Republic of Iraq
Ministry of Higher Education
And Scientific Research
University of Babylon
Collage of Engineering
Department of Material engineering

INVESTIGATION OF CERTAIN SHAPE MEMORY ALLOYS IN SPACE SYSTEMS .

A THESIS

SUBMITED TO THE COLLEGE OF ENGINEERING OF THE UNIVERSITY OF BABYLON IN PARTIAL FULFILLMENT OF THE REQUIREMENTS FOR THE DEGREE OF DOCTOR OF PHILOSOPHY IN MATERIAL ENGINEERING

BY

Abdul –Raheem Kadhim Abid-Ali

(Msc. In Material Engineering)

October 2007

وزارة التعليم العالي والبحث العلمي
جامعـــــــــة بابـــــــــل
كليـــــــة الهنـــــــــدسة
قسم هنـــــــــدسة المواد

استقصاء بعض السبائك
التي تستعيد شكلها في أنظمة الفضاء

أطروحة
مقدمة الى قسم هندسة المواد
كلية الهندسة جامعة بابل
كجزء من متطلبات نيل شهادة الدكتوراه فلسفة
في هندسة المواد

من قبل

عبدالرحيم كاظم عبد علي
(بكلوريوس وماجستير هندسة مواد)

تشرين اول 2007

Abstract

The rapid development of aerospace, military and medical industries required patents or development of certain materials. One of the most important ones in these fields is the shape memory alloys.

This study represents an attempt to prepare, alloying and investigate Cu Al Ni based shape memory alloys by using powder metallurgy technique. Several alloying elements are added from alloying elements such as (Ti, B, Fe, ,Si, Co, Zr,Ti+Mn and B+Mn) with (0.4 ,0.8 and 1.2 wt%) additives from each element taking into consideration several process parameters such as rate of loading , period of maximum load, compacting pressure , temperature and time of sintering. Different heat treatments have been employed to enhance shape memory effect of prepared alloys included solution heat treatment, aging and step-quench heat treatment .After deformation, shape recovery treatment is also used. Physical tests before and after sintering have been measured such as apparent density , green density and porosity , water absorption and expansion of sintered compacts. In addition , mechanical test such as hardness and compression have also studied. Compression test is conducted at room temperature and at 50 °C and then at constant stress of (100Mpa) and the change of strain as a function of temperature is recorded. SME is measured for prepared alloys by using hardness and compression tests after different heat treatments that is used in this study. Electrical resistance test has been measured as a function of temperature after direct quench heat treatment and after shape recovery treatment .
In addition ultrasonic technique is used to examine the shape memory effect after deformation and after shape recovery treatment.

Phase identification and analysis of alloys has been done using x-ray diffraction technique whereas SEM and LOM reveal microstructure

of alloys. In addition, pore size and its distribution as well as particle size and its distribution are calculated using image processing and image analysis technique in the matlab ver 7 environment for LOM image of unetched specimens.

Analysis of porous shape memory alloys is given based up on unit cell finite element technique taking into consideration square and hexagonal arrangement of pores to determine the response of porous shape memory alloys for both stresses and strains. Analysis of real microstructure of porous shape memory with different pore size , shape and distribution has been presented based upon LOM image analysis combination with finite element method in Ansys. version 9 software environment.

It is apparent that alloy with titanium addition (0.4 wt %) for (Cu +13 wt %Al+3.8wt% Ni) based shape memory alloy has a maximum shape effect (58.82 %) compared with other prepared alloys. With comparing to the standard very expensive cast (Ni/Ti) shape memory alloys, this value represent (80 %).The percentage of porosity is in the range of (10-38 %)for prepared alloys. It appears that lower the porosity the higher SME.

Direct quenching gives the highest martensitic transformation and eventually shape memory effect. On the other hand it seems that aging and step-quenched treatments have lower effect due to the presence of $\gamma 2$ phase.

Unit cell finite element analysis and real microstructure finite element analysis appear that stress-induced martensite regions are found around the pores which act as stress concentration positions.

الخلاصة

ان التطورات السريعة في الصناعات الفضائية و العسكرية و الطبية تتطلب العديد من براءات الاختراع او تطوير بعض المواد. إحدى أهم هذه التطورات في هذا المجال هو استخدام السبائك التي تستعيد شكلها.

في هذه الدراسة تم تحضير ودراسة سبائك ذات أساس من النحاس- الألمنيوم – النيكل(CuAlNi) باستخدام تقنية ميتالورجيا المساحيق وذلك بإضافة عناصر سبك مختلفة من (Ti,B,Fe,Si,Co,Zr,Ti+Mn,B+Mn) وبأضافات مختلفة تتضمن (0.4,0.8 ,1.2 wt %.) من هذه العناصر. تم دراسة متغيرات التصنيع مثل مقدار ضغط الكبس ومعدل تسليط الضغط و الفترة الزمنية لبقاء الضغط وكذلك درجة حرارة التلبيد و زمن التلبيد. تم استخدام عدة معاملات حرارية من شانها تأكيد خواص استعادة الشكل مثل المعاملة المحلولية ومعاملة التعتيق ومعاملة الإخماد بالإضافة إلى المعاملات الحرارية التي تستعيد الشكل. أجريت الفحوصات الفيزيائية و الميكانيكية للسبائك المحضرة بعد عملية الكبس وبعد عملية التلبيد مثل فحص الكثافة الضاهرية و المسامية وامتصاصية الماء وتغير أبعاد النموذج بالإضافة إلى قياس صلادة النماذج الملبدة. تم قياس تأثير استعادة الشكل من خلال نماذج فحص الصلادة ونماذج فحص الانضغاط بعد أن أجريت عدة معاملات حرارية.

تم قياس المقاومة الكهربائية عند درجات حرارية مختلفة باستخدام فرن أنبوبي وكذلك تم قياس زمن مرور الموجات فوق الصوتية للنماذج المعاملة بالإخماد المباشر بعد التشكيل ومن ثم المعاملة حراريا ولجميع السبائك المحضرة .اجري فحص حيود الأشعة السينية للنماذج بعد عملية الكبس وبعد عملية التلبيد للتحقق من نجاح عملية التلبيد وكذلك اجري الفحص بعد المعاملات الحرارية المختلفة للكشف عن التحولات الطورية في حين استخدم المجهر الضوئي والمجهر الإلكتروني الماسح لكشف البنية المجهرية للسبائك المحضرة .تم حساب حجم المسامات وطبيعة توزيعها بالاضافة الى حجم الدقائق

وتوزيعها باستخدام تقنية معالجة الصور وتحليلها المأخوذة من المجهر الضوئي باستخدام برنامج (Mat lab ver 7) .

اعتمدت طريقة الشرائح المتناهية باستخدام خلية أحادية مربعة وأخرى سداسية لتمثل توزيع دوري للمسامات الدائرية لتحليل البنية للسبائك المسامية التي تستعيد شكلها وكذلك تم اعتماد الطريقة لتحليل البنية المجهرية الحقيقية للسبائك المحضرة من خلال اخذ صور للبنى بالمجهر الضوئي ومعالجتها وتحليلها وتحويلها إلى شكل هندسي يمكن تحليله بواسطة الشرائح المتناهية باستخدام برنامج (Ansys ver 9) .

يبدو ان السبيكة(Cu+13 wt% Al+3.8wt%Ni) المضاف اليها (.4 wt % Ti) تمتلك أعلى تأثير لاستعادة الشكل (% 58.824) بالمقارنة مع السبائك المحضرة الأخرى.بالمقارنة مع السبائك القياسية ذات الاساس من(Ni/Ti) تمثل هذة النسبة (80%) من نسبة استعادة الشكل والتي تبلغ (% 12-8) .

تتراوح المسامية الضاهرية للسبائك المحضرة بين(% 38-10) ويبدو إن أعلى نسبة تأثير استعادة الشكل يكون عند اقل مسامية.

إن معاملات الإخماد المباشر أعطت أعلى تحول مارتنسايتي في حين معاملات التعتيق و الإخماد المرحلي أعطى اقل تحولا بسبب ترسب طور جاما في البنية.

اظهر تحليل الشرائح المتناهية باعتماد الخلية الأحادية وكذلك التمثيل الحقيقي للبنية المجهرية إن التحول المارتنسايتي الناتج بالإجهاد يكون في المناطق القريبة من المسامات والتي تعمل كمناطق لتمركز الاجهادات.

ACKNOWLEDGEMENTS

*First of all , Profusely all thanks for **ALLAH** Lord of all creation who enable me to achieve this work.*

*I would like to express my faithful gratitude to my supervisors **Prof. Dr. kahtan k. Al-kazraji and Prof.Dr.Eng. Abdul –Wahid k. Rajih** for their guidance and invaluable recommendations .*

I wish to express my thanks to Dr. Najim A. Saad, head of the department of material engineering for his kind help during my work especially in the use of experimental equipment used in this study.

I would like to thank the staff of workshop and Material laboratories at the university of Babylon .Special thanks for engineer Rihab S. Kadhim for her help in metallurgical lab.

I wish to express my gratitude to Faculty of Engineering , university of Tahran and staff of advance Metallurgical and material lab. Especially Dr. Kashani Bozorg, S.F. for his help in the examination of SEM specimens .

Special thanks to my family ,my mother ,all my brothers and my wife for their care and encouragement during this work.

Contents

NO.	Title	Page
	Acknowledgments	I
	Abstract	II
	List of symbols	III
	List of Contents	IV
	Chapter One : Introduction	**1-15**
1.1	General view	1
1.2	Shape memory effect	1
1.3	Shape memory alloys	6
1.4	Applications	9
1.5	Objectives	15
	Chapter two : Review of literature	**16-27**
2.1	General view	16
2.2	Ni-Ti based shape memory alloys	16
2.3	Copper-based shape memory alloys	19
2.4	Analysis of shape memory alloys	24
2.5	Summary	26
	Chapter three : theoretical Considerations	**28-84**
3.1	General view	28
3.2	Martensitic transformation	28
3.2.1	Microscopic perspective of martensite	29
3.2.1.1	Structure of martensite and morphology	34
3.2.1.2	Martensite crystallography	36
3.2.1.3	Martensite nucleation	38
3.2.1.4	Martensite growth	39
3.2.1.5	Origin of martensitic transformation .	39
3.2.2	Macroscopic perspective of Martensite	40
3.2.2.1	Stress- induced martensite and superelasticity	40
3.2.2.2	Martensite aging and stabilization	46
3.3	Martensitic transformation in Cu-based shape memory alloys.	47
3.4	Origin of shape memory alloys.	52
3.5	Copper-based shape memory alloys	56
3.5.1	Effect of alloying elements.	56
3.5.2	Effect of heat treatment	57
3.6	Powder metallurgy of Cu-based shape memory alloys	60
3.6.1	Preparation of copper powder.	60
3.6.1.1	Production of copper by the reduction of copper oxide	61
3.6.1.2	Production of copper powder by atomization	62
3.6.1.3	Production of copper powder by electrolysis	62
3.6.1.4	Production of copper powder by hydrometallurgical processes	63
3.6.2	Blending and mixing processes	63
3.6.3	Particle shape and powder density	65
3.6.4	Particles size and its distribution	66
3.6.5	Powder compaction of cu-based alloys	68
3.6.5.1	Die compaction	68

3.6.5.2	Isostatic pressing	71
3.6.5.3	Roll compacting	72
3.6.5.4	Powder extrusion	72
3.6.5.5	Powder forging	72
3.6.5.6	Hot isostatic pressing	73
3.6.6	Sintering of copper- based alloys	73
3.6.6.1	Stages of sintering	74
3.6.6.2	Mechanism of sintering	75
3.6.7	Liquid phase sintering	79
3.6.8	Homogenization during sintering	82
Chapter Four : (Experimental procedure)		**85-113**
4.1	General view	85
4.2	Materials	85
4.3	Equipments	86
4.4	Preparation of blended mixtures	87
4.5	Mixing	87
4.6	Compaction	90
4.7	Sintering	92
4.8	Heat treatment	96
4.8.1	betatizing heat treatment	96
4.8.2	Aging treatment	97
4.8.3	Step- quench heat treatment	97
4.8.4	Heat treatment including shape memory effect.	98
4.9.	Phase identification and analysis	98
4.10	LOM examination	99
4.11	Scanning electron microscopy	101
4.12	Physical test	101
4.12.1	Particle size and its distribution	101
4.12.2	Apparent density of powder and blended powders.	102
4.12.3	Green porosity and density	103
4.12.4	Pore size and pore distribution	104
4.12.5	Apparent density , porosity and water absorption of sintered compact.	105
4.12.6	Dimensional change of sintered compacts.	106
4.12.7	Electrical Resistance	106
4.12.8	Ultrasonic test	108
4.13	Mechanical tests	108
4.13.1	Microhardness measurements	108
4.13.2	Macrohardness measurements	108
4.13.2.1	Vicker's macrohardness test	109
4.13.2.2	Brinell macrohardness test	109
4.13.3	Compression test	109
4.13.4	Shape memory effect and shape recovery	111
Chapter Five : Modelling and Numerical simulation of shape memory alloys		**113-137**
5.1	General view	113
5.2	Shape memory models	113
5.2.1	Ozdemir model	113

5.2.2	*Cozzarelli model*	*115*
5.2.3	*Tanaka model*	*116*
5.2.4	*Auricchio model*	*117*
5.2.4.1	*Single variant martensite production*	*118*
5.2.4.2	*Austenite production.*	*119*
5.3	*Modeling of porous shape memory alloys*	*124*
5.4	*Unit cell Finite element method*	*125*
5.4.1	*Tetragonal (square) arrangement of pores*	*125*
5.4.2	*Hexagonal arrangement of pores.*	*125*
5.5	*Real representation of microstructure image using image analysis and processing*	*127*
5.5.1	*Image processing*	*127*
5.5.2	*Image Analysis*	*130*
5.6	*Finite element analysis of porous SMA using Ansys ver 9 software*	*131*
5.6.1	*Boundary conditions*	*132*
5.6.2	*Material properties*	*133*
5.7	*Verification of the SMA model used in this study.*	*135*
Chapter six : Results and Discussion		***138-350***
6.1	*General view*	*138*
6.2	*Results before sintering of compacts*	*138*
6.2.1	*Apparent density of elemental and blended powders.*	*138*
6.2.2	*Particle size and its distribution*	*140*
6.2.3	*Green density and green porosity of compacts*	*156*
6.2.3.1	*Effect of rate of loading*	*159*
6.2.3.2	*Effect of period of maximum load.*	*159*
6.2.4	*x-ray diffraction pattern of compacts*	*161*
6.2.5	*Microstructure of compacts and pore size and its distribution.*	*161*
6.3	*Results after sintering of compacts*	*161*
6.3.1	*x-ray diffraction analysis*	*163*
6.3.2	*Physical test results*	*170*
6.3.2.1	*Apparent density of sintered compacts*	*170*
6.3.2.2	*Apparent porosity and absorption of water*	*177*
6.3.2.3	*True porosity*	*186*
6.3.2.4	*Expansion of sintered compacts*	*190*
6.3.3	*Microstructure of sintered compacts*	*192*
6.3.4	*Pore size and its distribution*	*197*
6.3.5	*Vicker's macrohardness results*	*200*
6.4	*Effect of heat treatment after sintering .*	*202*
6.4.1	*X-ray diffraction patterns for Direct quench treatment.*	*202*
6.4.2	*Light optical microscope images for direct quench heat treatment.*	*233*
6.4.3	*Scanning electron microscope images*	*238*
6.4.4	*Hardness test results for direct quenching treatment*	*242*
6.4.5	*Electrical resistance test results*	*245*
6.4.6	*Ultrasonic test results*	*248*
6.4.7	*Shape memory effect and shape recovery*	*253*
6.5	*Aging heat treatment*	*288*

6.5.1	*X-ray diffraction for aged specimens*	*288*
6.5.2	*LOM image*	*292*
6.5.3	*SEM images*	*320*
6.5.4	*Vicker's macrohardness test results*	*320*
6.5.5	*Shape memory effect for aged treated specimens*	*324*
6.6	*Step- quenched heat treatment*	*324*
6.6.1	*x-ray diffraction patterns for step-quenched specimens*	*326*
6.6.2	*Light optical micrographs*	*329*
6.6.3	*SEM micrographs*	*334*
6.6.4	*Vickers's Marcohardness test results*	*334*
6.6.5	*Shape memory effect*	*335*
6.7	*Strain- temperature curves*	*338*
6.8	*Numerical results*	*340*
6.8.1	*Unit cell finite element results*	*340*
6.8.1.1	*Square arrangements of pores*	*340*
6.8.1.2	*Hexagonal arrangements of pores*	*341*
6.8.2	*Real representation of microstructure finite element analysis*	*341*
Chapter seven : conclusions and Recommendations for future work.		
7.1	*Conclusions*	*351*
7.2	*Suggestions and recommendations for future work*	*353*
	References	*354*
	Appendix A : powder diffraction data Cards	*A1*

Dedication

To spirit of my father and my sister

To My family specially for my Mother and my brothers

To my wife and My sons with my love and respect

بِسْمِ اللَّهِ الرَّحْمَنِ الرَّحِيمِ

﴿وَيَسْأَلُونَكَ عَنِ الرُّوحِ قُلِ الرُّوحُ مِنْ أَمْرِ رَبِّي وَمَا أُوتِيتُم مِّن الْعِلْمِ إِلاَّ قَلِيلاً ﴾

صدق الله العلي العظيم

{ سورة الإسراء / أية 85}

Chapter One

INTRODUCTION

Chapter Two

REVIEW OF LITERATURE

Chapter Three

THEORETICAL CONSIDERATION

Chapter Four

EXPERIMENTAL PROCEDURE

Chapter Five

MODELING AND NUMERICAL SIMULATION OF SHAPE MEMORY ALLOYS

Chapter Six

RESULTS AND DISCUSSION

Chapter Seven

CONCLUSION AND RECOMMENDATIONS FOR FUTURE WORKS

References

Appendix A

Appendix A

04-0850 Wavelength= 1.5405

Ni

Nickel

Nickel, syn

Rad.: CuKa1 λ: 1.5405 Filter: Ni Beta d-sp:

Cut off: Int.: Diffract. I/Icor.:

Ref: Swanson, Tatge, Natl. Bur. Stand. (U.S.), Circ. 539, I, 13 (1953)

Sys.: Cubic S.G.: Fm3m (225)

a: 3.5238 b: c: A: C:

α: β: γ: Z: 4 mp:

Ref: Ibid.

Dx: 8.911 Dm: SS/FOM: F_8 = 87(.0115 , 8)

Color: White

Pattern taken at 26 C. Sample obtained from Johnson Matthey Company, Ltd. CAS #: 7440-02-0. Spectrographic analysis show <0.01% each of Mg, Si and Ca. Cu type. Gold group, gold subgroup. PSC: cF4. Mwt: 58.70. Volume[CD]: 43.76.

2θ	Int	h	k	l
44.505	100	1	1	1
51.844	42	2	0	0
76.366	21	2	2	0
92.939	20	3	1	1
98.440	7	2	2	2
121.922	4	4	0	0
144.655	14	3	3	1
155.632	15	4	2	0

ICDD. 1997 JCPDS-International Centre for Diffraction Data. All rights reserved
PCPDFWIN v. 1.30

18-0019 Wavelength= 1.5418

Ti(Cu,Al)2

Aluminum Copper Titanium

Rad.: CuKa λ: 1.5418 Filter: Ni Beta d-sp:

Cut off: Int.: Estimation I/Icor.:

Ref: Rieger et al., Monatsh. Chem., 95, 1573 (1964)

Sys.: Hexagonal S.G.: $P6_3/mmc$ (194)

a: 5.023 b: c: 8.130 A: C: 1.6186

α: β: γ: Z: 4 mp:

Ref: Ibid.

Dx: Dm: SS/FOM: F_{27} = 5(0.117 , 46)

Mg Zn2 type. PSC: hP12. Volume[CD]: 177.64.

2θ	Int	h	k	l	2θ	Int	h	k	l
20.416	5	1	0	0	86.895	5	1	0	7
22.00	20	0	0	2	88.985	50	3	1	3
23.224	5	1	0	1	91.524	40	4	0	1
35.832	80	1	1	0	92.521	40	2	2	4
39.237	100	1	0	3	96.289	5	3	1	4
41.458	20	2	0	0					
42.333	100	1	1	2					
43.246	100	2	0	1					
44.637	50	0	0	4					
47.450	55	2	0	2					
49.510	40	1	0	4					
53.830	50	2	0	3					
56.039	5	2	1	0					
60.863	10	1	0	5					
64.434	50	3	0	0					
66.661	60	2	1	3					
68.887	60	3	0	2					
69.293	20	0	0	6					
72.676	60	2	0	5					
74.268	10	2	1	4					
75.868	60	2	2	0					
84.368	50	2	0	6					

ICDD. 1997 JCPDS-International Centre for Diffraction Data. All rights reserved
PCPDFWIN v. 1.30

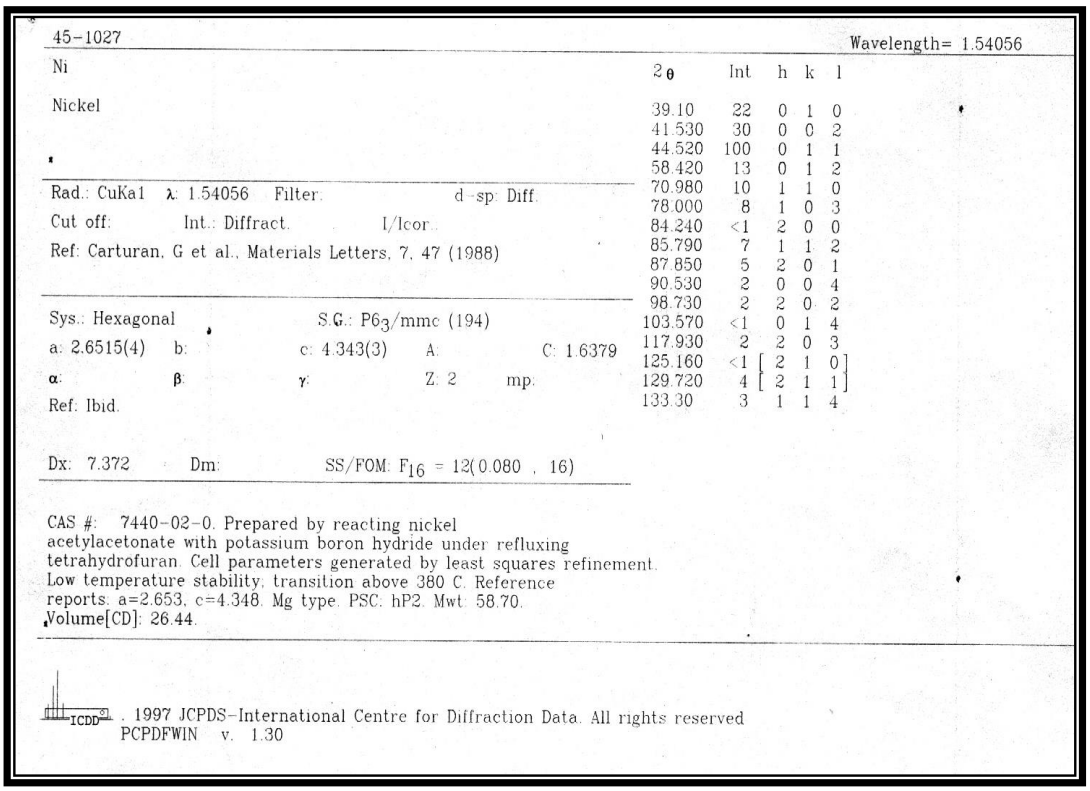

45-1027 Wavelength= 1.54056

Ni

Nickel

Rad.: CuKa1 λ: 1.54056 Filter: d-sp: Diff.

Cut off: Int.: Diffract. I/Icor.:

Ref: Carturan, G et al., Materials Letters, 7, 47 (1988)

Sys.: Hexagonal S.G.: $P6_3/mmc$ (194)

a: 2.6515(4) b: c: 4.343(3) A: C: 1.6379

α: β: γ: Z: 2 mp:

Ref: Ibid.

Dx: 7.372 Dm: SS/FOM: F_{16} = 12(0.080 , 16)

CAS #: 7440-02-0. Prepared by reacting nickel acetylacetonate with potassium boron hydride under refluxing tetrahydrofuran. Cell parameters generated by least squares refinement. Low temperature stability, transition above 380 C. Reference reports: a=2.653, c=4.348. Mg type. PSC: hP2. Mwt: 58.70. Volume[CD]: 26.44.

2θ	Int	h	k	l
39.10	22	0	1	0
41.530	30	0	0	2
44.520	100	0	1	1
58.420	13	0	1	2
70.980	10	1	1	0
78.000	8	1	0	3
84.240	<1	2	0	0
85.790	7	1	1	2
87.850	5	2	0	1
90.530	2	0	0	4
98.730	2	2	0	2
103.570	<1	0	1	4
117.930	2	2	0	3
125.160	<1	[2	1	0]
129.720	4	[2	1	1]
133.30	3	1	1	4

ICDD . 1997 JCPDS-International Centre for Diffraction Data. All rights reserved
PCPDFWIN v. 1.30

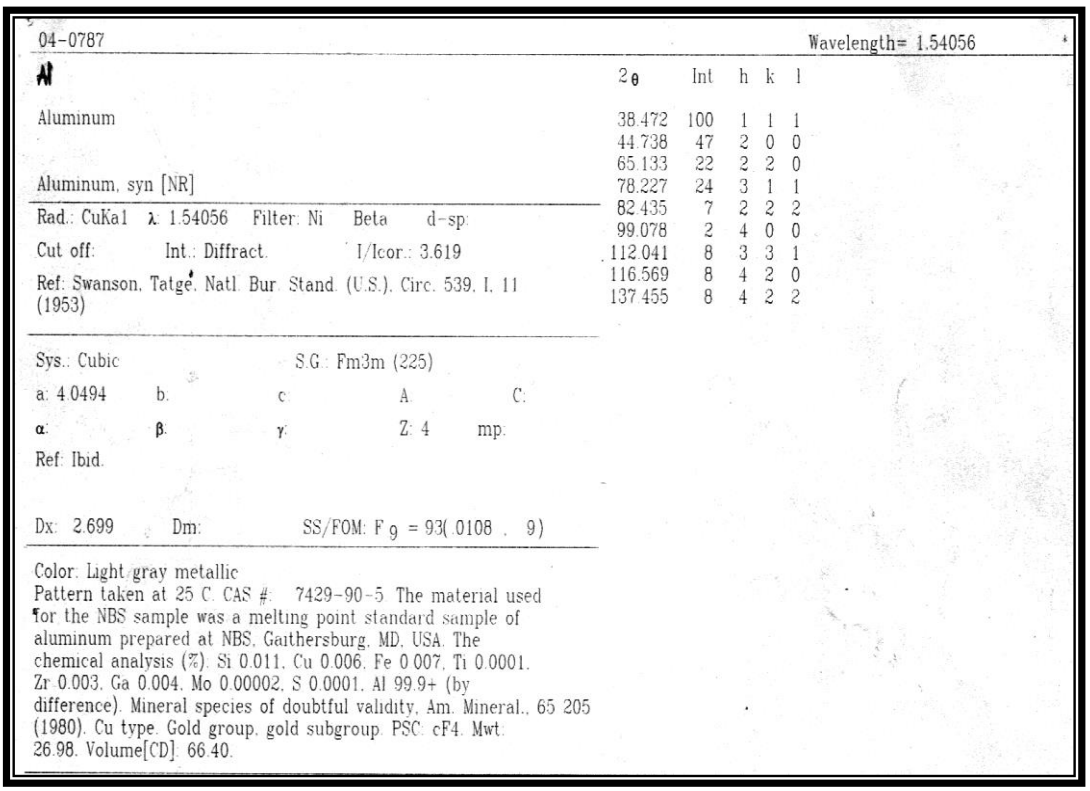

04-0787 Wavelength= 1.54056

Al

Aluminum

Aluminum, syn [NR]

Rad.: CuKa1 λ: 1.54056 Filter: Ni Beta d-sp:

Cut off: Int.: Diffract. I/Icor.: 3.619

Ref: Swanson, Tatge, Natl. Bur. Stand. (U.S.), Circ. 539, I, 11 (1953)

Sys.: Cubic S.G.: Fm3m (225)

a: 4.0494 b: c: A: C:

α: β: γ: Z: 4 mp:

Ref: Ibid.

Dx: 2.699 Dm: SS/FOM: F_9 = 93(.0108 , 9)

Color: Light gray metallic
Pattern taken at 25 C. CAS #: 7429-90-5. The material used for the NBS sample was a melting point standard sample of aluminum prepared at NBS, Gaithersburg, MD, USA. The chemical analysis (%): Si 0.011, Cu 0.006, Fe 0.007, Ti 0.0001, Zr 0.003, Ga 0.004, Mo 0.00002, S 0.0001, Al 99.9+ (by difference). Mineral species of doubtful validity, Am. Mineral., 65 205 (1980). Cu type. Gold group, gold subgroup. PSC: cF4. Mwt: 26.98. Volume[CD]: 66.40.

2θ	Int	h	k	l
38.472	100	1	1	1
44.738	47	2	0	0
65.133	22	2	2	0
78.227	24	3	1	1
82.435	7	2	2	2
99.078	2	4	0	0
112.041	8	3	3	1
116.569	8	4	2	0
137.455	8	4	2	2

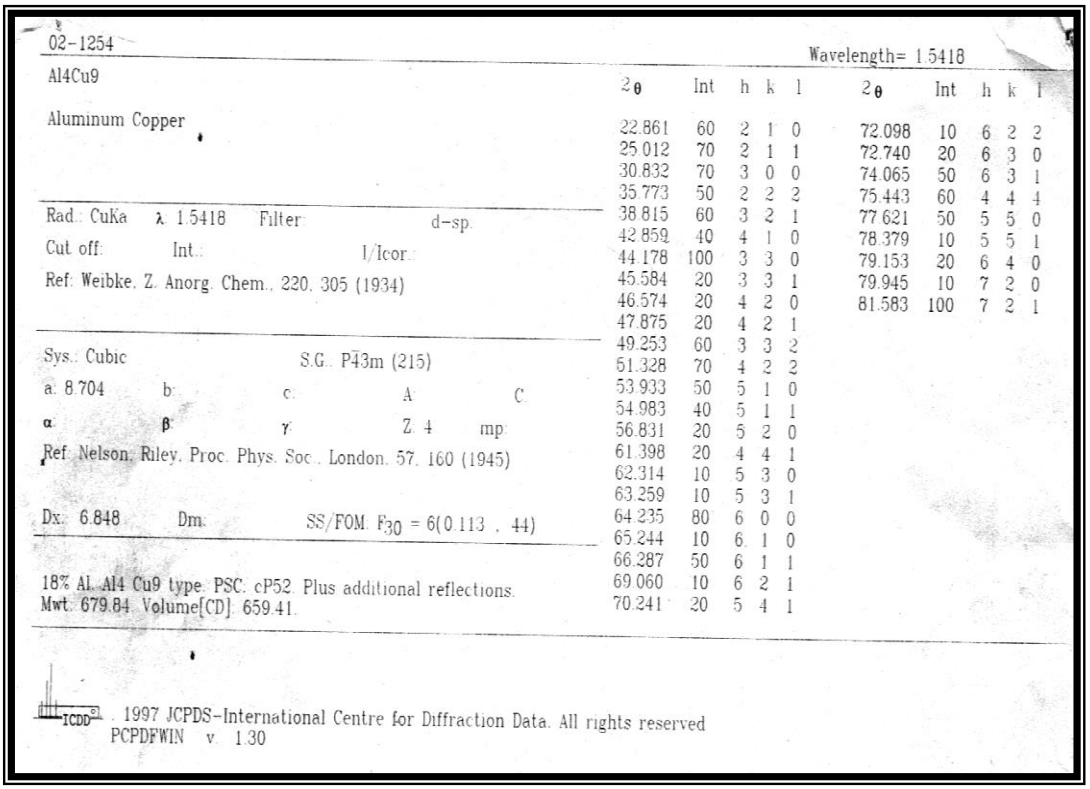

02-1254

Al4Cu9

Aluminum Copper

Rad.: CuKa λ: 1.5418 Filter: d-sp:

Cut off: Int.: I/Icor.:

Ref: Weibke, Z. Anorg. Chem., 220, 305 (1934)

Sys.: Cubic S.G.: P43m (215)

a: 8.704 b: c: A: C:

α: β: γ: Z: 4 mp:

Ref: Nelson, Riley, Proc. Phys. Soc., London, 57, 160 (1945)

Dx: 6.848 Dm: SS/FOM: F_{30} = 6(0.113 , 44)

18% Al. Al4 Cu9 type. PSC: cP52. Plus additional reflections.
Mwt: 679.84. Volume[CD]: 659.41.

Wavelength= 1.5418

2θ	Int	h	k	l	2θ	Int	h	k	l
22.861	60	2	1	0	72.098	10	6	2	2
25.012	70	2	1	1	72.740	20	6	3	0
30.832	70	3	0	0	74.065	50	6	3	1
35.773	50	2	2	2	75.443	60	4	4	4
38.815	60	3	2	1	77.621	50	5	5	0
42.859	40	4	1	0	78.379	10	5	5	1
44.178	100	3	3	0	79.153	20	6	4	0
45.584	20	3	3	1	79.945	10	7	2	0
46.574	20	4	2	0	81.583	100	7	2	1
47.875	20	4	2	1					
49.253	60	3	3	2					
51.328	70	4	2	2					
53.933	50	5	1	0					
54.983	40	5	1	1					
56.831	20	5	2	0					
61.398	20	4	4	1					
62.314	10	5	3	0					
63.259	10	5	3	1					
64.235	80	6	0	0					
65.244	10	6	1	0					
66.287	50	6	1	1					
69.060	10	6	2	1					
70.241	20	5	4	1					

ICDD©. 1997 JCPDS-International Centre for Diffraction Data. All rights reserved
PCPDFWIN v. 1.30

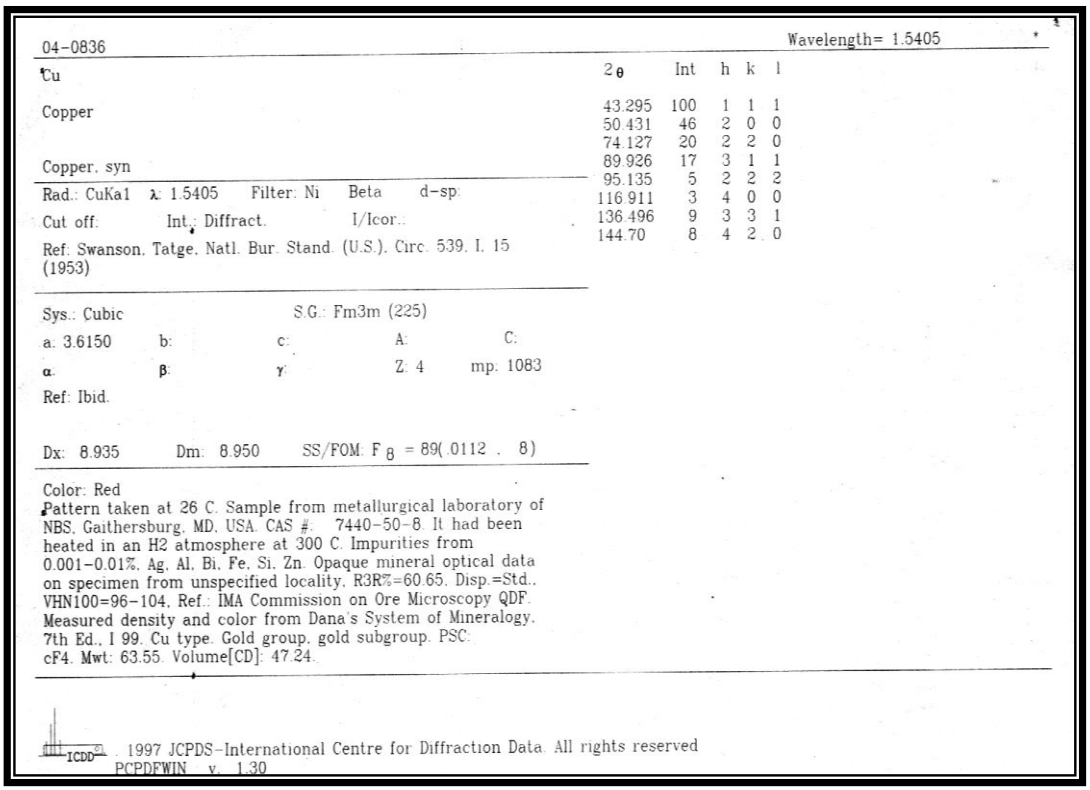

04-0836

Cu

Copper

Copper, syn

Rad.: CuKa1 λ: 1.5405 Filter: Ni Beta d-sp:

Cut off: Int.: Diffract. I/Icor.:

Ref: Swanson, Tatge, Natl. Bur. Stand. (U.S.), Circ. 539, I, 15 (1953)

Sys.: Cubic S.G.: Fm3m (225)

a: 3.6150 b: c: A: C:

α: β: γ: Z: 4 mp: 1083

Ref: Ibid.

Dx: 8.935 Dm: 8.950 SS/FOM: F_8 = 89(.0112 , 8)

Color: Red
Pattern taken at 26 C. Sample from metallurgical laboratory of NBS, Gaithersburg, MD, USA. CAS #: 7440-50-8. It had been heated in an H2 atmosphere at 300 C. Impurities from 0.001-0.01%: Ag, Al, Bi, Fe, Si, Zn. Opaque mineral optical data on specimen from unspecified locality. R3R%=60.65. Disp.=Std., VHN100=96-104. Ref.: IMA Commission on Ore Microscopy QDF. Measured density and color from Dana's System of Mineralogy, 7th Ed., I 99. Cu type. Gold group, gold subgroup. PSC: cF4. Mwt: 63.55. Volume[CD]: 47.24.

Wavelength= 1.5405

2θ	Int	h	k	l
43.295	100	1	1	1
50.431	46	2	0	0
74.127	20	2	2	0
89.926	17	3	1	1
95.135	5	2	2	2
116.911	3	4	0	0
136.496	9	3	3	1
144.70	8	4	2	0

ICDD©. 1997 JCPDS-International Centre for Diffraction Data. All rights reserved
PCPDFWIN v. 1.30

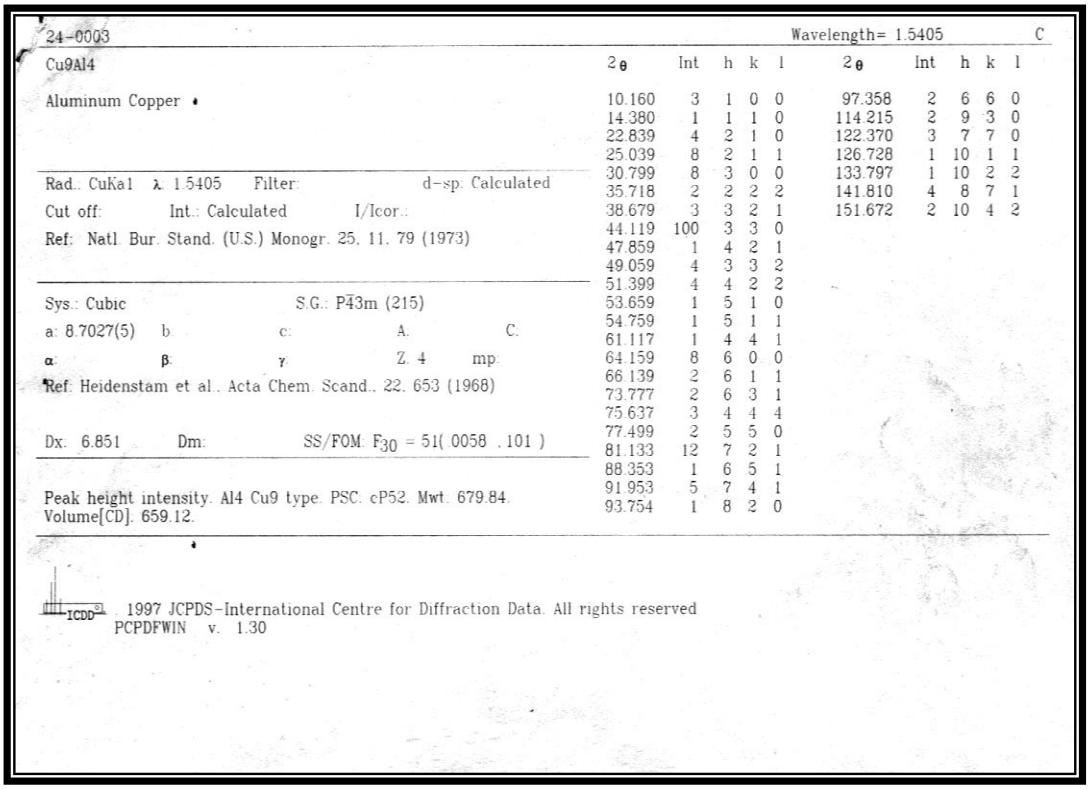

24-0003 Wavelength= 1.5405 C

Cu9Al4

Aluminum Copper

Rad.: CuKa1 λ: 1.5405 Filter: d-sp: Calculated

Cut off: Int.: Calculated I/Icor.:

Ref: Natl. Bur. Stand. (U.S.) Monogr. 25, 11, 79 (1973)

Sys.: Cubic S.G.: P$\bar{4}$3m (215)

a: 8.7027(5) b: c: A: C:

α: β: γ: Z: 4 mp:

Ref: Heidenstam et al., Acta Chem. Scand., 22, 653 (1968)

Dx: 6.851 Dm: SS/FOM: F_{30} = 51(.0058 , 101)

Peak height intensity. Al4 Cu9 type. PSC: cP52. Mwt: 679.84.
Volume[CD]: 659.12.

2θ	Int	h	k	l	2θ	Int	h	k	l
10.160	3	1	0	0	97.358	2	6	6	0
14.380	1	1	1	0	114.215	2	9	3	0
22.839	4	2	1	0	122.370	3	7	7	0
25.039	8	2	1	1	126.728	1	10	1	1
30.799	8	3	0	0	133.797	1	10	2	2
35.718	2	2	2	2	141.810	4	8	7	1
38.679	3	3	2	1	151.672	2	10	4	2
44.119	100	3	3	0					
47.859	1	4	2	1					
49.059	4	3	3	2					
51.399	4	4	2	2					
53.659	1	5	1	0					
54.759	1	5	1	1					
61.117	1	4	4	1					
64.159	8	6	0	0					
66.139	2	6	1	1					
73.777	2	6	3	1					
75.637	3	4	4	4					
77.499	2	5	5	0					
81.133	12	7	2	1					
88.353	1	6	5	1					
91.953	5	7	4	1					
93.754	1	8	2	0					

ICDD 1997 JCPDS-International Centre for Diffraction Data. All rights reserved
PCPDFWIN v. 1.30

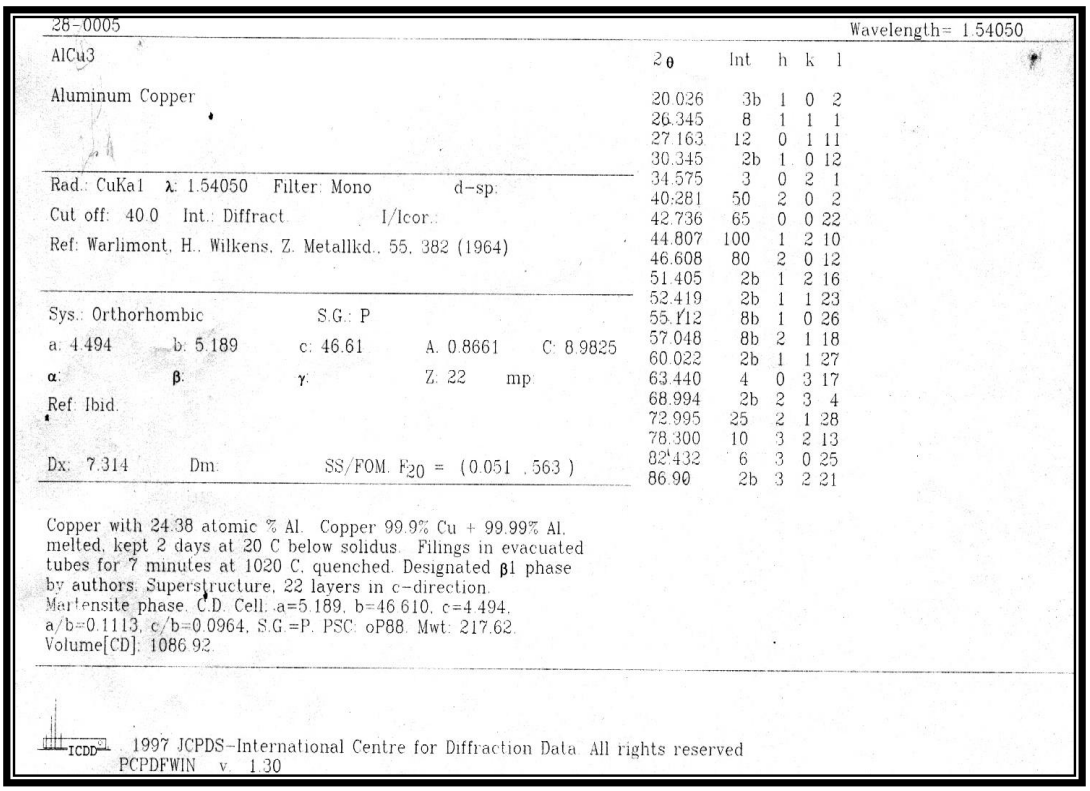

28-0005 Wavelength= 1.54050

AlCu3

Aluminum Copper

Rad.: CuKa1 λ: 1.54050 Filter: Mono d-sp:

Cut off: 40.0 Int.: Diffract. I/Icor.:

Ref: Warlimont, H., Wilkens, Z. Metallkd., 55, 382 (1964)

Sys.: Orthorhombic S.G.: P

a: 4.494 b: 5.189 c: 46.61 A: 0.8661 C: 8.9825

α: β: γ: Z: 22 mp:

Ref: Ibid.

Dx: 7.314 Dm: SS/FOM: F_{20} = (0.051 , 563)

Copper with 24.38 atomic % Al. Copper 99.9% Cu + 99.99% Al, melted, kept 2 days at 20 C below solidus. Filings in evacuated tubes for 7 minutes at 1020 C, quenched. Designated β1 phase by authors. Superstructure, 22 layers in c-direction. Martensite phase. C.D. Cell: a=5.189, b=46.610, c=4.494, a/b=0.1113, c/b=0.0964, S.G.=P. PSC: oP88. Mwt: 217.62. Volume[CD]: 1086.92.

2θ	Int	h	k	l
20.026	3b	1	0	2
26.345	8	1	1	1
27.163	12	0	1	11
30.345	2b	1	0	12
34.575	3	0	2	1
40.281	50	2	0	2
42.736	65	0	0	22
44.807	100	1	2	10
46.608	80	2	0	12
51.405	2b	1	2	16
52.419	2b	1	1	23
55.112	8b	1	0	26
57.048	8b	2	1	18
60.022	2b	1	1	27
63.440	4	0	3	17
68.994	2b	2	3	4
72.995	25	2	1	28
78.300	10	3	2	13
82.432	6	3	0	25
86.90	2b	3	2	21

ICDD 1997 JCPDS-International Centre for Diffraction Data. All rights reserved
PCPDFWIN v. 1.30

18-0019 Wavelength= 1.5418

Ti(Cu,Al)2

Aluminum Copper Titanium

Rad.: CuKa λ: 1.5418 Filter: Ni Beta d-sp:

Cut off: Int.: Estimation I/Icor.:

Ref: Rieger et al., Monatsh. Chem., 95, 1573 (1964)

Sys.: Hexagonal S.G.: $P6_3/mmc$ (194)

a: 5.023 b: c: 8.130 A: C: 1.6186

α: β: γ: Z: 4 mp:

Ref: Ibid.

Dx: Dm: SS/FOM: F_{27} = 5(0.117 , 46)

Mg Zn2 type. PSC: hP12. Volume[CD]: 177.64.

2θ	Int	h	k	l	2θ	Int	h	k	l
20.416	5	1	0	0	86.895	5	1	0	7
22.00	20	0	0	2	88.985	50	3	1	3
23.224	5	1	0	1	91.524	40	4	0	1
35.832	80	1	1	0	92.521	40	2	2	4
39.237	100	1	0	3	96.289	5	3	1	4
41.458	20	2	0	0					
42.333	100	1	1	2					
43.246	100	2	0	1					
44.637	50	0	0	4					
47.450	55	2	0	2					
49.510	40	1	0	4					
53.830	50	2	0	3					
56.039	5	2	1	0					
60.863	10	1	0	5					
64.434	50	3	0	0					
66.661	60	2	1	3					
68.887	60	3	0	2					
69.293	20	0	0	6					
72.676	60	2	0	5					
74.268	10	2	1	4					
75.868	60	2	2	0					
84.368	50	2	0	6					

ICDD. 1997 JCPDS-International Centre for Diffraction Data. All rights reserved
PCPDFWIN v. 1.30

Al5CuTi2

Aluminum Copper Titanium

Rad.: λ: Filter: d-sp:

Cut off: Int.: I/Icor.:

Ref: Tarnacki, J., Kim, Y.-W., Scr. Metall., 22, 329 (1988)

Sys.: Cubic S.G.: Pm3m (221)

a: 3.927 b: c: A: C:

α: β: γ: Z: 0.5 mp:

Ref: Ibid.

Dx: 4.034 Dm: SS/FOM: F γ = 6(0.127 , 9)

0 assigned because pattern contains several unindexed reflections probably from second Cu-rich phase. Prepared by arc melting pure elements in an Ar atmosphere in a copper crucible. Alloys were prepared by rapid solidification under pressurized He. Chemical analysis (wt.%): Al 43.6, Cu 22.2, Ti 34.1. Contains copper rich second phase. Au Cu3 type. PSC: cP4. To replace 42-1069. Mwt: 294.25. Volume[CD]: 60.56.

2θ	Int	h	k	l
22.625	16	1	0	0
32.199	2	1	1	0
38.990	3			
39.705	100	1	1	1
44.178	4			
44.406	3			
46.322	100	2	0	0
51.954	3	2	1	0
67.367	14	2	2	0
80.754	24	3	1	1
85.099	5			

ICDD. 1997 JCPDS-International Centre for Diffraction Data. All rights reserved
PCPDFWIN v. 1.30

دانشکدهٔ فنی
Faculty of Engineering
University of Tehran

To Whom It May Concern

21 May 2007

This is to certify that Scanning Electron Microscopic (Cam Scan Model MV2300) examination of twenty six metallic samples was carried out upon request of Mr. Abdul Raheem Kadhim Abid-Ali.

S.F. Kashani Bozorg

S.F. Kashani Bozorg,
Director of Advanced Metallography Lab
School of Metallurgy and Materials Engineering
University of Tehran

University of Tehran School of Metallurgy and Materials Eng.

Supervisors Certificate

We Certify that this thesis entitled *[Investigation of certain shape memory alloys in space systems*] prepared by ***Abdul-Raheem kadhim Abid-Ali*** has been carried out under our supervision at the department of material engineering , College of Engineering Babylon university in partial fulfillment of the requirements for the degree of Doctor of philosophy in Material Engineering .

Supervisors

Signature : K. Al-Kazraji

Prof .Dr. Kahtan H. Al-Kazraji

Date: / /2007

signature:

A. Rajih

Prof .Dr.Eng. Abdul-Wahid K.Rajih

Date: / /2007

SUPERVISORS CERTIFICATE

We Certify that this thesis entitled ***[Investigation of certain shape memory alloys in space systems***] prepared by ***Abdul-Raheem kadhim Abid-Ali*** has been carried out under our supervision at the department of material engineering , College of Engineering Babylon university in partial fulfillment of the requirements for the degree of Doctor of philosophy in Material Engineering .

Supervisors

Signature :

Prof .Dr. Kahtan K. Al-Kazraji

Date: / /2007

signature:

Prof .Dr.Eng. Abdul-Wahid K.Rajih

Date: / /2007

Introduction

1.1General view

During the early 1960 ´s ,the Naval Ordnance Laboratory discovered what is commonly referred to as the shape memory effect (SME) in binary NiTi alloys. This alloy ,dubbed " Nitinol" from [nickel- Titanium _Naval Ordnance Laboratory] ,exhibited a remarkable ability to recover its original dimensions after having been deformed ,simply by heating it above a certain transformation temp.[Buehler et al .1963].This alloy also exhibited drastic damping changes as a function of temperature .This important discovery inspired a greet deal of interest in understanding and developing smart materials with shape memory effect .

In recent years an increased efforts in engineering have been directed toward multi functional materials and so called smart structures which is defined as an assembly or its components which serve an engineering function in which the structure possesses an inherent ability to sense ,diagnose and actuate in order to perform their function [Addington and Schodek ,2005].In the case of an airplane wing ,for example ,the main purpose is to provide lift but it also serves as a container for the fuel.

1.2 Shape memory effect:

one of the recent discoveries in multifunctional materials is "shape memory alloys" (SMA).These alloys describe a unique group of materials which execute a solid to solid phase transformation of their crystallographic structure from the parent phase to another phase and back in response to temperature or stress.[Wayman .and Duerig, 1990].This property allows the materials to be

heavily deformed and regain its original shape upon heating .In other words shape memory refers to the ability of certain materials to remember a shape even after rather severe deformations, once deformed at low temperature these materials will stay deformed until heated where upon they will spontaneously return to their original predeformation shape .The basis for the shape memory effect is that the materials can easily transform to and from martensite phase.[Miyazaki,1999].Shape memory effect is associated with the crystallographically reversible nature of the martensitic transformation which appears in shape memory alloys. Such crystallographically reversible martensitic transformation was especially named thermoelastic martensitic transformation [Otsuka and Ren,1999].The martensitic transformation itself is not a new phenomenon ,but was first found longtime ago in a steel which was heat treated at a high temperature (austenite phase) followed by rapid quenching, the martensitic transformation in most iron and steels is not crystallographically reversible so that they will not show the shape memory effect .The quenched steel revealed a fine structure which was formed by the martensitic transformation and was named as martensite after the discoverer Adolf Martens .Which consists of fine structure that has long been used for strengthening steels .[Higgins,1983].

The martensitic transformation is a diffusionless transformation described by a shear-like mechanism as shown in Fig.(1.1) .When the parent phase (high temperature phase (Austenite)in Fig(1.1a) is cooled to some critical temperature called Ms(the temperature at which the martensitic phase started to form upon cooling), the structure changes into martensite which is lower temperature phase with lower symmetry as shown in Fig.(1.1b). Since the parent phase has higher symmetry than the martensitic phase ,multi formation of martensites with the same structure in different orientation is possible [Otsuka.and kakeshita,2002]

.These are called variants or domains of martensites .In fact, two or four variants of martensites are usually formed side by side as shown in Fig. (1,b). In order to accommodate elastic strains around the martensites .This is called self–accommodation.[Porter and Easterling 1992].The two neighboring variants are twin-related to each other and may contribute to deformation if the interface is mobile under stress.

The martensitic transformation is divided into two categories : thermoelastic and non thermoelastic .The thermoelastic phase transformation is characterized by a small temperature hysteresis (several ten of degrees)a mobile twin interface and a crystallographically reversible transformation and vice – versa for non thermo elastic transformation.[Otsuka.and kakeshita,2002].The shape memory and super elasticity effects are characteristic of thermo elastic transformation. The characteristic temperatures of a martensitic transformation are defined as follows:

M_s: martensite –start temperature upon cooling.

M_f: martensite –finish temperature upon cooling.

A_s: reverse-transformation start temperature upon heating .

A_f: reverse-transformation finish temperature upon heating .

When a unidirectional stress is applied to a martensitic specimen as shown in Fig.(1.2a).There is a critical value where upon the detwinning process of martensitic variants takes place .This process consists in the spatial re-orientation of the original martensitic variants .If there is a performed direction for the occurrence of the transformation often associated with a state of stress, only the most favorable variant is formed. The product phase is then termed single-variant martensite and it is characterized by a detwinned structure. During such a process ,the stress remains practically constant until the martensite is fully detwinned (theoretically having a single variant aligned with the strain

direction).Further straining causes the elastic loading of detwinned martensite. upon unloading , a large residual strain remains however, by heating above A_f ,martensite transforms into high temperature phase (Austenite) and the specimen recovers its initial undeformed shape. This shape is kept during cooling below M_f when the material re-transforms into twinned martensite this phenomenon is named as shape memory effect.[Lukkassen, and Meidell,2003] .

When a unidirectional stress is applied to an austenitic specimen as shown in Fig. (1.2b). at temperature greater than A_f ,there is a critical value where upon a transformation from austenite to detwinned martensite occurs .A_s deformation proceeds in isothermal conditions, the stress remains almost constant until the material is fully transformed .Further straining causes the elastic loading of detwinned martensite .Upon unloading since martensite is unstable without stress at temperature greater than A_f ,a reverse transformation takes place, but at a lower stress level than during loading so that a hysteretic effect is produced .If the material temperature is greater than A_f ,the strain attained during loading is completely and spontaneously recovered at the end of unloading. This remarkable process gives rise to an energy absorption capacity with zero residual strain which is termed super elasticity or pseudo elasticity .If the material temperature is less than A_f only a part of stress-induced martensite retransforms into austenite .A residual strain is then found at the end of unloading which can be recovered by heating above A_f .This phenomenon is generally referred to as partial super elasticity .[Penrod,2003].

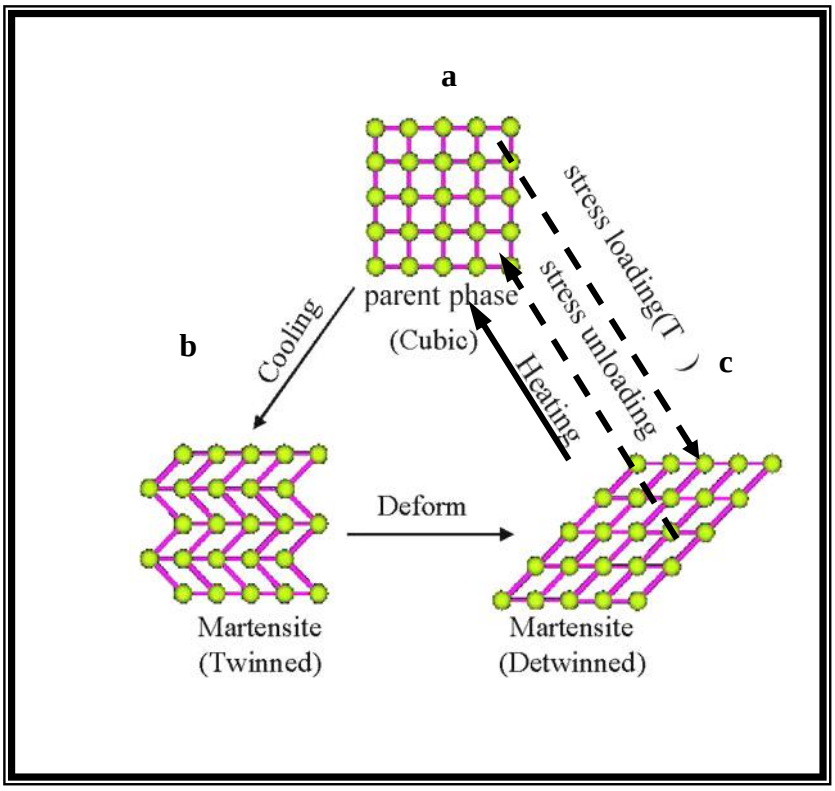

Fig.(1.1)a-c schematic illustration of mechanism of the shape memory effect and super elasticity(Penrod,2003)

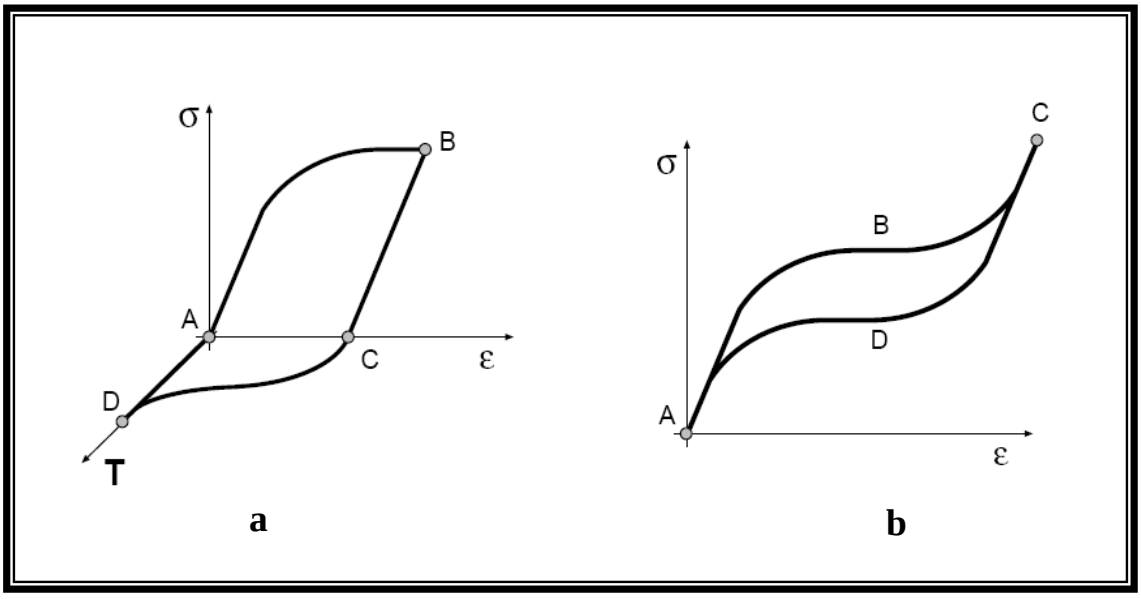

Fig .(1.2) schematic of : a. Shape memory effect at the end of a mechanical loading-unloading path ABC preformed at constant low temp .,material presents residual deformation (AC) which can be recovered through a thermal cycle (CDA)b. Super elastic effect .At a constant temperature the material is able to undergo large deformation with zero fild permanent strain. Note hysteresis loop.(Auricchio et al 1997)

1.3 Shape memory alloys

Although the shape memory effect was first discovered in a Au-Cd alloy in 1951[Porter and Easterling,1992] research became much more active after the effect was found in NiTi alloy in 1963 ,during the past decade smart materials and structures or intelligent material systems have received increasing attention because of their great scientific and technological significance .A smart structure is a structure system with macroscopically embedded or built-in sensors ,actuators and is usually monitored by an external microprocessor. While smart material refers to the material which has intrinsic sensing ,actuating and controlling in its microstructure [WEI et al.,1998] .

Shape memory alloys (SMA) are one of the major elements of smart materials due to their unusual properties such as the shape memory effect. Super elasticity ,high damping capacity and adaptive properties which are due to the reversible phase transitions in the alloys. Shape memory alloys can be classified into :

I.Bulk shape memory alloys:

This category include the following alloys:

1.Ni-Ti system alloys:

The nickel-titanium system is based on the equiatomic compound of nickel and titanium [Erbstoeszer et al ,2000] .Besides the ability of tolerating quite large amounts of shape memory strain, Nitinol alloys show high stability in cyclic applications possess an elevate electrical resistivity and are corrosion resistance. They also have a moderate solubility range, enabling changes in composition and alloying with other elements to modify bulk shape memory and their mechanical behavior. Third metal is usually added to the binary system in order to improve its properties .In particular ,a nickel quantity up to an extra 1% is the most common modification .This increases yield strength of the austenite phase while at the same time depressing the transformation temperatures.

Manufacture of NiTi alloys is not easy task as many machining techniques can only be used with difficulty. This facts explains the reason for the high cost of such alloys.[Scheiger,2002] .

When nickel in NiTi shape memory alloys is substituted by palladium ,platinum and gold metals by up to 50at% and titanium in NiTi is substituted by hafnium and zirconium by up to 20at% the martensitic transformation temperatures can be increased to as high as 600 °C while the shape memory performance still exists [Lindquist, and Wayman, 1990Queted in Wei et al,1998] .Shape memory effect of these alloys is in the range of (8-10 %).

2. Copper-based alloys:

Copper–based shape memory alloys have some advantages such as low cost and simple fabrication procedure compared to NiTi alloys. Copper zinc aluminum (CuZnAl) alloys are the first copper-based SMA_s to be commercially exploited[Humbeek et al ,1984] .This alloy originally comes from the copper-aluminum binary alloy, a system despite its shape memory characteristics ,has transformation temperatures considered to high for practical use. CuZnAl alloys have the advantage that they are made from relatively cheap metals using conventional metallurgical processes. Compared to other SMA_s , Cu Zn Al alloys have modest shape properties with a maximum recoverable strain of approximately (4 - 7%) ,also without the addition of grain growth control additives, their grain size can be quite large leading to brittleness problems.[Jianxin et al 1988].

Copper aluminum Nickel (CuAlNi) alloys have undergone extensive development and are now preferred to CuZnAl alloys [Schweiger,2002]. They are very popular for their wide range of useful transformation temperatures and because they are the only commercial shape memory alloys used above 100 °C . Despite CuAlNi alloys are made from relatively inexpensive metals, their processing is particularly difficult to machine. It can only be hot worked and the final heat treatment has to be tightly controlled to produce an alloy with the

desired transformation temperatures. These difficulties have mode this system more expansive than CuAlZn even if it is still cheaper than Nitinol.[Sampath,2005] .The other commercial alloys include CuAlMn and CuAlBe alloys .however ,the applications of these alloys have been much limited mainly for two reasons:

1. The poor ductility and workability of the polycrystalline alloys resulting from coarse grain and precipitation of brittle second phase particles.
2. The metastability of both the parent and martensite phases in the alloys which result in complicated aging effects and hence an undesirable reliability of the performance of the alloys [Wei. et al.,1998]. Because CuAlNi alloys have a much better thermal stability and higher operating temperatures than CuAlZn alloys, they may become one candidate for practical high temperature. Shape memory alloy if only their poor processibility can be improved. The group of these alloys has been taken in this study .

3. Iron base alloys:

Because price is one of the key considerations for applications ,the low cost iron based shape memory alloys have attracted considerable attention in recent years, and now some of them are also to a market introduction.[Zhao,2000].Of particular interest are Fe-Mn-Si,Fe-Ni-Mn and Fe-Cr-Ni-Mn-Si-Co.After complex thermo mechanical treatment ,these alloys exhibit nearly perfect SME due to stress-induced martensitic transformation and the reversion more recently, the Fe + Pt and Fe + Pd alloys which were previously investigated mainly as experimental materials have received more attention because the martensite transformations can be induced by magnetic fields and hence ferromagnetic shape memory alloys may be developed. [Szprynagcz et al.,2004].

4. Intermetallic compounds:

In the β-Ni Al alloys with nickel contents of 62-69 at % ,a thermo elastic martensitic transformation occurs on quenching .The M_s temperature shows a strong dependence on the nickel content and on the solution treatment temperature .[kim, and Wayman ,1990] .NiAl alloys still suffer from phase metastability,Ni_2Al,Ni_5Al_3 and phases may precipitate at temperature exceeding 250 $^{\circ}C$ .Some other β-phase intermetallic compounds such as NiMn,NiMnGa and ZrCoNi also exhibit shape memory effect and have some interesting potentials but still under development [Wei et al.,1998].

II. Thin –film shape memory alloys:

The bulk shape memory alloys exhibit large strokes and forces but at a show response. This is due to the fact that SMA_s are usually heat actuated and this heat must be removed between cycles and the cooling process usually results in a long cycle lifetime .Compared to bulk SMA_s ,SMA thin films provide a small amount of thermal mass to cool and hence the cycle lifetime can be decreased substantially. CuAlNi films can be sputter deposited on to heated aluminum foils and the as deposited films exhibited a good shape memory effect.[Wei et al,1998] .By coupling the SMA thin film with ferroelectric or ferromagnetic materials , SMA_s may be actuated electrically or magnetically and smart composites with optimized characteristics can be obtained.[Kim and Lee,2003] .

1.4 Applications

Since shape memory alloys have unique properties which are not present in many materials traditionally used in engineering applications, they have potentiality for many applications based on their particular characteristics. In the following ,the most important applications utilizing shape memory effect and super elasticity have been introduced.

1.Applications using shape memory effect:

The applications described in what follows take advantage of SMA ability to recover the configuration associated with the austenitic phase. In some devices the shape recovery is performed only once (one way shape memory alloys), in some other devices, through the use of a basic system ,it is possible to switch cyclically between two different configurations (two way SMA).[Wayman, and Duerig,1990] .This type of applications may be summarized as follows:

1. couplings
2. actuators
3. smart materials

A widely exploited use of SME is one in which an external constraint prevent the material from returning to its original shape on heating (constrained recovery) ,resulting in the generation of large recovery forces .[Auricchio,1995]. The main application of constrained recovery is in couplings and fasteners such as :

- ***Air plane –pipe coupling*.**

They give the possibility of obtaining closely packed hydraulic tubing assemblies and the freedom of designing the hydraulic system without the joining method providing constraints because of tool access. This system used in F-14 jet fighters by Raychem Corporation.[Otsuka, and Ren,1999].

- ***Electrical connectors*:**

Shape memory alloys are used to drive the opening and closure of connectors such as those on computer boards. In such cases, almost no insertion force is needed and very little if any of the mating force is transmitted to the supporting structure. Moreover ,once the connector is closed ,it exerts high retention forces , inhibiting any relative movement between connector member and preventing fretting corrosion from occurring .[Auricchio,1995] .SMA coupling

devices are also successfully used in marine deep-sea applications ,in braid termination missile retain rings and hermetic seals. An interesting application for joining of optical fibers has also been proposed.[Auricchio,1997] .Since the recoverable strain of SMA_s can be more than 10% and the shape recovery process can cause larger force generation if strain is constrained, SMA_s have attracted wide attention for their application as actuator materials in smart systems. [Qiu, J. et al,2000].In general ,a distinction is made between thermal and electrical actuators. Both do work upon heating ,the difference being that thermal actuator are heated by changes in the surrounding environment while electrical actuators are heated by passing electricity directly through the SMA .[Surbeld et al.,1998].

- ***Thermal acuators:***

Thermal actuators are usually designed to behave as sensors (detecting a temperature change) and so actuators. Both Nickel –Titanium and copper based alloys are used depending upon the exact requirements, NiTi alloys being better in fatigue and work output, while the cu-based alloys have higher transformation temperature and are cheaper. Compared to other actuation methods , SMA_s are generally simpler ,less expansive more compact and provide very large, sudden motion however, the presence of the hysteresis makes it difficult to perform an accurate temperature. control. [Saz et al.,1990].

- ***Electrical actuators:***

Electrical actuators are used to replace solenoids, servomotors, hydraulic and pneumatic devices. They are typically simpler in design, quieter more compact and less expensive.[Auricchio,1995]. SMA actuators have also

been used in conjunction with active vibration control for flexible linkage mechanisms ,active buckling of stiffened panels, control surfaces for adjustable chambers, bending and shape control of beams , shutters for air conditioners, fans for automobile radiators ,switches for automatic kettles, thermal valves for fire protection and liquid-gas switches .[Otsuka, and Ren,1999].

Another types of smart materials are composites of NiTi SMA_s with polymers or metal matrix .The NiTi wires embedded in polymers may be used for vibration control of space vehicles, since the elastic constants can be changed widely by changing the temperature in the transformation temperature range. The TiNi wires embedded in aluminum matrix may be used to strengthen aluminum matrix by the same mechanism of pre stressed concrete.[Cadegan et al,2002].

Shape memory effects have also been exploited for medical applications such as blood –clot fillers , intracranial aneurysm clips, artificial hearts ,ropes for the treatment of scoliosis , micropumps.[Koop et al.,2001] .Another area of interesting applications is orthopedics .The heating of fractured bones proceeds more rapidly if the fractured faces are under steady compressive stress. During surgery to reset fractures ,shape memory alloy plates can be attached on both sides of the fracture producing the necessary compressive stress in the fracture gap by exploiting the memory effect .[Li et al,1999].

The use of SMA has opened new frontiers also in terms of space applications. SM connectors are being developed to facilitate the joining of composite tube structural members. Such connectors are automatic catches and release systems based on SMA latching devices. SMA actuators are planned to be used to deploy shelters, control the dynamic of space structures and ensure the integrity of seals.[Turner, and patel,2004].There is also the promise of using

SMA_s in making high efficiency damping devices that are superior to those made of conventional materials, partially due to their hysteretic response ,specially ,porous shape memory alloys. The use of a torsion tube for trailing the edge trim tab control on helicopter rotors is a typical example of the smart blade technology whose main task is the attenuation of noise and vibrations in the surrounding environment.[Schweiger,2002].

2.Applications using superelasticity:

Super elasticity which is nonlinear pseudo elasticity as much as 7-8%,has been also applied in various fields. The first application was to orthodontic arch wire which made the orthodontic therapy much easier and effective.[Koop,K et al,2001].The second quite successful is to the antennas for cellular phones as shown in Fig.(1.3).Since superelastic wire is quite flexible and is not subject to damage. The third one is guide wires for catheters in medical use as shown in Fig.(1.4).A catheter which is a tube made of plastics , is a standard tool for diagnosing the circulatory system by injecting a contrast medium into vessels or for medical treatment by dilating a humen of blood vessel at the site of the obstruction .To introduce the catheter in a required place of the vessel in brain, heart , lever , a guide wire is necessary .It is being overtaken by NiTi superelastic wire recently since the Nitinol wire is more flexible and is not permanently bent, thus this application is expanding rapidly.[Mantovan,2000].By using the super elastic property of shape memory alloys, eyeglass frame components can withstand extreme deformations and spring back completely .[Chute,and Hodjson.1990 Queted in Aurcchio,1995].Further more ,many products in medical application such as braces, dental implants, stents and orthodontic wires are used of shape memory alloys.

Fig.(1.3) Superelastic antenna for a cellular phone.(adapted from Otsuka & Ren 1999)

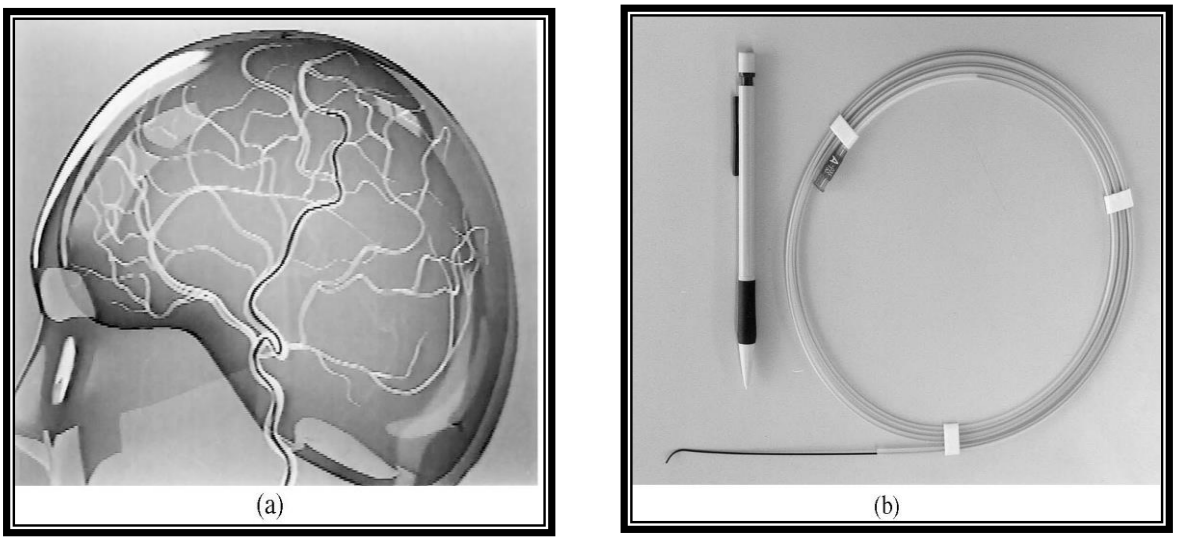

Fig.(1.4) Superelastic guide wire for a catheter in medical use.
(a)Applications for brain; (b) appearance of a guide wire. (adapted from Otsuka & Ren 1999)

1.5 Objectives

The objective of this work is to prepare, develop and investigate porous (CuAlNi) base shape memory alloys produced by powder metallurgy technique

in order to increase shape memory effect and super elasticity of copper based shape memory alloys. In this study ,several material parameters are studied through the addition of alloying element such as (Ti,B,Fe,Si,Co,Zr) and the combination of Ti and Mn and B and Mn in the other hand. In addition, different heat treatment such as solution treatment, direct quenching, aging and step quenched treatment.

Furthermore, different process parameters such as compacting pressure, rate of loading, period of maximum load, sintering time and sintering temperature have also been studied to know their effects on shape memory effect and super elasticity of prepared alloys.

On the other hand, numerical analysis and modeling of CuAlNi porous shape memory alloys are presented using finite element technique with two approaches. In the first ,unit cell finite element analysis with square and hexagonal arrangement of periodic distribution of pores has been used. In the second, the real microstructure of porous shape memory alloys is analyzed using image processing and image analysis for light optical microscope structure combination with finite element method to analyze stresses and strains in the real material microstructure.

Review of Literature

2.1 General view:

Research on shape memory alloys is becoming a target of physicists as well as materials scientists and engineers, and martensitic transformations are being studied by various approaches both experimental and theoretical. For these reasons, rapid progress has been made recently in both fundamentals and applications. one form of these studies current study for copper based high temperature shape memory alloys used for space systems based upon shape memory effect or super elasticity characteristics . Cu Al Ni shape memory alloys have been prepared using powder metallurgy process in the present study .

2.2 Ni-Ti based shape memory alloys:

In the 1960 Buehler and Wiley developed a series of nickel-titanium alloys with a composition of 53 to 57% nickel by weight, that exhibited an unusual effect: severely deformed specimens of the alloys with residual strains of 8-15%,regained their original shape after a thermal cycle. This effect became known as the shape memory effect and the alloys exhibiting it were named shape memory alloys.[Buehler and Wiley,1965 Quoted in Auricchio 1995].

Eucken and Duerig (1989),studied underage Ti-50.85 at % Ni wire tensile specimens which were pseudo elastically pre strained between 2 and 8% .A second deformation to the same strain was found to occur at stresses some 60Mpa lower than the flow stresses measured during the pre straining. The transformation temperatures were measured in the unstressed state using differential scanning calorimetric (DSC) and tensile testing was done using extensometer in a temperature chamber.

Li et al.,(1999) used TiH_2 powder which is added as a reactant and pore-forming agent to produce porous NiTi shape memory alloys. The transformation behavior of porous NiTi alloys was investigated as it has been relevant to engineering and medical applications of SMA_s .It was found that the behavior of porous NiTi alloys is different from that of cast NiTi alloys. They showed that the characteristic transformation temperatures of porous NiTi alloys are independent of sintering temperature, sintering time and TiH_2 content, but latent heats of transformation increase with increasing sintering temperature ,time and TiH_2 content.

Li et al.,(2000)prepared equiatomic porous NiTi SMA_s by self propagating high temperature synthesis (SHS) using elemental nickel and titanium powder. It was found that the combustion temperature increases with increasing preheating temperature and results in melting of NiTi compound above 450 $^{\circ}$C.

Erbstoeszr et al (2000) presented an experimental investigation for NiTi shape memory alloys to stabilize the shape memory effect in cast NiTi. It was found that the most stable one –way shape memory effect in NiTi was a five minutes 475°C salt bath followed by water quench .

Mantovni (2000) presented an overview about properties and biomedical applications of NiTi shape memory alloys. Detwining process and its anisotropy in Nitiol shape memory alloys have been studied by Liu (2001).He showed that the maximum shape recovery strain is intrinsically related to lattice geometry and twining mode. While the magnitude of shape recovery strain is related to a competition of detwinning versus dislocation generation responsible for the macroscopically observed martensite deformation . It has been shown that the anisotropy in detwinning process allows the possibility of maximizing the potential of the polycrystalline shape memory alloys.

Wu(2001) reviewed Nitiol fabrication processes such as melting , forming , shaping , cutting, joining and finishing commonly employed for manufacture of Nitinol material and components.

The thermally induced recovery of microscopic deformation in a Ni-Ti shape memory alloy was examined by Ni et al (2002). Surface deformation was evaluated by indenting the alloy in the martensite phase at room temperature using spherical and pyramidal indenters. They showed that deformation in spherical microindents can be almost completely reversed by heating whereas partial recovery observed for pyramidal impressions formed by Vickers indenter. It was shown that the recovery ratio is independent of load for Vickers geometry .

Crone et al (2002) prepared NiTi shape memory alloy with refined grain size synthesized by mechanical alloying process through a cold rolling fabrication of elemental nickel and titanium layered foils. After the layer thickness was reduced to the nano scale by multiple cold rolling and folding passes, an alloying and intermediate phase formation reaction was initiated. X-ray diffraction profiles confirmed that the present was intermetallic NiTi phase.

Tension-torsion tests were conducted on thin walled tubes of the polycrystalline super elastic and shape memory Nitinol alloy using various loading / unloading path under isothermal conditions by the workers Macnany et al (2003).Their experimental results showed significant variations in the mechanical response a long the two loading axes.

Brinson et al (2003) studies micro and macro mechanical transformation behavior of polycrystalline NiTi shape memory alloys. Special attention was paid to macroscopic banding , variant microstructure , effect of cyclic loading, strain rate and temperature effects. It has been shown that use of interference filter on the microscope enabled observation of grain boundaries and martensite plate formation and growth without recourse to etching or other chemical surface preparation.

Crone et al(2003) used atomic force microscopy (AFM) to reveal that the thermally induced martensitic transformation of NiTi shape memory thin films allows for partial indent recovery on the nano scale and the recovery was nearly complete at indentation depths of less than 100nm.

Fan et al (2004)presented comparative study between single crystals and polycrystals from NiTi shape memory alloys and found that all single crystals exhibit normal two stage transformation being independent of Ni content where as polycrystals with Ni content show three stage transformation but those with high Ni content (51.5 Ni %) exhibit normal two stage transformation.

Nasser et al(2005)investigated compressive response of NiTi shape memory alloys at high strain rates using modified split Hopkinson pressure bar and a mini- Hopkinson bar with specially designed striker bars. It was shown that the transition stress from the austenite to the martensite phase shows strain rate sensitivity. Porous NiTi alloy with several different porosities was processed by spark plasma sintering by Zhao et al (2005). The compression behavior of the porous NiTi was examined as a high energy absorbing material.

2.3 Copper base shape memory alloys:

Planes et al (1981) presented study of ordering in a β phase of CuZnAl alloy and the influence of ordering on the martensitic transformation temperature using differential scanning calorimetric. Barcelo and Ahlers (1982) showed that it is possible to induce a hexagonal long range ordered martensite phase in a Cu ZnAl alloy with $M_s = 50^{\circ}C$ and an electron concentration e/a=1.48. From their measurements of the critical stress and retransformation to β after re heating , it was concluded that the hexagonal and original 3R martensite have the same formation free energy thus, the two structures can not be described by their difference in stacking fault density (compared to a face centered lattice). The application of martensitic alloys in shape memory devices requires reproducible and stable transformation temperatures. In certain CuZnAl alloys,

the reverse transformation temperatures A_s and A_f progressively increase with prelonged holding at temperatures below A_s .

Study of the increase in A_s as a function of the stabilization temperature and time had been reported by Humbeeck et al(1984). The crystal structure and reordering of stabilized step-quenched copper zinc aluminum martensite using x-ray diffraction technique had been reported by Delacy et al (1984).

During the stabilization of step-quenched Cu Zn Al martensite

(quenching above the M_s temperature) ,precipitation and changes in the microstructure of martensite had been occurred. Extra contrasts were observed which are not present in non stabilized martensite by Graef et al (1985).

A study of crystallography of the martensitic transformation in a Cu-26.71Zn-4.15Al shape memory alloy by means of group theory was presented by Juany et al (1985). They had obtained the irreducible representation and 24 martensite variants associated with the martensitic transformation in this alloy system.

Thermal analysis data for CuZnAl in ribbon form were analyzed as a function of degree of stabilization by Scrasbrook and Stobbs (1987). The relatively high sensitivity of rapidly quenched ribbon material to both quench and equilibrium stabilization was discussed using differential calorimeter.

The influence of the average grain size and ordering degree of the parent phase on the starting temperature of thermoelastic martensitic transformation in a Cu-25.62 Zn-3.97 Al-0.0018B (wt %) shape memory alloy was studied by Jianxin et al (1988).

Adachi et al (1988) presented crystallographic analysis using transmission electron microscopy taking into account the various combinations of martensitic plate variants which meet at the boundaries formed between different self accommodating plates groups in CuZnAl martensites.

The process of the thermo elastic β´to martensite transformation and reverse transformation was studied as a function of temperature and applied

stress using electric resistance measurements and metallographic observation in a Cu-29%Zn-3%Al alloy by Deg, Ansell(1990).

Mellor et al (1990) presented the training of polycrystalline Cu-6.57%Al -20.18%Zn-0.72%Co alloy using stabilized stress induced martensite. The mechanism responsible for the development of two way SME by stabilized stress induced martensite had been studied using optical and scanning electron microscopy.

The ordering temperatures of β to B_2 (ordered body center cubic) and from B_2 to another order crystal lattice structure ($L2_1$ as shown in chapter three)had been studied in CuAlNi shape memory alloys with different concentrations using electrical resistively by Recarte et al, (1997).

Franz and Horbegen(1998) had been shown that the lattice defects in the stable austenite (β) phase of a Cu-27%Zn-4%Al shape memory alloy by a hot rolling and quenching process (Ausforming) lower the temperature range of martensitic transformation cycles and improve strength properties through increase dislocation density.

The neutron texture analysis had been perform on the pseudo elastically transforming CuAlZn Mn shape memory alloy specimens by Neov et al (1999). Pons and Cesari (1999) had been shown that variety of distribution of γ-phase precipitates in CuZnAl single crystals shape memory alloy with different size , shape , distribution density and nature can be obtained by some suitable heat treatments.

Recarte et al (1999) have studied the influence of quenching and post quench aging treatments on the atomic order of the β phase obtained by quenching in CuAlNi shape memory alloys using thermoelectric power measurements. The initial evaluation of thermoelectric power during aging showed two clear stages where thermoelectric power value decreases.

The microstructural and transformation characteristics were studied by Aslanidis et al (1999), including the effect of thermomechanical cycling and

using torsional actuation mechanism for Cu Al Ni shape memory alloy. Recent developments with nearly 10 years on shape memory alloys (specially for NiTi) and martensitic transformations on which shape memory effect and super elasticity are based, were reviewed by Otsuka and Ren (1999).

Ferreira et al (2000) were shown that boron and iron were refining and stabilizing the microstructure in the Cu-15.5%Zn-8.0%Al alloy. The pre-alloyed melt of Cu-13.1Al-3.16Ni alloy was atomized by argon at pressure of 2.3 Mpa by Raul et al(2000). They used hot isostatic pressing (140 Mpa pressure at 850 $^{\circ}$C)during 2hr to compact pre alloyed powder. After the compaction , hot rolling temperature of 850°C to improve mechanical properties of product was used . The main result had been shown that fracture occurred after deformation higher than 12% and the maximum recoverable tensile strain was 7 %.

Cakmak et al (2001) studied aging behavior of Cu-21.62%Zn-5.68%Al martensite at 24°C by analyzing diffraction line profiles obtained by x-ray diffractometry and change of the lattice parameters associated with aging time at room temperature .

In (2002) , Pana et al presented characterization of dry sliding wear behavior of the Cu Zn Al shape memory alloys in their different phases using adhesive wear tests (pin-on-Disk).Characterization of wear surfaces were carried out by optical microscopy , scanning electron microscopy , Dsc and x-ray diffraction.

The nucleation and propagation of cracks in Cu Al Ni shape memory alloy were observed using atom force microscope (AFM) by Lu et al(2002) . The results indicated that in Cu Al Ni shape memory alloy the martensitic transformation first occurred at crack tip upon loading and the micro crack nucleated and propagated along martensite interface. Neutron powder diffraction and texture studies of Cu Al Mn Zn shape memory alloy were preformed under tensile loads by Neov et al (2002) . The specimens were deformed up to 3% strain .

The effect of high velocity impact loading on the structure , transformation temperatures , elastic and an elastic properties had been studied for a CuAlNi shape memory alloy in the β'_1 martensitic phase by(Golyandin et al,2002). The impact loading of crystals had been preformed by means of a light gas gun producing compressive plain strain wave pulses with a duration of about $2*10^{-16}$ sec. It had been shown that the stability of the temperature range and hysteresis of martensitic transformation are a scribed to the rather stable martensitic variant structure .

Kim (2003) had used a simple constrained heating technique to realize the two-way shape memory effect (which is a phenomenon that a material can alternate between two shapes as it undergoes a thermal cycle) and had studied the effect of heating time and temperature for Cu-33.1%Zn-1.3%Al alloy prepared by induction furnace casting and hot rolled.

Silva and Lima(2005) prepared Cu-13%Al-2%Nb shape memory alloy by mixing pure elemental powders. A ball to powder weight ratio 6:1 and rotation rate of 15rpm in argon atmosphere were the main processing parameters changes in microstructure as a function of milling time were studied using x-ray diffraction analysis and scanning electron microscopy. Obtained results had been shown that high energy ball milling combined with pressing with (900Mpa) and sintering at 850°C , can be used to promote the formation of copper aluminum solid solution with density of 91% of theoretical density .

Sampath (2005) studied effect of addition of zirconium (0.2, 0.4 and 0.6%Zr) on the microstructure and transformation temperatures of Cu-11%Al-3.82%Ni shape memory alloy . The differential scanning calorimeter studies had been shown that zirconium increases the martensitic transformation temperature up to 0.4% additives but further addition of zirconium decreases M_s to below room temperature .

From the previous review , it has been clear that very little studies for copper base shape memory alloys by powder metallurgy technique using process

parameters and various alloying elements such as [B, Fe, Si, Co, Mn, Zr, Ti] were presented.

2.4 Analysis of shape memory alloys:

Turner et al(1994) presented finite element analysis of the random response suppression of composite panels reinforced with NiTi shape memory fibers. The preliminary results demonstrated that the SMA fibers can completely eliminate the thermal post buckling deflection and reduce the random response at elevated temperatures.

Lubliner and Auricchio(1996) presented a first attempt to apply generalized plasticity to the behavior of shape memory alloys. Trochu and Qian (1997) suggested a methodology to simulate the nonlinear thermo mechanical behavior of shape memory alloys by finite element method. A general and simplified constitutive law was formulated based on plastic flow theory using a bilinear model as uniaxial material law. Auricchio et al (1997) proposed constitutive models based upon generalized plasticity taking into account super elasticity and the single variant martensite reorientation only. Numerical simulation of uniaxial loading, four point bending and three point bending tests were presented . The computation tool to be used during the design of SMA-based devices had been also proposed by Auricchio & Taylor (1997). Constitutive model included super elastic behavior of shape memory alloy at finite strains.

Rebelo and Perry (1999)developed algorithms which allow for analysis of Nitinol medical devices by finite element method. They assumed multi linear elastic behavior to explain super elasticity of Ni-Ti shape memory behavior.

Thermo mechanical one dimensional constitutive model based on the use of strain and temperatures control variables and able to reproduce the basic response in tension and compression and shape memory effect had been presented by Auricchio and Sacco (1999) . The model was implemented in a small deformation beam finite element.

The structure of a twinned martensite plate in NiTi shape memory alloy was examined based on micro mechanics by Liang et al(1999).

Koop et al (2001) analyzed stent material Nitinol using Ansys type 4.5 software and user material program to present individual model for the material. They used multi linear elastic model with different Young ′s modulus for austenite and martensite phases to compute super elastic under loading and unloading behavior of Nitinol stent material. Thermo mechanical model of a super elastic shape memory wire under cyclic stretching –bending loading had been proposed by Auricchio and Sacco (2001).

Qidwai et al (2001) presented modeling of thermo mechanical behavior of porous shape memory alloy. The porous SMA was assumed to be made of two components , the dense shape memory alloy matrix and the pores . Rate – independent type constitutive model was employed to describe the matrix behavior using unit cell finite element method and averaging micro mechanic method . Cylindrical and spherical shape were considered as approximations of open and closed pores respectively.

The radial displacement control of an externally pressurizes elliptic composite cylinder where the SMA strip actuators are bonded on its in and out surface was studied numerically using finite element method by Kim and Lee(2003) .

Turner and Patel (2004) analyzed of shape memory alloy hybrid composite structure using thermo mechanical model of SMA actuators and hybrid composite models to implement in the commercial finite element codes.

2.5 Summary

Shape memory alloys (SMA) are being increasingly used in various industrial applications as actuators , connectors, eyeglass frames , stents or damping materials so that a significant a mount of research in last few years has

greatly advanced in thermo mechanical characterization, material fabrication and numerical modeling and simulation of SMA.

In the light of previous review of literature shape memory alloys included NiTi base alloys for medical and for fiber reinforced advanced composites and copper base shape memory alloys for space systems specially Cu Zn Al and Cu Al Ni alloys . Most of those studies were prepared by casting in control atmosphere (in Argon or in vacuum) except NiTi shape memory alloys for medical applications . The previous studies were emphasized on thermo mechanical characterization and martensitic transformation and their crystallographic changes during phase transformation . Very few work has been done for porous copper base shape memory alloys processed by powder metallurgy taking into consideration compacting and sintering parameters effects.

Perhaps, there is no comprehensive study on the copper base shape memory alloys prepared by powder metallurgy taking into consideration all manufacturing parameters and analysis of porous shape memory alloy depends upon real microstructure of size , shape and distribution of pores in the material.

In this study , CuAlNi shape memory alloys have been prepared from elemental powder and developed of their behavior by two ways as follows:

1. Chemical compositions of alloys through adding of various alloying element into base used alloys such as Ti, B, Co ,Zr ,Fe , Si, Mn.
2. Heat treatments in what solution heat treatments at different times and temperatures has been taken further more, effects of aging treatment and step-quenched treatment are also explained on the microstructure , shape memory effect and super elastic behavior of prepared alloys from different physical and mechanical tests.
3. Until cell finite element analysis of porous shape memory material has been presented in this study. Proposed square and hexagonal unit cell for

pore distribution have been used to represent periodic arrangement of pores.

4. Unit cell finite element analysis of real microstructure of porous shape alloy has been taken in this study. Real images from optical microscopy with suitable magnification have been pictured and analyzed using image analysis technique to calculate pores and their distribution in the image, further more transform these image to engineering geometry to analyze mechanical behavior using finite element method .

Theoretical Consideration

3.1 General View

The term shape memory alloy (SMA) is applied to that group of metallic materials that demonstrate the ability to return after deformation, to some previously defined shape or size when subjected to the appropriate thermomechanical procedure. Although a relatively wide variety of alloys and also compounds are known to exhibit the shape memory effect, only those that can recover substantial a mounts of strain are of commercial interest. To date , this has been the case for Ni-Ti and copper based alloys such as CuZnAl , CuAlNi or CuAlBe which are the subject of the present work.

In this chapter, shape memory effect and superelasticity behavior, martensitic transformations and their microscopic and macroscopic perspectives have been presented with enhanced for copper base alloys. Furthermore, theoretical considerations of powder metallurgy technique for copper base alloys taking into consideration types of compaction and sintering processes have been presented. Finally, effects of alloy elements, thermal treatments and aging treatments have also explained in this chapter, but we begin with martensitic transformation due to understand the origin of shape memory effect.

3.2 Martensitic Transformations:

One can not obtain an understanding of even the most elementary engineering aspects of shape memory effect without first becoming familiar with some basic principles of martensite and its formation. Martensitic transformation can be explained in two manners as follows:

3.2.1 Microscopic Prospective of Martensite

Solid state transformations are two types diffusion and diffusionless (displacive). Diffusion transformation are those in which a new phase can only

be formed by moving a toms randomly over relatively long distances . long rang diffusion is required because the new phase is of a different chemical composition than the matrix from which it is formed. Since atomic migration is required, the progress of this type of transformation is dependent upon both time and temperature. In contrast, displacive transformations do not require such long range movements in these cases atoms are cooperatively rearranged into a new more stable crystal structure but without changing the chemical nature of the matrix. Because no atomic migration is necessary, displacive transformations generally progress in a time –in dependent fashion . They are referred to as a thermal transformation since the amount of new phase present is usually dependent only on temperature and not the length of time at temperature. Martenesitic transformations are generally of this second type and are formed upon cooling from a higher temperature phase called the parent phase or austenite. (Wayman and Duerig 1990).

The terms "Martensite" and "austenite " were originally intended to refer only steel phases but the more generalized definition referring to the type of transformation product and not the particular material is now widely accepted. In physical metallurgy, the term martensite is used to describe any diffusionless transformation product which the individual atomic movements are less than one interatomic spacing. (Porter and Easterling 1992).

Martensitic transformations are first order transformations which mean that heat liberated when martensite is formed, there is a hysteretic associated with the transformation and there is a temperature range over which austenite and martensite coexist. [Ahlers 2002]. Martensite is formed based upon cooling with the volume fraction of martensite increasing as the temperature is reduced but with the volume fraction being independent of time, and that it inherits the composition and atomic order of the parent phase.[Wayman and Duerig,1990] .

The transformation from parent phase to martensite is often thought of in two parts, the Bain strain and the lattice invariant shear. The Bain strain or lattice deformation consists of all the atomic movements needed to produce the

new structure from the old.[Reed-Hill,1964].In Fig.(3.1),the austenite structure is illustrated in diagram(a)and the martensite structure is illustrated by diagram (d).

As the interface progresses one atomic layer, each atom is required to move by only a very small amount as shown in Fig. (3.1) c. The end results of all these small coordinated movements are the new martensitic structure. The movements needed to produce the new structure are called as Bain strain.(Reed-Hill, 1964) .

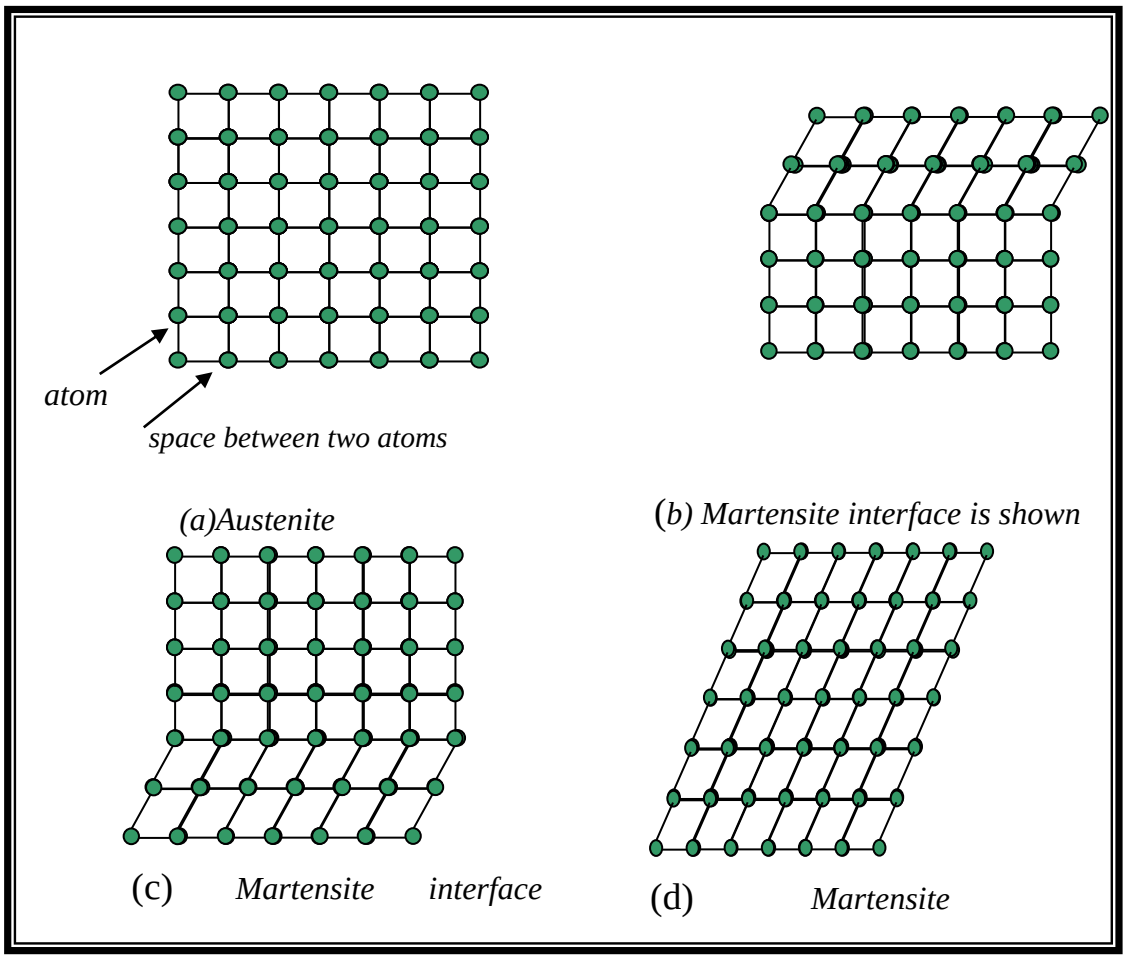

Fig.*(3.1) The transformation from austenite to martensite .a. austenitic phase b.and c. interface advance and d. completely martnsitic phase*

The second of a martensitic transformation, the lattice invariant shear which is an accommodation step. The martensitic structure produced by the Bain strain is of a different shape and often volume than the surrounding austenite.[Smallman and Bishop,1999].

Martensite in steel involves both volume and shape change where as shape memory alloys such as NiTi and Cu-base alloys undergo basically only a shape change. Either the overall shape of the new phase or the surrounding austenite must be attend to accommodate the new structure .[Wayman and Durig ,1990]. For example, one cannot change the shape of single brick in the center of brick wall, either the surrounding bricks must deform, or the new brick must accommodate its form to the space available.

There are two general mechanisms by which this can happen: slip and twinning as shown in Fig. (3.2) . In both cases, each individual cell has the new martensitic structure, but the overall shape is that of the original austenite. Slip is a permanent process and is a common accommodation mechanism in many martensites.[Reed-Hill,1964].

Twinning is unable to accommodate volume changes which should be necessary, but can accommodate shape changes in a reversible way [Porter and Easterlng,1992] . For shape memory to accur to any significant extent, the accommodation must be required fully reversible, in other words, twinning be the dominant accommodation process. [Otsuka and Kakestia,2002].

In the two–dimensional model shown in Fig. (3.2) , only two directions or variants of shear are required to restore the original overall shape of the matrix. In three dimensions, the situation can be complicated. For example, in CuZnAl martensites require four martensites variants for full three dimensional accommodation.

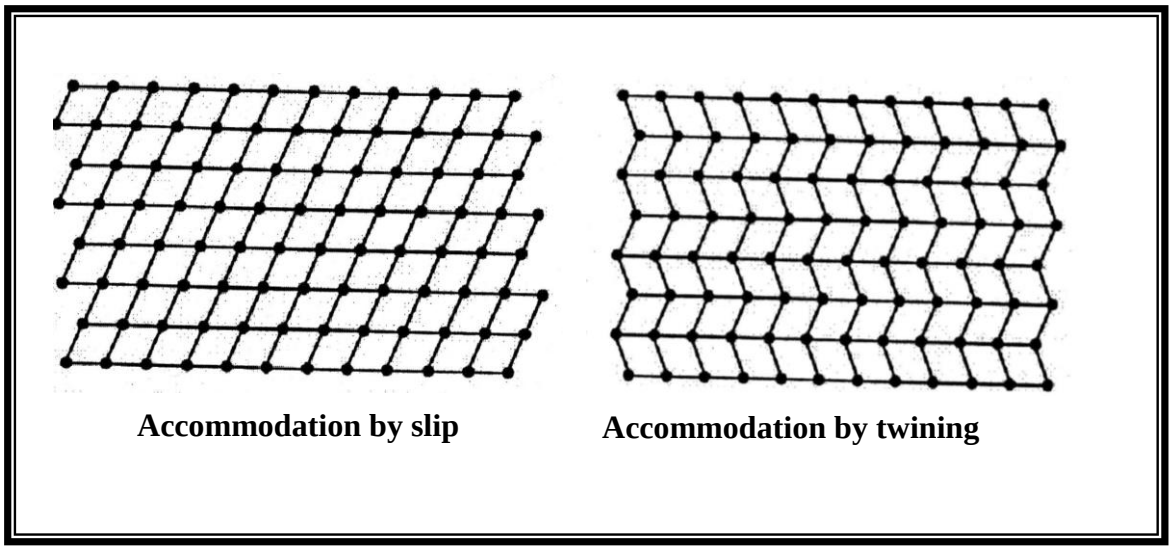

Fig.(3.2): The two mechanisms of accommodating the shape change due to atomic shear of a martensitic transformation a. by slip b. by twinning(Wayman and Duerig,1990)

The twin boundary is a mirror plane and when positioned on the boundary, the view in one direction is mirrors of the other as shown in Fig. (3.3).The atoms situated on the boundary have the same number and types of bonds in both directions. The twin boundaries have very low energy and they are quite mobile thus the relative stability of a martensite phase is not strongly affected by the number of location of these boundaries .[Reed-Hill,1964].

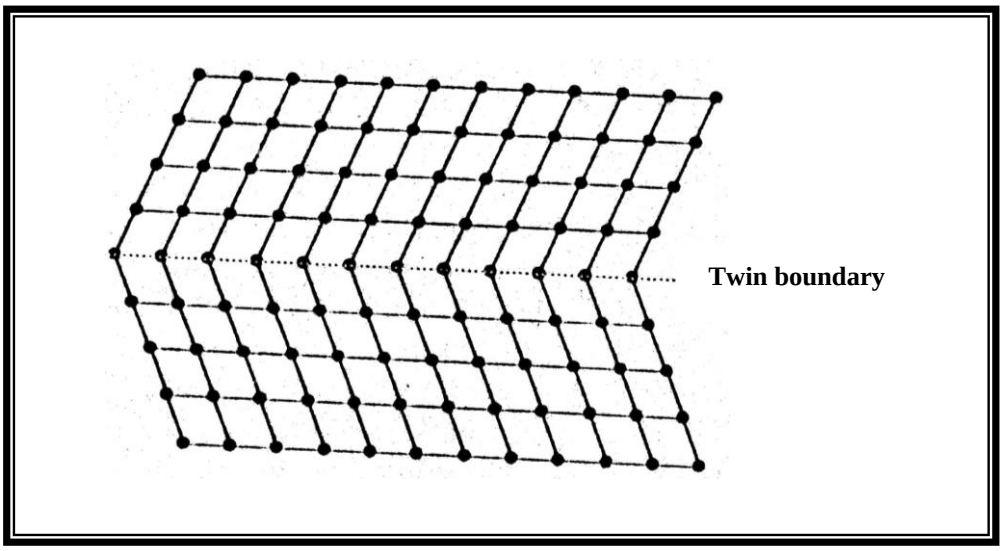

Fig.(3.3) Schematic view of a twin boundary.(Reed-Hill,1964)

Atomic bonds are broken in the slip accommodation while all bonds remain intact in the twinned structure. If a stress is applied to the structure as

shown in Fig. (3.2.b), the twin boundaries will easily move producing a shape which better accommodates the applied stress as clear in Fig.(3.4).

The result of moving a twin boundary is to convert one orientation or twin variant into another. That variant will be chosen which is most favorably oriented to the applied stress. A single variant of martensite can be produced by straining a sufficient amount. The condensation of many twin variants into a single favored variant is called as detwinning . The boundaries between martensite plats also behave as twin boundaries. [Reed-Hill,1964].

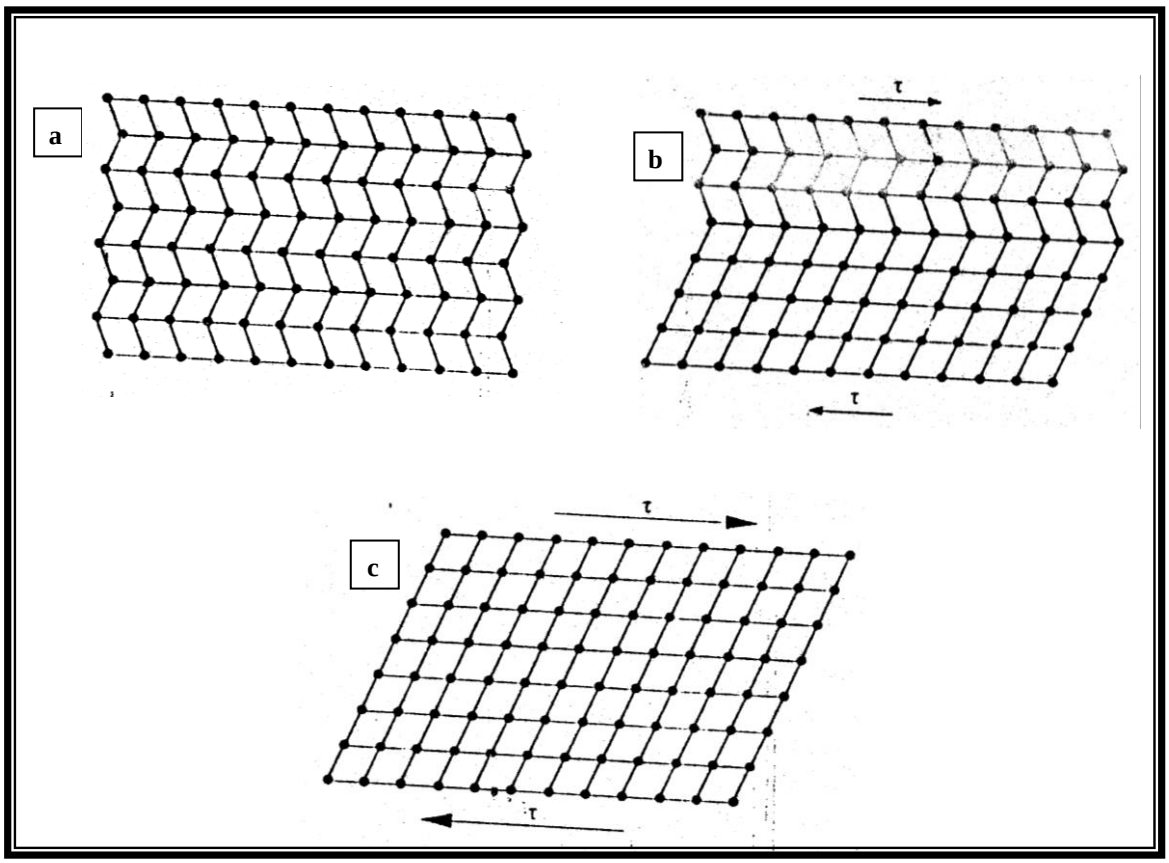

***Fig.(3.4) Twin boundaries in martensite can be removed by applied shear stress*(Reed-Hill,1964)**

In steel , the atoms are disordered , meaning that different elements are randomly distributed on the lattice sites, where as in CuZnAl and CuAlNi atoms are on very specific sites so that atoms are ordered.

During a martensitic transformation, the martensite takes on the same ordering of the austenite which is called inherited ordering. [Porter and Easterling,1992].

Shape memory alloys are generally based upon a Bcc symmetry , some with Bcc structure , more often with B_2 (premitive cubic) order structure and some with an even more complex ordering called Do_3 (face centered cubic) [Wayman and Duering ,1990].

3.2.1.1.Structure of martensite and morphology:

The formation of martensite appears from micrographs to be a random process and way it is observed to develop is illustrated in Fig. (3.5) . It has been shown that the martensitic phase is often in the shape of lens and spans initially an entire grain diameter. The density of plates does not appear to be a function of the grain size of the austenite . [Porter and Easterlng,1992] .

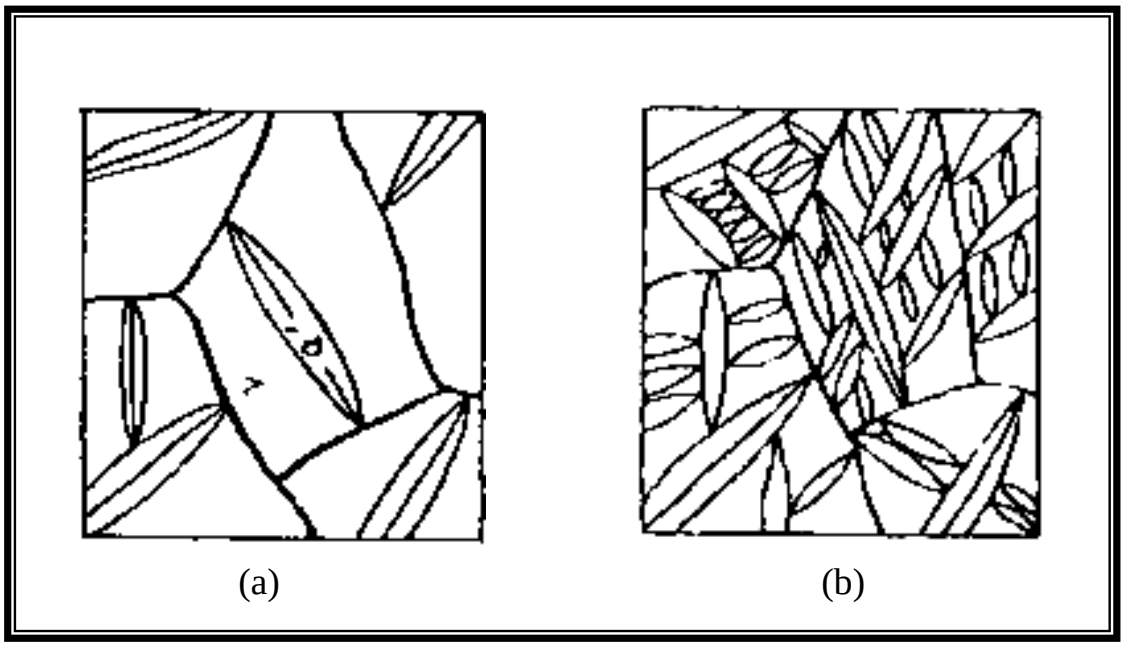

Fig.(3.5)growth of martensite with increasing cooling below M_s ,for both (a) and (b) **[Porter and Easterlng,1992]**

The transformed regions appear coherent with the surrounding austenite which means that intersection of the lenses with the surface of the specimen does not leads to any discontinuity . It has been shown that a fully grown plate spanning a whole grain may form within 10^{-7} second which means that the martensite / austenite interface reaches the speed of sound in a solid. Martensite is thus able to grow independently of thermal activation although some Fe-Ni

alloys to exhibit isothermal growth characteristics . This great speed of formation makes martensite nucleation and growth as a difficult process to study experimentally.[porter and Easterling,1992]. The volume fraction of martensite increases by the systematic transformation of the austenite remaining between the plates that have already formed as shown in Fig. (3.5.b). The first plates form at the martensite start temperature (M_s) which is associated with a certain driving force for the diffusionless transformation from austenite to martensite as shown in Fig. (3.6)

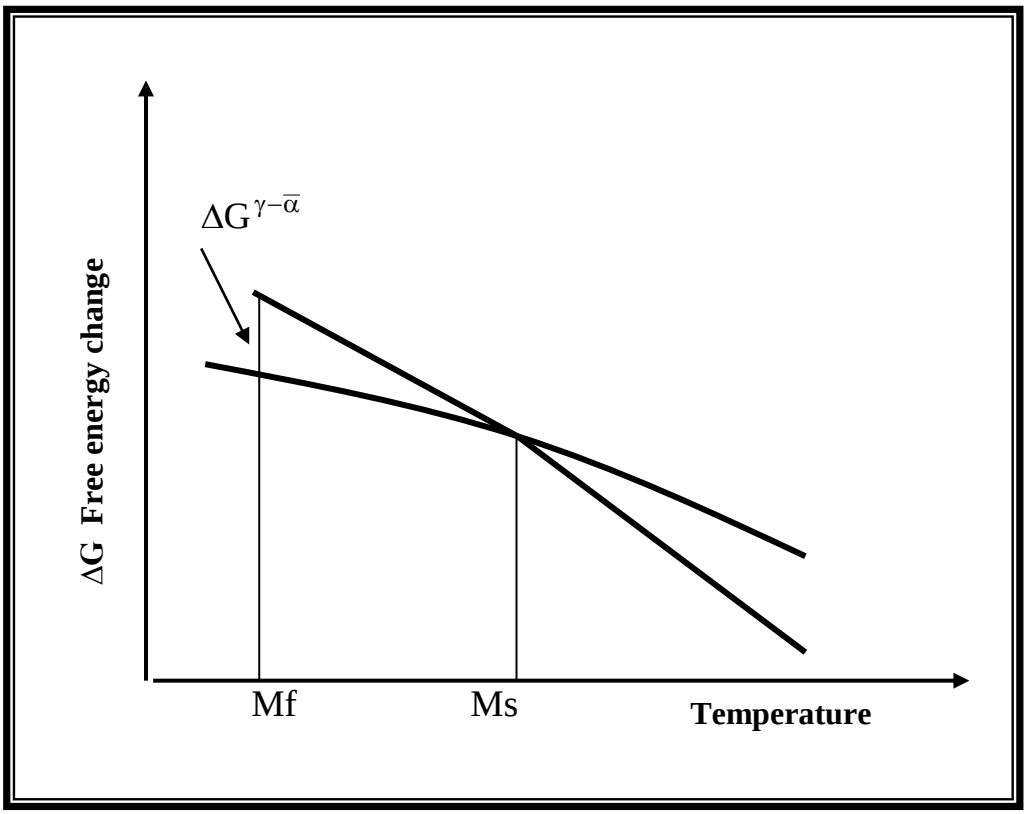

Fig.(3.6)Free energy temperature diagram for austenite to martensite phase change

The martensite finish temperature (M_f) correspond to that temperature below which further cooling does not increase the martensite amount.[Reed-Hill,1964]. Because the martensitic transformation is a lattice –distortional diffusionless structural change having a dominant deviatory component and an associated change in shape , strain energy dominates the kinetic and morphology of the transformation . The driving energy required for martensitic

transformation is much higher (especially for irreversible martensite) than that needed for diffusion decomposition such as precipitation.[Meyers and Chawla,1999]. If a diffusion-induced transformation competes with martensitic transformation, the cooling in the region where to M_s (Fig. 3.6), has to be fast enough to avoid the former transformation on the other hand, if to is low enough , there is essentially no diffusion and slow cooling leads to produce martensite .For irreversible martensites the gap in which $M_s \rightarrow A_s$ is a few handred Kelvin while for reversible martensites, the gab is a few tens of Kelvin.[Meyers and Chawla,1999].Martensite can be exhibited a variety of morphologies depending upon the composition of the alloy, conditions in which it is formed and its crystalline structure . The three most common morphologies are the lenticular (lens shaped), lath (a large number of blocks juxtaposed in a single like arrangement) and the a circular (needle shaped) .

In spite of these differences in morphology , some unique features are common to all martensites . The most important is the existence of an undistorted and un rotated plane which has the same indices in the two structures , parent and martensite phases. This undistorted and unrotated plane is called as the habit plane . The macroscopic shape deformation in the formation of martensite plate is believed to be shear parallel to the habit plane and a simple (uniaxial) tensile or compressive strain perpendicular to the habit plane . A strain of this nature called as invariant plane strain .[Reed-Hill,1964].

3.2.1.2.Martensite Crystallography:

Knowledge the crystal structure of martensite is a first step toward understanding the mechanism of the martensitic transformation. Lattice parameters and lattice correspondence between parent and martensite are required in the phenomenological theoretical calculation and the exact atomic positions are not required , since small suffles are considered not to a contribute to the shape strain . The correct band structure of martensite can not be obtained unless actuate atomic parameters are used . Since martensites usually appear in a

self-accommodating manner, a single crystal of martensite is not usually obtained.[Otsuka and Ren,1999].In Au-Cd alloys two types of martensite appear depending upon Cd content which are γ_2' (B19) martensite appear near Au-47.5% Cd while ζ'_2 martensite appear near Au-50.0%%Cd. The structure of the γ_2' martensite is an orthorhombic unit cell where as ζ'_2 martensite is Trigonal (R-phase)unit cell structure .[Otsuka and Ren,1999]. R –phase transformation is a martensitic transformation which competes with the monoclinic martensitic transformation. In Ti-50% Ni alloy , the structure of martensite is monoclinic (B19) martensite where as R-phase appears in Ti-Ni-Fe ternary alloys. Table (3.1) present a number of systems in which martensitic transformation have been observed .

Table (3.1) systems in which martensitic transformation occurs .

Adapted from (Meyers and Chawla,1999).

Alloy	***structure change***
Fe-Mn , Fe-Cr-Ni	Fcc→Hcp
Fe-Ni	Fcc→Bcc
Fe-Mn-C	Fcc→BcT
Fe-Ni-C	Fcc→BcT
Fe-C	Fcc→BcT
In-Ti and Mn-Cu	Fcc→FcT
Cu-Zn	Bcc→FcT
Cu-Sn	Bcc→FcT
Cu-Al	Bcc→disordered HcP Bcc→orthorhomic Bcc→monoclinic
Au-Cd	Bcc→orthorhomic Bcc→Trigonal
Mn-Cu	Fcc→BcT
Ti	Fcc→HcT
Ti-Cu	bcc→HcP
Ti-Fe	bcc→HcP

3.2.1.3.Martensite Nucleation:

The nucleation of martensite plates is a subject of great interest and also of considerable controversy. It is generally accepted that nucleation occurs heterogeneously at defects as is the case with nucleation in most other transformations or phase changes. (Ahlers,2002). Because of the great speed of growth of martensite , it is extremely difficult to study this transformation experimentally . It has been assumed that the initial nucleus should be coherent with the parent austenite phase. So the total increase in Gibbs free energy associated with the formation of a fully coherent inclusion of martensite in a matrix of austenite can be expressed as : [Porter and Easterling,1992].

$\Delta G = A\gamma + V\Delta G_s - V\Delta G_v$ ----------Eq.(3.1)

where :

γ –The interfacial free energy

ΔG_s –strain energy

ΔG_v –volume free energy

A- surface area

There is a balance between surface and elastic energy on the one side and volume free energy on the other .In the martensitic transformations , the strain energy of the coherent nucleus is much more important than the surface energy so that the Bain distortion strain produces large strains in the surrounding austenite .

The interfacial surface energy of a fully coherent nucleus is relatively small.[Porter and Easterling,1992]. It has been thought that surfaces and grain boundaries are not significantly contributing to nucleation so the transformation is being initiated with other defects within the crystal.[Reed-Hill,1964].

In order to reduce the elastic energy of martensite plate should be as thin as possible being determined by the decrease in volume free energy compared with the increase from the habit plane energy. In addition the amount of the martensite shear should be as small as possible.[Ahlers,2002].

3.2.1.4.Martensite Growth

Martensite plates grow to their final sizes with great rapidity. Recent measurements show that the growth velocity is of the order one –third the velocity of sound in the matrix , and the growth velocity is independent of temperature . If the growth of martensite plates occurred as the results of atoms jumping over energy barrier from the parent phase to the product phase then the jump rate should be a decreasing function of the temperature and at some finite temperature a noticeable dropping off in the martensite growth rate should become apparent. This does not occur. Martensite has been observed to form with great rapidity even at $4K^{\circ}$. [Reed-Hill,1964].

During the growth of the thin planar plates of a constant thickness a low-energy interface between the martensite and the matrix, the habit plane is created right to the tip of the growing plate. The orientation of this interface is found generally to have high miller indices.[Ahlers,2002].Because of the martensite shear the matrix around the tip is distorted elastically, provided that the stresses do not activate plastic deformation by the movement of dislocations in the martensite or matrix . All the redistributions of the atoms from the matrix to the martensite structure occur near the tip and thus must not consume too much energy in order to possible . Once a thin martensite plate is created it often but not always, thickness by the movement of interfaces. During this step the mobility is more important than the necessity to keep an undistorted habit plane which leads to a bending of the interface and to an change in microstructure as often observed .[Ahlers,2002].

3.2.1.5.Origin Of The Martensitic Transformation:

Although it is still a subject of dispute ,items that on the level of lattice dynamics almost all different first order martensitic transformations can find a common origin . First order martensitic transformations is driven dominantly by phonon entropy differences between parent phase and martensite .[Otsuka and Ren,1999]. The parent phase has higher vibrational entropy because its low

lying or soft phonon branch contributes significantly to the entropy of the system where as stiffer martensite has lower vibrational entropy due to its higher phonon energy . As a result, a transformation from a higher entropy state to a lower entropy state will occur at some temperature .

According to the basic principle of thermodynamics that a low entropy state is favored at low temperatures and a high entropy state is favored at high temperatures . It has been shown that a dominant phonon contribution to entropy in martensitic transformation of copper base shape memory alloys using elastic constant measurements and calorimetry measurements .[Comas and Manosa ,2000].It has been suspected that many martensitic transformation can be caused by certain electron effect which can induce a phonon a normally through electron phonon coupling where as in ferrous alloys, martensitic transformation has different origin which is largely due to the magnetic contribution.

For example , there has been some clear evidence indicating the softening in elastic constants in Fe-Ni and Fe-Pt alloy can be ascribed to the magnetoelastic coupling between magnetization and phonon. Therefore ,items that the microscopic origin of martensitic transformation may be diverse and depends upon specific alloy system .[Otsuka and Ren,1999].

3.2.2.Macroscopic Perspective Of Martensite :

Most of mechanical and physical properties of austenite and martensite are different so through the transformation variety of significant property changes will be occurred .The temperatures, M_s,M_f ,A_s and A_f are indicated in Fig. (3.7),which refer to the temperatures at which the transformation to martensite starts and finishes, and the temperature at which the reversion to austenite starts and finishes. As shown in Fig.(3.7),the transfer matrix temperatures differ upon heating and cooling .

This difference causes a hysteresis associated with martensitic transformation. Yield strength is an one property that changes in a most significant way. The martensitic structure can deform by moving twin

boundaries which are quite mobile so, the yield strength of martensite is extremely low compared with yield strength of austenite which must deform by dislocation generation and movement .[Wayman and Duerig,1990].

Only a certain a mount of martensitic deformation can be accommodated by this twin movement process and once this is exceeded , the material will deform elastically and eventually yield a second time , this time by irreversible processes (dislocation movement).

The tensile behavior of a twinned martensite material is explained in Fig.(3.8) .the plate all stress is related to thermal hysteretic in that both are controlled by the frictional stress of the twin boundaries . The ratio of resistances to reversible and irreversible deformation is characterized by the yield strength ratio of martensite to austenite . In general, in shape memory alloy , this ratio is maximized so that all deformation can be recovered upon heating .Typically ratios would be 0.1to 0.2. [Wayman and Duerig,1990] .

3.2.2.1.Stress Induced Martensite and Superelasticity:

The formation of martensite is a thermoelastic process. Which means that an incremental decrease in temperature between M_s and M_f results in a slight growth of existing martensite plates and the nucleation of new ones , but when the temperature is incrementally raised , the newly nucleated plates disappear and those which grew slightly on incremental cooling correspondingly shrink back a little . There is an equivalence between temperature and stress ,a decrease in temperature is equivalent to an increase in stress, both of them stabilizing martensite. The martensite is also crystallographically reversible.

Normally on cooling, the martensite forms at M_s under no stress , but in the same material ,martensite can form above M_s if a stress is applied , martensite is termed stress-induced martensite (SIM). The deriving force for the transformation in this case, is mechanical.

Above M_s the stress required to produce SIM increases with increasing temperature as shown in Fig. (3.9). The variation in the stress needed to produce

(SIM) increases linearly with temperature above M_s . The linear variation in stress to induce martensite as a function of temperature obeys the Clausius-Clapeyron equation written as : [Gaskel,1978]

$d\sigma/dM_s = - \Delta H/T\varepsilon_t$----------Eq.(3.2)

where:

σ-applied stress

ε_t- transformational strain resolved a long the direction of the stress

T-temperature

ΔH-The transformation latent heat

The increase in difficulty to stress induce martensite continues to increase with temperature until M_d ,above which the critical stress for inducing martensite is greater than that needed to move dislocations. M_d is the highest temperature at which it is possible to have martensite thus the temperature range for (SIM) is from M_s to M_d . Above the temperature M_d, superelastic behavior can not occur and M_d is above A_f with few degrees. [Keefe, 1999].

Fig. (3.10) shows typical measurements from differential scanning calorimeter (DSC)for shape memory alloy. The (DSC) plot illustrates the power required to heat the material at a constant rate of temperature increase versus temperature . Energy is either absorbed or released during phase changes resulting in sharp peaks when the heat flow is plotted versus temperature . The transformation temperatures are measured from the intersection of the slopes in the linear portions of the peaks and the single phase , horizontal sections [Keefe,1999].

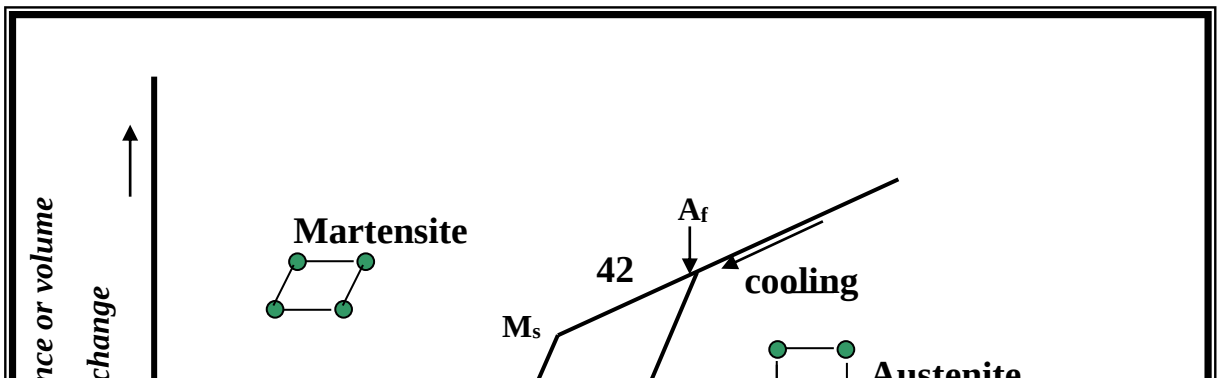

Fig. (3.7) property change with temperature for martensite transformation occurring in a shape memory alloy (Wayman and Duerig,1990).

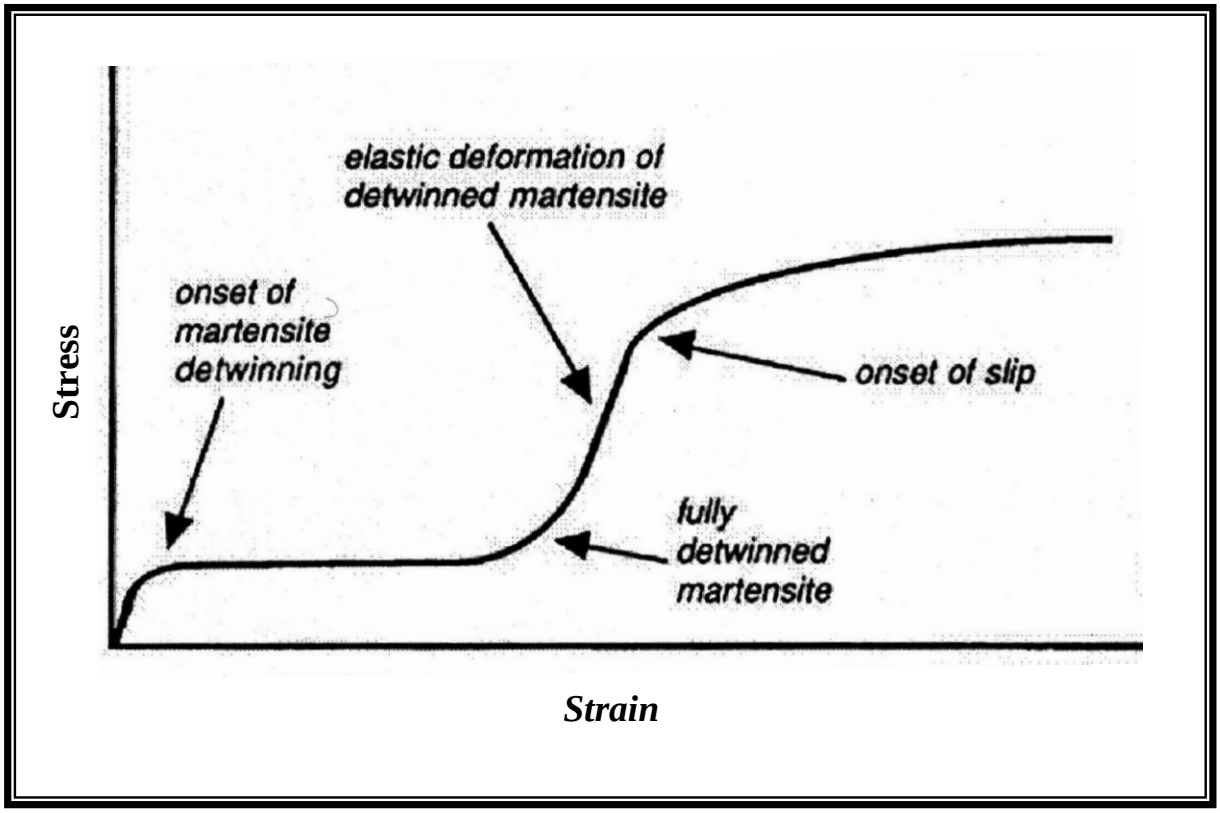

Fig. (3.8) typical stress-strain curve for a twinned martensitic material(Keefe,1999).

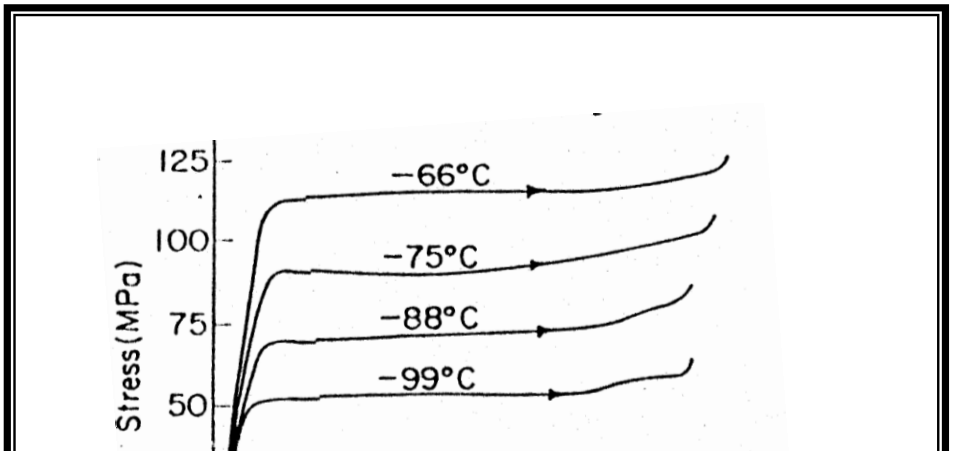

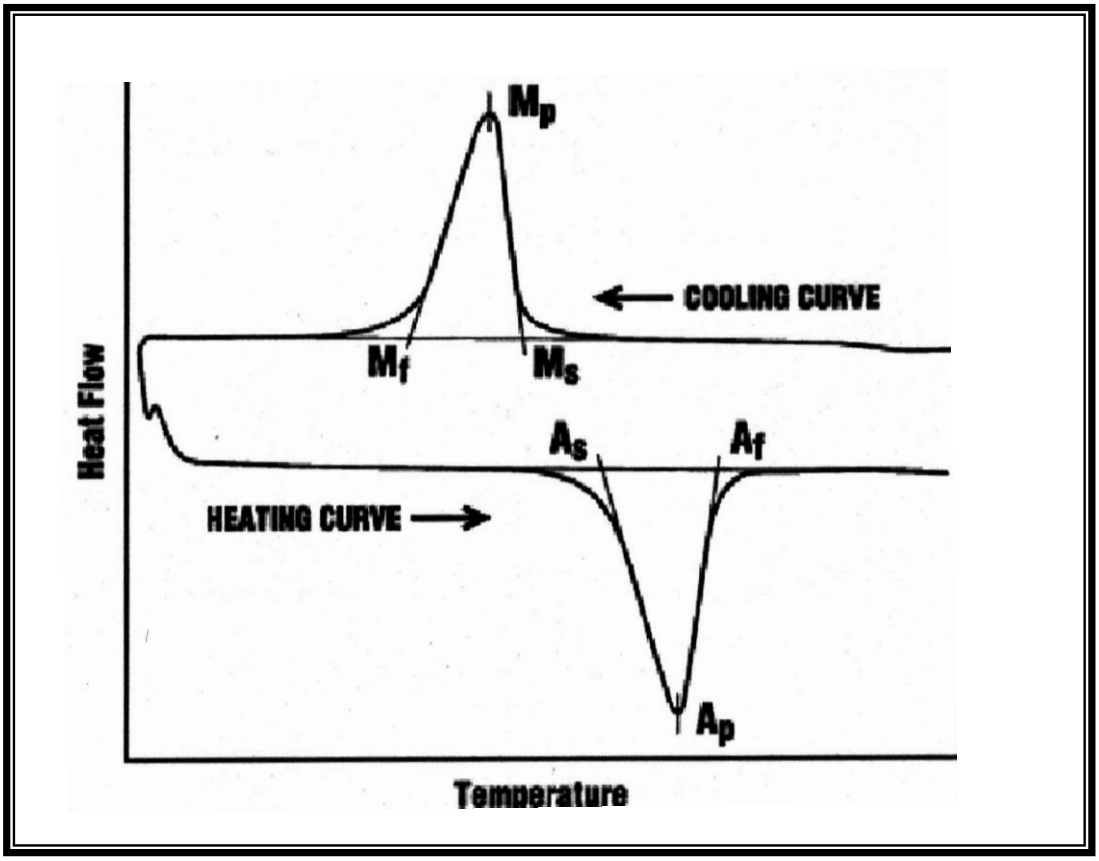

Fig. (3.10) A typical(DSC) curve for shape memory alloy **(Keefe,1999).**

Depending upon temperature , the material will generally behave in one of three ways: when cold below M_s the alloy will be in the martensitic phase, when hot above A_f the material will be in the austenitic phase and when between A_f and M_d ,the material can behave superelsticity alloy .

The behavior of the alloy is distinctly different in each temperature regime .Fig. (3.11) shows three different stress-strain responses for one shape memory alloy .[Keefe,1999].

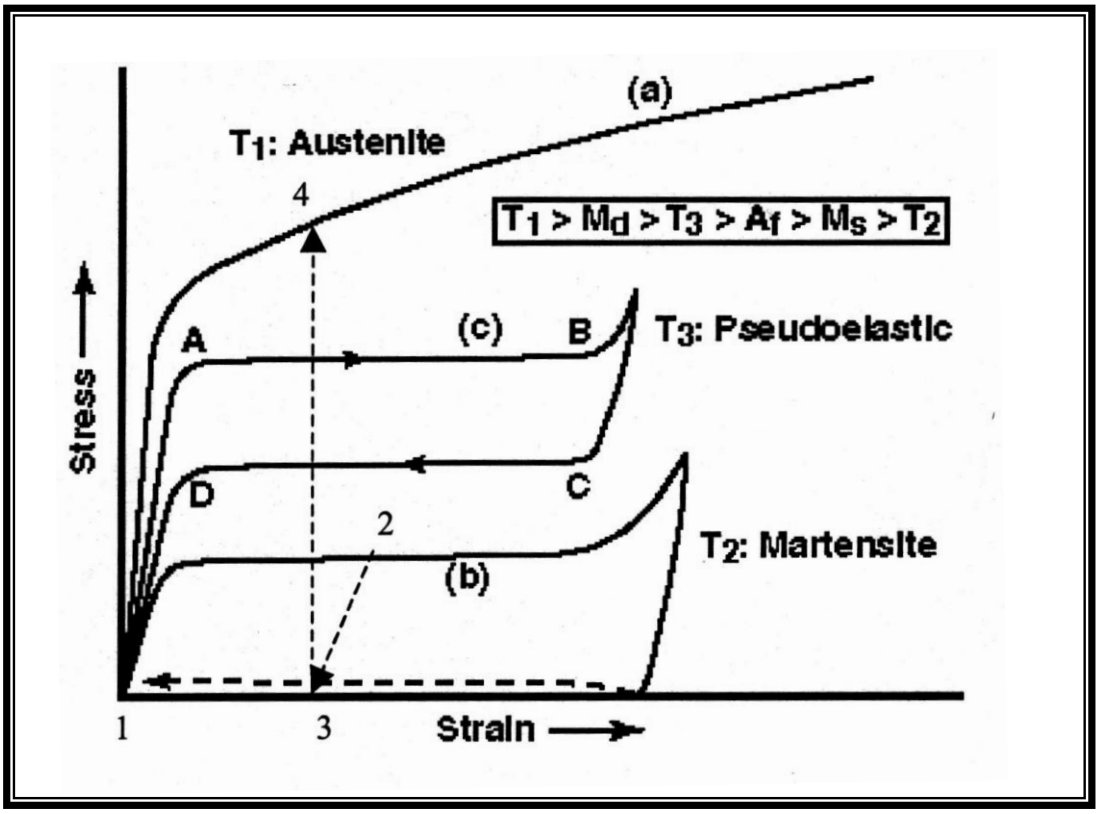

Fig. (3.11) Generic loading curve for SMA (Keefe,1999).

The shape memory effect is outlined in Fig.(3.11) by following numbers (1-4). The material is strained in martensite (1-2). At point 2, the specimen is unloading and left with some apparent plastic deformation at 3.If the simple is unconstrained and heated into austenite , all of this deformation will be completely recovered and return to point 1. However , if the piece were held fixed and heated , the stress would increase to point 4, when the (SMA) becomes fully austenitic .Point 4, corresponding to the maximum stress that can be achieved for the given amount of preset deformation .

3.2.2.2.Martensite Aging and Stabilization:

Martensite aging effect is a puzzling phenomenon unclear for over 60 years and has been found in Au-Cd ,Au-Cu-Zn,Cu-Zn-Al,Cu-Al-Ni and In-Tl . It involved two time dependent phenomena during martensite aging. One is called martensite stabilization , the other is called rubber like behavior .[Otsuka and Ren,1999].Martensite stabilization refer to the phenomenon that martensite appears to be more stable with respect to the parent phase during aging so that the reverse transformation temperatures are increased. The rubber like behavior refers to the phenomenon that martensite exhibits a recoverable or pseudo-elastic deformation behavior after aging together with an increase in critical stress as shown in Fig. (3.12).

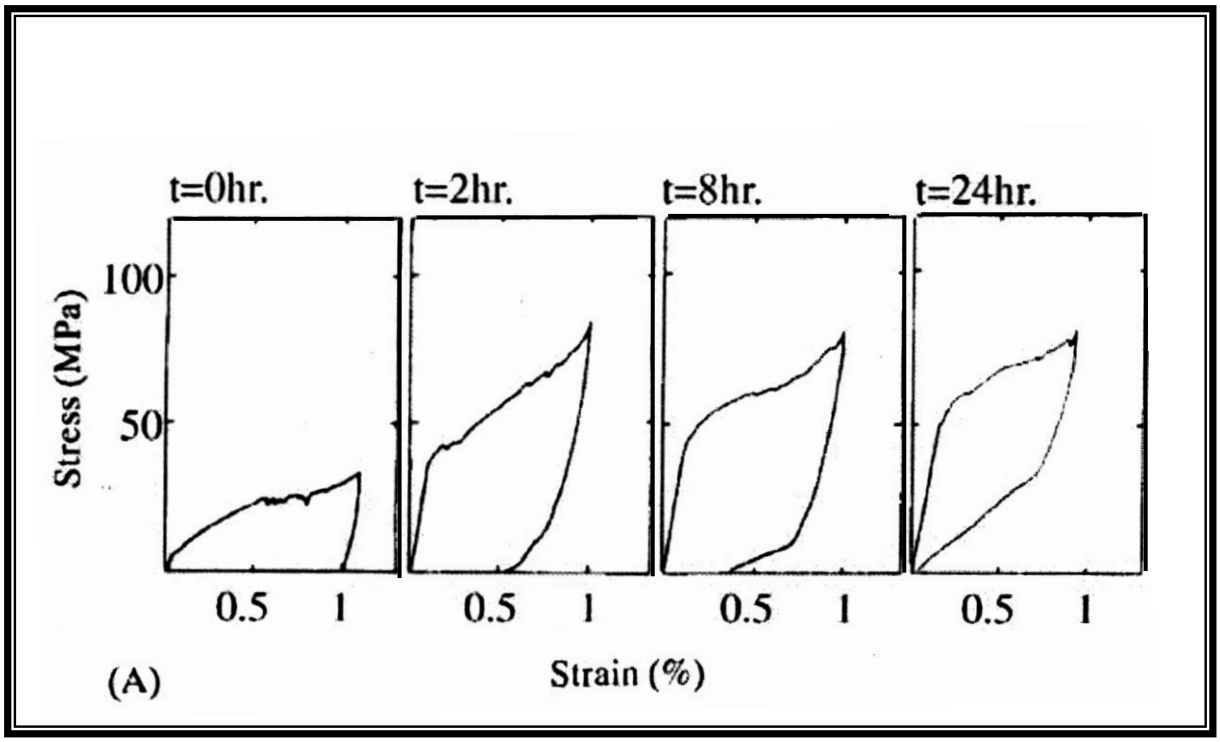

.

Fig. (3.12) The change of stress-strain curves of furnace-cooled Au-47.5Cd alloy after aging in martensite for various times t.[Otsuka and Ren ,1999]

Stabilization is a phenomenon associated with samples cooled to some temperature intermediate between M_s and M_d ,held there for a period of time and then cooled again. In such case , transformation does not immediately continue and the total amount of transformed martensite is less than obtained by

continuos cooling throughout transformation range. It has been observed that existing plates do not continue to grow after stabilization ,but the new plates are nucleated.

The degree of stabilization is a function of the time held at temperature.[Porter and Easterling,1992]. However , a general mechanism applicable to all martensites explained what is occurring during martensite aging which gives rise to stabilization and rubber like behavior , is not found.
Many previous studies using Cu-based alloys concluded that some structure change during aging in martensite is necessary to cause the aging effect.

However , martensite of these alloys are unstable and thus they have an born tendency to decompose simultaneously during aging. Therefore , the observed structure change may be just due to the inadvertent decomposition while aging itself may be independent of the decomposition. [Asanovic et al,2006].

3.3.Martensitic Transformation in Cu-based Shape Memory Alloys.

Cu-based alloys are Hume- Rothery alloys for which the phase stability is mainly controlled by the average number of valence electrons per atom. At high temperatures the crystal structure is bcc (β phase).

The β phase can be retained as a metastable phase below its stability limit by means of a suitable quench . During this quench the alloy becomes configurationally ordered.[Comas and Manosa,2000].

The body center cubic (β) phase is unstable thermodynamically at low temperature as shown in phase diagram of Cu-Al and Cu-Al-Ni in Fig.s(3.13)and (3.14).

It transforms martensitically to 3R,9R,18R or 2H . Its stability at elevated temperatures is due to the vibrational entropy from the low energy transverse phenon modes .[Ahlers ,2002].

Shears on the low –index {110} $<\bar{1}10>$ systems are therefore good candidates to describe the martensitic transformation .

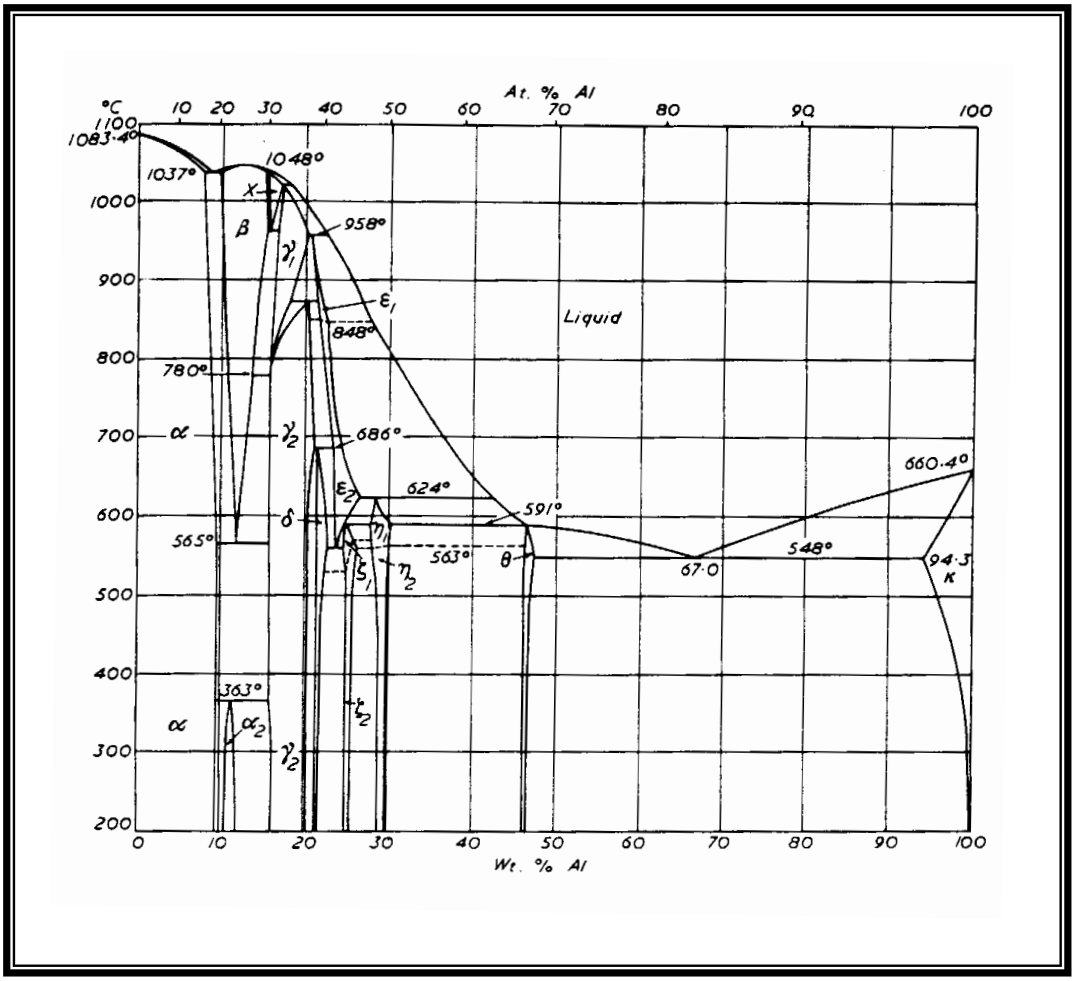

Fig. (3.13) Cu-Al equilibrium phase diagram(Higgins 1977)

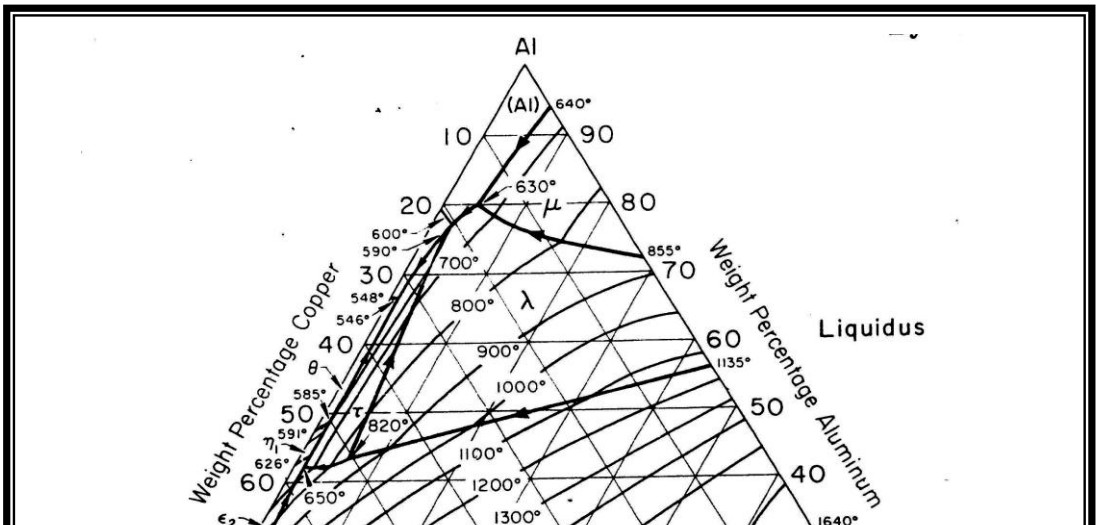

The {110} planes are also common slip planes in the bcc structures. A long wave "primary" shear combined with an additional secondary "shuffle" shear on an inclined (011) plane can indeed account for the movements of the atoms at the tip of growing thin martensite plates. It also leads to the correct martensite crystallography . For illustration consider Fig. (3.16)in which B_2 (Fig. 3.15) unit cell with the two sublattice sites and a(110) plane are indicated. The same (110) plane is plotted in Fig.(3.16)b . The circles belong to the atoms in one plane and the square to the atoms in the neighboring plane .The two different sublattice sites are shown as open and full symbols. Along-wave shear by which each consecutive plane is displaced with respect to the neighboring plane is indicated by the shifts A $\rightarrow A^{-}$ and D$\rightarrow D^{-}$, which place the atoms into the middle between the three atoms on the neighboring plane. This primary shear already transforms an inclined (011) plane into a close packed plane of martensite structure a shown in Fig. (3.16)c .[Ahlers,2002] .

Its stacking is not correct yet, and therefore additional secondary shear of these planes are required which is represented by the shift from D^{-} to $D^{=}$.

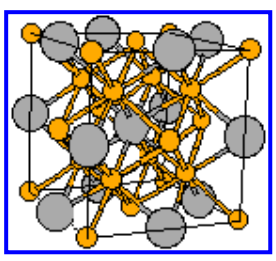

$D0_3$

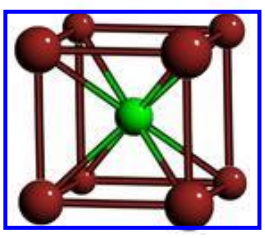

B2

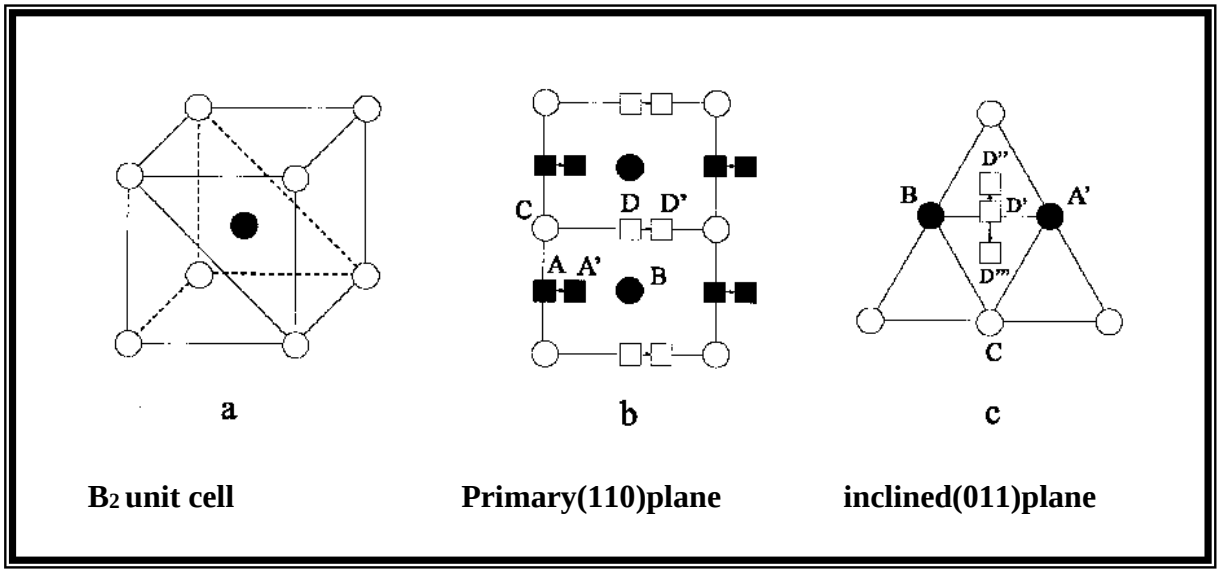

Fig. (3.16) The B_2 unit cell and primary (110) plane.(○),(●) positions in one plane whereas (□),(■), positions in the neighboring plane(Ahlers 2002).

The fraction of planes shuffled in one direction and in other direction is determined by the condition that an undistorted habit plane is created . The net amount of these shuffles has been calculated to be close to zero. This means that the number of planes shuffled the larger distance from D^{-} to $D^{=}$ must be compensated by double their number in the opposite direction .

The most homogenous distribution leads to the 9R structure with the stacking sequence ABC ,BCA,CAB .A less homogenous distribution is obtained by the shift of a whole stack of planes in one direction followed by a shift in the opposite direction . This configuration leads to the formation of twinned FCC martensite.[Ahlers,2002].

In reality the two shear occur simultaneously at the tip of the expanding martensite plate which means that the atoms on the shuffle plane are displaced continuously with its progressing distortion by the primary shear starting from the original positions on the inclined (011) secondary plane. They move symmetrically in the two possible opposite directions towards the final positions $D^{=}$ to $D^{\equiv}$ in the close-packed lattice . The 9R structure has a more homogenous interface than the twinned 3R.Once the thin plate has formed, it starts to thicken.

This process consumes little energy . It is due to the very favorable atom fit at the boundary between the two structures because of the small orientation change of the based planes.[Lovey et al,1987 Quoted in Ahlers, 2002]. Therefore the energy consuming process during martensitic transformation is the expansion of the thin plates at constant thickness in addition to nucleation.

The long range ordered Cu-based alloys retransform back to the original shape of β phase matrix. In order for this occur, two conditions have to be met .The first is that the flow stress of the matrix is so high that the distortion at the tip of the growing martensite is not relaxed by dislocation glide. A second important factor is the multiplicity of the transformation-retransformation paths of the atoms. It has been shown that in order to obtain a martensitic transformation with little energy loss two requirements have to be met. The resistance against the shears and shuffles should be small, and the transformation –retransformation path of the atoms must be single valued.[Ahlers,2002].

3.5.Origin of Shape Memory **:**

The martensite phase is generally a lower symmetry phase than is the austenite . The consequence of this is that there are several ways in which martensite can form from austenite but there is only one possible route which will return the austenite structure .Two shear directions can be applied to the squares to produce two different rhombus variants but there are no other possible variants of austenite so both of these rhombus shapes would have to return to same square geometry .This simple geometrical concept becomes the foundation for the shape memory effect. Upon cooling from austenite , the self accommodating variants of martensite are formed. The twin boundaries migrate during deformation resulting in a biased distribution of martensite variants. There is only one possible reverted structure and with reversion to austenite must return to original shape . Thus the shape accommodation due to twin boundary movement can only be supported by the less symmetrical martensitic structure and when the more symmetric austenite structure is return , the twinning deformation must also disappear .[Wayman and Duerig,1990].

The shape memory effect can be described according to the cooling and heating curves with respect to electrical resistance property.There is no change in shape of a specimen cooled from above A_f to below M_f.

When the specimen is deformed below M_f it remains so deformed until it is heated. The shape recovery begins at A_s and is completed at A_f .Once the shape is recovered at A_f , there is no change in shape when the specimen is cooled to below M_f and the shape memory can only be reactivated by deforming the martensitic specimen once again. The shape memory effect is a one time only occurrence which referred as one way shape memory. In contrast , in the two way shape memory behavior ,the specimen changes its shape upon cooling to below M_f .For example, way shape memory spring extends when heated above A_f and contracts again when cooled below M_f .Special thermomechanical treatment is required to produce two way shape memory behavior .[Wayman and Duerig ,1990].

When the external stress is applied , the variants that have shear strains tend to grow and the unfavorable oriented variants shrink as shown in Fig.

(3.17) only two variants are shown for simplicity. All unfavorable variants disappear and the favorable variant stakes over the structure. On heating, the structure reverts to the original one. Composed of equal distribution of the two variants giving the strain recovery.

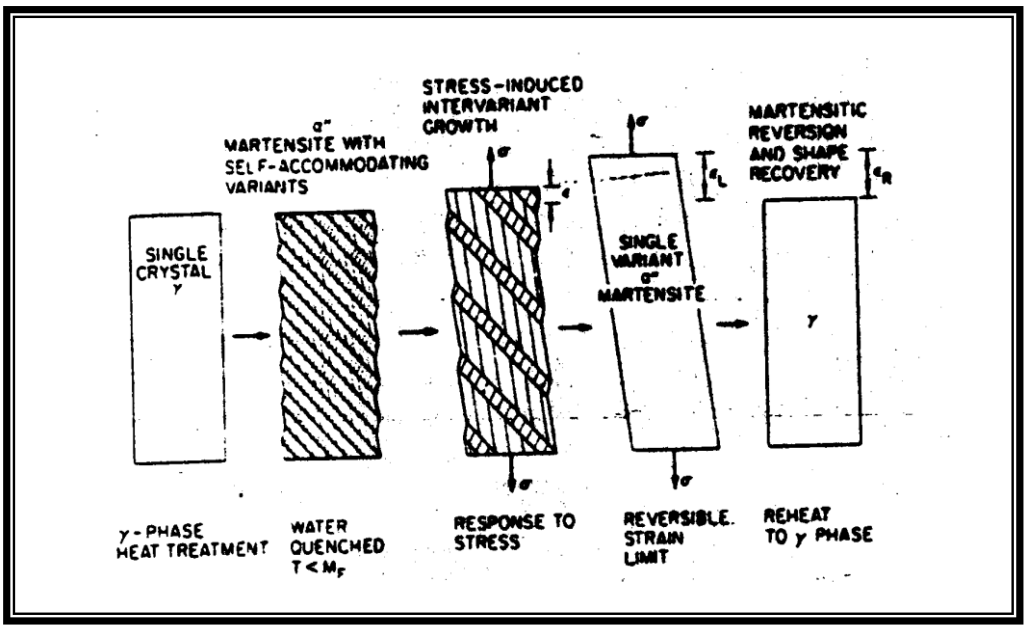

Fig. (3.17) Growth of one martensite variant and shrinkage of others.(adapted from Meyers and Chawla,1999)

The shape memory effect in tension, compression and bending loading are shown in Fig. (3.18).

Only two martensite variants are shown , A and B . variant B favors tensile strains where as variant A produces compression in the direction of loading. Under compressive stresses. Variant grows at the expense of B. Under tensile loading , the opposite is true. Under bending ,variant B grows in the outside while variant A grows in the inside. The situation in a real material is much more complex.

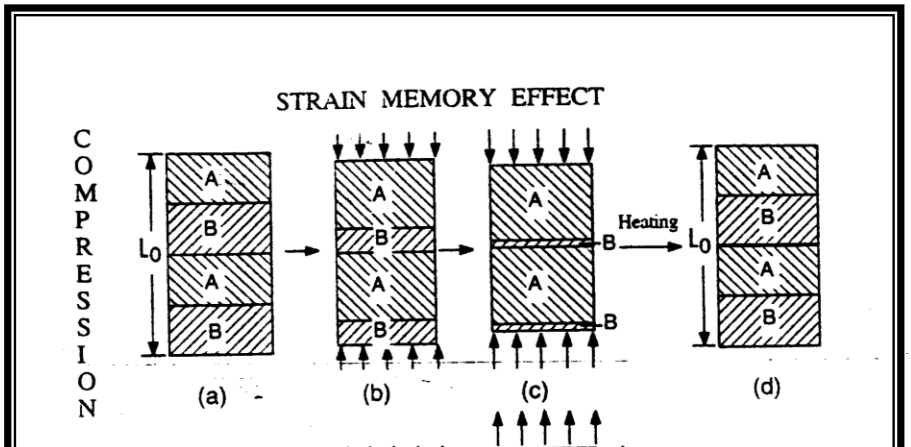

3.6. Copper-Based Shape Memory Alloys:

Both Ni-Ti and Cu-based shape memory alloys such as CuZnAl and CuAlNi, are presently available for commercial shape memory applications. In many applications, Cu-based alloys provide a more economical alternative to Ni-Ti.

Early Cu-based alloys suffered from intergranular failure causes by coarse grain structure but, recent development of fine–grain Cu-based alloys has improved mechanical properties.

Current Cu-based shape memory alloys are derived from three binary alloy systems: Cu-Zn and Cu-Sn. The martensitic transformation in Cu-Sn alloys is not ideally thermoelastic and suffers from a rapid degradation of shape memory properties during aging.[Wayman and Duerig,1990].

Cu-Zn base with al, Si, Ga, Mn as alloying elements and Cu-Al with alloying elements of Ni, Be, Zn, Mn have been explored for their shape memory properties.

In this study, CuAlNi alloys have been prepared using powder metallurgy process. These alloys are also grain refined by additives such as b, Ti, Co, Zr, Fe, Si and Mn. Further more , CuAlNi+(Ti+Mn) and CuAlNi+(B+Mn)with different percent of additives have also been studies.

3.6.1.Effect Of Alloy Elements :

The shape memory properties of Cu-based shape memory alloys are very sensitive to alloying elements which are added to adjust the martensitic transformation temperatures and to optimize mechanical properties.

The martensitic transformations in cu-based alloys occur from ordered bcc (β phase). The high temperature β phase has a disordered A_2 structure (Fig. (3.15))but upon cooling the structure goes through a nearest-neighbor ordering transition and develops the B_2 supperlattice structure .Further cooling induces next-nearest neighbor ordering and the structure eventually becomes the Do_3 or L_2,superlattice structure depend up on alloy composition and cooling rate .[Barrett and Massalski, 1980].

Martensite structure in Cu-based shape memory alloys are more complex than are those of Ni-Ti system. All are of along period stacking order type such as 3R, 6R, 9R, 18R and 2H or 4H. The thermally induced martensites in both CuZnal and CuAlNi alloys consist predominantly of β^{-}(9R) martensites. γ^{-}(2H) martensites are usually found in alloys with higher aluminum content. Mixtures of both β^{-} and γ^{-} martensites have been observed in cu-21.0Zn-5.95Al and Cu-13%Al+ 4.09% Ni. In both systems, the stability of γ^{-} martensite increases with aluminum content .

The stress–induced martensite from parent β phase normally have the same structure as thermally induced martensites ,further more , β^{-} martensites can also

be induced upon stressing the γ' martnsites .the stability of β' and γ' marteensites depend upon stress and temperature .[Wu,1990].

3.6.2.Effects Of Heat Treatment:

Cu-based shape memory alloys are affected by heat treatment such as solution (Betatizing) treatment and aging through changing of transformation temperatures (A_s,A_f,M_s.M_f) .All transformation temperatures are increased with increasing betatizing temperature.[Wu,1990].Also ,extending of betatizing time from 10 to 60minuts raises transformation temperature . This effect is related to grain growth during solution treatment.

Both the parent phase (β) and martensite in Cu-based shape memory alloys are susceptible to aging effects. For CuZnAl alloys, a direct quench into the austenite β phase results in depressed transformation temperatures which increase and stablize during subsequent aging at low temperatures.[Asanovic et al,2006].

When CuZnAl alloy is stabilized by post-quench aging and is then subjected to exposure at temperatures of 100-350 C°, the change in transformation temperatures can be classified into three stages as shown in Fig. (3.19). The first is characterized by a rapid drop of transformation temperatures which are then recoverable during subsequent aging at temperatures below 70 C° . The amount of depression increases with aging temperature up to 300 C° and then decreases with further increases in the aging temperature .

The transformation temperatures increase only moderately with time during the second stage.

The temperatures decrease drastically and the hysteresis is widened, in third stage. [Wu,1990].

It has been shown that the post quench aging effect and the first stage behavior are related to the ordering in CuZnAl alloys . The second stage is probably related to the growth of ordered domains where as the third stage aging

characteristics have been demonstrated to be caused by the decomposition of the β phase into bainite or α phase .[Asanovic et al,2006].

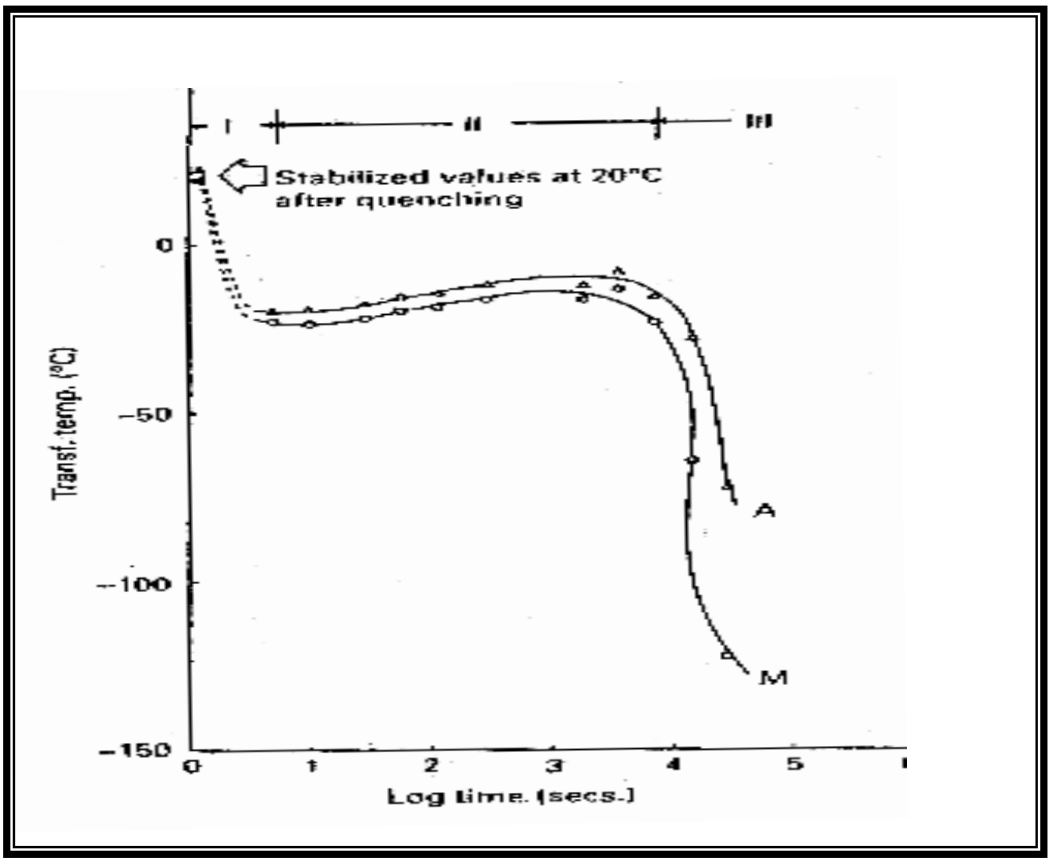

Fig. (3.19) Changes in M and A temperatures of cu-26.67Zn-4Al alloy during aging at 200 C° .(Wu,1990) .

Direct quenching of CuZnAl alloys into martensitic state causes stabilization of martensites which may not transform back to the parent phase during subsequent heating up to 150 C° as shown in Fig. (3.20) which clear the resistivity curve of Cu-25.8%Zn3.58Al alloy with M_s =100 C° after directly quenching from the solution treatment to the ambient. No transformation is detected whereas step-quench process with intermediate aneal in the parent phase(β) state at 150 C° gradually restore transformation as shown in Fig. (3.20) .[Wu,1990].

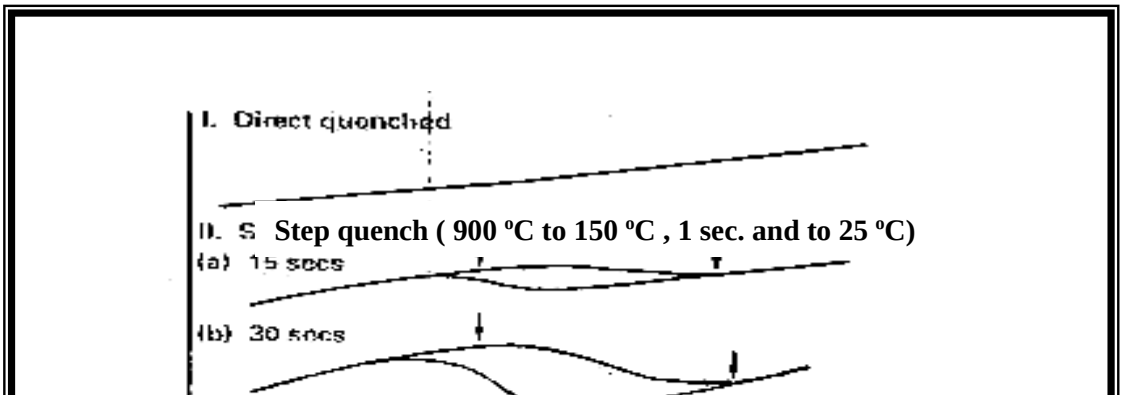

Fig. (3.20) Effects of quenching on transformation resistivity curve for Cu-25.8Zn-3.6%Al alloy. [Wu,1990].

Aging of CuZnAl martensites also causes martensite stabilization through increase A_s and A_f to higher temperature.[Asanovic,2006].

The aging effects in CuAlNi alloys are sensitive to Ni content. For most alloys containing 3-5%Ni, the transformation temperatures increase with aging time at 200-300 C° temperatures and decrease at higher aging temperatures .e.g.400 C° . The aging characteristics are related to reordering at the early stage and later to the precipitation of γ_2. Which causes the depression of transformation temperatures. [Wu,1990].

3.7.Powder Metallurgy of Cu-Based Shape Memory Alloys:

Fine grain copper based shape memory alloys without grain-refining element additions can be produced by powder metallurgy. A grain size of around 30μm has been obtained in a powder processed CuZnal alloy which was water atomized to an averaged particle size of 150 μm and subsequently cold

Powder processed CuZnAl shows better resistance to cycling degradation

in recoverable strain than conventionally processed alloys. A powder processed CuAlNi alloy with grain size of 20 μm exhibits a significantly improved ductility from 5 to 7% compared to 0.6% in cast alloys.[Wu,1990].

Porous shape memory alloys exhibit all the same properties as their dense counterparts but with added benefit of low density and the ability to undergo larger deformation before failure. Furthermore , porous SMA would take advantage of the inherent damping of shape memory alloys while at the same time providing structural rigidity and decreased weight.[Penrod,2003].

Porous SMA_s are manufactured by several different ways based upon application, structure and properties which can be adjusted to meet a specific need.In the following , general explanation for copper based alloys powders preparation , mixing, compacting and sintering have been presented.

3.7.1.Preperation of Copper Powder:

Because of the majority of copper content in copper base shape memory alloys , great attention for production of copper powders, has been presented in this section . Copper powder containing more than 99% Cu is available commercially . The four major methods for producing unalloyed copper powders are oxide reduction, atomization , electrolysis and hydrometallurgy .[stevenson,1984]. Brief description of these processes are presented in the following :

3.7.1.1.Production of copper Powder by the reduction of Copper Oxide:

reduction of copper oxide is the oldest and by tonnage ,the most extensively used process for the production of copper powder . In the this process , particulate copper oxide is reduced with gaseous reducing agents at elevated temperatures. The product is essentially a sintered porous cake of copper that must be ground to powder . Raw materials include copper scale, cement copper , particulate copper scrap and atomized copper. Particulate copper scrap and atomized copper are roasted to form cuprous and cupric oxide. Various approaches for producing copper powder by oxide reduction . They differ

mainly in the degree of oxidation of the starting material prior to reduction .[Stevenson,1984].

3.7.1.2 .Production of Copper powder by Atomization:

Atomization of copper is the disintegration of a molten stream of high quality copper with high pressure water jets, which produces copper powders of compacting grade quality. The resulting denied powder may be subjected to an elevated temperature treatment to modify its engineering properties.

Nearly spherical powders result from the atomization of liquid copper with inert gas or air. These powders are used to produce fake copper powders. Spherically shaped copper powders have insufficient green strength for use in conventional powder metallurgy.[Dowson,1990].

Liquid copper is superheated to about 1150 to 1200 C° utilizing flow rates of 27Kg/min or more with water pressures of 10-14Mpa.Atomization may be conducted in an air or inert(N_2 gas)environments.

3.7.1.3.Production of Copper Powder by Electrolysis:

Production of electrolytic copper powder as shown in Fig. (3.21) , depends upon electrochemical principles that apply to the electro refining of copper . The conditions of deposition are changed to yield spongy deposit instead of the strongly adherent product. The formation of powdery deposits is favored by low copper ion concentration, high acid content in the electrolyte and high cathode current density.

Although , these conditions yield spongy deposits, control of additional variables such as temperature, circulation rate of the electrolyte , size and type of anode and cathode and electrode spacing, is necessary to produce copper powders.[Jasim,2006].

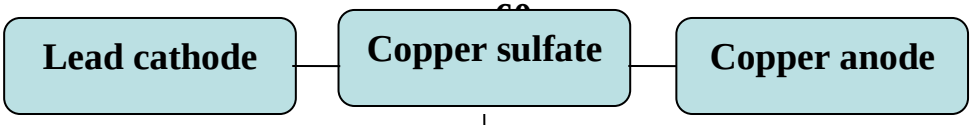

Fig.(3.21) flow chart for production of electrolytic copper powder[adapted from Klar,1984]

3.7.1.4.Production of Copper Powder by Hydrometallurgyical Processing :

Copper powder can be produced by hydrometallurgical methods which consist of preparing pregnant liquor by leaching ore or another suitable raw material followed by precipitation method of the metal from this solution. The most important precipitation methods are cementation , reduction with H_2 or sulter de oxide and electrolysis .Use of several leach precipitation steps or the inclusion of floatation , solvent extraction or ion exchange improves the purity of the final material.

3.7.2 Blending and Mixing processes:

Blending is an operation of through intermingling of powders of the same composition or substance while mixing is defined as the through intermingling of powders of several or more different materials .Mixing is extremely desirable in the preparation of alloys from elemental powders .[Sinha,1995].

Additives such as binders or lubricates are usually included in both types of processes to facilitate pressing and achieve the required green strength and controlled porosity in the final product. Mixing of powders is a most complex process which relies on the movement of mass of one powder component into that of another powder component. This movement is dependent upon powder material, particle size and shape and surface conditions.[Sinha,1995].

The main purpose of mixing is to produce uniform distribution of powder and to control the powder characteristics .It must produce a homogenous mixture in the least possible time .

Time of mixing is of great importance. It is very difficult to determine the optimum mixing time in advance because of our limited knowledge of the friction in powder mass. Some problem that can take place during mixing, are variation in particle size distribution through agglomeration , oxidation of powder particles and segregation of powder during transfer from the mixer.

Time of mixing may vary considerably from a few minutes to 24 hours or more. It may be accomplished in air , under protective atmosphere or under suitable liquid to avoid partially or completely oxidation or segregation.

Mixing is accomplished by various types of blenders and mills such as ball mills, road mills and double cone mixers.

It has been shown that there are three mechanisms which occur in mixing process included the following :

1.Transfer of groups of adjacent particle from one location to another called as "connective mixing".

2.Distribution of particles over a newly developed surface known as "diffusive mixing".

3.The formation of slipping planes within the mass called as "shear mixing"

All of them are always occurred in operation but the degree of any one of these will depend upon the mixing machine .[Sinha,1995].

Mixing may be either dry or wet based on the medium in which the milling is carried out. Wet mixing is used to produce more fine and uniform mixture of powder particles. Wet mixing may be obtained by the addition of alcohol, benzene, glycerin or acetone as a liquid medium in adequate amount in order to bring the powder to the consistency of a thin paste. After completion of the mixing process, benzene or acetone is removed by during the mix in air or in a controlled oven up to 50 C° .

Mechanical alloying is a relatively new technology that enables a large variety of advanced material obtaining. It consists of material milling in a high energy mill process producing repeated powder particle deformation ,work hardening , fracturing , clean surface , local heating and solid state welding. Re-fracturing and so on, under the impact energy transferred to them from collisions of the chaotic moving balls. Pure solid solutions of alloys of an extended solubility limit are obtained if components does not react each other.[Orban,2004].

It has been shown that mechanical alloying and powder metallurgy techniques can be used to prepare Cu-based shape memory alloys. Mechanical alloying can reduce oxidation because a new phase is formed and produces a pre-alloyed powder that shortens the sintering time. For CuAlNb shape memory alloy prepared by mechanical alloying, the ball to powder weight ratio is 6:1 with 150rpm rotation rate.[Silva and Lima,2005].

3.7.3.Particle Shape and Powder Density:

Although shape of powder particle is importance it is not normally specified or determined directly . It is not easy factor to measure and almost impossible to quantity. There is a number of commonly occurring shapes such as granular, a circular, irregular ,flaky and spheriodal. Particle shape has a major influence on the packing density of powders and this is a factor that can be measured.

Spherical powders pack most density and the density decreases as the irregularity of the particle shape increases.

There are two was of expressing this bulk density that are in general use in powder metallurgy. The most widely used is apparent density ($\rho_{ap.}$) which is

the density of powder mass expressed as grammes per cubic centimeter of a standard volume of powder gently loaded under specified conditions into a cylindrical container of specified volume .

In the other test a weighed sample is placed in a graduated cylinder which is tapped or otherwise vibrated in a standard way until the volume is constant. This gives the tap density or tapped density which is higher than the apparent density.[Dowson,1990].

Most powder are three dimensional in nature. These powder may be equiaxed and nodular but uniformity of shape does not completely exist within anyone type of powder. However, advancements in qualitative analysis are based on the use of the scanning electron microscope(SEM) for determination of particle shape. In addition to its high magnification capability, this device produces an image with a three dimensional appearance.

3.7.4.Particle Size and its Distribution:

particle size and size distribution have a significant effect on the behavior of metal powders during processing thus to a considerable extent, they govern the properties of the final products made from powder.

It affects most of the properties such as mould strength, density of compact, porosity , expulsion of gases, dimensional stability, flow and mixing characteristics .[Ullrich, 1984].

Particle size is expressed by the diameter for spherical shaped particles and by the average diameter for non-spherical particles. Average diameter is defined in different ways according to the method employed for size distribution .When the method involves sizing ,the particle size is measured as the opening of a standard screen which just retains or passes the particle. When determined by microcount method ,the diameter is measured by averaging several dimensions. According to the sedimentation method the particle size is defined as the diameter of the spherical particle having the same specific gravity and setting velocity as the non spherical particle under test. In practical metal powders are divided into three distinct classes sieve, sub sieve and sub micron or ultra fine . The screen with the opening of finest standard mesh sieve for production purposes is the 325 mesh screen having the aperture of 44 micron.

Whereas sub sieve particles are smaller than the aperture of mesh screen but greater than 1 micron. There are several techniques of particle size measurement which have been shown in table (3.2).

In this study optical microscopy has been used to analyze shape, size and distribution of particles for elemental powders and their alloys through taking digital images for optical microstructure with suitable magnification and analyzing of these image with image analysis program taking into consideration image analysis and image processing .

Table (3.2) Common methods of particle size measurement and their limit of useful size range.[Sinha,1995].

Method of analysis	*Particle size range (micron)*
1.i- sieving using mechanical shaking ii-Micro mesh sieve	44→840 5→44
2.Microscopic analysis i-light microscopy ii-SEM	 0.1→100 0.001→10
3.Sedimentation method i-Sedimentation and decantation ii-Gravitational iii-Centrifugal	 2→50 0.05→50 0.05→10
4.Elutration method i- Elutration ii-Roller air analyzer	 5→100 5→40
5.Permeability method i-Permeability ii-fisher sub-sieve size	 0.5→100 0.2→50
6.Adsorption method (gases)	0.002→20
7.Electrolytic resistivity method (coulter counter)	0.3→300

3.7.5.Powder Compaction of Cu-based Alloys:

Powder of copper–based alloys is usually preformed in a closed die although other means such as hot pressing, roll compaction, isostatic pressing, extrusion and forging can be used. Brief description of these processes has been presented as follows:[Stevenson,1984].

3.7.5.1.Die Compaction:

Compaction in metal dies is one of the most important methods for shaping metal powders. When the die cavity is uniformly filled with copper powder it gives rise to certain packing density (apparent density) but a certain amount of bridges are also formed, when the powder is slightly pressed by the application of one punch or more punches as shown in Fig.(3.22), the first densification occurs by particle movement and rearrangement causing improved packing density which all bridges are collapsed. The degree to which this occurs is dependent upon particle size distribution, particle shape, amount of lubricants.

The interparticle movement produces superficial abrasion of surface film comprising oxides which absorbed atmospheric gases which are usually present or wedged between the metallic surfaces. These films obstruct the occurrence of direct metal contact and thus the formation of appreciable interparticle bonding due to the interparticle movement, the films surrounding the particles are ruptured which are more brittle with respect to the metal underneath.

The initial contact areas between the particles are so small that even a slight punch load causes very high pressure on these areas there by breaking up the surface films at the areas of contact. At this stage compacting produces only dense packing of powder particles.

There is no deformation or adhesion between the individual particles. If the pressure is more increased, the clean particles are brought close enough together and they adhere to each other with some strength. Further increase in pressure causes deformation of particles and large areas of contact of neighboring grains will take place companied by filling of voids by the

squeezing of small particles, due to this , strength and density are increased.[Sinha,1995].

Deformation is the major mechanism of densification with regard to production of high density parts.

Both elastic and plastic deformation may be took place. Most of elastic deformation will be recovered on removal of stress from the compact. This occurs before, during and after ejection from the die cavity.

Most of metal powders work hardens to a suitable extent so that they become more difficult to improve densification of the compact by increasing pressure of compacting. However ,low pressures may be more effective since plastic deformation may occur at ease and the external pressure will be become less effective with increasing pressure.[Sinha,1995].

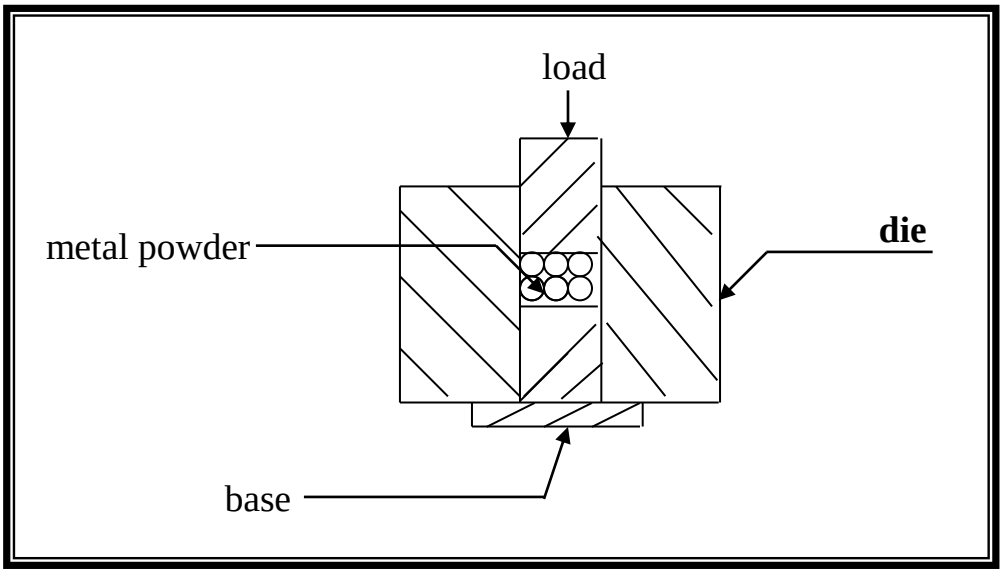

Fig. (3.22) Tools Die Compaction

During compaction, several types of friction will be occurred as follows:

1. Friction between moving punches and die wall which is relatively small.
2. Friction between adjacent particles which is insignificant and play a minor part in compaction .

3. Internal friction within the powder particles during deformation.
4. Friction between powder particles and the die wall which is the most important factors which effects the uniformity of density throughout thr compacted part.
5. Friction between the green compact and the die wall ejection which based upon powder material, die finish and compacting pressure.[Sinha,1995].
6. To reduce the effects of all above friction, lubricants from low melting materials such as Li, Zn, Al strearates can be used. It has been shown that the lubricant Zinc stearate forms a protective film on the powder surface and hinders diffusion between Aluminum and Copper in CuAlNb shape memory alloy.[Silva and Lima,2005].

There are several different types of die compaction techniques but here ,two important types are considered as follows:

1.Single-action compaction which is used for manufacture of flat, thin parts such as washers , discs and thin rings or short rods. The die and the lower punch are stationary during application of pressure by the motion of upper punch acting from one direction only on the powder placed in the die cavity. This type of compaction has been used in this study to prepare disc samples and cylindrical samples.

2. Double–action compaction denotes a system in which powder is compacted simultaneously from opposite directions by both the top and bottom punches. Equal or different amounts of movements and pressure may be used from each direction as shown in Fig.(3.23).

Upper punch

Fig.(3.23) Double action compaction system

3.7.5.2.Isostatic Pressing:

Isostatic pressing is the consolidation (refers to the production of coherent metal structures using metal powders as the major raw material) of powdered material contained in a tightly sealed flexible mould into shaped bodies in which uniform pressure is applied simultaneously and equally in all directions which leads to achieve uniform density and strength.

If the pressure transmitting medium is liquid such as water , glycerin or various hydraulic oils, the term more specifically used is hydrostatic pressing whereas gases, powders, rubber or plastic medium refers to as isostatic pressing process .[Sinha,1995].

3.7.5.3.Roll compacting:

Roll compacting refers to the continuous compaction of metal powders by a rolling mill in which metal powders are fed from a hopper to a set of rolls that produce a continuous green strip or sheet as shown in Fig. (3.24).[Knopp et al,1984].

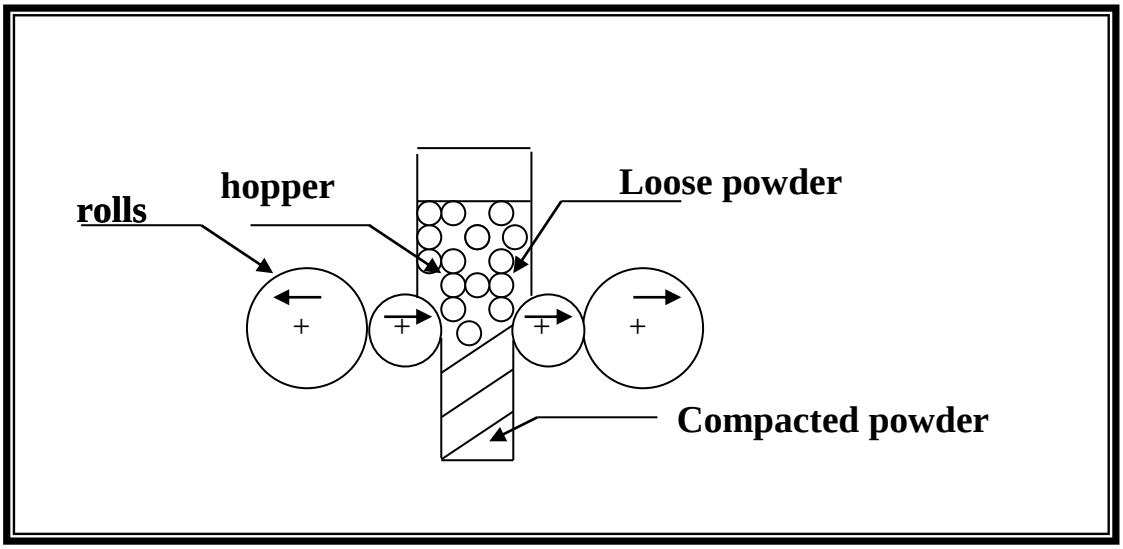

Fig. (3.24) Typical roll compaction of copper strip.

3.7.5.4.Powder Extrusion:

This process consists of extruding the mixture of powders at high pressures and high temperatures (850 for copper base alloys) through the suitable die.

In this process, binding material such as paraffin wax is used to binds the powder particles and to minimizes the friction against the die wall. Extrusion of bars, rods, tubes and thin sheets may be used to satisfy extremely high densities.[Sinha,1995].

3.7.5.5.Powder Forging :

In this process, pressed powder perform by die compaction or isostatic compaction is heated to hot working temperature in a protective atmosphere and immediately transferred to close die and forged. After forging, the component is quenched or cooled in protective medium to minimize oxidation. This produces densification up to 100% and involves lower sintering temperature. The green

compacts are given the combination of sintering and forging preheating instead of sintering in a normal way.

3.7.5.6.Hot Isostatic Pressing (HIP):

Hot isostatic pressing is a material processing technique in which high isostatic pressure is applied to powder compact at elevated temperatures to produce particle bonding. This process usually results in the manufacture of a fully dense body.

During compacting, the compact is subjected to equal pressure from every side. Elevated temperature ranges from 480 C° for aluminum alloy powders compacting to 1700 C° for tungsten powder compacting. High density argon gas is the most common medium used in the process and pressure range from approximately 20 to 300 Mpa .[Price and Kohler,1984].

A pressure of 140 Mpa at 850 C° which is applied during 2 hours, has been used to hot isostatic compacting of CuAlNi shape memory alloys.[Raul et al,2000] .

3.7.6.Sintering of Copper-base alloys:

Sintering is the thermal treatment of a powder or compact at a temperature below the melting point of the main constituent for the purpose of increasing its strength by bonding together of the particles.[Dowson,1990].

Sintering is carried out at a temperature in the range of 0.7-0.9 of the absolute melting point of the base metal in a multi component powder system. Sintering is a very complex process in which physical, chemical and metallurgical effects interact simultaneously. Sintering process is concerned with the following:

1. Diffusion of particle to particle.
2. Formation of grain boundaries.
3. The closing of voids present in the green compacts.

Furthermore, the decrease in free energy due to the decrease in surface area is the main driving force of sintering.[Sinha,1995] .

Typical sintering furnace temperatures for Bronze range from 815 to 860 C° with total sintering time in hot zone from 15 to 30min depending on the furnace temperature selected, required dimensional change and the mechanical properties desired after sintering .

For brasses, sintering temperatures range from 760 to 925 with time from 10 min to 45 min.[Mathews,1984].

3.7.6.1.Stages of Sintering:

The fundamental aspect of sintering is that it is carried out at constant temperature and time is varied to obtain the desired results. There are three stages of sintering as follows [Sinha,1995]:

I.Adhesion without shrinkage:

Initial bonding and neck growth occur rapidly and very early in the sintering process when the powder compact is being heated up. In this stage, great extended of bonding within the sinter mass may continue for some more time.

This first stage of consists of volume diffusion of vacancies from the neck region to the convex portion of the system remote from the neck and surface diffusion between surface regions with different radii of curvature.

II. Stage of Densification and Grain Growth:

Here, most of the shrinkage occurs in which more pore rounding takes place so that network of pores is formed and grain growth continue. Closed pores with increase pore size and decreased numbers of total pores are obtained by volume diffusion of voids from the interior towards the surface. Smaller pores must have been absorbed more rapidly by the larger ones.

III. Elimination of the last isolated and rounded pores:

Here, the spheroidization of isolated pores rapidly increases and pore shrinkage has been occurred more quickly in the vicinity of the grain boundary.

Further densification proceeds at a low rate.

3.7.6.2.Mechanisms of Sintering:

Several mechanisms of sintering are considered as follows:

I. Adhesion Mechanism:

Adhesion between metal surfaces is an elementary bonding process which does not involve material transport. Adhesion processes exert a decisive influence on sintering but not during intermediate and last stages of sintering.[Sinha,1995].

II. Material Transport Mechanisms:

There are six possible mechanisms of material transport which are briefly explained here in the following:

1.Recovery and Recrystallisation :

It involves the movement of atoms over very small distances which are observed in powders having severe lattice distortions and are related with grain growth during densification.

The removal of stress in the micro-contacts also promotes mutual binding between the particles in the initial stages.[Sinha,1995].

2.Viscous Flow:

under the effect of applied pressure , it is expected that the plastic flow of material will slowly fill up the pores. Viscous flow occurs according to the equation :

$\tau = \eta \, d\varepsilon_{xy} / dt$ ----------Eq.(3.2)

where :

τ –shear stress

η-viscosity

$d\varepsilon_{xy} / dt$ -shear strain rate

For other materials which behave as a solid with a yield point which vary with temperature, the equation of viscous flow becomes :

$r_n^2 / r_p = 3/2 \, (\gamma/\eta) \, t$ ----------Eq.(3.3).

where:

r_n -radius of neck between two particles

r_p - particle radius η- viscosity

γ- surface tension t-time

This mechanism relied on the rate of increased contact area between two spherical powder particles to calculate the rate of sintering solid mass. This theory has been established in hot pressing. [Sinha,1995].

3.Evaporation and Condensation Mechanism:

It involves material transport through a gas phase, in which evaporation from the convex portions or the surfaces of spheres and condensation in the neck area due to higher vapor pressure over the convex surface comparison with neck region have been occurred. Because most metals do not have high vapor pressures at temperatures near their melting points, evaporation and condensation contribute normally to material transport in metallic systems.[Lenel et al,1984].

4.Lattice Diffusion Mechanism:

Diffusion flow is the most important mechanism of material transport which is based on the concept that a certain concentration of vacancies exist in crystal lattice of a metal.

Vacancy gradient exists between neck area and the interior of the system , between points on the surfaces having different curvatures. Further more ,vacancy gradient exists between distorted and undistorted lattice and particles centenss and midpoints of contact with adjacent particles.

Vacancy diffusion during sintering is obtained by the geometrical arrangement and type of vacancy sources and sinks. Vacancies diffuse from the neck area or high curvature regions to the interior or regions of low curvature while atoms diffuse in opposite direction to cause welding.[Sinha,1995].

Smaller pores and concave surfaces act as the vacancy source and grain boundary, convex surfaces and larger pores act as vacancy sinks. Lattice or volume diffusion works at elevated temperatures at which the value of surface

diffusion diminishes due to the decrease in particle specific surface and large temperature dependence of the lattice (volume) diffusion coefficient at high temperature as shown in eq.(3.4).[Sinha,1995].

$r_n^2 / r_p^2 = (Kv\gamma/RT)^* D_v .t$ ----------Eq.(3.4)

where:

D_v -volume (lattice) self diffusion coefficient

K- constant dependents upon surface geometry of the system and nature of vacancy sinks.

R- gas constant, T- absolute temperature ,T-time,γ-surface tension , v- volume

Fig. (3.25 a) illustrates a cross section of a two shape model. The radius r_c is the radius of curvature , r_n is the neck radius and radius of particle r_p. In Fig.(3.28 b) volume diffusion indicated by path (a) and surface diffusion indicated by path (b).

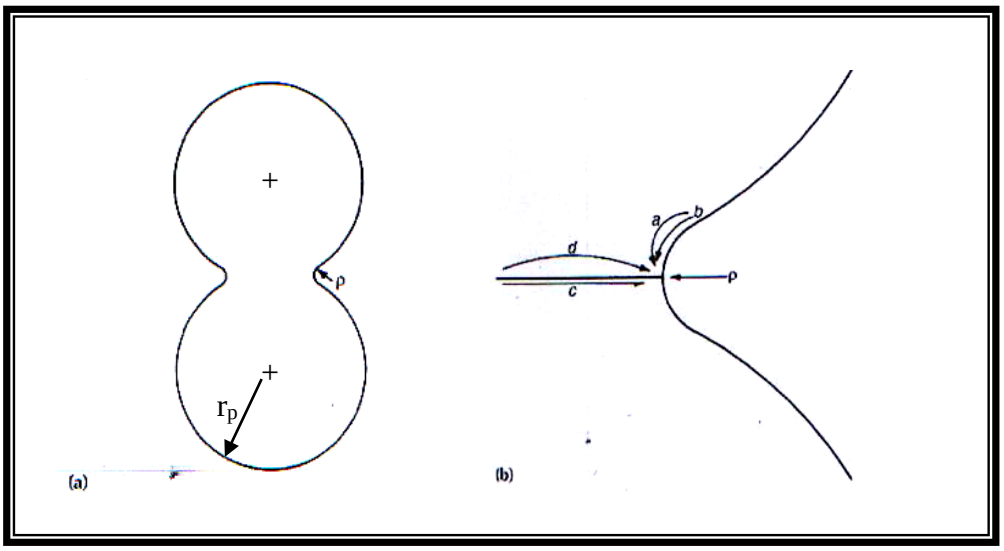

Fig. (3.25) Cross section through two spheres sintering together in [a] and volume diffusion and surface diffusion baths in [b], where path (a) , volume diffusion from flat surface to the neck. Path (b) , surface diffusion from the flat surface to the neck. Path (c), grain boundary diffusion from the grain boundarythe neck. Path (d) ,volume diffusion from the grain boundary to the neck.[Lenel et al,1984].

Assuming that the two particles are single crystals with different orientations, a grain boundary is formed at the neck. The difference in curvature at the neck with r_c and adjacent flat surfaces causes a difference in stress and chemical potential between two points which produces a gradient in the

concentration of vacancies between highly curved neck surface and the adjacent flat surface the high and low concentration of vacancies respectively.

5.Surface Diffusion Mechanism:

It refers to the movement of atoms on external surfaces therefore, exchange between surface atoms and surface vacancies is occurring during sintering. Surface diffusion occurs in all sintering processes which is responsible for the neck formation between adjacent particles. It is significantly important for sintering fine powders at low temperature where the effect of volume (lattice) diffusion is insignificant. Path (b) in Fig.(3.25 b) illustrates the surface diffusion . Surface and volume diffusion flow cause rounding and spheroidization of irregular pores in compacts. However, they do not explain shrinkage which may be represented by a decrease in the distance between the centers of the two spherical particles.

6.Grain Boundary diffusion Mechanism :

Grain boundary is considered to be formed between adjacent particles in the original sinter compact and it is expected that vacancies are moving directly along grain boundaries to external surfaces. In grain boundary diffusion, a slow displacement of grain boundaries takes place through a region of voids which remove them.

Elimination of last isolated pores during the last stage of sintering is due to grain boundary diffusion.[Sinha,1995].

The atoms from either the external surfaces or locations along the grain boundaries would diffuse down the grain boundaries which result in neck growth , rounding of pore or shrinkage of pore . This mechanism is found to be more effective with decreasing sintering temperature .

3.7.7.Liquid Phase Sintering :

In system involving mixed powders, liquid formation is possible because of differing melting ranges of the components. Common systems involving

liquid phase sintering for copper base alloys include copper-cobalt, copper-tin, copper-zinc, copper-phosphorous and copper-aluminum.

Heating of a mixed –phase system begins with a mixture of elemental powders. When the liquid forms, it flows and wets the solid particles and begins acting on the solid phase. Melt penetration between the solid particles can cause swelling of the compact especially if the green density is high and the particles are coarse. However, along with melt penetration, there is possible rearrangement of the particles.

The combination of wetting, liquid flow and particle rearrangement contributes to a rapid change in the volume of the compact. When heating is continuing in the presence of a liquid phase, the solid phase begins to dissolve.[Lenel et al,1984].

Based upon experimental observations, the stages of liquid phase sintering are given as follows:

1. Melting and liquid flow involving a rearrangement of the solid particles.
2. Rapid dissolution of the small solid constituent and reprecipitation on the larger ones.
3.coal essence of solid of solid particles involving slow densification.

The characteristics of typical liquid phase sintering include that the liquid phase wets the solid so there is a solubility of the solid in the liquid , and the amount of liquid phase should be large enough to occur an appreciable densification.[Sinha,1995].

The first stage refers to large scale bulk movement of particles within the liquid phase causing rearrangement of the particles and densification. It has been noted that densification increases with the increasing the amount of liquid phase. The densification is very rapid in this stage.

It has been shown that a liquid drop in contact with a solid surface (as shown in Fig. (3.26)) obeys the following equation [Parker ,1981]:

$\cos\theta = (\gamma_{GS} - \gamma_{SL}) / \gamma_{LG}$ ----------Eq.(3.5).

Where:

θ -contact angle

γ_{GS}-surface tension of solid –gas interface .

γ_{SL}-surface tension of solid-liquid interface.

γ_{LG}-surface tension of liquid –gas interface .

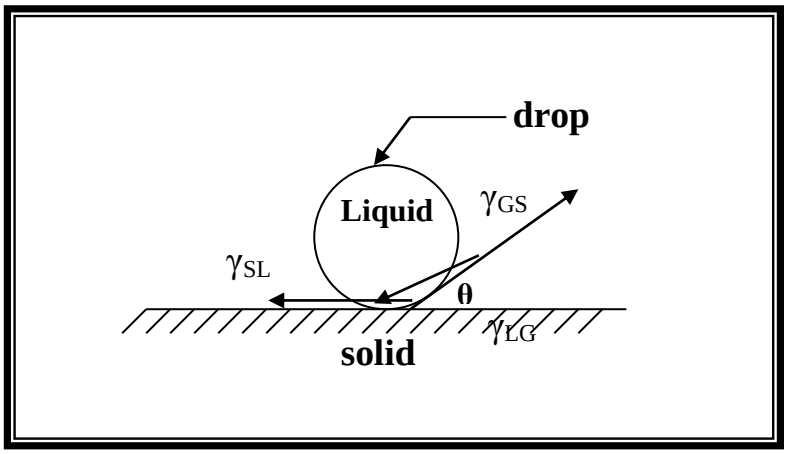

Fig. (3.26) Interfacial surface tension between gas, liquid and solid phases.

If the liquid phase completely wet the solid particles , contact angle θ=0. In order to liquid phase sintering successfully occurs, it is necessary that contact angle is less than 90˚. In case of non wetting liquid phase, contact angle equal or greater than 90˚. Therefore, partial exudations from the compact will occur in the form of droplets during sintering. It has been noted that partial exudations from CuZnAl and CuAlNi compacts occur during sintering at 850 C˚ as a droplets in many experiments of this work.

The amount of wetting can be improved by lowering the liquid-solid interfacial energy by diffusion or absorption method at the interface . A measure of penetration of a liquid phase by the liquid between the two grains is given by angle (φ) as shown in Fig.(3.27) . Complete penetration into grain boundary takes place when the liquid-solid interfacial energy or tension is less than one half of the grain boundary energy.[Sinha,1995].

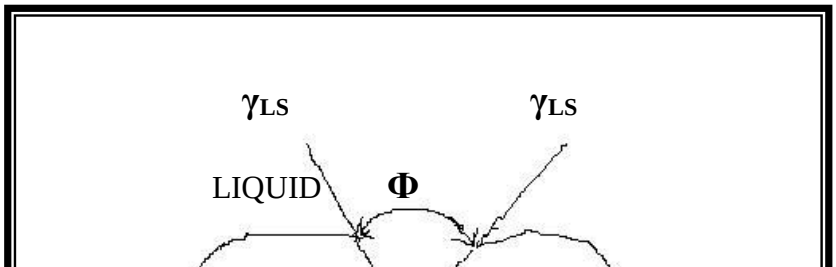

Fig. (3.27) Interfacial energy between solid and liquid phases when liquid phase penetrates between two grains.

The second stage is controlled by the surface and interfacial tension of the phases. After the completion of the rearrangement stage, second stage including solution and reprecipitation take place. It must be at least limited solubility of the solid in the liquid phase. Because there is dissolution and material transport by diffusion through the liquid, slow densification occurs as compared with first stage. Small particles have high curvature so they have interfacial tension and therefore higher solubility compared with large particles. These small particles dissolve first to form supersaturated liquid phase while re precipitation occurs on the largest solid particles having lower interface tension.

Third stage includes coalescence and grain growth. In the case of incomplete wetting of the solid by liquid, there is no complete separation of the solid particles by the liquid but there is some contact between solid particles. This may be considered in terms of low grain boundary energy with regard to one half the interfacial energy between the solid and the liquid .This condition causes the formation of solid skeleton within the compact.[Sinha,1995].

Liquid phase sintering kinetics generally are more sensitive to temperature than to sintering time. For solution and reprecipitation shrinkage, the transport path is through the liquid phase.

In the final stage, solid state sintering is predominant and the rate of densification is quite low. The combination of wetting, liquid flow and particle rearrangement contributes to a rapid change in the volume of the compact.

3.7.8.Homogenization During Sintering :

alloys may be produced by powder metallurgy techniques either by sintering compacts pressed from homogenous pre alloyed powder particles or by first mixing different powders for compacting and sintering which is based in this study . Compacted blends of powder exist as solute-rich particles surrounded by a matrix of solvent particles such as aluminum particles as solute particles and copper particles as solvent particles in the case of copper-aluminum alloys.

The density to which the powder is pressed determines the degree of residual inter particle porosity. Density differences between two different types of particles often cause mixing difficulties; therefore, such problems are minimized by varying the size of the particles used.

Sintering causes solid state diffusion of the solute atoms in to solvent matrix and diffusion of solvent atoms in to the solute-rich particles. Homogenization as a function of time at temperature may be described in terms of concentration and distance profiles that exhibit discontinuities in the as compact condition and that approach the average compact composition as concentration gradients are eliminated due to inter diffusion.

The compact behaves as a collection of many small diffusion couples that are allowed to undergo inter diffusion to the point where atomic fluxes become negligible and homogenization is achieved. [Lenel et al,1984].

Variation in sintered density with sintering temperature and time during homogenization is frequently different compared to the variation that exists if compacts are composed of particles of identical composition.

This is due two phenomena which have opposing effects on the densification of the compact and occur simultaneously. The matrix is densified due to pore shrinkage .A net flow of vacancies from one particle to other occurs if there is a difference in the fluxes of the atomic species to and away from a specific type of particle.

These vacancies can accumulate in the form of fine pores which called as Kirkendall porosity. The formation of Kirkendall porosity may cause expansion of the compact with subsequent reduction in density of compact.[Lenel et al,1984].

There are several parameters can affect the rate and extent of densification or expansion during homogenization such as:

1. Extent of the difference in the diffusivities of the particles.
2. Size of the particles in the compact.
3. Composition of the compact.
4. Compacting pressure.
5. Oxygen content of the starting powders.
6. Entrapped gases within powder particles.

The form of the density-time relationship for a specific homogenization treatment may vary and is more complicated for multi phase systems.

Multi phase binary systems must be described by the solute solubility and inter diffusion coefficients of each of the phases present. In such complexities the parameters required to analyze the homogenization process are not available.

The duration of sintering required to achieve a desired degree of homogeneity is dependent on temperature because inter diffusion coefficient (D) are exponentially dependent on temperatures in the following equation.

[Thornton and Colangelo,1985].

$D=D_{\circ} \exp(-Q/RT)$----------Eq.(3.6)

Where:

D- diffusion coefficient (cm^2 /sec)

$D_{\circ}$-diffusivity coefficient(cm^2 /sec)

Q- activation energy (cal/mol/K)

R- gas constant

T-absolute temperature (K)

Direct experimental techniques for the determination of the progress of homogenization include microscopy , composition analysis of microstructure using atomic probe analysis, scanning electron microscope and by x-ray diffraction technique .[Lenel et al ,1984].

Experimental Procedure

4.1. General View

In this chapter, materials and equipment used in this study are presented. Experimental procedure used to prepare samples from the elemental powders through the blending of powders in the mixing operation, compaction and finally sintering based upon typical steps of powder metallurgy technique, have been also presented in detail. Several physical tests such as apparent density, porosity expansion, etc and mechanical test such as hardness and compression in different form, furthermore, phase identification by X-ray diffraction and microstructure are also explained.

4.2. Materials

The elemental powders used in this study to prepare several alloys with average particle size, purity and origin are shown in table 4.1.

Table 4.1. powders used in this study.

Powder	Average particle size (μm)	Purity %	Origin.
Copper	75	99.98	Merck co.
Aluminum	75	99.80	Merck co.
Nickel	150	99.98	Bucks Fluka AG Co. Germany
Iron	150	99.9	Merck co.
Titanium	150	99.9	Merck co.
Cobalt	2	99.8	Merck co.
Zirconium	600	99.8	Merck co.
Manganese	45	99.8	Merck co.
Boron	22	99.9	Indian product.
Silicon	45	99.0	Merck co.

4.3. Equipments

The preparation of blended powders with different chemical compositions requires many equipments and instruments which are used not only in preparation of powder mixture but also in compaction and sintering stages. These equipments and instruments include the following:

1-Microbalance type L2205-D with accuracy (±0.001) manufactured by sartorius GMBH Gottigen –Germany.

2-Polyethylene zip-lock bags.

3-Calibrated micrometer with accuracy ±0.001mm.

4-Electrical oven up to 350 C.

5-Quartz type (0.038m in diameter with 0.38 m length).

6-Alumina gars with alumina balls manufactured by Berlin-Germany.

7-Dial gage with accuracy ±0.01mm manufactured by Germany with magnetic arm.

8-Proving ring with max. 50KN with dial gage ±0. 001mm accuracy manufactured by England.

9-Hydraulic press with hand-lever pressing with 32 ton maximum power.

10-Electric hydraulic press type soil test, Inc. USA with 120-ton capacity.

11-Electric tube furnace manufactured in this study up to 1200°C with alumina tube and type K thermocouple and digital thermostat controller with accuracy ±1.0 °C.

12-Double action dies with different dimensions made from alloy steel treated with suitable heat treatment have been used in this study.

13-Lithium striate lubricant.

14-Electric tube furnace up to 750°C manufactured in this study with type k thermocouple.

15-Argon cylinders with pressure gages from 1 to 15 bars.

16-Digital multimeter type (Honeytek A930)

17-Digital miliohmeter type (Hioki 3220 mΩ Hi tester)

18-Magnetic stirrer with thermostat hot plate up to 350°C. type (Gallenhamp)

19-Digital camera type (Mercury, Cyberpix S-550V).

20-Transparency glass slides.

21-Electric rolling mixer.

4.4. Preparation of blended mixtures

Blended mixtures from elemental powder given in table (4.1) with different weight percent have been prepared in this stage. Three main mixtures include Cu +13% Al + 3.98% Ni and Cu + 11% Al + 3.82% Ni , have been prepared. Furthermore; additives from Ti, B, Fe, Si, Co, Zr and Ti + Mn and B + Mn to the base mixture of Cu + 13Al + 3.98% Ni have also been prepared to explain the effects of alloying element on the shape memory effect and super elasticity of prepared alloys. Compositions of prepared alloys from elemental powders used in this study have been shown in table (4.2).

4.5. Mixing

The blending of an elemental powders mixture improves as the number of contacts between the different components of the mixture increases . Wet mixing for constituents of the mixtures has been done by electric rolling mixers as shown in Fig.(4.1).Alumina balls with different diameters as shown in Fig.(4.2) and alumina gars have been used to mix and refine metal powders for about 15 hours. Athyle alcohol has been used in wet mixing. In the light of this statement, mechanical mixing by hand for 2 hours has been used at first for alloys 1,2,3and 6 using athyle alcohol but it has been shown that chemical segregation in the final samples is found. Therefore, mechanical mixing by hand in zip-polyethylene locked bags is not satisfied. Chemical segregation of powder components has been shown macroscopically in samples as shown in Fig. (4.3).

Table 4.2. Mixtures and their compositions prepared in this study.

Alloy No.	Composition (weight parent of powders)
1	Cu + 11.0 Al + 3.82 Ni
2	Cu + 13.0 Al + 3.98 Ni
3	Cu + 12.6 Al + 3.98 Ni + 0.4 Ti
4	Cu + 12.2 Al + 3.98 Ni + 0.8 Ti
5	Cu + 11.8 Al + 3.98 Ni + 1.2 Ti
6	Cu + 12.6 Al + 3.98 Ni + 0.4B
7	Cu + 12.2 Al + 3.98 Ni + 0.8B
8	Cu + 11.8 Al + 3.98 Ni + 1.2B
9	Cu + 12.6 Al + 3.98 Ni + 0.4 Fe
10	Cu + 12.2 Al + 3.98 Ni + 0.8 Fe
11	Cu + 11.8 Al + 3.98 Ni + 1.2 Fe
12	Cu + 12.6 Al + 3.98 Ni + 0.4Si
13	Cu + 12.2 Al + 3.98 Ni + 0.8 Si
14	Cu + 11.8 Al + 3.98 Ni + 1.2 Si
15	Cu + 12.6 Al + 3.98 Ni + 0.4 Co
16	Cu + 12.2 Al + 3.98 Ni + 0.8 Co
17	Cu + 11.8 Al + 3.98 Ni + 1.2 Co
18	Cu + 12.6 Al + 3.98 Ni + 0.4 Zr
19	Cu + 12.2 Al + 3.98 Ni + 0.8 Zr
20	Cu + 11.8 Al + 3.98 Ni + 1.2 Zr
21	Cu + 12.2 Al + 3.98 Ni + (0.4 Ti + 0.4 Mn)
22	Cu + 11.8 Al + 3.98 Ni + (0.4 Ti + 0.8 Mn)
23	Cu + 11.4 Al + 3.98 Ni + (0.4 Ti + 1.2 Mn)
24	Cu + 12.2 Al + 3.98 Ni + (0.4 B + 0.4 Mn)
25	Cu + 11.8 Al + 3.98 Ni + (0.4 B + 0.8 Mn)
26	Cu + 11.4 Al + 3.98 Ni + (0.4 B + 1.2 Mn)

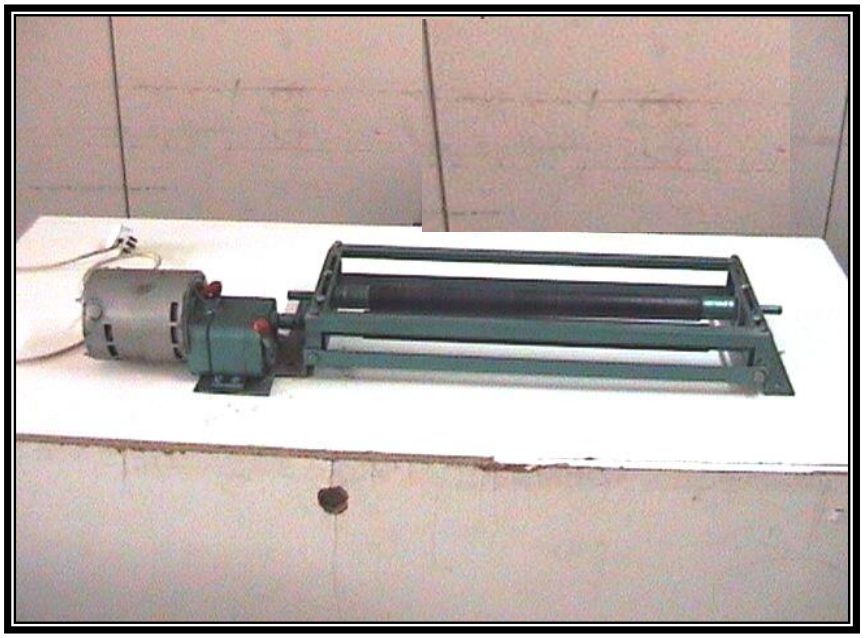

Figure.(4-1) Electric rolling mixing equipment.

Figure.(4.2) Alumina balls used for mixing powders mixture.

The wet mixtures of powdered alloys are dried in air at room temperature for about 1.0 hour and placed in polyethylene zip-locked bags. Lubricants are

not used in the mixture in order to avoid any oxide formation through the sintering process which leads to inhibit martensitic transformation. Based upon knowledge of oxide formation from lubricant in sintering process in Cu + 13% Al + 2% Nb which presented (Silva and Lima, 2005).

They showed that lubricant zinc stearate with milling and mixing of blended powders leads to form protective film on the powder surface and hinders diffusion between Aluminum and copper,

4.6. Compaction

In this stage, cold uniaxial pressing in double action dies has been used. Electric hydraulic press with uniaxial pressing as shown in Fig. (4.4) is used to compact green samples for compression test and disc samples for physical and micro structural tests.

Various compression stresses from (118.695; 237390; 356.086, 474.781, 593.476, 712.171, 830.867 and 949.562 Mpa) using double action alloy steel dies fixed in the electric hydraulic press with 120 ton capacity.

Alloy steel dies are heat treated by quenching from 850 for 1 hour in oil at room temperature and tempered in 200°C for 30 min to stress relieve due to quenching.

Samples with dimension (14.5 mm in diameter and 5mm thickness) and (10 mm diameter and 20mm height) have been prepared for hardness, microstructure tests and compression tests respectively.

Three loading rates have been used to press green compact as follows:
a-Rate (1) = 10 ton/ min,b-Rate (2) = 5 ton/ min , c-Rate (3) = 0.3 ton/ min

Furthermore; period of applied pressure time at maximum amount taken into consideration as a process parameter which are 1, 5, 10 minutes. Several

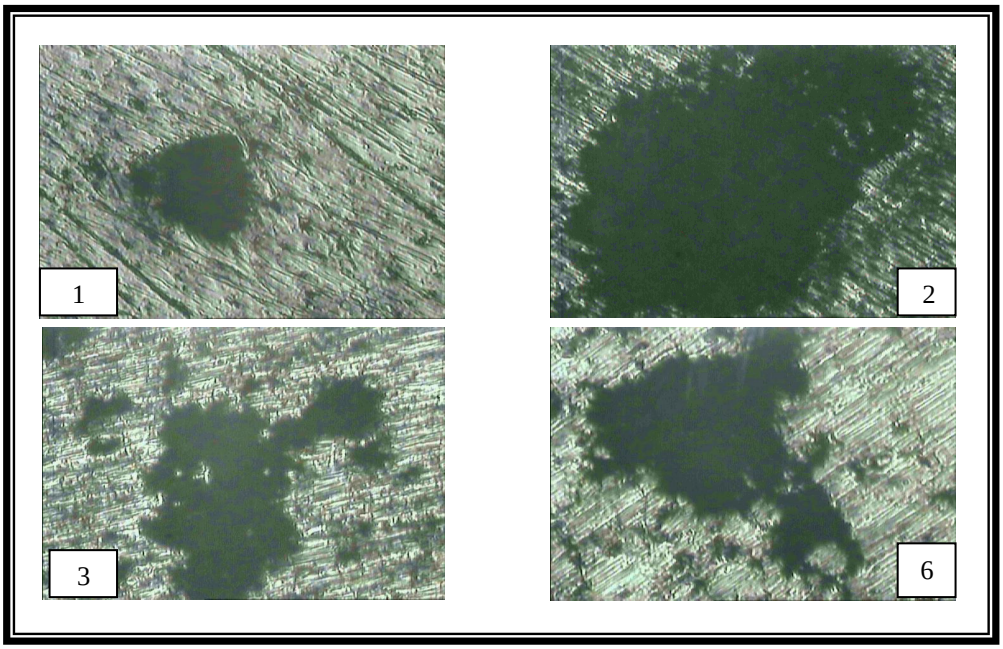

Fig.(4-3) chemical segregation of alloying element prepared by hand mixing for alloys 1.2.3 and 6.

Figure.(4-4) Uniaxial hydraulic press machine

physical tests such as apparent density, porosity, expansion and macrocracking after final sintering are based to determine optimum amount of pressure, rate of loading and period of time of maximum compression stress.

From experiments during experimental works, it has been shown that very small amounts from lithium stearate as lubricant for double action alloy steel die walls avoid cracking in the sample through the ejecting process from die specially cracks in the surface of samples. After each cycle of pressing, cleaning of die parts by acetone is used. Essential steps to form green compact from metal powder mixture include:

1-Full die cavity by some what 6 gram of mixture.

2-Pressing of mixture in double action dies by movement of upper punch and remain the base of frame fixed completely up to maximum load (tons) with different rates of loading and different soaking time.

3-Ejecting of green compact from the die by remove of the base and movement of the same upper punch.

Amount of compression stresses, rate of loading and periods of applying maximum compression stresses have been used for mixtures from alloy 1, 2, 3 and 6 .

4.7. Sintering

Several attempts have been used in this study to sinter green compacts from alloys, 1, 2, 3 and 6 using different heating cycles. Many of these attempts have been failed where complete cracking or melting of some particles on the surface causes burst of samples in the other hand, have been occurred. However, some of other attempt has been succeeded but with high porosity so, optimal experimental procedure for sintering of green compacts prepared in this study, has been reached in this investigation. All samples are placed in quartz tube which placed in tube furnace as shown in Fig. (4.5). Attempts used in this study include the following heating cycles.

I. First attempt

1. Heating green compacts from room temperature (27°C to 850 °C) with heating rate 5°C/min.
2. Soaking time for 15 min at 850°C.
3. Slow cooling in furnace.

All samples are failed with cracking and burst completely as shown in Fig.(4.6).

II. Second attempt

1-Heating green compact up to 850 from R. T. with 5°C/ min rate of heating.

2-Soaking time 15 min in 850°C.

3-Air cooling.

All the samples are also failed by creaking.

I*II. Third attempt*

1-Heating the furnace up to 550°C and entered the samples immediately and continue the heating up to 850°C.

2-Remain the green compacts in 850 for 10 minutes.

3-Air cooling.

All the samples are also failed by cracking and formation of melt bubbles on the surface.

IV. Fourth attempt

1-Heating the furnace up to 550°C and the green compact have been entered and closed the furnace to continue heating up to 900°C for 10 minutes.

2-Slow cooling in furnace.

All samples are also failed completely.

V. Fifth attempt

1. Heating the furnace up to 850°C.
2. Entered the green compact immediately.
3. Remain the samples in 850°C for 10 minutes.
4. Air cooling.

This cycle has been satisfied and accessed but with high porosity of final sintered samples and with low apparent density. (Porosity in the range of 16 - 35%).

The proposed heating cycle for sintering of prepared alloys in this study includes two stages of sintering as the following.

VI. Sixth attempt

1-Heating green compact from room temperature up to 600°C.

2-Soaking time is 3 hours.

3-Increase heating of samples in the furnace up to 850 for different times 10 min, 30 min, 1, 2 and 3hr.

4-Slow cooling in furnace.

This sintering heating cycle is shown in Fig.(4.7). The sintering of all samples has been satisfied and successfully occurred with low porosity (approximately 8~14).

Several higher sintering temperatures such as 850, 900, and 950°C have been taken to study their effects on the final physical properties. It has been shown that sintering in 850°C gives low evaporation of zinc in alloy I and low thermal effects compared with sintering in 900 or 950°C.All previous attempts of sintering have been done using argon atmosphere with 1.5 bar/min at a first minute to remove all air in quartz tube and with 0.5 bar/min for remain time.

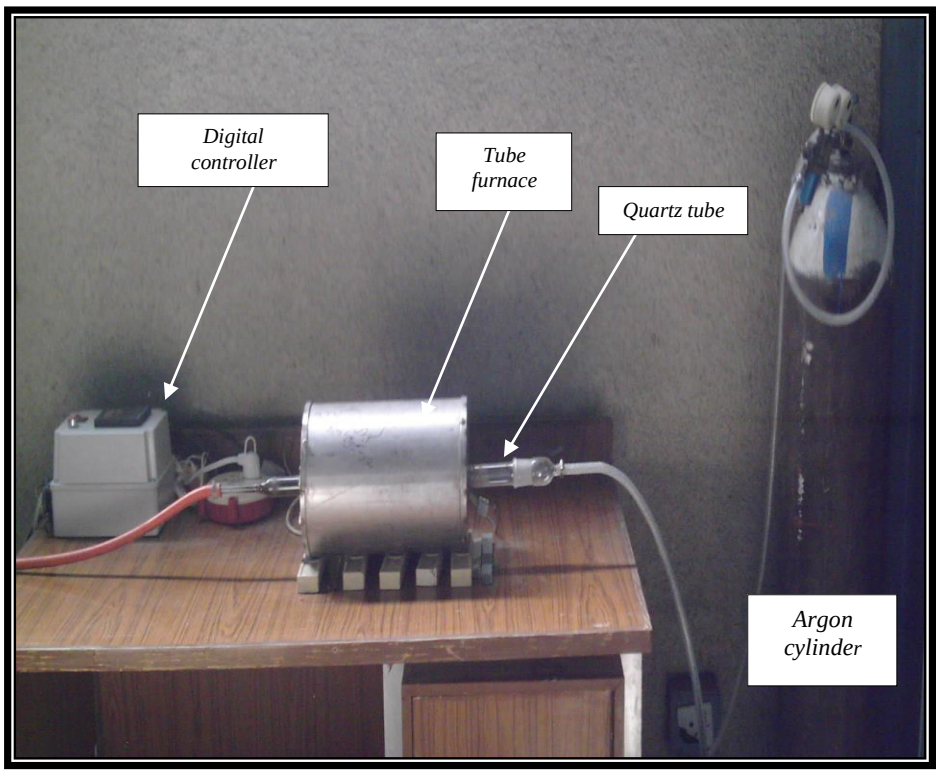

Figure. (4-5) Tube furnace used in this study.

Figure.(4-6) Failed samples in 1,2,3,4 attempts on sintering.

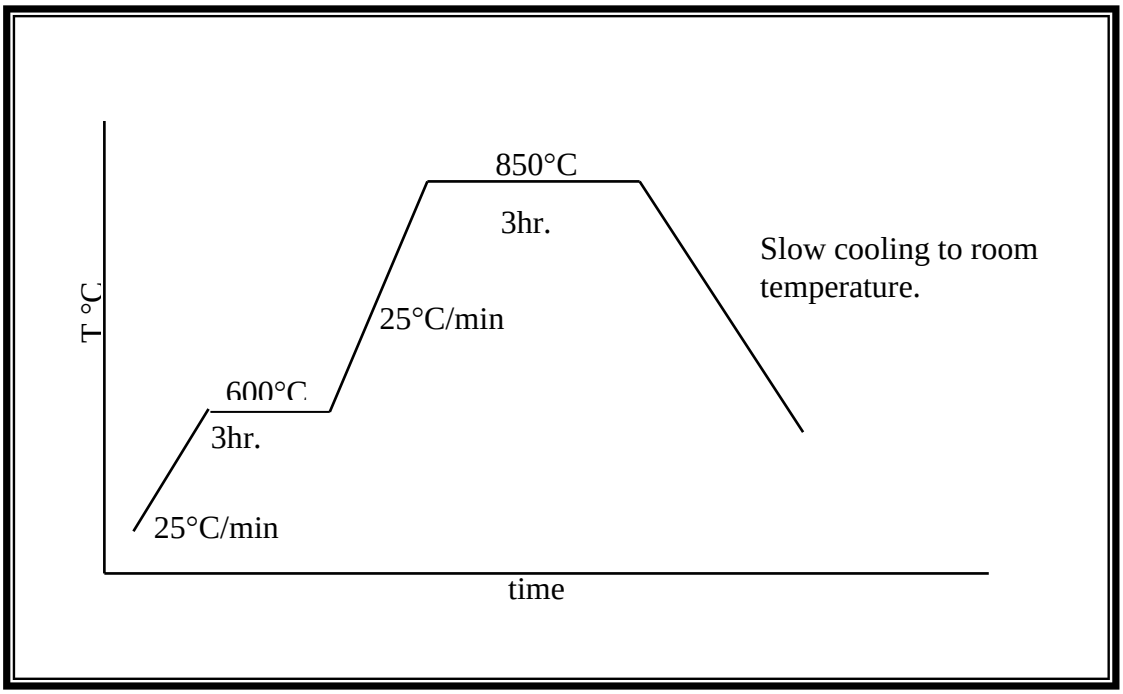

Fig. (4.7) heating cycle used in sixth attempt of sintering

Temperature in heating zone of type furnace is calibrated using external digital thermometer type (ELD Mod.9710,prodit ,Italy) and with digital multimeter with type k thermocouple. For different furnace temperature include

(250, 350, 500, 550, 600, 750, 800, 850, 900, 950). Digital controller of tube furnace has ±5 degrees as a temperature interval for switch on and switch-off of conductor operation.

4.8. Heat treatment

Several heat treatments have been used in this study including solution (betatizing) heat treatment , step quench treatment and aging heat treatment (post quench). Furthermore , heat treatment including shape memory effect of prepared alloy. The details of these treatment are given in the following:

4.8.1. Solution (betatizing) heat treatment

After sintering, all sample are solution treated by heating the samples up to (850°C) for different time as (30,60 and 140 min) and followed by rapid quenching in ice water at 3 ~ 4°C in order to avoid decomposition of β phase into equilibrium phases including ($\alpha + \gamma_2$) which is eutectoid reaction. taken in 565°C for aluminum bronze (Cu + 0.4 $\rightarrow$ 15.6 wt % Al). solution treatments are occurred in argon atmosphere with 0.5 Bar per min as a flow rate to avoid oxidation of samples. One of the most important and used of solution treatment in this study is shown in Fig. (4.8).

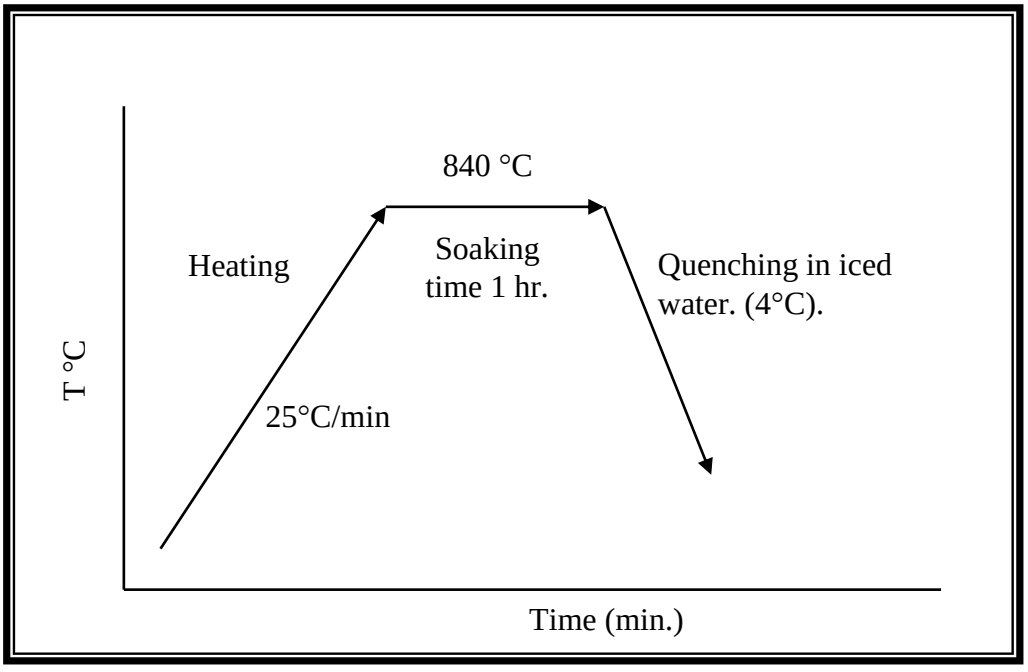

Fig. (4.8): solution treatment heating cycle for CuAlNi base alloys

.

4.8.2. Aging Treatment

Aging treatment is a thermal treatment occurred after rapid quenching in ice water to age some intermetallic compounds in the microstructure to modify their properties in suitable temperature. Here 200°C for 30 min is taken as aging treatment for all prepared alloys. Thermal cycle is shown in Fig. (4.9).After aging, samples are also post aging quench in iced water (3~4°C) in order not to occur any phase decomposition during slow cooling. There is no enough time to decompose β phase to $\alpha+\gamma_2$ phase.

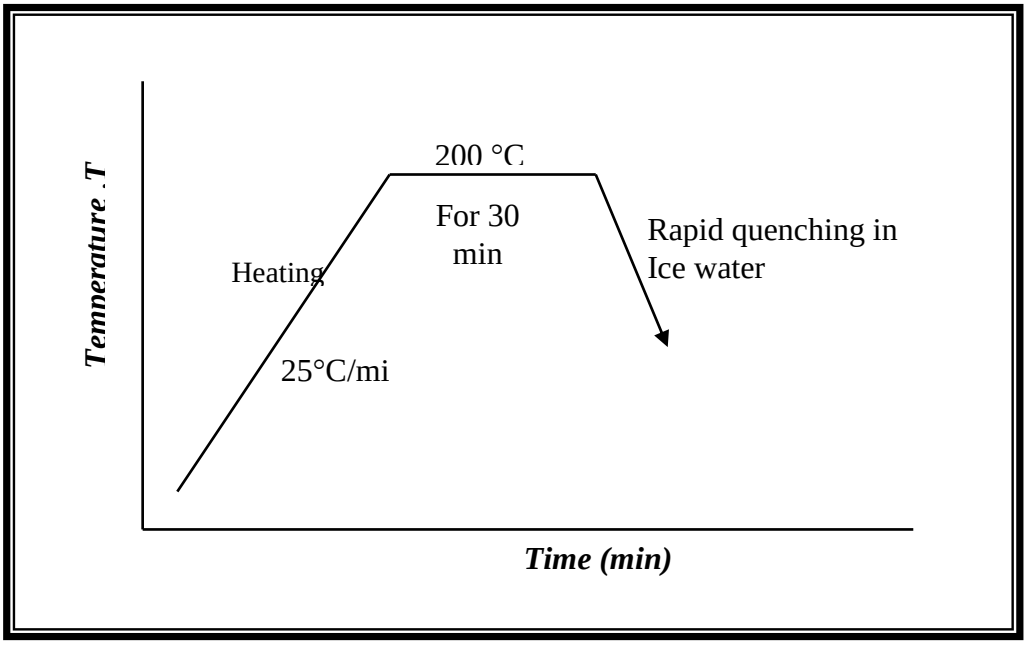

.

Fig. (4.9) Post quenching, aging treatment

4.8.3. Step quench heat treatment

Step quench treatment is not continuous rapid cooling but, it is an isothermal cooling through quenching from 850°C to 95°C at approximately (2-3) seconds. After this, remain in 95°C for 15 min and quenching in ice water at later. Thermal cycle of step quench is shown in Fig. (4.10).

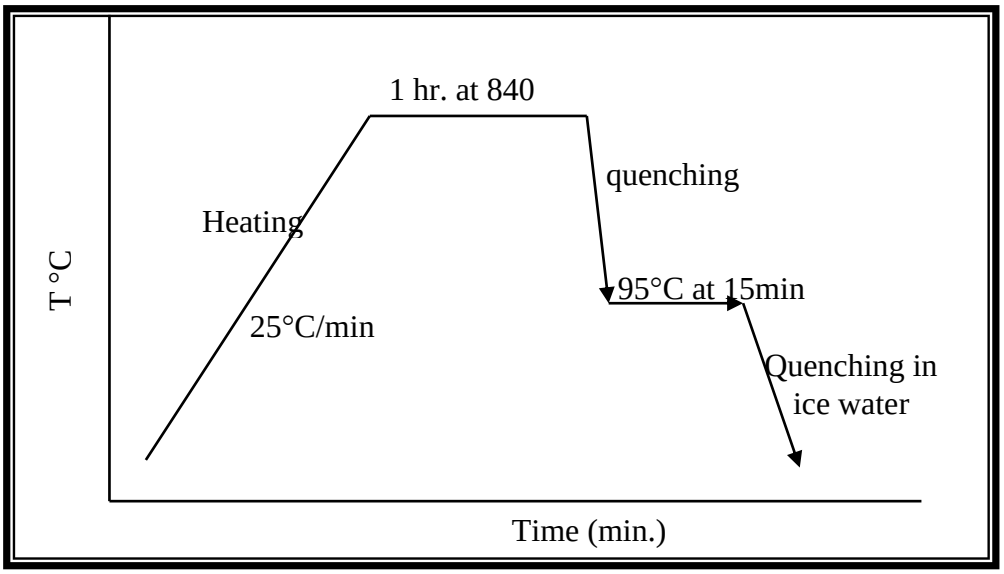

Fig. (4.10) Step quench heating cycle for prepared alloys.

4.8.4. heat treatment including shape memory effect

In order to obtain shape memory effect , which is determined by cold working by hardness indenter not only Brinell indentor but also micro and macro Vickers indenter and by compression test in different temperatures, heating to several temperatures such as 150°C, 200°C and 450°C for 10 and 30 minutes have been taken into consideration.

Different temperature and times have been taken into consideration due to different composition of prepared alloys and wide ranges of alloying element.

4.9. Phase identification and analysis

Phases analysis of prepared alloys is based upon X-ray diffraction technique and microstructures examination using optical microscope with different magnification. At a first, mixture of blended powders from alloys, 1, 2, 3 and 6 samples has been identified by X-ray diffraction technique in order to compare these diffraction pattern with sintered diffraction pattern for the same samples to enhance good sintering process. Furthermore, after solution

treatment, aging treatment and step quench heat treatment X-ray diffraction have been taken.

All X-ray diffraction tests are carried out at S.C. of Geological survey and mining. Low angle X-ray diffraction is preformed. X-ray generator with Cu Kα radition at 40 Kv and 20 mA is used.

The X-ray is generated by general electric diffraction type Philips (Pw 1840) operating at scanning speed of 6°(2θ) per minute. The specimen has been held at a fixed angle of θ=5 degrees relative to the incident X-ray been while the detector is moved through an angle of 2θ= 10° to 90 degrees.

4.10 Light Optical Microscopy (LOM)

Microstructure evolution with (40, 75, 100, 150, 400, 600 and 1000 X) magnification using two different microscope as shown in Fig.(4.11) has been examined for (40, 100, 400 and 1000X) Olympus microscope manufactured by Japan has been used where as with (75, 150, 600) union microscope has been used which is also made in Japan –in the metallurgical laboratory in material engineering department. Carl Zeiss. Microscope with low magnification (1.0, 1.6 and 5x) has also used to capture the macroscopically Brinell indentors. With all microstructure examination, digital camera type (Mercury, Cyberpix S-550V) has been used. The prepared samples from all categories with dimensions of (14.5 mm in diameter and 5mm in thickness) as can be seen in Fig.(4.12) have been wet ground using 180, 400, 800 and 1200 grit silicon carbide papers. These samples are then cleaned with water and dried with hot air. After drying , the samples are stored in polyethylene zip – lock bags with silica gel and sent to X-ray diffraction test where as another categories of the same alloys are polished with fine alumina type (0.02μm fine polishing alumina, struers made in Denmark) with fire cloth for ductile non ferrous alloys. Polishing and grinding wheel has been used to prepare metallographic sample. Samples are etched with two etching solution which are:

1-5 gram $FeCl_3$ + 10 ml HCl + 100ml H_2O

2-20 ml NH40H + 10 ml H_2O_2 + 20 ml H_2O

The ammonium hydroxide / hydrogen peroxide/ water solution (etching two) is the most widely used etching for copper and copper alloys. [Récksecker, 1985].

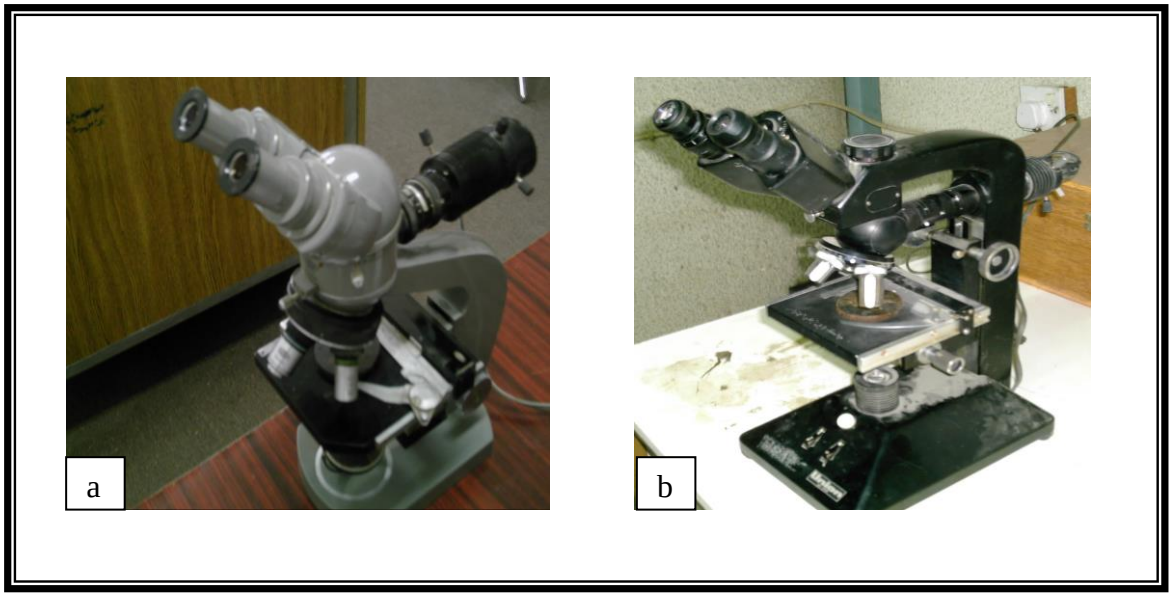

Figure.(4-11) Light optical microscopes.(a.Olympus and b.Union type).

Fig.(4.12) samples used for metallographic examination and physical tests.

4.11 Scanning electron microscopy (SEM)

Scanning electron microscope examination is used to reveal the microstructure of specimens for both unetched and etched conditions. SEM is used after direct quench , aging treatment and after step-quenched heat treatment . Several magnification has been captured with box, 2500x, 5000 x and 1000x for all specimens. SEM examination has been done in advanced metallurgical and material laboratory in the faculty of engineering, university of Tehran.Its specification is vega tescan, obducat camscan,Oxford instrument ,U.K.

4.12. Physical Tests

Several physical tests for elemental powders, green compacts and sintered samples as well as heat treated samples have been carried out. These tests include the following:

4.12.1. Particle size and particle distribution

Particle size of elemental powders [Cu, Al, Zn, Ni, Zr, Co, Fe, Mn, Ti, Si and B and blended powders from alloys, 1,2 ,3 and 6 is determined by image analysis technique..

Digital image for microstructure of certain powder sample using low magnification light optical microscope (LOM) has been captured by digital camera. This image is analyzed through image processing and image analysis using matlab program. The main steps for image processing and analyzing are shown in Fig. (4.13).

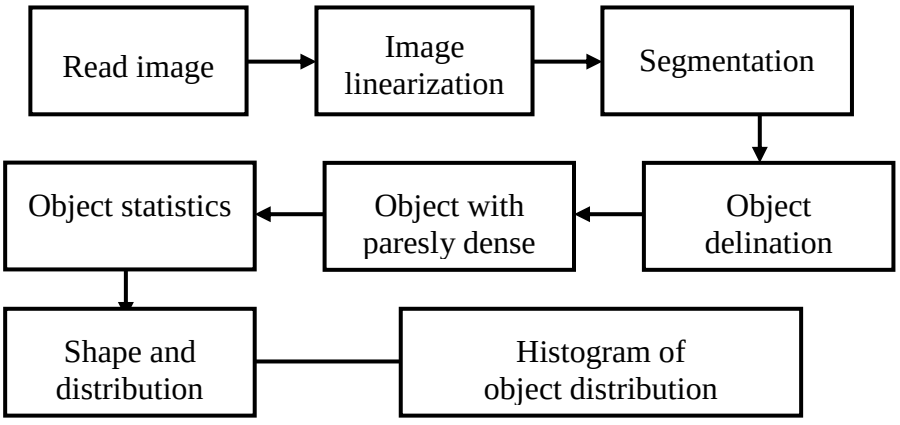

Figure. (4.13). Image processing and image analyzing using matlab version 7 program

Various techniques are used to measure the size of irregularly shaped particle when viewed through a microscope. This has resulted in different measurements which are used to classify these two dimensional particle image in terms of an equivalent spherical particle or equivalent rectangle in the direction of particle with feret's length and width, as shown in Fig. (4.14).

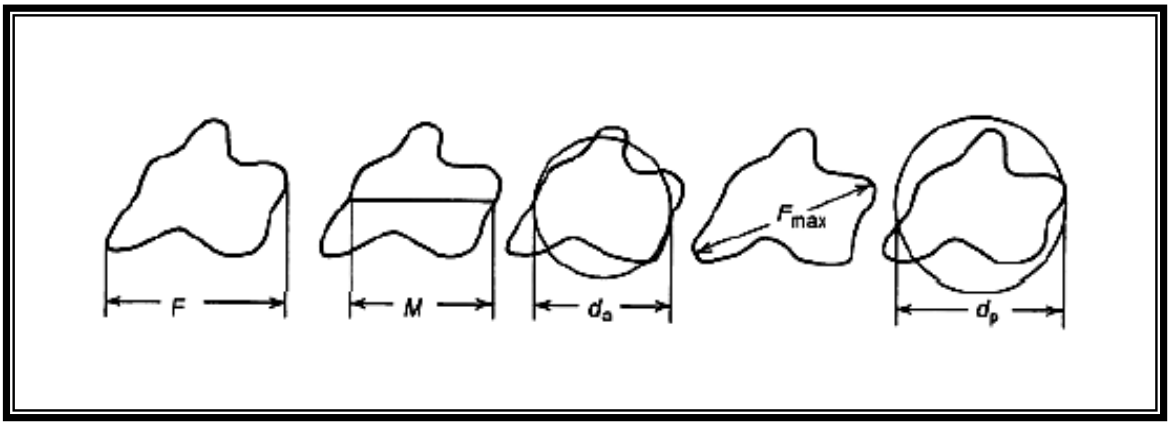

Figure. (4.14) Techniques for measuring size of irregular shaped particles.

Where M the Martin's diameter is the length of the line that bisects the area of the particle image, all particles measured in the same direction. [Hubbard, 1984].

In this study, direct measurement of particle dimensions in X and Y direction or any directions for one particle and for all particles can be used. Average of these dimensions has been taken as average particle size based upon equivalent spherical shape for spherical particle shape and equivalent elipse for non spherical particles.

Histogram curves for normal particle size distribution and acumulative plot used in determining median particle size have been also obtained by image analysis of LOM image.

4.12.2. Apparent density of powders and blended powders

The weight of unit volume of loose powder expressed in grams per cubic centimeter is the apparent density of a metal powder which is the one of the

fundamental properties of a powder. This characteristic defines the actual volume occupied by a mass of loose powder which directly affects processing parameters such as the design of compacting tooling and the magnitude of press motions required to compact and density loose powder.

Apparent density determinations are made by pouring powder into standard graded cub with 10 ml maximum volume into suitable grade. Care must be exercised to prevent physical densification of the powder in the cup when leveling. Weight of cup with and without powder is calculated using microbalance with accuracy of ±0.001 grams. Apparent density in grams per cubic centimeter is then determined by the following equation.

$$\rho_A = \frac{m_2 - m_1}{V_p} \quad \text{.....Eq.(4.1)}$$

Where:

ρ_A = Apparent density of powder (g/ cm^3).

m_1 = weight of cup without powder (unfilled cup (g).

m_2 = weight of cup with powder (g).

V_p = volume of powder in cup (cm^3)

4.12.3. Green porosity and density

The weight of unit volume of compacted blended powder expressed in grams per cubic centimeter is the green density of the compact. It is calculated from dimensions evaluations and weighting of compact sample as follows:

$$\rho_g = \frac{m_g}{V_g} \text{.....Eq. (4.2)}$$

Where:

ρ_g = green density (g/ cm^3). , m_g = green mass of the compact (g).

V_g = volume of the compact (cm^3).

Green porosity is determined from the knowledge of the theoretical density of blended powders (mixture) which is calculated by the weight percent of elemental powder multiply by it's theoretical density as follows:

$$\rho_{tB} = \sum_{i=1}^{n} Wt_1 * \rho_1 + Wt_2 * \rho_2 + Wt_3 * \rho_3 + ... + Wt_n * \rho_n \quad \text{.....Eq.(4.3)}$$

Where:

ρ_{tB} = theoretical density of blended powder (g/cm^3). , n = No. of elemental powders.

W_t = weight percent (%). , $\rho_{1,2,3,....n}$ = density of elemental powder (g/ cm^3).

So the green porosity is calculated from the equation:

$$P_g = \left(1 - \frac{\rho_g}{\rho_{tB}}\right) \times 100\% \quad \text{.....Eq. (4.4)}$$

Where:

P_g = green porosity (%). , ρ_g = green density (g/ cm^3).

ρ_{tB} = theoretical density of blended mixture (g/cm^3).

4.12.4. Pore size and pore distribution

The pore size and pore distribution in the samples for both compacted and sintered states have been determined by using image processing and analyzing through capture of light optical microscopy digital image for compacts and two stages of sintering. Histogram of natural distribution of pores and acumulative distribution have also determined.

4.12.5. Apparent density, porosity and water absorption of sintered compacts

The following procedure is used to evaluate apparent density, apparent and true porosity and water absorption of sintered samples according to ASTM-C 373 standard.

1-The specimen is dried up to 100°C for 24 hours in argon atmosphere then cooled to room temperature. The weight dry specimen is measured as (m_d).

2-The specimen is placed in a beaker of distilled water for 24 hours. The weight wet specimen is measured as (m_w).

3-The specimen is placed in a bayrex beaker of distilled water and boiled for 3 hours taking into consideration that the specimen must be covered by the water at all time. After boiling time , the specimen is left to soak form an additional 24 hours. After impregnation of the tested specimen, suspended mass (m_s) is measured when the specimen is suspended in water.

4-Directly, after calculation of (m_s), the specimen is cleaned with cotton cloth to remove all excess water from its surface. Immediately the specimen is weighted to determine the saturated mass (m_{sa}). The apparent density, apparent and true porosity and absorption of water are calculated from the following relations:

$$\underset{(g/cm^3)}{\text{apparened density}}\ (\rho_a) = \frac{m_d}{(m_{sa} - m_s)/\rho_w} \quad \text{.....Eq.(4.5)}$$

Where ρ_w = density of water (1.0 g/cm^3).

$$\underset{(\%)}{\text{apparened porosity}} = \frac{(m_w - m_d)}{(m_{sa} - m_s)} \times 100 \quad \text{.....Eq.(4.6)}$$

$$\text{true porosity} = (m_{sa} - m_d) \quad \text{.....Eq.(4.7)}$$

$$\underset{(\%)}{\underset{(cm^3)}{\text{absorption of water}}} = \frac{m_w - m_d}{m_d} \times 100 \quad \text{.....Eq.(4.8)}$$

4.12.6. Dimensional change of sintered compacts

Dimensional change for the sintered compact specimen is calculated from the following equation [Feerby, 1984].

$$\text{Dimensional change}(\%) = \frac{L_S - L_D}{L_D} \times 100 \quad \text{.....Eq. (4.9)}$$

Where:

L_D = is the die cavity dimension (mm). ,

L_S = is the sintered specimen dimension (mm).

Expansion is indicated by a plus sign and shrinkage is indicated by a minus sign (-). Dimensional changes are determined as the difference in dimensions between green and sintered compacts in the parallel and/or perpendicular direction of pressing. From a technological stand point , the dimensional change during sintering of greatest importance is the difference between the dimensions of the die and the sintered compact in the radial direction that is the direction perpendicular to that of pressing. Therefore, L_s and L_D in equation (4.9) refer to diameter of sintered compact and diameter of die compact respectively in this work.

4.12.7. Electrical resistance

Electrical resistance for sintered compacts and heat treated alloys [step quenched, direct quenched and aging specimens] has been determined using mili ohmmeter type [Hoyki 10100] manufactured in Japan as shown in Fig.(4.15). Electrical resistance is evaluated in different temperatures [8°C to 250°C] with increment of 1°C degree. Small tube furnace up to 750°C with type k thermocouple manufactured in this study has been used to carry out electrical resistance measurements with different temperature. Voltage transformer (variac) has been used to control heating rate through the experiments. Specimen is placed in alumina cell and both of furnace and sample in cell have been insulated with glass wool and E-glass fabric ravings to insulate heat to the surroundings as low as possible. Fig.(4.16) shows the tube furnace and cell used to calculate electrical resistance as a function of temperature. This test is used to know phase transformation temperatures which indicate suddenly variation in electrical resistance of the specimen with tested temperature.

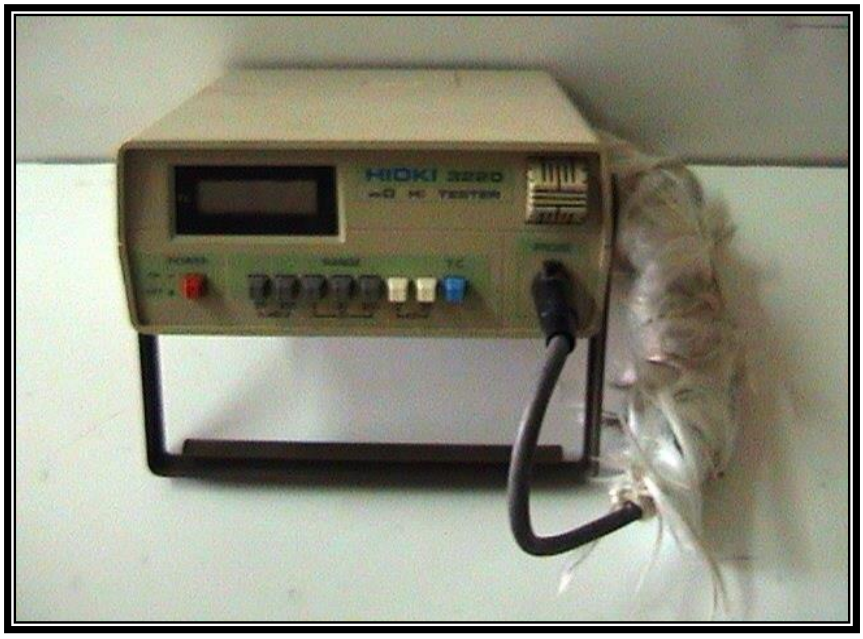

Figure(4-15) milliohm-meter equipment.

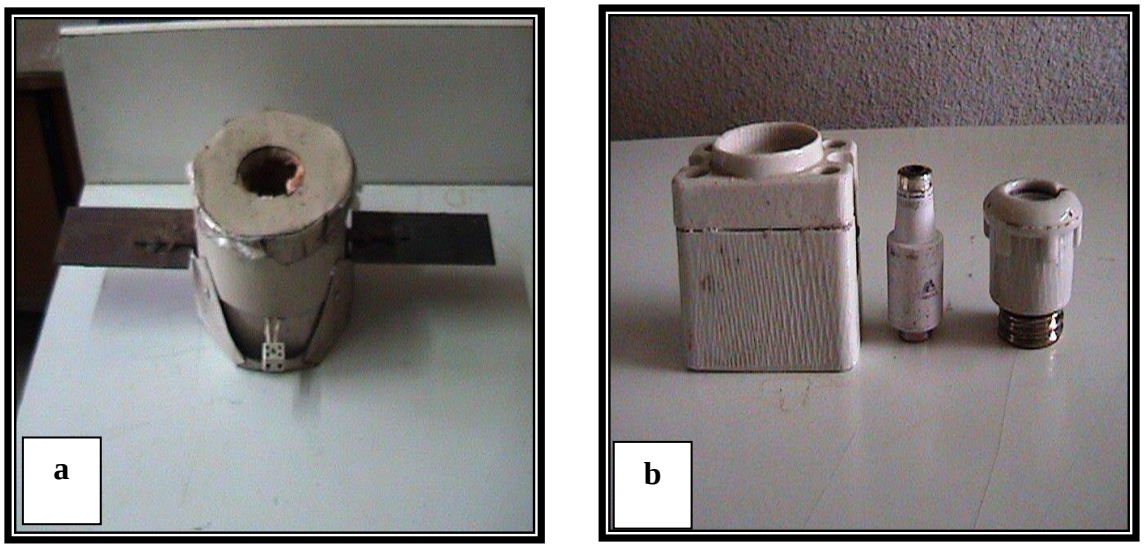

Figure(4.16) tube furnace (a)and the cell (b) used for electrical resistance with different temperatures.

4.12.8 Ultrasonic wave test.

Ultrasonic wave test is used for cylindrical specimens (10 mm in diameter , 35mm in length). This test has been done after compressing the direct quenched specimens up to 10 % strain and after recovery heat treatment which include heating the specimen upt to 150 ^{o}C for 15 min. Low frequency with high wave length of Ultrasonic equipment used especially for test the reinforced concrete is used . Digital monitor appears directly the time of transferred of ultrasonic wave. The wave length is 2.5 cm .

4.13. Mechanical Tests.

Mechanical tests including micro and macro hardness and compression test are done for sintered and heat treated samples. Shape memory effect has been concered in all mechanical tests.

4.13.1. Microhardness measurements

Microhardness Vickeres tester type [Microhardness Tester Hv-1000] is used to measure hardness with 100, 200 and 500g load and holding time of 20 seconds compined with optical microscopy to measure the diagonal length of Vicker's impression. The Vicker's microhardness (H.V.) is defined as follows:

$$HV = 1.854\,P/d^2 \quad \text{.....Eq.(4.10)}$$

Where P = applied load.

d = average length of diagonal μm.

Two reading are reordered for each sample. This test shows great variation in hardness number 50, it is based for shape memory effect only not to determine the hardness value of tested sample because there are many pores in the surface of the sample.

4.13.2. Macrohardness measurements

Two main methods are used not only to determine hardness values of tested specimens but also to evaluate shape memory effect through the indentation of tests impression. These include the following:

4.13.2.1. Vicker's macro harness measurements

Macrohardness Vicker's tester type [Hardness Tester model mat24/crbv,Brooks inspection equipment Ltd.] is used to measure the hardness with 3Kg primary load and 30 Kg as major load. Four readings are recorded for each specimen. Macrohardness is given directly by digital monitor with test machine. Dimensions of Vicker's impression are calculated using low magnification light optical microscopy type [Carl Zeiss] and by image analysis.

4.13.2.2. Brinell macrohardness measrments

Brooks universal hardness tests is used to measure Brinell hardness with 2.5mm ball diameter as indentation ball and 137.5Kg major load with 10Kg as micro load digital readings for Brinell hardness number is given directly-where as the impression of indentation ball is given by using low magnification light optical microscopy with digital camera and by image analysis and image processing.

4.13.3. Compression test

Sample with (10 mm in diameter and 20 mm height) dimension as shown in Fig.(4.17) have been compressed using calibrated universal testing machine as shown in Fig. (4.18) at room temperature and at 50 ^{o}C. However, strain-temperature test curves of prepared direct quench samples achieved using Calibrated, compression equipment. Proving ring manufactured in England with 50 KN maximum load is used to measure the load applied in to specimen and dial gage with 0.01mm accuracy is used to evaluate displacement in the designed equipment as a shown in Fig. (4.19). All equipment are calibrated with three compression machine, universal testing machine with 30KN max. load type phwye, Marshal compression machine with 20KN max. load and with another universal testing machine manufactured in Germany in Kufa university.

Compression tests are done in room temperature and in different temperature using tube furnace with digital controller and type K-thermocouple which is stacked with sample directly.

It has been shown that samples from Cu+45%Ti+5%Co with 6mm in diameter and 8mm height have the following experimental data:

Table (4.3) verification of compression equipment

Type of equipment	Max. load	Max. displacement
Universal testing machine with 30KN max. load type phywe	17	2.1
Universal testing machine with 20KN max. load.	16.9	2.2
Hydraulic compression machine used in this study	16.87	2.25

Therefore; due to the limit of loads in universal testing machine and there is slight or small variation in he corded readings for max. load and max. displacement furthermore , no one accept heating system placed with universal testing machine, hydraulic compression machine with designed heating equipment has been used in this study.

Fig.(4.17) compression samples

4.13.4. Shape memory effect

Shape memory effect is determined from Vickers impression or brinell indentation follows:

$$\text{Shape memory effect (SME \%)} = \frac{d_b - d_a}{d_b} \times 100 \quad \text{.....Eq. (4.11)}$$

Where:

d_b = average impression diameter in (μm) before heating.,

d_a = average impression diameter in (μm) after heating.

Shape memory effect is also determined from compression test as follows [Ariapour, 1998]:

$$SME\ (\%) = \frac{L_2 - L_1}{L_0 - L_1} \times 100 \quad \text{.....Eq. (4.12)}$$

Where:

L_0 = initial distance between two indentation reference marks on the surface of a specimen parallel to the compression direction.

L_1 = is the distance between the indentation marks after compression and direction.

L_2 = is the distance between the indentation marks after recovery heating.

The reported values are the average of three measurements. Further more, strain recovery percentage during shape memory effect is also calculated as follows:

$$\in_r = \frac{L_2 - L_1}{L_0} \times 100 \quad \text{.....Eq.(4.13)}$$

Where :

$\in_r$ = recovery of strain percentage (%). ,

The reported values are the average of three measurements.

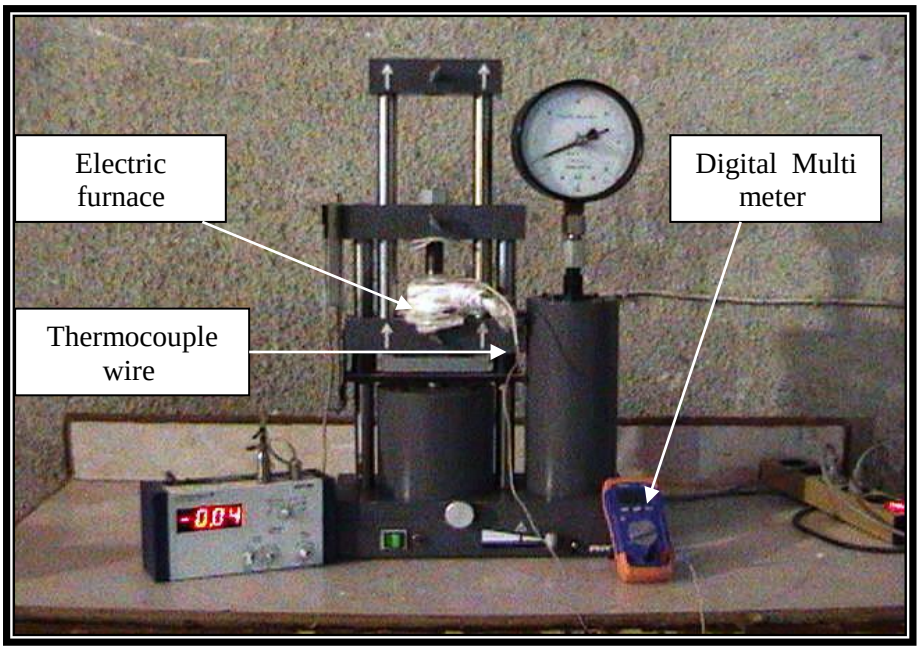

Fig.(4.18) Universal testing machine used for compression test in room temperature and 50 ^{o}C.

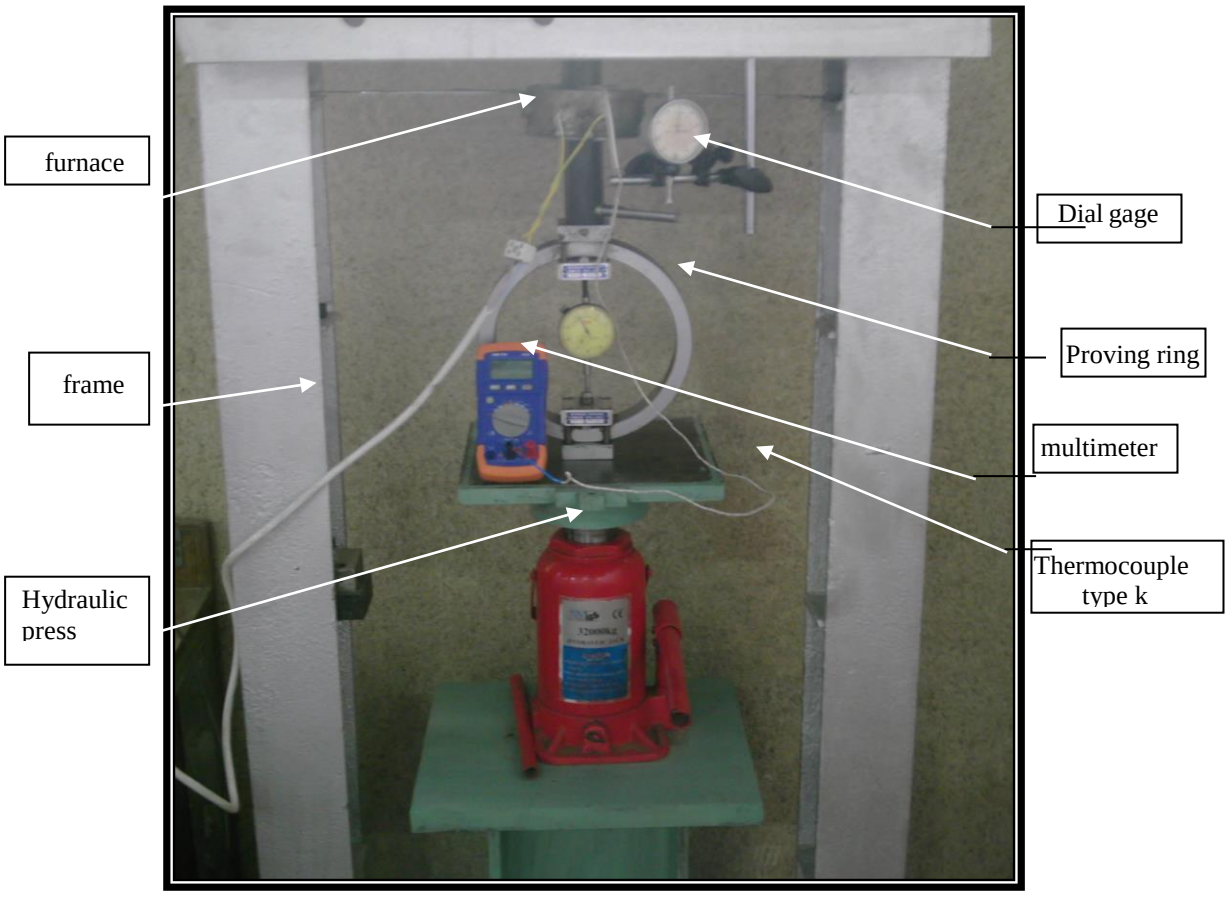

Fig.(4.19) compression equipment with required heating system.

Modeling and Numerical Simulation of Shape memory Alloys

5.1.Gernal View

In this Chapter , the attention on the constitutive modeling of shape memory alloys has been presented. Several shape memory alloys models have been explained in attention to temperature- dependent inelastic model of shape memory alloys used in packages such as Abquas and Ansys version 9.

In this study, two approaches are used to analyze shape memory effect through using unit cell finite element analysis using square and hexagonal unit cell to study of shape memory structures with pores and, the real microstructure using digital image have been used to analyze porous shape memory alloy with finite element method. For both of the two approach ansys ver. 9. has been employed. Verification of used model with case studies has also been presented.

5.2. Shape memory models

Constitutive laws which according to the recent literature ,seem to be the most used and efficient for simulating the response of shape memory allays based devices , are present in the following:

5.2.1 Ozdemir model

This model introduced by Ozdemir [Queted in Fugazza , 2003] allows to study the mechanical responded material showing hystersis. The mathematical expressions that described it are the following :

$$\frac{d\sigma}{dt} = E[\frac{d\varepsilon}{dt} - \left|\frac{d\varepsilon}{dt}\right|(\frac{\sigma-\beta}{Y})^n] \qquad \text{------- Eq.(5.1)}$$

$$\frac{d\beta}{dt} = \alpha E\left|\frac{d\varepsilon}{dt}\right|(\frac{\sigma-\beta}{Y})^n \qquad \text{------- Eq.(5.2)}$$

Where

σ : Stress

ε : strain

E : elastic modulus (Gpa)

Y: Yield stress (MPa) which represents the beginning of the stress-induced transition from austenite to martersite in SMA.

β : one dimensional back stress (N/m^2).

α : Constant controlling the slope of the $\sigma - \varepsilon$ curve .

n : Constant Controlling the sharpness of transition form elastic to plastic state.

The equation (5.1) can be rearranged as following :

$$\frac{d\varepsilon}{dt} = \frac{d\sigma/dt}{E} + \left|\frac{d\varepsilon}{dt}\right|\left(\frac{\sigma-\beta}{Y}\right)^n \qquad \text{------- Eq.(5.2)}$$

The total strain as shown in equation (5,3) is made up of two separate components as follows :-

1. Linear elastic component σ/E and .
2. nonlinear strain component $\dot{\varepsilon}$, described by the expression

   $\dot{\varepsilon} = |\dot{\varepsilon}|[(\sigma-\beta)/Y]^n$.

Where (.) is the ordinary time derivative. This inelastic component is a function of both the strain rate ($\dot{\varepsilon}$) and the over stress ($\sigma-\beta$).

It would be possible to show that for equation (5.1 and 5.2) , the strain is in dependent of the applied rates of loading which means not dependent on either $\dot{\sigma}$ or $\dot{\varepsilon}$). By subtracting expression in equation (5.2) from expression (5.1), we may obtain the following equation :

$$\dot{\sigma} - \dot{\beta} = E\,\dot{\varepsilon}\left[1 - (1+\alpha)\left(\frac{\sigma-\beta}{Y}\right)^n\right] \qquad \text{Eq.(5.4)}$$

Which it is useful to rewrite in a more Convenient differential form as :

$$d\varepsilon = \frac{d(\sigma - \beta)}{E\left[1 - (1+\alpha)\left(\frac{\sigma - \beta}{Y}\right)^n\right]} \qquad \text{...Eq.(5.5)}$$

and by integration , we get the solution for the total strain .

$$\varepsilon = \frac{Y}{E(1+\alpha)^{1/n}} \int \frac{d(\sigma - \beta)}{1 - (\sigma - \beta)^n} \qquad Eq.(5.6)$$

The integral in Equation (5.6) is a function only of the overstress $\sigma - \beta$ therefore , equations (5.1 and 5.2) represent a rate – independent stress – strain behavior . and this model does not permit to capture the behavior exhibited by shape memory alloys .

5.2.2.Cozzarelli model :

Here , the mechanical characterization of shape memory alloys is accomplished by extending the rate independent model of Ozdemir [Graesser and Gozzerelli 1991] when equation (5.1) is divided by $\dot{\varepsilon}$, the slope of the stress –strain curve is obtained as :

$$\frac{d\sigma}{d\varepsilon} = E\left[1 - Sgn(\dot{\varepsilon})\left(\frac{\sigma - \beta}{Y}\right)^n\right] \qquad \text{Eq.(5.7)}$$

Where

$$Sgn(\dot{\varepsilon}) = \begin{cases} -1 & \text{if} \quad \dot{\varepsilon} < 0 \\ 0 & \text{if} \quad \dot{\varepsilon} = 0 \\ +1 & \text{if} \quad \dot{\varepsilon} > 0 \end{cases} \qquad \text{...Eq. (5.8)}$$

This model has ability to predict super elastic and simplicity to be extended to three dimensional case but still rate and temperature independence . It is unabled to predict the behavior after that the transition from austenite to martensite is completed .

5.2.3 Tanaka model

On the basis of the analysis of thermo- mechanics and Continuum mechanics . Tanaka presents the following constitutive relation [Fugazza ,2003]

$$\dot{\sigma} = D\dot{\varepsilon} + \theta\dot{T} + \Omega\dot{\zeta} + \psi\dot{\eta} \qquad \text{...Eq}(5.9)$$

Where ,

σ - Stress tensor

ε - Strain tensor

T - Temperature

D - Stiffness matrix

θ - Thermo elasticity tensor

Ω - Range of strain resulting from martensite

ψ - Range of strain resulting from R-phase transformation

ζ - Volume percentage of martensite phase

η - Volume percentage of R phase .

It is also possible to evaluate the volume percentage of austenite phase which results from the expression $1-(\zeta+\eta)$ the volume Percentage of martensite transformation ζ Can be written as :

$$\zeta = 1 - \exp\left[b_M C_M (M_S - T) + b_M \sigma\right] \qquad \text{Eq}(5.10)$$

and for austenite

$$\zeta = \exp\left[b_A C_A (A_S - T) + b_A \sigma\right] \qquad \text{Eq}(5.11)$$

Where b_M ,C_M ,b_A and C_A are material coefficient for martensite and austenite phase respectively .

M_S and A_S represent the initial temperature of the martensite and austenite transformation under no stress conditions respectively

The volume Percentage of R-phase , η assume the form :

$$\eta = b'_M C'_M (T - M'_S) - b'_M \qquad \text{...Eq.(5.12)}$$

and

$$\eta = 1 + b'_A C'_A (T - M'_S) - b'_A \sigma \qquad \text{...Eq.(5.13)}$$

Where again b'_M, C'_M, b'_A, C'_A are material coefficients .M`s and A`s are the temperature of initial of the martensite and reversed R-phase transformation under condition of no stress . This model has an ability to account for the R-phase and temperature dependence but it is still rate independent ..

5.2.4. Auricchio model :

The general inelastic theory used for development of constitutive models for materials has been presented by Auricchio (1995) and Lubliner and Auricchio (1995) .

Auricchio applied generalized plasticity to analyse shape memory alloy behavior .For simplicity , a one dimensional model is presented here .

Auricchio model assumed that the stress and strain are – rate independent and isotropy of martensite single variant and austenite phase , Therefore , in the most general case , three phase transformation are considered as follows :

1) Conversion of austenite to single Variant martensite($A \to M$) .

2) Conversion of Single Variant martensite to austenite phase ($M \to A$) .

3) Single Variant martensite reorientation ($M \to M$)

As control Variables , we assume the uniaxial stress , σ and relative temperature T , As internal Variables we may choose either Single –Variant martensite fraction ζ_M or austenite fraction ζ_A [Auricchio et.al,1997] which are assumed to satisfy the following relation at each time :

$$\zeta_M + \zeta_A = 1 \qquad \text{...Eq.(5.14)}$$

Accordingly there is only one independent internal variable , chosen herein to be ζ_M . From equation (5.14) we get relation between the rates of the fractions as :

$$\dot{\zeta}_M + \dot{\zeta}_M = 0 \qquad \text{...Eq.(5.15):}$$

To reproduce the Superelastic behavior in a uniaxial State of stress only two phase transformations Can be considered , the conversion of austenite into single Variant martensite($A \rightarrow M$) and the conversion of single variant martensite into austenite ($M \rightarrow A$).

As showed experimentally , for uniaxial stress- temperature changes and in the usual range of applications , the region s in which phase transformation may be occurred are delimited with good approximation by straight lines [Melton , 1990] So that ,

$$\dot{\zeta}_M = \dot{\zeta}_M^{A\rightarrow M} + \dot{\zeta}_M^{M\rightarrow A} \quad \text{...Eq.(5.16)}$$

$$\dot{\zeta}_A = \dot{\zeta}_A^{A\rightarrow M} + \dot{\zeta}_A^{M\rightarrow A} \quad \text{...Eq.(5.17)}$$

5.2.4.1 Single Variant martensite Production :

To describe the region corresponding to the Single variant martensite production Process , the following functions are introduced (Auricchio et al 1997) .

$$F^{A\rightarrow M} = \sigma - C^{A\rightarrow M} * T \quad \text{...Eq.(5.18)}$$

$$F_S^{A\rightarrow M} = F^{A\rightarrow M} - R_S^{A\rightarrow M} \quad \text{...Eq.(5.19)}$$

$$F_f^{A\rightarrow M} = F^{A\rightarrow M} - R_f^{A\rightarrow M} \quad \text{...Eq.(5.20)}$$

With

$$R_S^{A\rightarrow M} = C^{A\rightarrow M} M_S \quad \text{...Eq.(5.21)}$$

$$R_F^{A\rightarrow M} = C^{A\rightarrow M} M_F \quad \text{...Eq.(5.22)}$$

Where $C^{A\rightarrow M}, M_S$ and M_f are material Parameter include stress to temperature Coefficient , initial and final transformation temperatures from $A \rightarrow M$ at zero stress respectively . whereas σ is the applied stress and F is the pressure causes flow in the Material . The region in which the transformation may take place is evaluated from

$$F_S^{A\rightarrow M} > 0 \text{ and } F_f^{A\rightarrow M} < 0 \quad \text{…Eq.(5.23)}$$

As can be shown in Fig. .(5.1) .

To activate the production of single – variant martensite , the stress should be increased or temperature should be decreased . so ,we require to,

$$\dot{F}^{A\to M} > 0 \qquad \text{Eq.(5.24)}$$

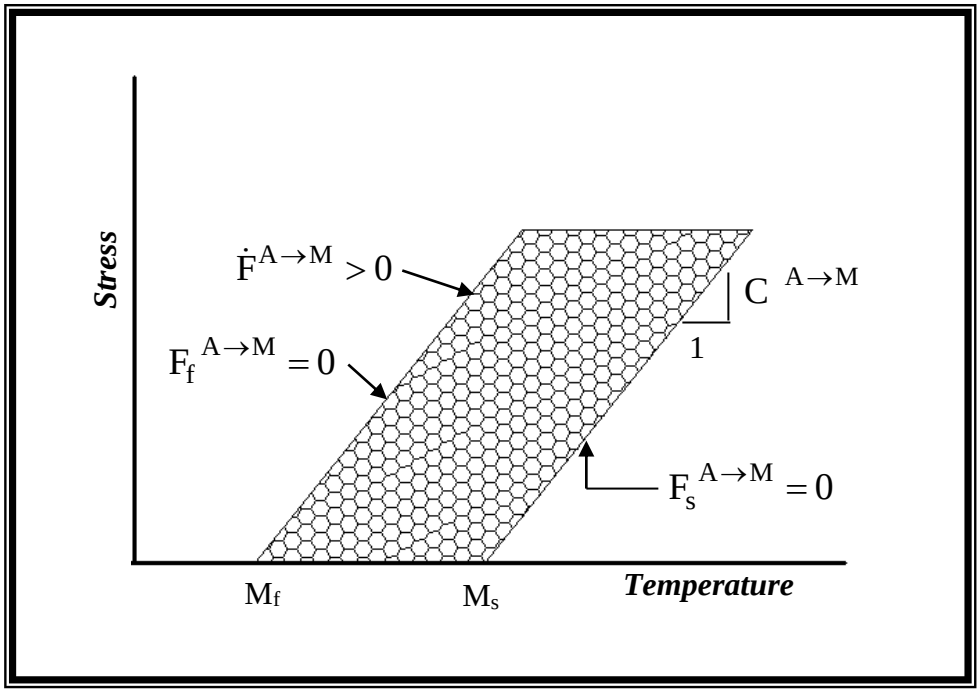

Fig.(5.1) production of single variant martensite

5.2.4.2. Austenite production

Similarly to the previous equations , the functions are introduced as :

$$F^{M\to A} = \sigma - C^{M\to A}T \qquad \text{...Eq.(5.25)}$$

$$F_S{}^{M\to A} = F^{M\to A} - R_S{}^{M\to A} \qquad \text{...Eq.(5.26)}$$

$$F_f{}^{M\to A} = F^{M\to A} - R_f{}^{M\to A} \qquad \text{...Eq.(5.27)}$$

With

$$R_S^{M\to A} = C^{M\to A}A_S \qquad \text{...Eq.(5.28)}$$

$$R_f^{M\to A} = C^{M\to A}A_f \qquad \text{...Eq.(5.29)}$$

Where $C^{M\to A}$ is the stress to temperature coefficient for reveries direction of transformation A_S and A_f are the initial and final transformation temperature from martensite to austenite zero stress .The region in which the transformation may take place is described by Fig. (5.2) as :

$$F_S^{M\to A} < 0 \quad \text{and} \quad F_f^{M\to A} > 0 \qquad \text{Eq.(5.30)}$$

So , to activate the production of austenite ,the stress should be decreased or the temperature should be increased or proper combination of these actions should be occurred , so.

$$\dot{F}^{M\to A} < 0 \qquad \text{...Eq.(5.31)}$$

The material behavior is assumed to be isotropic. The pressure dependency of the phase transformation is modeled by introducing the Drucker –Prager loading Function as [Auricchio , 2001]

$$F = q + 3\alpha p \qquad \text{Eq.(5.31)}$$

Where

α – material parameter

p- pressure

$$p = \mathrm{Tr}(\sigma)/3 \qquad \text{...Eq.(5.32)}$$

Where :

Tr – trace operater

σ – stress vector

$$q = \left[\frac{1}{2}\sigma^T[M]\sigma\right]^{1/2} \qquad \text{...Eq.(5.33)}$$

σ^T - Transpose of stress vector

M – matrix defined as

$$[M]=\begin{bmatrix}1&0&0&0&0&0\\0&1&0&0&0&0\\0&0&1&0&0&0\\0&0&0&2&0&0\\0&0&0&0&2&0\\0&0&0&0&0&2\end{bmatrix} \quad \text{...Eq.(5.34)}$$

Auricchio model (1997) assumed the linear form for evolution of the Volume fraction of martensite and which is defined as :

$$\dot{\zeta}_M=\begin{cases}-H^{A\to M}(1-\zeta_M)\dfrac{\dot{F}}{F-R_f^{A\to M}} & A\to M \text{ Transformation}\\ H^{M\to A}\zeta_M\dfrac{\dot{F}}{F-R_f^{M\to A}} & M\to A \text{ Transformation}\end{cases} \quad \text{..Eq.(5.35)}$$

where :

$$R_f^{A\to M}=\sigma_f^{A\to M}(1-\alpha) \qquad \text{Eq.(5.36)}$$

$$R_f^{M\to A}=\sigma_f^{M\to A}(1+\alpha) \qquad \text{Eq.(5.37)}$$

Where $\sigma_f^{A\to M}$ and $\sigma_f^{M\to A}$ are material Parameters as shown in Fig. .(5.3)

$$H^{A\to M}=\begin{cases}1 & \text{if}\begin{pmatrix}R_S^{A\to M}<F<R_f^{A\to M}\\ \dot{F}>0\end{pmatrix}\\ 0 & \text{otherwise}\end{cases} \quad \text{...Eq(5.38)}$$

$$H^{M\to A}=\begin{cases}1 & \text{if}\begin{pmatrix}R_f^{M\to A}<F<R_s^{M\to A}\\ \dot{F}>0\end{pmatrix}\\ 0 & \text{otherwise}\end{cases} \quad \text{...Eq(5.39)}$$

Where :

$$R_S^{A\to M} = \sigma_S^{A\to M}(1+\sigma) \qquad \text{Eq.(5.40)}$$

$$R_S^{A\to M} = \sigma_S^{M\to A}(1+\sigma) \qquad \text{Eq.(5.41)}$$

Where $\sigma_S^{A\to M}$ and $\sigma_S^{M\to A}$ are the material Parameter as shown in Fig.. (5.3).

Fig. (5.3) idealized stress – strain carve of linear super elastic behavior of SMA .The incremental stress relation is

$$\Delta\sigma = [D]\,(\{\Delta\varepsilon\} - \{\Delta\varepsilon^{tr}\}) \qquad \text{Eq.(5.41)}$$

$$\{\Delta\varepsilon^{tr}\} = D\overline{\zeta}_M\bar{\varepsilon}_L\frac{\partial F}{\partial\{\sigma\}} \qquad \text{Eq.(5.42)}$$

Where

$\{D\}$- elastic –strain matrix. , $\{\Delta\varepsilon^{tr}\}$ = incremental transformation strain

$\bar{\varepsilon}_L$ = maximum transformation strain which is the material parameter as shown in Fig. (5.3).

This model assumed isotropic behavior for both austenite and martensite phase , furthermore , it is applied to evaluate only super elastic behavior not the shape memory effect for both linear and exponential approach in this study , Ansys version 9 is taken for modeling super elastic behavior of shape memory alloy which is based upon Auricchio model for only linear approach .up to date , there is no unique model for modeling and numerical simulation for both super elastic an shape effect of shape memory materials further more , there is no package or software deals with porous shape memory alloys not only for modeling but also for numerical simulation of engineering devices.

Many workers in the field of analysis of shape memory alloys assume the multilinear elastic model to analyze super elastic behavior of shape alloys especially for nitinol devices with appropriate approximations and assumptions . [koop et al , 2001]

The previous material parameters as shown in Fig. (5.3), are determined from experimental tensile or compression tests for shape memory alloy sample .

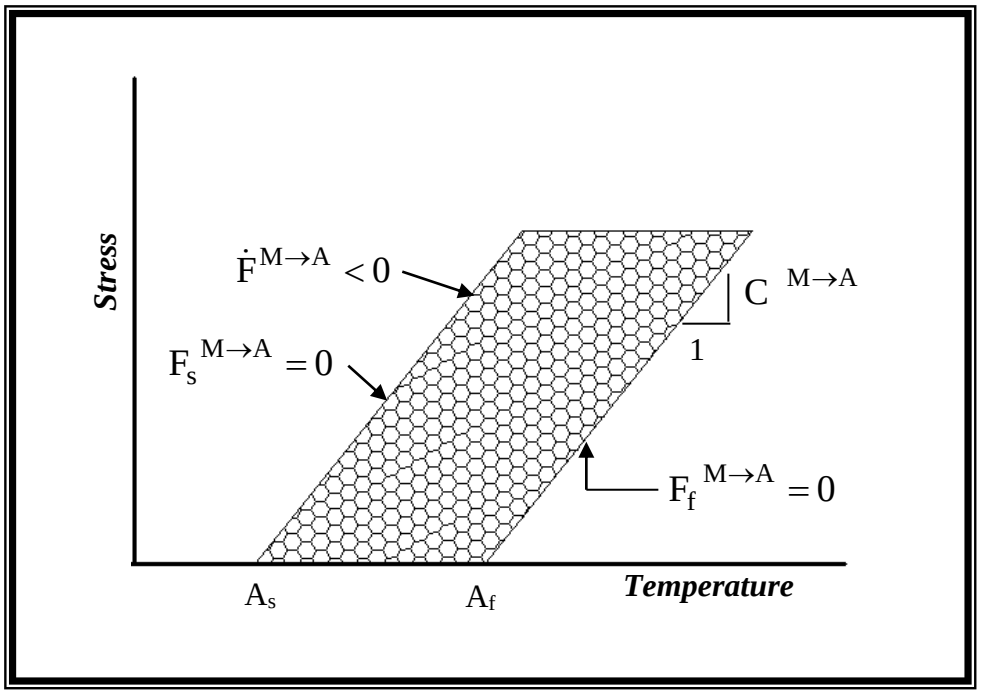

Fig.(5.2) production of austenite phase .

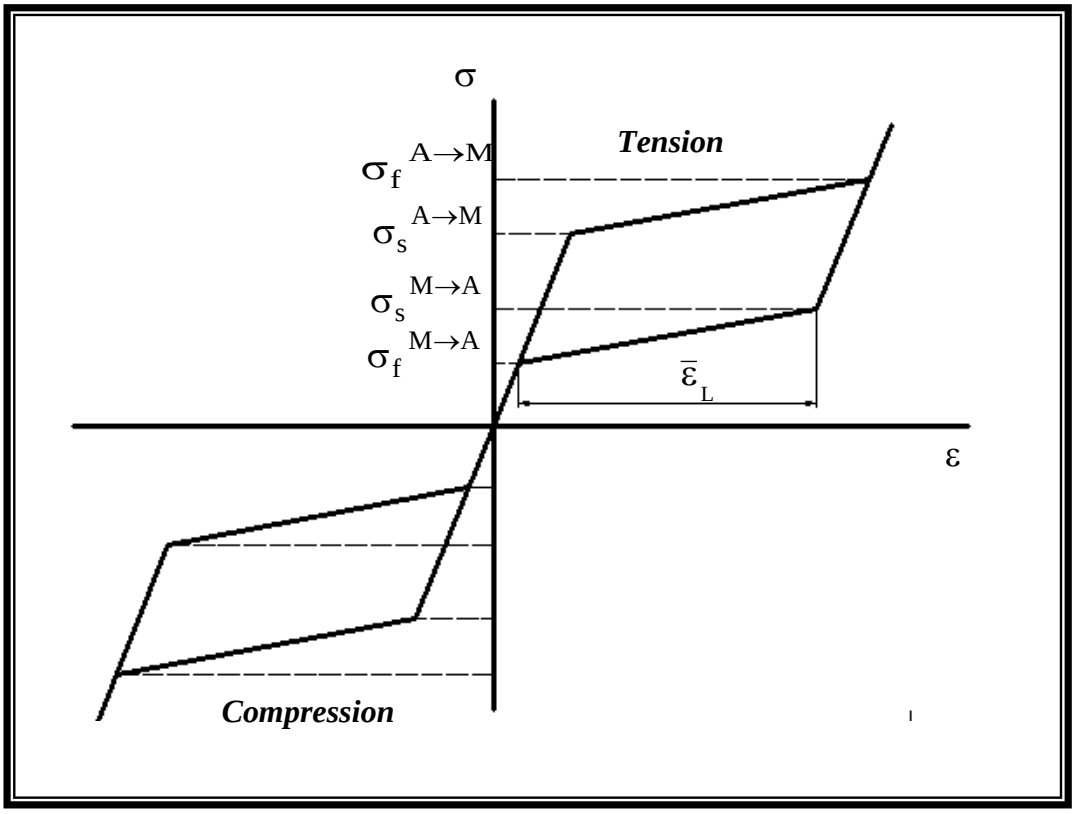

Fig.(5.3) idealized stress-strain curve of linear super elastic behavior of SMA.

5.3 modeling of porous shape memory alloys :

Porous shape memory alloys have been developed and used primary for bone be construction (Ni – Ti base) also due to it's lower density compared to fully dense shape memory alloys, they use in a number of light weight applications. Another advantage of porous shape memory alloys is the possibility of creating a functionally gradient material by controlling the porosity . The expectation is that the porous SMAs will retain some of the desirable characteristics of fully dense SMAs such as shape memory effect and super elasticity while enhancing shape recovery and energy absorption capabilities.

While both theoretical and experimental work are equally important, in this section focuses on the micromechanical modeling of porous shape memory alloys under quasi- static loading.

The modeling of porous materials has been performed assuming either periodic or random distribution of pores. Periodic arrangement of pores in a real porous shape memory material is an approximation assumption, but this assumption provides insight into global material behavior in the form of useful limiting values for the overall properties.

Furthermore, an approximate local variation of various field such as stress and strain indicating areas of concentration due to porosity can be obtained. So , these results may give design limitations in order to minimize or even avoid micro-buckling , yielding and consequently loss of capacity of phase transformation. The assumption of periodicity and symmetry boundary conditions reduce the analysis of porous shape memory material to the analysis of the unit cell. Thus , appropriate loading conditions need to be used. In the case of the porous material with random distribution of pores , micromechanical averaging techniques can be used to determine the averaged macroscopic response. In this case the material is treated as a composite with two phases, dense matrix and pores. The two most widely used are the self- consistent method and the Mori-Tanaka method. Both methods are based on the assumption that the effective response of the composite can be obtained by considering a single in homogeneity embedded in an infinite matrix.

Furthermore , the two approaches are assumed uniform shape of pores such sphere or cylindrical . but with random distribution.

In this study , unit cell finite element analysis taking into consideration tetragonal and hexagonal distribution of pores has been studied using Ansys. version 9.

Furthermore , randome distribution with non uniformed shape of pores in shape memory alloy matrix has also studied using real microstructure image taken from digital camera sticked with light optical microscope. Microstructure images have analyzed and processed in order to know the two phases, matrix shape memory alloy and embedded pores clearly and to convert image (pixels) into geometry (area in X and y coordinates) . This object is not easy due to the complex image of microstructure of porous shape memory alloy because there are multiphase in addition of pores.

Two dimension analysis is used for both approaches. Circle, ellipse or any non uniformed shape can be used as pore shape In the image of microstructure porous shape memory alloy may contain open, closed pores or a combination of both types. In this study two dimension analysis is based , so either open or closed pores are assumed to exist in the sample.

5.4. Unit Cell Finite element method

Two main periodic arrangement of pores are studies as follows:-

5.4.1. Tetragonal arrangement of pores.

An in plane square arrangement of pores is assumed at a first step in the present study. the cross section of such arrangement for open pores is shown in Fig.. (5.4) . The xy-plane forms the cross section of the material specimen and z is the out of plane axis along the length of the specimen.

As shown in Fig.(5.4) the open pores are assumed to be in the form of cylinders with circular cross-section and generators parallel to the out of plane z-axis

5.4.2. Hexagonal arrangement of pores. :-

Hexagonal arrangement of pores is also assumed in this study. The cross section of hexagonal arrangement of pores is shown in Fig..(5.5).

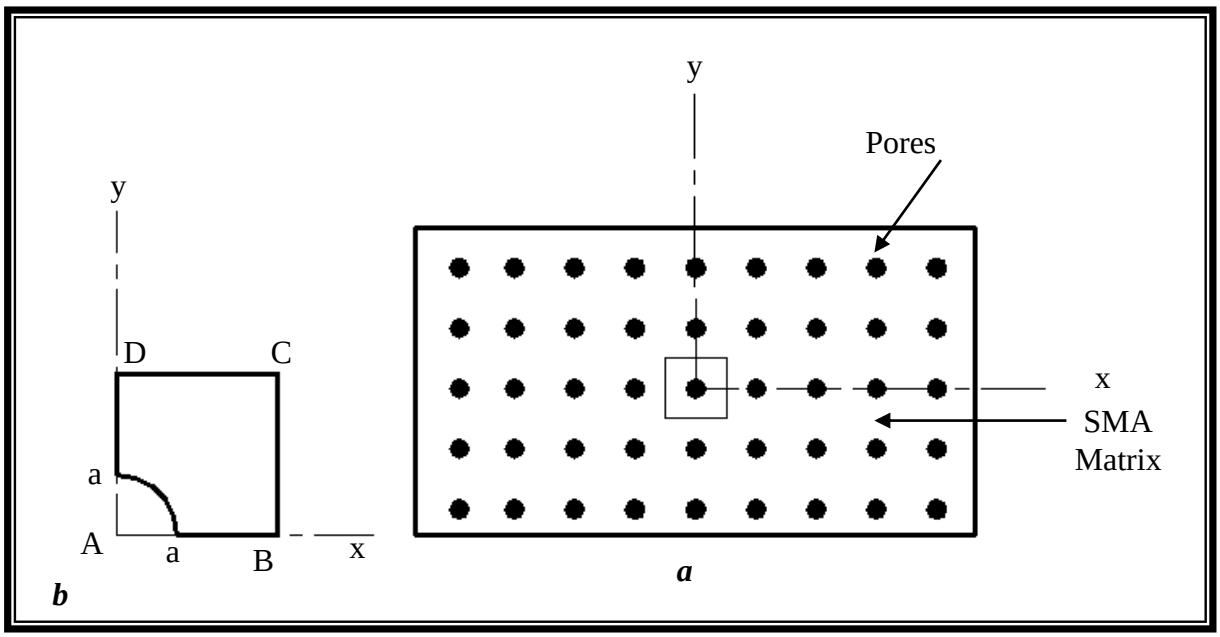

Fig..(5.4) square arrangement of pores in a and b squire unite cell

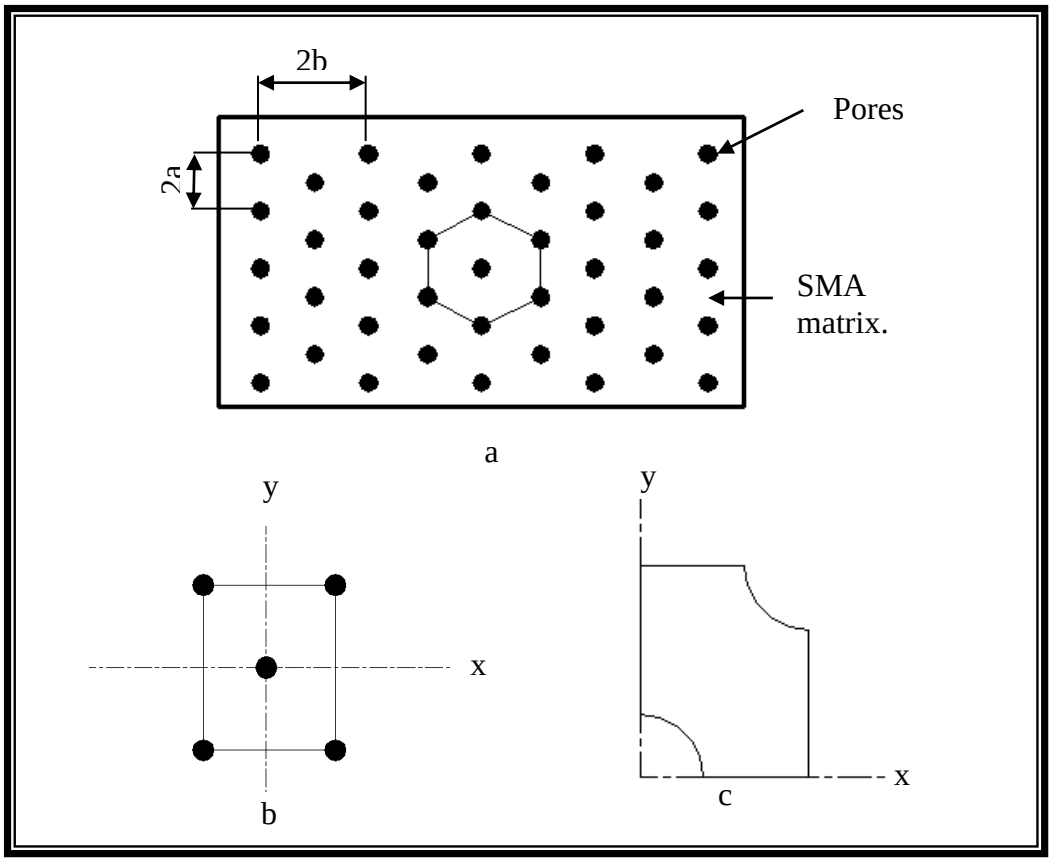

Fig.(5.5) Cross-section schematic of periodic hexagonal arrangement of open pores in a dense shape memory alloy matrix. a. Hexagonal arrangement of pore b. Repeated unite of pore arrangement C. Hexagonal unit cell .

In this case , the unit cell is a rectangle with length a and width b, So the cross section of each unit cell is a rectangle with cross section [2a × b]where b= 0.866 a . The unit cell has a uniform depth in the z- direction. Assuming that the applied loads do not violate the geometric symmetry of the unit cell.

5.5.1 real representation of microstructure image using image analysis and processing.

In this section several parameters and topics must be explained as follows:-

5.5.1. Image processing :-

Scanned surface section images of microstructure examination specimens have been used in both experimental and modeling studies. Image processing is applied to the microstructure light optical microscope image. The image is processed by Microsoft picture manger at first to obtain image without black edges taken from optical microscope as shown in Fig. (5.6).

Matlab version 7 imaging toolbox is used in order to convert the original images to a binary (black and white) image , with white signifying the shape memory alloy matrix and black being the pores. The image has a resolution of (118 pixels /cm) which captured by digital camera fitted by hand on the microscope. The processing of image involves creating a uniform background in the image and converting the image in to binary image . This stage includes the following steps in matlab version 7:-

Step 1. Read and display an image .

Clear the matlab workspace of any variable and read and display the microstructure image such alloy I image for example as shown in Fig. (5.7) using the command : I = imread (alloy I. JPg); imview(I)

Step 2. Estimate the value of background pixels:

This is very important step to recognize objects and background of image .There are many functions in morphological operations used to see the estimated background of image in matlab Toolbox software.

Step3. Create an image with uniform background .

step4. Create a binary version of the image .

Create a binary version of the image by using there sholding. The function gray threshold automatically computes an appropriate there to use to convert the image to binary as shown in Fig. (5.8).

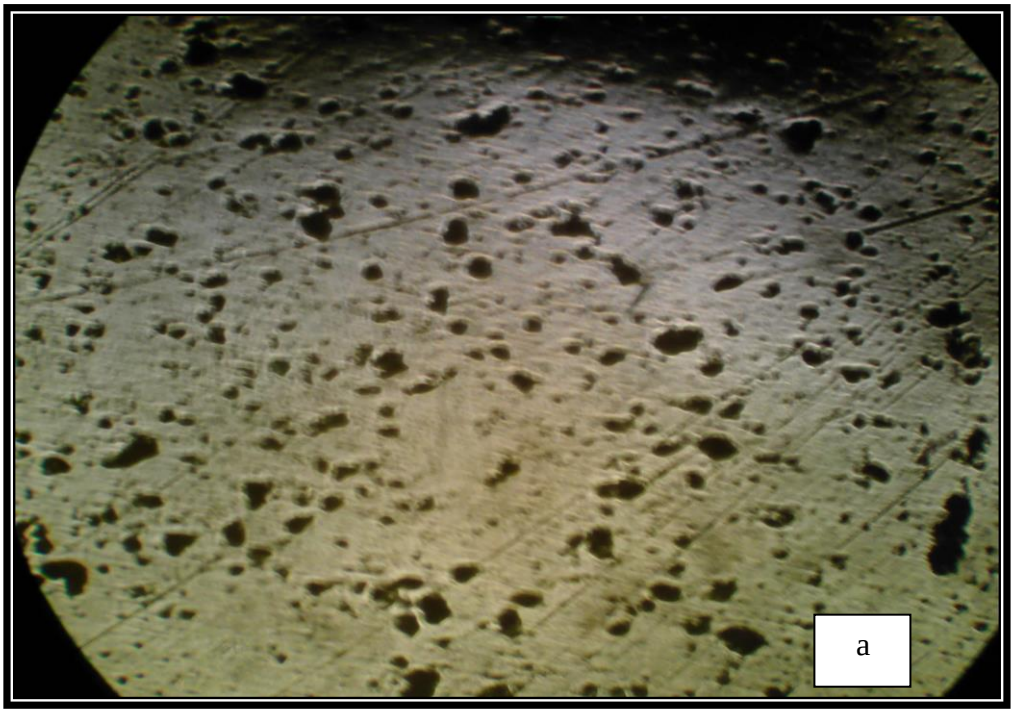

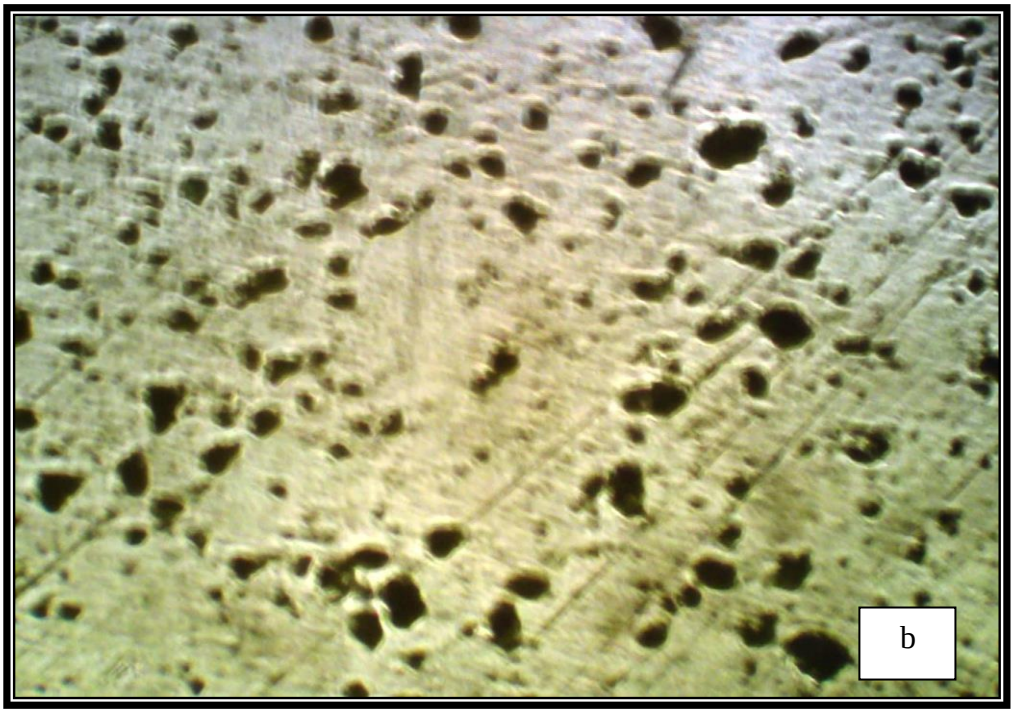

Fig. (5.6)LOM images for alloy 13 in the case of : a. original image b.neutralized image with Microsoft picture manger.

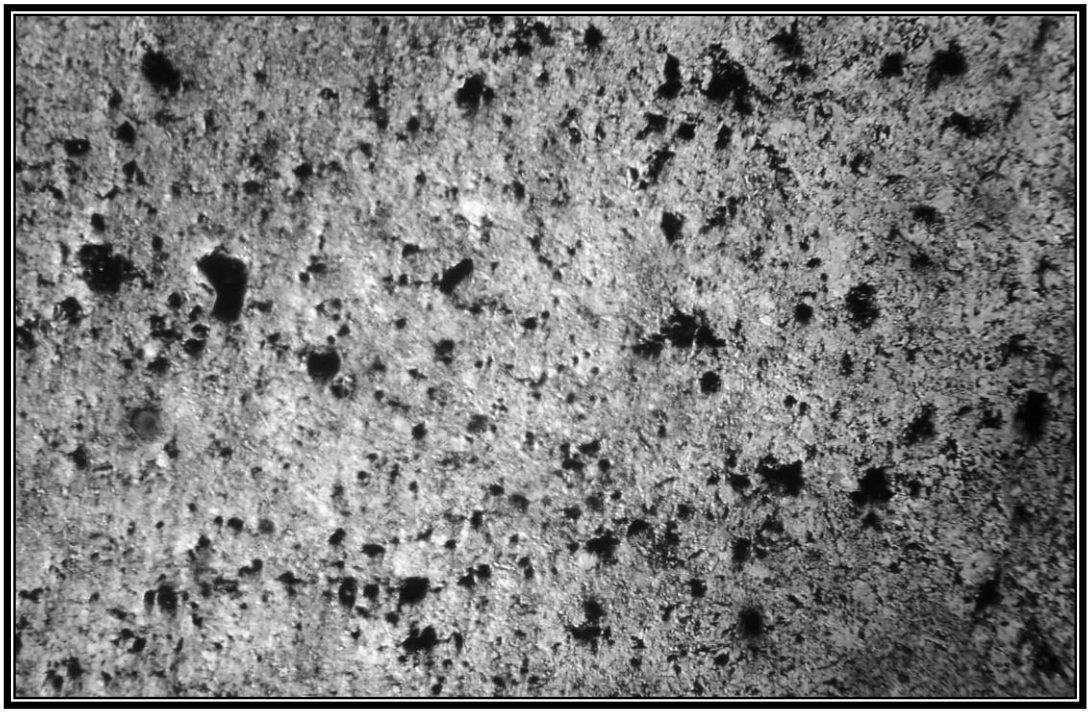

Fig.(5.7) LOM image with uniform background for alloy 10.

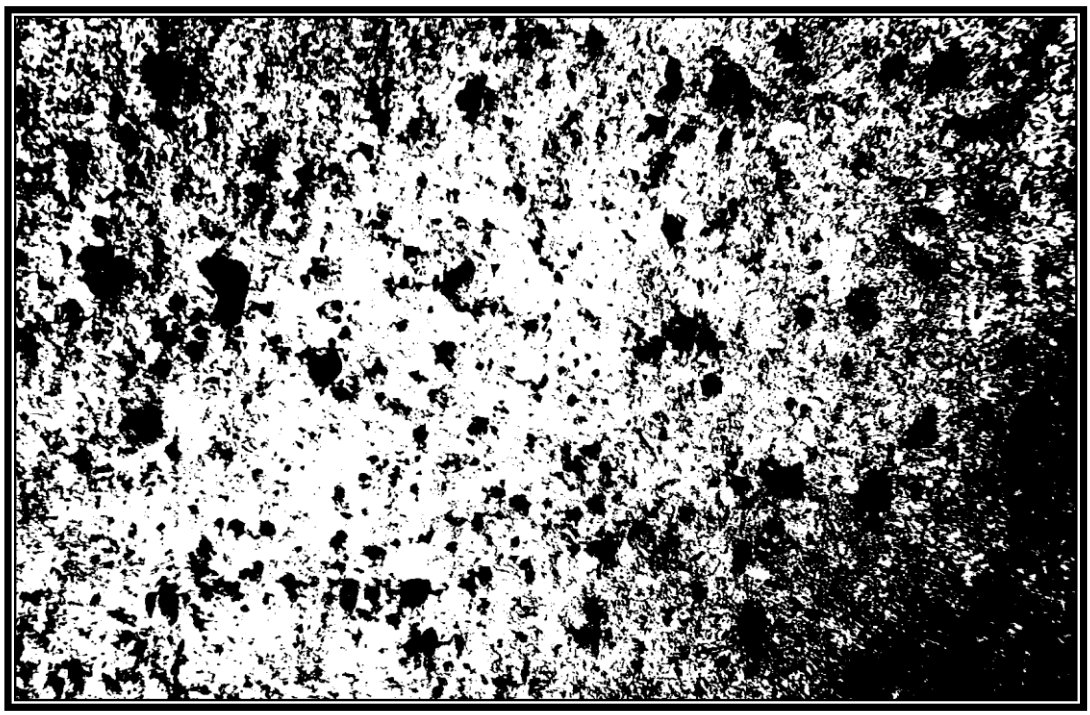

Fig.(5.8) LOM binary image for alloy 10.

5.5.2. Image Analysis:

After converting the image to a binary image (white and black), several functions have been used to determine the number of objects (black in image) which are pores , their distribution ,area , centroid and bounding box. The bounding box represents the smallest rectangle that can contain a region on in this case a pore. Further more , statistical properties of objects in the image may be obtained using matlab functions . statistical properties include maximum diameter of pore area , circle or ellipse fitted object and mean of all pore sizes.
This field of knowledge is new and very important in material engineering applications such as analysis of particles , shape and size and distribution of particles in the field of powder metallurgy as in this study, and in the analysis of final product microstructure for example pores size and their distribution , grain size and grain growth in complex metallurgy microstructure. The main problem in the field of image processing and analysis is the image segmentation which is the hardest task and main problem in computer vision . If target objects cannot be detected correctly, it is difficult to do object measurement , analysis and reconstruction. Since objects are complex in shape and size and its distribution, there is no universal segmentation algorithm.

There are several Segmentation algorithms based upon the type of images and requirements of measuring objects. These algorithms include:-

- ***threshold .***
- ***split and touching objects on shape.***
- ***edge detection.***

The algorithm based on edge detection is very useful for delineating objects with a valuable edge whereas threshold is suitable for image with either uniform object or uniform background. The algorithm based on split and merge is suitable for image on that objects have similar surface properties[wojnar,1999]. Object in our images are the pores in the analysis of microstructure of porous shape memory alloys and are the particles in the analysis of particles of pure

powders and blended powders before compaction. In this study image analysis and processing used to give the following :-

1. Particle size and shape using suitable scale calibration .
2. particle distribution based up on accumulated particle number and histogram of particle sizes.
3. particle size with suitable circle ellipse and Feret rectangle best fit with Particle shape .
4. pore size and shape in the sintered compact image .

5.6.Finite element Analysis of porous shape memory alloys using Ansys Software:

Ansys program is an open system where the user has various possibilities for constricting an individual model for the material .Ansys program is based up on finite element analysis. Our problem which in reality is composed of continuous fields (fields of displacements , strains , stresses temperature and state variables) can be solved by an approximate discrete element based solution.

Shape memory alloys have a complex behavior and are not similar than all other material behavior .They have several non linearities such as follow:

1. The deformations in the model are so large that the relationship between strains and displacements become non linear .
2. Material behavior is non linear .

3- The loadings may be non linear .

Thus all geometrical non linearities and material non linearities are employed in the analysis of shape memory alloys alone , further more the presence of pores also increased the complexity of the analysis .

After processing and analyzing microstructure images of porous shape memory alloys , Ansys parametric Design Language (APDL) script is used to input coordinates of pores with best fit ellipse , best Fit ferret rectangles and / or best fit circle .In Ansys version 9 (2005) there are two elements deal with shape

memory alloy which are plane 182 and plane 183. These element may be used to model only the super elastic behavior of shape memory alloys depend up on Auricchio model .

Plane 182 element is used for two dimensional modeling which is defined by four nodes having two degree of freedom at each node .where as plane 183 is defined by eight nodes with also two degree of freedom per node as shown in Fig..(5.9)

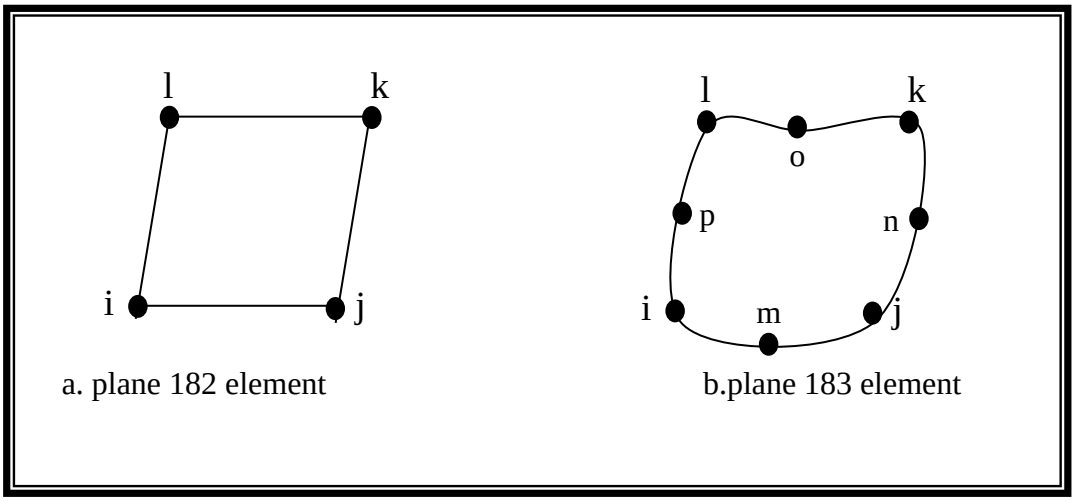

.

Fig.(5.9) Plane element use to model super elastic behavior of shape memory alloy in Ansys ver 9 Environment

5.6.1. Boundary Conditions

The following boundary conditions need to be applied regardless of pore geometry for unit cell finite element analysis .

$$U(0,y) = V(x,0) = 0 \qquad \text{Eq.}(5.43)$$

$$U_{max}(x,y) = C_1 \quad \text{and} \quad V_{max}(x,y) = C_2 \qquad \text{Eq.}(5.44)$$

Where U and V are displacements in the X and Y directions respectively and C_1 and C_2 are constants which impose the boundary conditions that all material points on respective unit cell boundaries have the same normal displacement. The stress and strain field in the unit cell can be extended for the whole porous shape memory alloy by virtue of the periodicity and symmetry conditions .

The reflective symmetries imply that shear stresses components are vanished on all boundaries of the unit cell (square and hexagonal Unit cell). So .

$$\tau_{xy}(0,y)=\tau_{xy}(x,0)=0 \qquad \text{...Eq.(5.45)}$$

Where τ_{xy} - in plane shear stress .

Fig.(5.10) shows the meshes of the unit cells used and mesh of real microstructure image with plane 182 element. Plane 182 with four nodes is used and based for finite element analysis formulation in order to decrease time of analysis and running addition to complexity of the structure.

Non linear load increment procedure has been done for 10 load steps with 50 steps with 50 and 5 sub steps of loads for maximum and minimum sub steps respectively.

5.6.2. Materials properties

In this study Auricchio model is based to model the superelastic behavior of shape memory alloy which described by six constants previously mentioned as follows:

$\sigma_S^{A\to M}$-starting stress value for austenite phase toward martensite phase (martensite starting stress).

$\sigma_f^{A\to M}$ - Martensite finishing stress.

$\sigma_s^{M\to A}$- starting stress value for martensite to austenite reverse phase transformation.

$\sigma_f^{M\to A}$- Final stress value for martensite to austenite reverse phase transformation.

ε_L^- - maximum transformation strain.

α - parameter measuring the difference between material responses in tension and compression.

These constants are input in the ansys program as show in Fig. (5.11). All material constants are measured experimentally from compression test of compression samples prepared in the experimental work..

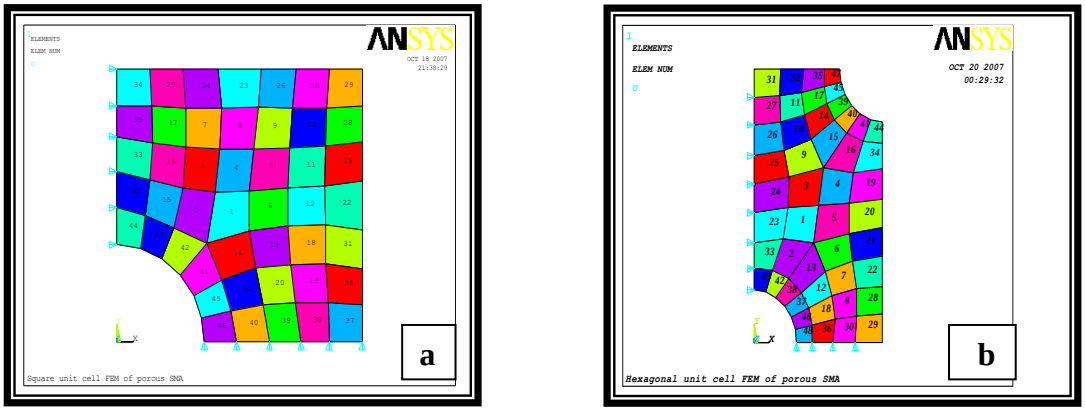

Fig.(5.10) Mesh of Square (a) and hexagonal (b) unit cell FE.

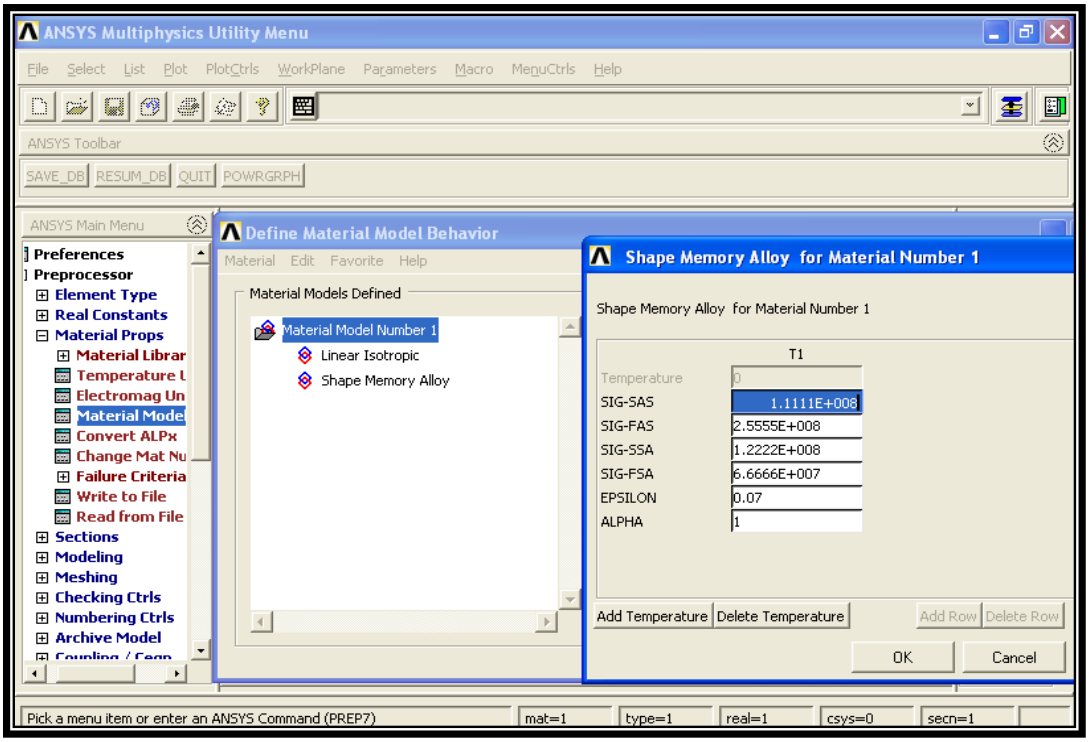

Fig.(5.11) Material properties of shape memory alloy input in Ansys program .

5.7. verification of the shape memory alloy model.

According to review of literature , there is very few papers about the analysis of porous shape memory alloys used unit cell finite element method. Perhaps there is no study of porous shape memory alloy based upon real micro structural image with ansys program. All previous studies deal with dense shape memory alloy manufactured by casting and their models have been done in another programs with user material subroutine (such as in Abquas program) . All researchers used unit cell finite element method and no one depend upon real microstructure of porous shape memory alloys. Therefore in this section two case studies have been presented for dense shape memory alloy.

1.First verification case study:

The First case study is a circular wire of diameter D= 1.49 mm and length 20 mm. The experimental loading unloading history was applied to the specimen reaching a maximum 8% strain by wick 1994(Queted in Auricchio etal 1997). The material parameters are in the following :

$E = 60$ GPa , $\nu = 0.3, \varepsilon'_L =$ 7.5 % , $\sigma_s^{A\to M} = 520MPa$, $\sigma_f^{A\to M} = 600MPa, \sigma_s^{M\to A} = 300MPa,$ $\sigma_f^{M\to A} = 200MPa$

In our verification, element plane 182 is used to mesh the specimen with its material parameters and applied incremental nonlinear loads as tensile stress. Fig.(5.12) showed the comparison between experimental and analyzed behavior. Good agreement has been obtained.

2. Second verification case study.

Nitinol tube (49.2 wt % Ti ,50.8 wt% Ni) with a 4.64 mm outer diameter and .37 mm thickness had prepared by (McNaney et. al, 2003) The tube was cut into 75 mm long specimens and ground along 25 mm long center test section to an outer diameter of 4.3 mm in order to obtain tensile specimen with 0.2mm thickness ,with the following material properties:

$E = 180\ GPa$, $\nu = 0.3, \varepsilon'_L = 6\%$, $\sigma_s^{A\to M} = 360\,MPa$, $\sigma_f^{A\to M} = 440\,MPa, \sigma_s^{M\to A} = 150\,MPa,$ $\sigma_f^{M\to A} = 100\,MPa$

Good agreement has been obtained with experimental study as show in Fig.. (5.13). For both examples , the material is nitinol 50/50 Ni-Ti base shape memory alloy. We choose these experimental studies because all material parameters are defined experiments alloy whereas many other studies on Ni-Ti or copper base alloys are studied from the point of view either focuses on physical properties such as x-ray diffraction , electrical resistance, DSC studies of some mechanical tests such as stress-strain curves or only hardness with nanoscale so we not comparison with these studies as a numerical study.

Note.

It must be shown that numerical modeling and simulation of porous shape memory alloys either by unit cell finite element analysis or by microstructure-based finite element analysis where the porous shape memory matrix and pore as particulate impeded in the matrix, shape memory material parameter for fully densed material must be presented. In this study all samples prepared by experimental work are porous so the following acceptable relation are based to calculate dense material parameters (See Zhao etal, 2005).

$$\sigma_{sp}^{M\to A} = (1-P)\sigma_{sD}^{M\to A} \quad \text{---------- Eq(5.46)}$$

$$\sigma_{fp}^{M\to A} = (1-P)\sigma_{fD}^{M\to A} \quad \text{---------- Eq(5.47)}$$

$$\sigma_{sp}^{A\to M} = (1-P)\sigma_{sD}^{A\to M} \quad \text{---------- Eq(5.48)}$$

$$\sigma_{fp}^{A\to M} = (1-P)\sigma_{fD}^{A\to M} \quad \text{---------- Eq(5.49)}$$

Where :

p-apparent porosity

p and D subscript refer to porous and fully densed respectively for all stresses which defined as material parameters .

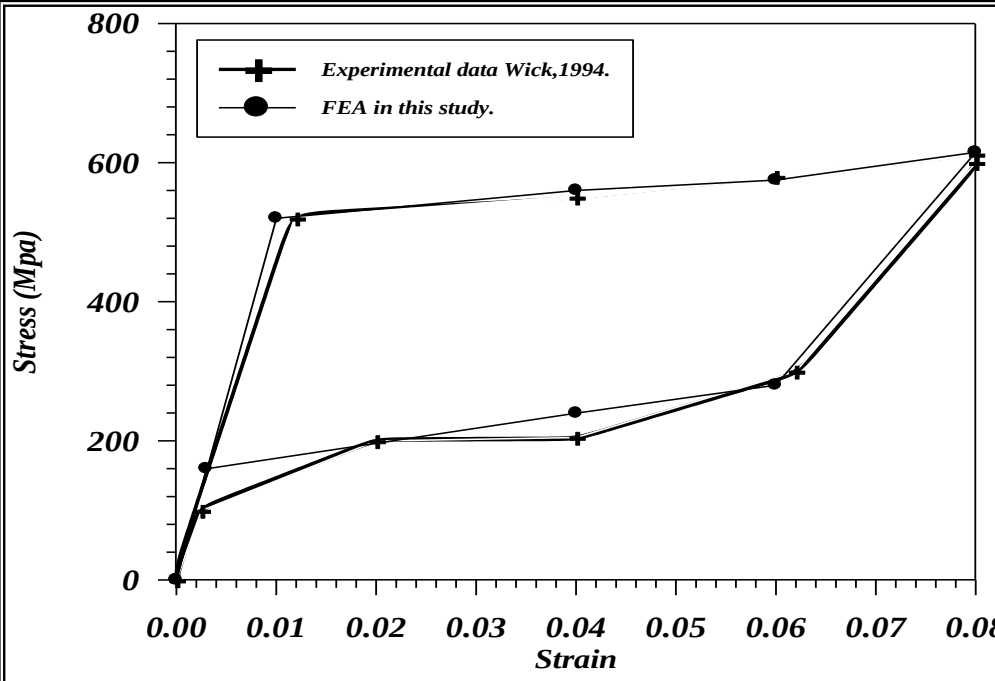

Fig.(5.12) Stress-Strain curve for nitinol wire under tension ,comparison between experimental and FEA for case study 1.

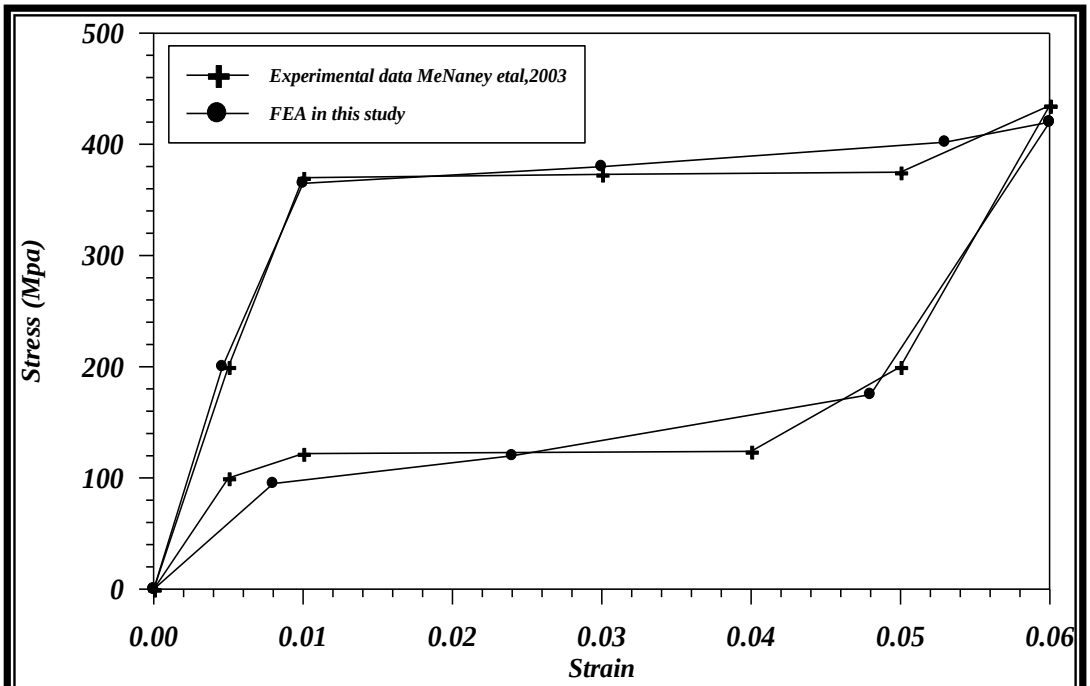

Fig.(5.13) Stress- strain curve for nitinol tube under tension, comparison experimental with FEA for case sudy 2.

Results and Discussion

6.1 General View :

In this chapter , experimental results which include physical and mechanical tests results for both before sintering and after sintering process have been presented . At a first , physical properties measured in this study for elemental and blended powders such as apparent density , particle size and shape and particle distribution have been presented .It has been Concluded that all experimental results are classified into before sintering and after singeing in order to avoid any ambiguous arrangement of results . Furthermore, numerical results and comparison with experimental work based up on unit cell finite element analysis and microstructure based finite element analysis have also presented .

6.2.Results before sintering of compacts :

In this part many physical tests results and several parameters have been studied and presented as follows:

6.2.1 Apparent density of elemental and blended powders :

Apparent density of elemental powders used to prepare blended mixture of alloys has been measured and shown in Fig.(6.1). The apparent density of iron and nicked are the highest density compared with other powders due to high density of the solid material for be both iron and nicked .

Apparent density of a metal powders depends upon the density of the solid material , particle size and its distribution , particle shape and surface area , Apparent density is strongly affected by particle size and its distribution, in

addition , As particle shape becomes less spherical apparent density decreases due to the increase in frictional surface area and less uniformity powder particle during packing .

Apparent density of blended powders for mixtures of alloys [1,2,3 and 6] is shown in Fig .(6.2). Apparent density of mixture of alloy (1) is the highest with comparison with other mixtures due to the high content of higher solid density of copper. The measured apparent density of blended powders and elemental powders , has been affected by the flow rate and internal friction between particles in the same or different composition and friction between particles and wall of baffle box and small funnel . Decreasing surface area to volume ratios and decreasing surface roughness tends to reduce frictional forces between setting particles , This tendency thus increases apparent density by allowing the particles to move with more effectively to fill the free spaces between previously settled particles. An effective way to increase the apparent density of the elemental or blended powders is to fill the spaces between particles with smaller particles as can be seen in the next section.

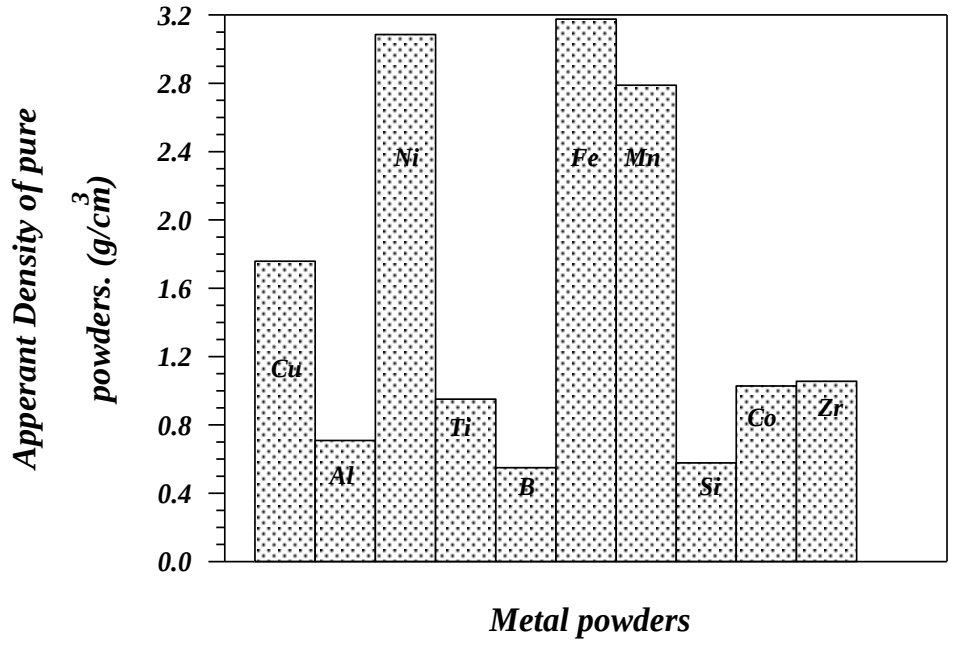

Fig.(6.1) Apperant density of pure metal powders used in this study.

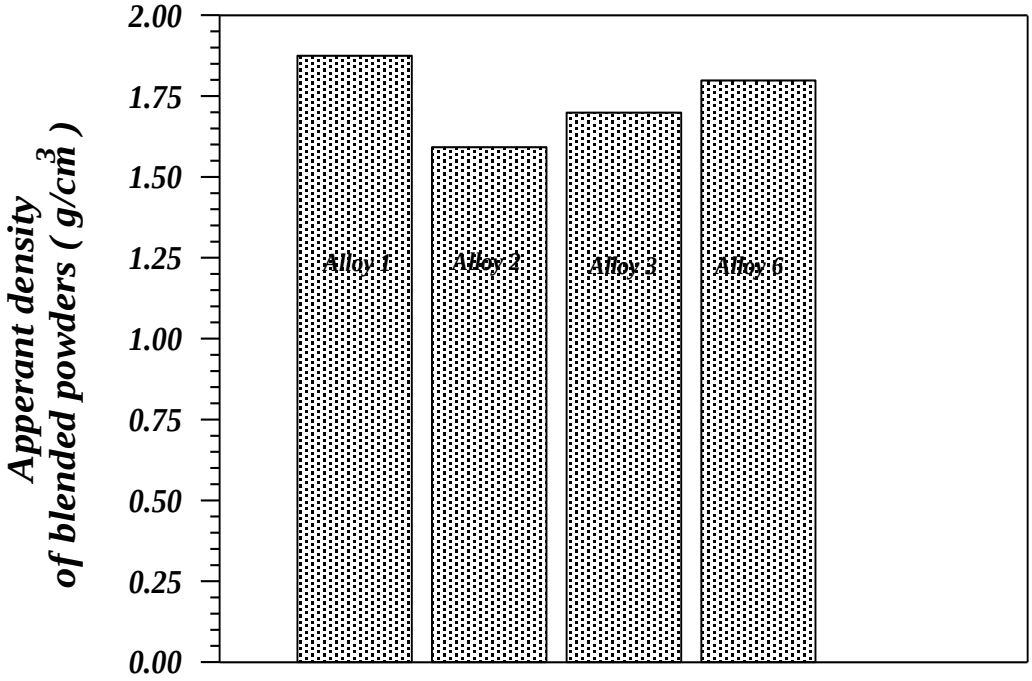

Fig.(6.2) Apparent density of blended mixtures of alloys.

6.2.2 particle size and distribution :

Particle size and its distribution for both elemental and blended powders have been measured in this work using light optical microscopy images which are analyzed and processed using image analysis toolbar in matlab version 7 program image in white and black (binary image) and accumulative plot for each powders are shown in Figures (6.3 - 6.12).

In all these image middle particle size are used in the image analysis to find particle size of metal powders. Mean particle size is determined at 50 % point on the accumulative plot , accumulative plot is weighted by particle size .In all these image , agglomerate of particles in the glass slide is the main problem which may be occurred so wrong result about particle size may be obtained .Furthermore ; the best fit ellipse or circle or feret width and feret length used to capture particles shape and size are estimated technique and affected on the final results accuracy . Mean of particles size for elemental and blended powders are given in table (6.1) .

Decreasing particle size generally decreases apparent density because the smaller particles have greater specific surface of the powder which the later leads to increase the friction between particles and subsequently decreases the apparent density.

On the other hand , most powders used for compaction have irregular shape. The addition of fine spherical powder such as powder Ni effectively increases apparent density while the addition of flake powders such as Cu decreases apparent density .

The relative amount of coarsest and finest particles and the percentage of particles between the two types determine apparent density .

Binary image and accumulative plot for blended mixture of powders from alloy(1,2,3and 6) are shown in Fig .(6.13-6.16) .respectively .

Different particle size ranges are preferred for good compacts and also for good properties of the final sintered Products .

Table(6.1) Average particle size of metal powders and blending mixtures

No.	Material	Average particle size
1	Cu	1
2	Al	2
3	Ni	8
4	Ti	75
5	B	80
6	Co	0.8
7	Zr	8.2
8	Fe	20
9	Mn	1.2
10	Si	4
11	Alloy 1	9
12	Alloy 2	5
13	Alloy 3	16
14	Alloy 6	8

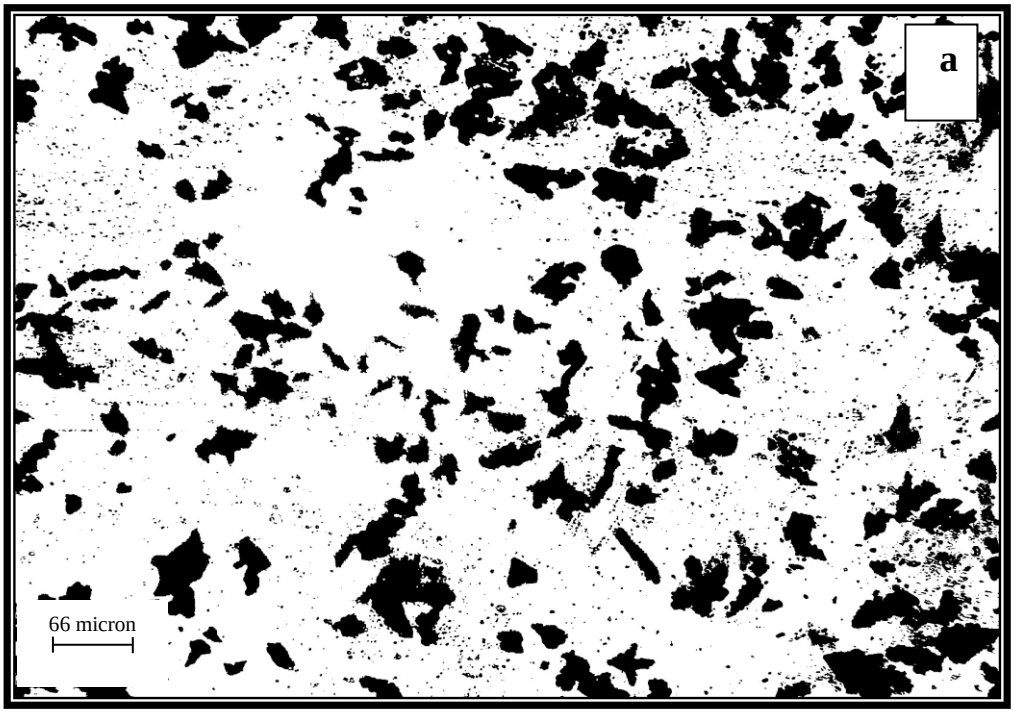

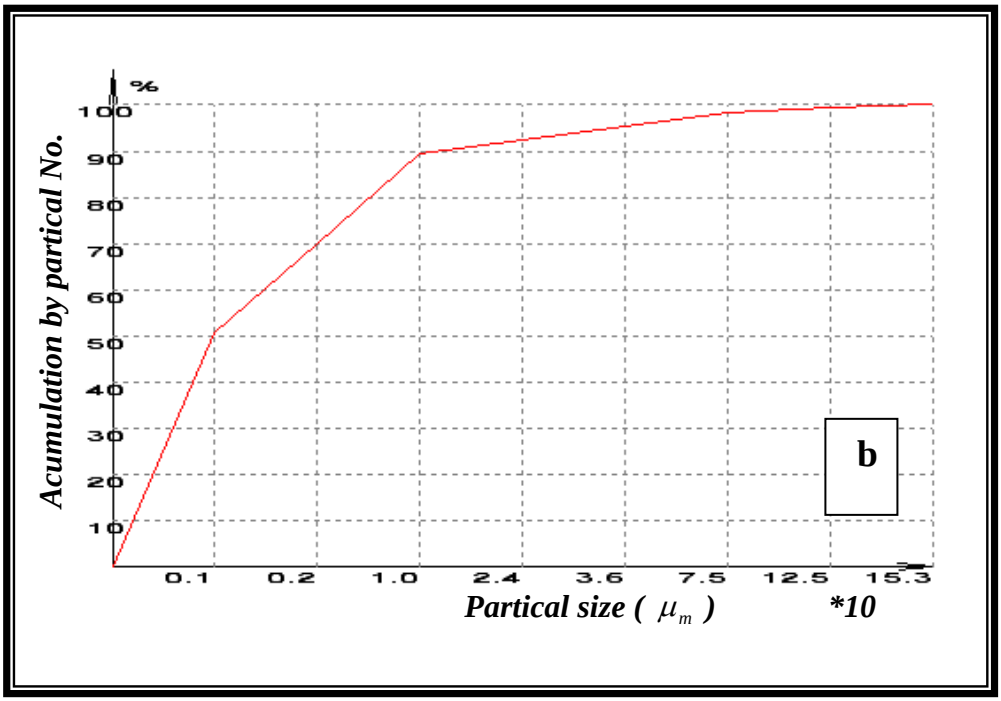

Fig.(6.3) Binary Image and Accumulative size Distribution in (a) and (b) respectively of Cu Powder.

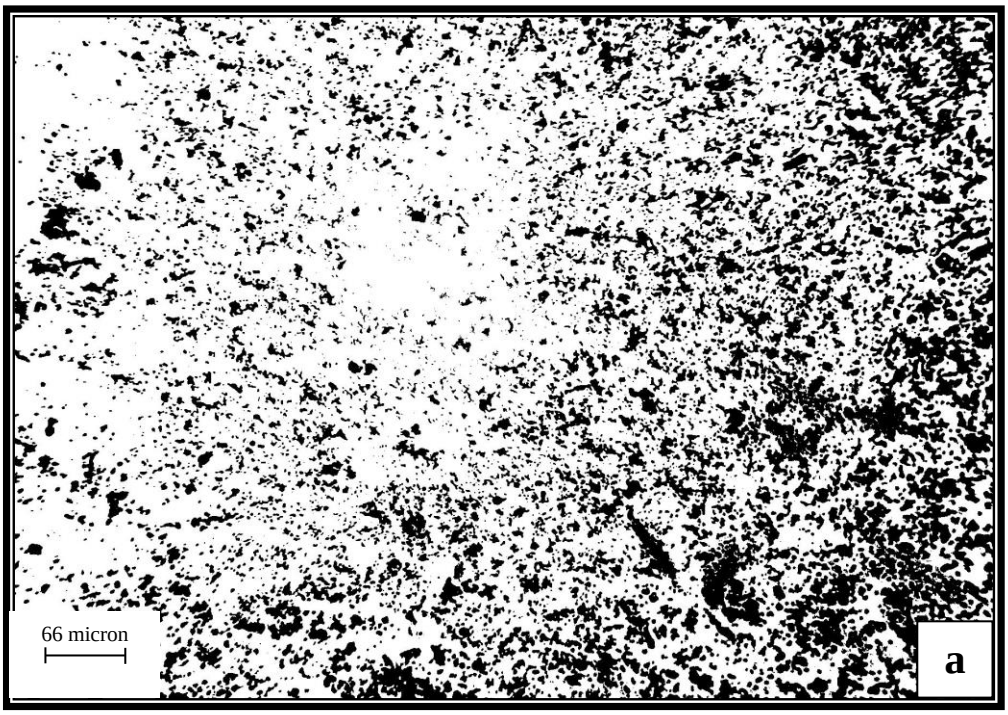

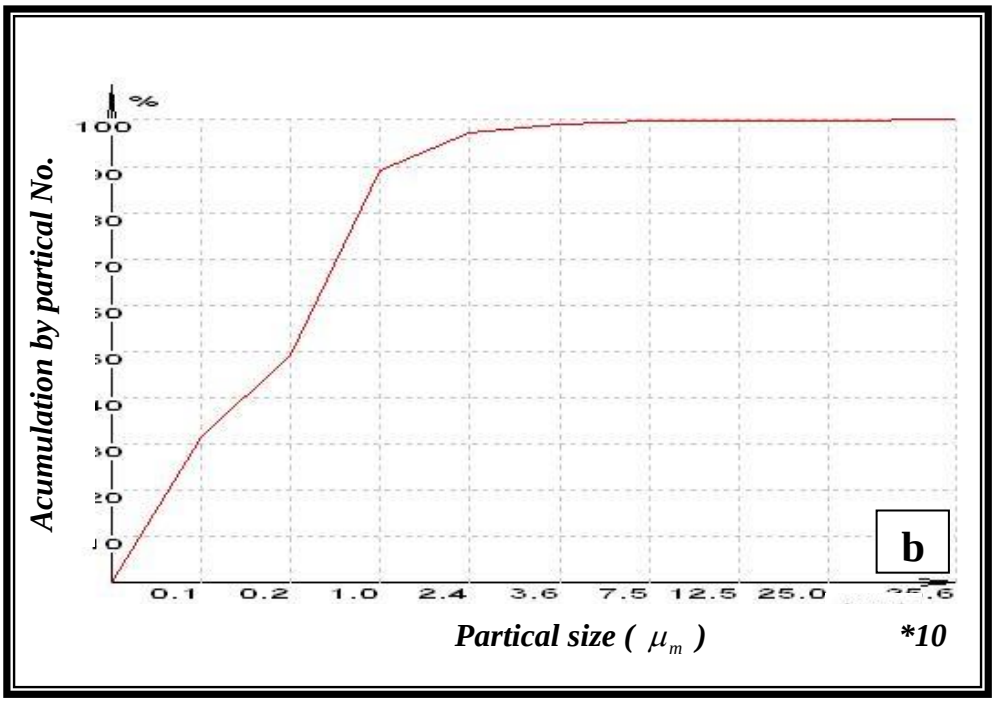

Fig.(6.4) Binary Image and Accumulative size Distribution in (a) and (b) respectively of Al Powder.

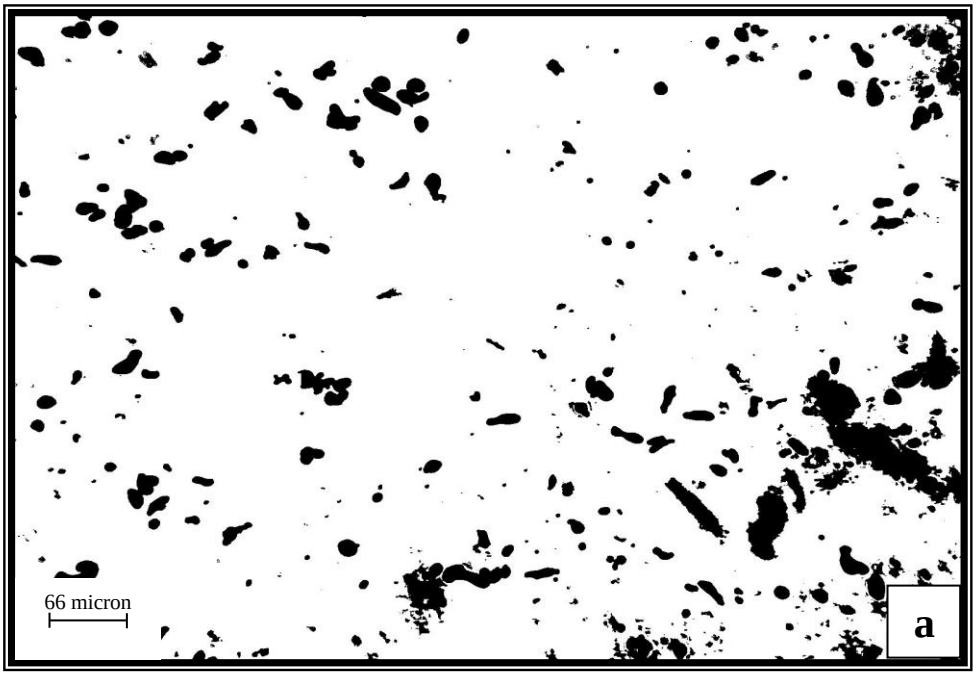

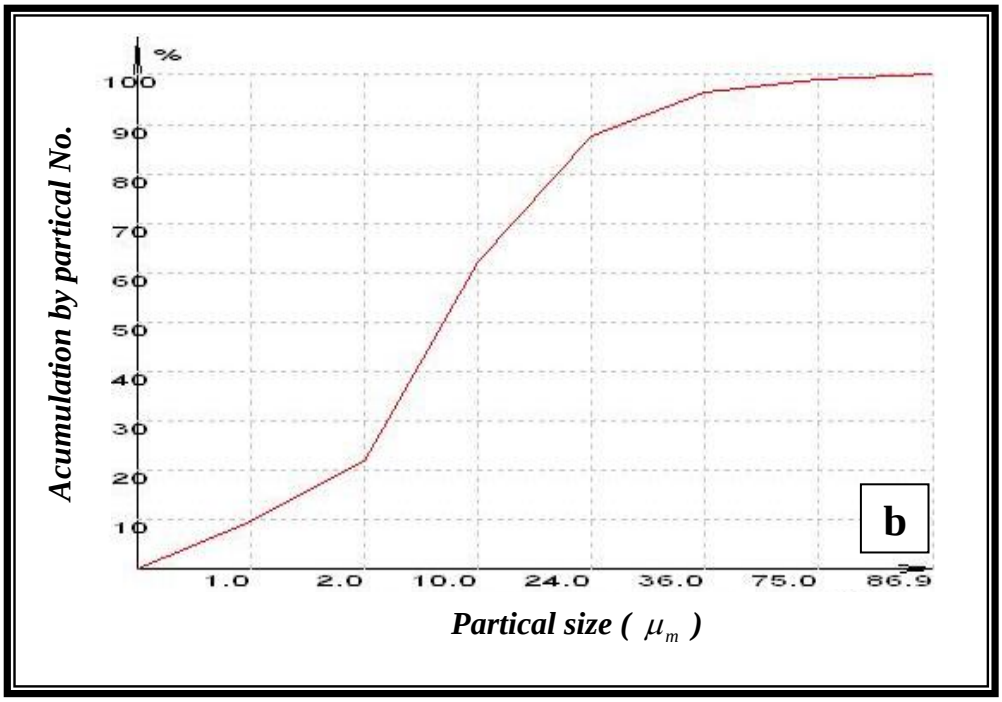

Fig.(6.5) Binary Image and Accumulative size Distribution in (a) and (b) respectively of Ni Powder.

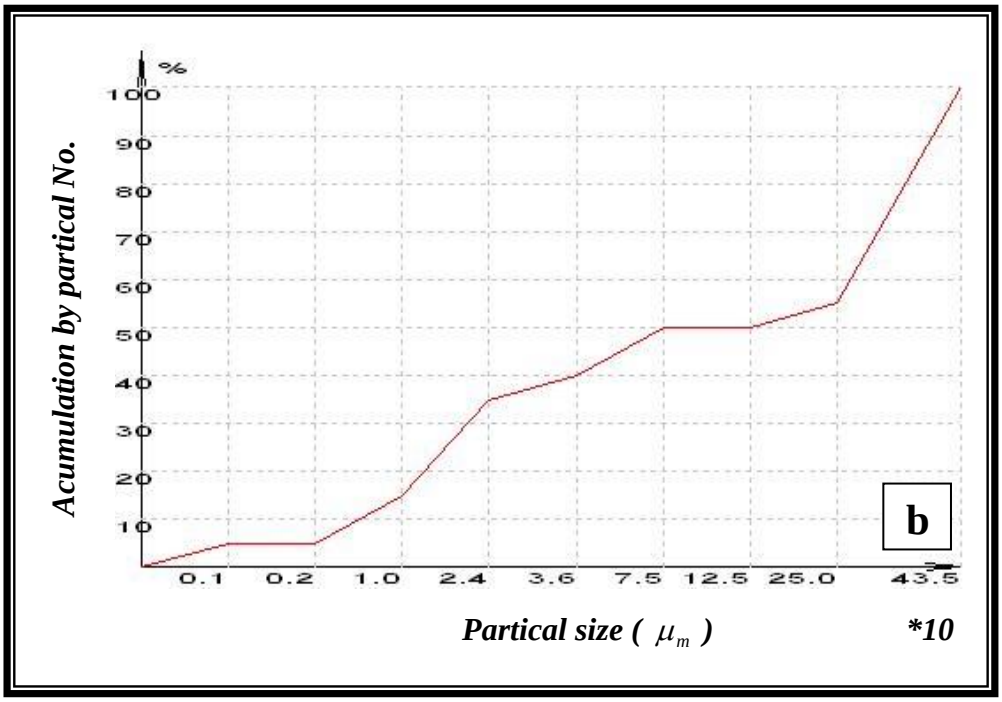

Fig.(6.6) Binary Image and Accumulative size Distribution in (a) and (b) respectively of Ti Powder

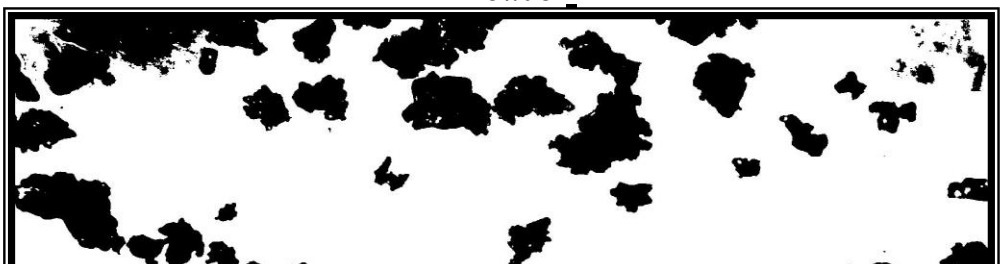

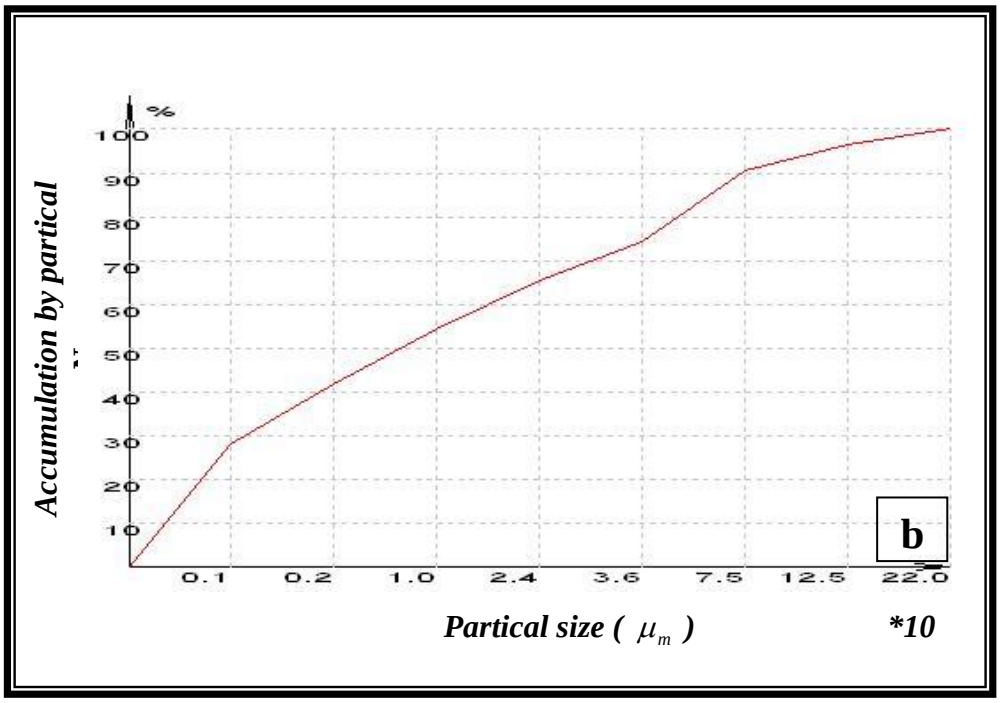

Fig.(6.7) Binary Image and Accumulative size Distribution in (a) and (b) respectively of B Powder

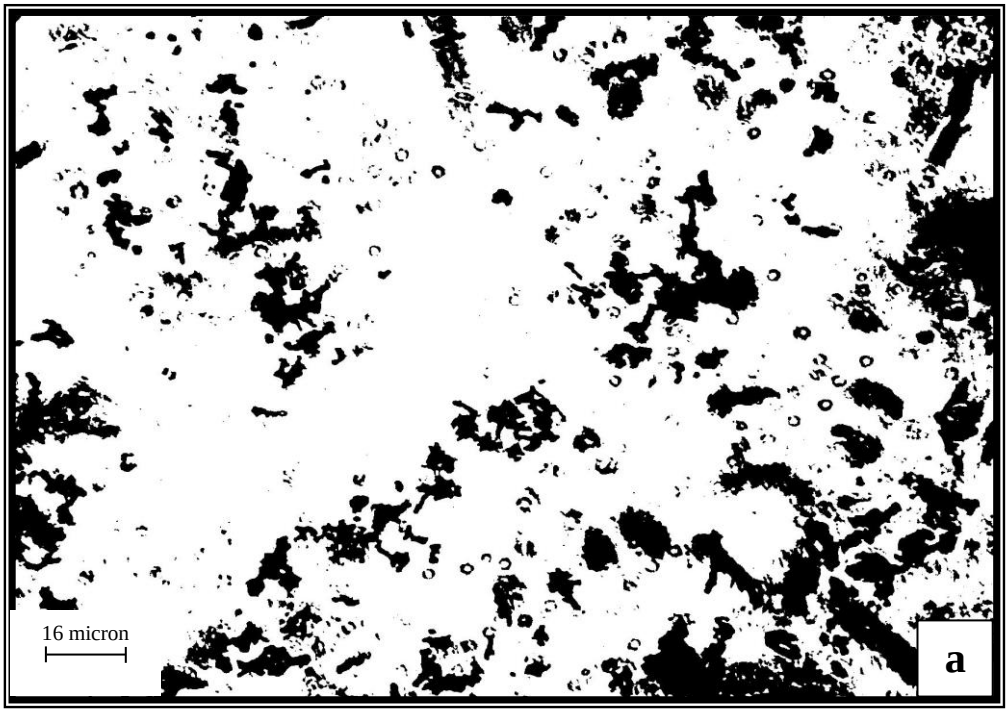

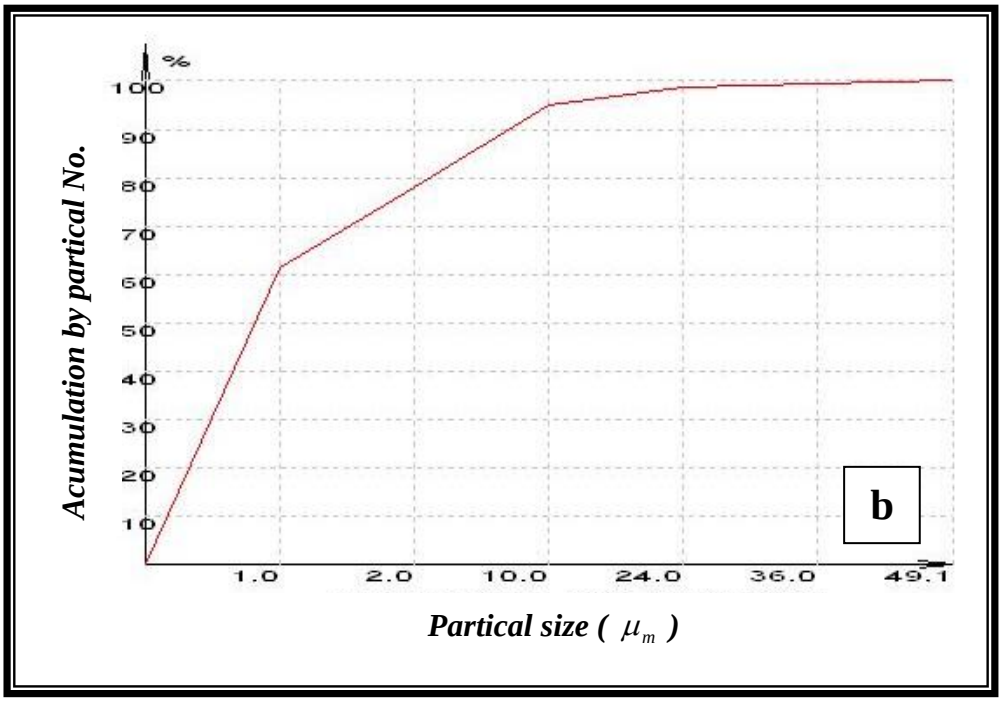

Fig.(6.8) Binary Image and Accumulative size Distribution in (a) and (b) respectively of Co Powder

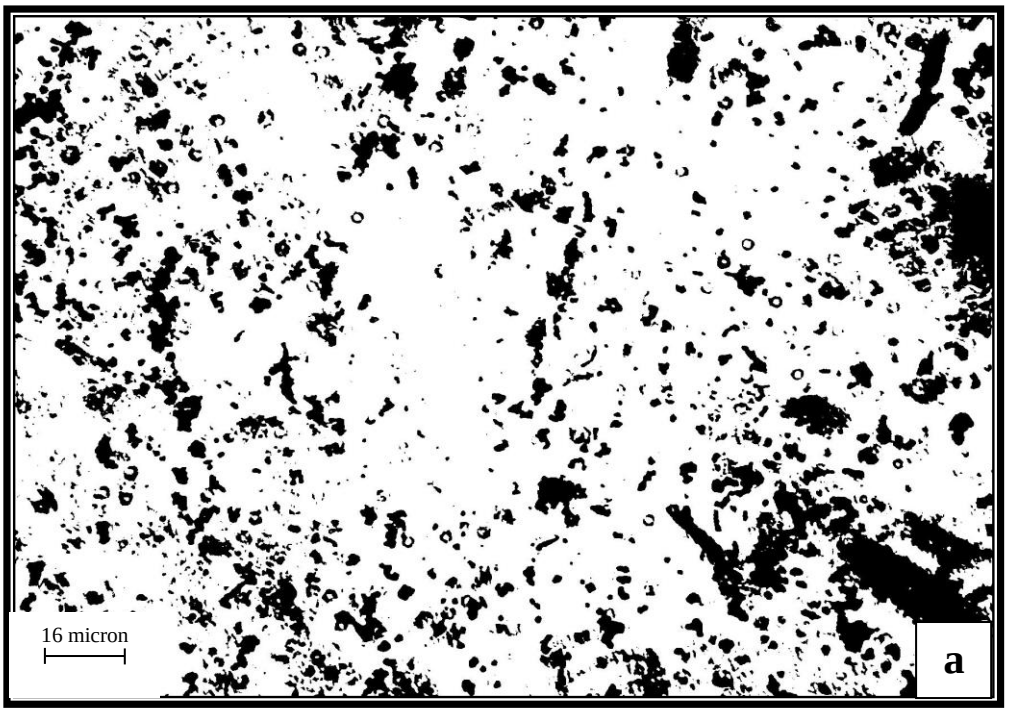

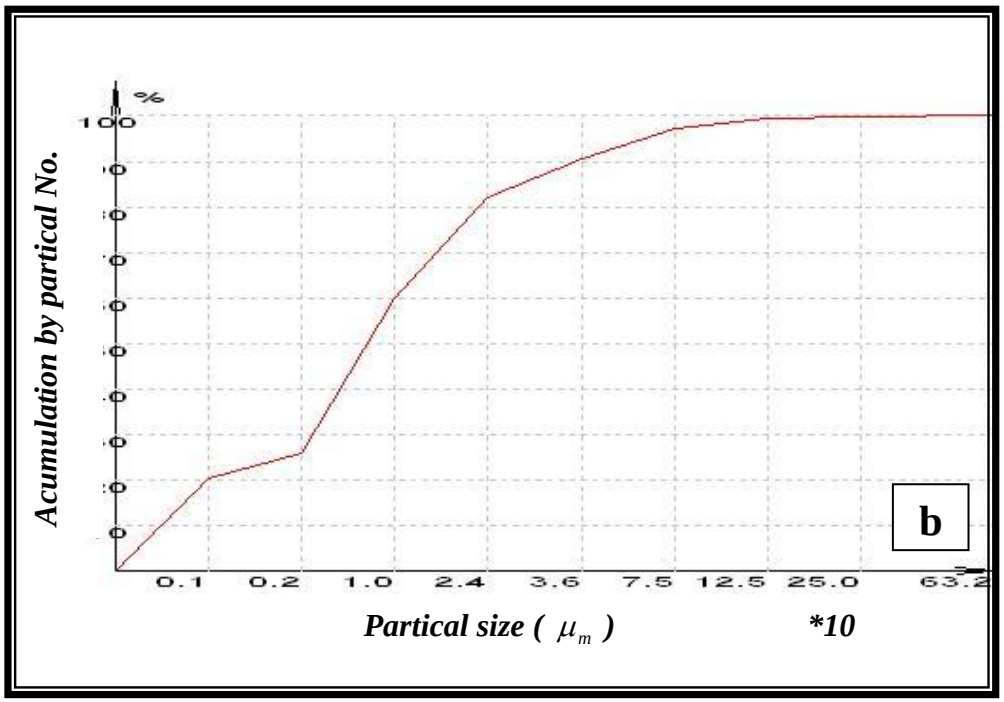

Fig.(6.9) Binary Image and Accumulative size Distribution in (a) and (b) respectively of Zr Powder

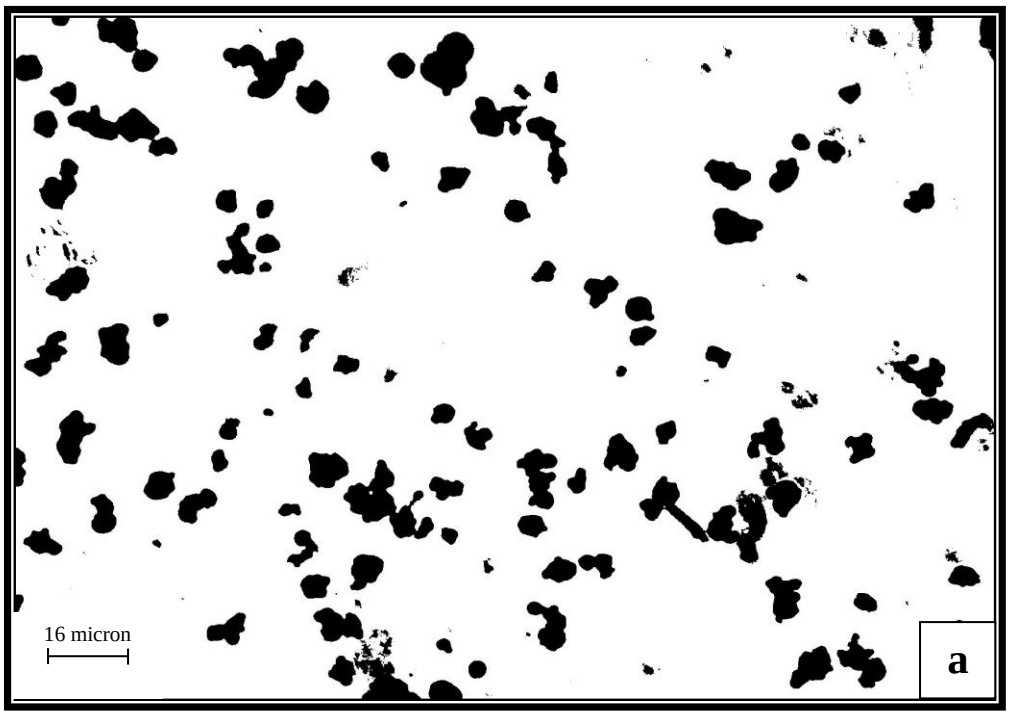

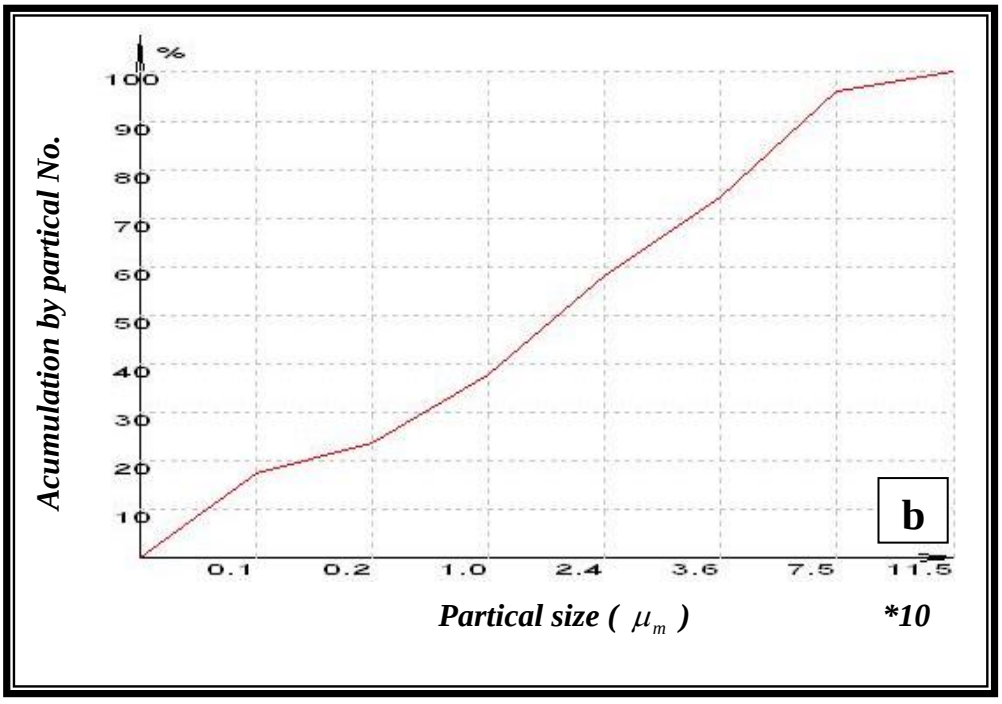

Fig.(6.10) Binary Image and Accumulative size Distribution in (a) and (b) respectively of Fe Powder

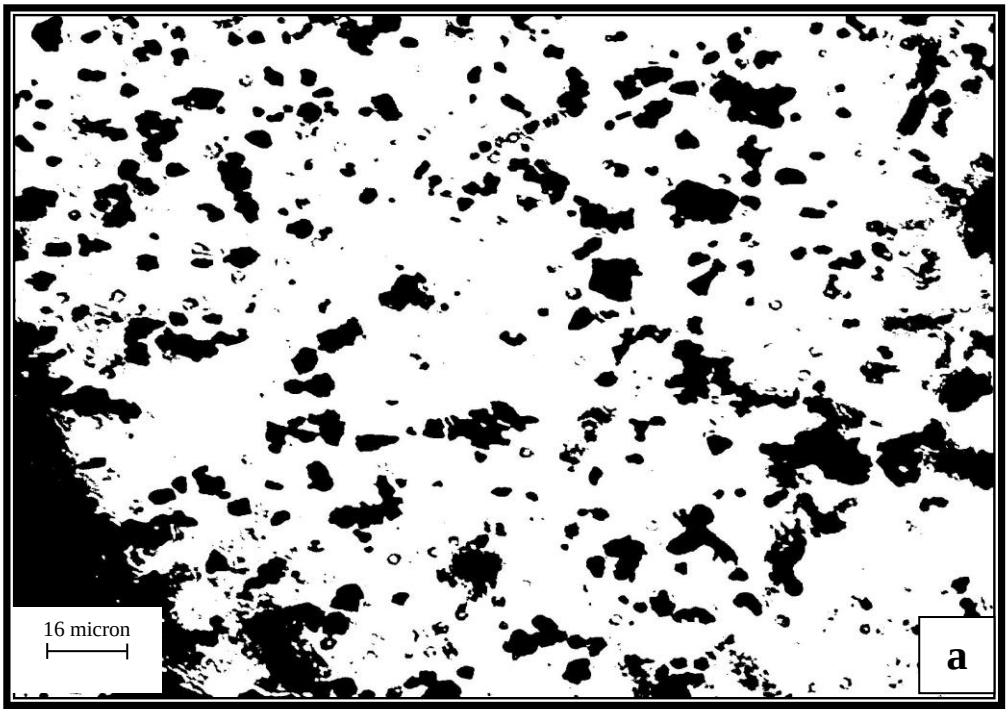

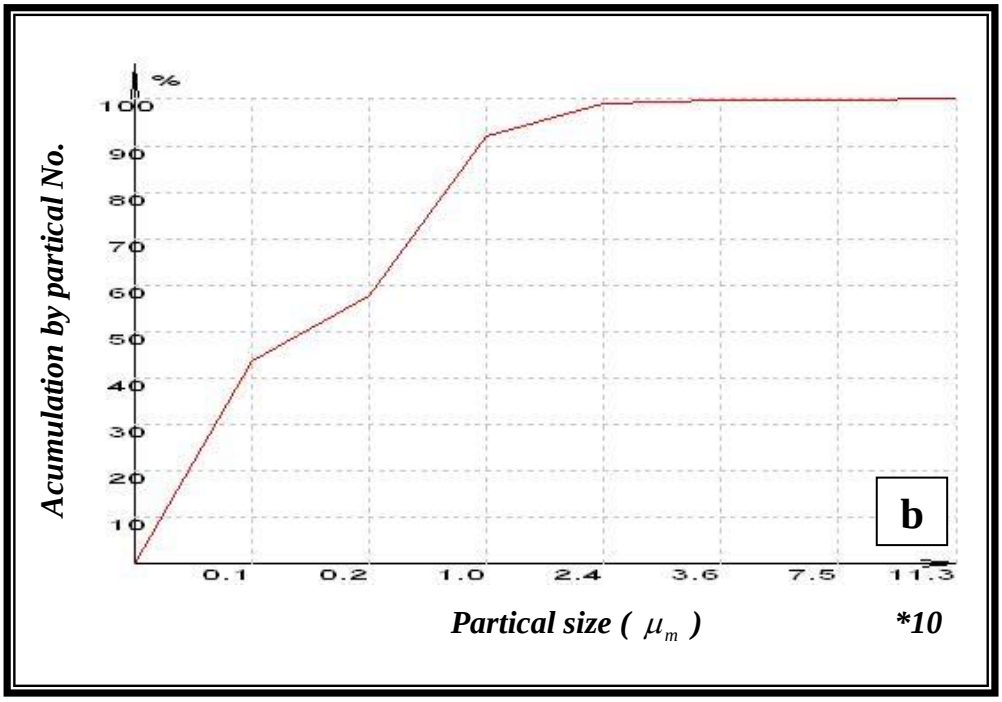

Fig.(6.11) Binary Image and Accumulative size Distribution in (a) and (b) respectively of Mn Powder

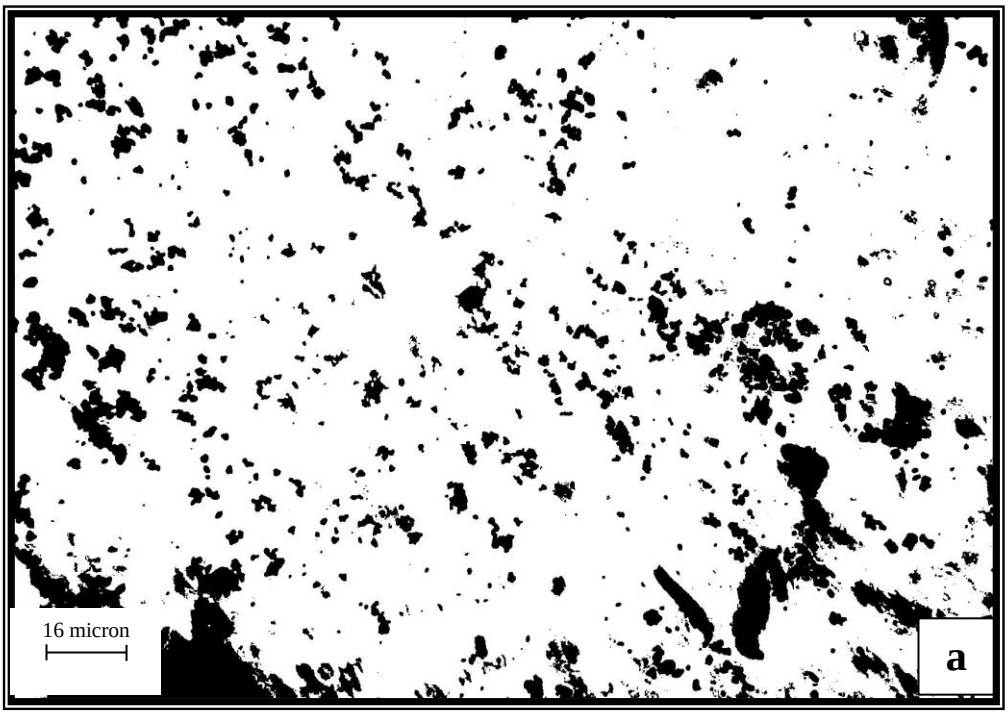

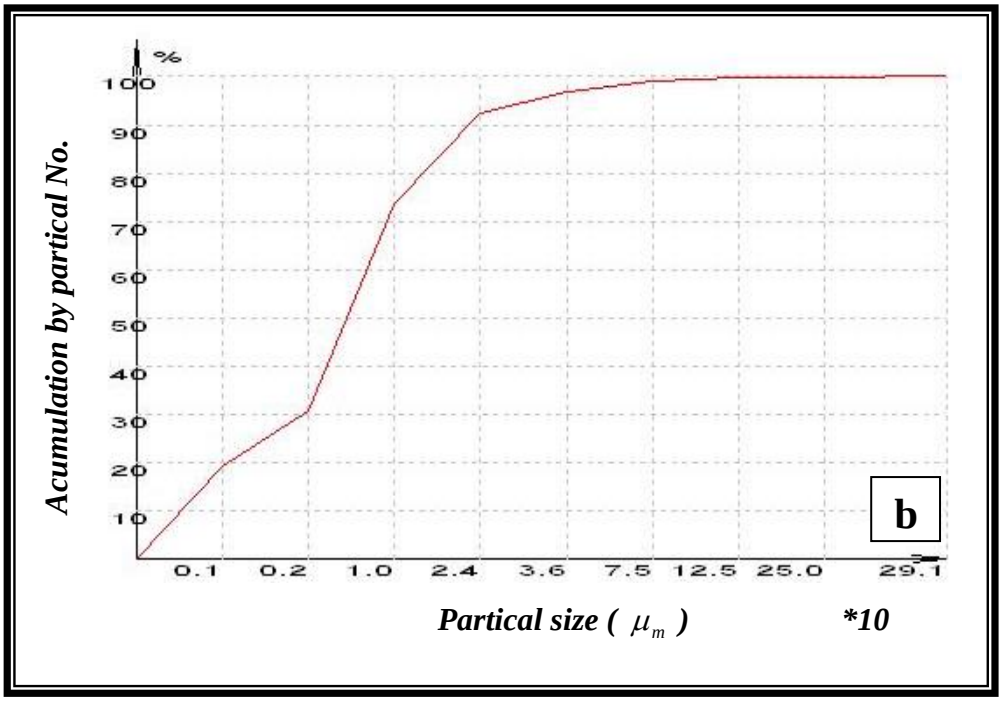

Fig.(6.12) Binary Image and Accumulative size Distribution in (a) and (b) respectively of Si Powder

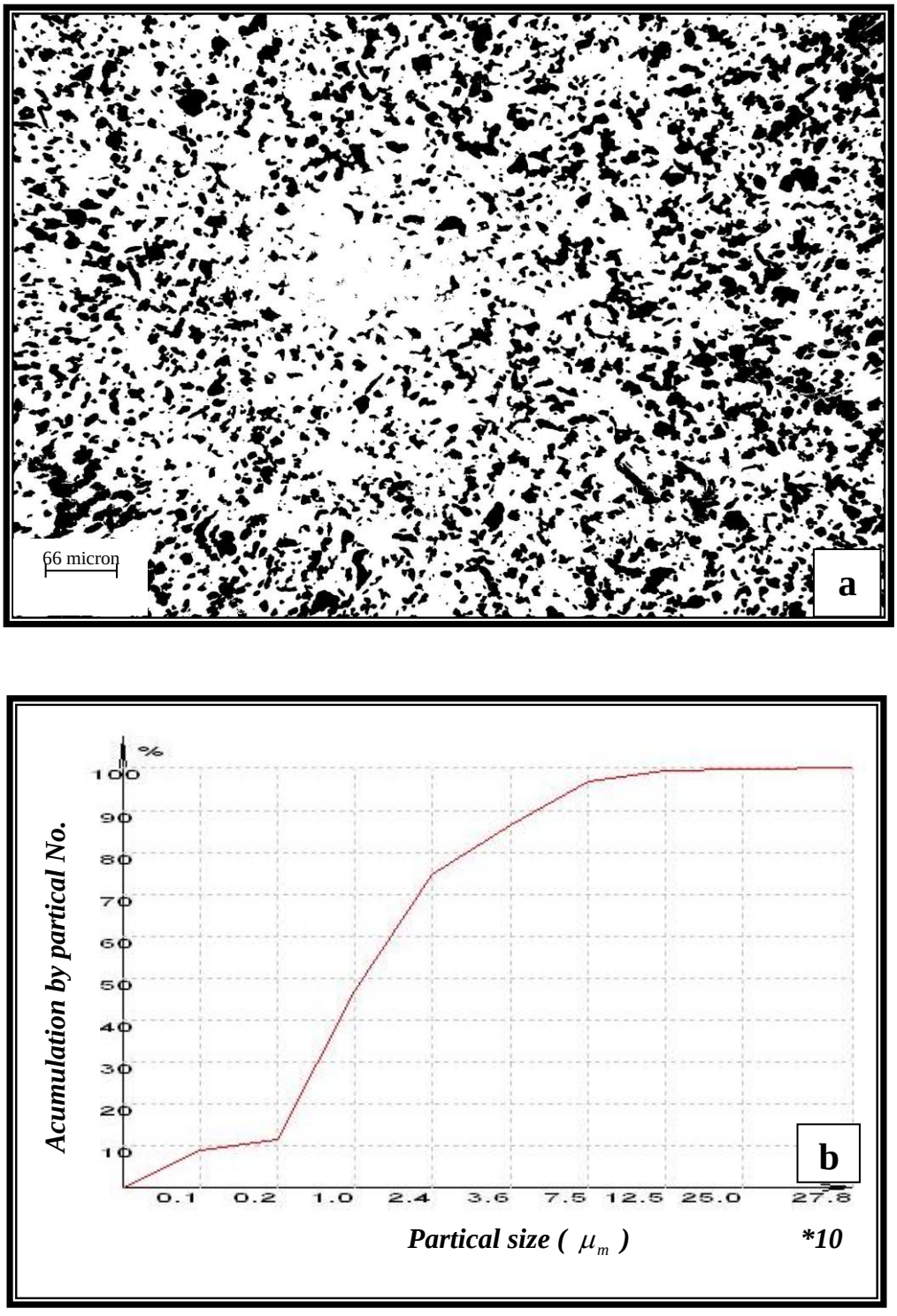

Fig.(6.13) Binary Image and Accumulative size Distribution in (a) and (b) respectively of blended mixture of alloy1 Powder.

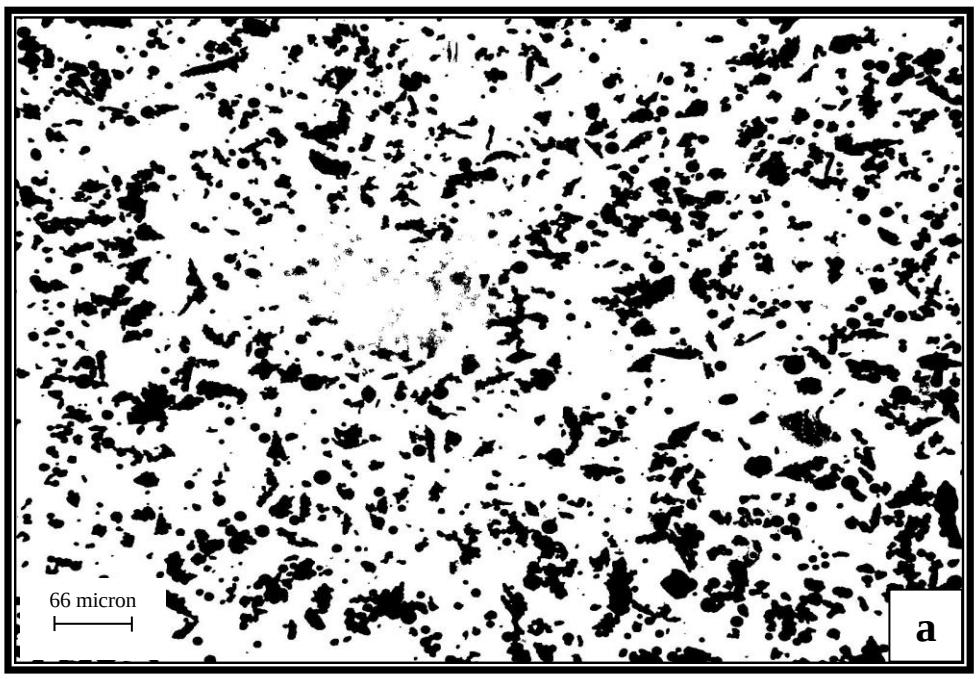

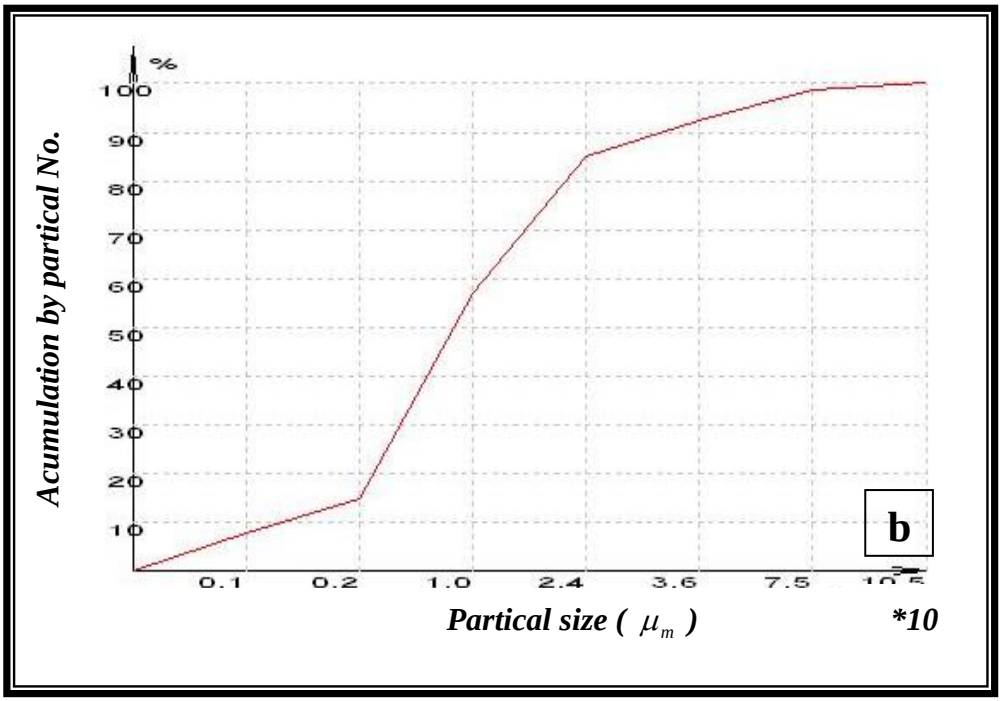

Fig.(6.14) Binary Image and Accumulative size Distribution in (a) and (b) respectively of blended mixture of alloy2 Powder

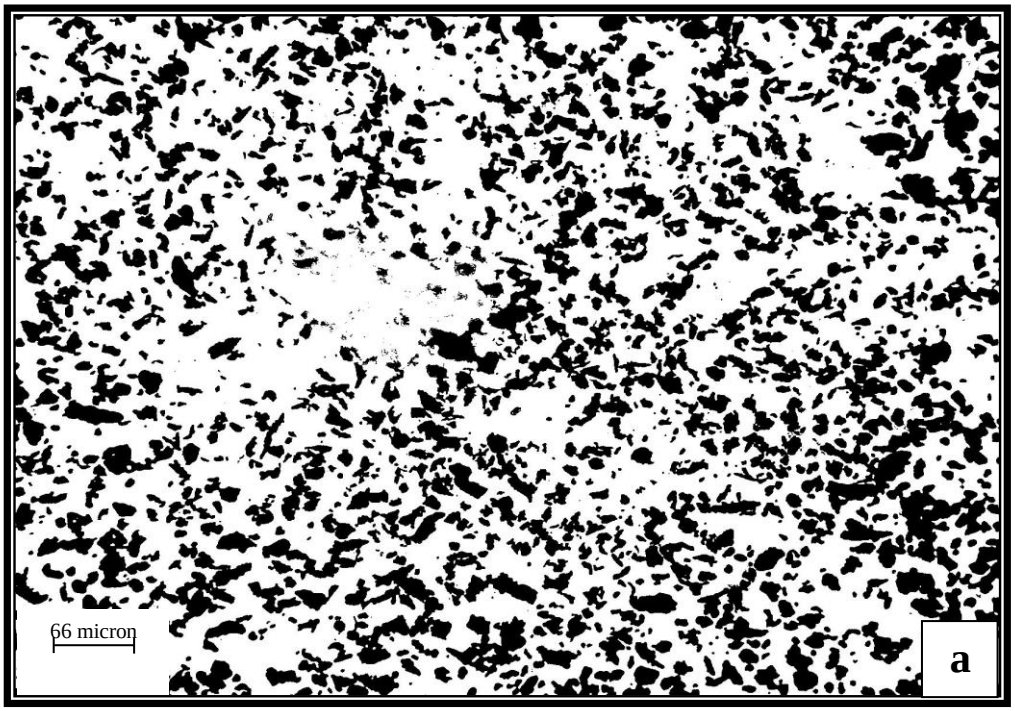

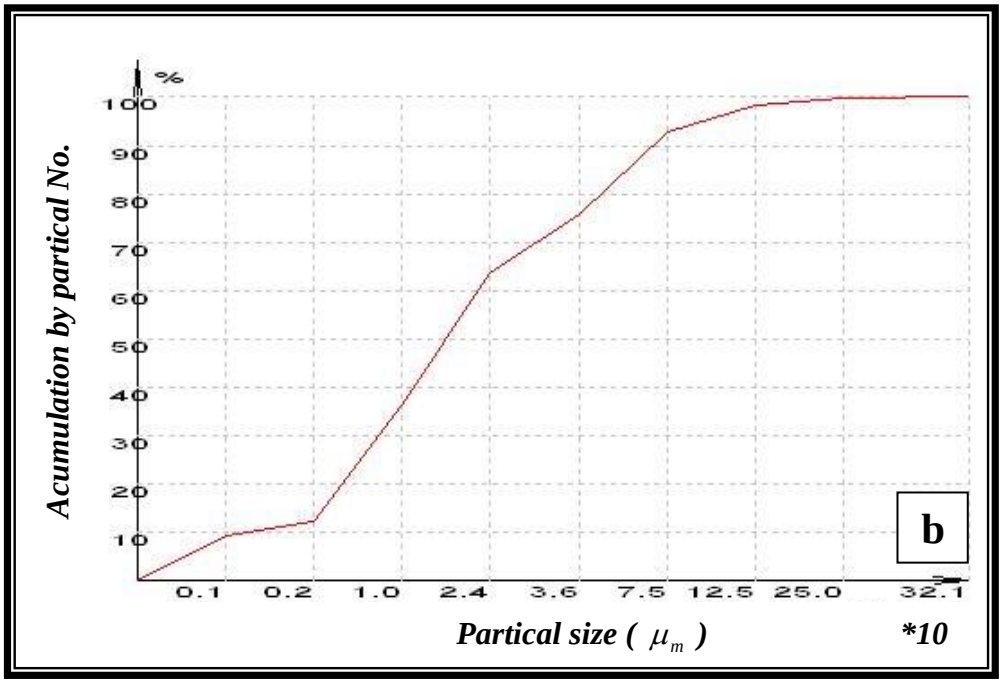

Fig.(6.15) Binary Image and Accumulative size Distribution in (a) and (b) respectively of blended mixture of alloy3 Powder

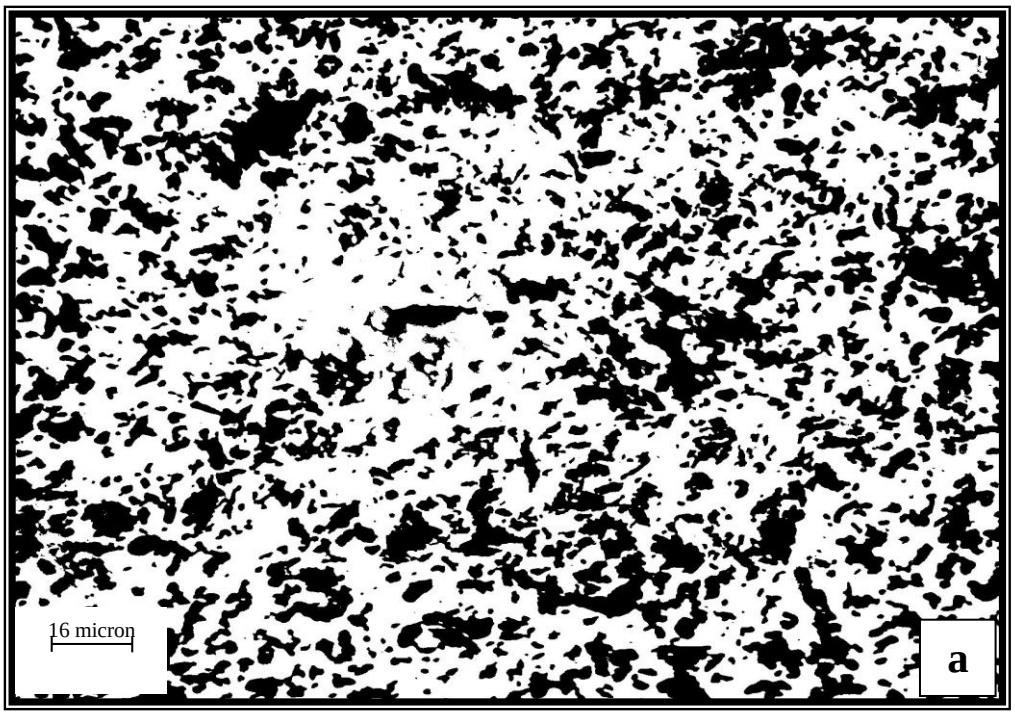

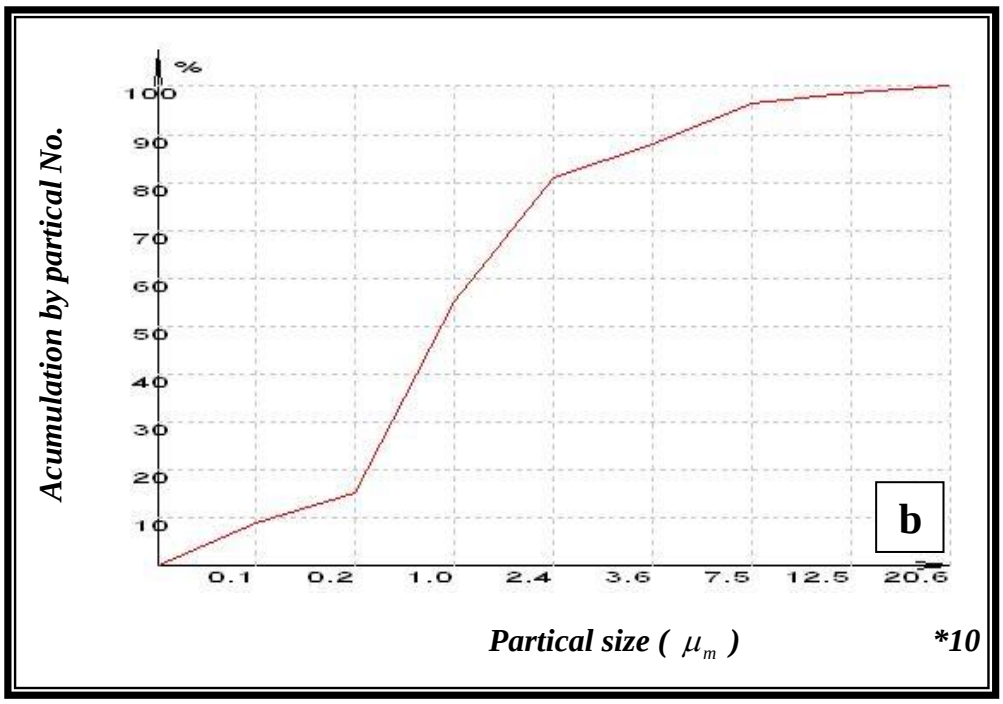

Fig.(6.16) Binary Image and Accumulative size Distribution in (a) and (b) respectively of blended mixture of alloy6 Powder

6.2.3.Green density and green Porosity of compacts :

Green density of alloys 1,2,3 and 6 compacts are shown in Fig.(6.17) .with respect to compacting pressure . For all Compacts , green density increases with increasing pressing stress , from 100 MPa to 950 MPa .As show from Fig.(6.17) , slight increment in green density for all blended compacts are obtained when compacting pressure increases from 800 MPa to 1000 MPa thus , 850 MPa as compacting pressure is based for all next studies of all other parameters such as rate of loading , period of maximum load and all parameters in the sintering process.

In the first stage of compaction , powder particles are rearranged so that bridging that alloys occurs in a randomly arranged stack of loose powder particles is partially eliminated. In the second stage elastic and plastic deformation of the particles have been took place . The amount of plastic deformation depends up on the ductility of the powder material which is here the matrix copper Powder , copper powder has much ductility than the other powders such as Al, Ni , Ti, B, Co , Mn , Si, Fe and Zr. In the light of this statement , when plastic deformation of powder particles has been done , powder Particles are strain hardened.

The third stage of compaction includes fracture of powder particles which have been embrittled through work hardening , under the applied stress increment . The plastic flow stage of densification of powders may be divided in to two substages as deformation in the region surrounding the particles contacts and filling of remaining cavities by local extrusion.

Green porosity which the complimentary of green density , has been shown in Fig.(6.18) for green compacts from alloys number 1, 2, 3 and 6 . With increasing of compacting pressure , the density of the powder mass increases because the total amount of porosity in the mass decreases , however , the pore size and pore distribution will change as well. The uniform compacting stress

applied to the upper punch when a single level cylindrical compact is pressed from one direction as used in this study, is not transmitted uniformly for both direction and magnitude of the stress. throughout the compact. This leads to variation in density in the pressing direction due to the friction between the die wall and the powder. This friction is reduced by using lubricants . In this study, Paraffin lubricant has been applied as a thin coating to the wall of rigid dies. The ratio of the compact to which pressure is applied to the area of contact between the powder and the side walls of the die also affects density. The highest density is found at the top of the outer circumference where wall friction causes maximum relative motion between particles. The density at the circumference decreases rapidly from the top downward with the lowest compact density near the bottom. Density distribution at the centerline of the compact is more uniform due to minimum influence of friction between die wall and powder.

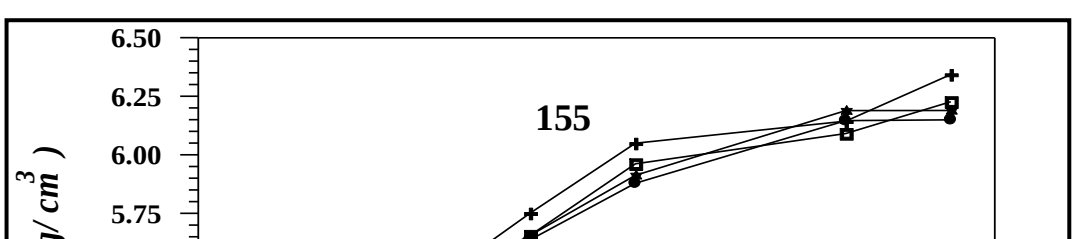

6.2.3.1. Effect of rate of loading

To explain effect of rate of loading on the green density of compacts , three rates (0.2 ,6 and 10 ton/ min) have been studied. Figure (6.19) shows effect of loading rate on the green density of blended mixtures of alloys 1,2,3 and 6. It has been shown that increasing rate of loading leads to decrease green density for all blended powders . when the rate is slow (0.2 ton/ min) , there is a period that the powder particles move and slide together so many pores are filled with small particle size. In addition , most gases are remove from the compact under action of stress because there is enough time to escape gases. Furthermore ,any motion of powder particles requires increasing applied stress and period of time as well like the diffusion process which depends upon time , temperature and activation energy which is a function of stress.

6.2.3.2 Effect of period of maximum load.

when pressing stress is applied to metal powders, behavior is not similar to solid material. The maximum compacting (850 MPa) is applied to powder particles in the metal die at the first moment but this amount of pressure is decreased gradually through the period of time . Thus, powder particles in die have smaller compressive stress than at first moment . In the light of this statement, there is a relaxation time that the elastic deformation of powder particles will be returned and this deformation will not grow to give additional plastic deformation so the green density of compacts decreases with more time of loading as shown in Fig. (6.20) for all alloys.

Powdered compacts have spring-back behavior therefore their mechanical stress- strain curves do not obey traditional elasto-plastic metallic behavior It is like soil behavior thus , Drucker-Prager model may be used to analyze mechanical behavior of powders in the dies during compaction process.

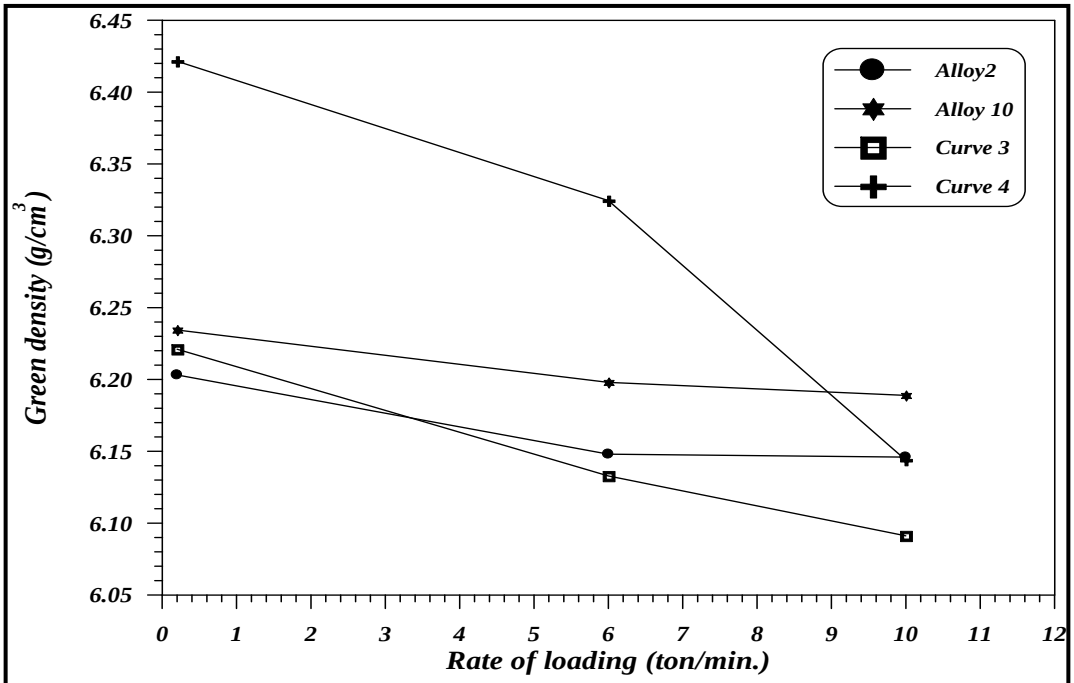

Fig.(6.19) Green density of compacts as a function of rate of loading at 850 Mpa compacting pressure and 1 min. as period of load.

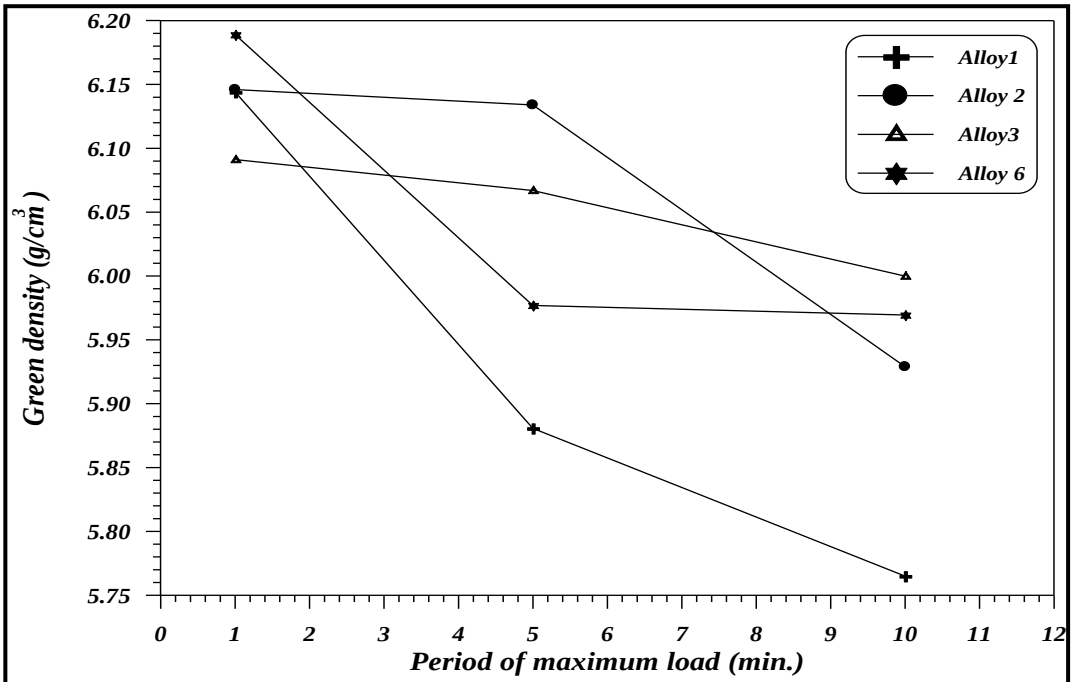

Fig(6.20) Green density as a function of period of maximum load at rate 3 and 850 Mpa compacting pressure.

6.2.4. x-ray diffraction pattern of compacts:

X-ray diffraction analysis of powdered compacts form alloy 1,2,3 and 6 has been studied in order to identify metal powders used in this study and to satisfy two stages of sintering later. In order not to repeat figures and to comparison with sintering samples x-ray diffraction pattern of compacts have been discussed later with sintering results.

6.2.5. Microstructure of compacts and pore size and its size distribution.

Microstructures of unetched samples from alloy compacts 1,2,3 and 6, have been taken using light optical microscope and digital camera. 0.2 ton/ min and one minute as period of maximum loading which is 850 MPa are based. Pore size at 50% point in the accumulative plot is calculated and shown in Fig.(6.21). It has been shown that grinding with 1200 grit silicon carbide paper may be closed then open pores in the surface which is affected on the microstructure and next affected on the accuracy of pore size and pore size distribution analysis. In the pore size distribution analysis using digital image analysis technique , best fit circle has used to represent the pores.

6.3 Result after sintering of compacts.

X- ray diffraction patterns for alloy 1,2,3 and 6 for both stage I and stage II sintering have been studied. In addition physical tests include apparent density, apparent porosity , water absorption and true porosity for different temperatures of sintering and different time of sintering have also been explained. At a first , It must be satisfied that all powdered compacts transform to alloys, so , we begin discussion about x-ray diffraction patterns as follows:

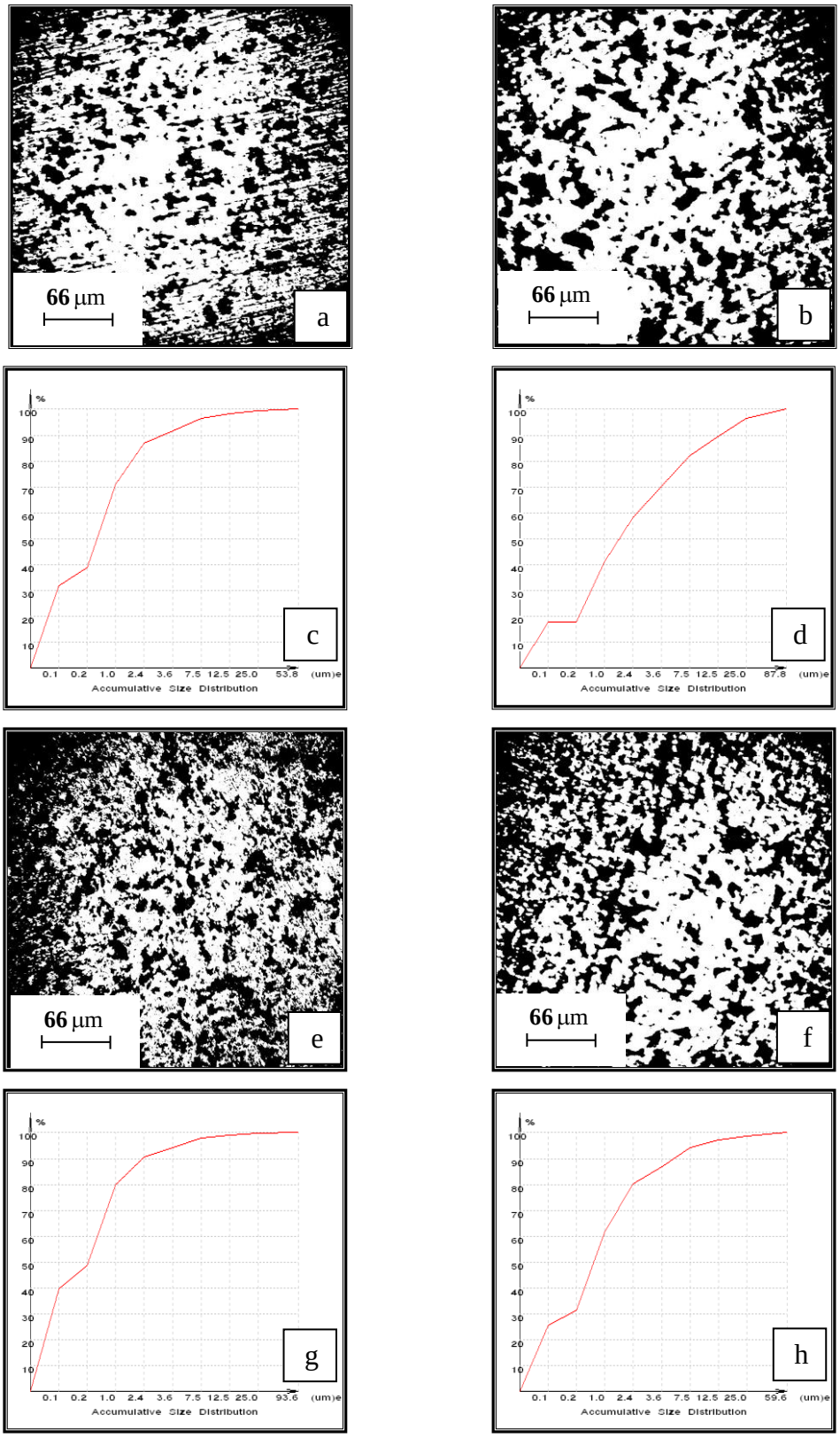

Fig.(6.21) LOM binary images and pore distribution for compact:

a. alloy1 b. alloy2 e. alloy 3 f.alloy 6 for images.

c. alloy1 d.alloy2 g.alloy 3 h.alloy 6 for accumulative distribution .

6.3.1. x-ray diffraction analysis.

x-ray diffraction patterns for compacts 1,2,3 and 6 and for these sample after 3 hours at 600 ^{o}C stage one sintering and after 3 hours at 850 ^{o}C stage two sintering are shown in Fig. (6.22) ,Fig. (6.23), Fig.(6.24) and Fig.(6.25) respectively .

From Fig. (6.22) , It has been shown that most elemental powders (Cu, Al and Ni) form the intermetallic compound γ_2 (Cu_9Al_4) according to Cu-Al phase diagram. The phase (Al_4Cu_9) is the same phase formula (Cu_9Al_4) but is different by density and interatomic space parameter as can be seen from x-ray diffraction card in Appendix A. for (Cu_9Al_4) intermetallic compound the unitcell is cubic with a=b=c= 8.7027 ^{o}A whereas cubic unit cell of (Al_4Cu_9) compounds has a=b=c= 8.704 ^{o}A. This is for the first stage of sintering (600 ^{o}C for 3 hours soacking time) whereas all elemental powders which remained in the first stage of sintering, form the intermetallic compound γ_2. Of course, in this system there are α phase with nickel dissolves in the unit cell of Cu+Al and γ_2 phase . It has been shown that sintering of alloy one in the final stage for three hours is enough to get microstructure with solid solution alloy (α) and with intermetallic compound γ_2 which precipitates on the grain boundaries of α phase.

In the Fig.(6.23) , standard peeks of x-ray diffraction pattern for copper, Aluminum and Nickel are obtained for compact 2. These peeks tend to remove partially in the first stage of sintering. whereas completely new peeks are formed in the second stage of sintering which refers to success of sintering process.Due to the composition of alloy 2 which is hypereutectoid , the phase are α solid solution and γ_2 intermetallic compound. there is enough time to get (Al_4Cu_9) compound with bigger unit cell dimensions than (Cu_9Al_4) Compound.

The intermetallic compound from titanium aluminum copper $(Cu,Al)_2Ti$ is formed in alloy 3 system. In addition , complete formation of $(Cu,Al)_2Ti$ Compound from compact3 has been satisfied in the second stage of sintering. The small additives from titanium (0.4 Ti) to the base alloy 2 in not clear in the x-ray diffraction pattern of compact whereas the effect of titanium is clear in the alloy formation by forming the completely $(Cu,Al)_2Ti$ compound as can be seen from Fig.(6.24).

From Fig.(6.25), it has been shown that all element powders form combination between two phases which are intermetallic compounds (Al_4Cu_9) and (Cu_9Al_4) which are the same phases except the length of cubic unit cell and furetherly, theoretical density. Boron addition affects on the positions of pecks and their intensities compared with the base alloy 2. As can be seen from Fig.(6.25) , addition of Boron deos not lead to form boron compounds with copper or another constituent such as aluminum and /or nickel , in this amount of addition. This is probably due to not enough amount of boron addition which led to week affinity to form intermetallic compound.

X-ray diffraction technique may be used for the rapid determination of the degree of homogeneity. The progress of homogenization is seen clearly although qualitatively in Figs. (6.22) , (6.23) , (6.24) and Fig.(6.25). The copper (111) peak occurs at diffraction angle $2\theta = 43.0$ and the aluminum (111) peak at a diffraction angle $2\theta = 38.0$ as can be seen in Fig.(6.23a) for example . In Fig.(6.23 b). , it has been shown that the initial stages of homogenization (low temperature (600 ^oC) first stage of sintering) proceed by forming the complete range of compositions from copper and aluminum. This is the manifestation of the intial interdiffusion across the copper- aluminum interparticle boundaries. As shown in Fig. (6.23) C, later stage of homogenization (high temperature 850 ^oC

for three hours second stage of sintering) result in the formation 100% intensity of Al_4Cu_9 internetallic compound. Intermetallic compound (Al_4Cu_9) formation occurs at a diffraction angle between those of pure copper and pure aluminum. from Fig. (6.23) , it is shown that diffraction angle of 100% intensity of the product (Al_4Cu_9) is 42.2 deg. Which lies between 43 for copper and 38.0 for Aluminum pure metal respectively.

The characteristic of the powder particles either copper powder or aluminum powder that compose the mixture exert a significant effect on homogenization kinetics. The sizes of the particles in the mixture establish the distance over which interdiffusion must occur to achieve homogeneity. [Lenel et al , 1984] . In alloy mixtures where the elemental solvent particles from a continuous matrix around the dispersed solute – rich particles ,particle size of the dispersed particles become the important parameter in establishing the interdiffusion distance.

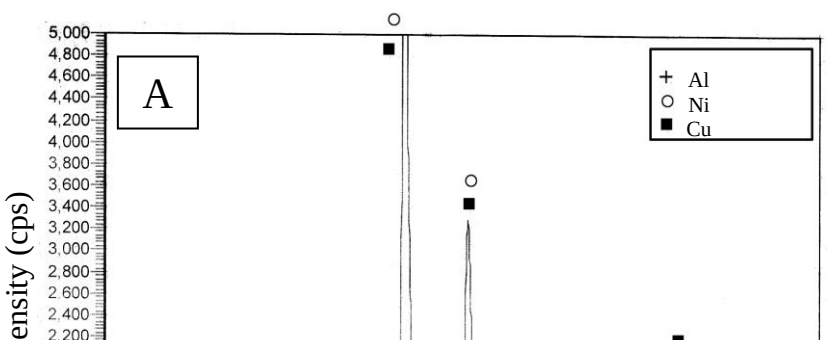

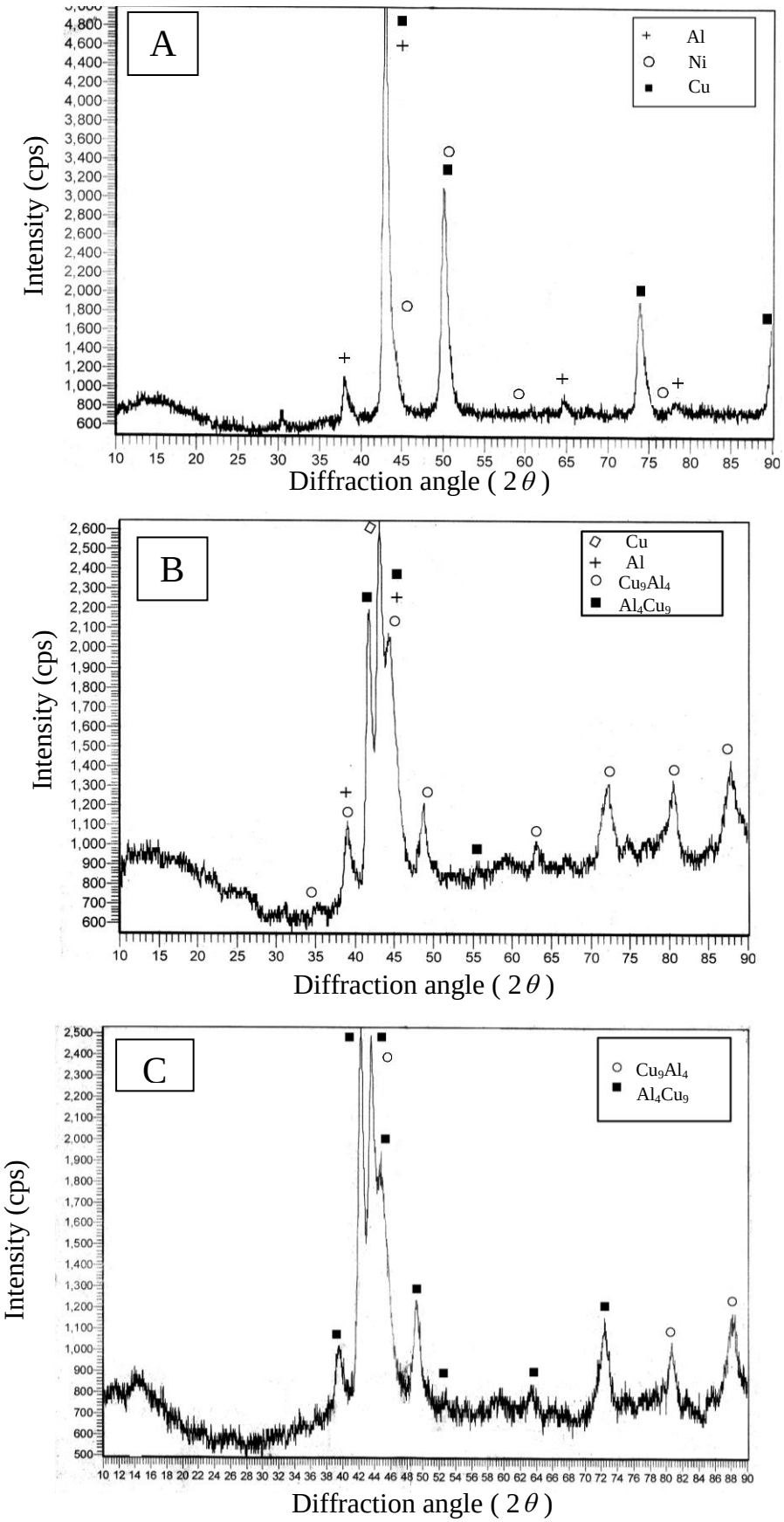

Fig.(6.23) XRD patterns for alloy 2 for :a. Compact . b. stage I sintering c.stage II sintering

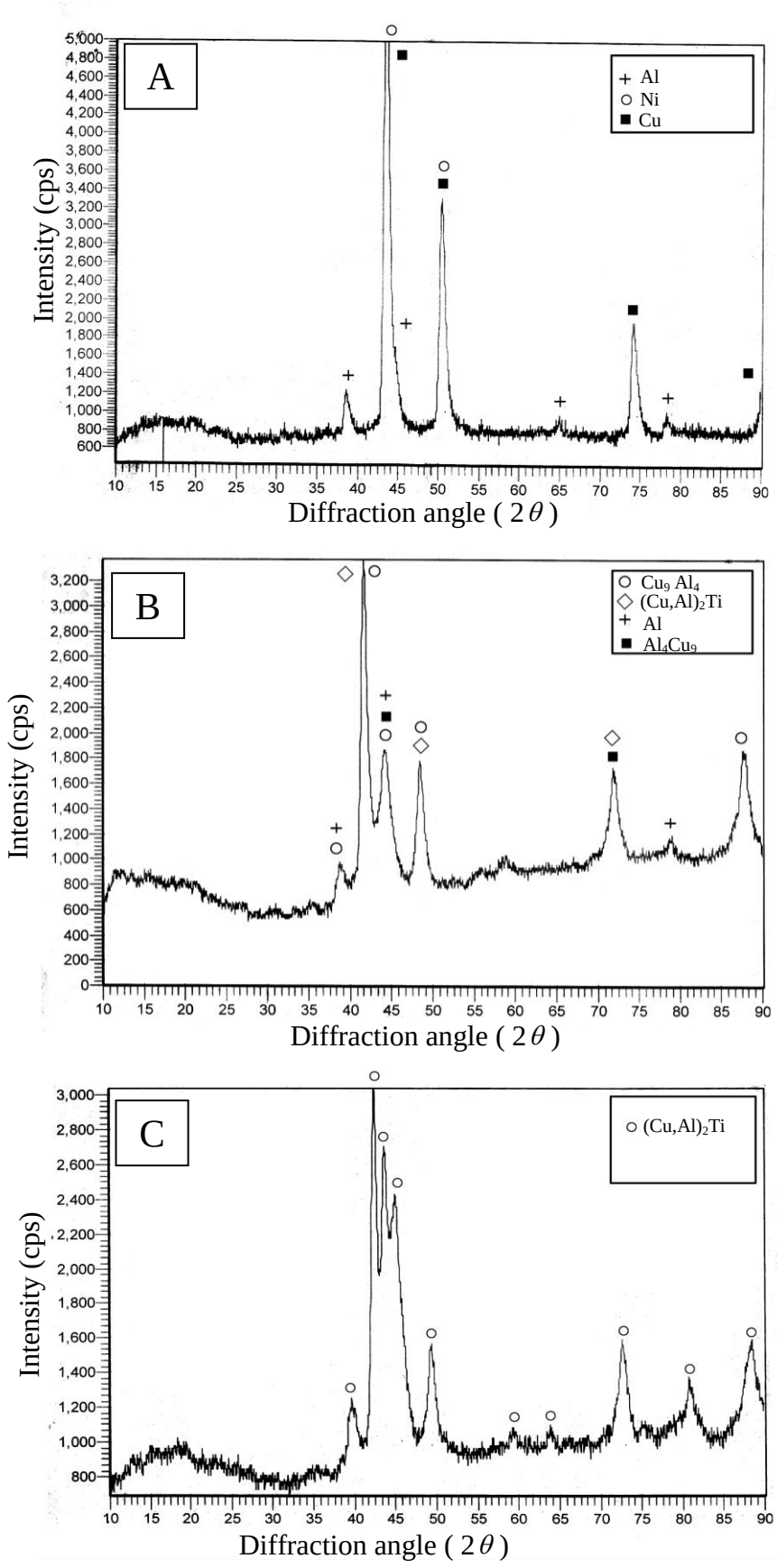

Fig.(6.24) XRD patterns for alloy 3 for :a. Compact . b. stage I sintering c.stage II sintering

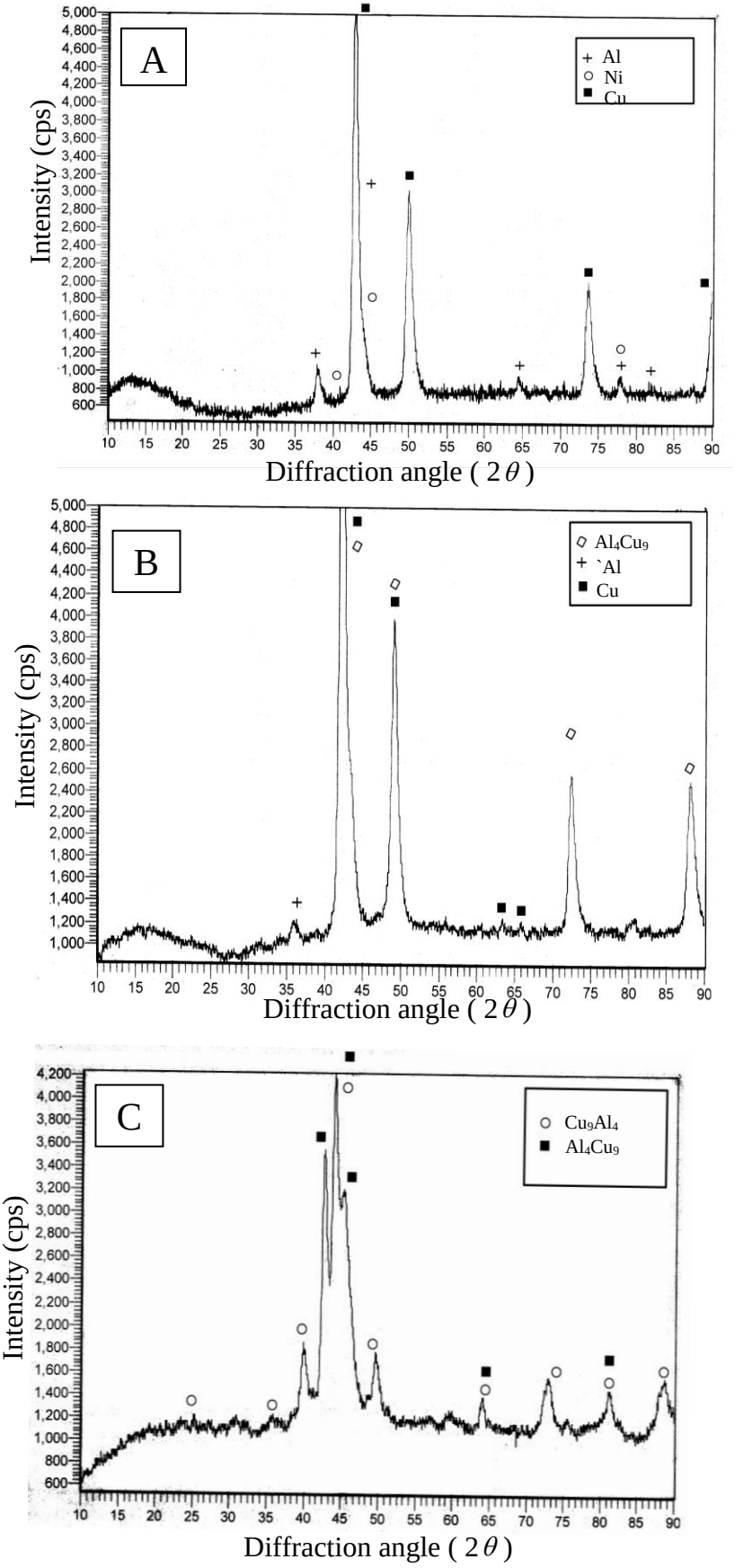

Fig.(6.25) XRD patterns for alloy 6 for :a. Compact . b. stage I sintering c.stage II sintering

6.3.2 physical test Results :

Several physical properties included apparent density , apparent porosity , water absorption , true porosity and expansion have been studied with respect to several parameter such as compacting pressure , time of sintering , temperature of sintering and rate of loading .These results are discussed and presented in the following :

6.3.2.1 Apparent density of sintered Compacts :

Apparent density of sintered compacts at 600^{c}c for three hours and at 850 ^{o}C for 10 minutes in addition , for alloy 1,2 ,3 and 6 is shown in Fig.(6.26) and Fig .(6.27) with respect to pressure of Compaction. the apparent density of alloys 1,2,3 and 6 in creases with increasing compacting pressure due to increase contacts regions in higher pressure which are the region of densification of compact under sintering . After 650 MPa Compacting pressure , slow increment in apparent density has been occurred Therefore , Compacts under sintering have traditional little pores and with high green density at higher Compacting pressure than that at lower Compacting pressure which lead to in crease apparent density at the final .It has been shown that sintered compacts have 72.3% from the theoretical density of Al_4Cu_9 compound (6.848 g/ cm^3) which measured from x-ray diffraction pattern for alloy 1,2,3 and 6 , at 950 M Pa compacting pressure . This ratio of density (apparent density relative to theoretical density) is not enough due to low time of sintering (10 min.) .The effect of time of sintering and sintering temperature have been explained later .It must be known that theoretical density of sintered compact is not calculated from elemental powders by summation of weight percent of constituents of compacts after sintering new material has been obtained and can not be compared with green elemental powders. So , theoretical density may be calculated from the equation :

$$\text{Theoretical density} = \frac{\text{No. of atoms per unit cell} \times \text{molecular weight}}{\text{Volume of unit cell} \times \text{Avogadro No.}} \qquad \text{Eq.(6.1)}$$

on the other hand , the effect of time of sintering on the apparent density of sintered compact has been shown in Fig.(6.28) and Fig.(6.29) for alloys 1,2,3 and 6. It has been shown that apparent density increases with increasing sintering time due to increase diffusion through the sintering process which leads to decrease porosity of sintered compacts .It is shown , density ratio between 80 -84% from the theoretical density , has been obtained alloy 1 and alloy 2 are more sensitive than alloys 3 and 6 for time of sintering because there is no fourth element additives (Ti or B) as in alloy 3 and 6 respectively These alloying elements need to more time and more temperature to diffuse in the matrix of alloy Some times , Compact swelling has been occurred .compact swelling is attributed to the diffusion of the primary or transient Al-metal into copper which is not transformed in the first stage sintering process (600 ^{o}C for 3 hours).

The effect of rate of loading of compacting pressure on the final apparent density of sintered compact has been shown in Fig.(6.30) and Fig .(6.31) .It is shown that apparent density is decreased loading because green density is decreased with increasing rate of with increasing rate of loading in beginning ,At low rate of loading , Compacts enter the sentencing process with low pores and with high initial green density so that all the activation thermal energy during sintering is went to density the compact through the diffusion of solute a tomes in the solvent a toms to form an alloys . whereas Compacts with high pores (low green density) heed more activation thermal energy either time or temperature in order to density through reduce the pores .

Apparent density as a function of temperature of sintering has been shown in Fig.(6.32) and Fig.(6.33) for alloy 2,6 and 1.3 respectively .

It is shown that apparent density increases from 850 ^{o}C to 900 ^{o}C for to min . as time of sintering . The highest point of apparent density is at 900 ^{o}C and after , this apparent density dropped in to lower amount at 950 ^{o}C . Variation in

sintered density with sintering temperature during homogenizations is frequently quite different compared to the variation that exists if compacts are composed of particles of identical composition . This is due to two phenomena which have opposing effects on the densification of the compacts which occur simultaneously .The matrix densities due to pore shrinkage .The net flow of vacancies from one particle to the other occurs if there is a difference in the fluxes of the atomic species to a specific type of particle Those vacancies may be accumulated in the form of fine pores which is called kirkendall porosity (Lenel et al , 1986) The formation of kirkendall porosity can result in expansion of the compact under sintering effect companied by reduction in density of the compact. From Fig .(6.32) and (6.33) , It has been shown that density of compact first increases and then decrease until a minimum is reached . It the initial stage of sintering (short time , low temperatures) the densification mechanism dominates and apparent density in creases sharply , later , a point is reached where density begins to decrease indicating that formation of kirkendall porosity has begin to dominate .Expansion of sintered compacts has been given for all compacts .The following processing parameters may affect the rate of densification and / or expansion during homogenization :

1. extent of difference in diffusivities of the particles in the compact (D_o for Cu, Al, Ni , Ti ,B, …etc)
2. size of the particles in the compact .
3. mean composition of the powder compacts .
4. Compacting pressure .
5. rate of loading during Compacting .
6. oxygen content of the starting Powders .

So , the form of the density –time – temperature relationship is frequently more complex for multi-phase systems .

Transient liquid phase sintering

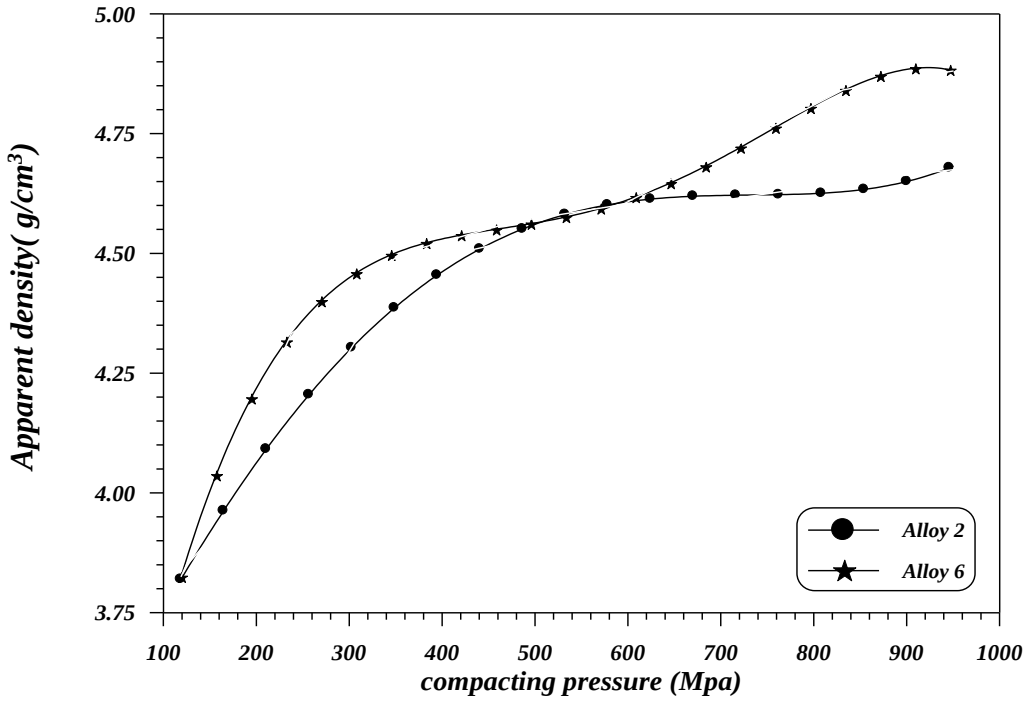

Fig.(6.26) Apparent density of alloy 2 and alloy 6 with respect to compacting perssure .

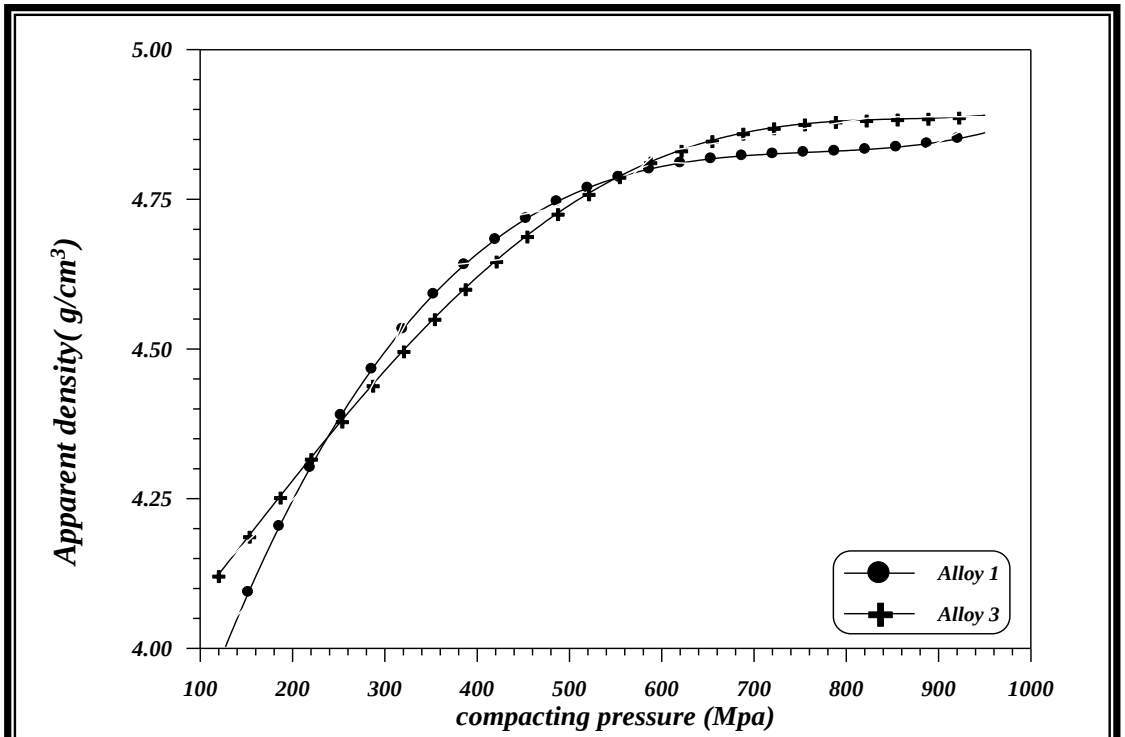

Fig.(6.27) Apparent density of alloy 1 and alloy 3 with respect to compacting perssure .

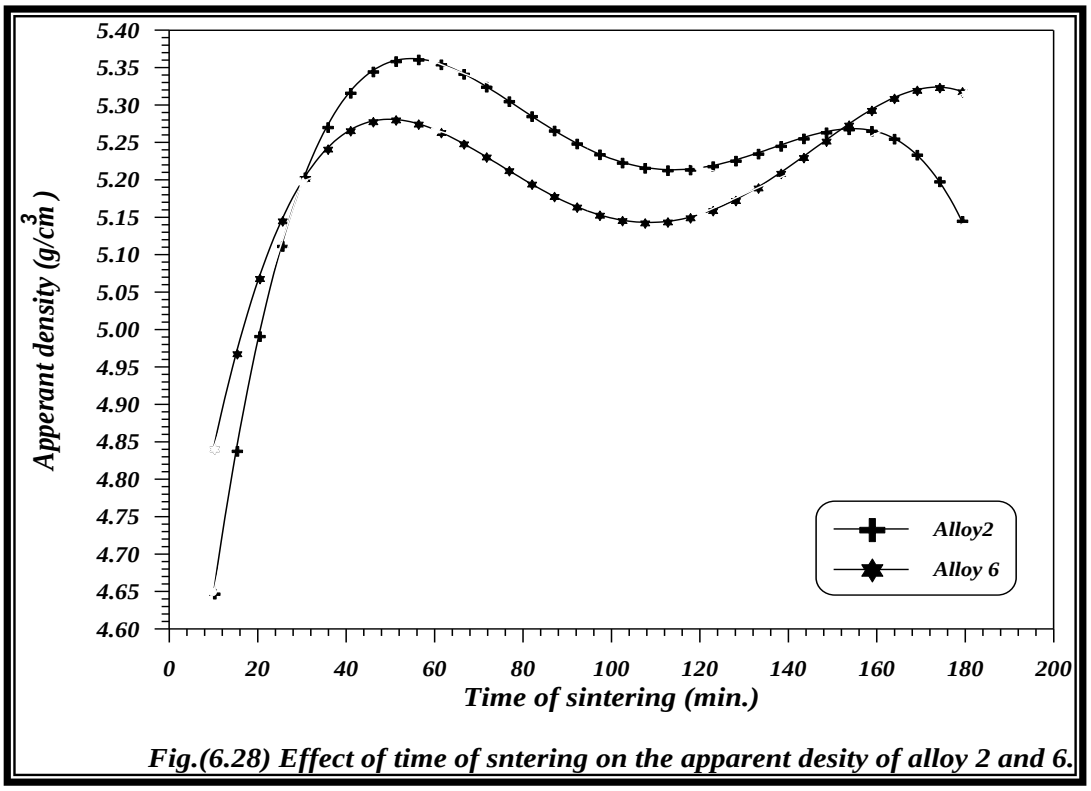

Fig.(6.28) Effect of time of sntering on the apparent desity of alloy 2 and 6.

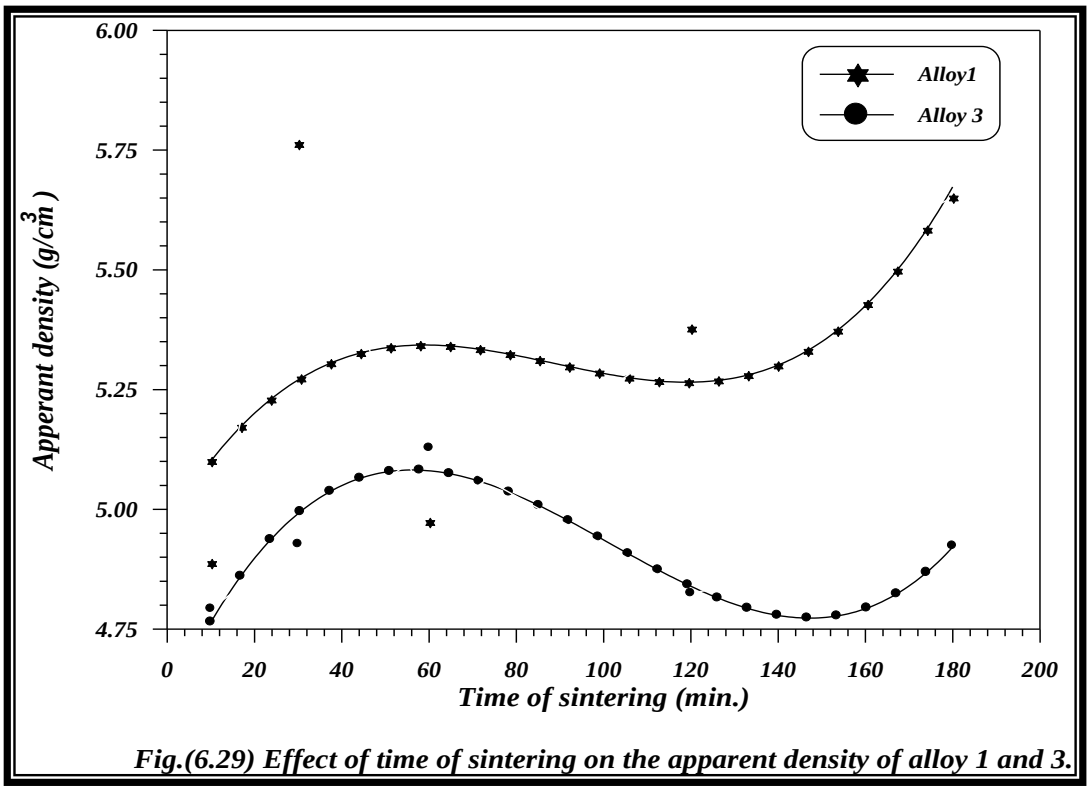

Fig.(6.29) Effect of time of sintering on the apparent density of alloy 1 and 3.

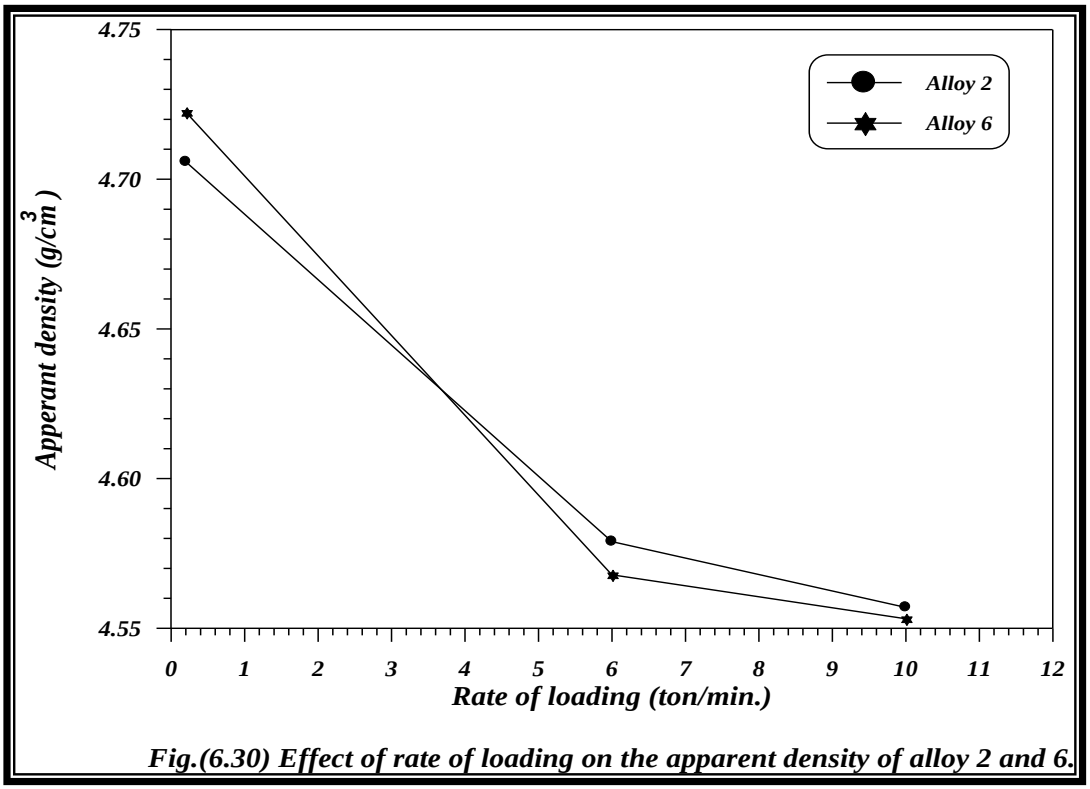

Fig.(6.30) Effect of rate of loading on the apparent density of alloy 2 and 6.

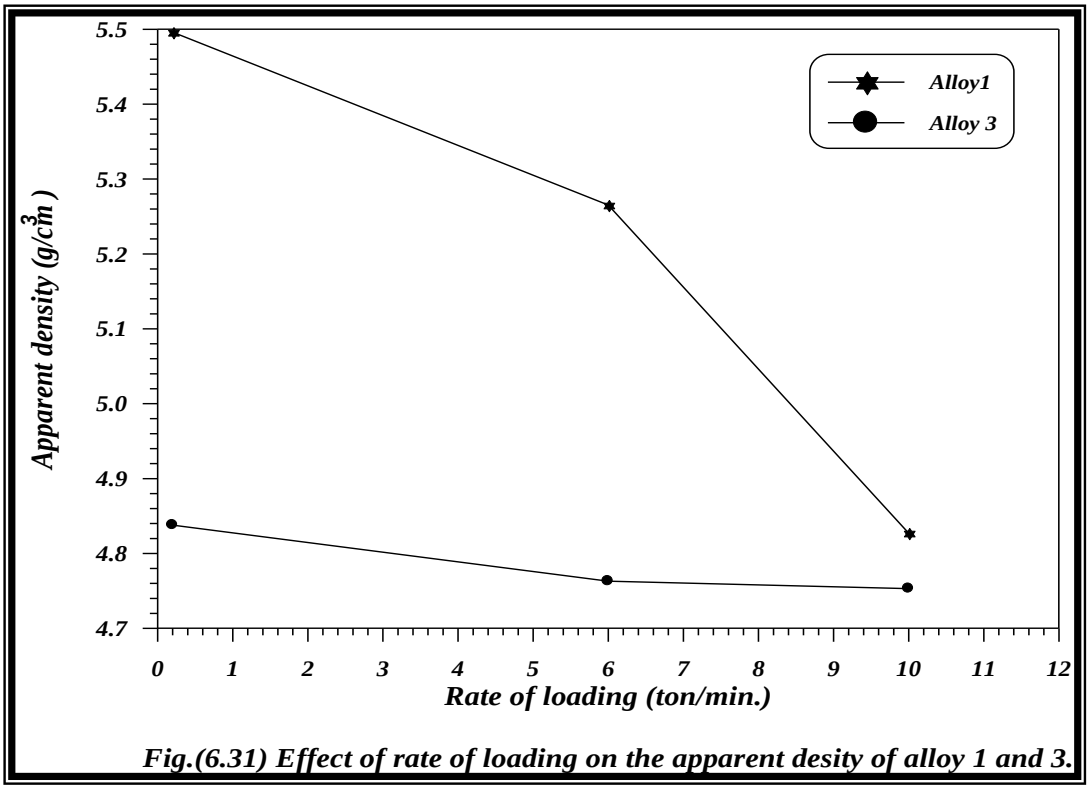

Fig.(6.31) Effect of rate of loading on the apparent desity of alloy 1 and 3.

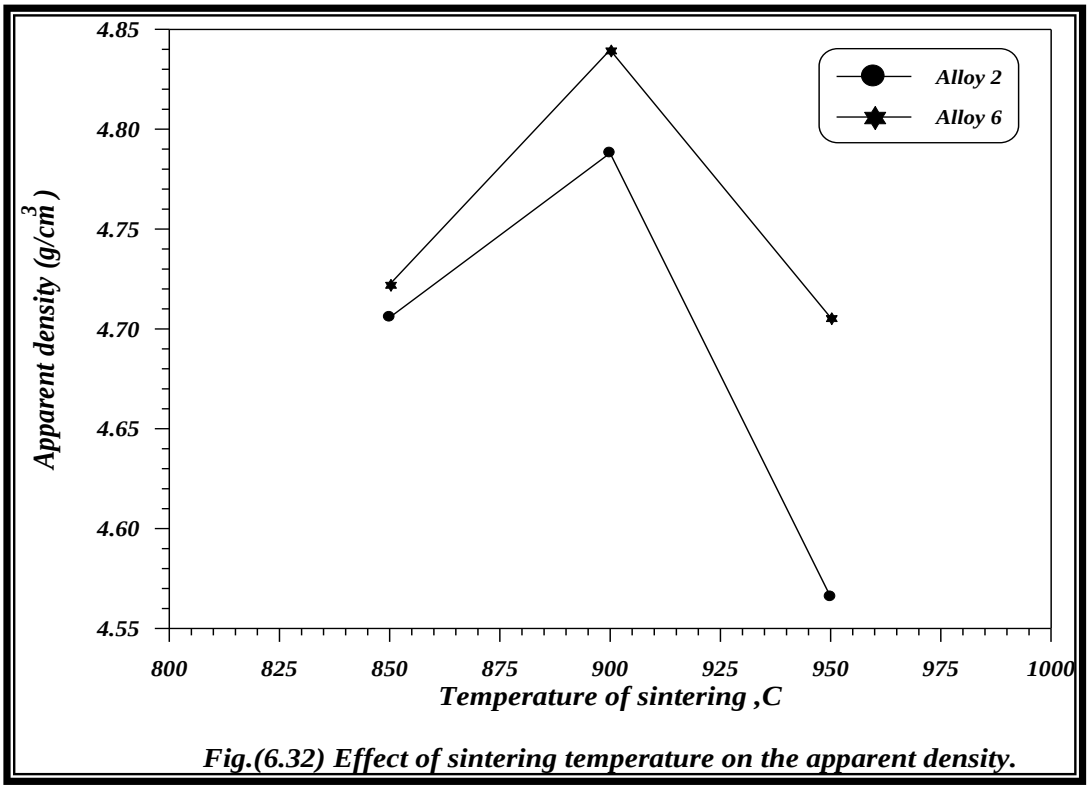

Fig.(6.32) Effect of sintering temperature on the apparent density.

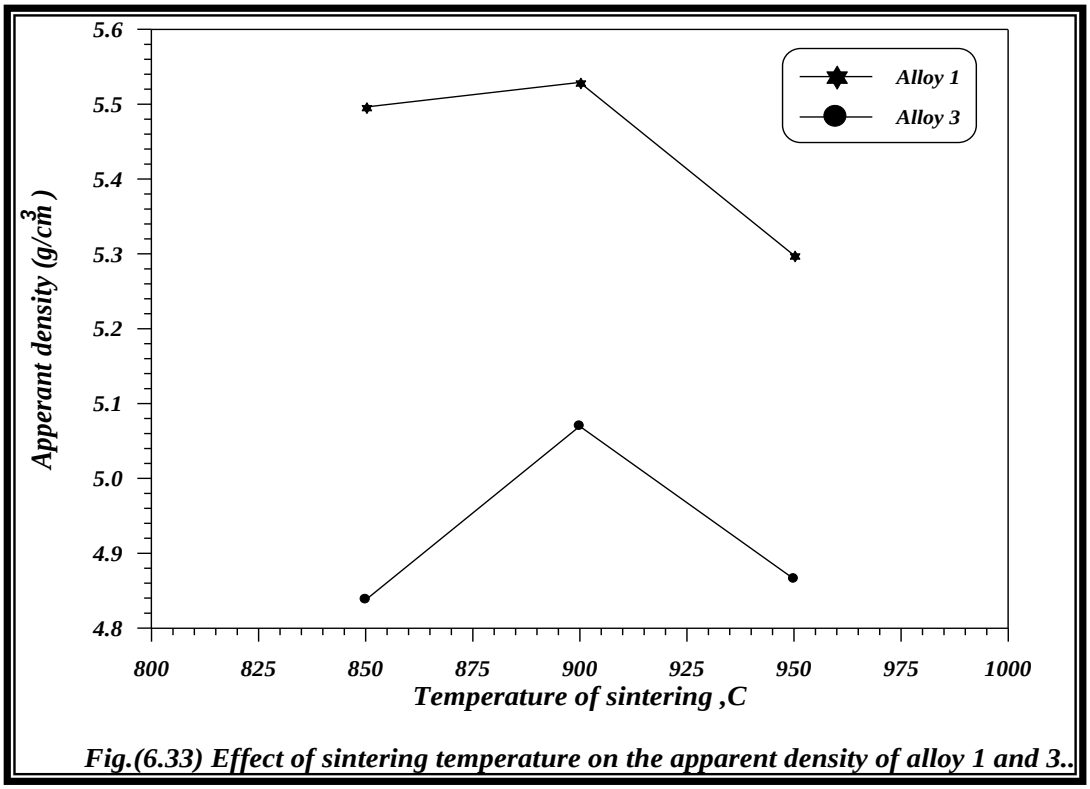

Fig.(6.33) Effect of sintering temperature on the apparent density of alloy 1 and 3..

6.3.2.2. Apparent porosity and absorption of water .

Apparent porosity is the amount of open pores in the volume of sintered compact. Apparent porosity as a function of compaction pressure is shown in Fig. (6.34) and Fig (6.35) for alloys 1,2,3 and 6.It has been shown that open pores volume fraction or apparent porosity for alloy 1,2,3 and 6 are decreased due to obtain densification at high compacting pressure so the pores are reduced on the other hand, apparent porosity is increased when rate of loading is increased due to decrease density of sintered compacts for alloy 1,2,3 and 6 as can be seen from Fig (6.36) and Fig.(6.37).

apparent porosity is the complimentary of apparent density as well, So the apparent porosity will be increased when temperature of sintering and or time of sintering increase because kirkendall porosity is simultaneously formed and reduce densification in the final stages of sintering as can be seen from Fig.(6.38) , (6.39) , (6.40) and Fig.(6.41). for temperature and time of sintering effects respectively.

Some open pores are connectedly between them in channels which facilitate water absorption from the surface to the bottom of alloy 1,2,3 and 6. This effect has been shown in polishing and wet grinding with water which leads to corrode the surface of specimens. Absorption of water is important property in wet or aqueous corrosion. Absorption water as a function of compacting pressure has been shown in Fig. (6.42) and Fig.(6.43) for alloy 2 and 6 for alloy 1 and 3 respectively. Water absorption is decreased for all alloys when compacting pressure is increased due to increase density of sintered compacts and decreased open pores.

when high loading rate is used in compaction of compacts , there is no enough time to escape air from pores and there is no time required to reduce pores by displacing of particles . thus absorption of water is increased when rate

of loading is increased as can be, seen in Fig.(6.44) and Fig.(6.45).It has been shown that alloy 2 and 3 are less sensitive than alloy 1 and 6 for absorption of water with rate of loading. Absorption of water is increased from 3.2% to 4.2% for alloy 6 and to 6.4% for alloy 2 respectively as can be seen from Fig.(6.46).

This is because of increasing of apparent porosity with increasing of sintering temperature . However, for alloy 1 and 3 , absorption of water decrease the beginning with increasing temperature of sintering but at later, water absorptions is increased at 900 ^{o}C for alloy 3 whereas water absorption of alloy 1 is continuously reduced with further increasing of sintering temperature as shown in Fig.(6.47) . This is probably due to kirkendall porosity which depends upon chemical composition of compact during sintering. In the light of this statement , alloy 1 has a smaller aluminum content than the other alloys so that compact swelling is not preferred in this alloy. Thus densification phenomena is the predominant at these temperatures.

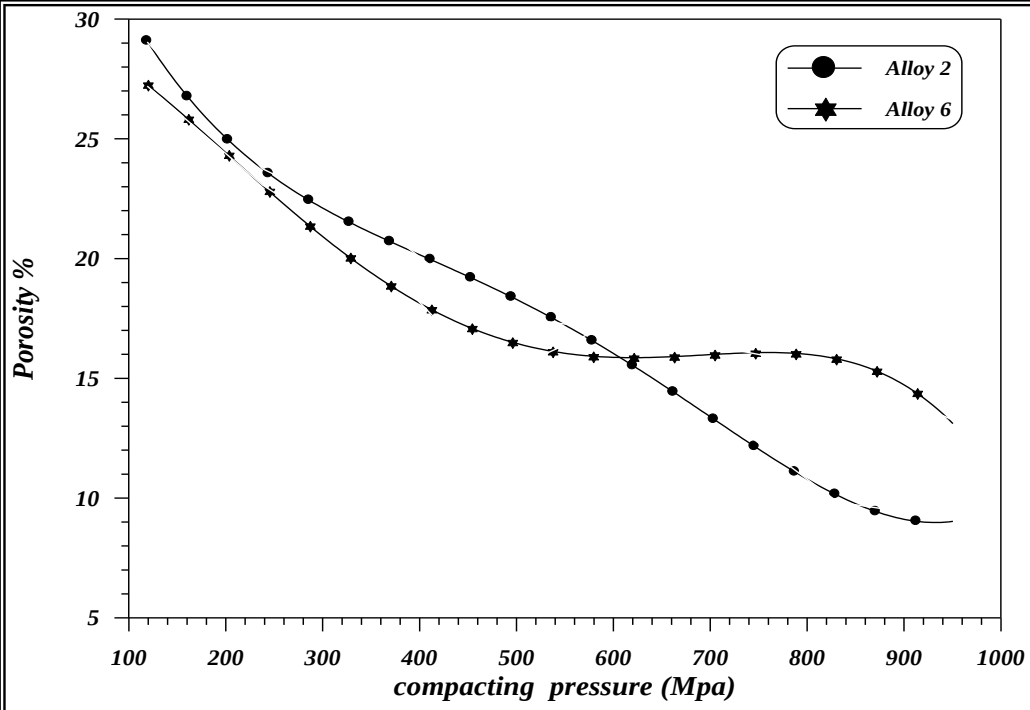

Fig(6.34) Effect of compacting pressure on th e apparent porosity of alloy 2 and 6.

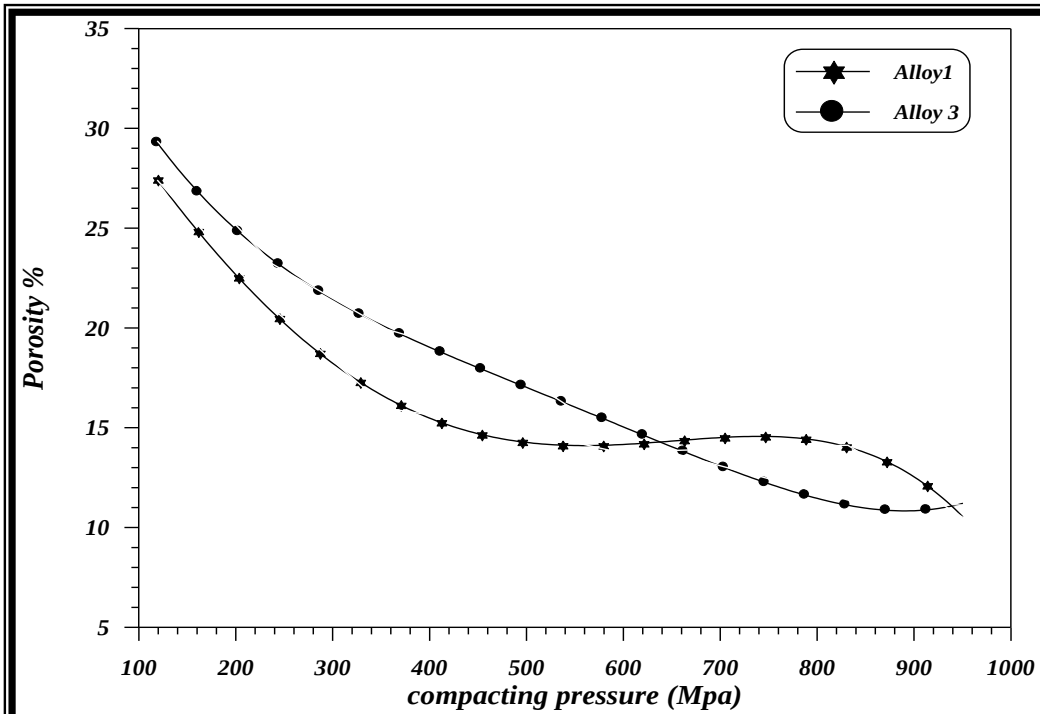

Fig.(6.35) Effect of compacting pressure on the apparent porosity of alloy 1 and 3.

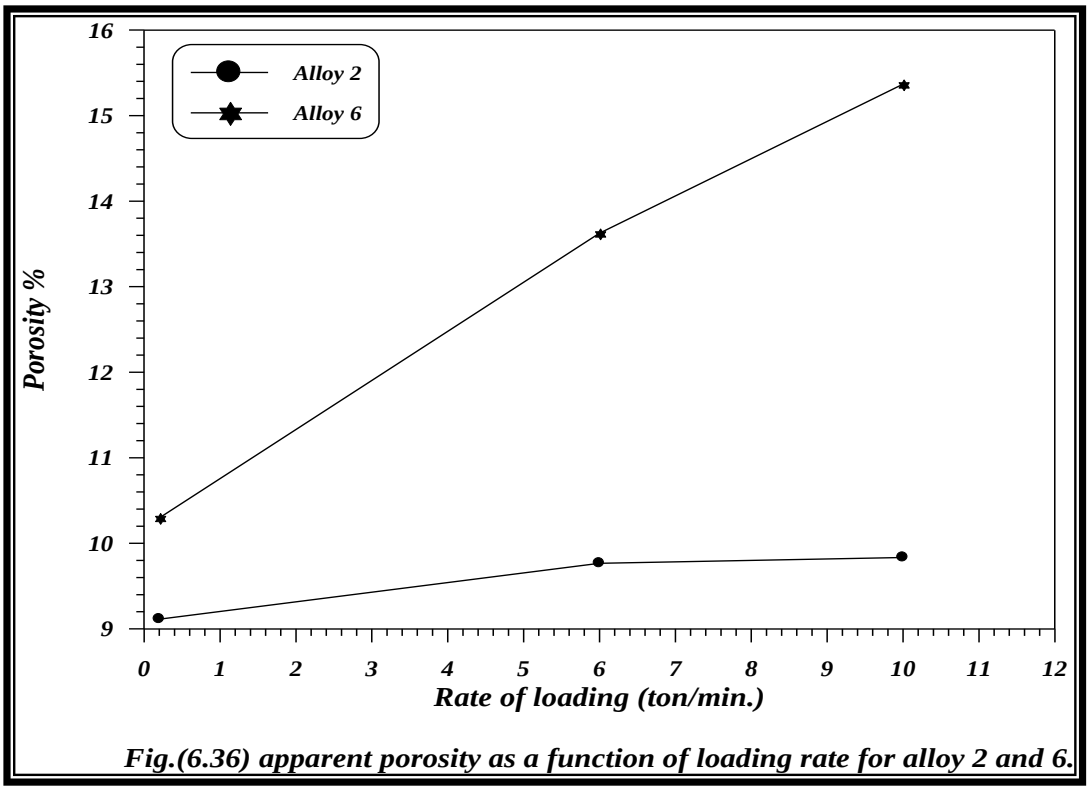

Fig.(6.36) apparent porosity as a function of loading rate for alloy 2 and 6.

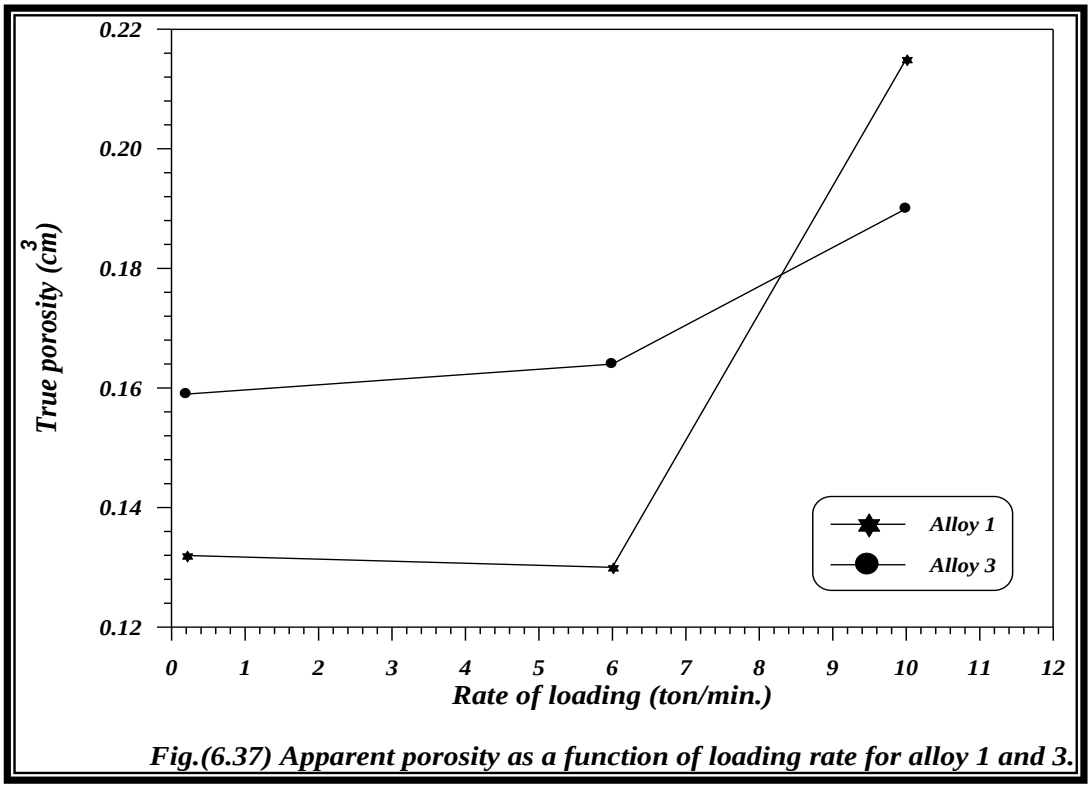

Fig.(6.37) Apparent porosity as a function of loading rate for alloy 1 and 3.

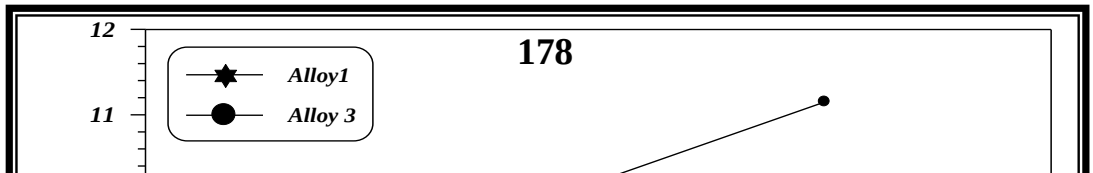

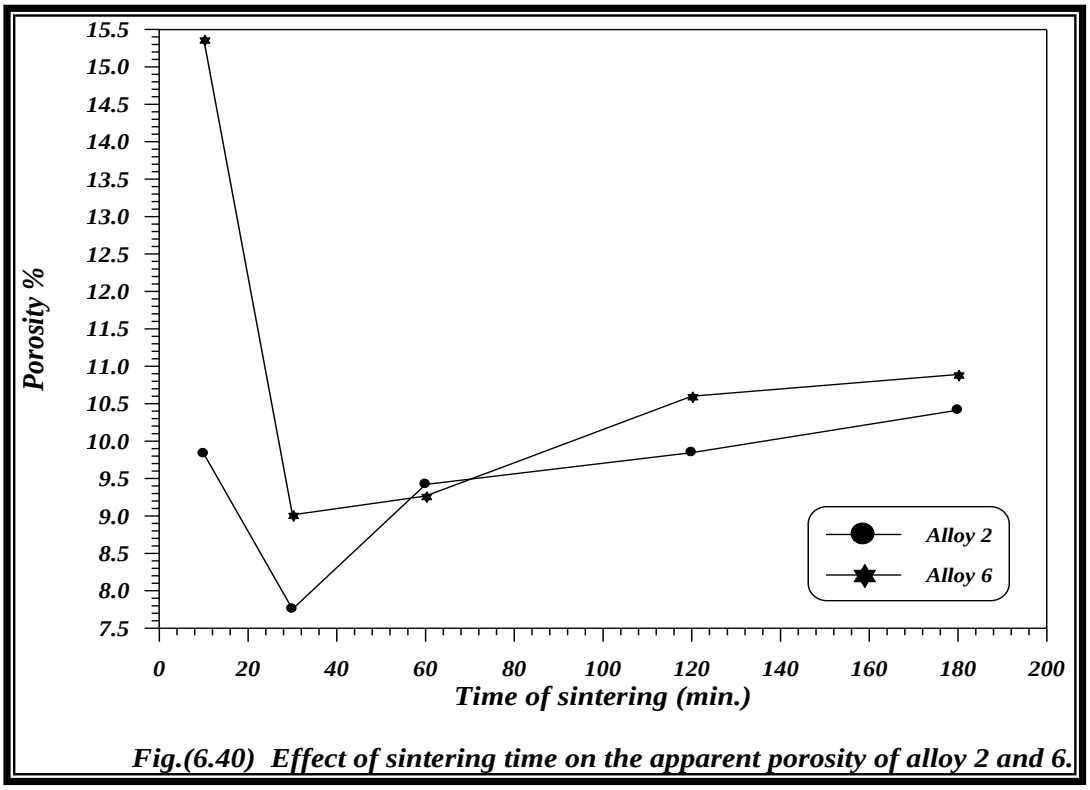

Fig.(6.40) Effect of sintering time on the apparent porosity of alloy 2 and 6.

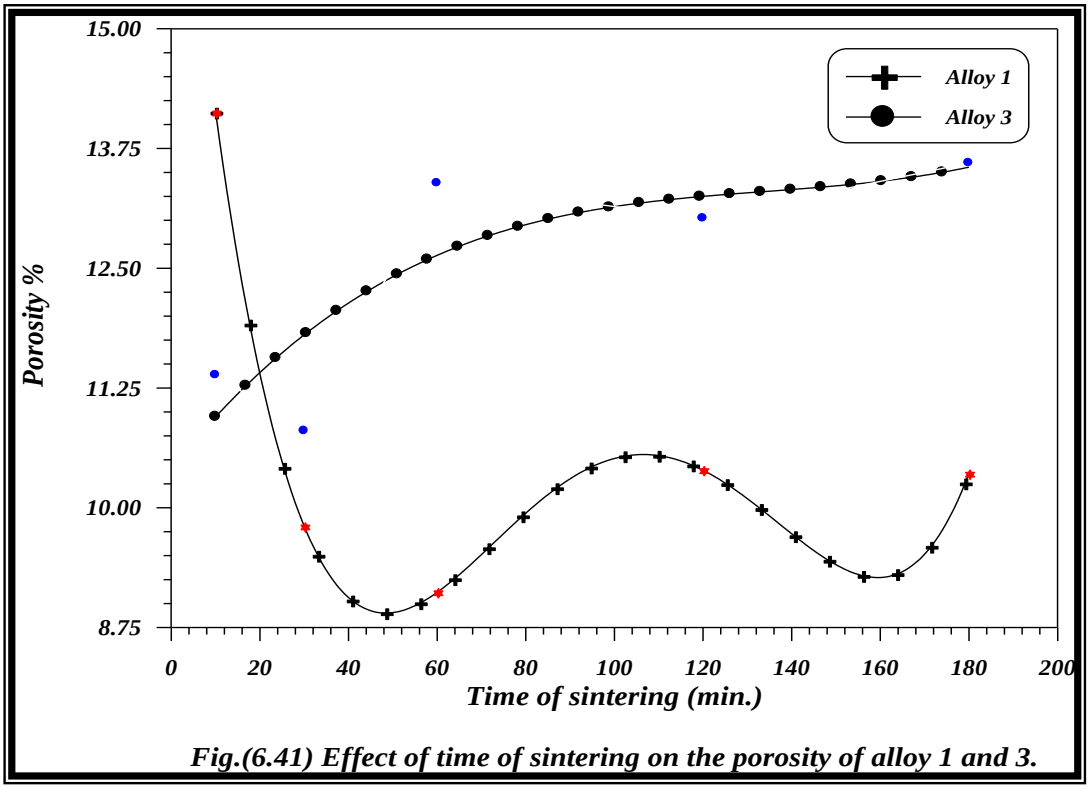

Fig.(6.41) Effect of time of sintering on the porosity of alloy 1 and 3.

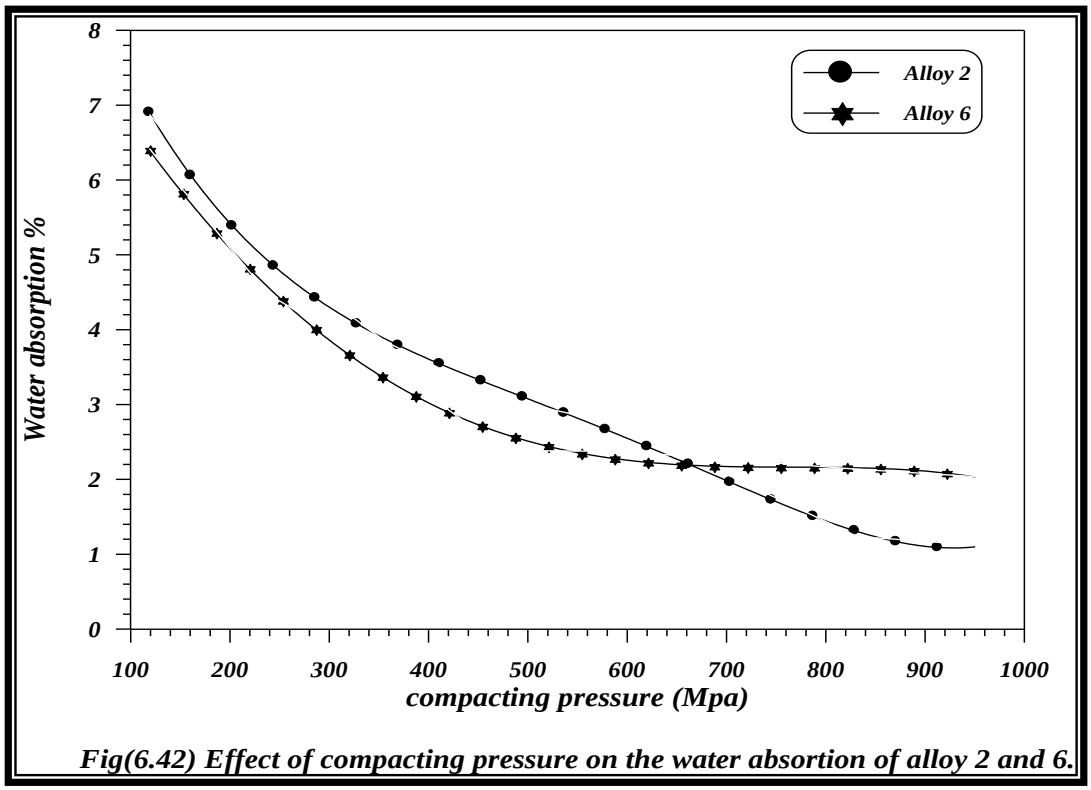

Fig(6.42) Effect of compacting pressure on the water absortion of alloy 2 and 6.

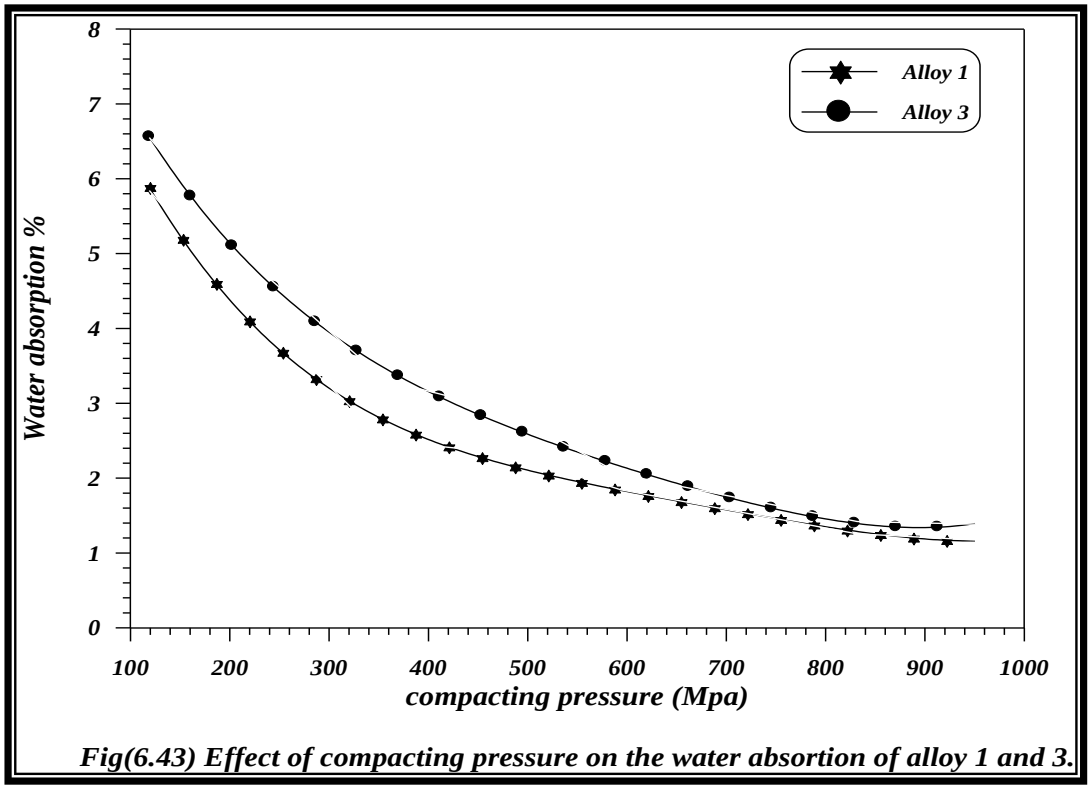

Fig(6.43) Effect of compacting pressure on the water absortion of alloy 1 and 3.

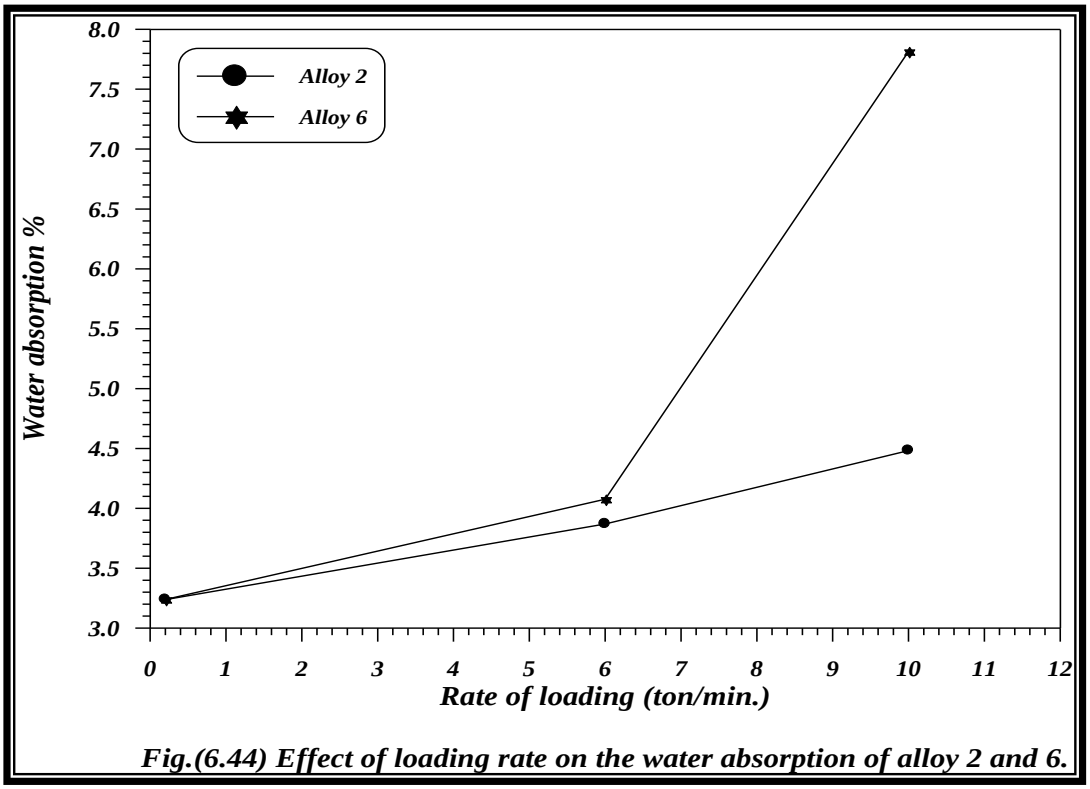

Fig.(6.44) Effect of loading rate on the water absorption of alloy 2 and 6.

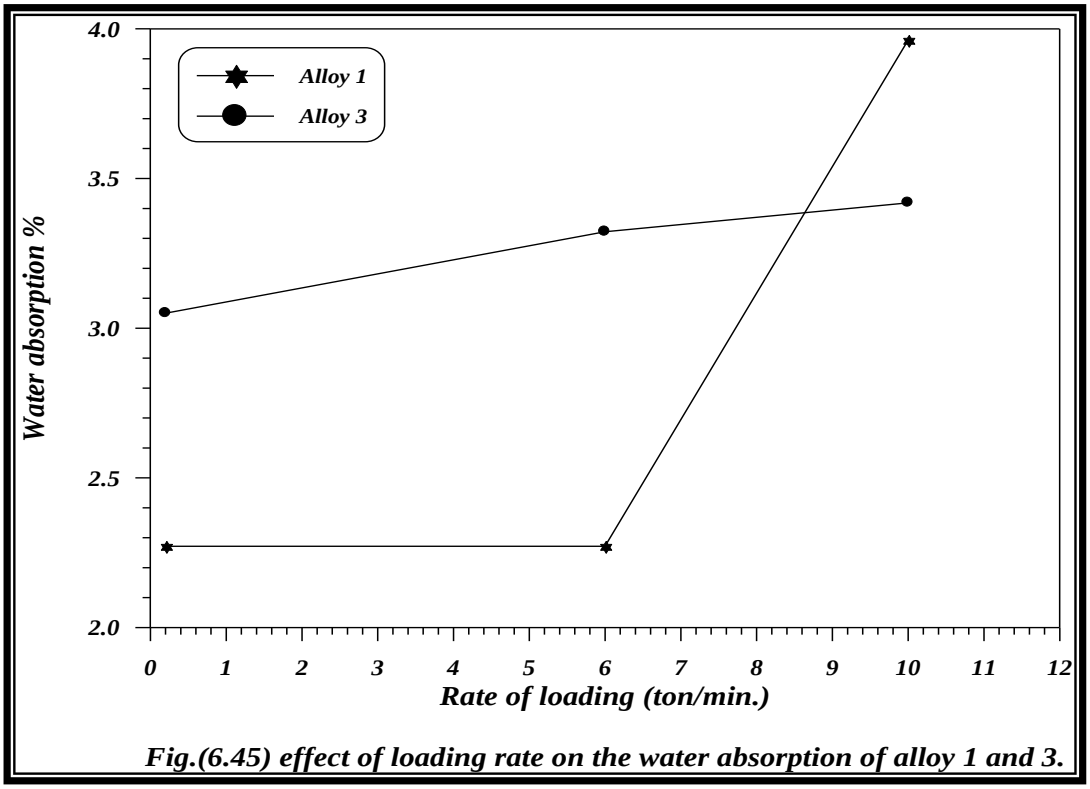

Fig.(6.45) effect of loading rate on the water absorption of alloy 1 and 3.

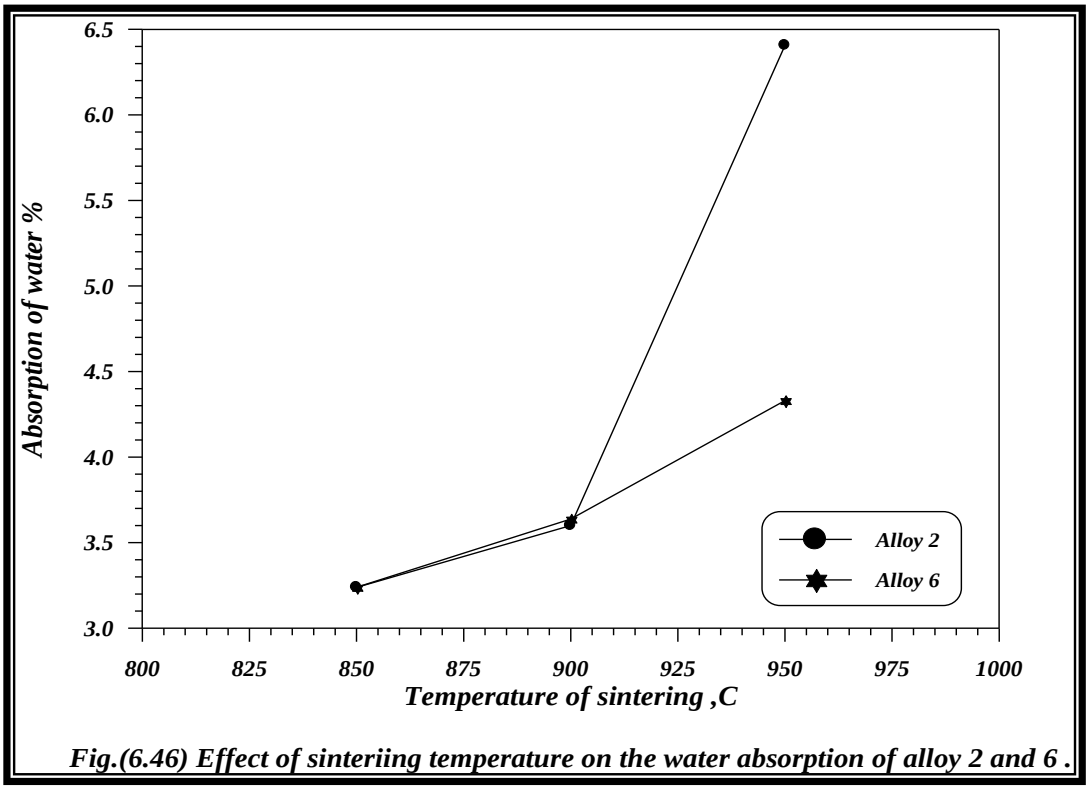

Fig.(6.46) Effect of sinteriing temperature on the water absorption of alloy 2 and 6 .

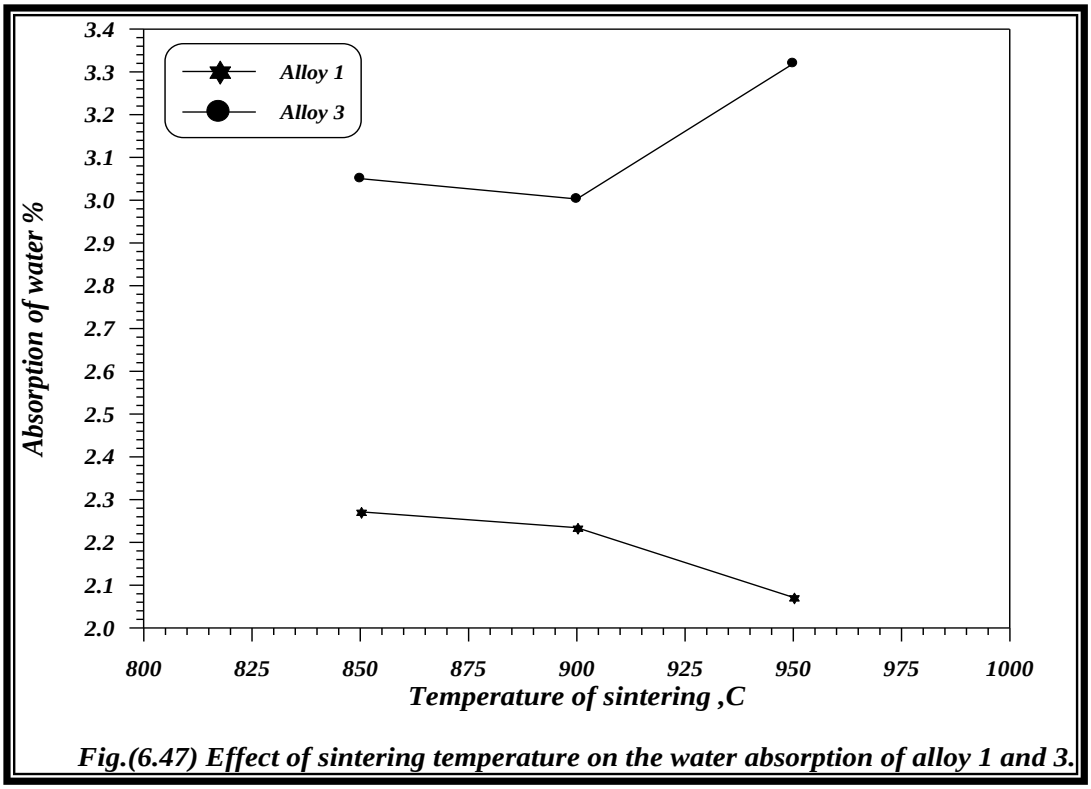

Fig.(6.47) Effect of sintering temperature on the water absorption of alloy 1 and 3.

6.3.2.3. True Porosity

True porosity is the measuring of closed and open pores in the volume of sintered compacts. True porosity decreased with increasing of compacting pressure for alloys 1,2,3 and 6 in Fig.(6.48) and (6.49).

In has been shown that closed pores is decreased when the compacting pressure is increased initial green density and increase apparent density with increasing pressing stress. On the other hand the effect of rate of loading on the true porosity of alloy 1,2,3 and 6 has been taken in to consideration as shown in Fig.(6.50) and Fig.(6.51).

High closed and opened pores concentration at high loading rate because the is no time to move of diffuse particles in the compact under the action of sintering. In the light of this statement, true porosity has been increased when temperature of sintering increased. It is probably due to form kirkendall porosity at high temperature which lead to occur the expansion of compacts under sintering. This is truly took place in all specimen. So that sintering at 850 ^{o}C is taken and higher temperatures (900 or 950 ^{o}C) have been avoided. The effect of sintering temperature on the true porosity is shown in Fig.(6.52) and Fig.(6.53). Because the expansion of compacts under sintering condition depends upon composition of alloy and because the lower aluminum content in alloy 1 tan in the other alloys , true porosity has been decreased up to (0.116 cm^3) at the sintering temperature of 900 ^{o}C. After this , open and close pores have been increased with increasing sintering temperatures.

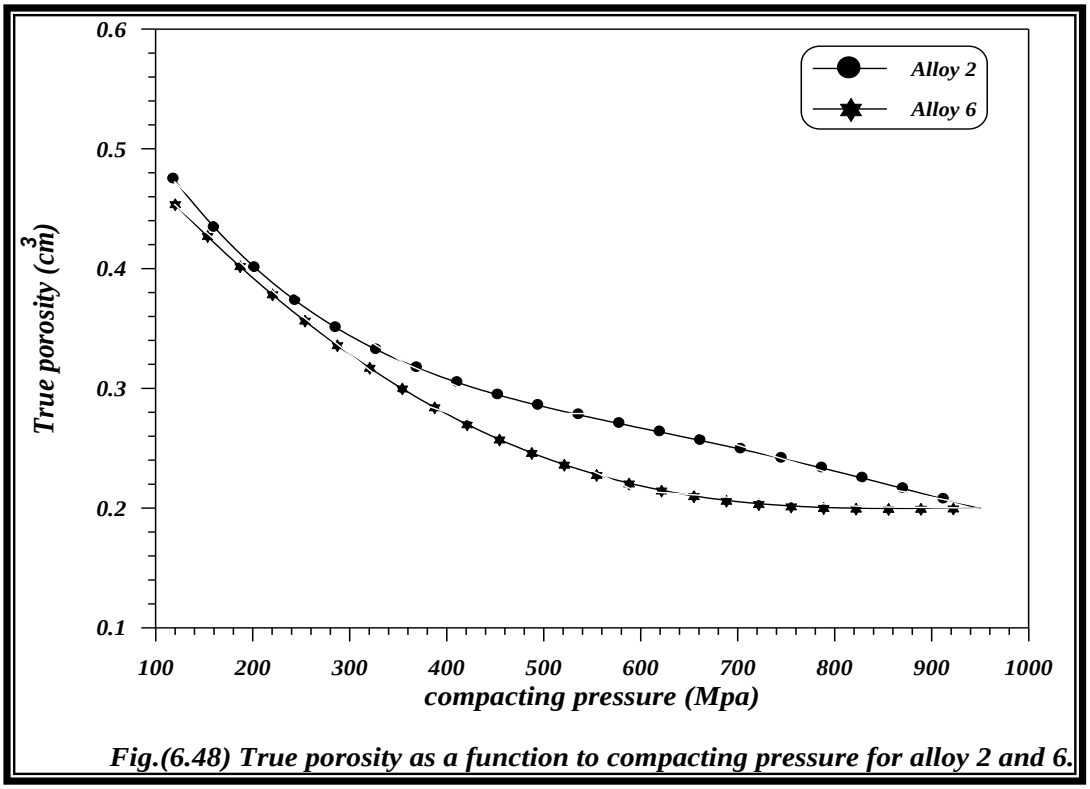

Fig.(6.48) True porosity as a function to compacting pressure for alloy 2 and 6.

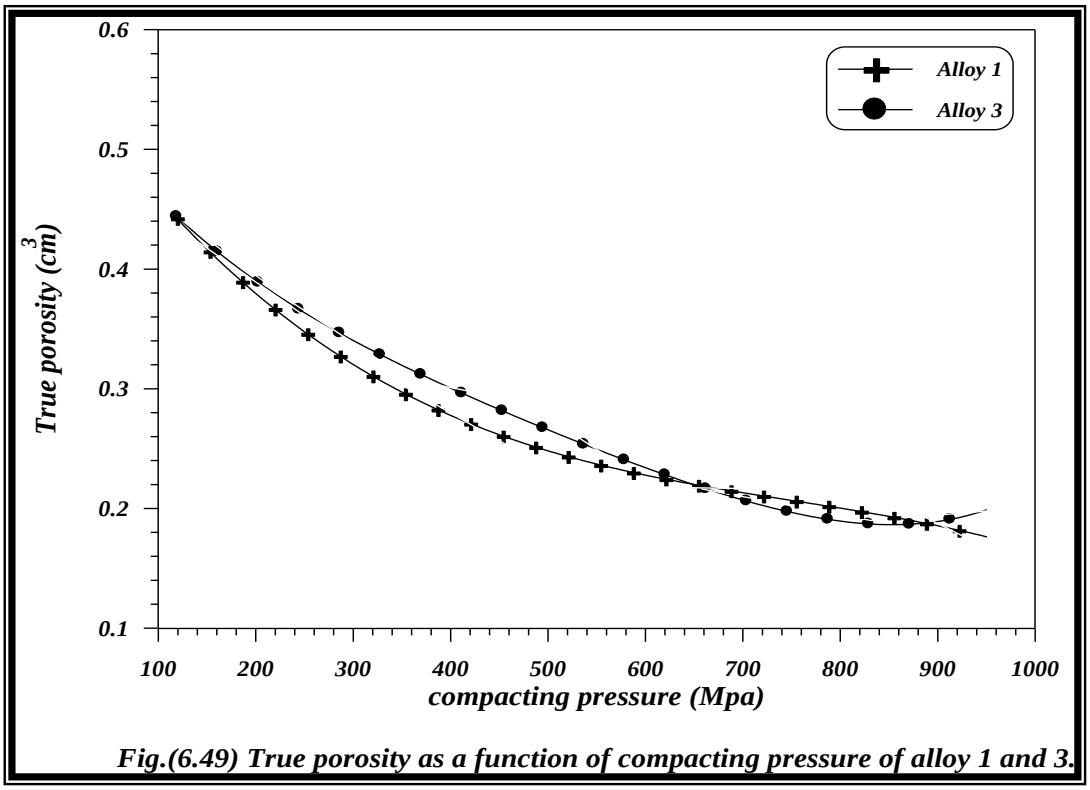

Fig.(6.49) True porosity as a function of compacting pressure of alloy 1 and 3.

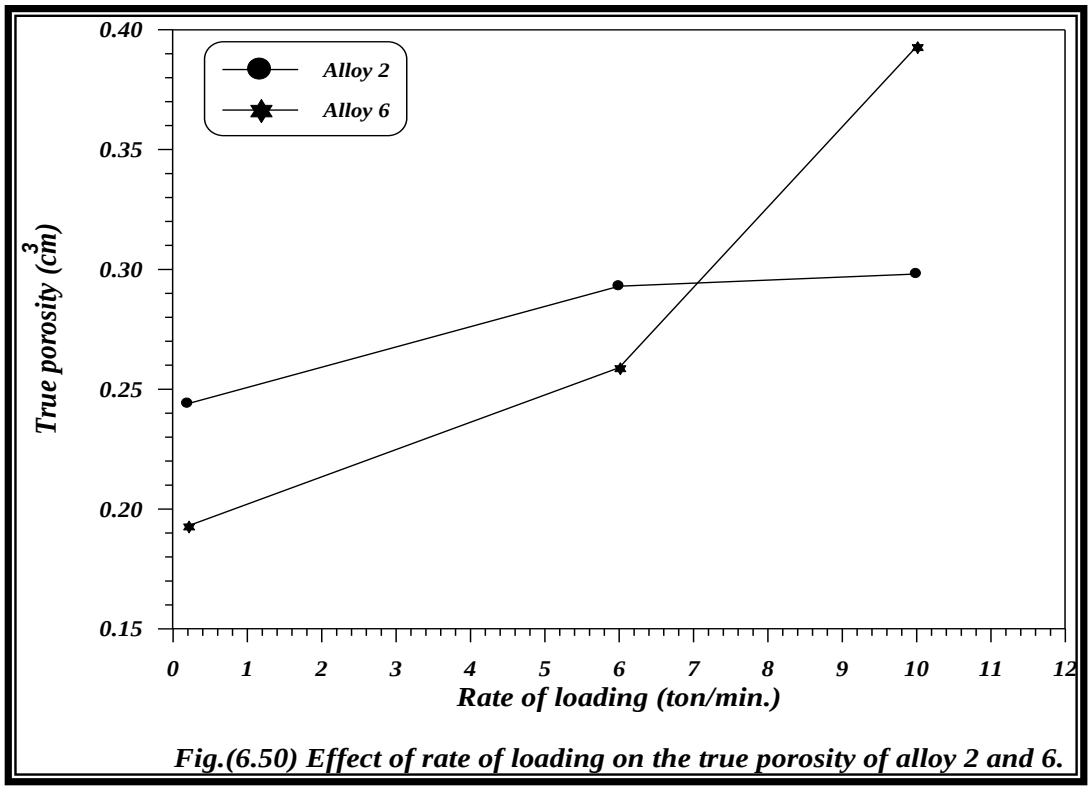

Fig.(6.50) Effect of rate of loading on the true porosity of alloy 2 and 6.

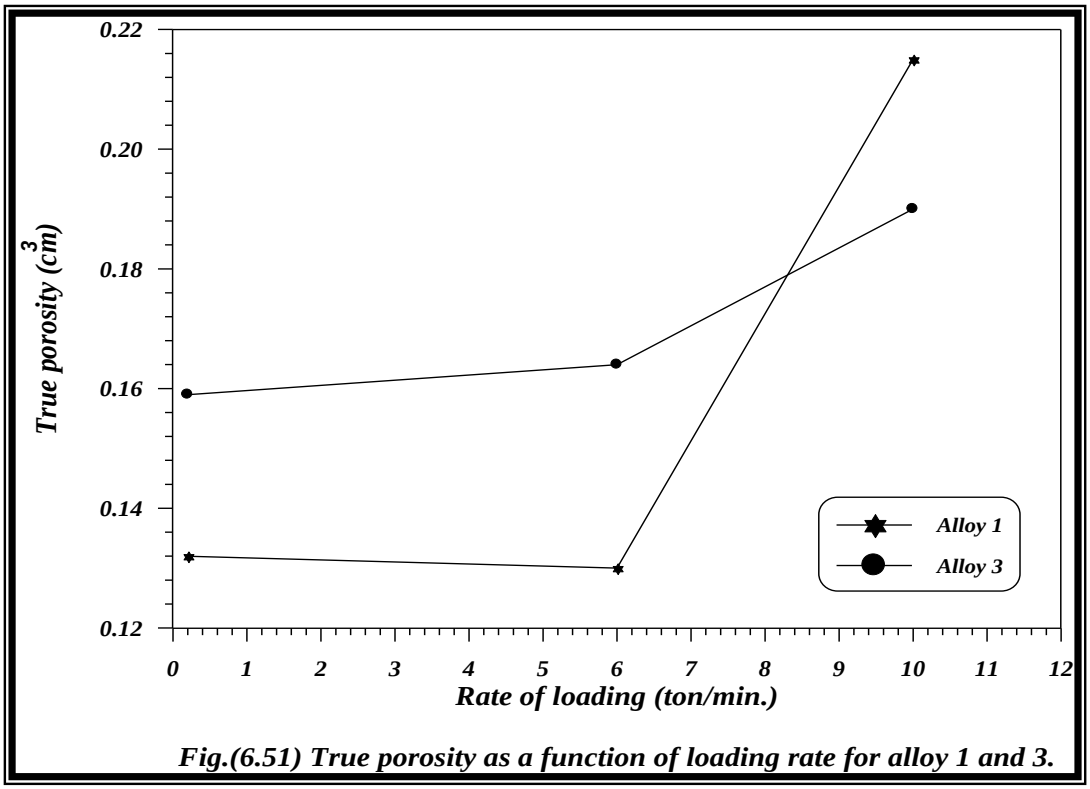

Fig.(6.51) True porosity as a function of loading rate for alloy 1 and 3.

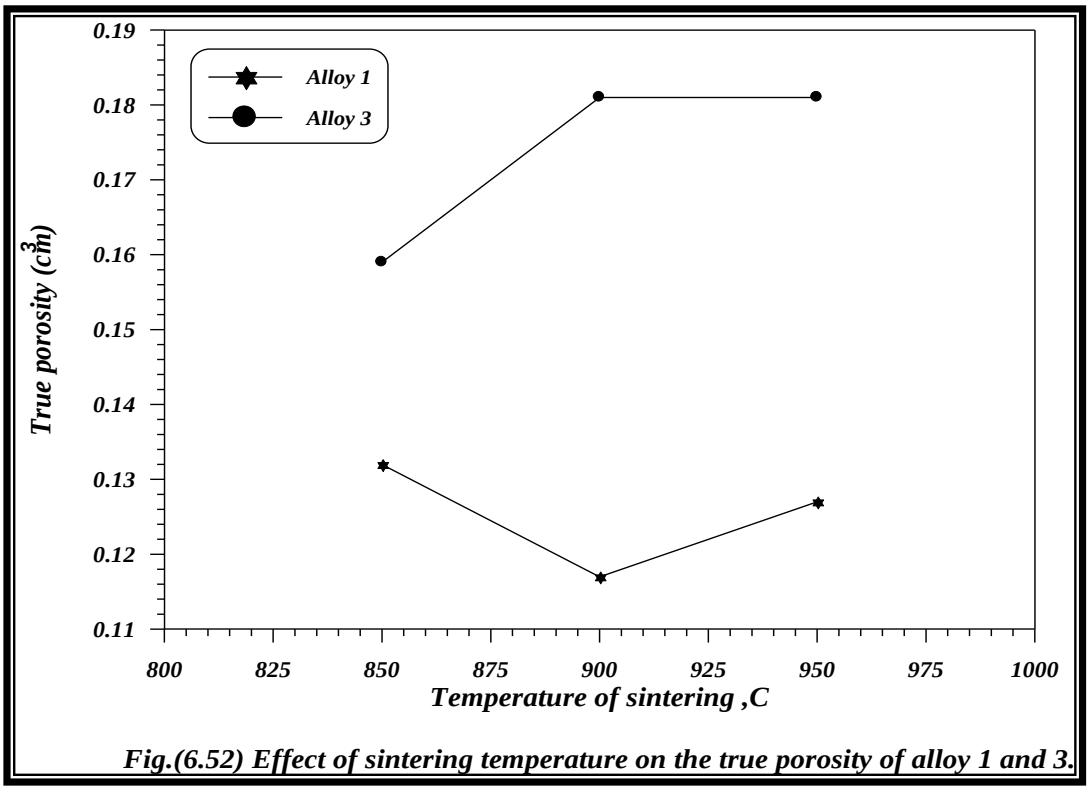

Fig.(6.52) Effect of sintering temperature on the true porosity of alloy 1 and 3.

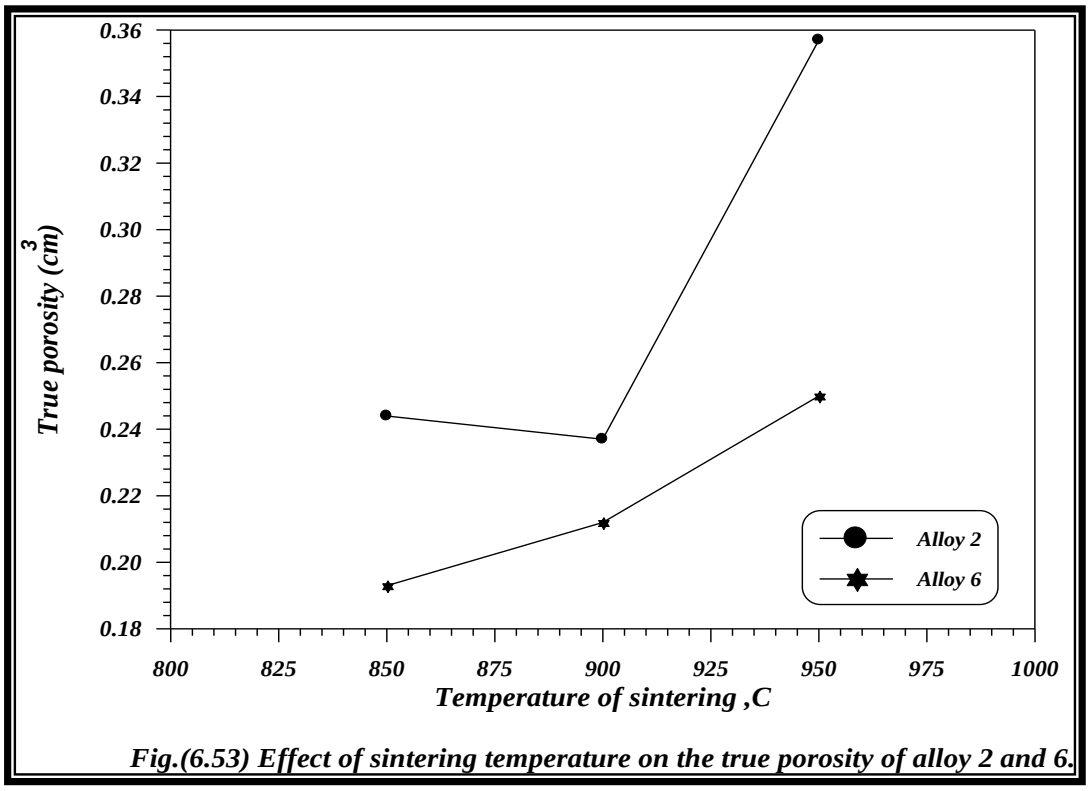

Fig.(6.53) Effect of sintering temperature on the true porosity of alloy 2 and 6.

6.3.2.4. Expansion of sintered compacts

Changes in the dimensions of compacts are important considerations in the sintering. Dimensional changes are determined as the difference in dimensions between green and sintered compacts parallel and perpendicular to the direction of pressing and are expressed in the percent of the green dimensions.

The effect of compacting pressure on the expansion of alloy 1,2,3 and 6 has shown in Fig. (6.54) and Fig.(6.55) . It has been shown that expansion of alloy 1,2,3 and 6 are increased with increasing compacting pressure from 1.32 % at 120 MPa a study state value of 3.35 % at compacting pressure greater than 660 MPa. This expansion is due to gases entrapped in closed off pores of the compact. Gases may be entrapped during compacting or may be formed by chemical reactions such as the formation of water vapor by reaction of oxide skins on the surface of the particles with the hydrogen of the sintering atmosphere which diffuses in to the closed pores. In the case of Aragon atmosphere , there is no hydrogen but it is probably that Aragon enters the closed pores at high temperature sintering which leads to expand the compact under sintering .

Furthermore, thermal expansion due to increase in temperature of sintering with high coefficient of thermal expansion of copper particles , increases and arises from high thermal expansion coefficients of other constituents under cooling of sintered compacts.

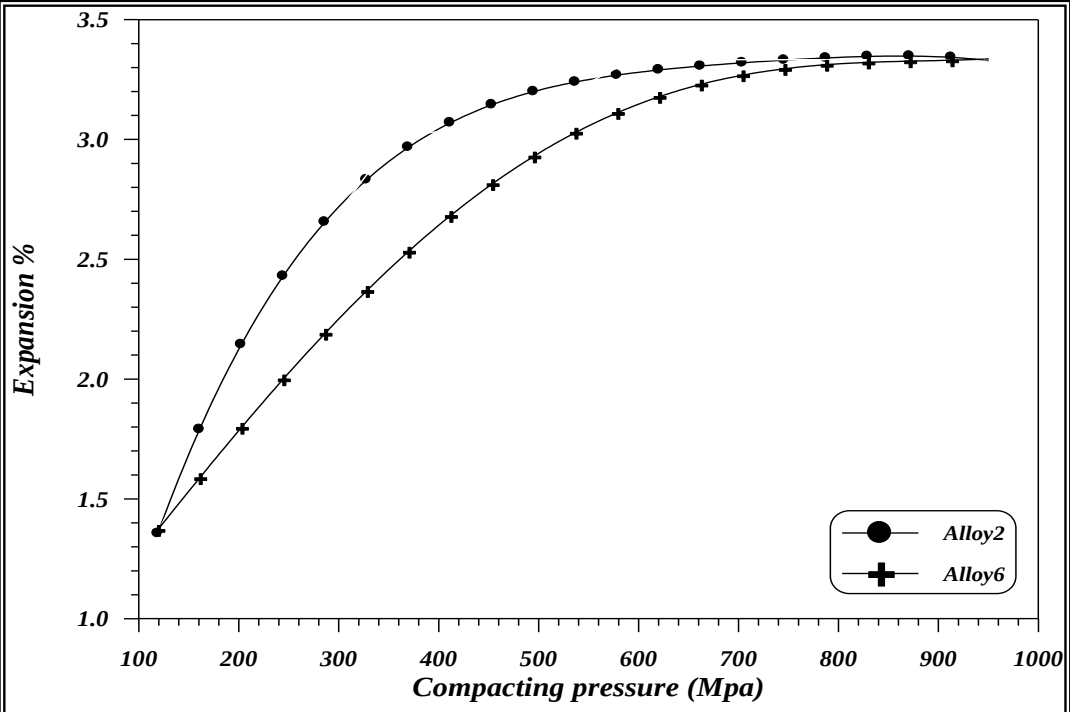

Fig(6.54) Expansion as a function to compacting pressure for alloy 2 and 6.

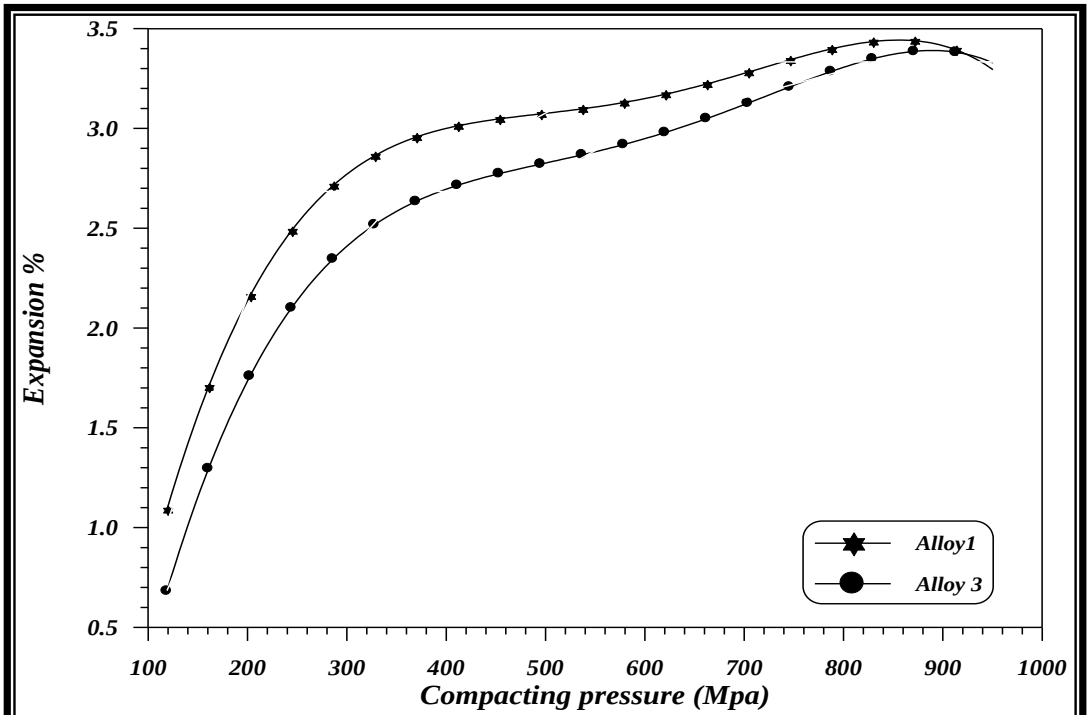

Fig.(6.55) Expansion as a function to compacting pressure for alloy 1 and 3.

6.3.3 Microstructure of sintered compacts.

The microstructure image by (LOM) for first stage sintering (3 hr at 600 ^{o}C) and second stages sintering (3 hr. at 600 ^{o}C and 3 hr. at 850 ^{o}C) have been shown in Fig.(6.56). The principal difference between the microstructures of the first and second stage sintering is in the shape of pores within the powder particles which have become rounded during sintering. The first stage sintering temperature is in the shape of pore within the powder particles which have become rounded during sintering. the first stage sintering temperature is too low to produce adequate bonding between powder particle. The specimens have been etched with ($NH_4OH + H_2O_2 + H_2O$) etchent to reveal the grain boundaries in the microstructure. Pores of different size are no longer cusp-shaped and irregular but have become rounded. The transition in microstructure form that of a green compacts to that of a well sintered compacts is a function of sintering time and temperature.

The effect of time of sintering which achieved at 850 ^{o}C on the microstructures has been shown in Fig. (6.57). While the temperature of sintering at constant time (10 min.) effect on the microstructures of alloys 1,2,3 and 6 has been shown in Fig.(6.58) and Fig.(5.59).

During annealing of cold worked wrought material, a recrystallization temperature is reached. The nuclei of strain-free grains are formed which grow into the recrystallized structure so that grain growth has been occurred. recrystallization temperature and amount of cold work. However, the temperature of sintering is higher than the recrystallization temperature of wrought material. Compacting pressure has a relatively minor effect on the temperature range at which the sintering structure is formed. The effect of compacting pressure on grain growth during sintering may be to facilitate contact between particles. Sintered structure of compact requires that grain growth occurs across particle boundaries. This grain growth is restricted until material transport has progressed to point where a substantial increase in the contact area between particles has been took place.

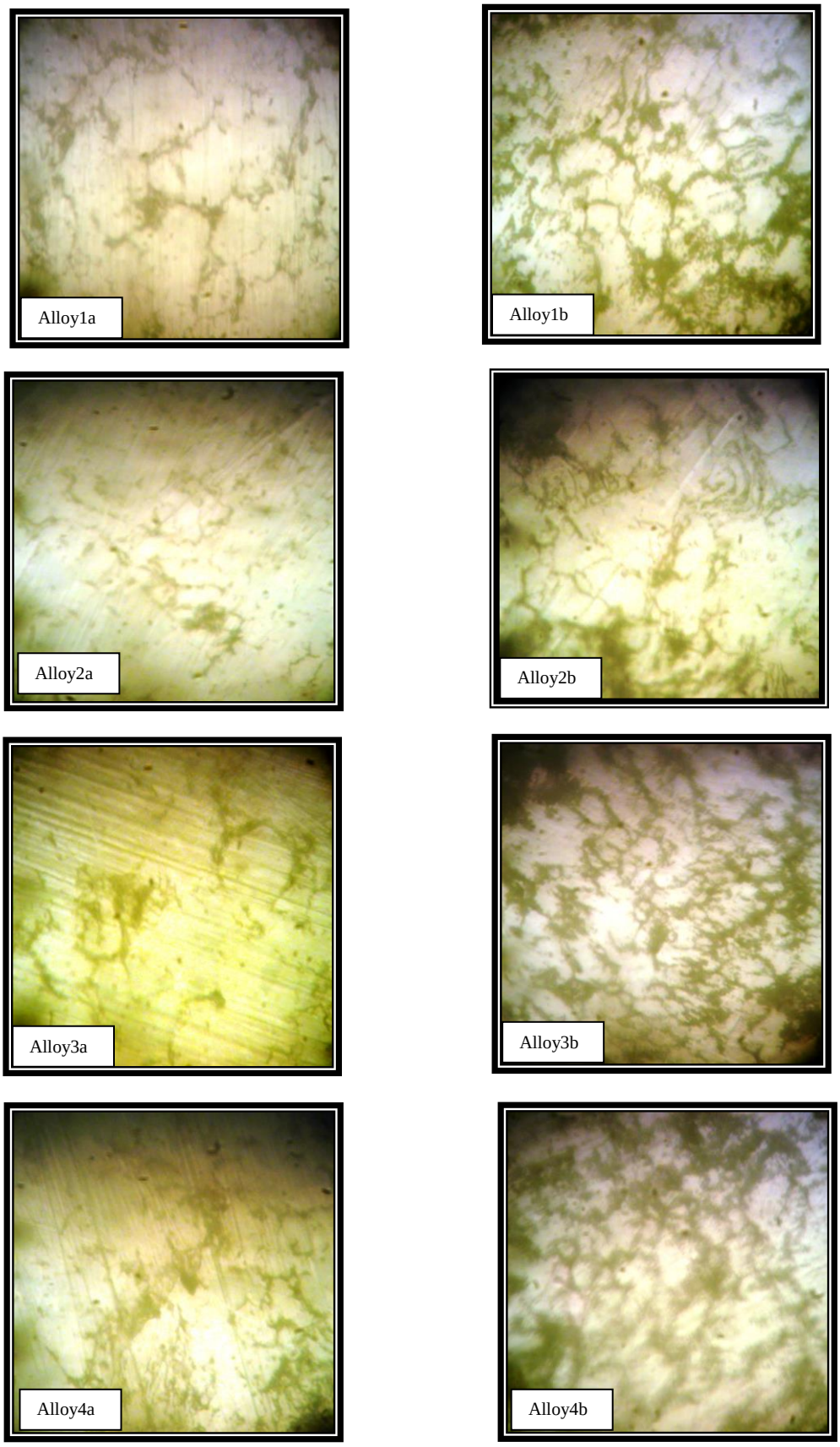

Fig.(6.56) LOM images for the microstructure of alloys1,2,3,6 for: a.stage I sintering b.stage II sintering 1000X .

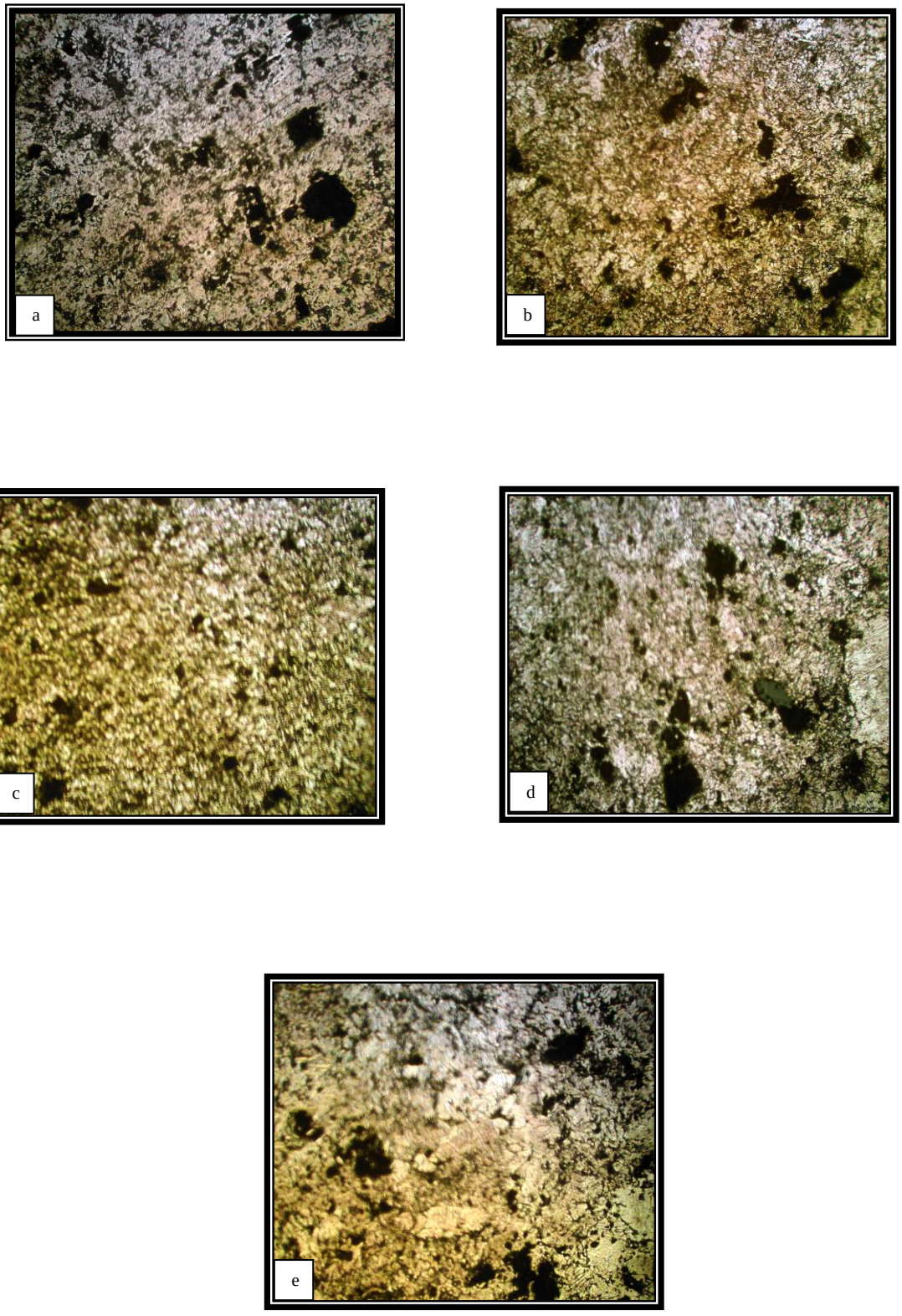

Fig.(6.57) LOM images for the microstructure of alloys2 for different sintering time as: a.10 min. b.30 min. c.60 min. d.120 min. e.180 min 150X.

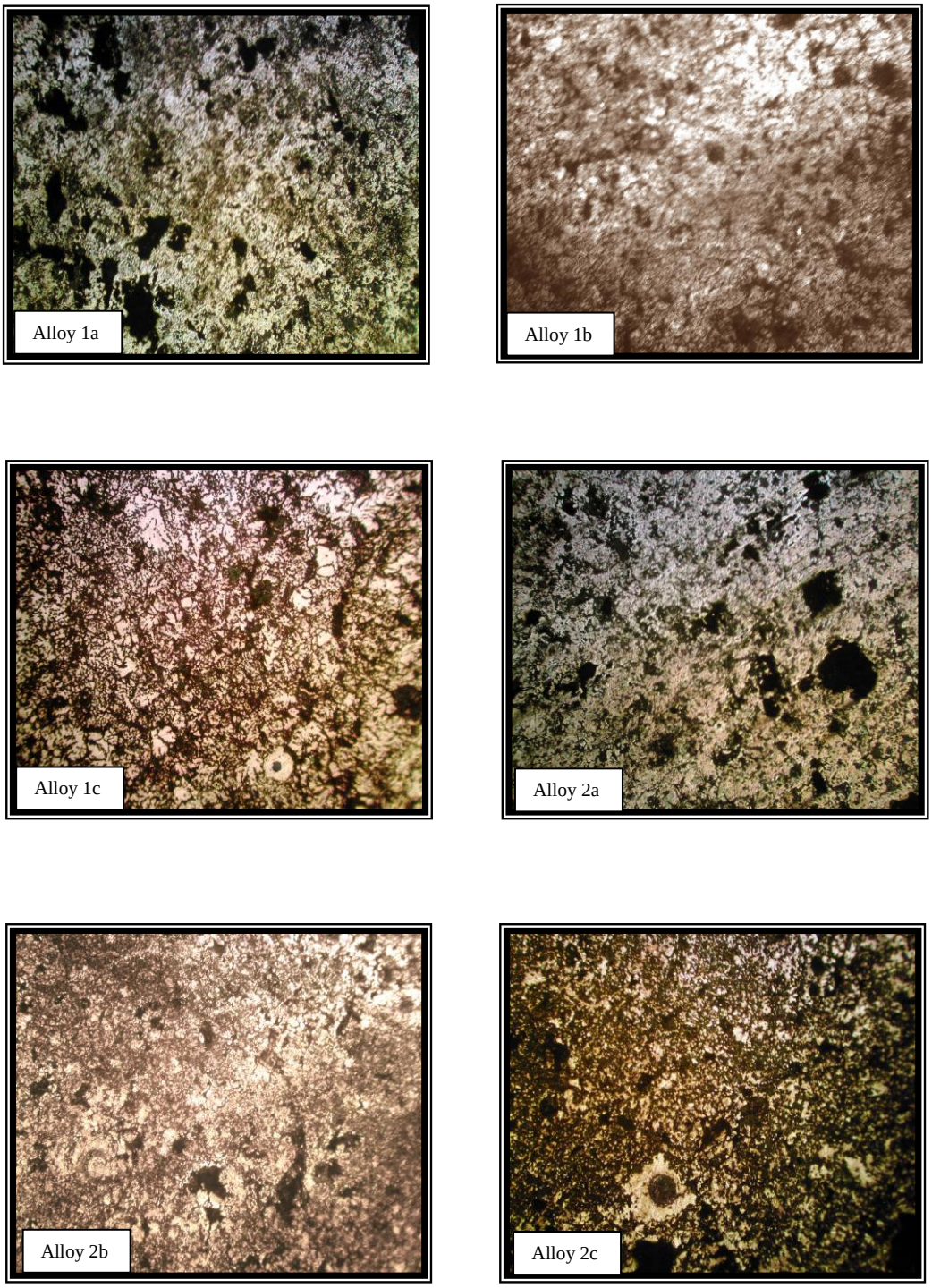

Fig.(6.58) LOM images for the microstructure of alloys 1 and 2 for different sintering temperature as: a.850 ^{O}C. b.900 ^{O}C. c.950 ^{O}C 150 X.

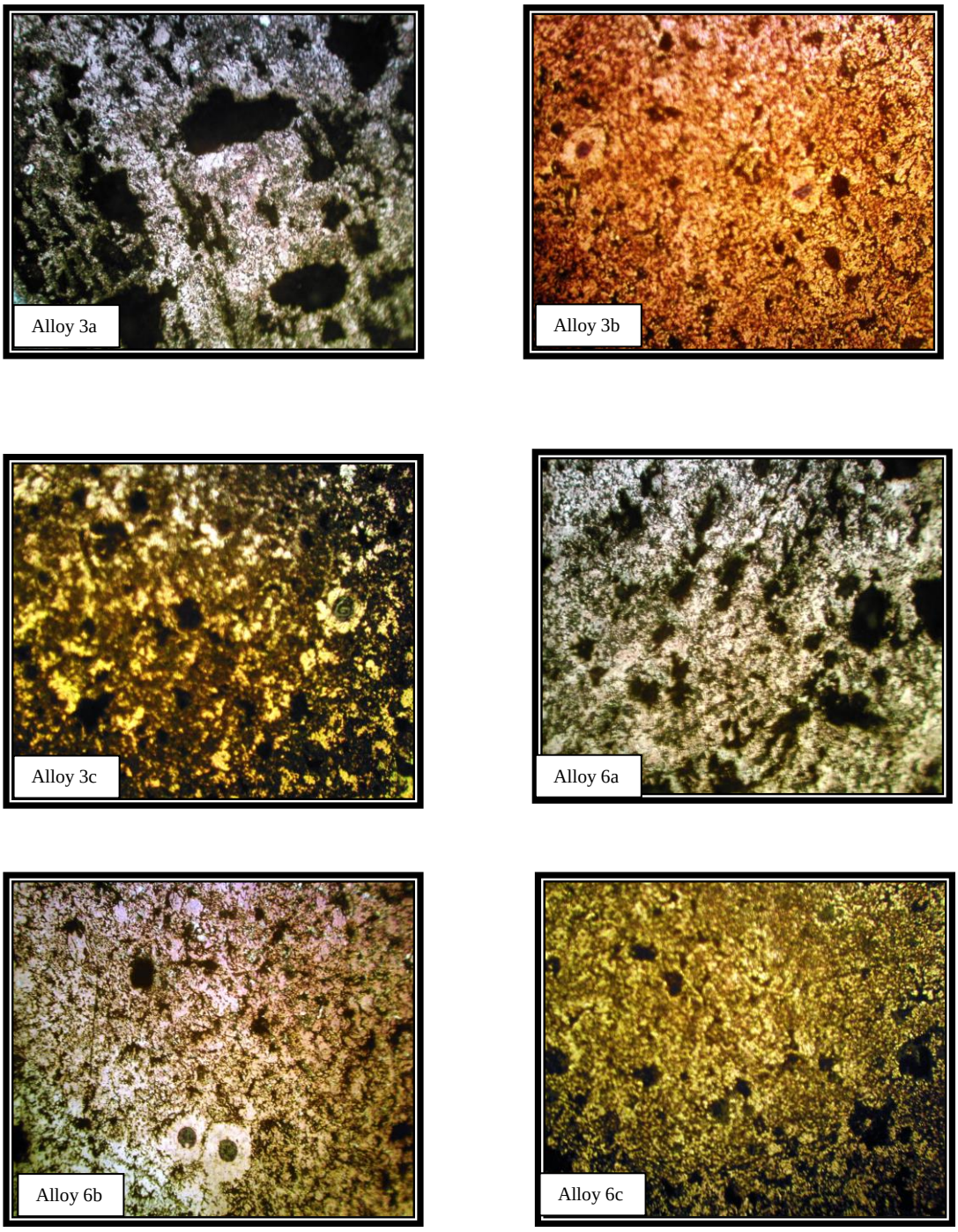

Fig.(6.59) LOM images for the microstructure of alloys 3 and 6 for different sintering temperature as: a.850 ^{O}C. b.900 ^{O}C. c.950 ^{O}C 150 X.

6.3.4. Pore size and distribution

LOM image of microstructures for first stage sintering and second stage sintering with corresponding a accumulative plots for alloy 1,2,3 and 6 have been shown in Fig.(6.60) and Fig.(6.61).

It is shown that pores are irregular and non uniform in shape and distribution in the first stage sintering due to low temperature of sintering with respect to the matrix alloying element (Cu). However , pores are rounded some what at the second stage sintering. The average pore size is determined at 50% point on the accumulative plot which is (8 , 10 , 7 and 10 μm) for alloys 1,2,3 and 6 respectively. For first stage sintering. However. the average pore size of alloys 1,2,3 and 6 for second stage sintering case is determined form Fig.(6.61) as [2,8,6 and 6 μm] respectively. Sometimes ,powder particles which are not formed alloy in the first stage sintering, appear as black regions in binary image so that not all black regions are pores. Any way , pores tend to round in the second stage sintering as possible.

Difference in composition and quantity of phases $(\alpha + \gamma_2)$ in the microstructure of sintered specimens affect on the distribution , of pores in the microstructures. In addition, silicon carbide particles of grinding paper may be impeded in sectioned surface of polished specimens specially alloy 1 due to low content of aluminum in the chemical composition which leads to lower γ_2 concentration phase in the matrix of ductile α. This effect may also affect on the real pore distribution which based upon binary image analysis. Therefore , more attention must be taken in the preparation of polished specimen to reveal real pores and the next pore distribution base up on white and black objects image analysis. Rounded and less of pores in the second stage of sintering refer to access of sintering process of compacts.

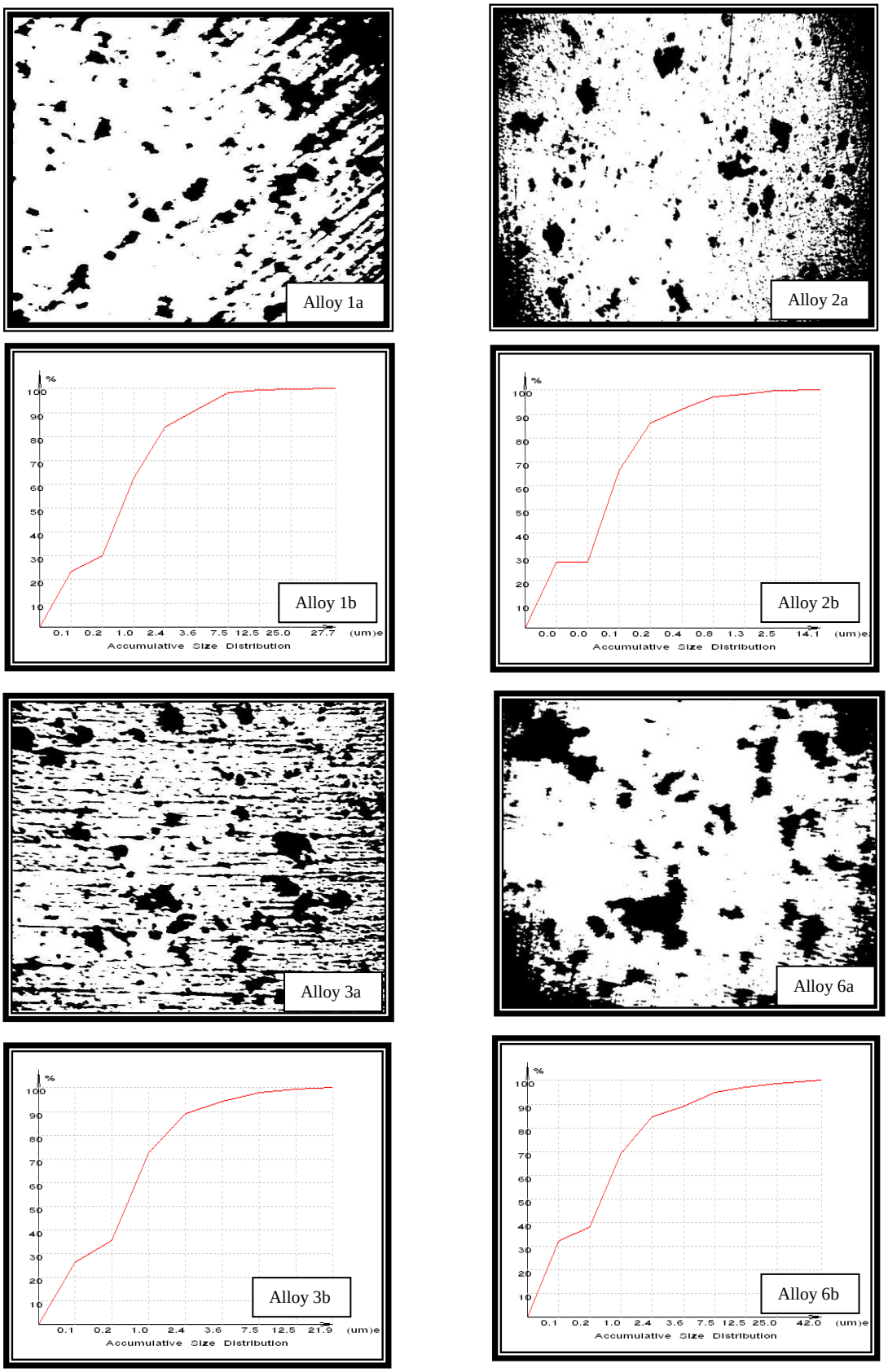

Fig.(6.60) LOM binary images and accumulative pore distribution of alloys 1 , 2 ,3 and 6 as: a. micrograph stage I sintering b. accumulative plot for stage I sintering 150 X .

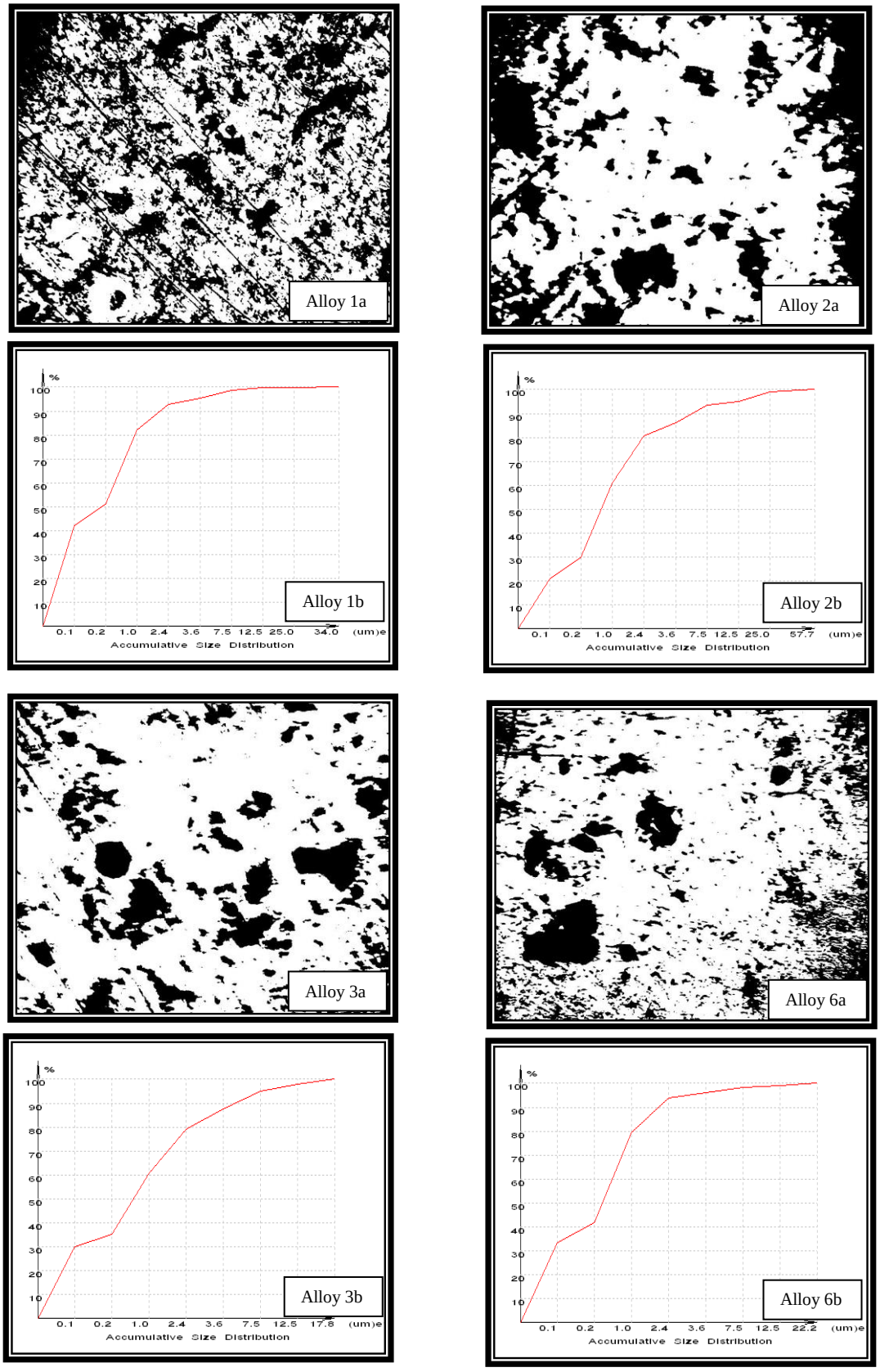

Fig.(6.61) LOM binary images and accumulative pore distribution of alloys 1 , 2 ,3 and 6 as: a. micrograph stage II sintering b. accumulative plot for stage II sintering 150 X .

6.3.5. Vicker's macrohardness test results

Vicker's macrohardness tester with digital monitor is used to determine the macrohardness of sintered compacts for both first and second stage sintering. Four readings are based for each specimen and apply this condition for all alloys Fig.(6.62) shows Vicher's macrohardness with 30 kg majer load and 3 kg as minor load, for alloys 1,2,3 and 6 . It has been shown that vicker's macrohardness for first stage sintering of alloy 1,2,3 and 6 are higher than that in the second stage sintering of these alloys because the sintering of alloy 1,2,3 and 6 at 600 ^{o}C and 3hr. as holding time is not enough to transform all intermetallic compound (γ_2) in to solid solution of β at the temperature greater than 564 ^{o}C for Eutectiod composition. In other words , sintering in temperature of 600 ^{o}C leads to form microstructure in $(\alpha+\gamma_2)$ region according to (Cu +Al) phase diagram. Alloy 1 consists of 11 % Al so that it is not enough to form β phase. Alloys 2,3 and 6 have 13% Al percent so that they are hypereutectoid and also sintering in 600 ^{o}C hot from β phase . There fore , γ_2 in $(\alpha+\gamma_2)$ microstructure is the predominant phase and because this intermetallic compound is very hard , alloys 1, 2,3 and 6 have high hardness. while the sintering in 600 ^{o}C for 3 hr and the next 850 ^{o}C for 3hr. addition , produce β' phase in this temperature and during cooling (Which is high rate in type furnace used in this study) Small amount from γ_2 phase may be precipitated in the matrix of α phase specially at grain boundaries regions. This reason produce low hardness of α phase with comparison with $(\alpha+\gamma_2)$ in the first stage sintering case.

Furthermore, in the first stage sintering case, not all metal powders transform to alloy so that these particles impeded in the matrix and not solved in the α phase and no form any intermetallic compound which lead to remain these particles near the surface and affect on the vicker's macrohardness. Thus ,

in the second stage there is no powdered particles not dissolved in the microstructure which form alloyed solid solution that the third and /or fourth alloying elements dissolve in the matrix of solvent metal.

After presentation of studying of process parameters for both in green and sintered compacts, martensitic transformation during different heat treatment are being presented in the following :-

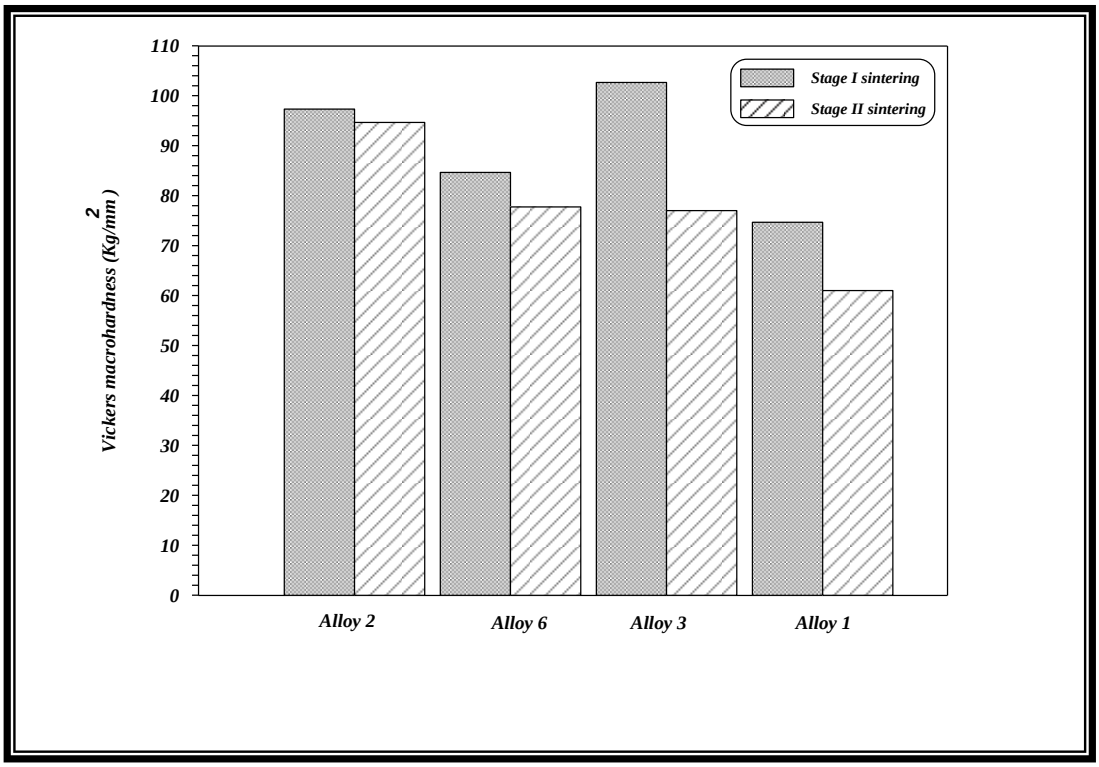

Fig.(6.62) Vickers macrohardness for sintered compacts 1,2,3 and 6 after stage I and stage II sintering.

6.4. Effect of heat treatment after sintering .

Different heat treatment such as direct quenching step – quench and aging after quenching are studied. Effects of these heat treatments on the X- ray diffraction patterns, LOM image, SEM image , hardness and compression are discussed and presented as follows:

6.4.1 X-ray diffraction Patterns for Direct quench treatment .

The sintered samples from (1 to 26) are heated from room temperature to 840 ^{o}C for 30 min., 60 min, and 140 min . After this , all heated samples are quenched in ice water at 2- 4 ^{o}C. To identify martensitic structure, x-ray diffraction technique is based . It is achieved from 10 deg. to 90 degree of diffraction angle (2θ). After x-ray diffraction patterns for alloys (from 1 to 26) are obtained , the same samples are heated to 450 ^{o}C for 30 min. and slow cooling in furnace up to 150 ^{o}C and cooling air from 150 ^{o}C. These reheated specimens are analyzed with x-ray diffraction in order to identify phases and to identify phases and to compare with direct quench x-ray diffraction patterns.

Fig. (6.63) shows x-ray diffraction patterns of alloy 1 for direct-quench treatment in a whereas b. shows x-ray diffractogram for reheating up to 450 ^{o}C for 30 min. treatment. It is shown that typical pattern of $\beta'(Cu_3Al)$ martensite phase has been formed during quenching. The crystallographic of β' phase is orthorhombic with primitive space group. Whereas $\gamma_2(Al_4Cu_9)$ precipitates in the reheating heat treatment without any retained $\beta'(Cu_3Al)$ which has cubic unit cell. It is probably that martensite is decomposed in to $\alpha + \gamma_2(Al_4Cu_9)$ phase completely due to low transformation temperatures with respect to the other alloys due to low content of aluminum in alloy 1.

Several empirical relationships are useful in obtaining estimated transformation temperature as: [Wu, 1990].

$$M_s(^oC) = 2020 - 45(wt\%Ni) - 134(wt\%Al) \quad \text{----- (6.2)}$$

It is shown from Fig.(6.63) that the intensity of (1210) plane is 3117 whereas the intensity of γ_2 in the plane (330) is 3313 (cps) which is greater than the first. Most intensities of martensitic structure (orthorhombic) is lower that in the case of $\gamma_2\,(Al_4Cu_9)$ phase due to high atomic packing in the γ_2 phase which cubic.

Fig.(6.64a) shows the diffractogram of martensitic transformation in alloy 2 which is hybereutectoid alloy. There is only one phase which is martensite in the x-ray diffraction pattern of retained martensite and γ_2 phase are explained in Fig.(6.64b.).Note that in order to decompose all β' phase into $\alpha + \gamma_2$ phase , it is required additional timer or high temperature. 30 min at 450 ^oC is not enough decompose $\beta' \rightarrow \alpha + \gamma_2$ Completely. Therefore, It is probably that alloy 2 has shape memory properties at higher temperature than alloy 1 because there is remain martensite phase up to 450 ^oC . High intensity about 2568 (cps) occurs at diffraction angle (2θ) = 44.6 degree for β' phase whereas the maximum intensity (4176 cps) of γ_2 phase at diffraction (2θ) = 42.5 degree.

For Fig. (6.65) which has titanium additive to alloy 2 as base alloy as (0.4 wt %) , It is shown that this alloy forms completely martensite phase ($\beta' = Cu_3Al$) when their sample are quenched in ice water at (2-4 ^oC) Titanium additive refine the microstructure and rise the martensitic transformation temperatures. Thus these alloys have desired shape memory properties at reasonable high temperatures. It is apparent that an addition of Ni in combination with Al form strong intermetallic compounds which leads to increase hardness in copper-aluminum base alloys. In addition , it is also apparent that Titanium functions together with Ni and Al to stabilize the bata phase (β) of Cu- Al alloys and retard the eutectoid reaction of

$\beta \rightleftarrows \alpha + \gamma_2$ and prevent emergence of the brittle ($\alpha + \gamma_2$) structure. It is shown that during heating up to (450 ^{o}C) there is intermetallic compound with titanium alloying element as $[Cu, Al]_2 Ti$

The effect of boron additive as 0.4 wt% on the x-ray diffraction patterns is shown in Fig.(6.66) . It is dear that decomposition of β phase into $\alpha + \gamma_2$ phase is occurred even though high rate of cooling has been used. Addition of boron in Cu Al Ni shape memory alloys effectively suppress subsequent grain growth during betatizing heat treatments. Boron additives have remarkable effects in refining the microstructure. Refining is largely due to the formation of small insoluble particles which either assist grain nucleation or inhibit grain growth so that boron additives have only very slight effects on transformation temperature. It is also shown that there is retained martensite (β') phase during reheating heat treatment as can be seen from Fig. (6.66b) .However , the predominate phase is γ_2 phase which refers to decompose of β phase through eutectoid reaction.

From all x-ray diffraction patterns of most alloys, It has been shown that direct quenching heat treatment promote and stabilize martensite phase for both quench state and even after reheating . It is apparent later that in order to promote reverse direction $\beta \rightleftharpoons \alpha + \gamma_2$ we need to step quench and / or aging treatments However , phase change included martensitic transformation has been satisfied during quenching.

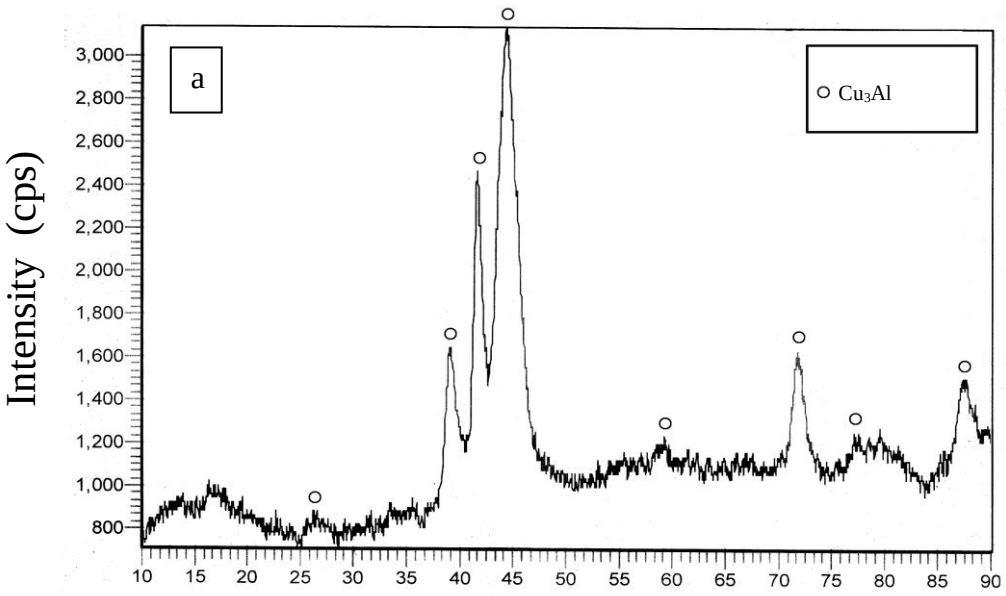

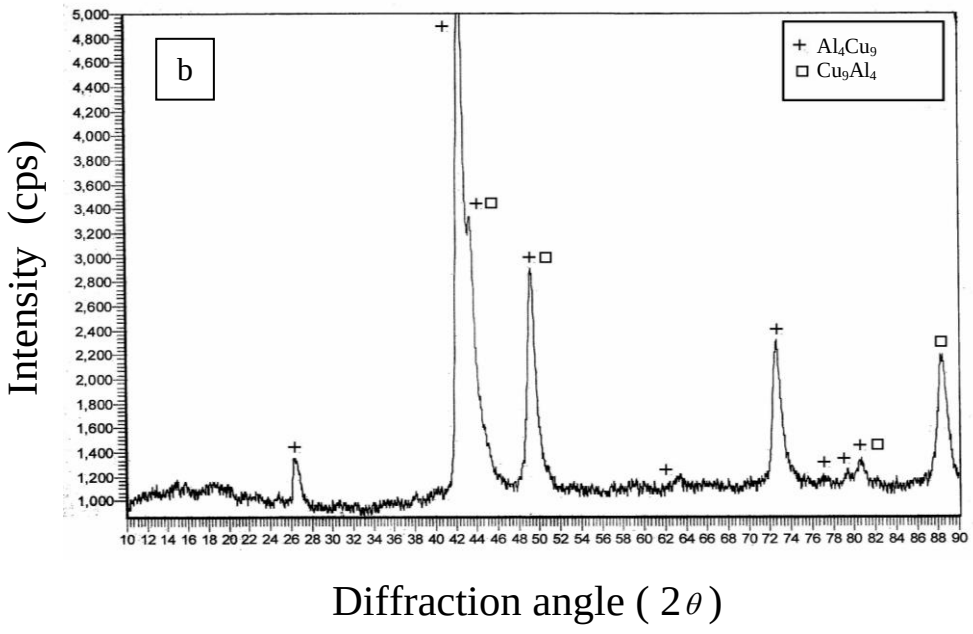

Fig.(6.63) XRD patterns for alloy1 at: a. after quenching from 840 °C for 60 min.to ice water. B. after reheating up to 450 °C for 30 min heat treatment

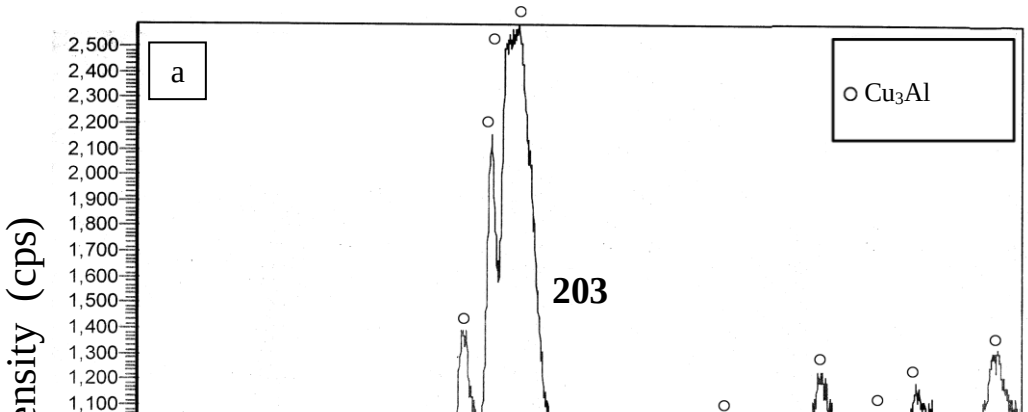

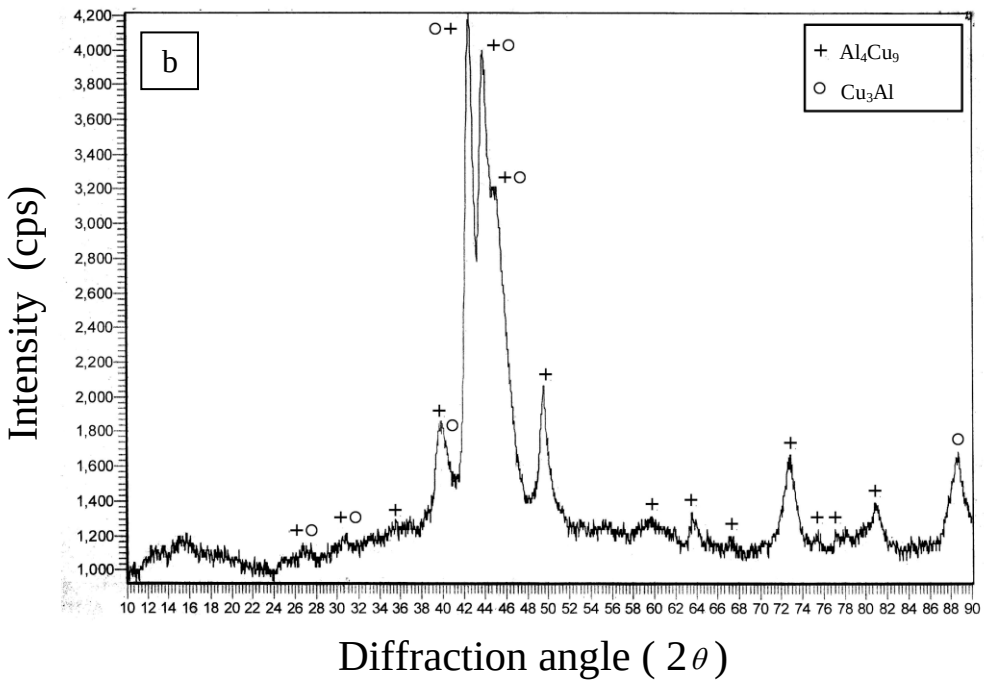

Fig.(6.64) XRD patterns for alloy2 at: a. after quenching from 840 °C for 60 min.to ice water. B. after reheating up to 450 °C for 30 min heat treatment

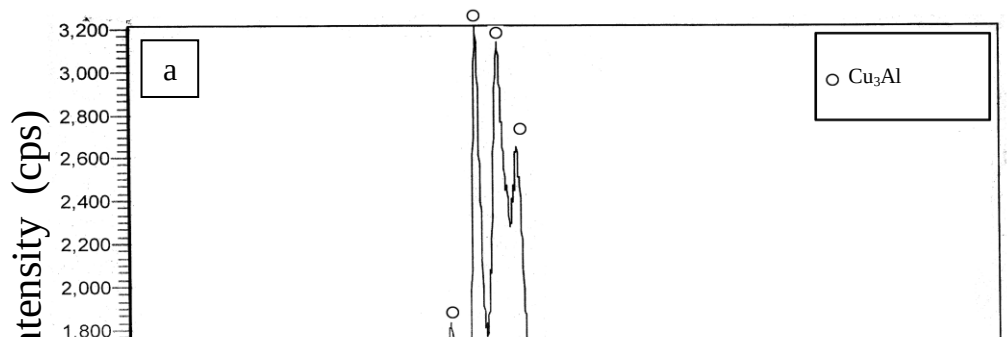

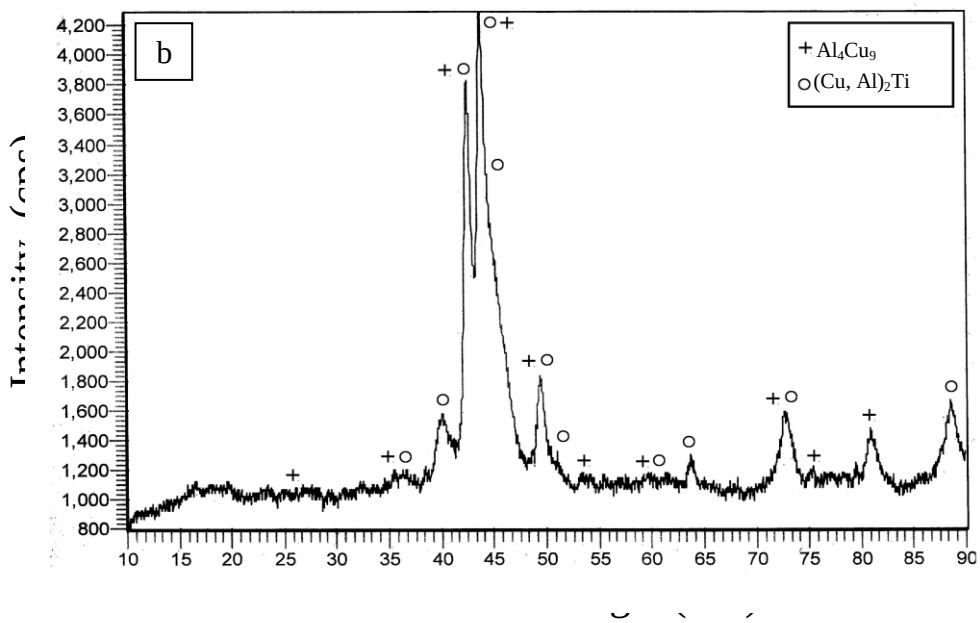

Fig.(6.65) XRD patterns for alloy3at: a. after quenching from 840 ºC for 60 min.to ice water. B. after reheating up to 450 ºC for 30 min heat treatment.

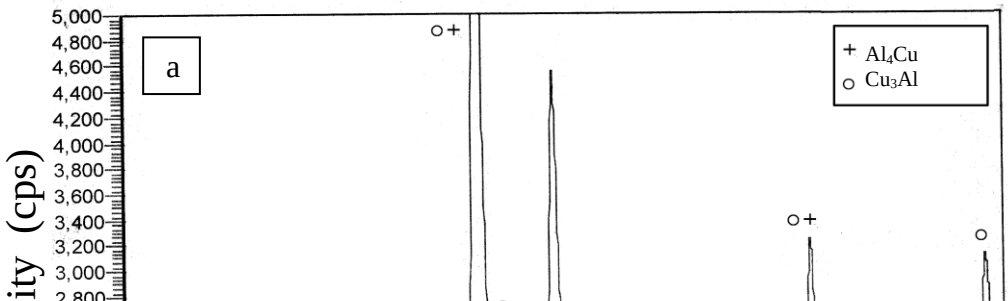

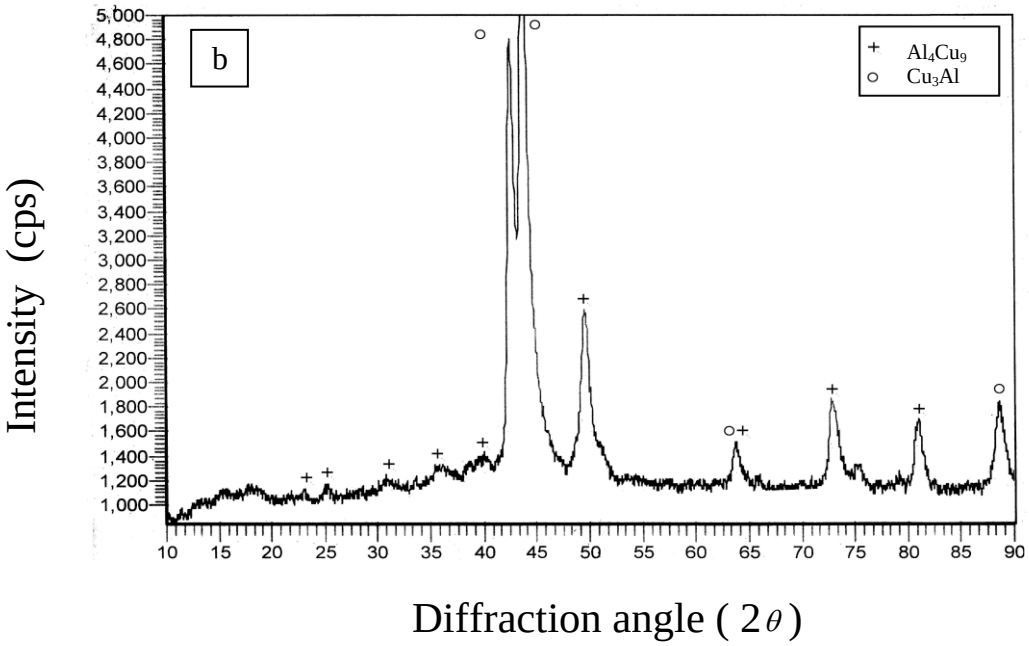

Fig.(6.66) XRD patterns for alloy 6 at: a. after quenching from 840 °C for 60 min.to ice water. B. after reheating up to 450 °C for 30 min heat treatment.

6.4.2.Light optical microscope images for Direct quench heat treatment.

Light optical microscope images for alloys (1,2,3, ….. 26) have been shown in Figs. (6.67) , (6.68) , (6.69) and Fig.(6.70).

The microstructure of these alloys are fine grains for etched specimens with [NH_4OH+ H_2O_2 + H_2O] etching . Sometime , martensite platelet has been clear but others is not clear due to fine structures and probably due to type of used etching.

It is apparent that martensite phase is formed near the pores in all specimen microstructures. Thus , pores as a defect may be promoted the martensitic phase transformation in porous alloys. It has been shown that martensitic structures viewed using (LOM) nearly always consist of plates that are very similar in appearance regardless of the alloys composition in which they have formed.

The internal microstructure of the martensite however , varies greatly among different alloys and con not be resolved by LOM.

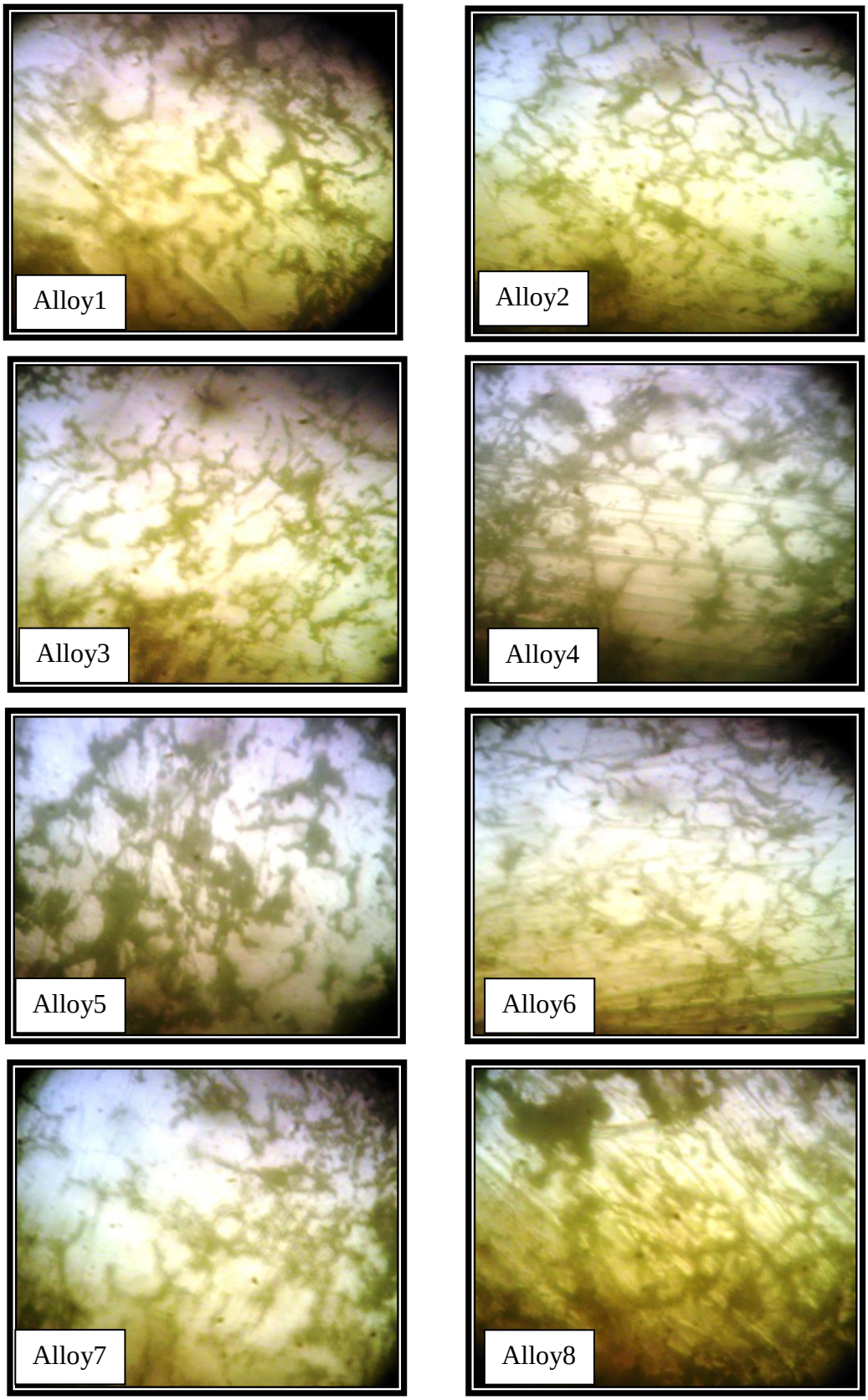

Fig.(6.67) LOM images for direct quench alloys 1,2,3,4,5,6,7 and 8 1000X.

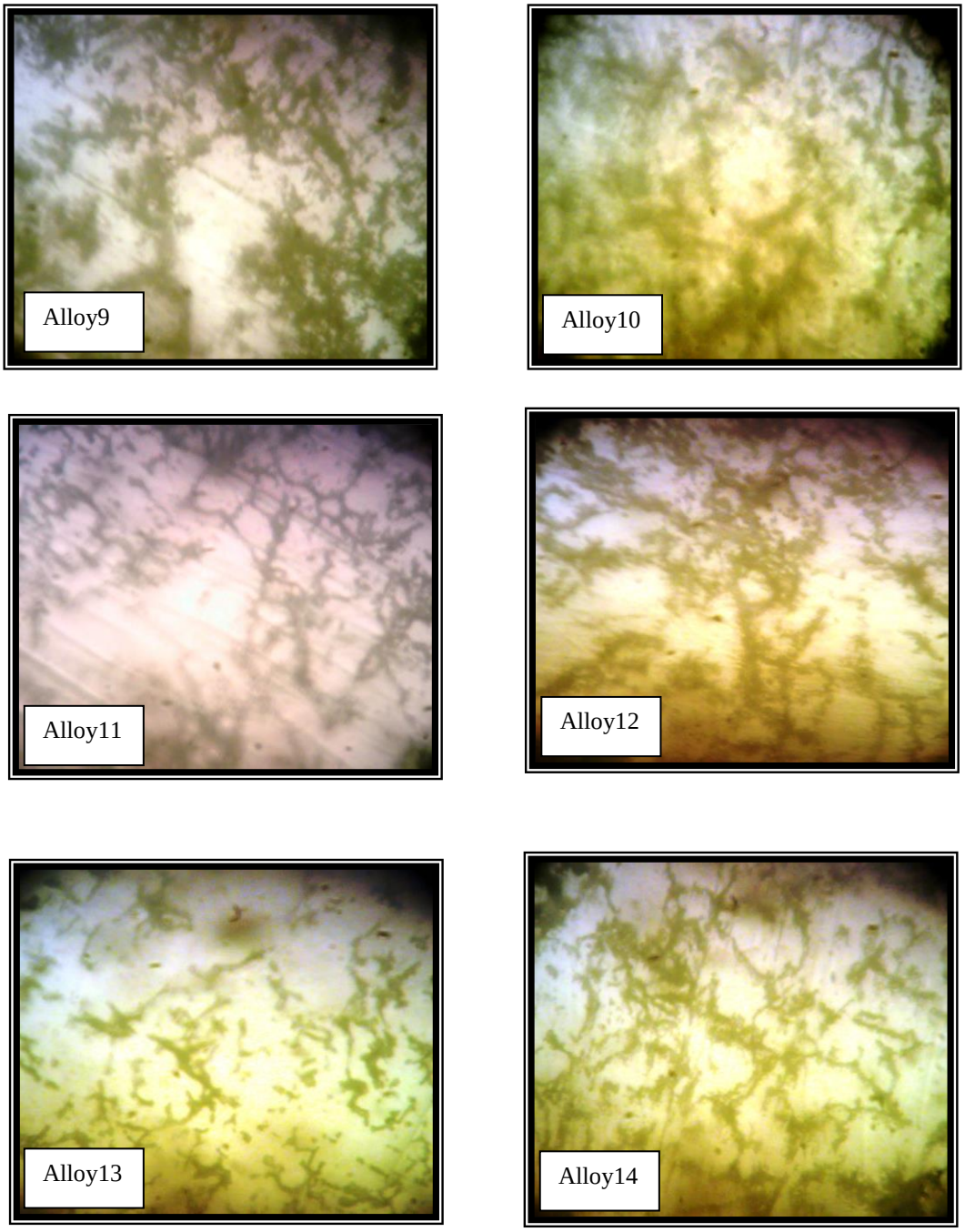

Fig.(6.68) LOM images for direct quench alloys 9,10,11,12,13 and 14 1000X.

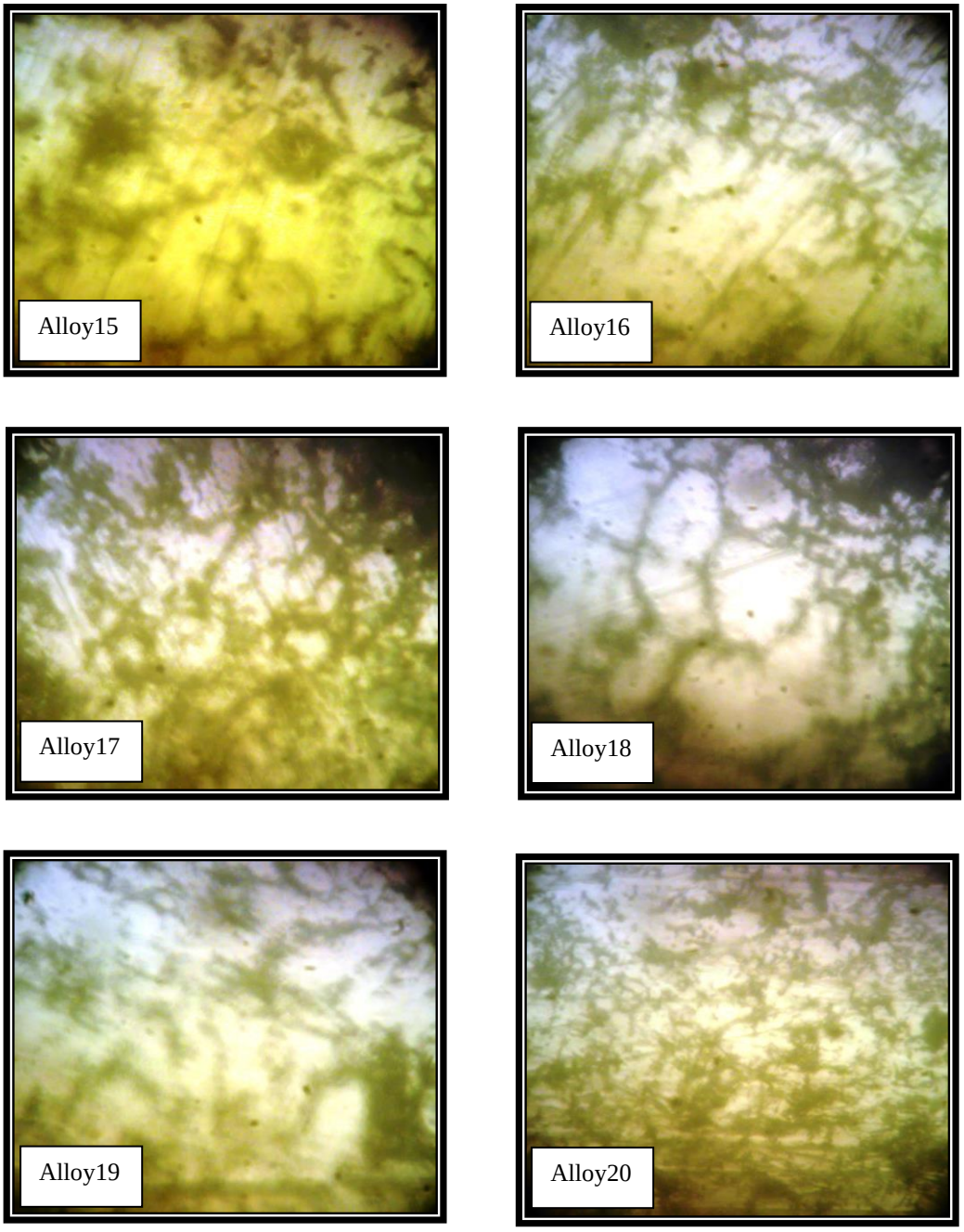

Fig.(6.69) LOM images for direct quench alloys 15,16,17,18,19 and 20 1000X.

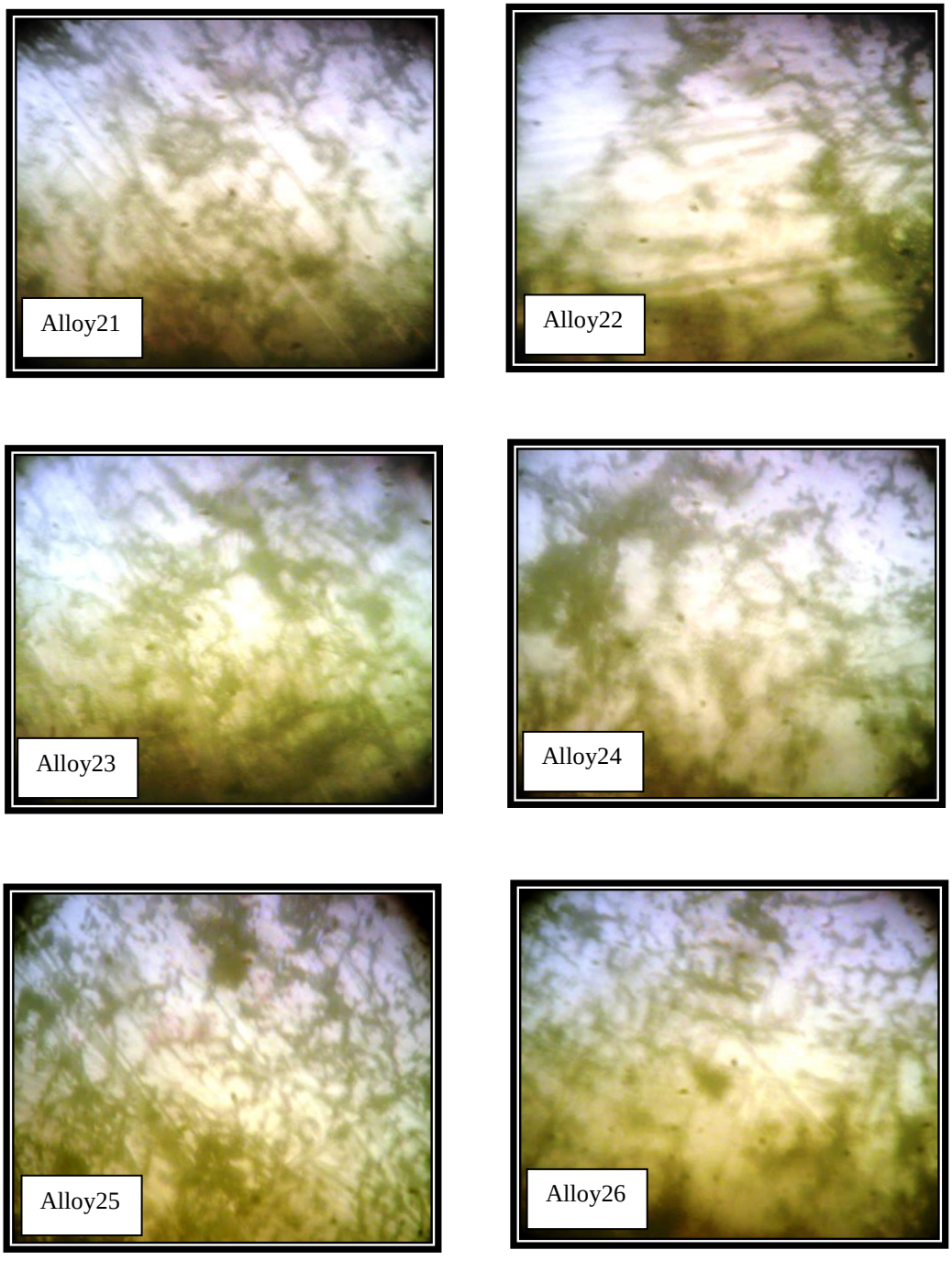

Fig.(6.70) LOM images for direct quench alloys 21,22,23,24,25 and 26 1000X.

6.4.3 Scanning electron microscope images.

Scanning electron microscope images for unetched specimen of alloys 1,2,3 and 6 are shown in Fig.(6.71), (6.72) , (6.73) and Fig. (6.74) .It is very important to examine sintered parts in the unetched condition which displays the number and distribution of original particle boundaries present.

Scanning electron microscope images for etched specimen of alloys 3 and alloy 6 are shown in Fig.(6.75) and Fig.(6.76) respectively. Etching reveal grain boundaries which are easily confused with the particle boundaries that also appear as thin gray or black lines. Cracks , particles and pore shape are easier to locate in the absence of distracting features.

The martensite formed in all alloys has a plate shape . This appearance is independent of the following parameters: -

1) The crystal structure of the martensite phase.
2) Whether the internal structure is twinned or faulted.
3) The presence or absence of crystallographic order.

Because of diffusionless feature of martensitic transformation , the order or disorder of the parent phase (β) is transferred in to martensite. Disordered B_2 copper- aluminum alloys (β) form disordered hcp martensite (β') whereas ordered B2 in Cu- Al system forms ordered orthorhombic martensite that is internally faulted (β').Growth of martensite plates is restricted by the grain boundaries of the parent phase or by previously formed plates.

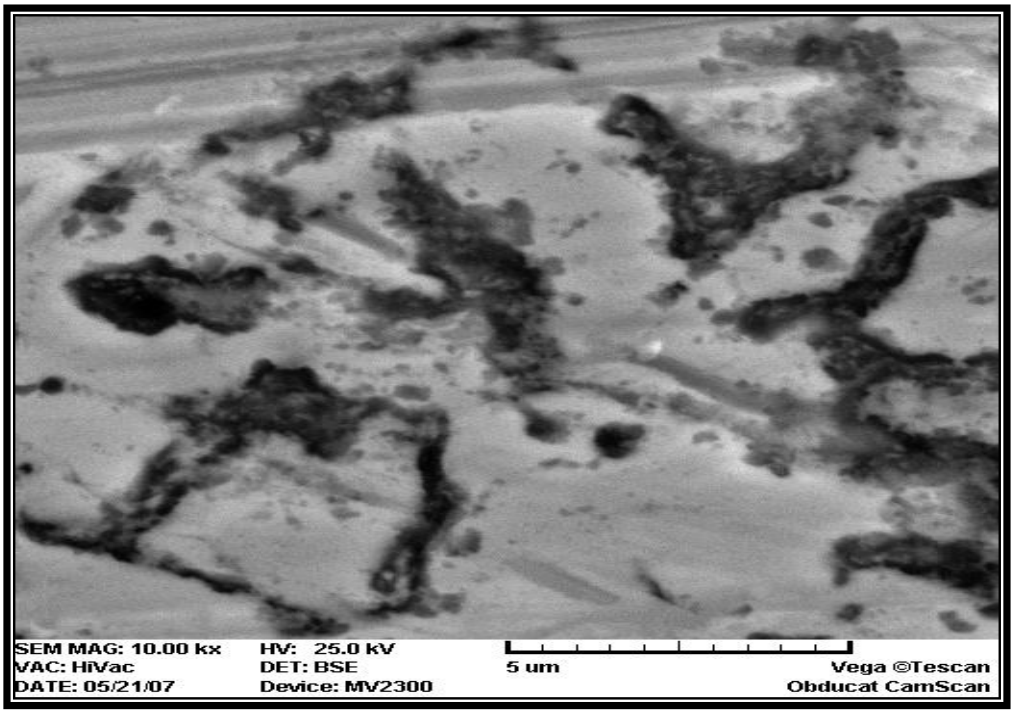

Fig.(6.71) SEM image for unetched alloy 1 in direct quenching state.

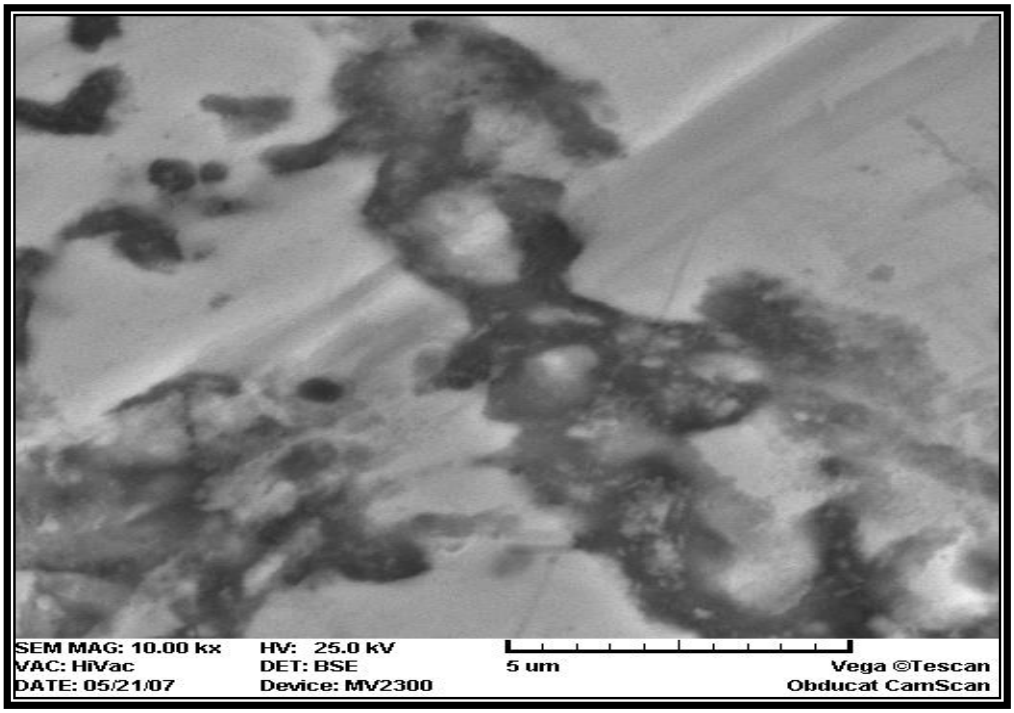

Fig.(6.72) SEM image for unetched alloy 2 in direct quenching state.

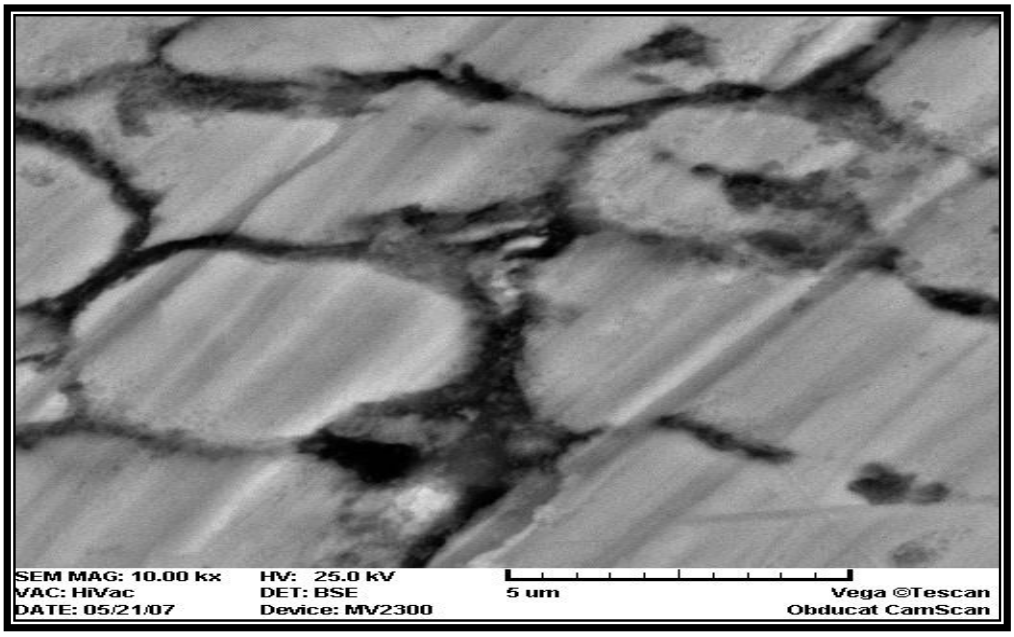

Fig.(6.73) SEM image for unetched alloy 3 in direct quenching state.

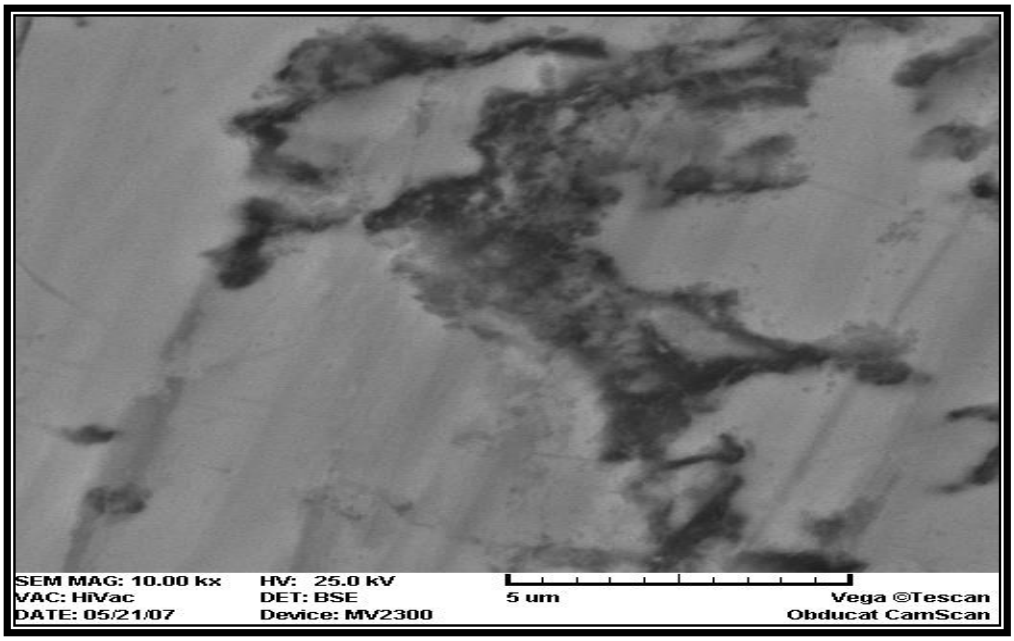

Fig.(6.74) SEM image for unetched alloy 6 in direct quenching state.

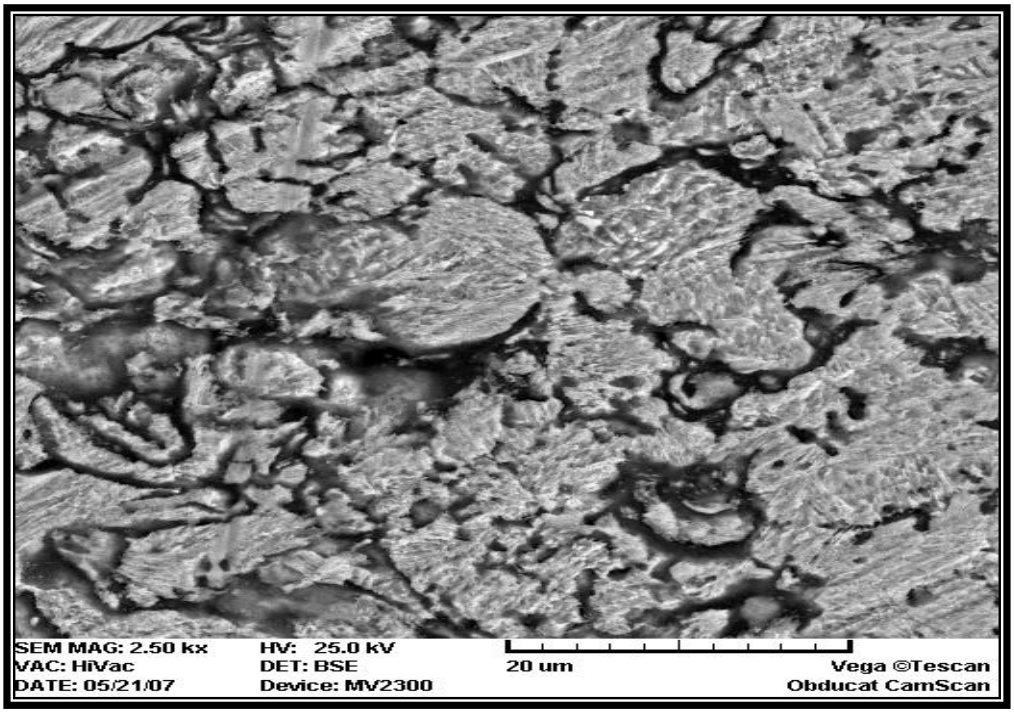

Fig.(6.75) SEM image for etched alloy 3 in direct quenching state.

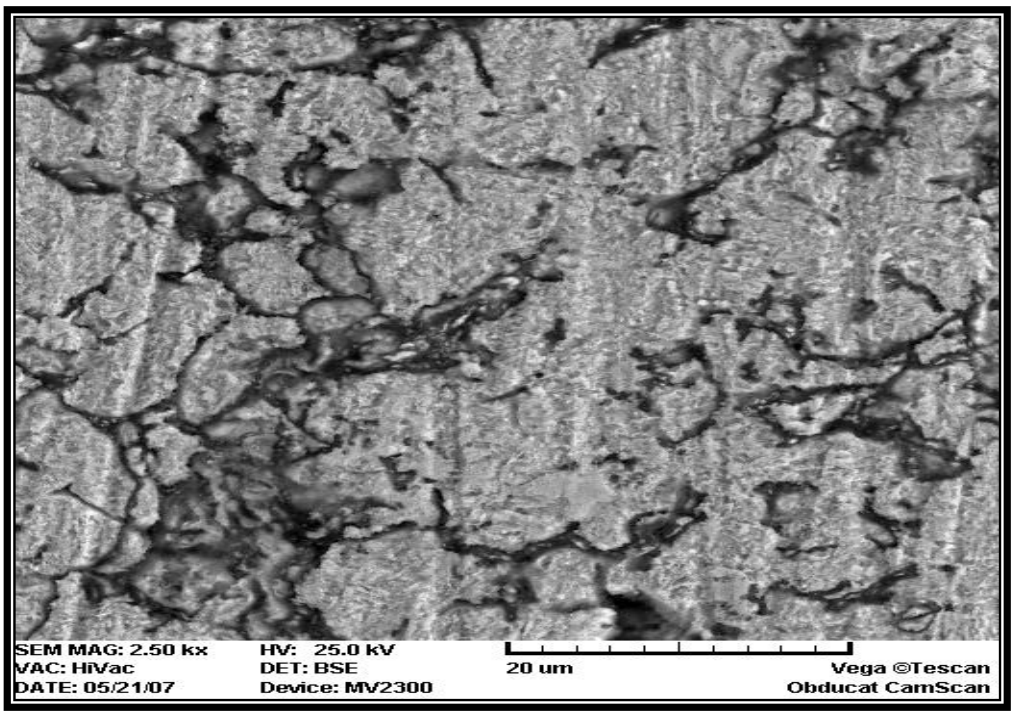

Fig.(6.76) SEM image for etched alloy 6 in direct quenching state

6.4.4 Hardness Test results for direct quenching heat treatment .

Vicker's microhardness using 500 g as maximum load as a function of weight percent of alloying element is shown in Fig.(6.77). These results for 26 alloys with three readings when the holding time at 840 ^{o}C is 60 min. when holding time is 30 min. microhardness is shown in Fig.(6.78) whereas for 140 min. as holding time of direct quench heat treatment it's results for microhardness is shown in Fig.(6.79).

It has been clear that Vicker's microhardness is fluctuated according to weight percent of most alloying element. This is probably due to presence of pores and its distribution through the specimen. Furthermore , Vicker's microhardness indenter may be lied on the pore or pore edge which leads to fluctuate reading results. In addition , not all alloying element added to based alloy have the same function on the hardness. Thus ,some of these alloying elements such as silicon gives hardness increment with its weight percent whereas a combination of(Ti+ Mn) leads to give higher hardness of the base alloy. It is probably that manganese stabilizes the intermetallic compound formed with fourth element (Ti or Zr for example) with Cu+Al+Ni systems. In general 0.4 wt % of alloying element has the greatest value of vicker's microhardness for most holding time from (30 min to 140 min.).

Brinell macrohardness with returned ball tester , has been shown in Fig.(6.80) for alloying element action . It is apparent that fluctuating of Brinell hardness valves are less than that is for vicker's microhardness. This is due to the large indentation ball with comparison with vicker's indenter. It is also apparent that Brinell hardness decreases with higher content of alloying element as 1.2 wt% of these elements. This is probably that when alloying weight percent is increased, holding time to dissolve this percent must also be increased to diffuse this higher weight percent so that it is probably that 60 min.as holding time is not enough so some intermetallic compounds does not form. Martensite phase during quenching through promoting decomposition of β phase $\alpha + \gamma_2$ phases.

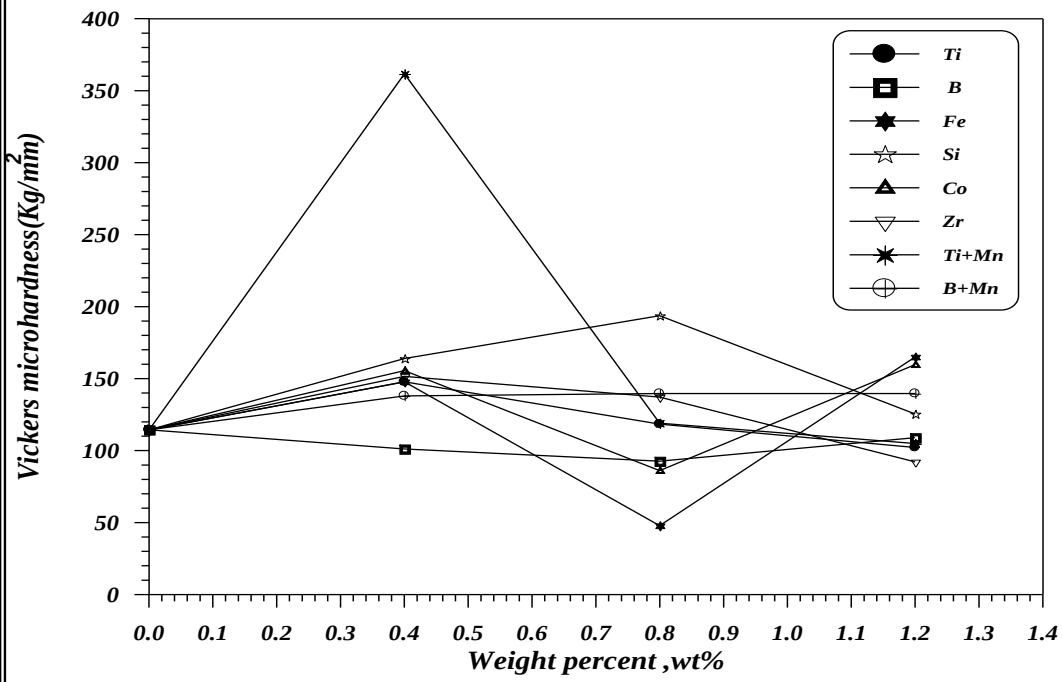

Fig.(6.77) Vickers microhardness as a function of alloying element for30 minute holding time of solution treatment.

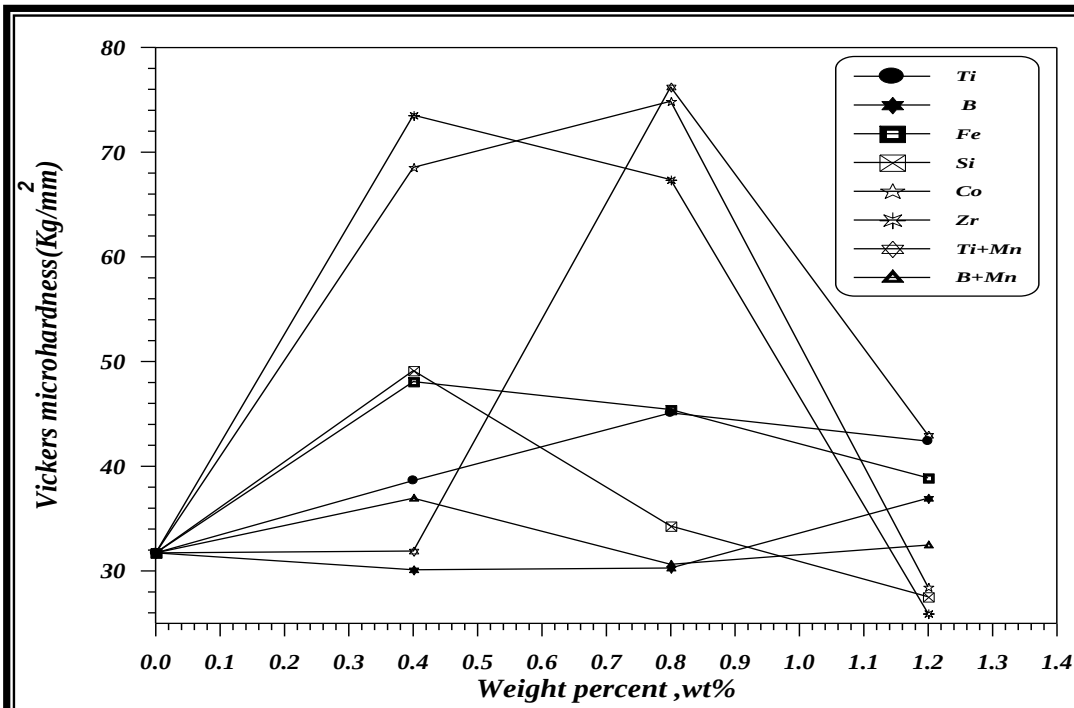

Fig.(6.78) Vickers microhardness as a function of alloying element for60 minute holding time of solution treatment.

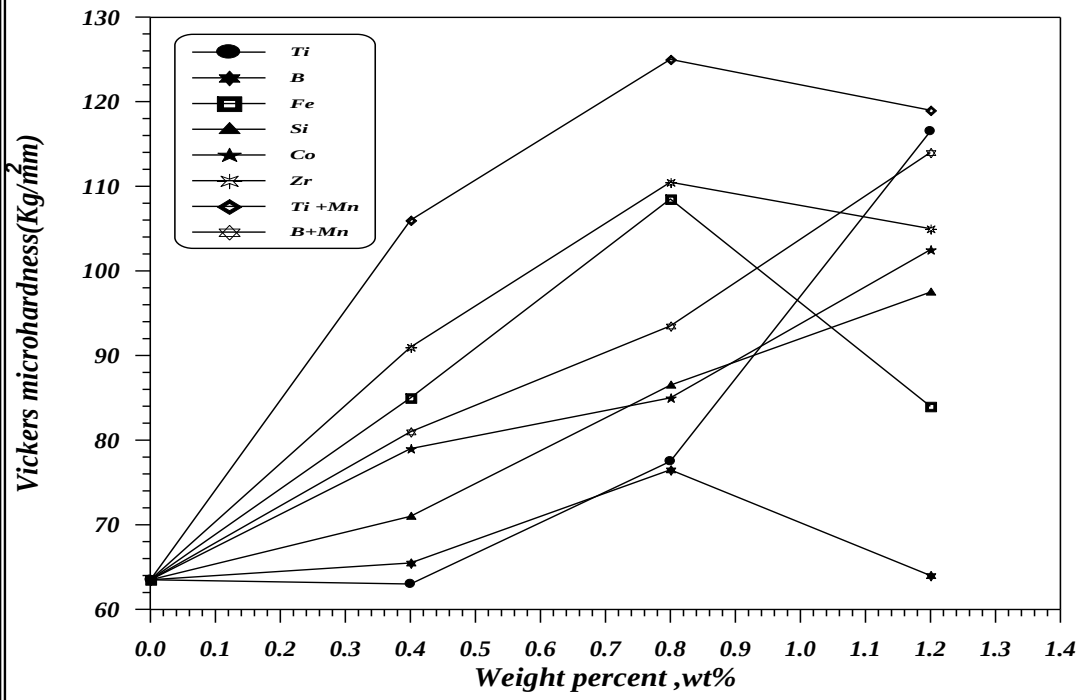

Fig.(6.79) Vickers microhardness as a function of alloying element for140 minute holding time of solution treatment.

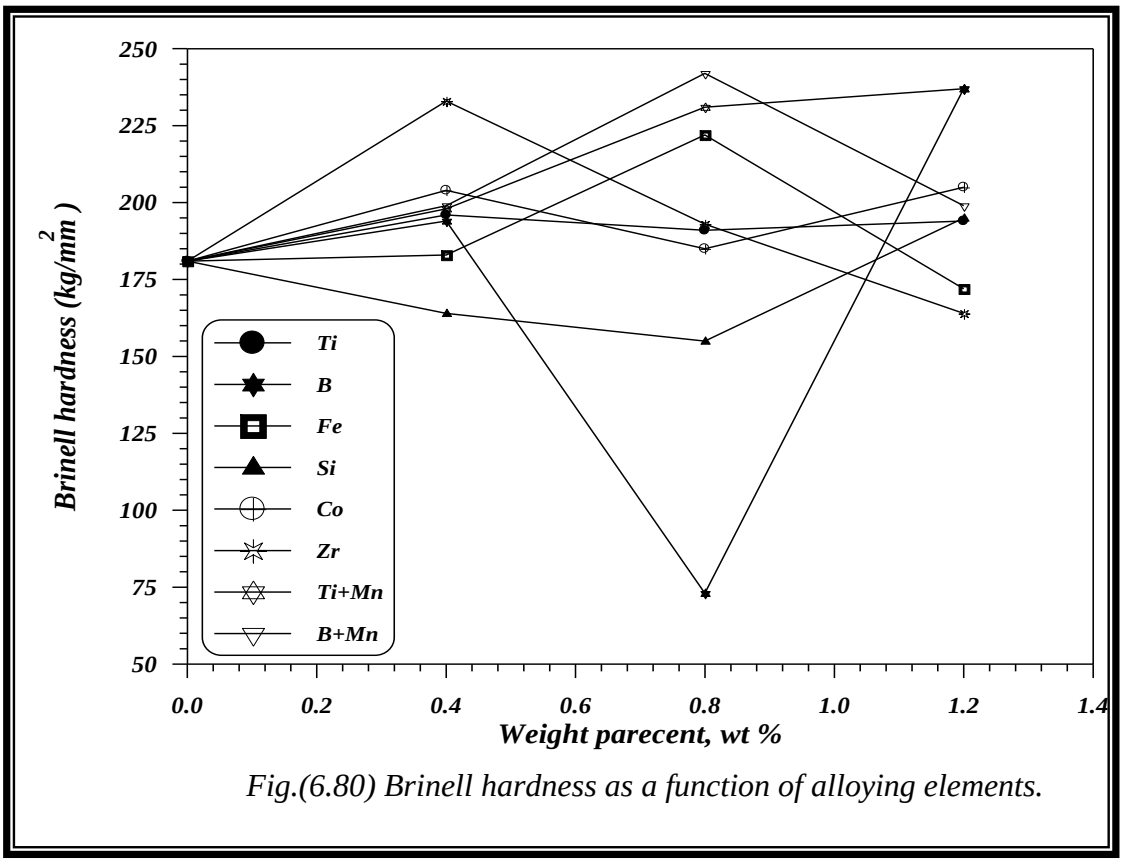

Fig.(6.80) Brinell hardness as a function of alloying elements.

6.4.5 Electrical Resistance test results

Electrical resistance test has been done for quenched specimen by heating them up to 170 ^{o}C and further cooling them to room temperature or slow below room temperature using cold water in the surrounding container. Electrical resistance results for both heating and cooling for alloy 1 have been shown in Fig. (6.81).

It is clear that there is wide range of transformation temperature during heating (A_s and A_f) and through cooling (Ms and Mf) . This is probably due to presence of pores which isolate the internal structure for heating and cooling. Thus , the specimen has been required more time to stabilize the temperature .During heating ,the first peek is referred to begin transformation in to parent phase (β) but the second peek or sharp change in electrical resistance curve referred to end of phase transformation. However, during cooling the first peek is referred to martensite final and the second referred to martensite final. Electrical resistance as a function of temperature for alloy 2 has been shown in Fig. (6.82) , whereas Figs. (6.83) and (6.84) show the electrical resistance results as a function of temperature for both heating and cooling for alloys 3 and 6 respectively.

It is apparent that the same wide range of transformation temperature for both of heating and cooling have been occurred due to presence of pores and non uniform pores distribution which are affected on the distribution of heat or temperatures through the specimen. Relative units of electrical resistance of specimen refer to divide electrical resistance for specimen to electrical resistance of the equipment (wires and cell).

It is clear that electrical resistance of metals and alloys are increased when temperature is raised but here, when phase transformation is occurred , drop or peak. Of electrical resistance readings have been obtained where the internal phase change is occurred in the specimen.

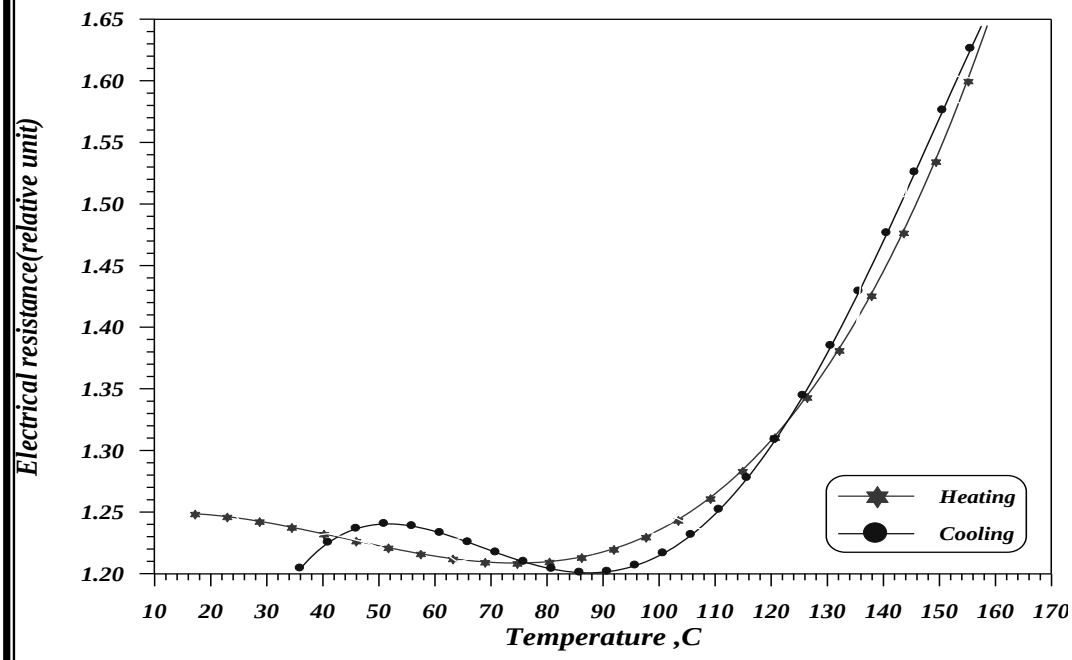

Fig.(6.81) Electrical resistance as a function of temperature for direct quench alloy 1 specimen.

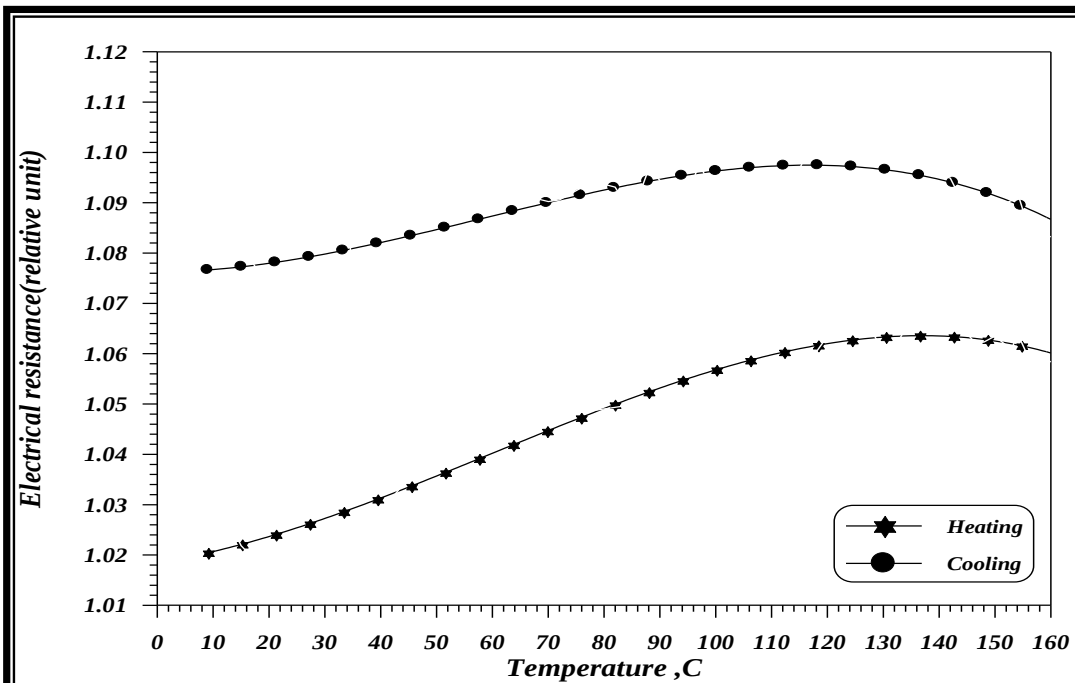

Fig.(6.82) Electrical resistance as a function of temperature for direct quench alloy 2 specimen.

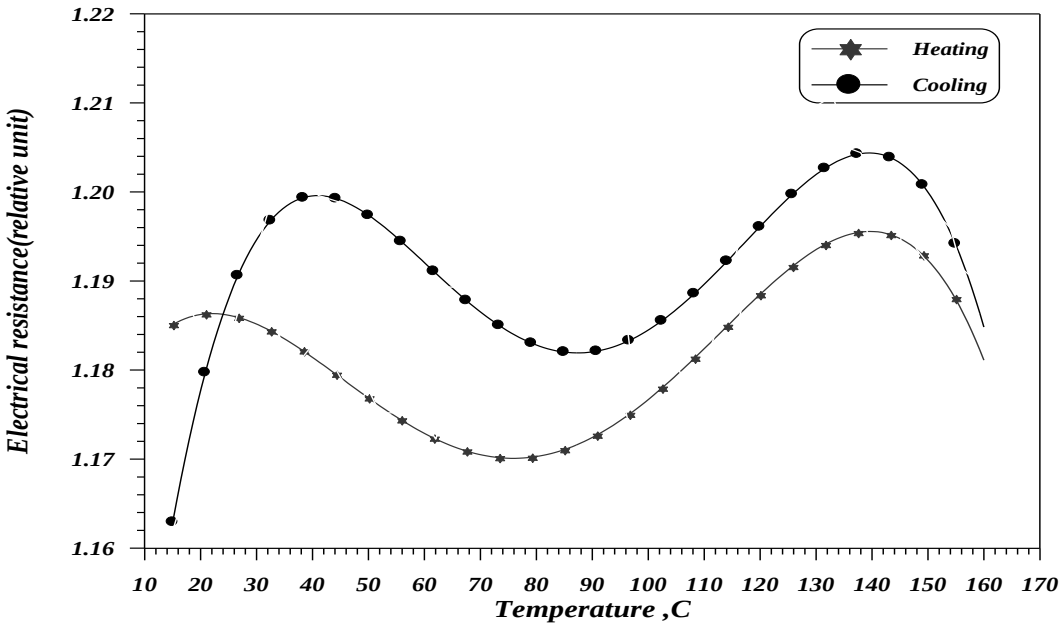

Fig.(6.83) Electrical resistance as a function of temperature for direct quench alloy 3 specimen.

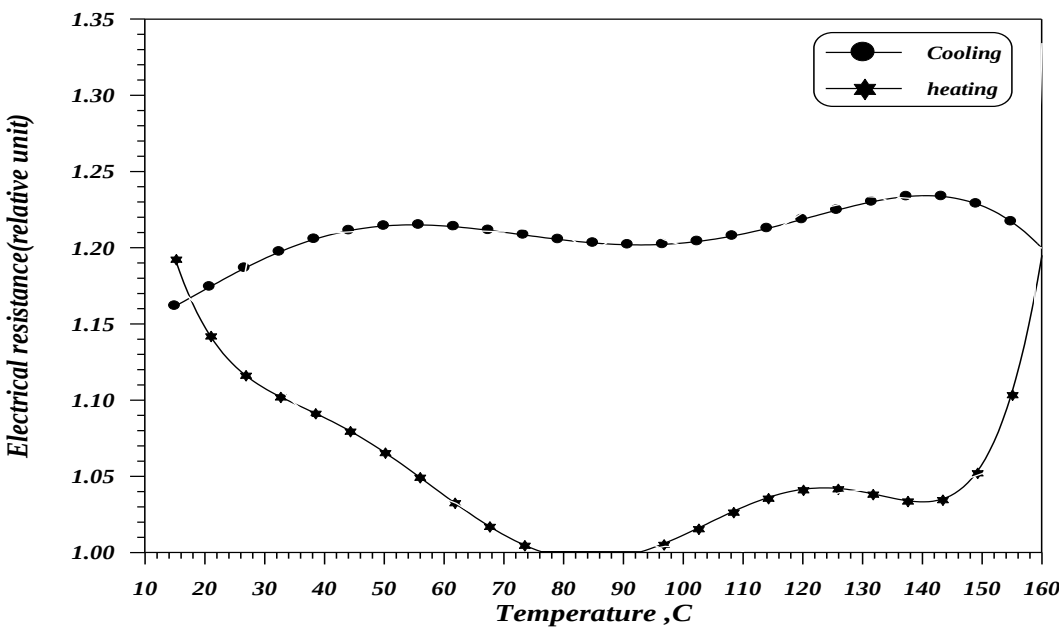

Fig.(6.84) Electrical resistance as a function of temperature for direct quench alloy6 specimen.

6.4.6. Ultrasonic test results

The aim of ultrasonic test is to satisfy the phase transformation of all specimens in quenched states and in reheating states.

Ultrasonic test has been done for cylindrical specimens with (0.01) m diameter and (0.04) m height.

After compression up to 8 % total strain in martensitic state and after reheating up to 150 ^{o}C for 10 min. state , ultrasonic test has been carried out. Time of ultrasonic test has been carried out. Time of ultrasonic wave transferred as a function of weight percent of Ti , B , Fe ,Si , Co, Zr, Ti+ Mn and B+Mn for both two case are shown in Figs.(6.85) , (6.86) , (6.87) (6.88) ,(6.89), (6.90) , (6.91) and Fig. (6.92) respectively.

It is clear that all alloying elements decrease time of wave transferred except Boron element. In addition , there is a difference between time of wave transferred through compressed specimens and reheated specimens due to change in phases for both cases. It is also apparent that time of ultrasonic wave for parent phase is lower than martensitic phase in the range of addition between (0.8 % to 1.2 %).

Ultrasonic test as nondestructive inspection is useful to calculate mechanical properties such as young modulus , shear modulus and poison's ratio. In this study , modulus of elasticity and other mechanical properties have been determined by destructive compression tests. Any way , comparison between experimental data in cases may be given with suitable correcting factor.

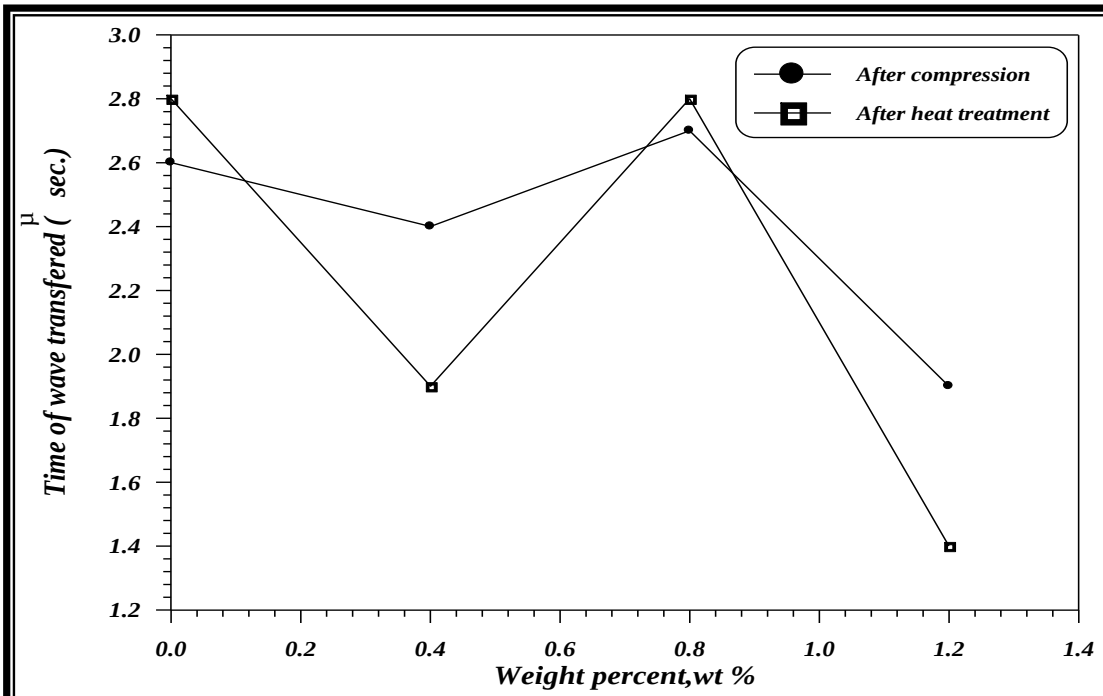

Fig.(6.85) Time of wave transferred as a function of weight percent of Ti.

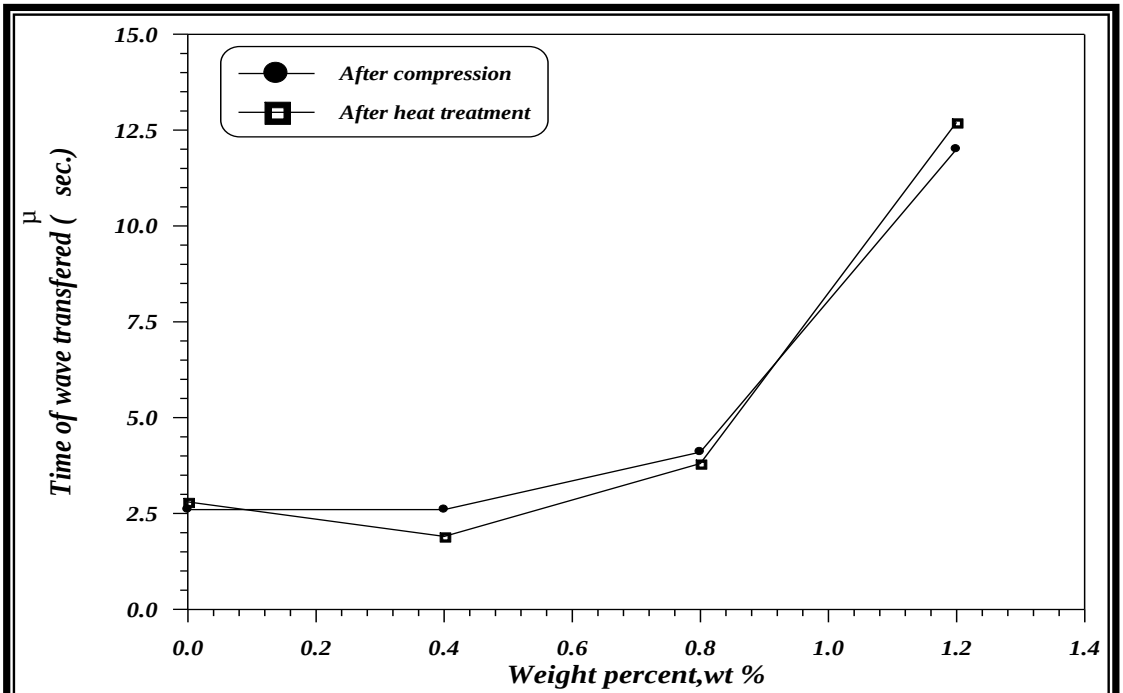

Fig.(6.86) Time of wave transferred as a function of weight percent of B.

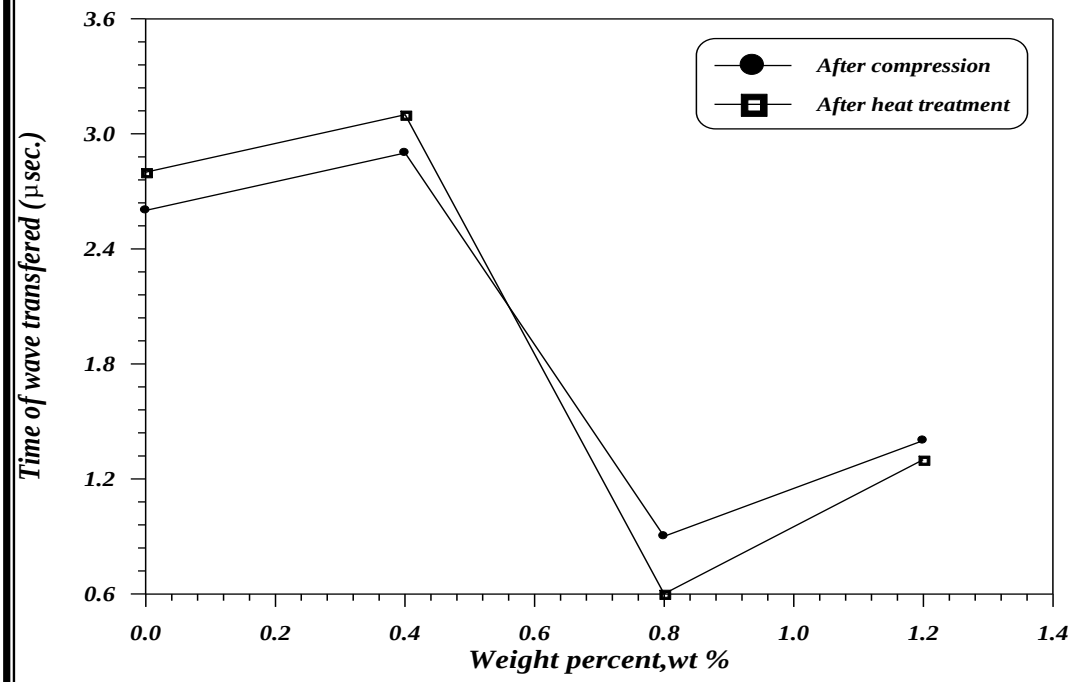

Fig.(6.87) Time of wave transferred as a function of weight percent of Fe.

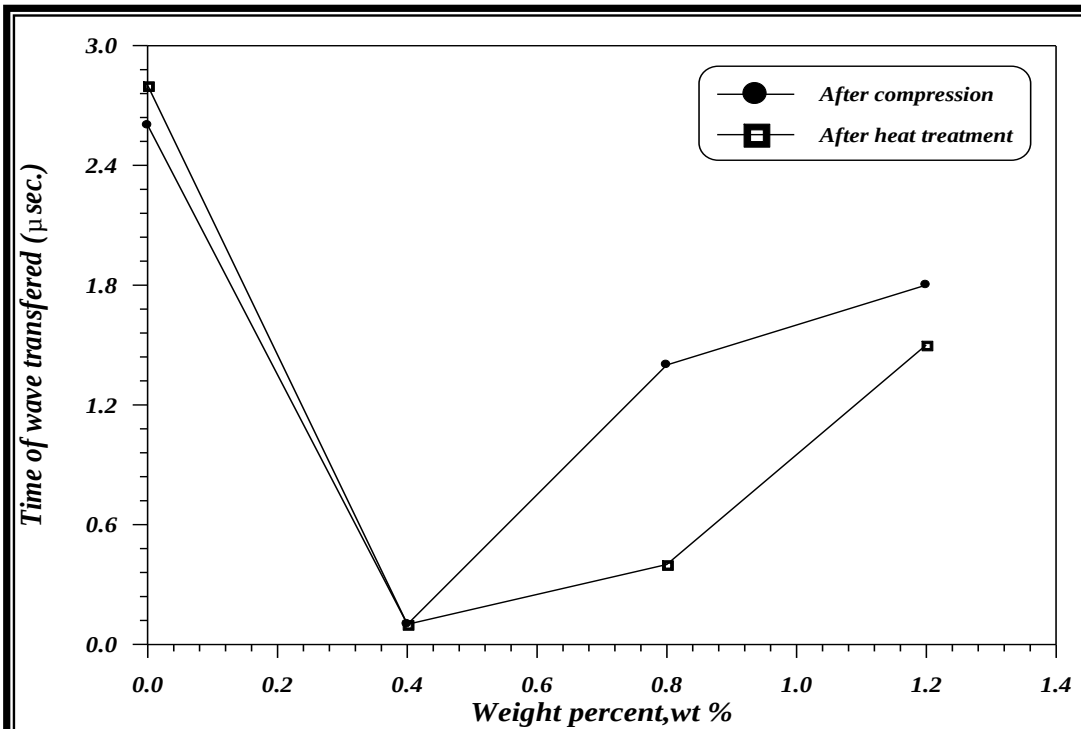

Fig.(6.88) Time of wave transferred as a function of weight percent o f Si.

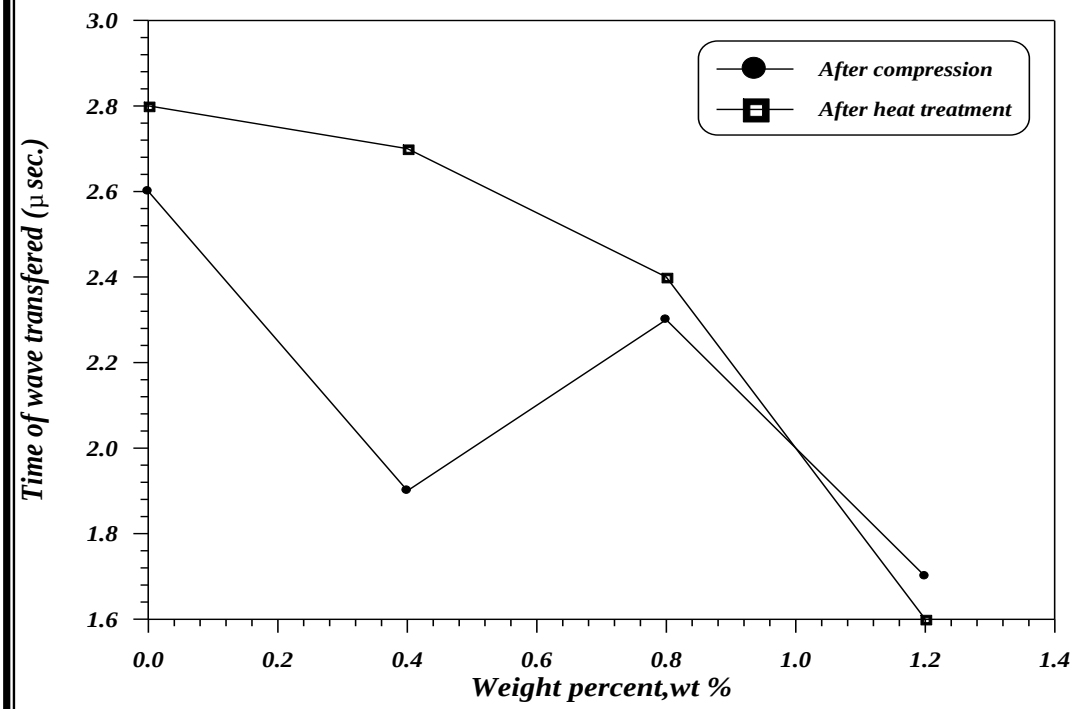

Fig.(6.89) Time of wave transferred as a function of weight percent of Co.

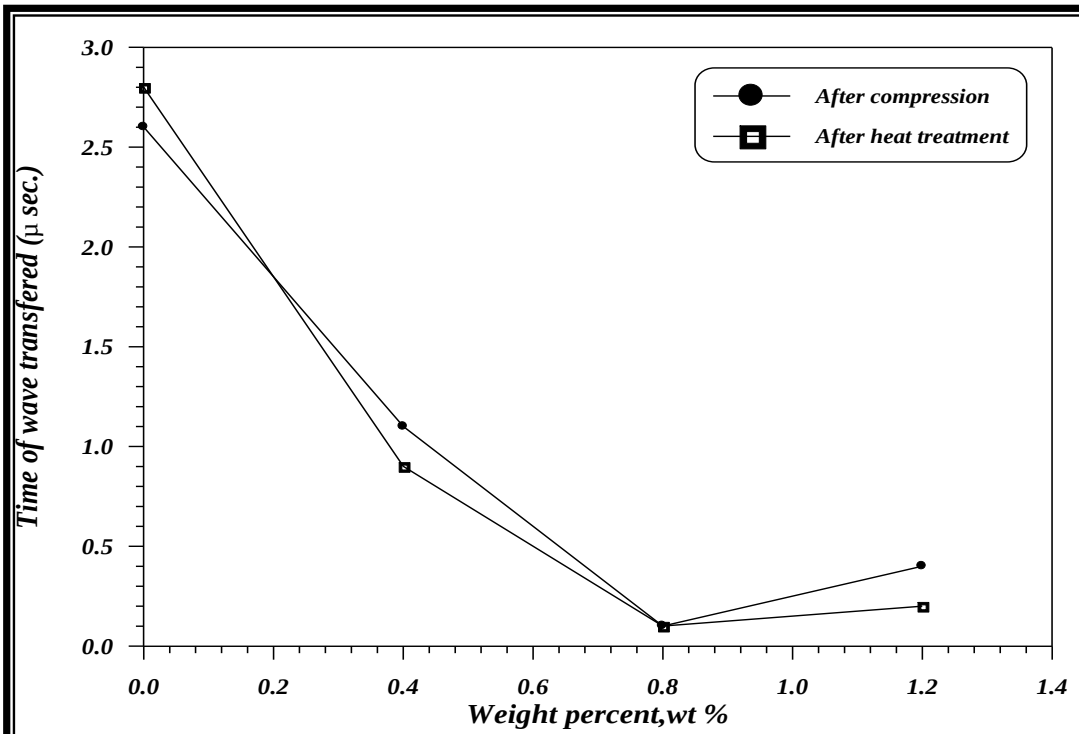

Fig.(6.90) Time of wave transferred as a function of weight percent of Zr.

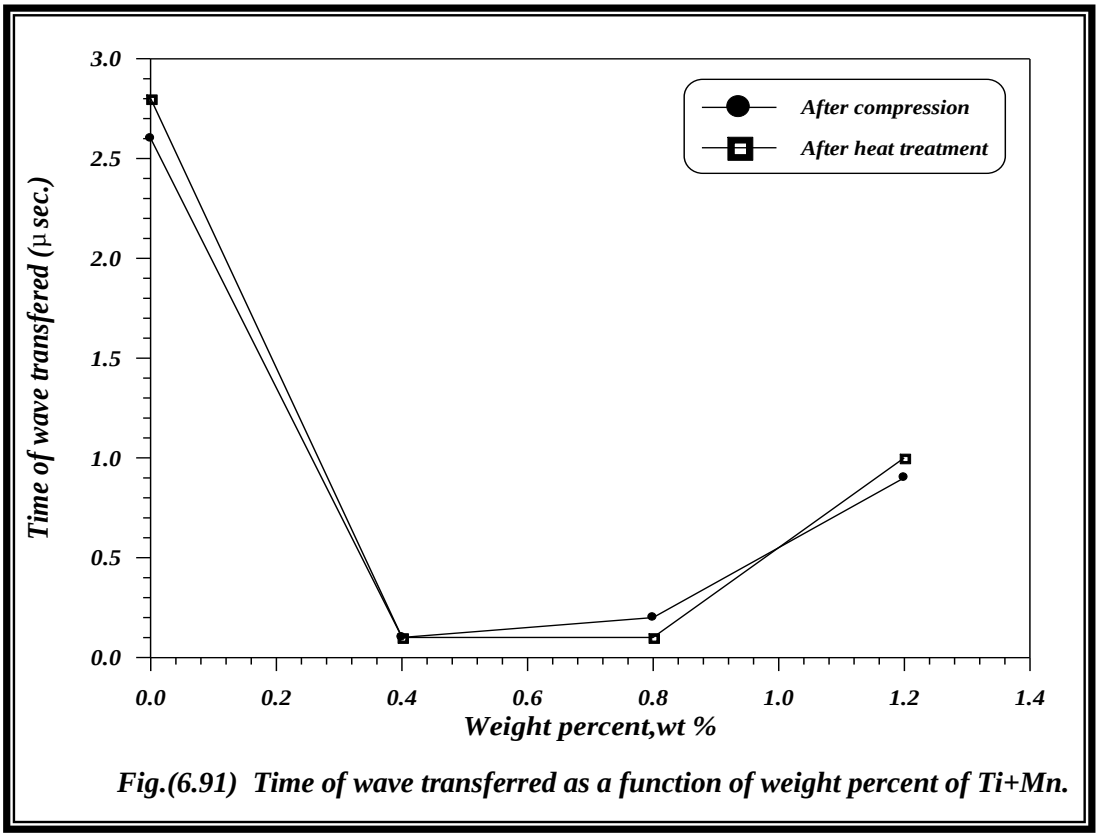

Fig.(6.91) Time of wave transferred as a function of weight percent of Ti+Mn.

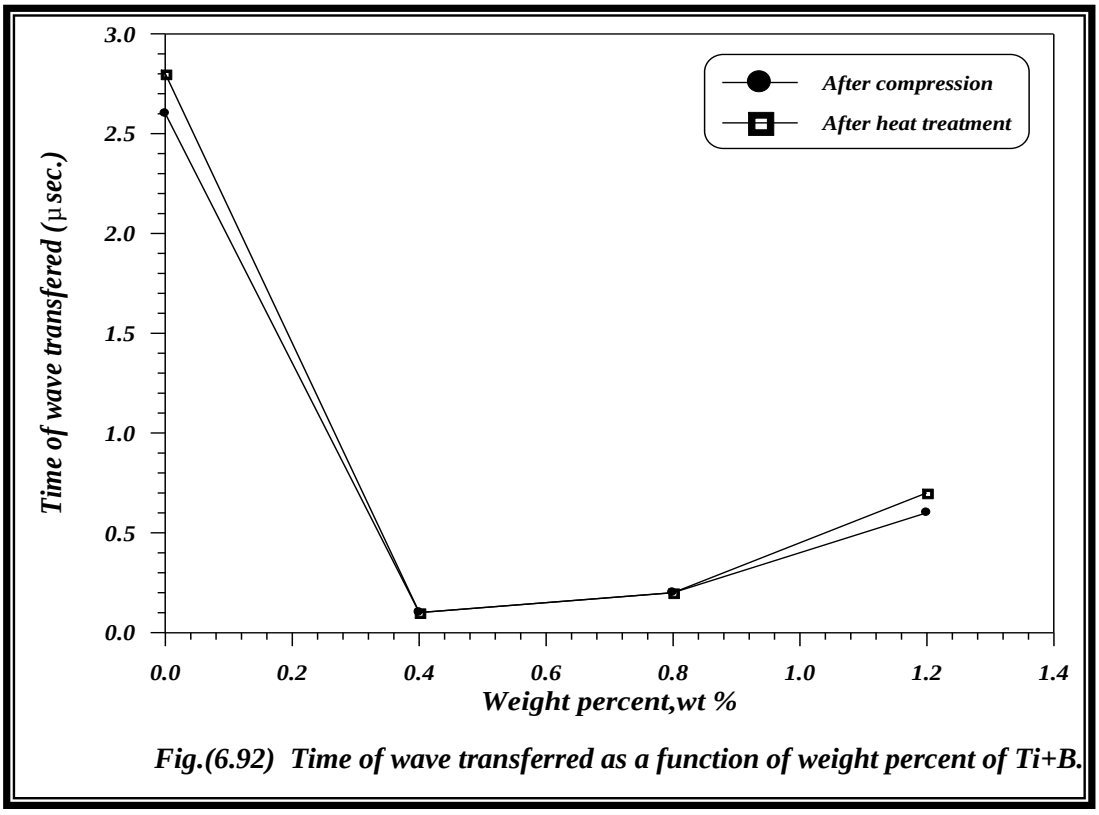

Fig.(6.92) Time of wave transferred as a function of weight percent of Ti+B.

6.4.7. Shape memory effect and shape recovery:

In order to test for shape effect and shape memory and shape recovery , the specimen is cooled below martensite finish temperature (M_f) and then loaded at a temperature at least below starting of parent phase (austenite) temperature (A_s) to detwin the martensite. After unloading , the sample is heated to recover austenite and the original shape.

Fig.(6.93) shows compression stress-strain curve for alloy1 under two conditions at room temperature as shown in a. and at 50 ^oC as shown in b. respectively.It is clear that hyctersis of stress- strain for loading and unloading is different for both cases. It is also clear that elastic recovery during unloading is approximately 3 % from the total strain – However , after heating up to 150 ^oC for min., shape memory effect and shape recovery are (5.52% and 0.294%) respectively for specimen compressed at room temperature In addition , shape memory effect and shape recovery are 3.85 % and 0.134 % respectively for specimen compressed at 50 ^oC as test temperature. It is apparent that specimen under loading unloading conditions has martensitic structure so that shape effect and shape recovery are obtained through heating cycle not at unloading condition so as to take place for super elastic behavior.

Compression stress- strain curve for alloy 2 tested at R.T. and at 50 ^oC have been shown in a. and b. in Fig. (6.94). It has been shown that low elastic strain (2%) with comparison with alloy 1 has been recovered during unloading. Thus this alloy has shape memory effect greater than alloy1 when tested at room temperature. However , low strength (approximately 150 Mpa) has been obtained for specimen tested in 50 ^oC and the specimen tends to have super elastic behavior during the first stage of loading. Any way , After heating specimen , shape memory effect is 24.996 % when tested this specimen at room temperature whereas specimen tested at 50 ^oC , shape memory effect is 1.44 % which is very low amount comparison with that at room temperature It is

probably that alloy2 specimen has superelastic behavior at 50 ^{o}C So it returns to original shape at unloading condition and not required to addition heating this is apparent from Fig.(6.94b.) by increasing superelastic strain as 3.4%.

Effect of titanium addition as (0.4 wt %) to base alloy (alloy2) on the compression stress strain curves for both cases at R.T. and at 50 ^{o}C are shown in Fig. (6.95) .

It is clear that titanium addition leads to increase strength at 50 ^{o}C and tends to browder hystersis of stress- strain loading- unloading cycle specially for specimens tested at 50 ^{o}C. Thus this alloys may be used as energy absorber material for damping application. It is probably that increasing titanium content leads to change martensitic transformation temperatures (M_s, M_f) which affects up on shape memory effect and shape recovery.

Effect of boron additions on the stress- strain curve have been shown in Fig. (6.96) for 0.4 wt% B. It is apparent that elastic strain is decreased when boron addition is increased and hystersis of loading and unloading is narrow specially for samples tested at 50 ^{o}C. However, shape memory effect after heating at 150 ^{o}C for 10 min. is (44.2 % , 9.6 % and 2.5 %) for (0.4 %, 0.8 % and 1.2 %) respectively when sample tested at room temperature thus , small additions from boron are preferred more than greater quantity due to boron effect on grain size of base alloy as grain refiner. For each content of boron, specimens tested at 50 ^{o}C have more Superelastic behaviors than that compressed at room temperature , this is probably that martensitic structure $(\bar{\beta})$ tends to transform into parent phase (β) under stress as possible in this temperature.

In addition , Summery of shape memory effect shape recovery for all alloys (1,2,3,4,…….., 26) are Presented in table (6.2).

Table (6.2) shape memory effect and shape recovery for all alloy under compression at room temperature at 50 °C.

Alloys	Compression R.T.		Compression at 50	
	SME%	S.R%	SME%	S.R.%
1	5.52	0.294	3.85	0. 134
2	24.99	0.0363	1.44	0.0116
3	58.82	1.382	2.94	0.110
4	5.90	0.113	2.97	0.131
5	15.34	0.290	10.28	0.149
6	44.18	0.217	1.96	0.034
7	9.58	0.238	4.53	0.115
8	2.49	0.113	2.05	0.057
9	14.35	0.365	2.84	0.120
10	12.80	0.319	2.50	0.066
11	28.01	0.443	1.64	0.061
12	19.16	0.465	6.63	0.184
13	27.23	0.365	10.58	0.214
14	11.71	0.180	8.69	0.189
15	1.36	0.030	1.67	0.103
16	8.45	0.177	7.53	0.220
17	5.23	0.166	2.16	0.048
18	53.97	1.357	2.25	0.084
19	11.84	0.154	5.78	0.147
20	25.93	0.564	8.69	0.111
21	5.29	0.056	1.10	0.025
22	7.71	0.156	4.92	0.171
23	7.53	0.185	1.35	0.043
24	5.21	0.0896	0.36	0.0061
25	35.45	0.896	0.99	0.024
26	6.92	0.142	2.31	0.104

It is clear that maximum shape effect is 58.82% from total strain (10%) at 0.4 wt % Ti of alloy3 whereas the minimum shape memory effect is

1.36 % for alloy 15 which contains 0.4 wt % Co. In addition , alloy 3 has a maximum shape recovery as 1.357%.

Furthermore , shape memory effect is calculated from hardness test by using image analysis technique for ball indenter of Brinell hardness and / or vicker's macrohardness indenter. Shape memory effect and shape recovery are function of load , temperature and composition as well as transformation temperature. Thus, it is believed that shape memory effect for microhardness is more than shape memory effect for vicker's macrohardness or Brinell hardness due to (large applied load used in the last two tests. Figs.(6.97), (6.98) and Fig.(6.99) show indenter image for alloys (1,2,3,4, …., 26) after direct quenching heat treatment in (a) and after heating up to 150 ^{o}C for 10 min. and air cooling in (b) . It is clear that difference in indentation dimension between a and b image is apparent in these Figures. This difference refer' to obtain shape memory effect for prepared alloys in this study. Brinell test with reciprocal ball is used to generate indenter which is taken an image using suitable magnification of optical microscope.

It must be taken the same digital camera to the same magnification of equipment in order and really compare between the two images.

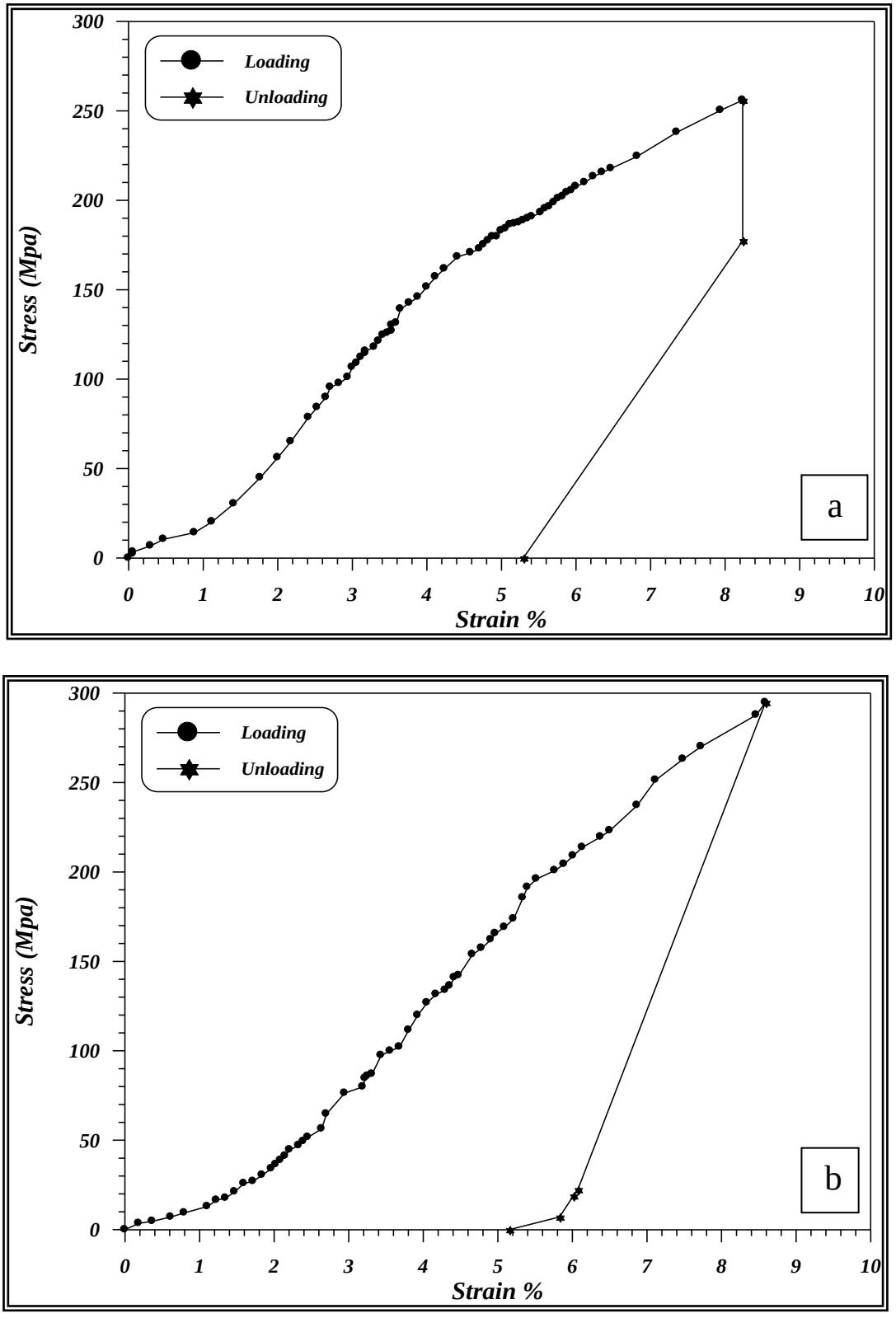

Fig.(6.93) Compression stress strain curve for alloy 1 at R.T. in a. And at 50 ˚C in b.

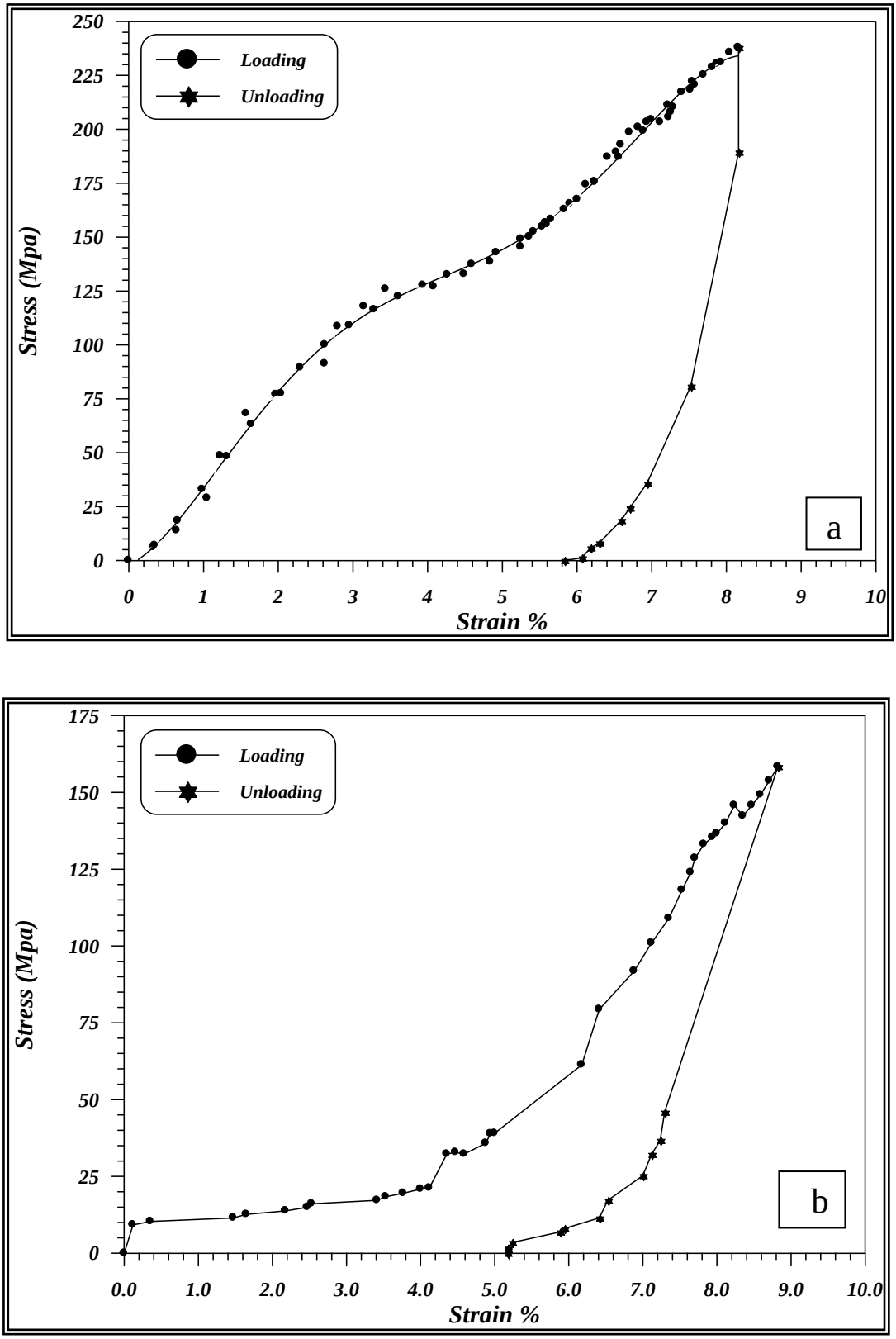

Fig.(6.94) Compression stress strain curve for alloy 2 at R.T. in a. And at 50 ˚C in b.

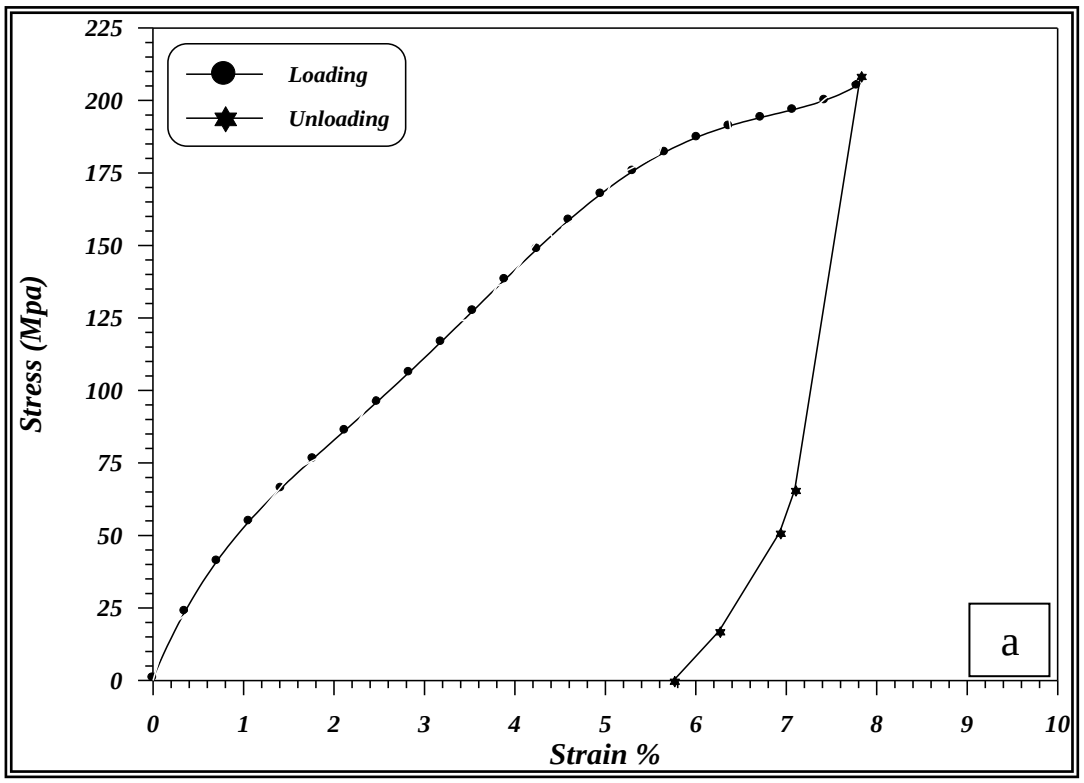

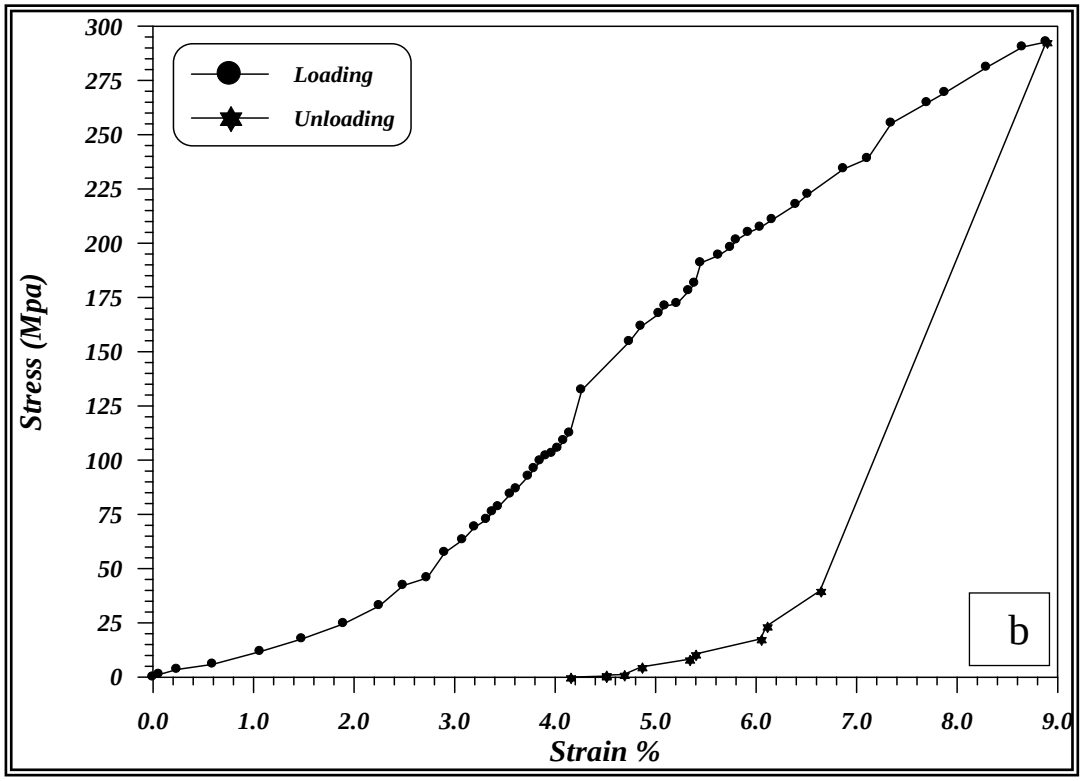

Fig.(6.95) Compression stress strain curve for alloy 3 at R.T. in a. And at 50 ˚C in b.

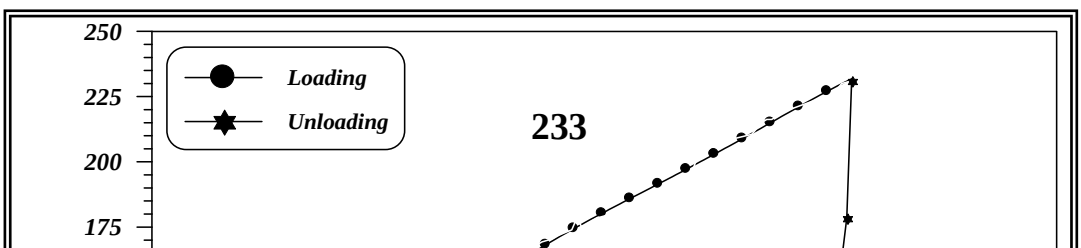

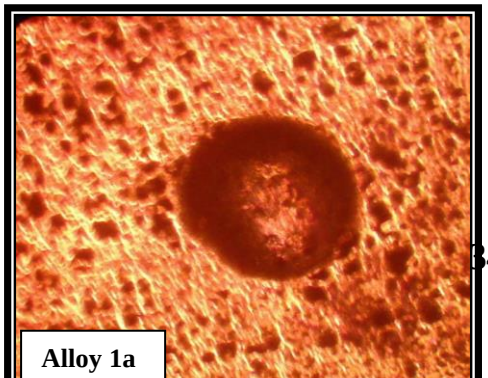
Alloy 1a

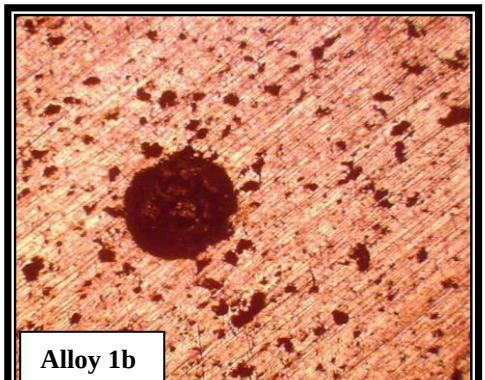
Alloy 1b

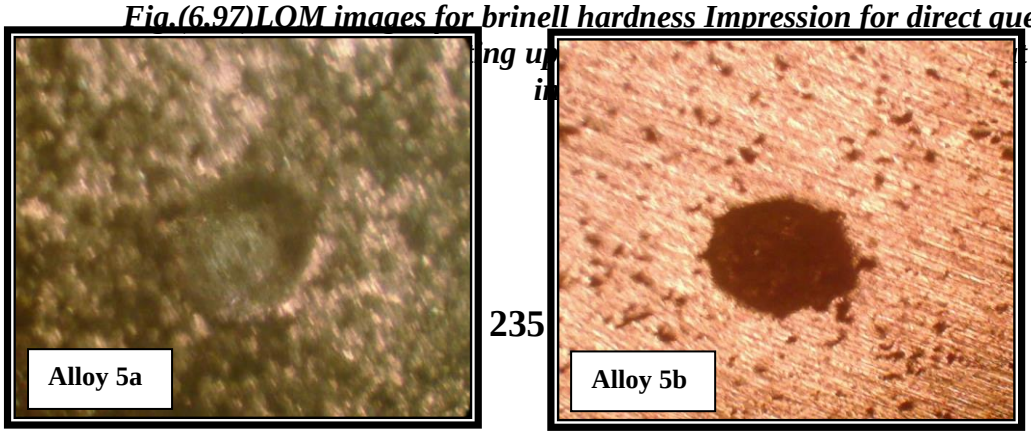

Fig.(6.97)LOM images for brinell hardness Impression for direct quenched ng up treatment in

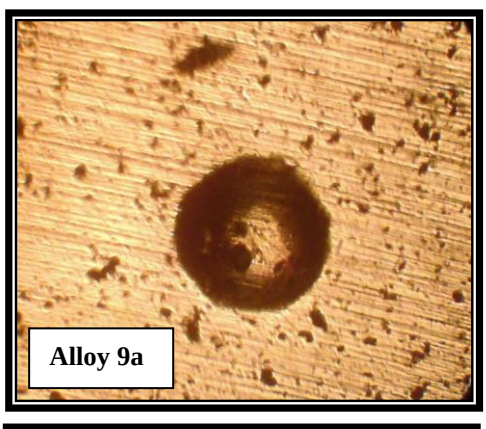
Alloy 9a

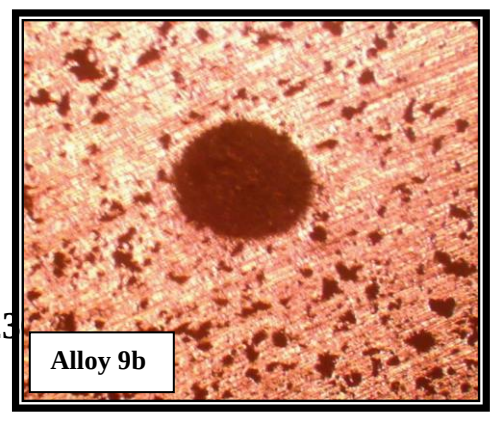
Alloy 9b

6.5. Aging heat treatment .

Aging heat treatment includes heating the direct quenched specimens up to 200 ^{o}C for 30 min. and followed by quenched in ice water . The origin of

martensite aging and the associated superelastic behavior has been a long standing puzzle for alloys having martensite transformation.

The martensite aging causes an increase in reverse transformation temperatures. Martensite aging includes martensite stabilization by which martensite becomes more stable with aging such that it is probably that the reverse transformation temperature (A_s and A_f) increase with aging time. In the following, X-ray diffraction technique has been done for aged specimen. In addition, optical microscopy image and scanning electron microscopy image have been presented. Furthermore , Vicker's macrohardness and shape memory effect have also been presented.

6.5.1. X-ray diffraction for aged specimens

X- ray diffraction pattern for alloy 1 which heat treated by aging treatment has been shown in Fig. (6.100).

It is clear that intermetallic compound (Al_4Cu_9) has been formed during aging of martensite $\overline{\beta}$ at 200 ^oC for 30 min. It has been shown that martensite of this alloy is unstable (i.e non equilibrium phase) and thus it has tendency to decompose simultaneously during aging decomposition of $\overline{\beta}$ phase which may be partially took place in this alloy because the martensite phase ($\overline{\beta}$) is the major phase in this alloy system.

Decomposition process is a diffusion process which is time dependent effect. It is required to more time or high temperature above (200 ^oC) to decompose all martensite phase in to ($\alpha + \gamma_2$) phase which are more stable (equilibrium phase than martensite phase).

Decomposition has also been occurred in alloy 2 as can be seen from X-ray diffraction pattern in Fig.(6.101). However, small amount of γ_2 phase has been form by decomposing of martensite phase with comparison with that it is occurred in alloy 1.

This is due to low transformation temperature of $\beta \rightleftharpoons \alpha + \gamma_2$ reaction as can be seen from (Cu+Al) phase diagram for for hypereutectoid alloys.

Fig.(6.102) shows x-ray diffraction pattern for alloy3 which aged in 200 ^{o}C for 30 min. It has been shown that the intermetallic compound (Cu, Al)$_2$ Ti precipitates in martensite matrix ($\overline{\beta}$) phase. In this temperature martensite phase is stable and may not be decomposed in to ($\alpha + \gamma_2$) through eutectoid reaction. It is probably that 0.4 wt % Ti addition satisfies this stability at 200 ^{o}C So that this alloy has shape memory effect at higher temperatures compared with alloy 1 and alloy 2.

In addition, aging of martensite structure of alloy 6 is more stable because there is no decomposition into $\alpha + \gamma_2$ phase during aging treatment as can be seen from x-ray diffraction pattern in Fig. (6.103). It is believed that boron addition as 0.4 wt % stabilized martensite phase and prevent decomposition by increasing transformation or increasing activation energy that is required to decompose ($\overline{\beta}$) in to $\alpha + \gamma_2$ phases. Thus , it is also apparent that alloy 6 may be used as high temperature shape memory alloy applications. In addition , it has been shown that aging is not dependent on the structure of martensite and it is occurred in any martensite for both ordered and disordered martensite. Aging of martensite is a time- dependent process so that it is diffusion process. Furthermore, it has been shown that points defects in shape memory alloys play a central role in determining martensite aging effects. Most shape memory alloys are ordered alloys or intermetallic and the defect structure and its concentration is quite different from that in pure metal or disordered alloys. Therefore, information on the defect structures and concentration is important for deep understanding of effect of defects on aging .

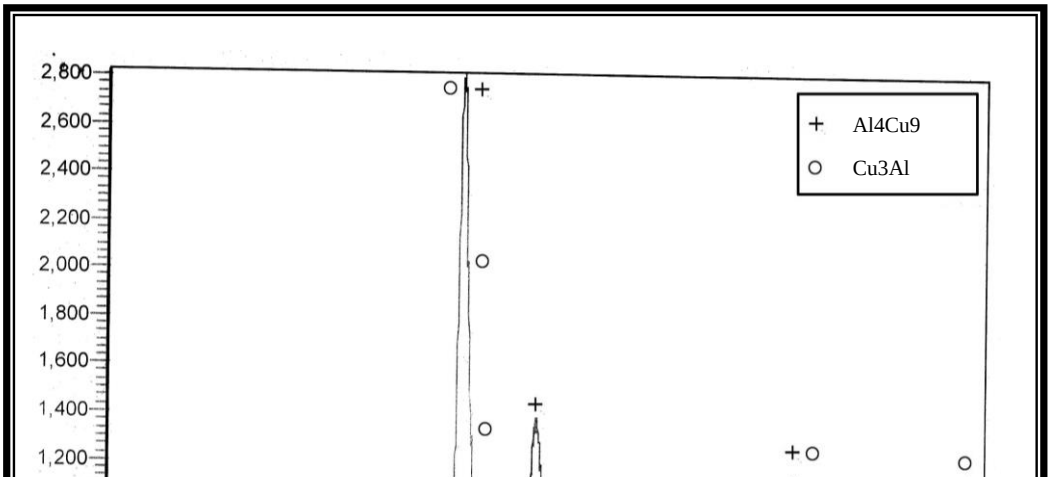

Fig.(6.100) XRD pattern for alloy1 which aged in 200 °C for 30 min.

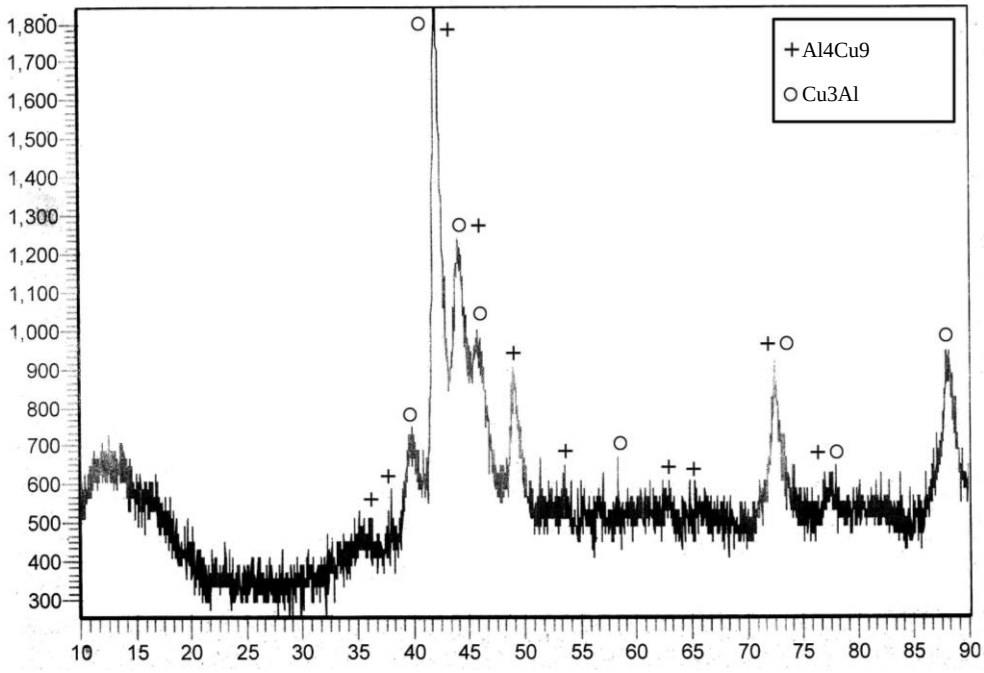

Fig.(6.101) XRD pattern for alloy2 which aged in 200 °C for 30 min.

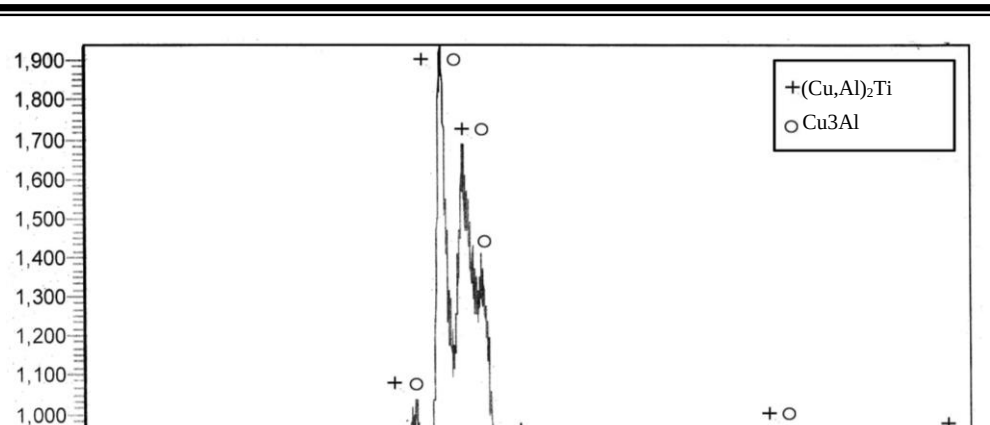

Fig.(6.102) XRD pattern for alloy3 which aged in 200 °C for 30 min.

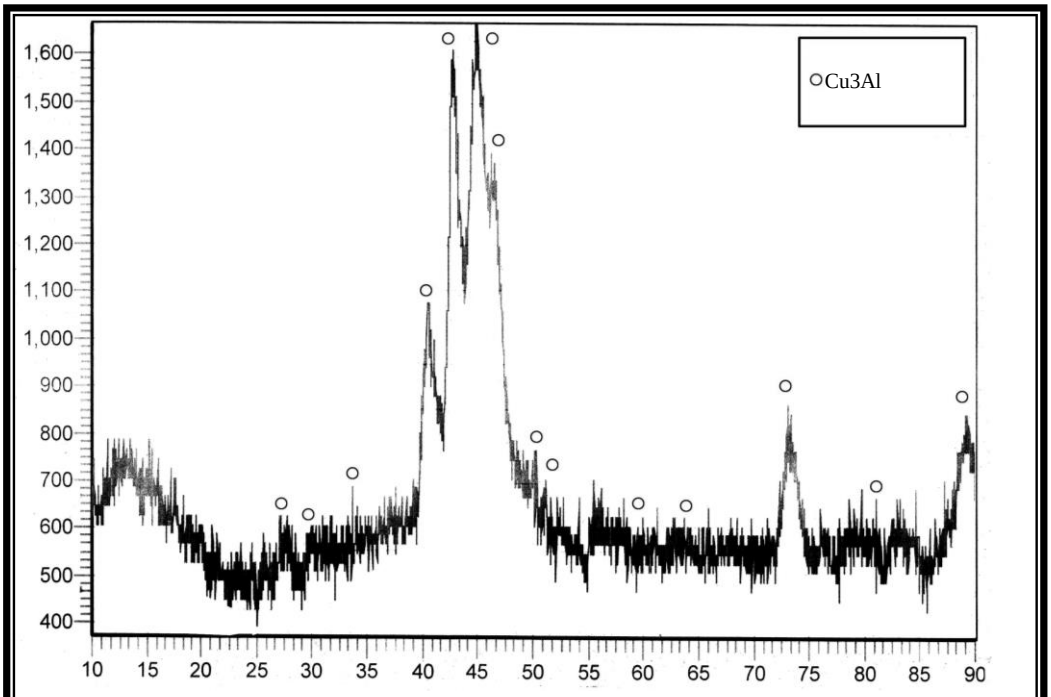

Fig.(6.103) XRD pattern for alloy6 which aged in 200 °C for 30 min.

6.5.2 Light optical microscope image:

Microstructure of twenty-six alloys using two etchants by optical microscope with two different magnification (1000 X and 2400 X) has been shown in Fig.(6.104 to 6.107) for alloy 1,2,3 and 6 respectively. Unfortunately , it has been shown that etching with ($NH_4OH + H_2O_2 + H_2O$) for all alloys dos not appear precipitation of intermetallic compounds in the microstructure but it is good etchant to appear grains and grain boundaries as shown from these Figures in a. Therefore , another etchant which is (Fecl3 + HCl + H2O) solution has been used to appear precipitates of intermetallic compounds in all alloys during aging treatment with (2400X) as magnification force . It has been shown that intermetallic compounds appear as gray or black fine spots in the microstructure near the grain boundaries or near the particles edges. It is also apparent that etching with ($NH_4OH + H_2O_2 + H_2O$) Solution reveals grain boundaries more than the second etchant which are easily confused with the particle boundaries that also appear as thin gray or black lines. Light optical microscope with polarized light is better than normal light optical microscope to reveal microstructure of martensite in non ferrous alloys. Unfortunately, there is no polarized light optical microscope in the university of Babylon.

During aging treatment ,(Cu, Al)2Ti intermetallic compound precipitates on the grain boundaries of martensite phase ($\overline{\beta}$) for alloy 3,4 and 5 . However, intermetallic compound of γ_2 phase (Cu_9Al_4) may be precipitated as gray fine spot near the boundaries in the region which do not include titanium intermetallic compound. However, the presence of precipitates produce changes in the martensitic transformation temperatures and the hystersis accompanying the forward and reverse transformations. Precipitates of γ_2 phase may be uncleared and grown through aging heat treatment which depend upon time , temperature and chemical composition of alloy. The γ_2 precipitates are rather well accommodated with the parent phase (β) . They are either fully coherent or at most semi coherent depending on the precipitates size. This is due to the cubic-cubic orientation relationship between (β) parent phase γ_2 phase.

Nevertheless , when the matrix surrounding one precipitate is transformed to single variant martensite , the hole left in the β matrix phase occupied by the precipitate is quite severely deformed due to the intrinsic deformation accompanying the transformation.

However, the precipitate itself maintains its shape which means that the γ_2 phase does not transform mathematically. Deep understanding of the interaction between γ_2 phase precipitates and martensite phase required high resolution transmission electron microscope (TEM).

However, the precipitation of γ_2 phase in the matrix of ($\overline{\beta}$) martensite phase is considered as one of strengthening the copper based shape memory alloys through producing dual phase shape memory alloys. Matrix of martensite in dual phase is responsible for shape memory properties and the precipitates (γ_2) is responsible to give high strength and high hardness of overall alloy.

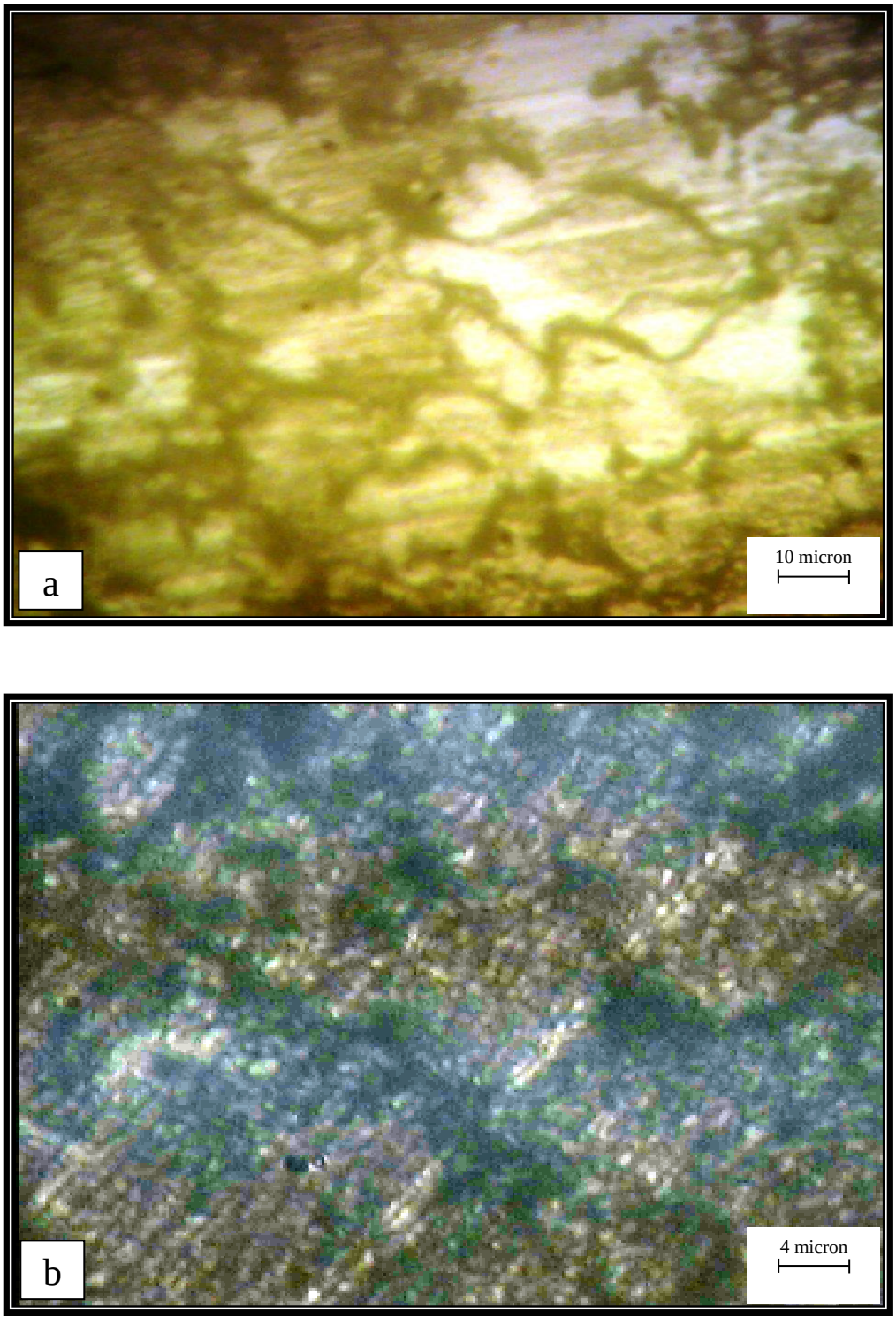

Fig(6.104) LOM images for alloy 1 aging in 200 C for 30 min. and followed by quenching in ice water for a:etched in (NH4OH+H2O2+H2O) solution, b: etched in(FeCl3+HCl+H2O) solution.

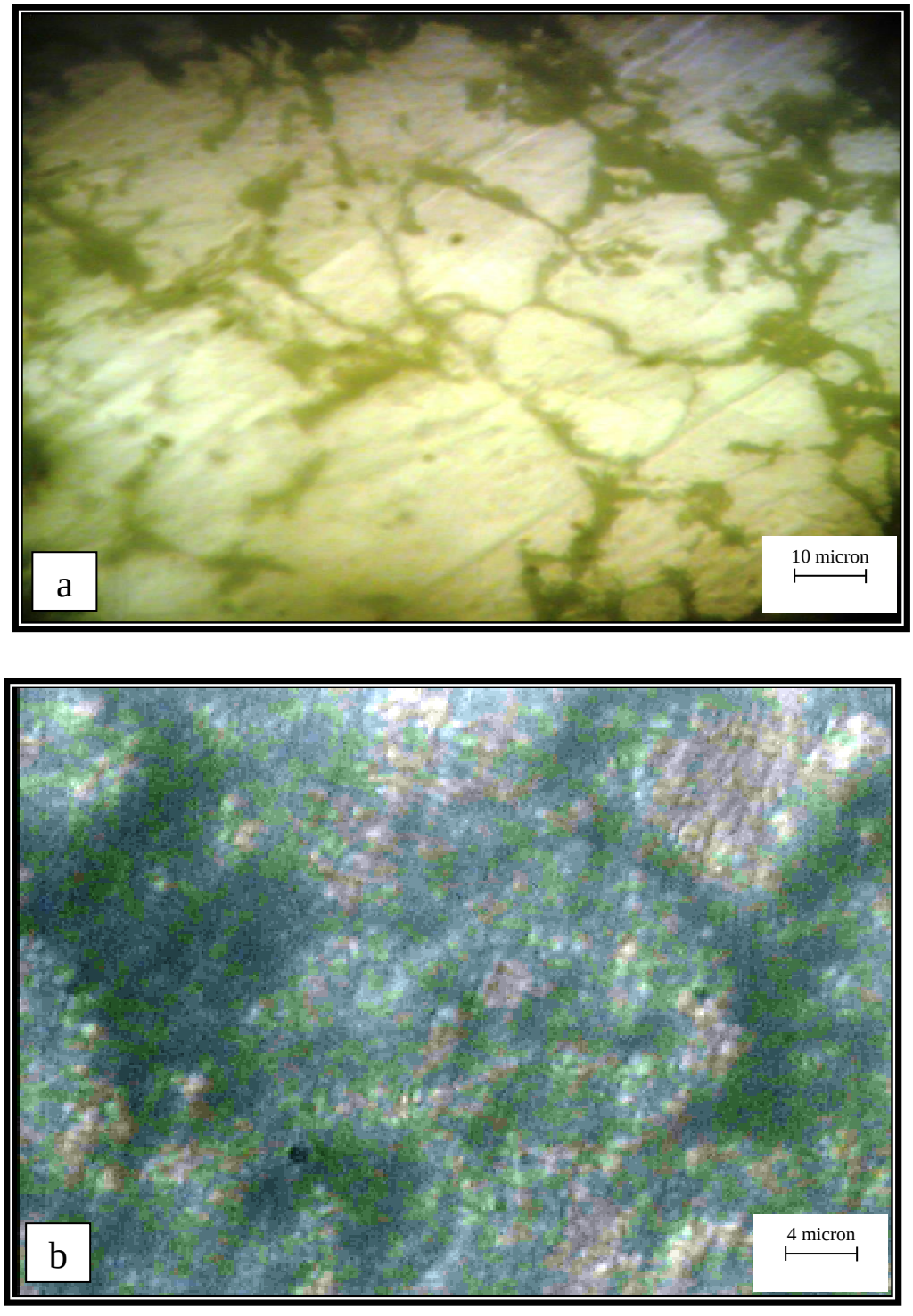

Fig(6.105) LOM images for alloy 2 aging in 200 C for 30 min. and followed by quenching in ice water for a:etched in (NH4OH+H2O2+H2O) solution.b: etched in(FeCl3+HCl+H2O) solution.

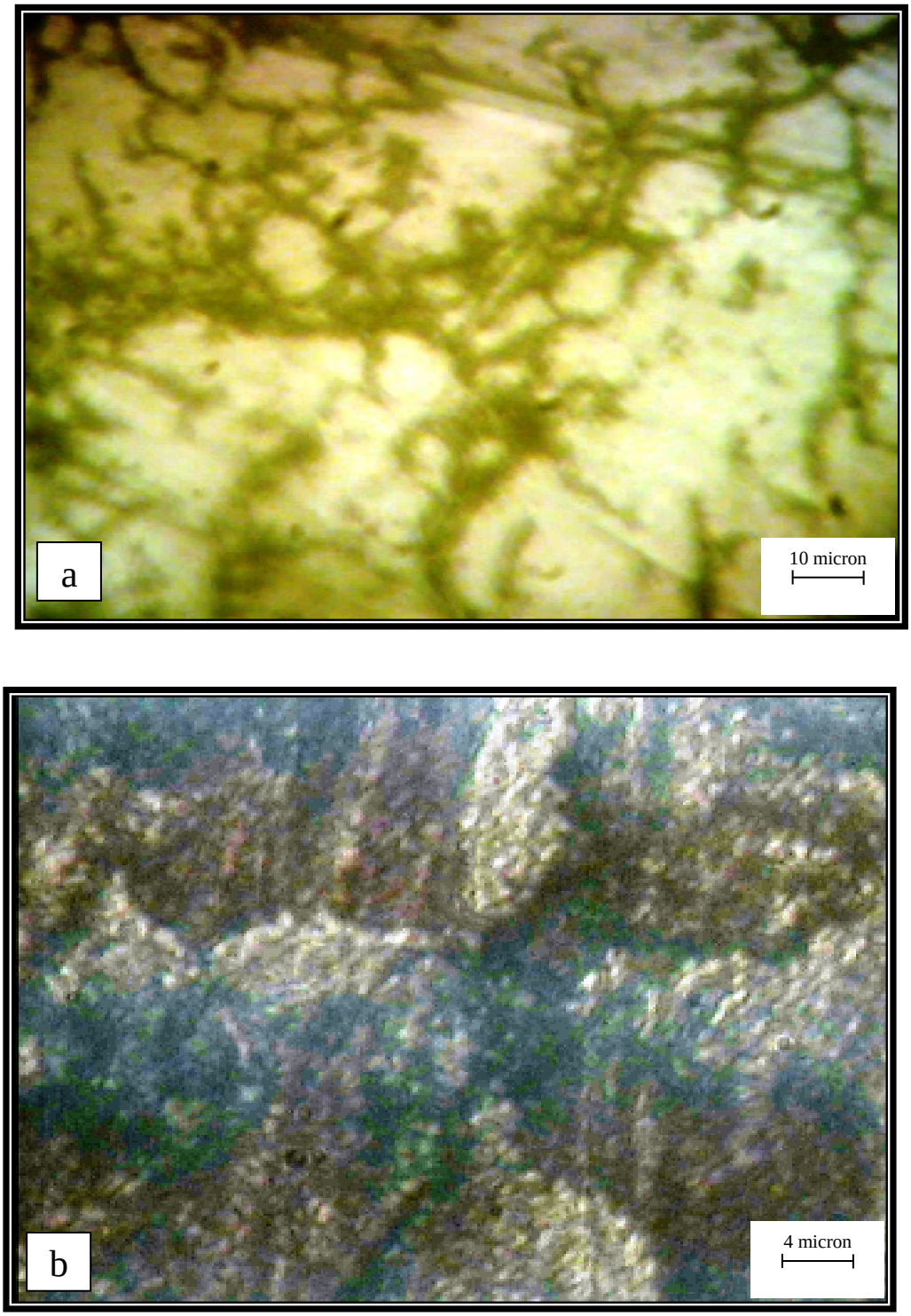

Fig(6.106) LOM images for alloy 3 aging in 200 C for 30 min. and followed by quenching in ice water for a:etched in (NH4OH+H2O2+H2O) solution.b: etched in(FeCl3+HCl+H2O) solution.

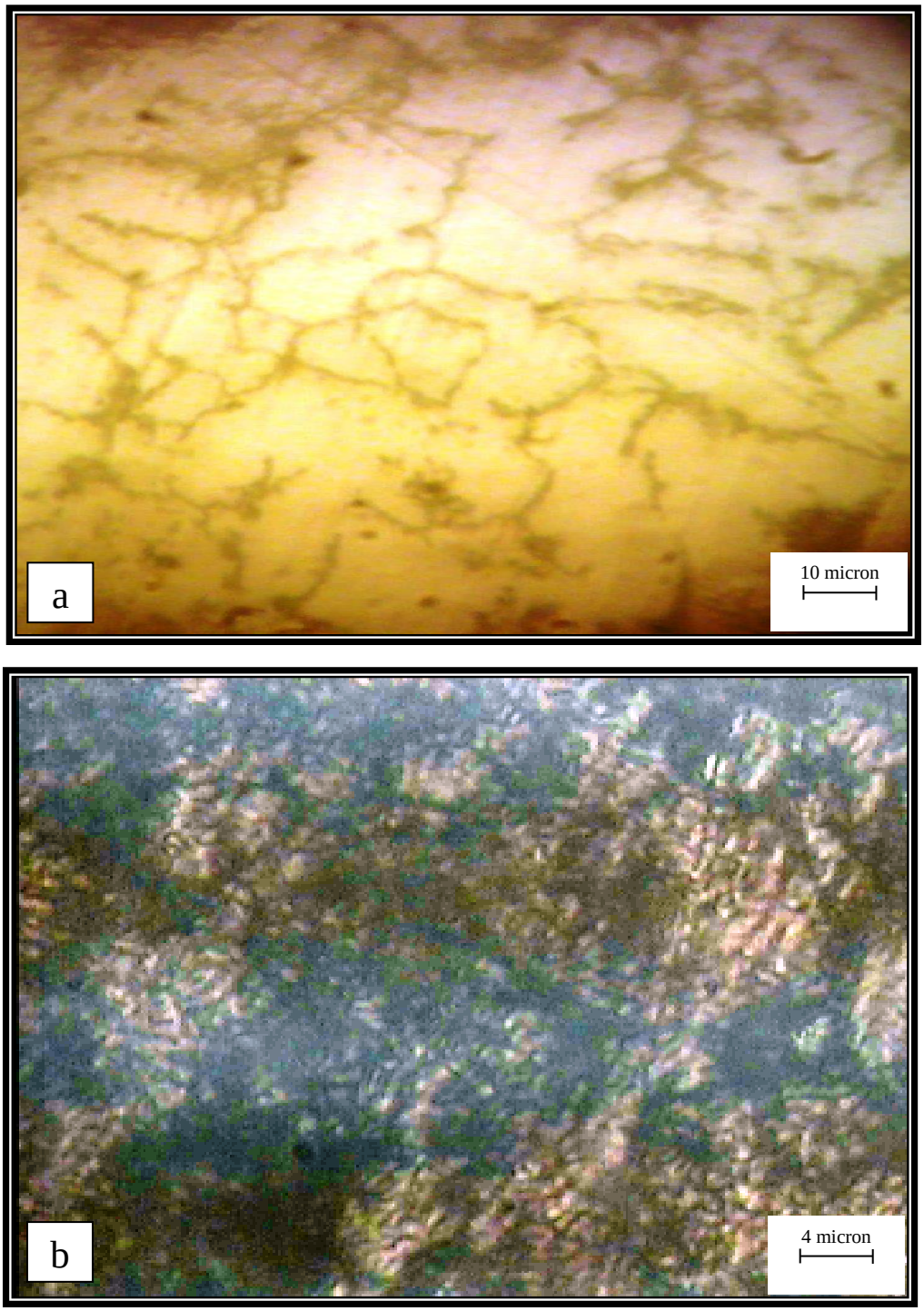

Fig(6.107) LOM images for alloy 6 aging in 200 C for 30 min. and followed by quenching in ice water for a:etched in(NH4OH+H2O2+H2O) solution.b: etched in(FeCl3+HCl+H2O) solution

6.5.3 Scanning electron microscope images:

Scanning electron micrographs of alloy 1, 2,3 and alloy 6 have been shown in Figs.(6.108) , (6.09) , (6.110) and Fig.(6.111) respectively. It has been shown that precipitates from γ_2 phase (dark black regions).blue precipitates are the intermetallic compounds of the above phases. It is also clear that scanning electron after solution treatment and aging treatment. It is apparent that pores and precipitates are lied near the grain boundaries or near the particle boundaries. Scanning electron micrographs for etched specimen of alloy2 and alloy3 etching with [$FeCl_3$+ HCl + H_2O] solution have been shown in Fig. (6.112) and Fig.(6.113) respectively.

6.5.4 Vicker's macrohardness test results

Vicker's macrohardness results as a function of weight percent of alloying elements have been shown in Fig. (6.114). It is apparent that vicker's hardness is decreased when weight percent of alloying elements is increased up to 0.8 wt%. After this decreasing, Vicker's hardness tends to increase secondly at 1.2 of alloying element except boron addition which continue in decreasing . It is probably that 0.4 % of alloying element forms critical weight percent which makes the precipitates of intermetallic compounds coherent with martensite matrix phase. This leads to increase hardness of alloys. However, when the weight percent of alloying elements is increased , precipitates of intermetallic compounds (γ_2 or $(Cu,Al)_2Ti$) may be semi coherent or no adherent stick with martensite matrix phase which also leads to decrease hardness. In addition, presence of pores make hardness data random in its distribution.

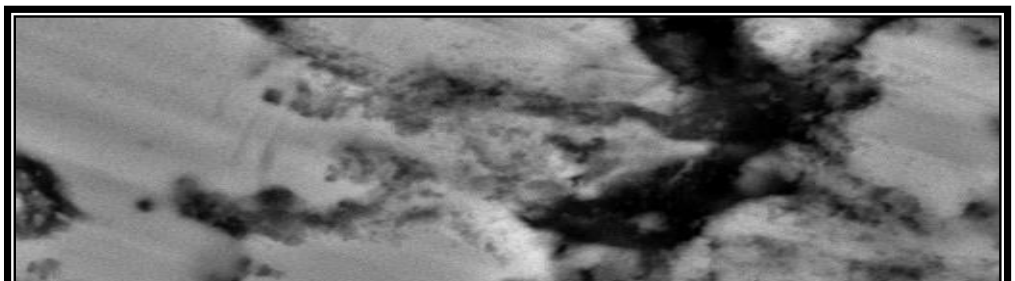

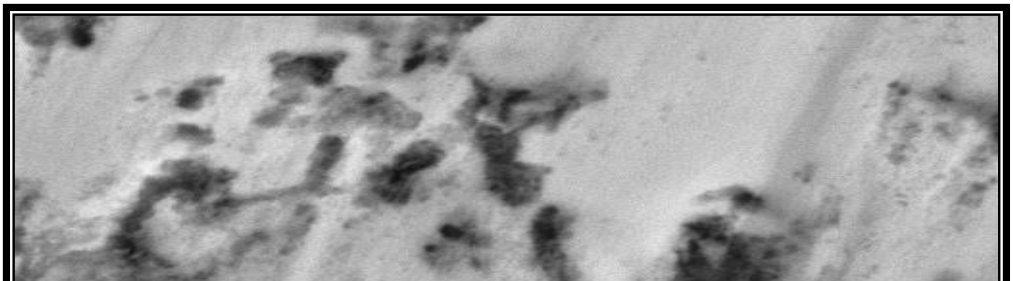

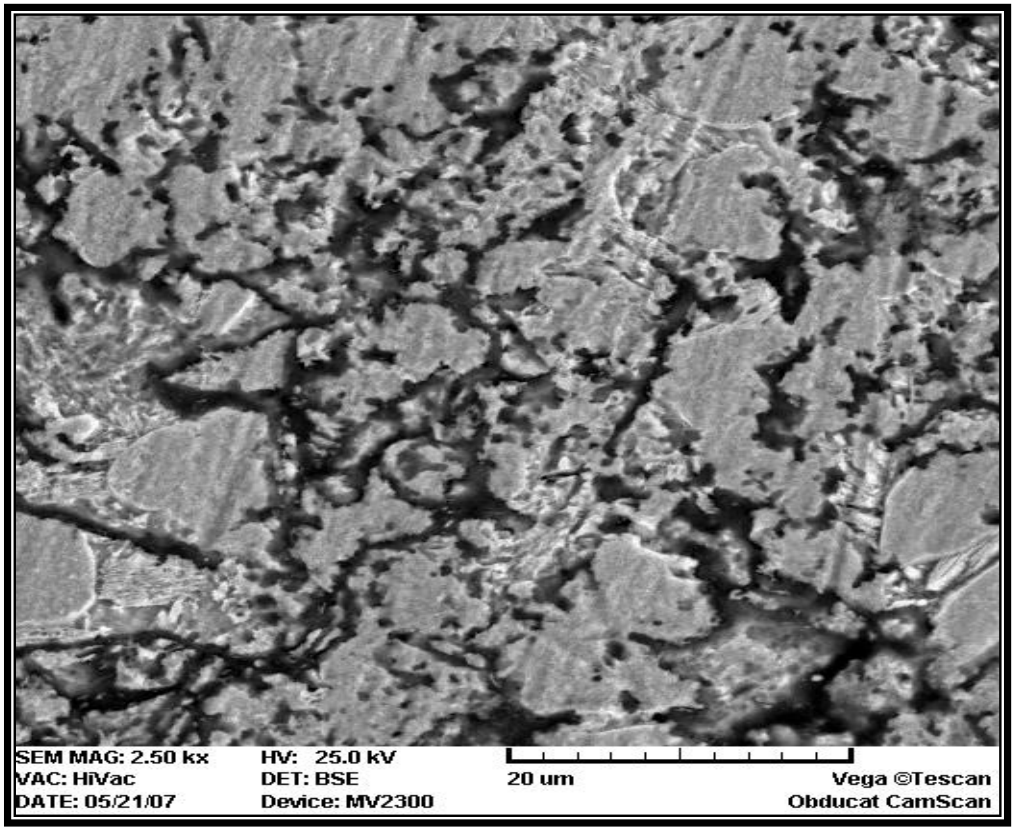

Fig.(6.112) SEM image for alloy 3 etched in (FeCl3+HCl+H2O) solution.

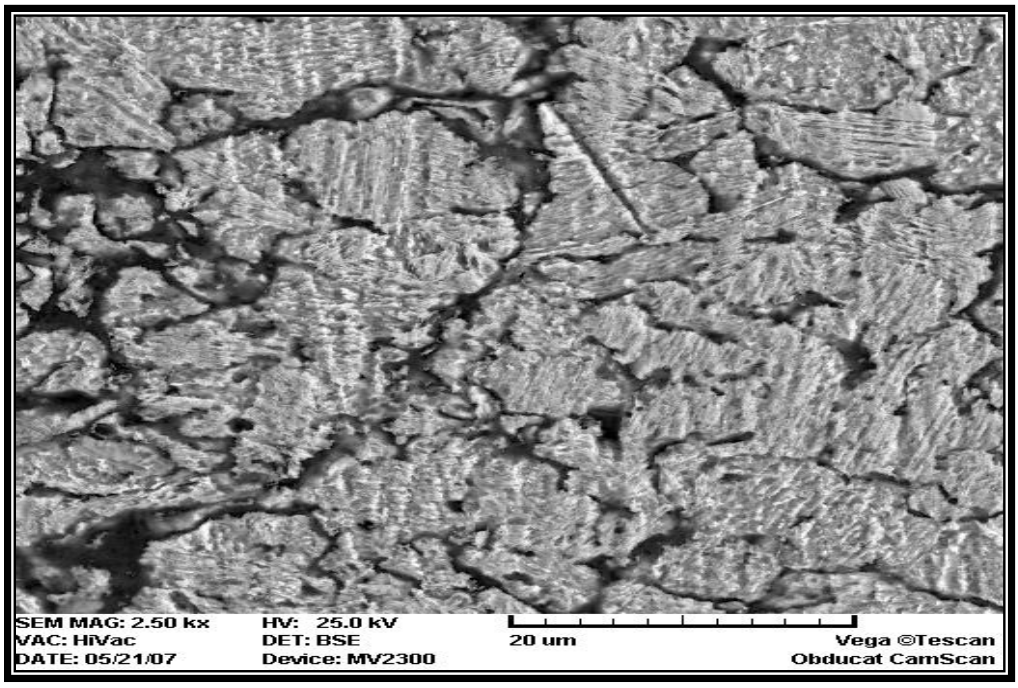

Fig.(6.113) SEM image for alloy 6 etched in (FeCl3+HCl+H2O) solution

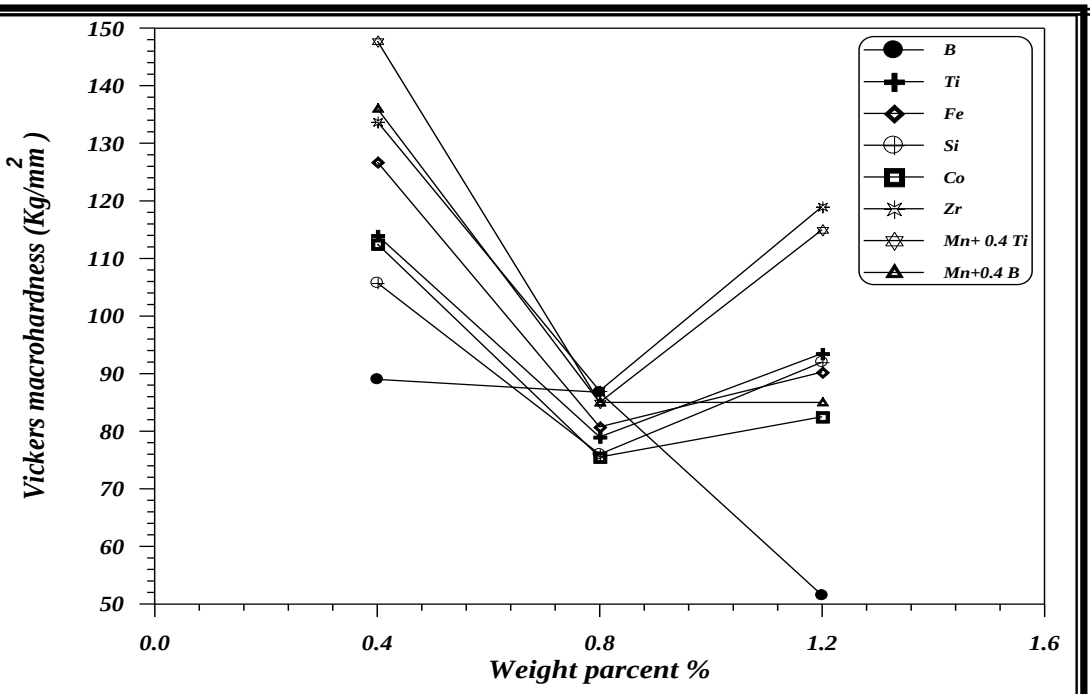

Fig.(6.114) Vickers macrohardness results for aged specimens with respect to weight percent of alloying elements

6.5.5 Shape memory effect for aged treated specimens:

Shape memory effect for aging heat treated specimen in calculated by using macrohardness test indenter. Vicker's macrohardness indenter after aging treatment is pictured for all alloys. After this , indenter for reheating up to 150 ^{o}C for 10 min. specimens is also pictured using digital camera fitted with light optical microscope with low magnification. These two image are analyzed and processed in real dimensions in order to determine dimensions of indenter (d1 and d2) before and after reheating heat treatment. Shape memory effect is calculated and presented in table (6.3). It is clear that alloy 6 has the maximum shape memory effect (**4.288365** %) whereas alloy 1has a minimum shape memory effect (**0.821182** %) in the other hand.

6.6. Step- quenched heat treatment:

Step- quenched heat treatment consists of solution treatment up to 840 ^{o}C for one hour and quenching in hot water at 95 ^{o}C for 15 min. After this , quenching in ice water has been done . In most copper—based shape memory alloys, the reverse transformation temperatures (A_s and A_f) increase with prolonged holding at temperatures below A_s[Humbeeck et. al , 1984] .

Therefore , transformation temperature may be changed after direct quenching treatment through the application of shape memory alloy and because the application of martensitic alloys in shape memory devices requires reproducible and stable transformation temperatures, martensitic structure must be stabilized either by aging or by step- quenched heat treatment. In this study, step-quenched specimen are used for the following reasons:

1. The disordered β-phase undergoes upon quenching disordered- ordered transformation. This transformation can not be suppressed even by rapid quenching and the degree of long range order is not equilibrium. Because M_s and A_s are affected by the degree of order in β-phase , holding the specimen at a temperature above M_s for a suitable time will be necessary in order to obtain equilibrium degree of order prior to transformation. The Transformation temperatures such as A_s , A_f , Ms and M_f obtained after step-quench treatment are Considered as true transformation temperatures.
2. quenching stresses which might affect the transformation temperatures , are minimized by step-quench heat treatment.

Table(6.3).Shape memory effect by impression Vickers's hardness for aged specimen.

Alloy No.	After aging treatment (by ferret's rectangle)		After recovery treatment		SME %	
	Length (Pixel)	Width (Pixel)	Length (Pixel)	Width (Pixel)	by length	by width
1	404.45	390.9	400.12	387.69	1.07059	0.821182
2	380.85	344.88	372.23	332.25	2.263358	3.662143
3	445.55	392.64	441.75	386.13	0.852878	1.658007
6	435.56	377.3	431.31	361.12	0.975755	4.288365

6.6.1. X-ray diffraction patterns for step- quenched specimens.

x-ray diffraction pattern for alloy 1 which step- quenched heat treated has been shown in Fig.(6.115). It is clear that intermetallic compound which is γ_2 , is precipitated through step- quench treatment with enough amount so as to appear in x-ray diffraction pattern. However, there is still martensite ($\overline{\beta}$) phase in the microstructure of alloy.

1.During step – quench treatment , decomposition of β phase in to $\alpha + \gamma_2$ phase through eutectoid reaction may be occurred. This is due to high temperature of decomposition line of alloy 1 which has low content of aluminum (11% Al) . It is hypoeutectiod alloy as can be seen from (Cu-Al) alloy phase diagram.

In addition X-ray diffraction pattern for alloy2 has been shown in Fig.(6.116). It is clear that the predominant phase is ($\overline{\beta}$) martensite phase but with small percent of intermetallic compound (γ_2) phase. This alloy is hypereutectoid alloy with (13% Al) . According to equation (6.2) , alloy 2 has M_s equal to 102 ^oC so that step- quench treatment temperature (95 ^oC) may be made the instable disordered ($\overline{\beta}$) phase suffer from decomposition into $\alpha + \gamma_2$ phase which are more stable and equilibrium than disordered ($\overline{\beta}$) at this temperature. It is also apparent from Fig.(6.18) that ratio of γ_2 phase is less that the ratio of ($\overline{\beta}$) martensite phase in the internal structure of step-quenched alloy2.

On the other hand, Fig(6.117) shows the x-ray diffraction pattern for alloy3 which contains titanium additions of 0.4% Ti. It has been shown that the major phase is ($\overline{\beta}$) martensite phase in which high intensity of ($\overline{\beta}$) phase has been obtained. It is also apparent that precipitates from [(Cu9Al)2Ti] intermetallic compound in the matrix of martensite phase are precipitated through step- quench treatment .It is clear that the ratio of intermetallic

compound is very little compared with the presence of major matrix phase from $(\overline{\beta})$ phase.

X-ray pattern for alloy 6 which contains boron addition is shown is Fig.(6.118). Decomposition of unstable (β) phase in to $\alpha + \gamma_2$ phase through eutectoid reaction has been occurred. However, most of the matrix of alloy 6 is still $(\overline{\beta})$ martensite phase. It is clear that step-quench treatment of alloys 1,2,3 and 6 leads to form dual phase shape memory alloys in which martensite is the matrix which intermetallic compounds precipitates.

This means that step-quenched shape memory alloys may be more strength as well more stable transformation temperature than that indirect quench specimens .

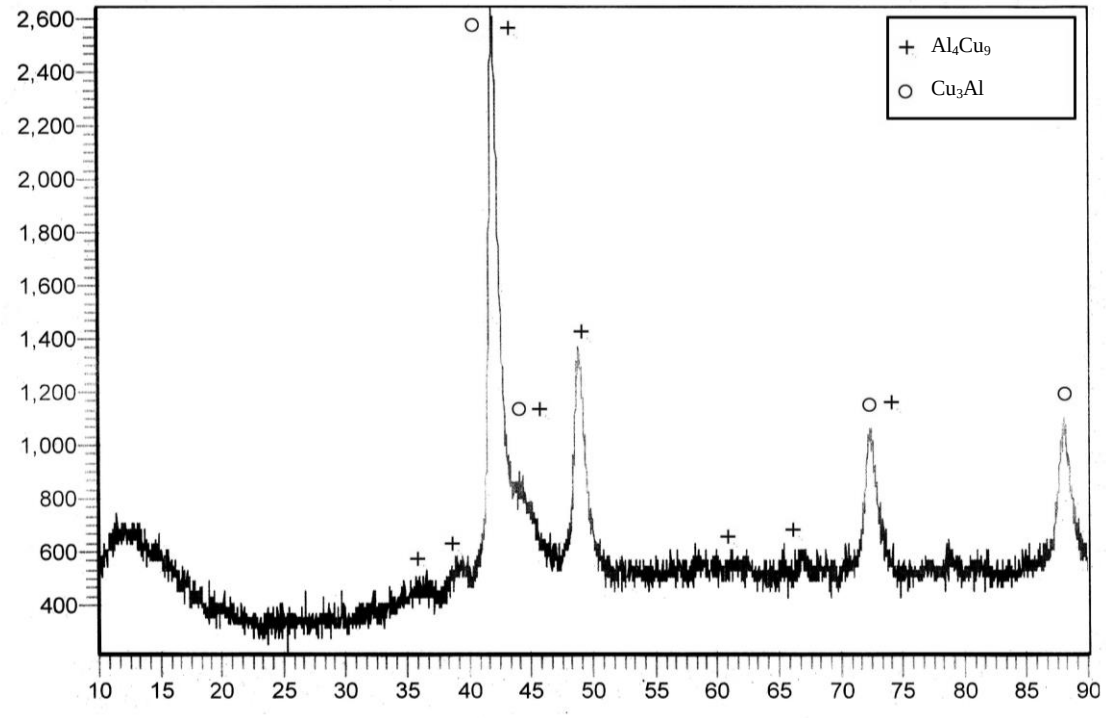

Fig.(6.115) XRD pattern of alloy 1 for step - quenched in 95 °C for 15 min.

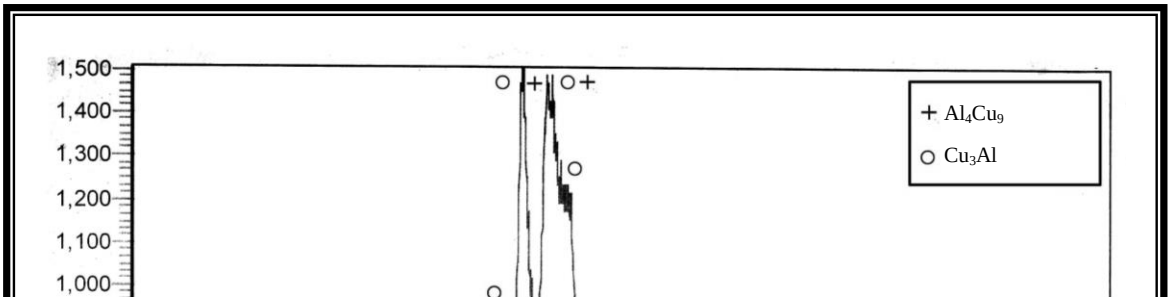

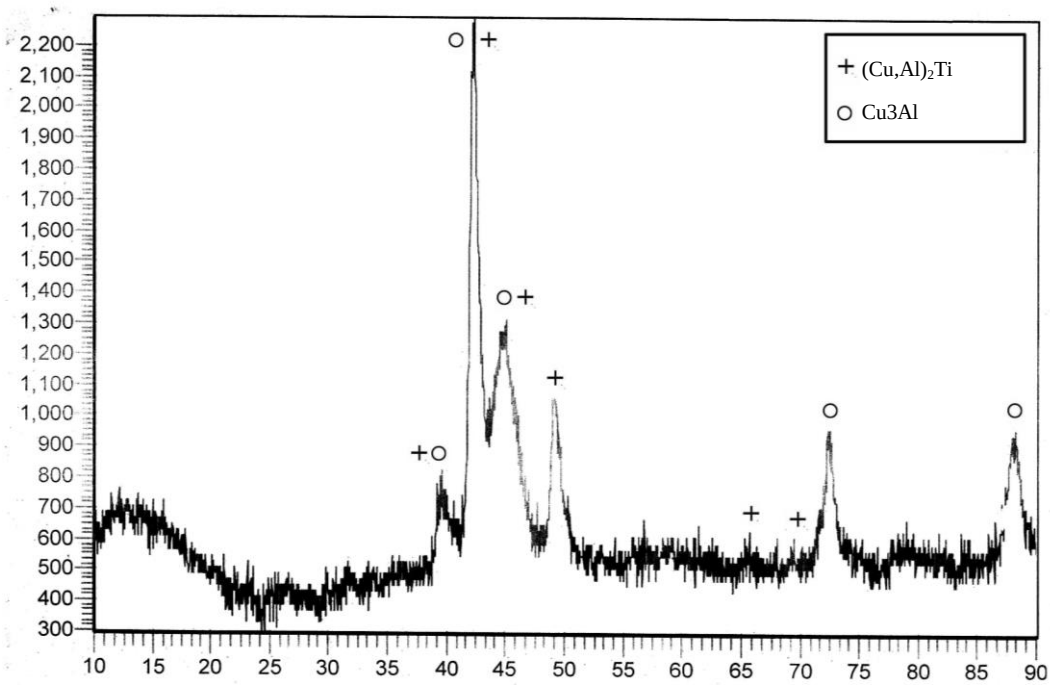

Fig.(6.117) XRD pattern of alloy 3 for step - quenched in 95 ºC for 15 min.

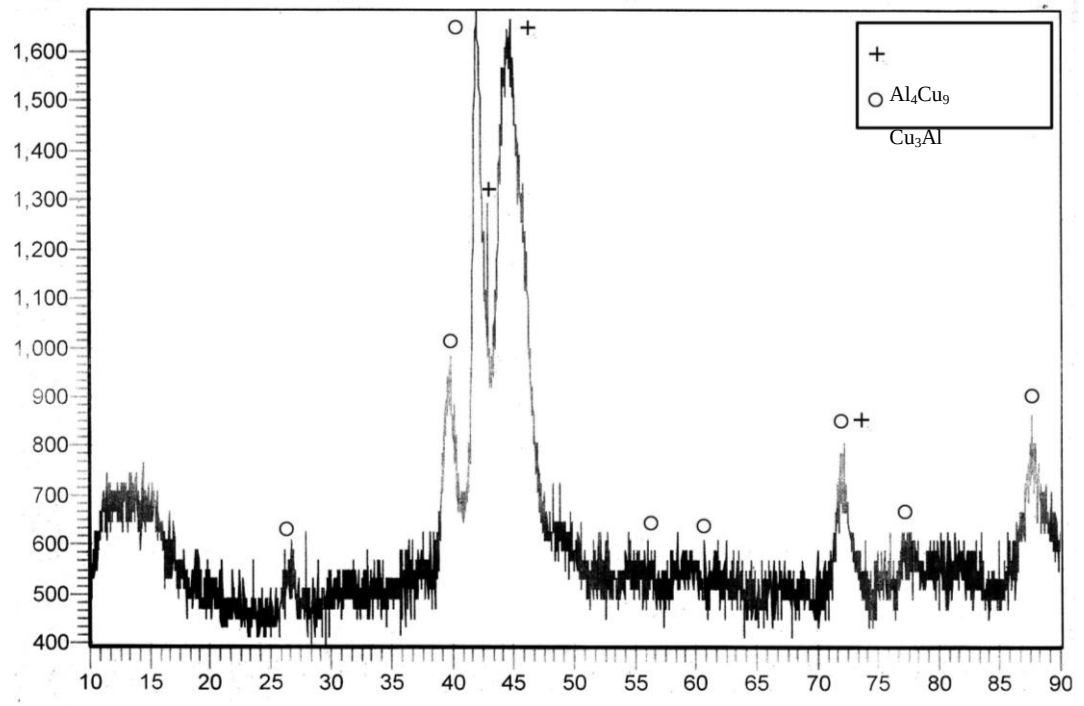

Fig.(6.118) XRD pattern of alloy 3 for step - quenched in 95 ºC for 15 min.

6.6.2. Light optical micrographs:

Here ,light optical micrographs for alloy 1,2,3 and 6 are considered to be attention in order not to scatter many microstructure image Two magnification resolution have been used as 1000 X and 2400 X . In addition two etchant solutions are also used to reveal grain boundaries and phases in the alloys microstructures. Etching the specimens with (NH_4OH + H_2H_2 +H_2O) solution reveals grain boundaries whereas etching specimens with (FeCl3+ HCl + H2O) solution reveal particle boundaries which is similar than grain boundaries in colors , and phases in the microstructure of alloys. The microstructure of alloys is complex due to presence of pores , multiphase and sometimes quench micro cracks rear pores which avoided them by step-quench treatment as possible.

Fig.(6.119) shows microstructure of alloy1 with 1000 x in a with(NH_4OH + H_2O_2+ $2O_2$+ H_2O) solution as etchant and 2400 x in b which the alloy is etched with solution of ($FeCl_3$ + HCl + H_2O). Note some intermetallic compounds from γ_2 precipitate near the grain boundaries or particle boundaries. This case it self may be applied in Figs.(6.120) , (6.121) , and Fig.(6.122) but for alloy 2,3 and 6 respectively . Unfortunates intermetallic compounds do not clearly appear in the micrographs. This is probably due to presence of pores and their distribution which makes complexity of microstructure in addition which

makes complexity of micrographs. This is probably due to presence of pores and their distribution which makes complexity of microstructure in addition to very fine structure of intermetallic compound itself.

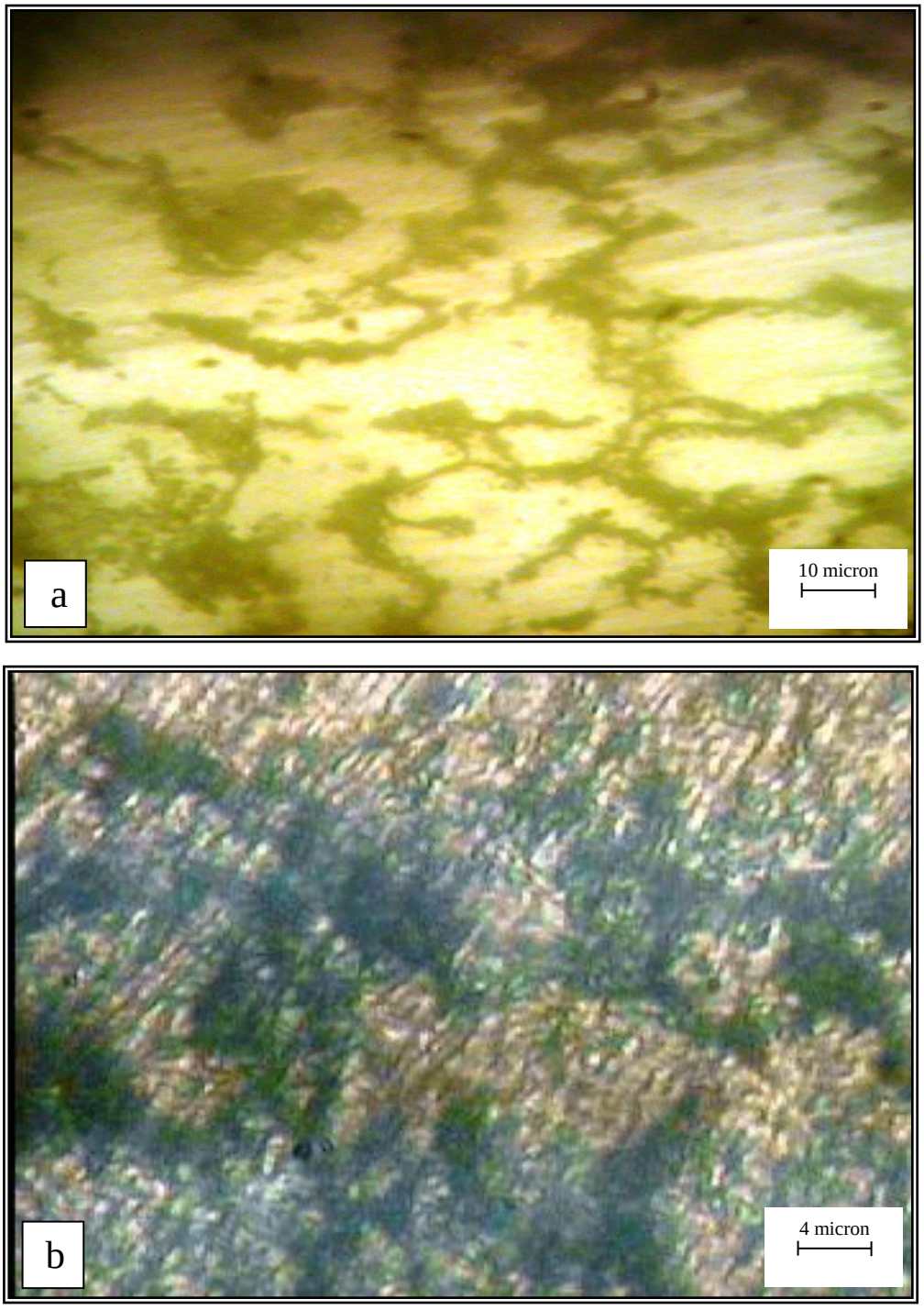

Fig.(6.119)LOM image for step-quenched of alloy 1 in 95 C followed by quenching in ice water for :a. etched in (NH4OH+H2O2+H2O) solution, b: etched in(FeCl3+HCl+H2O) solution.

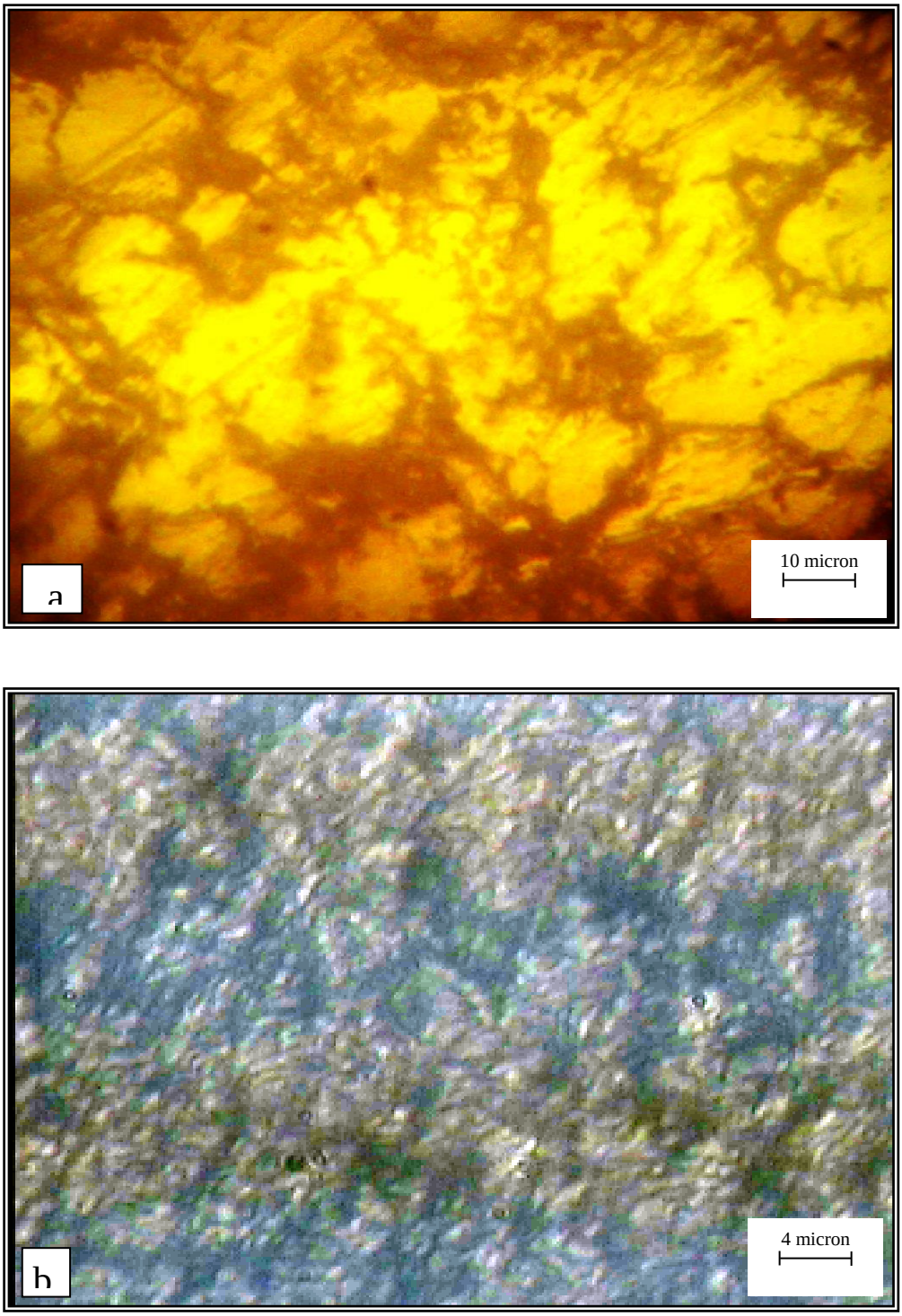

Fig.(6.120)LOM image for step-quenched of alloy 2 in 95 C followed by quenching in ice water for :a. etched in (NH4OH+H2O2+H2O) solution, b: etched in(FeCl3+HCl+H2O) solution

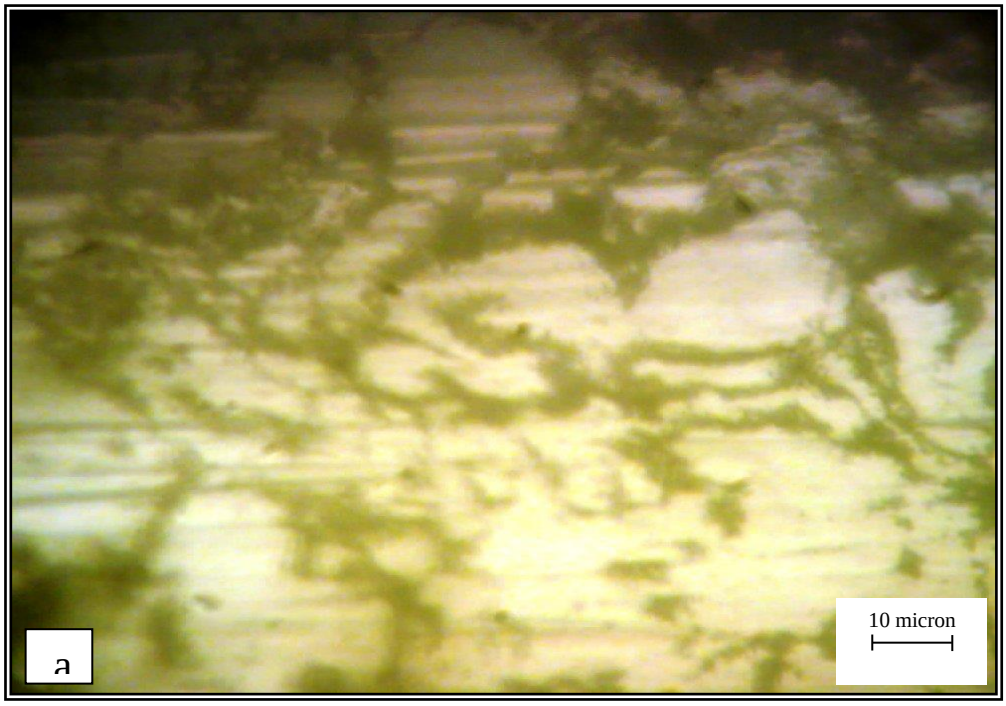

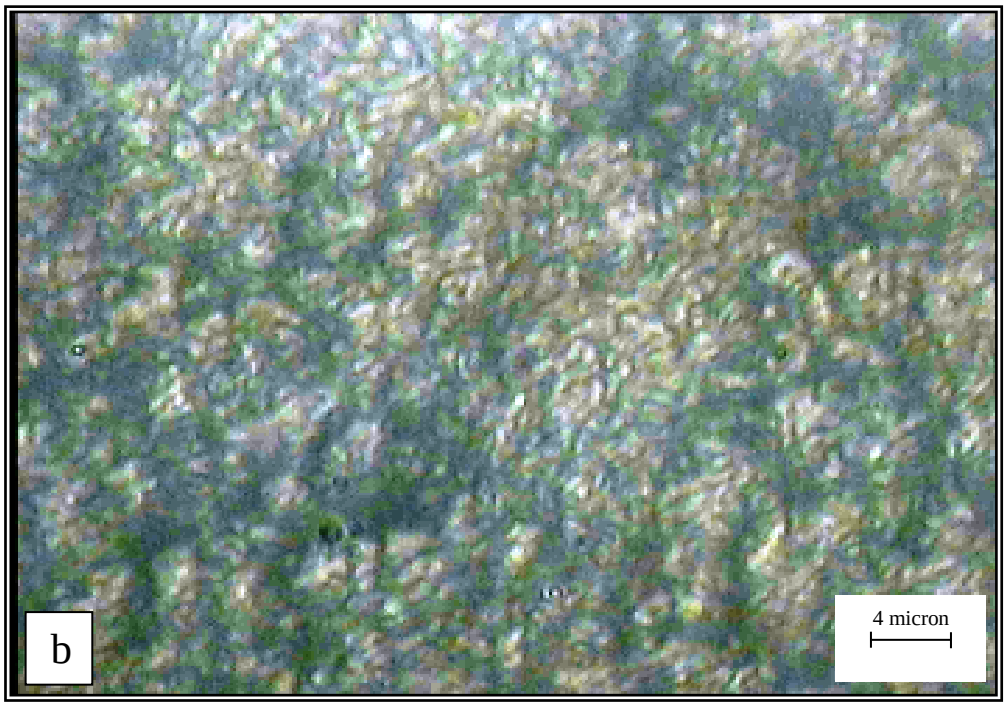

Fig.(6.121)LOM image for step-quenched of alloy 3 in 95 C followed by quenching in ice water for ∶a. etched in (NH4OH+H2O2+H2O) solution, b: etched in(FeCl3+HCl+H2O) solution

10 micron

4 micron

6.6.3. Scanning electron micrographs :

Scanning electron image for alloy 1 in the case of unetched has been shown in Fig.(6.123). The image reveals pores size and pores distribution on the surface of specimen. It has been shown that sintering difficulties of (Cu+Al) systems arise from aluminum content when aluminum content increase , porosity may be raised. All pores are agglomerated on the particle boundaries. Pores have non uniform shape as can be seen from Fig.(6.122).

It is clear that some regions in the surface of specimen are corroded when they are step- quenched in hot water. Unetched scanning electron image for alloys 2,3 and 6 are shown in Figs.(6.124) , (6.125) and Fig.(6.126) respectively. It is clear that using alloying element as grain refiner such as Ti or B causes small and low content of pores in the microstructure as can be seen in Fig.(6.125). It is probably that precipitates of intermetallic compounds require to high resolution of transmission electron microscope in which nanoscale has been taken into consideration. As clearly seen in Figs.(6.124) , (6.125) and Fig.(6.126), only distribution of pores and their shapes are clearly revealed whereas precipitates are not clearly appeared in the SEM image.

6.6.4. Vicker's macrohardness test results .

Vicker's macrohardness value as a function of alloying elements for step-quenched specimens, is shown in Fig.(6.127) In general speaking, aged martensitic specimens have vicker's macrohardness than in step- quenched specimens due to precipitate fine intermetallic compound in the aged treatment. However, the behavior of hardness profile is similar to the behavior of hardness profile of aged specimen in which the hardness is decreased with increasing weight percent of alloy elements. This is clearly seen is Fig.(6.127) . Generally , 0.4 wt % of alloying elements is optimum value for most elements to satisfy

suitable hardness number . In spite of using four readings for vicker's macrohardness value , standard deviation is high for each specimen. This is probably due to presence of pores in different shape and in nonuniform distribution .

6.6.5. Shape memory effect

Shape memory effect for step-quenched specimens has been determined using image analysis and image processing technique for impression of vicker's indenter using suitable low magnification resolution of optical microscope. Shape memory effect of all step- quenched specimens is shown in table (6.4).

As clearly seen from table (6.4) alloy 1 has maximums shape effect value (**23.63**%) whereas alloy 6 has a minimum value(**2.89934** %).

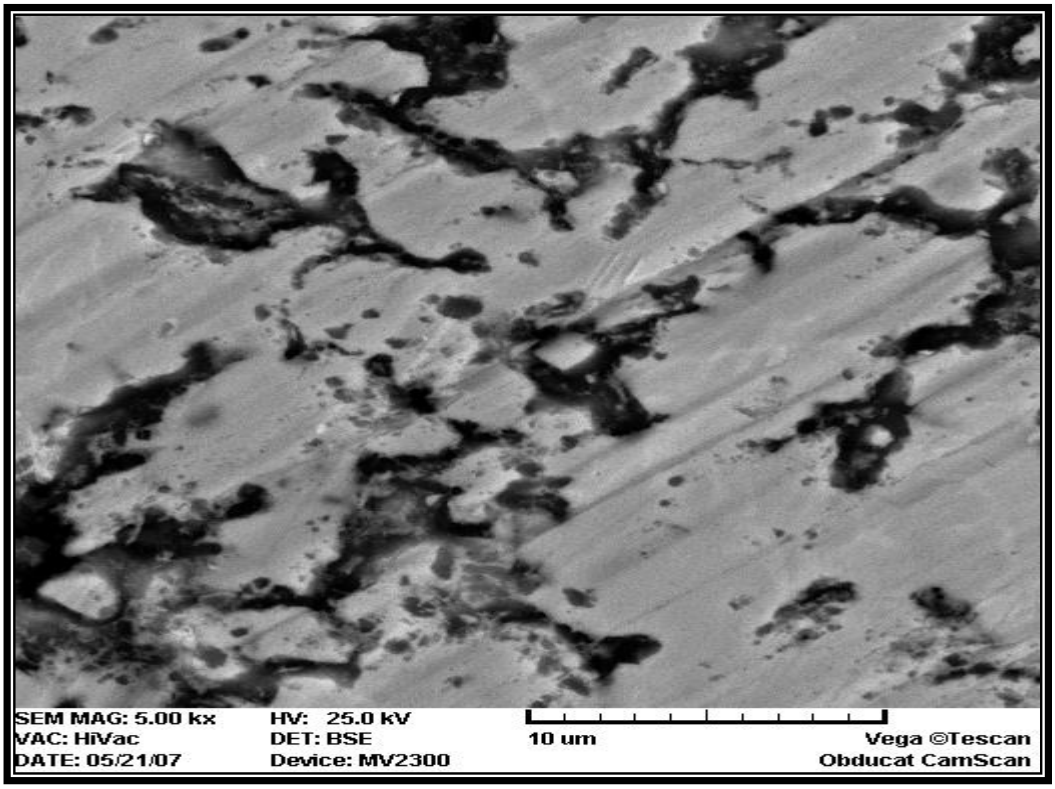

Fig.(6. 123) SEM image for alloy 1 under step quenched at 95 C for 15 min. and quenched in ice water.

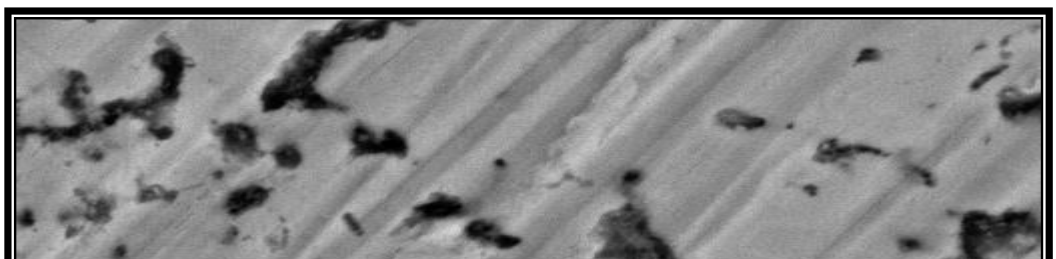

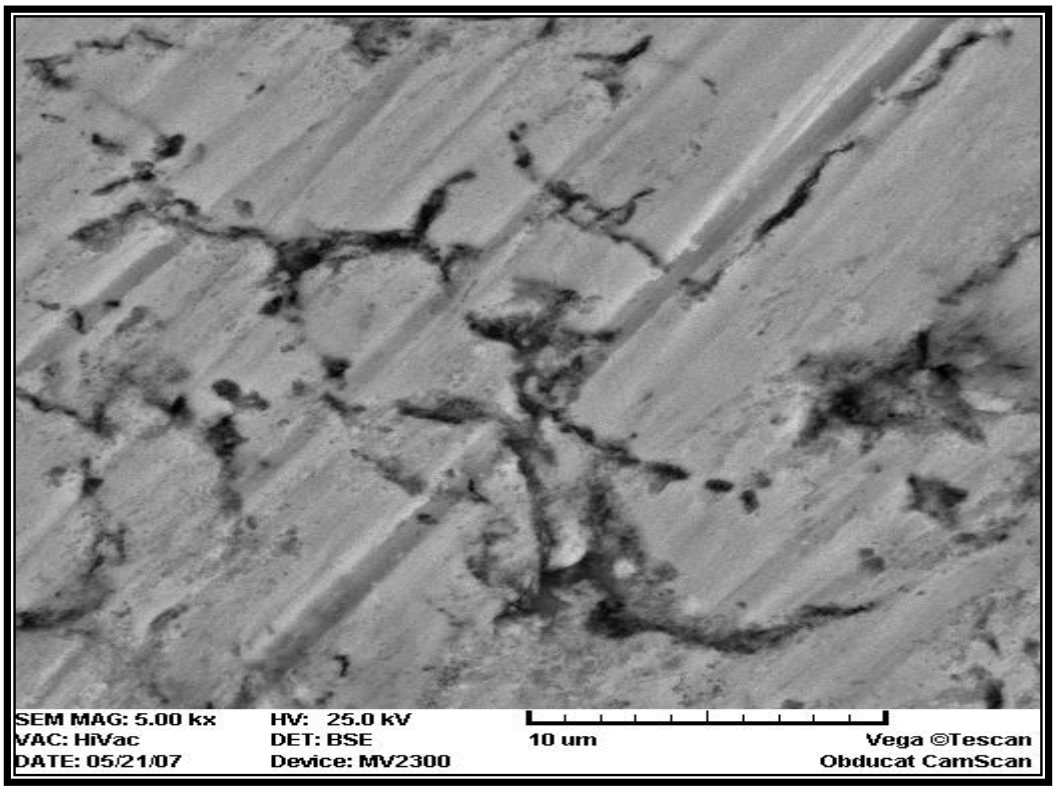

Fig.(6. 125) SEM image for alloy 3 under step quenched at 95 C for 15 min. and quenched in ice water

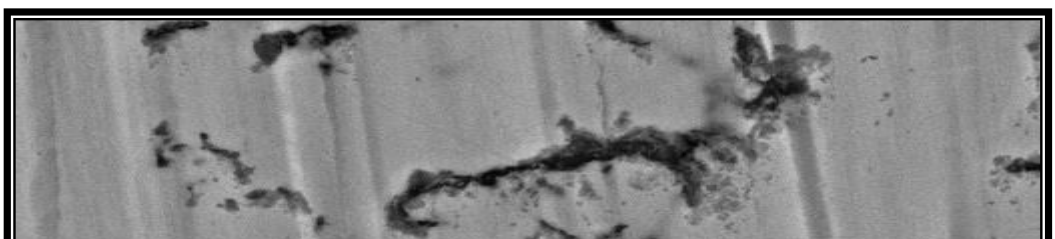

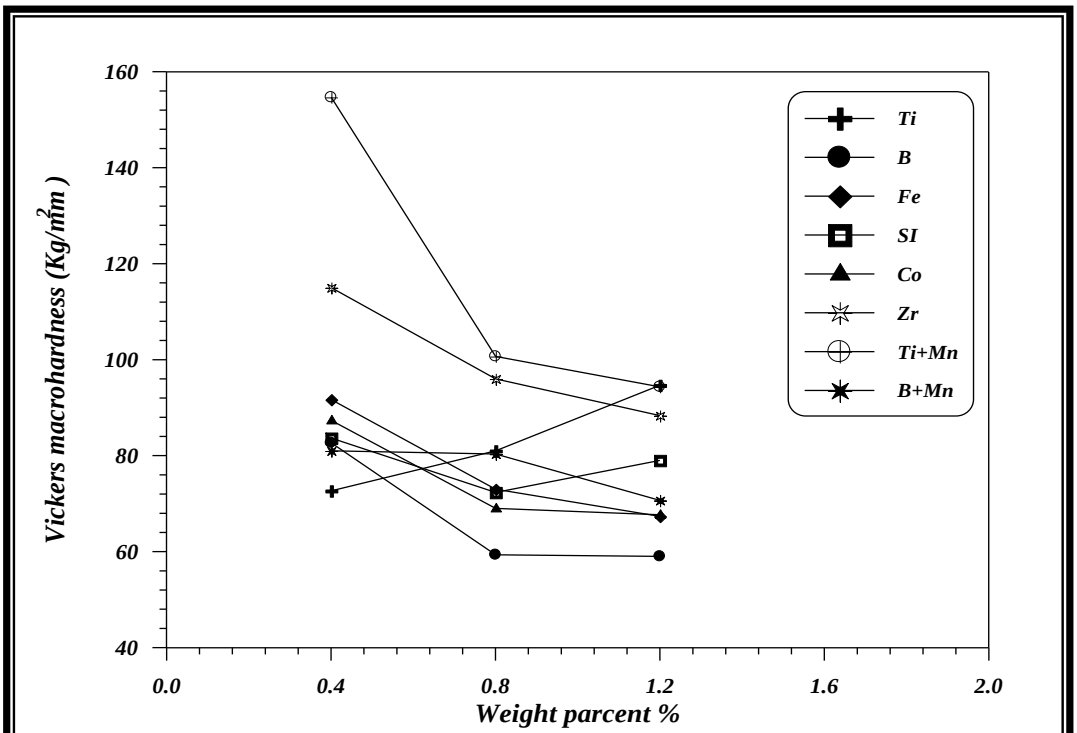

Fig.(6.127) Vickers macrohardness results for step-quenched samples according to weight percent of alloying elements.

Table(6.4).Shape memory recovery by Vickers hardness for step queched specimen.

Alloy No.	After aging treatment (by ferret's rectangle)	After recovery treatment	SME %

	Length(Pixel)	Width(Pixel)	Length(Pixel)	Width(Pixel)	by length	by width
1	824.73	661.83	629.84	570.46	23.63076	13.80566
2	446.29	434.58	434.52	414.73	2.637299	4.567629
3	526.04	491.95	470.67	455.84	10.52582	7.340177
6	422.51	417.50	410.26	403.43	2.89934	3.37006

6.7 Strain-temperature curves

Strain as a function of temperature at constant stress (100 Mpa) has been studied in order to know the amount f strain recovery and to know the range of transformation temperature during heating and cooling specimen. To conduct this test, direct quenched specimen in compressed up to the amount of stress of 100 Mpa and then placed in the furnace. The furnace was the heated from just above room temperature to (175 – 250 ^{o}C) according to tupe of alloy content of the specimen.Strain – temperature data is recorded by by dial guage with (0.001mm) accuracy and digital thermocouple curve for alloy 5 and alloy 6 has been shown in Fig.(6.128) and Fig.(6.129) respectively. The features of importance on these graphs are the two sharp changes in slope which corresponding to the beginning and end of transformation from martensite to oustensite during heating . Although the temperatures seen to have wide range and shiffed slightly slightly from that predicted form equation (6.2), the difference con be accounted for by consideration that the heating rate of the furnace in too high to allow stabilization at each temperature. This causes that the outer sections of the specimen reachs temperature before the inner section which which means that the majority of the specimen material is cooler than the indicated temperature. This may cause that the strain readings is to lag slightly behind the temperature readings . It is clear from this test that the compression testing does not significantly permanently impact the transformation temperatures . As can be seen Fig.(6.128) that small strain (0.16 %) is recovered during heating up to 225 ^{o}C. This is probably due to pore connections reopening or from edge effects. In addition, as can be seen from Fig.(6.129) , the recovery strain is 0.25 % but there a difference between the hystersis compared with that in Fig.(6.128) of alloy 5. After testing, specimen may be heated up to 450 ^{o}C and the strain measured to know the total shape recovery when the temperature just above A_s.

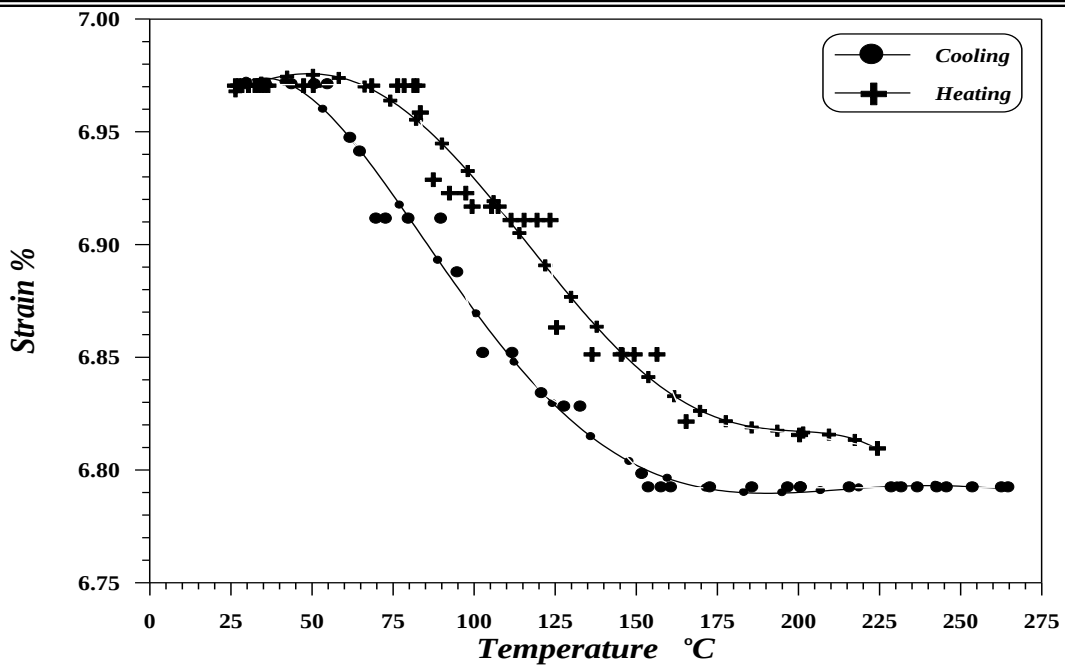

Fig.(6.128) Strain – temperature curve for alloy 5 at constant stress (100 MPa)

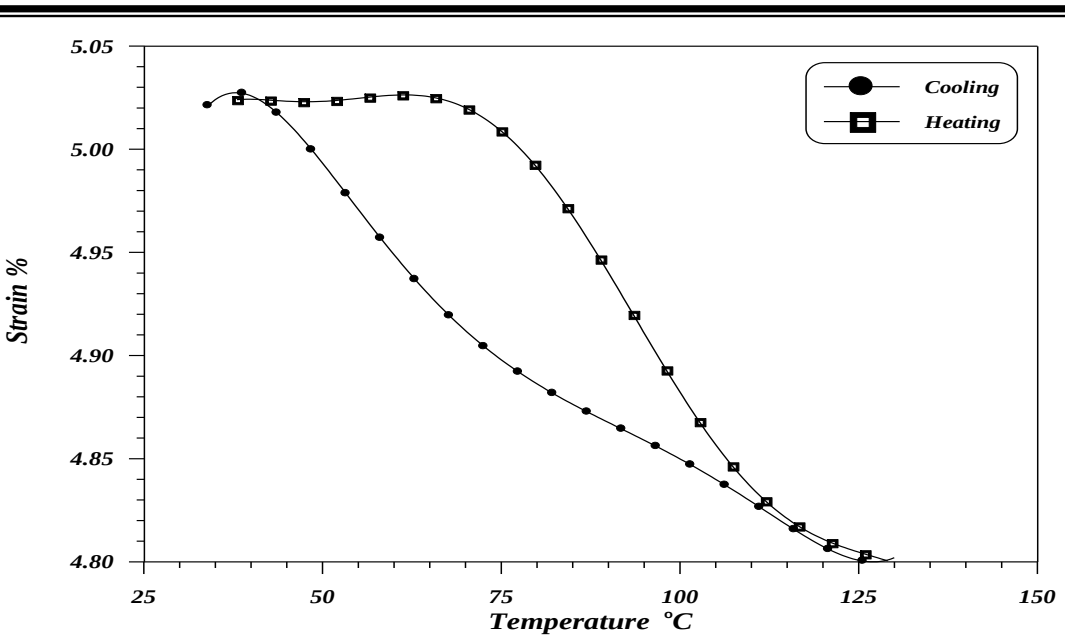

Fig.(6.129) Strain – temperature curve for alloy 6 at constant stress (100 MPa)

6.8 Numerical Results

Finite element analysis results for porous shape memory alloys prepared by powder metallurgy technique have presented here according to the pores distribution as follows:

6.8.1 Unit cell finite element results

Results obtained from unit cell finite element can be classified into the following manner according to assumption of periodic pores distribution.

6.8.1.1 Square unit cell FEA.

Fig.(6.130)shows the stress contour for (0.01*0.01mm) dimension of square unit cell for 10% as volume fraction of pores. This figure shows the distribution of normal stress in the x direction in which the maximum value of stress is obtained near the pore region in the last step of load increment. However, Fig.(6.131) shows the stress contour in the x direction for unloading case which also represents the maximum values near the holes (pores) which considered as stress concentration. It is clear that the region near pores are stressed enough to enhance stress-induced martensite more than the other regions.

In addition, Fig.(6.132) and Fig.(6.133) show the strain contour in x direction for the last load increment and unloading case (very small amount of loading but not equal to zero) respectively. It is apparent that some regions in the unit cell are strained up to 6.82 % that they will recover during unloading case up to 0.1 % which is very small elastic strain .furthermore, Fig.(6.134) and Fig.(6.135)show the stress- strain curve for loading and unloading cases for stress in the x and y direction respectively. It is apparent that small hystersis during loading and unloading paths has been observed. It is also apparent that the slope of the first stage of stress-strain curve is the same for the third stage due to the assumption of Auricchio model.

6.8.1.2.Hexagonal unit cell FEA results.

Fig.(6.136) shows the stress contour of x component in maximum load increment. It is apparent that maximum values of stress are occurred near the pores which means that pores may be promoted stress- induced martensite. In addition Fig.(6.137) shows the same stress contour but at the unloading case. It is clear that stresses may be released through unloading case in which phase transformation is occurred. Fig.(6.138)shows the high super elastic strain in which 9.46 % strain is given that is recovered into 1.0 % through unloading case as can be seen in Fig.(6.139).

In addition ,stress- strain curve for node 55 in x and y components are shown in Fig.(6.140) and Fig.(6.141) respectively. It is clear that hystersis throughout loading-unloading cases has been obtained for both components.

6.8.2.Real representation of microstructure FEA results.

Fig.(6.142) shows the image of microstructure of unetched alloy 12 specimen with 150X magnification. The equivalent finite element mesh of this image is shown in Fig.(6.143).

Fig.(6.144) and Fig.(6.145) show the total strain in the x direction for maximum load increment and during unloading step. It is apparent that regions strained up to 6.19 % are recovered into 1.2 % throughout unloading.

Fig.(6.146) shows the stress contour in the x direction for last load step. It is appeared that maximum stress is obtained near the pore region. However, Fig.(6.147)shows the same stress contour but at the unloading increment step. It is apparent that regions near the pores are stressed regions even after unloading case with comparison with the other regions which mean that these regions firstly transform into martensite and finally return to austenite during unloading.

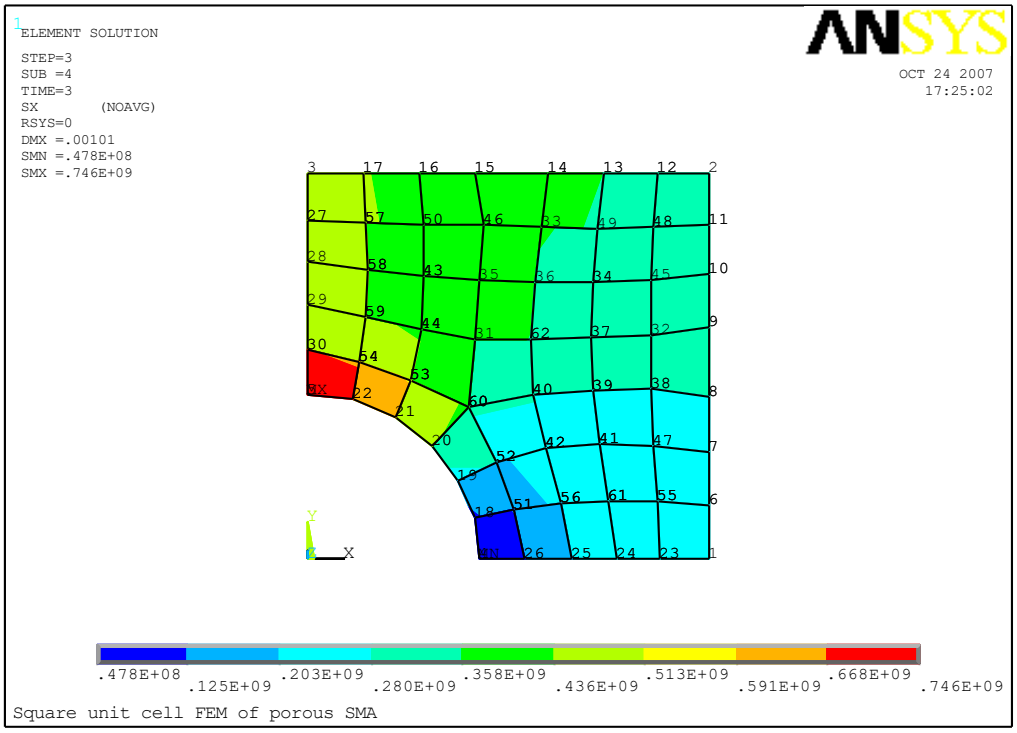

Fig.(6.130) Stress contour in x direction for square unit cell FEA For final maximum increment load step.

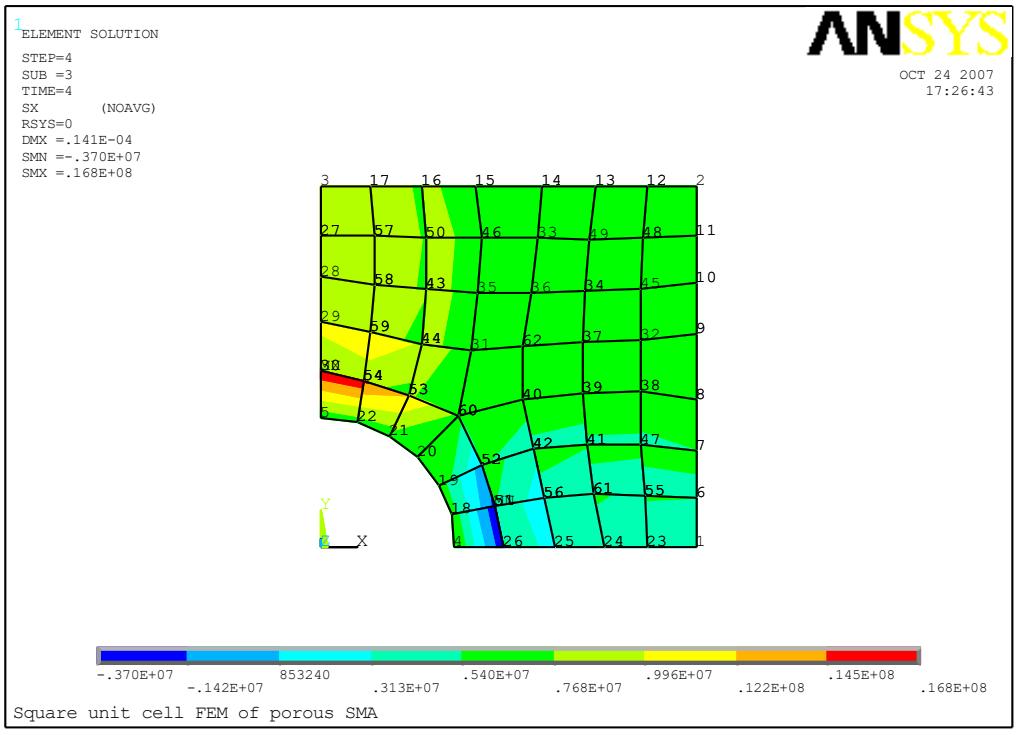

Fig.(6.131) Stress contour in x direction for square unit cell FEA For unload step.

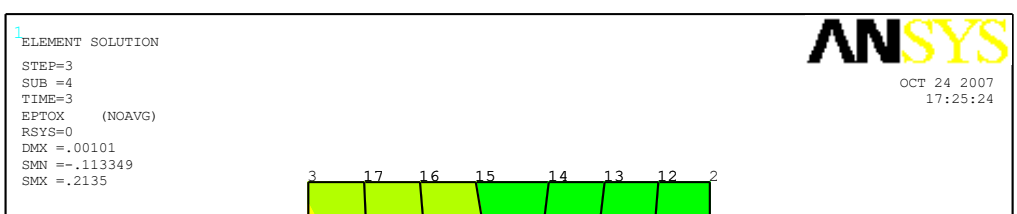

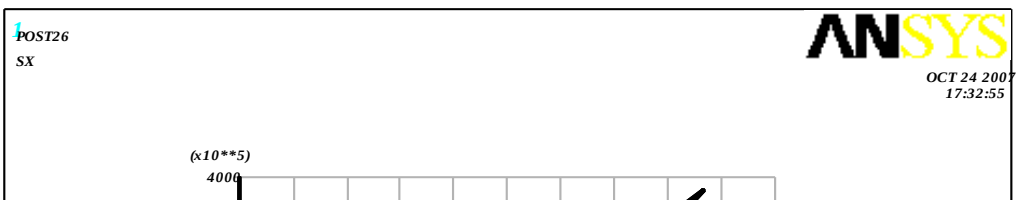
1
POST26
SX
ANSYS
OCT 24 2007
17:32:55
(x10**5)
4000

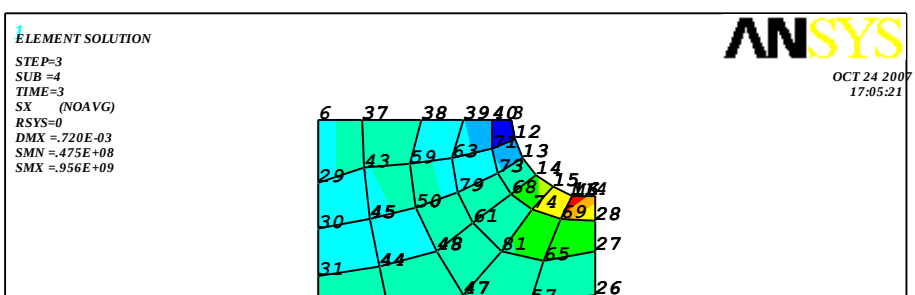
1
ELEMENT SOLUTION
STEP=3
SUB =4
TIME=3
SX (NOAVG)
RSYS=0
DMX =.720E-03
SMN =.475E+08
SMX =.956E+09
ANSYS
OCT 24 2007
17:05:21

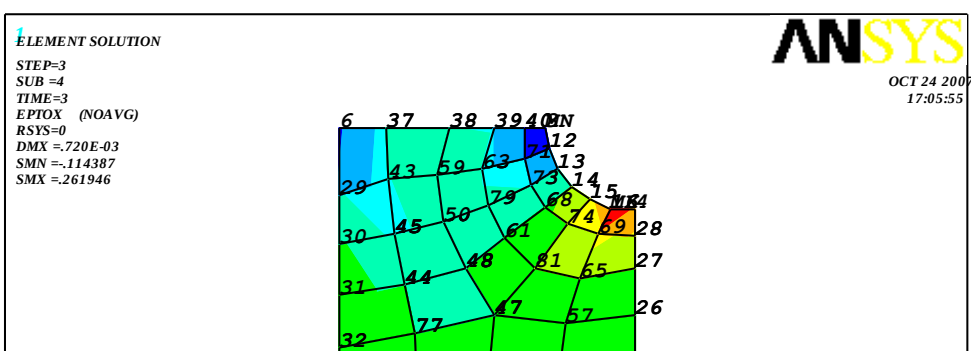
1
ELEMENT SOLUTION
STEP=3
SUB =4
TIME=3
EPTOX (NOAVG)
RSYS=0
DMX =.720E-03
SMN =-.114387
SMX =.261946
ANSYS
OCT 24 2007
17:05:55
6
37
38
39
40
MN
12
13
14
15
43
59
63
73
29
79
68
74
69
28
30
45
50
61
27
48
81
65
31
44
47
57
26
77
32

1
POST26
SX
ANSYS
OCT 24 2007
04:32:37
(x10**5)
4500
4000
3500
3000
2500
2000
ss (N/m2),Sx

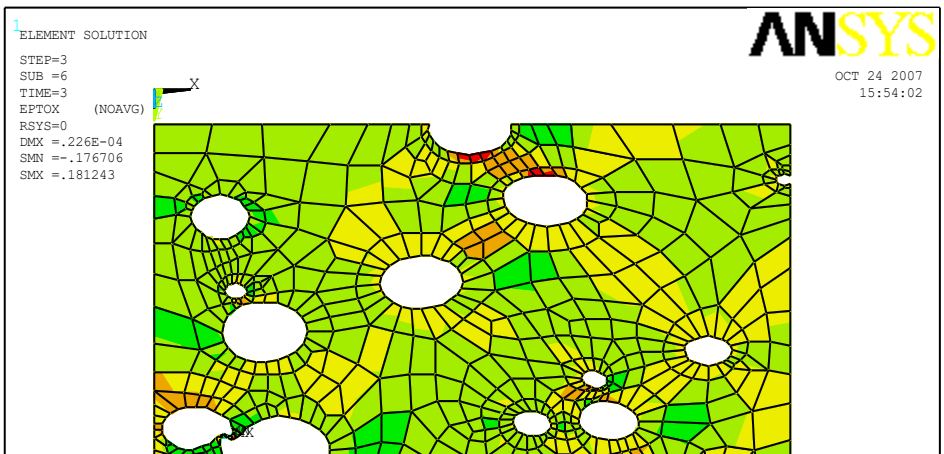
1
ELEMENT SOLUTION
STEP=3
SUB =6
TIME=3
EPTOX (NOAVG)
RSYS=0
DMX =.226E-04
SMN =-.176706
SMX =.181243
ANSYS
OCT 24 2007
15:54:02
Y
Z
X
MN
MX

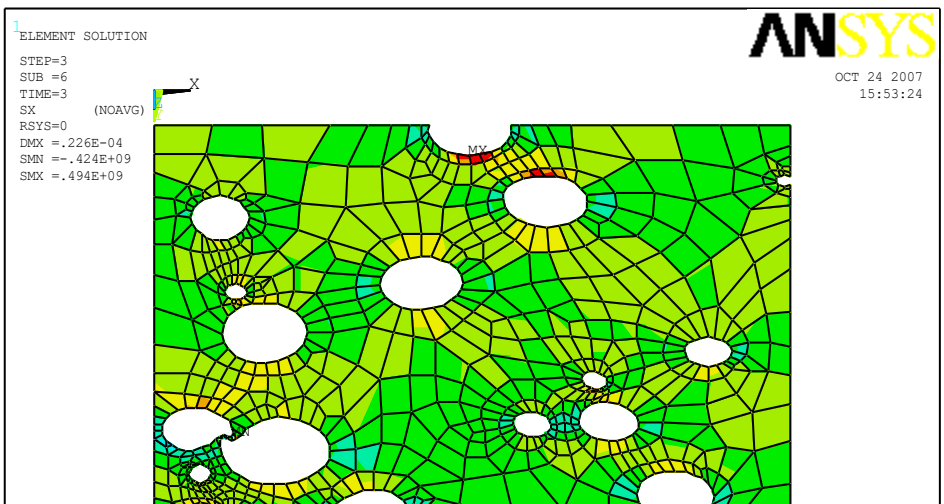
ELEMENT SOLUTION
STEP=3
SUB =6
TIME=3
SX (NOAVG)
RSYS=0
DMX =.226E-04
SMN =-.424E+09
SMX =.494E+09
ANSYS
OCT 24 2007
15:53:24
X
MX
MN

Conclusion and Recommendations For future works.

7.1 Conclusions

The main conclusions form the experimental and numerical study of the examined copper-based shape memory alloys in this research are :

1. The addition of (0.4 wt% Ti) to (Cu +13wt %Al +3.8wt % Ni) alloy causes a shape memory effect of (59 %) from 10 % of total strain.
2. shape memory effect obtained in this work is (5.9 %) in comparison with standard copper aluminum nickel base shape memory alloys of (4-7 %).
3. In comparison with standard (Ni/Ti) base shape memory alloys (8-10%) the SME observed in this study is (80 %).
4. It appears that the lower porosity leads to the higher SME.
5. Using image processing and images analysis of LOM images of elemental and blended powders is efficient to determine particle size and particle distribution before compacting of powders in addition to pore size and pore distribution in the microstructure of sintered compacts.
6. x-ray diffraction technique used to identify phases, shows that sintering at 600 ^{o}C for 3hr followed by sintering at 850 ^{o}C for 3hr. is efficient to satisfy sintering process in which elemental powders are completely transformed into alloy structure.
7. Martensitic transformation is occurred in Cu Al Ni based shape memory alloys completely by direct quenching form 840^{o}C into ice water(2-4 ^{o}C) whereas aging and step-quenched heat treatments tend to stabilize martensite phase with γ_2 intermetallic compound precipitates in the microstructure as clearly shown from x-ray diffraction analysis.
8. Phase transformations occurred in a temperature range of (70-130 °C) as indicated by electrical resistance test.
9. Ultrasonic results also support the occurrence of shape memory effect in all the examined alloys.

10. The use of unit cell finite element technique with periodic square and hexagonal arrangement of pores is efficient for analysis of porous shape memory alloys prepared with powder metallurgy technique.
11. Real represent of microstructure LOM image using image analysis with combination of finite element analysis is more accurate than unit cell finite element approach.
12. It has been shown that titanium addition to Cu Al Ni base shape memory alloys tends to form (Cu, $Al)_2Ti$ as intermetallic compound rather than $\gamma_2 (Al_4Cu_9)$ through recovery heating up to 450 ^oC and during aging treatment.
13. Numerical analysis for the hystersis of SMAs showed that regions around pores are preferred sites for martensitic transformations.
14. porous Cu Al Ni based shape memory alloys have suitable shape memory effect and shape recovery in addition to law weight which make them as suitable material for energy absorption applications.
15. It appears that Auricchio model is only applied to analyze superelastic behavior of shape memory alloy.

7.2 Suggestions and recommendation for future work.

The following suggestions should be taken into consideration for future work of copper-based shape memory alloys prepared by powder metallurgy technique.

1. Differential scanning calorimetric (DSC) test should be used in order to measure transformation temperature for the prepared alloys in heating and cooling cycles.
2. Transmission electron microscopy (TEM) should be used to reveal the structure of martensite, its form and the degree of ordering for obtained martensite .
3. In order to increased density of sintered compacts, double action press or hot isostatic pressing should be used.
4. To investigate shape recovery and superelastic behavior of prepared alloys in high temperature , stress- strain curve should be tested at high temperature in heating cycle and cooling subzero temperature during cooling cycle .
5. Corrosion and wear behavior of prepared alloys may be investigated in future in different mediums.
6. Advanced composite material in which metal matrix reinforced with shape memory alloy particles of prepared alloys may be studied and developed in future.
7. Fatigue behavior of copper based shape memory alloys should be studied to use them in space applications.

Examining committee Approval sheet

We certify that we have read this thesis entitled (***Investigation of Certain Shape Memory Alloys in Space Systems***) and as an examining committee, we have examined the student (***Abdul-Raheem Kadhim AbidAli)*** in its contents and what is related to it, and that in our opinion it meets the standard of a thesis for the degree of Doctor of Philosophy in Material Engineering.

Signature:
Prof.Dr.Mohammad H. Al-Taaie
Committee Chair
Date: / /2008

Signature:
Asst.Prof.Dr.Nabeel K. Abid Al-Sahib
Committee Member
Date: / /2008

Signature:
Asst.Prof.Dr.Ahmed A. Moosa
Committee Member
Date: / /2008

Signature:
Asst.Prof.Dr.Najim A. Saad
Committee Member
Date: / /2008

Signature:
Asst.Prof.Dr. Mohammad H.Al-Maamory
Committee Member
Date: / /2008

Signature:
Prof.Dr.K.H.Al khazraji
Supervisor
Date: / /2008

Signature:
Prof.Dr.Abdul-Wahid K. Rajih
Supervisor
Date: / /2008

Approval of the Department of Material Engineering
Head of Material Engineering Department.

Signature:
Asst.Prof.Dr.Najim A. Saad
Date: / /2008

Approval of the College of Engineering

Dean of the College of Engineering.

Signature:
Asst.Prof.Dr. Salah T.Ali Al-Bazzaz
Date: 18/5 /2008

List of symbols and Abbreviation

Symbols	*meaning*	*Units*
SME	*Shape memory effect*	*%*
SMA	*Shape memory alloy*	
SMAs	*Shape memory alloys*	
Ms	*Martensite start temperature up on cooling*	^oC
M_f	*Martensite final temperature up on cooling*	^oC
A_s	*reverse (austenite) transformation start temperature up on heating*	^oC
A_f	*reverse (austenite) transformation final temperature up on heating*	^oC
Nitinol	*Ni-Ti naval ordnance laboratory*	
SE	*Super elastic behavior*	
S.R.	*Shape recovery*	*%*
DSC	*differential Scanning calorimetric*	
SEM	*Scanning electron microscopy*	
AFM	*atomic force microscope*	
B_2	*Ordered body centered Cubic*	
R	*Trigonal or Rambohedral phase*	
BCC	*body center cubic*	
FCC	*Face center cubic*	
HCP	*Hexagonal closed packed*	
BCT	*Body center tetragonal*	
FCT	*Face center tetragonal*	
ΔG	*Change in Gibbs free energy*	*J*
A	*Surface area*	m^2
ΔG_s	*Change in strain energy*	J/m^3
ΔG_v	*Volume free energy*	j/m^3
v	*volume*	m^3
ΔH	*Change in enthalpy (Latent heat of transformation)*	*J*
T	*Temperature*	^oC
M_P	*peek temperature of martensite*	^oC
A_P	*Peek temperature of austenitic (reverse) transformation Dsc curve*	^oC
M_d	*deformation Matensite temperature*	
r_n	*radius of neck between two particles*	*m*
r_f	*particle radius*	*m*
t	*Time*	*min*
rc	*Curvature radius of particle*	*m*

R	*Universal gas constant*	
k	*Constant*	
D_θ	*volume (lattice) self diffusion coefficient*	
D	*diffusion coefficient*	cm^2/sec
D_O	*diffusivity Coefficient*	cm^2/sec
Q	*activation energy*	*(cal /mole /k)*
m	*mass of powder*	g
V_P	*Powder volume*	cm^3
m_g	*green mass of Compact*	g
V_g	*green volume of compact*	cm
w_t	*weight percent of elemental powders*	%
md	*dry mass of sample*	g
m_W	*met mass of sample*	g
m_s	*suspended mass of sample*	g
m_{sa}	*saturated mass of specimen*	g
LD	*die Cavity dimension (diameter)*	m
LS	*Sintered specimen dimension*	m
Hv	*Vicker`s hardness No.*	kg/mm^2
p	*load*	N
d	*average diameter of impression*	
HB	*Brinell hardness No.*	kg/mn^2
db	*average impression diameter before heating*	m
da	*average impression diameter after heating*	m
Lo	*original length of sample*	m
L_1	*Length after compression of specimen*	m
L_2	*Length after recovery heating of sample*	m
n	*strain hardening coefficient*	
$[D]$	*elastic stiffness matrix*	N/m^2
Y	*Yield strength*	MPa
E	*Elastic modulus*	GPa
b_M *and* C_M	*Material Coefficients for martensite phase*	
b_A*and* C_A	*Material Coefficient for austenite phase*	
b'_m, C'_m, b'_A, C'_A	*Material coefficients for R phase forward and backward transformation .*	
$F_{A\to M}$	*Flow pressure f material*	N/m^2

F	*Flow pressure for austenite to martensite transformation*	N/m^2
$F^{M\to A}$	*Flow pressure for martensite to austenite transformation .*	N/m^2
$C^{M\to A}$	*Stress to temperature coefficient for martensite to austenite transformation*	
Tr	*Trace operator*	
a	*length of unit cell*	*m*
b	*width of unit cell*	*m*
APDL	*Ansys parametric design language*	
U	*displacement in x direction*	*m*
V	*displacement in y direction*	*m*
C_1,C_2	*Constants refer to boundary conditions*	*m*
P	*apparent porosity*	*%*
LOM	*Light optical microscope*	

Greek Symbols

Symbols	***meaning***	***Units***
θ	*Contact angle*	*radian*
γ_{SG}	*Surface tension of solid –gas interface*	*N/m*
γ_{SL}	*Surface tension of solid –liquid interface*	*N/m*
γ_{LG}	*Surface tension of liquid –gas interface*	*N/m*
γ	*interfacial surface energy*	J/m^2
$\overline{\beta}$	*martensite phase in Cu-Al systems .*	
β	*Parent phase at high temperature in Cu-Al systems*	
η	*Viscosity*	*Pa.s*
σ	*Normal stress*	N/m^2
τ	*Shear stress*	N/m^2
ε	*Strain*	*%*
ε_{xy}	*Shear strain in x-y plane*	*%*
$[\theta]$	*thermo elastic tensor*	
ρ_A	*apparent density of powder*	g/cm^3
ρ_G	*green density of compact*	g/cm^3
ρ_{tB}	*Theoretical density of blended powders*	g/cm^3
p_g	*green porosity*	*%*
ρ_a	*apparent density of sintered compact*	g/cm^3

ρ_w	*water density*	g/cm^3
ε_r	*recovery strain*	%
β	*one dimensional back stress*	N/m^2
$\dot{\varepsilon}$	*strain rate*	*1/sec*
ε^{ain}	*inelastic nonlinear strain rate*	*1/sec*
$[\Omega]$	*range of strain result from martensite transformation*	
$[\Psi]$	*range of strain result and phase transformation*	
ζ	*volume percentage of martensite phase*	
η	*Volume percentage of R phase*	
ζ_M	*Martensite volume fraction*	%
ζ_A	*Austenite Volume fraction*	%
α	*material parameter shows the difference tension and Compression.* $(0 \to 1)$	
$\{\Delta\varepsilon^{\tau}\}$	*incremental transformation strain vector*	%
$\bar{\varepsilon}_L$	*Maximum transformation strain*	%
τ_{xy}	*shear stress in plane xy.*	N/m^2
$\sigma_s^{A\to M}$	*Martensite starting stress*	N/m^2
$\sigma_f^{A\to M}$	*martensite finishing stress*	N/m^2
$\sigma_f^{M\to A}$	*austenite starting stress*	N/m^2
$\sigma_f^{M\to A}$	*austenite finishing stress*	N/m^2

Subscript

s	*starting transformation*
f	*finishing transformation*
P	*Porous*
D	*Fully dense*
L	*Length*
M	*martensite phase*
A	*reverse austenite phase*
r	*recovery*
b	*before recovery heating*
a	*after recovery heating*
o	*original*
d	*dry*
s	*suspended*

Sa	*saturated*

w	*wet*
g	*green*
Tb	*theoretical for blended mixture*
A	*Apparent*
P	*Powder*
sl	*solid-liquid interphase*
sg	*solid –gas interphase*
lg	*liquid-gas interphase*
n	*neck between two Particle*
v	*volume*
t	*transformation*
s	*strain*

Super script symbols

$A \rightarrow M$	*Austenite to marten site phase transformation*
$M \rightarrow A$	*Martensite to reverse austenite phase transformation*
$\bullet$	*first derivative of time*
-	*degree of ordering of Martensite*
tr	*transformation*

Republic of Iraq
Ministry of Higher Education
And Scientific Research
University of Babylon
Collage of Engineering
Department of Material engineering

INVESTIGATION OF CERTAIN SHAPE MEMORY ALLOYS IN SPACE SYSTEMS .

A THESIS

SUBMITED TO THE COLLEGE OF ENGINEERING OF THE UNIVERSITY OF BABYLON IN PARTIAL FULFILLMENT OF THE REQUIREMENTS FOR THE DEGREE OF DOCTOR OF PHILOSOPHY IN MATERIAL ENGINEERING

BY

Abdul –Raheem Kadhim Abid-Ali

(Msc. In Material Engineering)

October 2007

وزارة التعليم العالي والبحث العلمي
جامعـــــــــة بابـــــــــل
كليـــــــة الهنـــــــــدسة
قسم هنـــــــــدسة المواد

استقصاء بعض السبائك
التي تستعيد شكلها في أنظمة الفضاء

أطروحة
مقدمة الى قسم هندسة المواد
كلية الهندسة جامعة بابل
كجزء من متطلبات نيل شهادة الدكتوراه فلسفة
في هندسة المواد

من قبل

عبدالرحيم كاظم عبد علي
(بكلوريوس وماجستير هندسة مواد)

تشرين اول 2007

بِسْمِ اللَّهِ الرَّحْمَنِ الرَّحِيمِ

﴿وَيَسْأَلُونَكَ عَنِ الرُّوحِ قُلِ الرُّوحُ مِنْ أَمْرِ رَبِّي وَمَا أُوتِيتُم مِّن الْعِلْمِ إِلاَّ قَلِيلاً ﴾

صدق الله العلي العظيم

{ سورة الإسراء / أية 85}

Dedication

To spirit of my father and my sister

To My family specially for my Mother and my brothers

To my wife and My sons with my love and respect

SUPERVISORS CERTIFICATE

We Certify that this thesis entitled ***[Investigation of certain shape memory alloys in space systems***] prepared by ***Abdul-Raheem kadhim Abid-Ali*** has been carried out under our supervision at the department of material engineering , College of Engineering Babylon university in partial fulfillment of the requirements for the degree of Doctor of philosophy in Material Engineering .

Supervisors

Signature :

Prof .Dr. Kahtan K. Al-Kazraji

Date: / /2007

signature:

Prof .Dr.Eng. Abdul-Wahid K.Rajih

Date: / /2007

Supervisors Certificate

We Certify that this thesis entitled *[Investigation of certain shape memory alloys in space systems*] prepared by ***Abdul-Raheem kadhim Abid-Ali*** has been carried out under our supervision at the department of material engineering , College of Engineering Babylon university in partial fulfillment of the requirements for the degree of Doctor of philosophy in Material Engineering .

Supervisors

Signature : K. Al-Kazraji

Prof .Dr. Kahtan H. Al-Kazraji

Date: / /2007

signature:

A. Rajih

Prof .Dr.Eng. Abdul-Wahid K.Rajih

Date: / /2007

دانشکدهٔ فنی
Faculty of Engineering
University of Tehran

To Whom It May Concern

21 May 2007

This is to certify that Scanning Electron Microscopic (Cam Scan Model MV2300) examination of twenty six metallic samples was carried out upon request of Mr. Abdul Raheem Kadhim Abid-Ali.

S.F. Kashani Bozorg

S.F. Kashani Bozorg,
Director of Advanced Metallography Lab
School of Metallurgy and Materials Engineering
University of Tehran

University of Tehran School of Metallurgy and Materials Eng.

Examining committee Approval sheet

We certify that we have read this thesis entitled (***Investigation of Certain Shape Memory Alloys in Space Systems***) and as an examining committee, we have examined the student (***Abdul-Raheem Kadhim AbidAli)*** in its contents and what is related to it, and that in our opinion it meets the standard of a thesis for the degree of Doctor of Philosophy in Material Engineering.

Signature:
Prof.Dr.Mohammad H. Al-Taaie
Committee Chair
Date: / /2008

Signature:
Asst.Prof.Dr.Nabeel K. Abid Al-Sahib
Committee Member
Date: / /2008

Signature:
Asst.Prof.Dr.Ahmed A. Moosa
Committee Member
Date: / /2008

Signature:
Asst.Prof.Dr.Najim A. Saad
Committee Member
Date: / /2008

Signature:
Asst.Prof.Dr. Mohammad H.Al-Maamory
Committee Member
Date: / /2008

Signature:
Prof.Dr.K.H.Al khazraji
Supervisor
Date: / /2008

Signature:
Prof.Dr.Abdul-Wahid K. Rajih
Supervisor
Date: / /2008

Approval of the Department of Material Engineering
Head of Material Engineering Department.

Signature:
Asst.Prof.Dr.Najim A. Saad
Date: / /2008

Approval of the College of Engineering

Dean of the College of Engineering.

Signature:
Asst.Prof.Dr. Salah T.Ali Al-Bazzaz
Date: 18/5 /2008

ACKNOWLEDGEMENTS

*First of all , Profusely all thanks for **ALLAH** Lord of all creation who enable me to achieve this work.*

*I would like to express my faithful gratitude to my supervisors **Prof. Dr. kahtan k. Al-kazraji and Prof.Dr.Eng. Abdul –Wahid k. Rajih** for their guidance and invaluable recommendations .*

I wish to express my thanks to Dr. Najim A. Saad, head of the department of material engineering for his kind help during my work especially in the use of experimental equipment used in this study.

I would like to thank the staff of workshop and Material laboratories at the university of Babylon .Special thanks for engineer Rihab S. Kadhim for her help in metallurgical lab.

I wish to express my gratitude to Faculty of Engineering , university of Tahran and staff of advance Metallurgical and material lab. Especially Dr. Kashani Bozorg, S.F. for his help in the examination of SEM specimens .

Special thanks to my family ,my mother ,all my brothers and my wife for their care and encouragement during this work.

Abstract

The rapid development of aerospace, military and medical industries required patents or development of certain materials. One of the most important ones in these fields is the shape memory alloys.

This study represents an attempt to prepare, alloying and investigate Cu Al Ni based shape memory alloys by using powder metallurgy technique. Several alloying elements are added from alloying elements such as (Ti, B, Fe, ,Si, Co, Zr,Ti+Mn and B+Mn) with (0.4 ,0.8 and 1.2 wt%) additives from each element taking into consideration several process parameters such as rate of loading , period of maximum load, compacting pressure , temperature and time of sintering. Different heat treatments have been employed to enhance shape memory effect of prepared alloys included solution heat treatment, aging and step-quench heat treatment .After deformation, shape recovery treatment is also used. Physical tests before and after sintering have been measured such as apparent density , green density and porosity , water absorption and expansion of sintered compacts. In addition , mechanical test such as hardness and compression have also studied. Compression test is conducted at room temperature and at 50 °C and then at constant stress of (100Mpa) and the change of strain as a function of temperature is recorded. SME is measured for prepared alloys by using hardness and compression tests after different heat treatments that is used in this study. Electrical resistance test has been measured as a function of temperature after direct quench heat treatment and after shape recovery treatment .
In addition ultrasonic technique is used to examine the shape memory effect after deformation and after shape recovery treatment.

Phase identification and analysis of alloys has been done using x-ray diffraction technique whereas SEM and LOM reveal microstructure

of alloys. In addition, pore size and its distribution as well as particle size and its distribution are calculated using image processing and image analysis technique in the matlab ver 7 environment for LOM image of unetched specimens.

Analysis of porous shape memory alloys is given based up on unit cell finite element technique taking into consideration square and hexagonal arrangement of pores to determine the response of porous shape memory alloys for both stresses and strains. Analysis of real microstructure of porous shape memory with different pore size , shape and distribution has been presented based upon LOM image analysis combination with finite element method in Ansys. version 9 software environment.

It is apparent that alloy with titanium addition (0.4 wt %) for (Cu +13 wt %Al+3.8wt% Ni) based shape memory alloy has a maximum shape effect (58.82 %) compared with other prepared alloys. With comparing to the standard very expensive cast (Ni/Ti) shape memory alloys, this value represent (80 %).The percentage of porosity is in the range of (10-38 %)for prepared alloys. It appears that lower the porosity the higher SME.

Direct quenching gives the highest martensitic transformation and eventually shape memory effect. On the other hand it seems that aging and step-quenched treatments have lower effect due to the presence of $\gamma 2$ phase.

Unit cell finite element analysis and real microstructure finite element analysis appear that stress-induced martensite regions are found around the pores which act as stress concentration positions.

List of symbols and Abbreviation

Symbols	*meaning*	*Units*
SME	*Shape memory effect*	*%*
SMA	*Shape memory alloy*	
SMAs	*Shape memory alloys*	
Ms	*Martensite start temperature up on cooling*	^oC
M_f	*Martensite final temperature up on cooling*	^oC
A_s	*reverse (austenite) transformation start temperature up on heating*	^oC
A_f	*reverse (austenite) transformation final temperature up on heating*	^oC
Nitinol	*Ni-Ti naval ordnance laboratory*	
SE	*Super elastic behavior*	
S.R.	*Shape recovery*	*%*
DSC	*differential Scanning calorimetric*	
SEM	*Scanning electron microscopy*	
AFM	*atomic force microscope*	
B_2	*Ordered body centered Cubic*	
R	*Trigonal or Rambohedral phase*	
BCC	*body center cubic*	
FCC	*Face center cubic*	
HCP	*Hexagonal closed packed*	
BCT	*Body center tetragonal*	
FCT	*Face center tetragonal*	
ΔG	*Change in Gibbs free energy*	*J*
A	*Surface area*	m^2
ΔG_s	*Change in strain energy*	J/m^3
ΔG_v	*Volume free energy*	j/m^3
v	*volume*	m^3
ΔH	*Change in enthalpy (Latent heat of transformation)*	*J*
T	*Temperature*	^oC
M_P	*peek temperature of martensite*	^oC
A_P	*Peek temperature of austenitic (reverse) transformation Dsc curve*	^oC
M_d	*deformation Matensite temperature*	
r_n	*radius of neck between two particles*	*m*
r_f	*particle radius*	*m*
t	*Time*	*min*
rc	*Curvature radius of particle*	*m*

R	*Universal gas constant*	
k	*Constant*	
D_θ	*volume (lattice) self diffusion coefficient*	
D	*diffusion coefficient*	cm^2/sec
D_O	*diffusivity Coefficient*	cm^2/sec
Q	*activation energy*	*(cal /mole /k)*
m	*mass of powder*	g
V_P	*Powder volume*	cm^3
m_g	*green mass of Compact*	g
V_g	*green volume of compact*	cm
w_t	*weight percent of elemental powders*	%
md	*dry mass of sample*	g
m_W	*met mass of sample*	g
m_s	*suspended mass of sample*	g
m_{sa}	*saturated mass of specimen*	g
LD	*die Cavity dimension (diameter)*	m
LS	*Sintered specimen dimension*	m
Hv	*Vicker`s hardness No.*	kg/mm^2
p	*load*	N
d	*average diameter of impression*	
HB	*Brinell hardness No.*	kg/mn^2
db	*average impression diameter before heating*	m
da	*average impression diameter after heating*	m
Lo	*original length of sample*	m
L_1	*Length after compression of specimen*	m
L_2	*Length after recovery heating of sample*	m
n	*strain hardening coefficient*	
$[D]$	*elastic stiffness matrix*	N/m^2
Y	*Yield strength*	MPa
E	*Elastic modulus*	GPa
b_M *and* C_M	*Material Coefficients for martensite phase*	
b_A*and* C_A	*Material Coefficient for austenite phase*	
b'_m, C'_m, b'_A, C'_A	*Material coefficients for R phase forward and backward transformation .*	
$F_{A\to M}$	*Flow pressure f material*	N/m^2

F	*Flow pressure for austenite to martensite transformation*	N/m^2
$F^{M\to A}$	*Flow pressure for martensite to austenite transformation .*	N/m^2
$C^{M\to A}$	*Stress to temperature coefficient for martensite to austenite transformation*	
Tr	*Trace operator*	
a	*length of unit cell*	*m*
b	*width of unit cell*	*m*
APDL	*Ansys parametric design language*	
U	*displacement in x direction*	*m*
V	*displacement in y direction*	*m*
C_1,C_2	*Constants refer to boundary conditions*	*m*
P	*apparent porosity*	*%*
LOM	*Light optical microscope*	

Greek Symbols

Symbols	***meaning***	***Units***
θ	*Contact angle*	*radian*
γ_{SG}	*Surface tension of solid –gas interface*	*N/m*
γ_{SL}	*Surface tension of solid –liquid interface*	*N/m*
γ_{LG}	*Surface tension of liquid –gas interface*	*N/m*
γ	*interfacial surface energy*	J/m^2
$\overline{\beta}$	*martensite phase in Cu-Al systems .*	
β	*Parent phase at high temperature in Cu-Al systems*	
η	*Viscosity*	*Pa.s*
σ	*Normal stress*	N/m^2
τ	*Shear stress*	N/m^2
ε	*Strain*	*%*
ε_{xy}	*Shear strain in x-y plane*	*%*
$[\theta]$	*thermo elastic tensor*	
ρ_A	*apparent density of powder*	g/cm^3
ρ_G	*green density of compact*	g/cm^3
ρ_{tB}	*Theoretical density of blended powders*	g/cm^3
p_g	*green porosity*	*%*
ρ_a	*apparent density of sintered compact*	g/cm^3

ρ_w	*water density*	g/cm^3
ε_r	*recovery strain*	%
β	*one dimensional back stress*	N/m^2
$\dot{\varepsilon}$	*strain rate*	*1/sec*
ε^{ain}	*inelastic nonlinear strain rate*	*1/sec*
$[\Omega]$	*range of strain result from martensite transformation*	
$[\Psi]$	*range of strain result and phase transformation*	
ζ	*volume percentage of martensite phase*	
η	*Volume percentage of R phase*	
ζ_M	*Martensite volume fraction*	%
ζ_A	*Austenite Volume fraction*	%
α	*material parameter shows the difference tension and Compression.* $(0 \to 1)$	
$\{\Delta\varepsilon^{\tau}\}$	*incremental transformation strain vector*	%
$\bar{\varepsilon}_L$	*Maximum transformation strain*	%
τ_{xy}	*shear stress in plane xy.*	N/m^2
$\sigma_s^{A\to M}$	*Martensite starting stress*	N/m^2
$\sigma_f^{A\to M}$	*martensite finishing stress*	N/m^2
$\sigma_f^{M\to A}$	*austenite starting stress*	N/m^2
$\sigma_f^{M\to A}$	*austenite finishing stress*	N/m^2

Subscript

s	*starting transformation*
f	*finishing transformation*
P	*Porous*
D	*Fully dense*
L	*Length*
M	*martensite phase*
A	*reverse austenite phase*
r	*recovery*
b	*before recovery heating*
a	*after recovery heating*
o	*original*
d	*dry*
s	*suspended*

Sa	*saturated*

w	*wet*
g	*green*
Tb	*theoretical for blended mixture*
A	*Apparent*
P	*Powder*
sl	*solid-liquid interphase*
sg	*solid –gas interphase*
lg	*liquid-gas interphase*
n	*neck between two Particle*
v	*volume*
t	*transformation*
s	*strain*

Super script symbols

$A \rightarrow M$	*Austenite to marten site phase transformation*
$M \rightarrow A$	*Martensite to reverse austenite phase transformation*
$\bullet$	*first derivative of time*
-	*degree of ordering of Martensite*
tr	*transformation*

Contents

NO.	Title	Page
	Acknowledgments	I
	Abstract	II
	List of symbols	III
	List of Contents	IV
	Chapter One : Introduction	**1-15**
1.1	General view	1
1.2	Shape memory effect	1
1.3	Shape memory alloys	6
1.4	Applications	9
1.5	Objectives	15
	Chapter two : Review of literature	**16-27**
2.1	General view	16
2.2	Ni-Ti based shape memory alloys	16
2.3	Copper-based shape memory alloys	19
2.4	Analysis of shape memory alloys	24
2.5	Summary	26
	Chapter three : theoretical Considerations	**28-84**
3.1	General view	28
3.2	Martensitic transformation	28
3.2.1	Microscopic perspective of martensite	29
3.2.1.1	Structure of martensite and morphology	34
3.2.1.2	Martensite crystallography	36
3.2.1.3	Martensite nucleation	38
3.2.1.4	Martensite growth	39
3.2.1.5	Origin of martensitic transformation .	39
3.2.2	Macroscopic perspective of Martensite	40
3.2.2.1	Stress- induced martensite and superelasticity	40
3.2.2.2	Martensite aging and stabilization	46
3.3	Martensitic transformation in Cu-based shape memory alloys.	47
3.4	Origin of shape memory alloys.	52
3.5	Copper-based shape memory alloys	56
3.5.1	Effect of alloying elements.	56
3.5.2	Effect of heat treatment	57
3.6	Powder metallurgy of Cu-based shape memory alloys	60
3.6.1	Preparation of copper powder.	60
3.6.1.1	Production of copper by the reduction of copper oxide	61
3.6.1.2	Production of copper powder by atomization	62
3.6.1.3	Production of copper powder by electrolysis	62
3.6.1.4	Production of copper powder by hydrometallurgical processes	63
3.6.2	Blending and mixing processes	63
3.6.3	Particle shape and powder density	65
3.6.4	Particles size and its distribution	66
3.6.5	Powder compaction of cu-based alloys	68
3.6.5.1	Die compaction	68

3.6.5.2	Isostatic pressing	71
3.6.5.3	Roll compacting	72
3.6.5.4	Powder extrusion	72
3.6.5.5	Powder forging	72
3.6.5.6	Hot isostatic pressing	73
3.6.6	Sintering of copper- based alloys	73
3.6.6.1	Stages of sintering	74
3.6.6.2	Mechanism of sintering	75
3.6.7	Liquid phase sintering	79
3.6.8	Homogenization during sintering	82
Chapter Four : (Experimental procedure)		**85-113**
4.1	General view	85
4.2	Materials	85
4.3	Equipments	86
4.4	Preparation of blended mixtures	87
4.5	Mixing	87
4.6	Compaction	90
4.7	Sintering	92
4.8	Heat treatment	96
4.8.1	betatizing heat treatment	96
4.8.2	Aging treatment	97
4.8.3	Step- quench heat treatment	97
4.8.4	Heat treatment including shape memory effect.	98
4.9.	Phase identification and analysis	98
4.10	LOM examination	99
4.11	Scanning electron microscopy	101
4.12	Physical test	101
4.12.1	Particle size and its distribution	101
4.12.2	Apparent density of powder and blended powders.	102
4.12.3	Green porosity and density	103
4.12.4	Pore size and pore distribution	104
4.12.5	Apparent density , porosity and water absorption of sintered compact.	105
4.12.6	Dimensional change of sintered compacts.	106
4.12.7	Electrical Resistance	106
4.12.8	Ultrasonic test	108
4.13	Mechanical tests	108
4.13.1	Microhardness measurements	108
4.13.2	Macrohardness measurements	108
4.13.2.1	Vicker's macrohardness test	109
4.13.2.2	Brinell macrohardness test	109
4.13.3	Compression test	109
4.13.4	Shape memory effect and shape recovery	111
Chapter Five : Modelling and Numerical simulation of shape memory alloys		**113-137**
5.1	General view	113
5.2	Shape memory models	113
5.2.1	Ozdemir model	113

5.2.2	*Cozzarelli model*	*115*
5.2.3	*Tanaka model*	*116*
5.2.4	*Auricchio model*	*117*
5.2.4.1	*Single variant martensite production*	*118*
5.2.4.2	*Austenite production.*	*119*
5.3	*Modeling of porous shape memory alloys*	*124*
5.4	*Unit cell Finite element method*	*125*
5.4.1	*Tetragonal (square) arrangement of pores*	*125*
5.4.2	*Hexagonal arrangement of pores.*	*125*
5.5	*Real representation of microstructure image using image analysis and processing*	*127*
5.5.1	*Image processing*	*127*
5.5.2	*Image Analysis*	*130*
5.6	*Finite element analysis of porous SMA using Ansys ver 9 software*	*131*
5.6.1	*Boundary conditions*	*132*
5.6.2	*Material properties*	*133*
5.7	*Verification of the SMA model used in this study.*	*135*
Chapter six : Results and Discussion		***138-350***
6.1	*General view*	*138*
6.2	*Results before sintering of compacts*	*138*
6.2.1	*Apparent density of elemental and blended powders.*	*138*
6.2.2	*Particle size and its distribution*	*140*
6.2.3	*Green density and green porosity of compacts*	*156*
6.2.3.1	*Effect of rate of loading*	*159*
6.2.3.2	*Effect of period of maximum load.*	*159*
6.2.4	*x-ray diffraction pattern of compacts*	*161*
6.2.5	*Microstructure of compacts and pore size and its distribution.*	*161*
6.3	*Results after sintering of compacts*	*161*
6.3.1	*x-ray diffraction analysis*	*163*
6.3.2	*Physical test results*	*170*
6.3.2.1	*Apparent density of sintered compacts*	*170*
6.3.2.2	*Apparent porosity and absorption of water*	*177*
6.3.2.3	*True porosity*	*186*
6.3.2.4	*Expansion of sintered compacts*	*190*
6.3.3	*Microstructure of sintered compacts*	*192*
6.3.4	*Pore size and its distribution*	*197*
6.3.5	*Vicker's macrohardness results*	*200*
6.4	*Effect of heat treatment after sintering .*	*202*
6.4.1	*X-ray diffraction patterns for Direct quench treatment.*	*202*
6.4.2	*Light optical microscope images for direct quench heat treatment.*	*233*
6.4.3	*Scanning electron microscope images*	*238*
6.4.4	*Hardness test results for direct quenching treatment*	*242*
6.4.5	*Electrical resistance test results*	*245*
6.4.6	*Ultrasonic test results*	*248*
6.4.7	*Shape memory effect and shape recovery*	*253*
6.5	*Aging heat treatment*	*288*

6.5.1	*X-ray diffraction for aged specimens*	*288*
6.5.2	*LOM image*	*292*
6.5.3	*SEM images*	*320*
6.5.4	*Vicker's macrohardness test results*	*320*
6.5.5	*Shape memory effect for aged treated specimens*	*324*
6.6	*Step- quenched heat treatment*	*324*
6.6.1	*x-ray diffraction patterns for step-quenched specimens*	*326*
6.6.2	*Light optical micrographs*	*329*
6.6.3	*SEM micrographs*	*334*
6.6.4	*Vickers's Marcohardness test results*	*334*
6.6.5	*Shape memory effect*	*335*
6.7	*Strain- temperature curves*	*338*
6.8	*Numerical results*	*340*
6.8.1	*Unit cell finite element results*	*340*
6.8.1.1	*Square arrangements of pores*	*340*
6.8.1.2	*Hexagonal arrangements of pores*	*341*
6.8.2	*Real representation of microstructure finite element analysis*	*341*
Chapter seven : conclusions and Recommendations for future work.		
7.1	*Conclusions*	*351*
7.2	*Suggestions and recommendations for future work*	*353*
	References	*354*
	Appendix A : powder diffraction data Cards	*A1*

04-0850 Wavelength= 1.5405

Ni

Nickel

Nickel, syn

Rad.: CuKa1 λ: 1.5405 Filter: Ni Beta d-sp:

Cut off: Int.: Diffract. I/Icor.:

Ref: Swanson, Tatge, Natl. Bur. Stand. (U.S.), Circ. 539, I, 13 (1953)

Sys.: Cubic S.G.: Fm3m (225)

a: 3.5238 b: c: A: C:

α: β: γ: Z: 4 mp:

Ref: Ibid.

Dx: 8.911 Dm: SS/FOM: F_8 = 87(.0115 , 8)

Color: White

Pattern taken at 26 C. Sample obtained from Johnson Matthey Company, Ltd. CAS #: 7440-02-0. Spectrographic analysis show <0.01% each of Mg, Si and Ca. Cu type. Gold group, gold subgroup. PSC: cF4. Mwt: 58.70. Volume[CD]: 43.76.

2θ	Int	h	k	l
44.505	100	1	1	1
51.844	42	2	0	0
76.366	21	2	2	0
92.939	20	3	1	1
98.440	7	2	2	2
121.922	4	4	0	0
144.655	14	3	3	1
155.632	15	4	2	0

ICDD. 1997 JCPDS-International Centre for Diffraction Data. All rights reserved
PCPDFWIN v. 1.30

18-0019 Wavelength= 1.5418

Ti(Cu,Al)2

Aluminum Copper Titanium

Rad.: CuKa λ: 1.5418 Filter: Ni Beta d-sp:

Cut off: Int.: Estimation I/Icor.:

Ref: Rieger et al., Monatsh. Chem., 95, 1573 (1964)

Sys.: Hexagonal S.G.: $P6_3/mmc$ (194)

a: 5.023 b: c: 8.130 A: C: 1.6186

α: β: γ: Z: 4 mp:

Ref: Ibid.

Dx: Dm: SS/FOM: F_{27} = 5(0.117 , 46)

Mg Zn2 type. PSC: hP12. Volume[CD]: 177.64.

2θ	Int	h	k	l	2θ	Int	h	k	l
20.416	5	1	0	0	86.895	5	1	0	7
22.00	20	0	0	2	88.985	50	3	1	3
23.224	5	1	0	1	91.524	40	4	0	1
35.832	80	1	1	0	92.521	40	2	2	4
39.237	100	1	0	3	96.289	5	3	1	4
41.458	20	2	0	0					
42.333	100	1	1	2					
43.246	100	2	0	1					
44.637	50	0	0	4					
47.450	55	2	0	2					
49.510	40	1	0	4					
53.830	50	2	0	3					
56.039	5	2	1	0					
60.863	10	1	0	5					
64.434	50	3	0	0					
66.661	60	2	1	3					
68.887	60	3	0	2					
69.293	20	0	0	6					
72.676	60	2	0	5					
74.268	10	2	1	4					
75.868	60	2	2	0					
84.368	50	2	0	6					

ICDD. 1997 JCPDS-International Centre for Diffraction Data. All rights reserved
PCPDFWIN v. 1.30

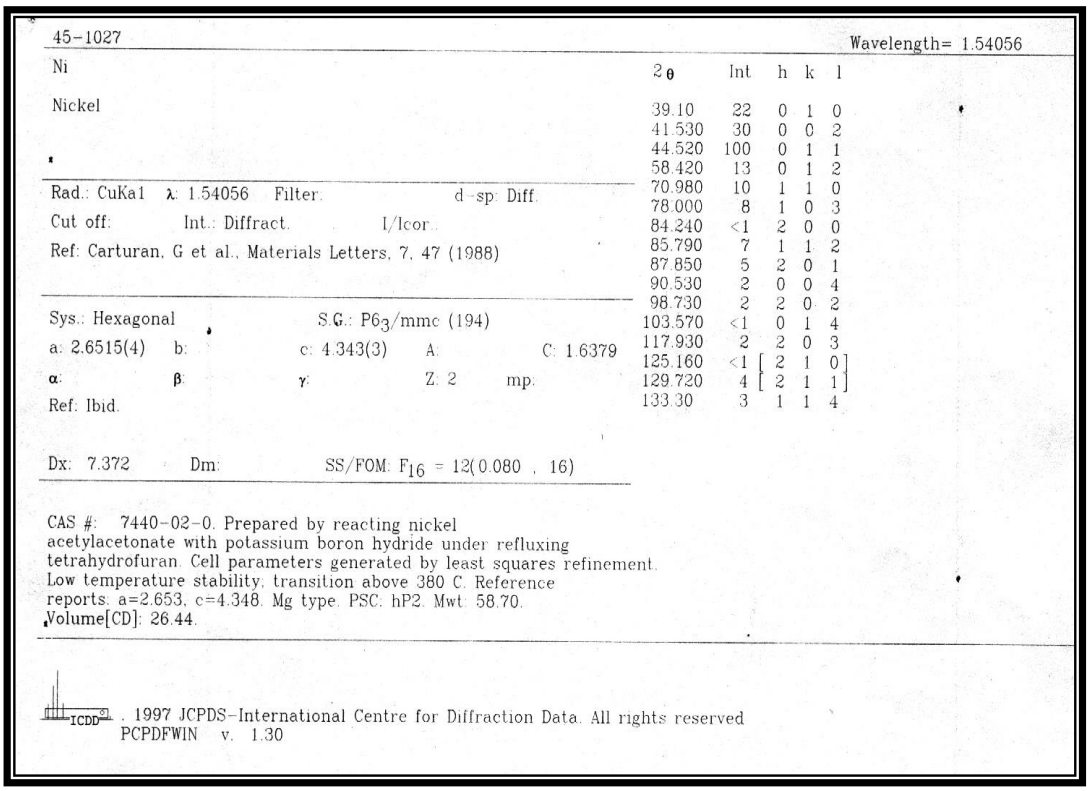

45-1027 Wavelength= 1.54056

Ni

Nickel

Rad.: CuKa1 λ: 1.54056 Filter: d-sp: Diff.

Cut off: Int.: Diffract. I/Icor.:

Ref: Carturan, G et al., Materials Letters, 7, 47 (1988)

Sys.: Hexagonal S.G.: $P6_3/mmc$ (194)

a: 2.6515(4) b: c: 4.343(3) A: C: 1.6379

α: β: γ: Z: 2 mp:

Ref: Ibid.

Dx: 7.372 Dm: SS/FOM: F_{16} = 12(0.080 , 16)

CAS #: 7440-02-0. Prepared by reacting nickel acetylacetonate with potassium boron hydride under refluxing tetrahydrofuran. Cell parameters generated by least squares refinement. Low temperature stability, transition above 380 C. Reference reports: a=2.653, c=4.348. Mg type. PSC: hP2. Mwt: 58.70. Volume[CD]: 26.44.

2θ	Int	h	k	l
39.10	22	0	1	0
41.530	30	0	0	2
44.520	100	0	1	1
58.420	13	0	1	2
70.980	10	1	1	0
78.000	8	1	0	3
84.240	<1	2	0	0
85.790	7	1	1	2
87.850	5	2	0	1
90.530	2	0	0	4
98.730	2	2	0	2
103.570	<1	0	1	4
117.930	2	2	0	3
125.160	<1	[2	1	0]
129.720	4	[2	1	1]
133.30	3	1	1	4

ICDD . 1997 JCPDS-International Centre for Diffraction Data. All rights reserved
PCPDFWIN v. 1.30

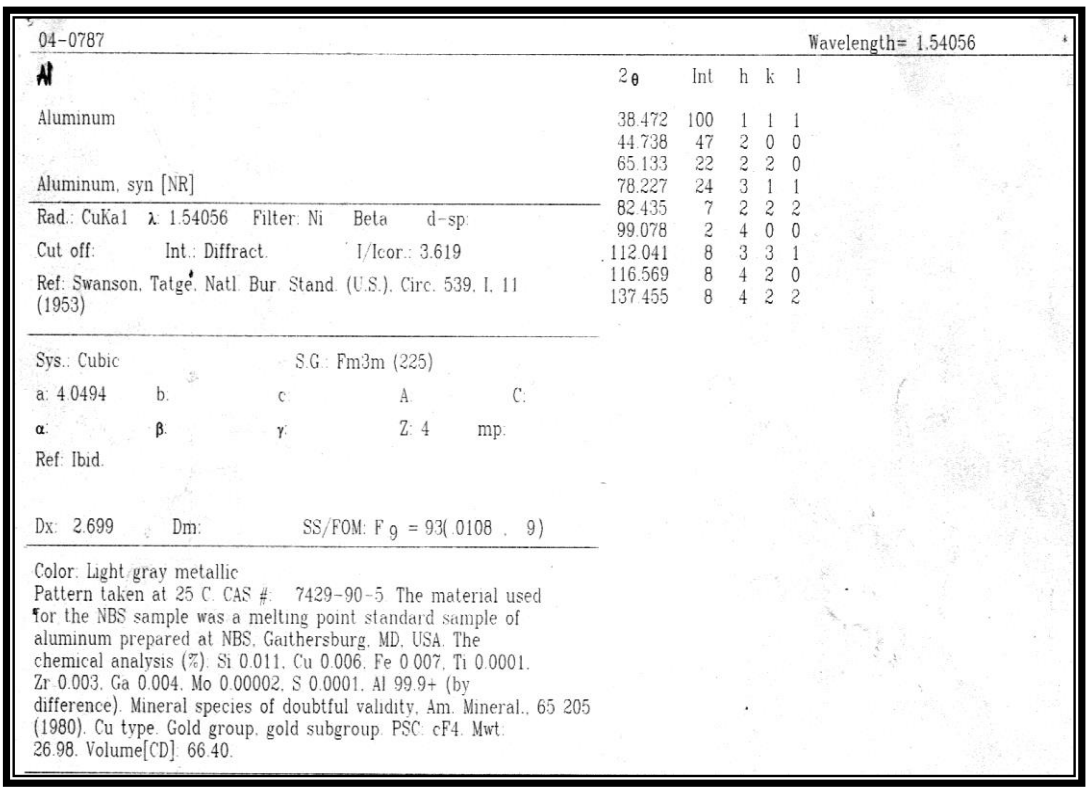

04-0787 Wavelength= 1.54056

Al

Aluminum

Aluminum, syn [NR]

Rad.: CuKa1 λ: 1.54056 Filter: Ni Beta d-sp:

Cut off: Int.: Diffract. I/Icor.: 3.619

Ref: Swanson, Tatge, Natl. Bur. Stand. (U.S.), Circ. 539, I, 11 (1953)

Sys.: Cubic S.G.: Fm3m (225)

a: 4.0494 b: c: A: C:

α: β: γ: Z: 4 mp:

Ref: Ibid.

Dx: 2.699 Dm: SS/FOM: F_9 = 93(.0108 , 9)

Color: Light gray metallic
Pattern taken at 25 C. CAS #: 7429-90-5. The material used for the NBS sample was a melting point standard sample of aluminum prepared at NBS, Gaithersburg, MD, USA. The chemical analysis (%): Si 0.011, Cu 0.006, Fe 0.007, Ti 0.0001, Zr 0.003, Ga 0.004, Mo 0.00002, S 0.0001, Al 99.9+ (by difference). Mineral species of doubtful validity, Am. Mineral., 65 205 (1980). Cu type. Gold group, gold subgroup. PSC: cF4. Mwt: 26.98. Volume[CD]: 66.40.

2θ	Int	h	k	l
38.472	100	1	1	1
44.738	47	2	0	0
65.133	22	2	2	0
78.227	24	3	1	1
82.435	7	2	2	2
99.078	2	4	0	0
112.041	8	3	3	1
116.569	8	4	2	0
137.455	8	4	2	2

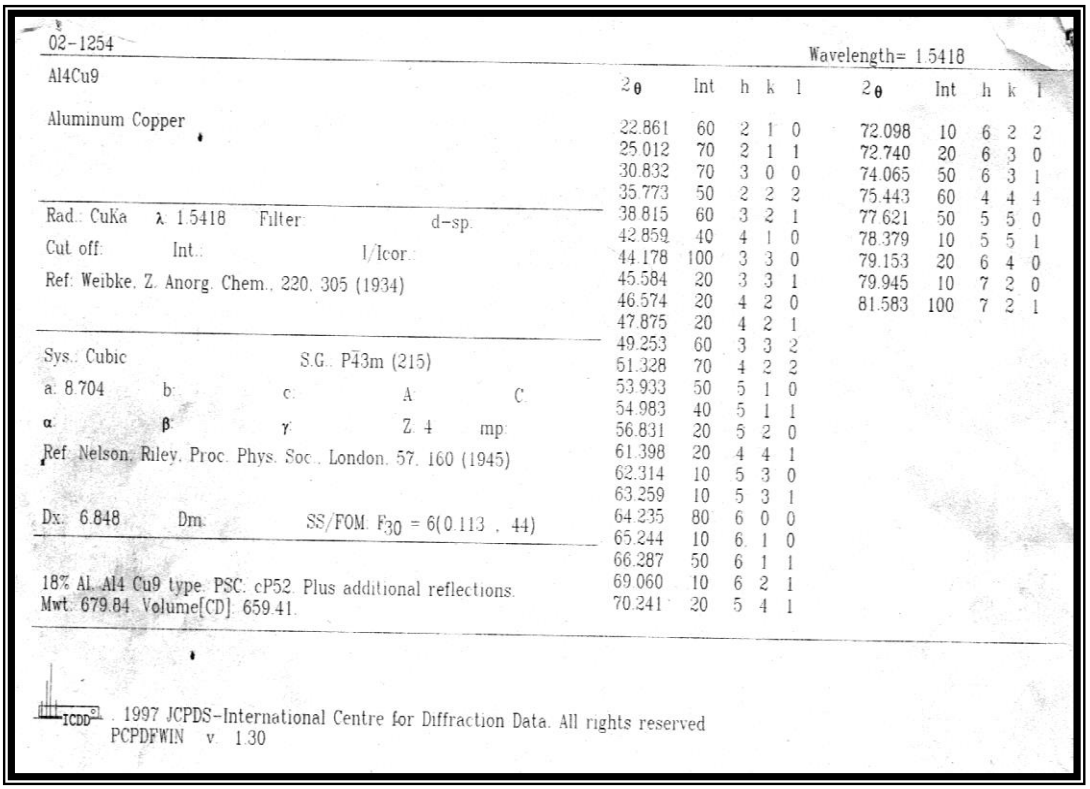

02-1254

Al4Cu9

Aluminum Copper

Rad.: CuKa λ: 1.5418 Filter: d-sp:

Cut off: Int.: I/Icor.:

Ref: Weibke, Z. Anorg. Chem., 220, 305 (1934)

Sys.: Cubic S.G.: P43m (215)

a: 8.704 b: c: A: C:

α: β: γ: Z: 4 mp:

Ref: Nelson, Riley, Proc. Phys. Soc., London, 57, 160 (1945)

Dx: 6.848 Dm: SS/FOM: F_{30} = 6(0.113 , 44)

18% Al. Al4 Cu9 type. PSC: cP52. Plus additional reflections.
Mwt: 679.84. Volume[CD]: 659.41.

Wavelength= 1.5418

2θ	Int	h	k	l	2θ	Int	h	k	l
22.861	60	2	1	0	72.098	10	6	2	2
25.012	70	2	1	1	72.740	20	6	3	0
30.832	70	3	0	0	74.065	50	6	3	1
35.773	50	2	2	2	75.443	60	4	4	4
38.815	60	3	2	1	77.621	50	5	5	0
42.859	40	4	1	0	78.379	10	5	5	1
44.178	100	3	3	0	79.153	20	6	4	0
45.584	20	3	3	1	79.945	10	7	2	0
46.574	20	4	2	0	81.583	100	7	2	1
47.875	20	4	2	1					
49.253	60	3	3	2					
51.328	70	4	2	2					
53.933	50	5	1	0					
54.983	40	5	1	1					
56.831	20	5	2	0					
61.398	20	4	4	1					
62.314	10	5	3	0					
63.259	10	5	3	1					
64.235	80	6	0	0					
65.244	10	6	1	0					
66.287	50	6	1	1					
69.060	10	6	2	1					
70.241	20	5	4	1					

ICDD©. 1997 JCPDS-International Centre for Diffraction Data. All rights reserved
PCPDFWIN v. 1.30

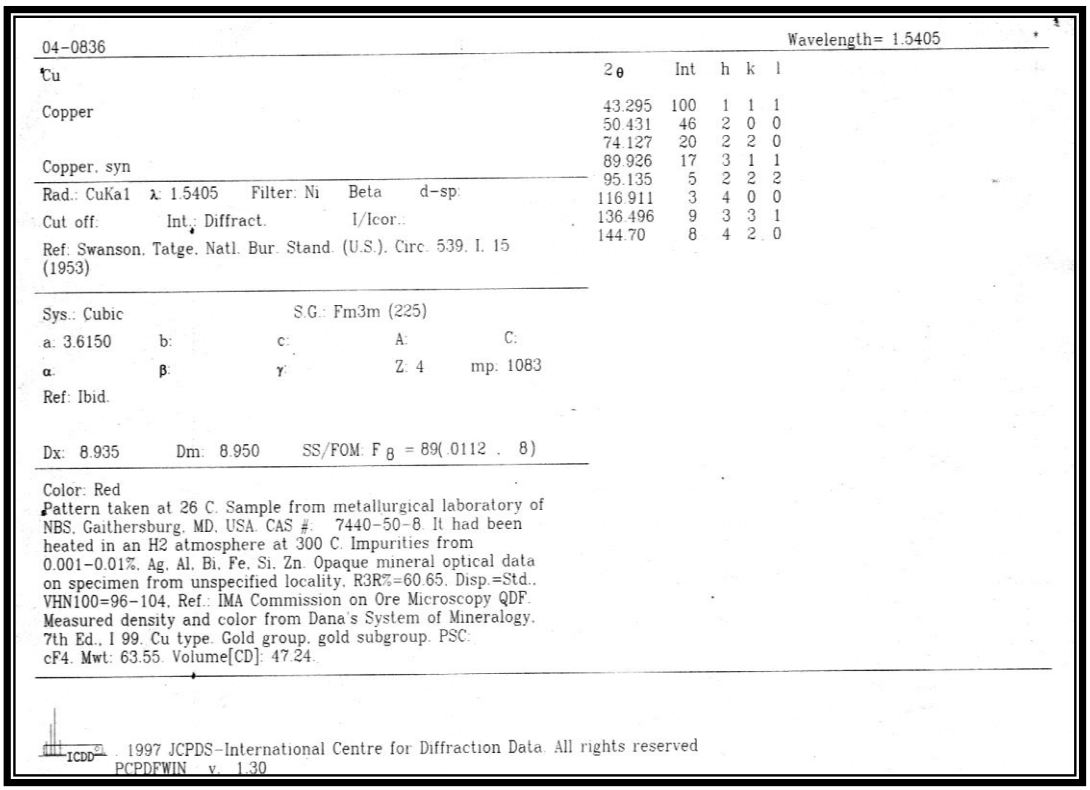

04-0836

Cu

Copper

Copper, syn

Rad.: CuKa1 λ: 1.5405 Filter: Ni Beta d-sp:

Cut off: Int.: Diffract. I/Icor.:

Ref: Swanson, Tatge, Natl. Bur. Stand. (U.S.), Circ. 539, I, 15 (1953)

Sys.: Cubic S.G.: Fm3m (225)

a: 3.6150 b: c: A: C:

α: β: γ: Z: 4 mp: 1083

Ref: Ibid.

Dx: 8.935 Dm: 8.950 SS/FOM: F_8 = 89(.0112 , 8)

Color: Red
Pattern taken at 26 C. Sample from metallurgical laboratory of NBS, Gaithersburg, MD, USA. CAS #: 7440-50-8. It had been heated in an H2 atmosphere at 300 C. Impurities from 0.001-0.01%: Ag, Al, Bi, Fe, Si, Zn. Opaque mineral optical data on specimen from unspecified locality. R3R%=60.65. Disp.=Std., VHN100=96-104. Ref.: IMA Commission on Ore Microscopy QDF. Measured density and color from Dana's System of Mineralogy, 7th Ed., I 99. Cu type. Gold group, gold subgroup. PSC: cF4. Mwt: 63.55. Volume[CD]: 47.24.

Wavelength= 1.5405

2θ	Int	h	k	l
43.295	100	1	1	1
50.431	46	2	0	0
74.127	20	2	2	0
89.926	17	3	1	1
95.135	5	2	2	2
116.911	3	4	0	0
136.496	9	3	3	1
144.70	8	4	2	0

ICDD©. 1997 JCPDS-International Centre for Diffraction Data. All rights reserved
PCPDFWIN v. 1.30

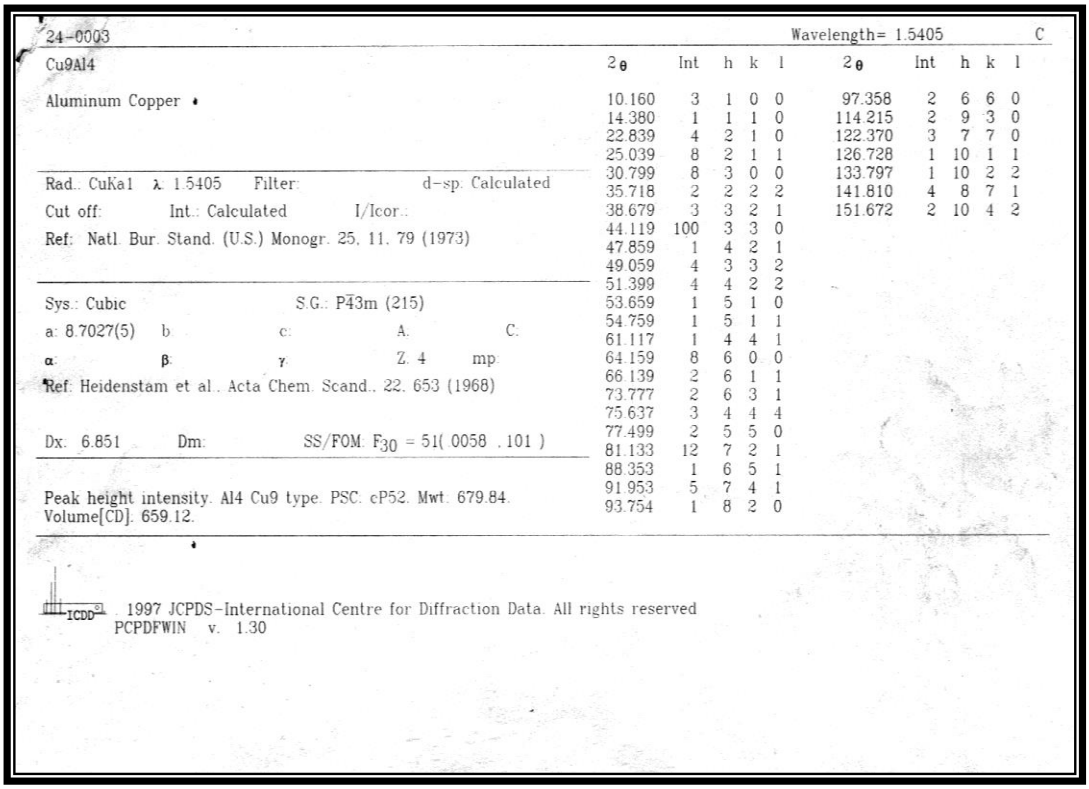

24-0003 Wavelength= 1.5405 C

Cu9Al4

Aluminum Copper

Rad.: CuKa1 λ: 1.5405 Filter: d-sp: Calculated

Cut off: Int.: Calculated I/Icor.:

Ref: Natl. Bur. Stand. (U.S.) Monogr. 25, 11, 79 (1973)

Sys.: Cubic S.G.: P$\bar{4}$3m (215)

a: 8.7027(5) b: c: A: C:

α: β: γ: Z: 4 mp:

Ref: Heidenstam et al., Acta Chem. Scand., 22, 653 (1968)

Dx: 6.851 Dm: SS/FOM: F_{30} = 51(.0058 , 101)

Peak height intensity. Al4 Cu9 type. PSC: cP52. Mwt: 679.84.
Volume[CD]: 659.12.

2θ	Int	h	k	l	2θ	Int	h	k	l
10.160	3	1	0	0	97.358	2	6	6	0
14.380	1	1	1	0	114.215	2	9	3	0
22.839	4	2	1	0	122.370	3	7	7	0
25.039	8	2	1	1	126.728	1	10	1	1
30.799	8	3	0	0	133.797	1	10	2	2
35.718	2	2	2	2	141.810	4	8	7	1
38.679	3	3	2	1	151.672	2	10	4	2
44.119	100	3	3	0					
47.859	1	4	2	1					
49.059	4	3	3	2					
51.399	4	4	2	2					
53.659	1	5	1	0					
54.759	1	5	1	1					
61.117	1	4	4	1					
64.159	8	6	0	0					
66.139	2	6	1	1					
73.777	2	6	3	1					
75.637	3	4	4	4					
77.499	2	5	5	0					
81.133	12	7	2	1					
88.353	1	6	5	1					
91.953	5	7	4	1					
93.754	1	8	2	0					

ICDD 1997 JCPDS-International Centre for Diffraction Data. All rights reserved
PCPDFWIN v. 1.30

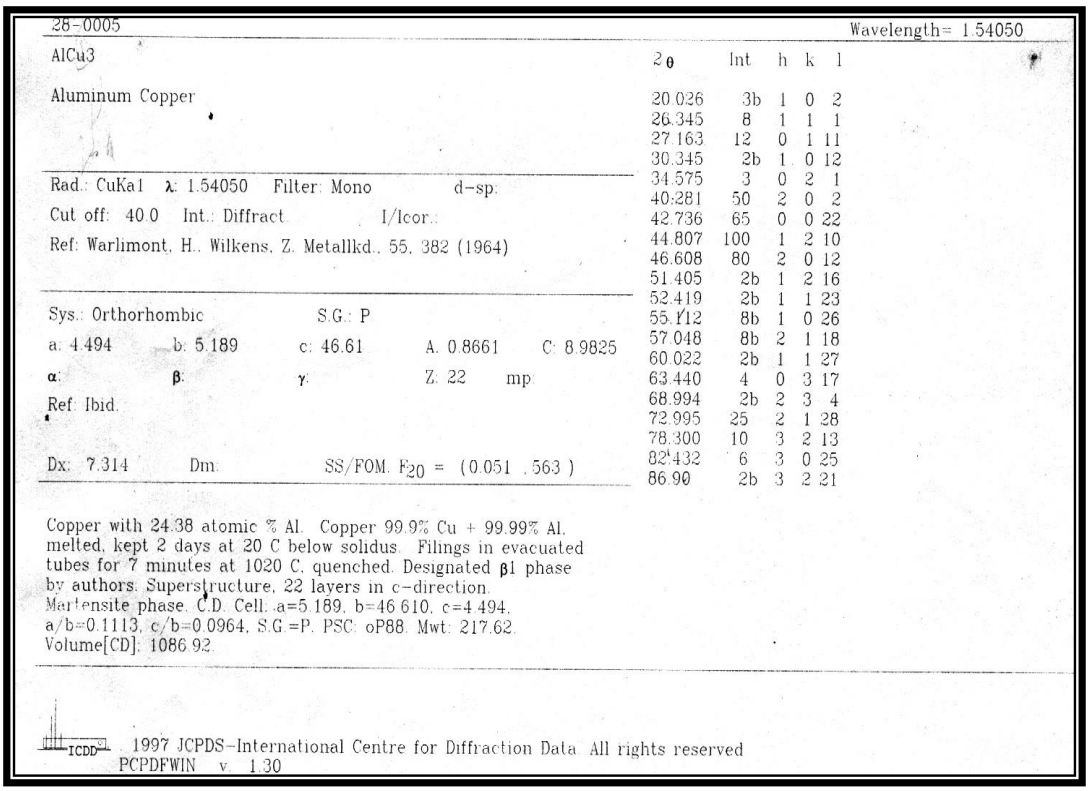

28-0005 Wavelength= 1.54050

AlCu3

Aluminum Copper

Rad.: CuKa1 λ: 1.54050 Filter: Mono d-sp:

Cut off: 40.0 Int.: Diffract. I/Icor.:

Ref: Warlimont, H., Wilkens, Z. Metallkd., 55, 382 (1964)

Sys.: Orthorhombic S.G.: P

a: 4.494 b: 5.189 c: 46.61 A: 0.8661 C: 8.9825

α: β: γ: Z: 22 mp:

Ref: Ibid.

Dx: 7.314 Dm: SS/FOM: F_{20} = (0.051 , 563)

Copper with 24.38 atomic % Al. Copper 99.9% Cu + 99.99% Al, melted, kept 2 days at 20 C below solidus. Filings in evacuated tubes for 7 minutes at 1020 C, quenched. Designated β1 phase by authors. Superstructure, 22 layers in c-direction. Martensite phase. C.D. Cell: a=5.189, b=46.610, c=4.494, a/b=0.1113, c/b=0.0964, S.G.=P. PSC: oP88. Mwt: 217.62. Volume[CD]: 1086.92.

2θ	Int	h	k	l
20.026	3b	1	0	2
26.345	8	1	1	1
27.163	12	0	1	11
30.345	2b	1	0	12
34.575	3	0	2	1
40.281	50	2	0	2
42.736	65	0	0	22
44.807	100	1	2	10
46.608	80	2	0	12
51.405	2b	1	2	16
52.419	2b	1	1	23
55.112	8b	1	0	26
57.048	8b	2	1	18
60.022	2b	1	1	27
63.440	4	0	3	17
68.994	2b	2	3	4
72.995	25	2	1	28
78.300	10	3	2	13
82.432	6	3	0	25
86.90	2b	3	2	21

ICDD 1997 JCPDS-International Centre for Diffraction Data. All rights reserved
PCPDFWIN v. 1.30

18-0019 Wavelength= 1.5418

Ti(Cu,Al)2

Aluminum Copper Titanium

Rad.: CuKa λ: 1.5418 Filter: Ni Beta d-sp:

Cut off: Int.: Estimation I/Icor.:

Ref: Rieger et al., Monatsh. Chem., 95, 1573 (1964)

Sys.: Hexagonal S.G.: $P6_3/mmc$ (194)

a: 5.023 b: c: 8.130 A: C: 1.6186

α: β: γ: Z: 4 mp:

Ref: Ibid.

Dx: Dm: SS/FOM: F_{27} = 5(0.117 , 46)

Mg Zn2 type. PSC: hP12. Volume[CD]: 177.64.

2θ	Int	h	k	l	2θ	Int	h	k	l
20.416	5	1	0	0	86.895	5	1	0	7
22.00	20	0	0	2	88.985	50	3	1	3
23.224	5	1	0	1	91.524	40	4	0	1
35.832	80	1	1	0	92.521	40	2	2	4
39.237	100	1	0	3	96.289	5	3	1	4
41.458	20	2	0	0					
42.333	100	1	1	2					
43.246	100	2	0	1					
44.637	50	0	0	4					
47.450	55	2	0	2					
49.510	40	1	0	4					
53.830	50	2	0	3					
56.039	5	2	1	0					
60.863	10	1	0	5					
64.434	50	3	0	0					
66.661	60	2	1	3					
68.887	60	3	0	2					
69.293	20	0	0	6					
72.676	60	2	0	5					
74.268	10	2	1	4					
75.868	60	2	2	0					
84.368	50	2	0	6					

ICDD. 1997 JCPDS-International Centre for Diffraction Data. All rights reserved
PCPDFWIN v. 1.30

Al5CuTi2

Aluminum Copper Titanium

Rad.: λ: Filter: d-sp:

Cut off: Int.: I/Icor.:

Ref: Tarnacki, J., Kim, Y.-W., Scr. Metall., 22, 329 (1988)

Sys.: Cubic S.G.: Pm3m (221)

a: 3.927 b: c: A: C:

α: β: γ: Z: 0.5 mp:

Ref: Ibid.

Dx: 4.034 Dm: SS/FOM: F γ = 6(0.127 , 9)

0 assigned because pattern contains several unindexed reflections probably from second Cu-rich phase. Prepared by arc melting pure elements in an Ar atmosphere in a copper crucible. Alloys were prepared by rapid solidification under pressurized He. Chemical analysis (wt.%): Al 43.6, Cu 22.2, Ti 34.1. Contains copper rich second phase. Au Cu3 type. PSC: cP4. To replace 42-1069. Mwt: 294.25. Volume[CD]: 60.56.

2θ	Int	h	k	l
22.625	16	1	0	0
32.199	2	1	1	0
38.990	3			
39.705	100	1	1	1
44.178	4			
44.406	3			
46.322	100	2	0	0
51.954	3	2	1	0
67.367	14	2	2	0
80.754	24	3	1	1
85.099	5			

ICDD. 1997 JCPDS-International Centre for Diffraction Data. All rights reserved
PCPDFWIN v. 1.30

Introduction

1.1General view

During the early 1960 ´s ,the Naval Ordnance Laboratory discovered what is commonly referred to as the shape memory effect (SME) in binary NiTi alloys. This alloy ,dubbed " Nitinol" from [nickel- Titanium _Naval Ordnance Laboratory] ,exhibited a remarkable ability to recover its original dimensions after having been deformed ,simply by heating it above a certain transformation temp.[Buehler et al .1963].This alloy also exhibited drastic damping changes as a function of temperature .This important discovery inspired a greet deal of interest in understanding and developing smart materials with shape memory effect .

In recent years an increased efforts in engineering have been directed toward multi functional materials and so called smart structures which is defined as an assembly or its components which serve an engineering function in which the structure possesses an inherent ability to sense ,diagnose and actuate in order to perform their function [Addington and Schodek ,2005].In the case of an airplane wing ,for example ,the main purpose is to provide lift but it also serves as a container for the fuel.

1.2 Shape memory effect:

one of the recent discoveries in multifunctional materials is "shape memory alloys" (SMA).These alloys describe a unique group of materials which execute a solid to solid phase transformation of their crystallographic structure from the parent phase to another phase and back in response to temperature or stress.[Wayman .and Duerig, 1990].This property allows the materials to be

heavily deformed and regain its original shape upon heating .In other words shape memory refers to the ability of certain materials to remember a shape even after rather severe deformations, once deformed at low temperature these materials will stay deformed until heated where upon they will spontaneously return to their original predeformation shape .The basis for the shape memory effect is that the materials can easily transform to and from martensite phase.[Miyazaki,1999].Shape memory effect is associated with the crystallographically reversible nature of the martensitic transformation which appears in shape memory alloys. Such crystallographically reversible martensitic transformation was especially named thermoelastic martensitic transformation [Otsuka and Ren,1999].The martensitic transformation itself is not a new phenomenon ,but was first found longtime ago in a steel which was heat treated at a high temperature (austenite phase) followed by rapid quenching, the martensitic transformation in most iron and steels is not crystallographically reversible so that they will not show the shape memory effect .The quenched steel revealed a fine structure which was formed by the martensitic transformation and was named as martensite after the discoverer Adolf Martens .Which consists of fine structure that has long been used for strengthening steels .[Higgins,1983].

The martensitic transformation is a diffusionless transformation described by a shear-like mechanism as shown in Fig.(1.1) .When the parent phase (high temperature phase (Austenite)in Fig(1.1a) is cooled to some critical temperature called Ms(the temperature at which the martensitic phase started to form upon cooling), the structure changes into martensite which is lower temperature phase with lower symmetry as shown in Fig.(1.1b). Since the parent phase has higher symmetry than the martensitic phase ,multi formation of martensites with the same structure in different orientation is possible [Otsuka.and kakeshita,2002]

.These are called variants or domains of martensites .In fact, two or four variants of martensites are usually formed side by side as shown in Fig. (1,b). In order to accommodate elastic strains around the martensites .This is called self–accommodation.[Porter and Easterling 1992].The two neighboring variants are twin-related to each other and may contribute to deformation if the interface is mobile under stress.

The martensitic transformation is divided into two categories : thermoelastic and non thermoelastic .The thermoelastic phase transformation is characterized by a small temperature hysteresis (several ten of degrees)a mobile twin interface and a crystallographically reversible transformation and vice – versa for non thermo elastic transformation.[Otsuka.and kakeshita,2002].The shape memory and super elasticity effects are characteristic of thermo elastic transformation. The characteristic temperatures of a martensitic transformation are defined as follows:

M_s: martensite –start temperature upon cooling.

M_f: martensite –finish temperature upon cooling.

A_s: reverse-transformation start temperature upon heating .

A_f: reverse-transformation finish temperature upon heating .

When a unidirectional stress is applied to a martensitic specimen as shown in Fig.(1.2a).There is a critical value where upon the detwinning process of martensitic variants takes place .This process consists in the spatial re-orientation of the original martensitic variants .If there is a performed direction for the occurrence of the transformation often associated with a state of stress, only the most favorable variant is formed. The product phase is then termed single-variant martensite and it is characterized by a detwinned structure. During such a process ,the stress remains practically constant until the martensite is fully detwinned (theoretically having a single variant aligned with the strain

direction).Further straining causes the elastic loading of detwinned martensite. upon unloading , a large residual strain remains however, by heating above A_f ,martensite transforms into high temperature phase (Austenite) and the specimen recovers its initial undeformed shape. This shape is kept during cooling below M_f when the material re-transforms into twinned martensite this phenomenon is named as shape memory effect.[Lukkassen, and Meidell,2003] .

When a unidirectional stress is applied to an austenitic specimen as shown in Fig. (1.2b). at temperature greater than A_f ,there is a critical value where upon a transformation from austenite to detwinned martensite occurs .A_s deformation proceeds in isothermal conditions, the stress remains almost constant until the material is fully transformed .Further straining causes the elastic loading of detwinned martensite .Upon unloading since martensite is unstable without stress at temperature greater than A_f ,a reverse transformation takes place, but at a lower stress level than during loading so that a hysteretic effect is produced .If the material temperature is greater than A_f ,the strain attained during loading is completely and spontaneously recovered at the end of unloading. This remarkable process gives rise to an energy absorption capacity with zero residual strain which is termed super elasticity or pseudo elasticity .If the material temperature is less than A_f only a part of stress-induced martensite retransforms into austenite .A residual strain is then found at the end of unloading which can be recovered by heating above A_f .This phenomenon is generally referred to as partial super elasticity .[Penrod,2003].

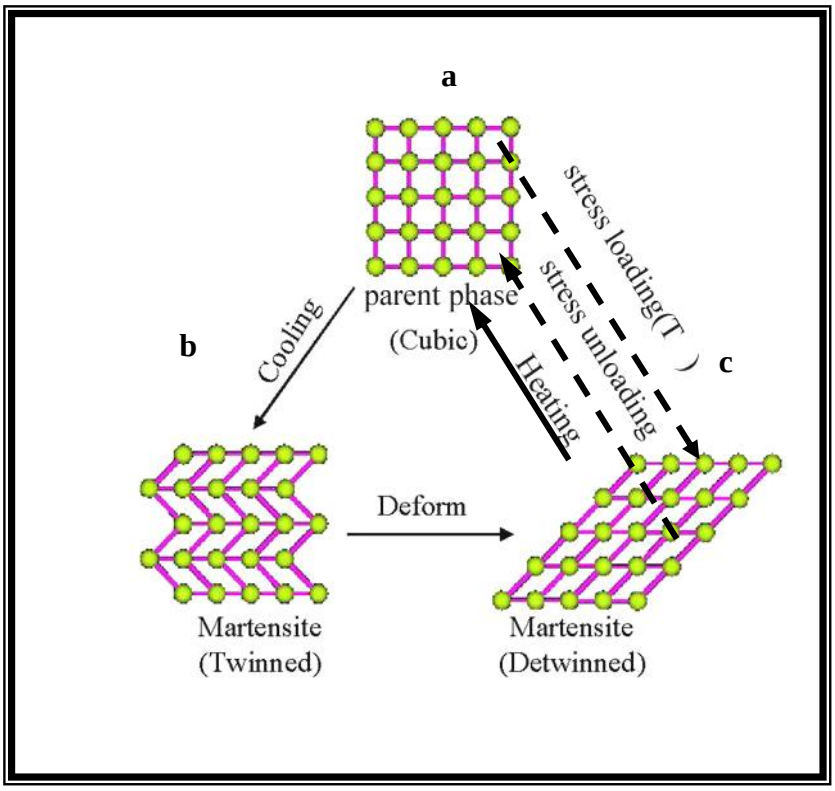

Fig.(1.1)a-c schematic illustration of mechanism of the shape memory effect and super elasticity(Penrod,2003)

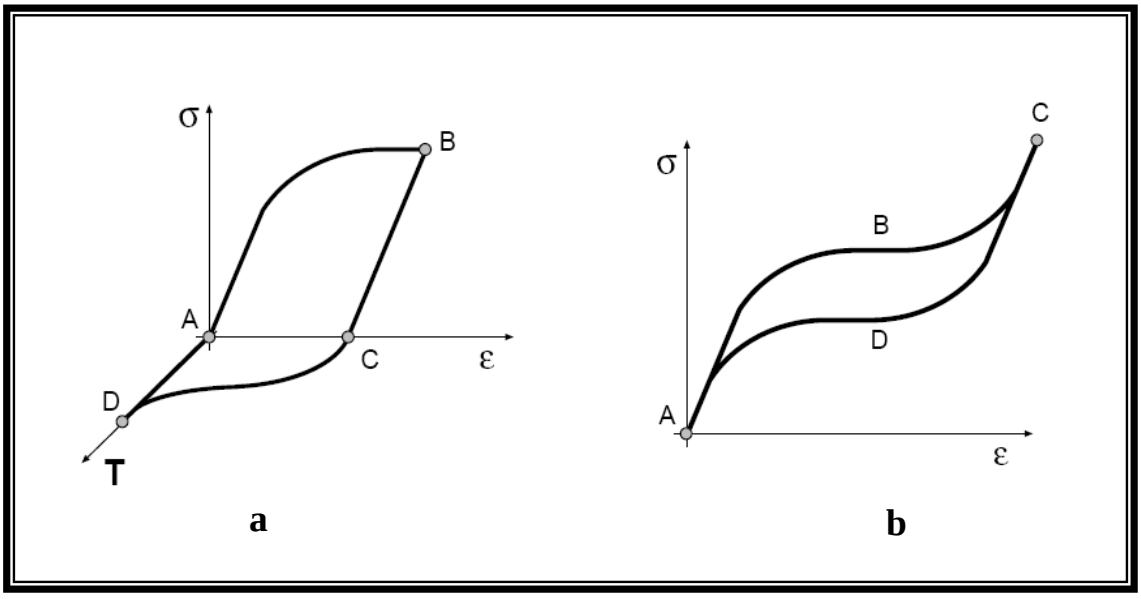

Fig .(1.2) schematic of : a. Shape memory effect at the end of a mechanical loading-unloading path ABC preformed at constant low temp .,material presents residual deformation (AC) which can be recovered through a thermal cycle (CDA)b. Super elastic effect .At a constant temperature the material is able to undergo large deformation with zero fild permanent strain. Note hysteresis loop.(Auricchio et al 1997)

1.3 Shape memory alloys

Although the shape memory effect was first discovered in a Au-Cd alloy in 1951[Porter and Easterling,1992] research became much more active after the effect was found in NiTi alloy in 1963 ,during the past decade smart materials and structures or intelligent material systems have received increasing attention because of their great scientific and technological significance .A smart structure is a structure system with macroscopically embedded or built-in sensors ,actuators and is usually monitored by an external microprocessor. While smart material refers to the material which has intrinsic sensing ,actuating and controlling in its microstructure [WEI et al.,1998] .

Shape memory alloys (SMA) are one of the major elements of smart materials due to their unusual properties such as the shape memory effect. Super elasticity ,high damping capacity and adaptive properties which are due to the reversible phase transitions in the alloys. Shape memory alloys can be classified into :

I.Bulk shape memory alloys:

This category include the following alloys:

1.Ni-Ti system alloys:

The nickel-titanium system is based on the equiatomic compound of nickel and titanium [Erbstoeszer et al ,2000] .Besides the ability of tolerating quite large amounts of shape memory strain, Nitinol alloys show high stability in cyclic applications possess an elevate electrical resistivity and are corrosion resistance. They also have a moderate solubility range, enabling changes in composition and alloying with other elements to modify bulk shape memory and their mechanical behavior. Third metal is usually added to the binary system in order to improve its properties .In particular ,a nickel quantity up to an extra 1% is the most common modification .This increases yield strength of the austenite phase while at the same time depressing the transformation temperatures.

Manufacture of NiTi alloys is not easy task as many machining techniques can only be used with difficulty. This facts explains the reason for the high cost of such alloys.[Scheiger,2002] .

When nickel in NiTi shape memory alloys is substituted by palladium ,platinum and gold metals by up to 50at% and titanium in NiTi is substituted by hafnium and zirconium by up to 20at% the martensitic transformation temperatures can be increased to as high as 600 °C while the shape memory performance still exists [Lindquist, and Wayman, 1990Queted in Wei et al,1998] .Shape memory effect of these alloys is in the range of (8-10 %).

2. Copper-based alloys:

Copper–based shape memory alloys have some advantages such as low cost and simple fabrication procedure compared to NiTi alloys. Copper zinc aluminum (CuZnAl) alloys are the first copper-based SMA_s to be commercially exploited[Humbeek et al ,1984] .This alloy originally comes from the copper-aluminum binary alloy, a system despite its shape memory characteristics ,has transformation temperatures considered to high for practical use. CuZnAl alloys have the advantage that they are made from relatively cheap metals using conventional metallurgical processes. Compared to other SMA_s , Cu Zn Al alloys have modest shape properties with a maximum recoverable strain of approximately (4 - 7%) ,also without the addition of grain growth control additives, their grain size can be quite large leading to brittleness problems.[Jianxin et al 1988].

Copper aluminum Nickel (CuAlNi) alloys have undergone extensive development and are now preferred to CuZnAl alloys [Schweiger,2002]. They are very popular for their wide range of useful transformation temperatures and because they are the only commercial shape memory alloys used above 100 °C . Despite CuAlNi alloys are made from relatively inexpensive metals, their processing is particularly difficult to machine. It can only be hot worked and the final heat treatment has to be tightly controlled to produce an alloy with the

desired transformation temperatures. These difficulties have mode this system more expansive than CuAlZn even if it is still cheaper than Nitinol.[Sampath,2005] .The other commercial alloys include CuAlMn and CuAlBe alloys .however ,the applications of these alloys have been much limited mainly for two reasons:

1. The poor ductility and workability of the polycrystalline alloys resulting from coarse grain and precipitation of brittle second phase particles.
2. The metastability of both the parent and martensite phases in the alloys which result in complicated aging effects and hence an undesirable reliability of the performance of the alloys [Wei. et al.,1998]. Because CuAlNi alloys have a much better thermal stability and higher operating temperatures than CuAlZn alloys, they may become one candidate for practical high temperature. Shape memory alloy if only their poor processibility can be improved. The group of these alloys has been taken in this study .

3. Iron base alloys:

Because price is one of the key considerations for applications ,the low cost iron based shape memory alloys have attracted considerable attention in recent years, and now some of them are also to a market introduction.[Zhao,2000].Of particular interest are Fe-Mn-Si,Fe-Ni-Mn and Fe-Cr-Ni-Mn-Si-Co.After complex thermo mechanical treatment ,these alloys exhibit nearly perfect SME due to stress-induced martensitic transformation and the reversion more recently, the Fe + Pt and Fe + Pd alloys which were previously investigated mainly as experimental materials have received more attention because the martensite transformations can be induced by magnetic fields and hence ferromagnetic shape memory alloys may be developed. [Szprynagcz et al.,2004].

4. Intermetallic compounds:

In the β-Ni Al alloys with nickel contents of 62-69 at % ,a thermo elastic martensitic transformation occurs on quenching .The M_s temperature shows a strong dependence on the nickel content and on the solution treatment temperature .[kim, and Wayman ,1990] .NiAl alloys still suffer from phase metastability,Ni_2Al,Ni_5Al_3 and phases may precipitate at temperature exceeding 250 $^{\circ}C$ .Some other β-phase intermetallic compounds such as NiMn,NiMnGa and ZrCoNi also exhibit shape memory effect and have some interesting potentials but still under development [Wei et al.,1998].

II. Thin –film shape memory alloys:

The bulk shape memory alloys exhibit large strokes and forces but at a show response. This is due to the fact that SMA_s are usually heat actuated and this heat must be removed between cycles and the cooling process usually results in a long cycle lifetime .Compared to bulk SMA_s ,SMA thin films provide a small amount of thermal mass to cool and hence the cycle lifetime can be decreased substantially. CuAlNi films can be sputter deposited on to heated aluminum foils and the as deposited films exhibited a good shape memory effect.[Wei et al,1998] .By coupling the SMA thin film with ferroelectric or ferromagnetic materials , SMA_s may be actuated electrically or magnetically and smart composites with optimized characteristics can be obtained.[Kim and Lee,2003] .

1.4 Applications

Since shape memory alloys have unique properties which are not present in many materials traditionally used in engineering applications, they have potentiality for many applications based on their particular characteristics. In the following ,the most important applications utilizing shape memory effect and super elasticity have been introduced.

1.Applications using shape memory effect:

The applications described in what follows take advantage of SMA ability to recover the configuration associated with the austenitic phase. In some devices the shape recovery is performed only once (one way shape memory alloys), in some other devices, through the use of a basic system ,it is possible to switch cyclically between two different configurations (two way SMA).[Wayman, and Duerig,1990] .This type of applications may be summarized as follows:

1. couplings
2. actuators
3. smart materials

A widely exploited use of SME is one in which an external constraint prevent the material from returning to its original shape on heating (constrained recovery) ,resulting in the generation of large recovery forces .[Auricchio,1995]. The main application of constrained recovery is in couplings and fasteners such as :

- ***Air plane –pipe coupling*.**

They give the possibility of obtaining closely packed hydraulic tubing assemblies and the freedom of designing the hydraulic system without the joining method providing constraints because of tool access. This system used in F-14 jet fighters by Raychem Corporation.[Otsuka, and Ren,1999].

- ***Electrical connectors*:**

Shape memory alloys are used to drive the opening and closure of connectors such as those on computer boards. In such cases, almost no insertion force is needed and very little if any of the mating force is transmitted to the supporting structure. Moreover ,once the connector is closed ,it exerts high retention forces , inhibiting any relative movement between connector member and preventing fretting corrosion from occurring .[Auricchio,1995] .SMA coupling

devices are also successfully used in marine deep-sea applications ,in braid termination missile retain rings and hermetic seals. An interesting application for joining of optical fibers has also been proposed.[Auricchio,1997] .Since the recoverable strain of SMA_s can be more than 10% and the shape recovery process can cause larger force generation if strain is constrained, SMA_s have attracted wide attention for their application as actuator materials in smart systems. [Qiu, J. et al,2000].In general ,a distinction is made between thermal and electrical actuators. Both do work upon heating ,the difference being that thermal actuator are heated by changes in the surrounding environment while electrical actuators are heated by passing electricity directly through the SMA .[Surbeld et al.,1998].

- ***Thermal acuators:***

Thermal actuators are usually designed to behave as sensors (detecting a temperature change) and so actuators. Both Nickel –Titanium and copper based alloys are used depending upon the exact requirements, NiTi alloys being better in fatigue and work output, while the cu-based alloys have higher transformation temperature and are cheaper. Compared to other actuation methods , SMA_s are generally simpler ,less expansive more compact and provide very large, sudden motion however, the presence of the hysteresis makes it difficult to perform an accurate temperature. control. [Saz et al.,1990].

- ***Electrical actuators:***

Electrical actuators are used to replace solenoids, servomotors, hydraulic and pneumatic devices. They are typically simpler in design, quieter more compact and less expensive.[Auricchio,1995]. SMA actuators have also

been used in conjunction with active vibration control for flexible linkage mechanisms ,active buckling of stiffened panels, control surfaces for adjustable chambers, bending and shape control of beams , shutters for air conditioners, fans for automobile radiators ,switches for automatic kettles, thermal valves for fire protection and liquid-gas switches .[Otsuka, and Ren,1999].

Another types of smart materials are composites of NiTi SMA_s with polymers or metal matrix .The NiTi wires embedded in polymers may be used for vibration control of space vehicles, since the elastic constants can be changed widely by changing the temperature in the transformation temperature range. The TiNi wires embedded in aluminum matrix may be used to strengthen aluminum matrix by the same mechanism of pre stressed concrete.[Cadegan et al,2002].

Shape memory effects have also been exploited for medical applications such as blood –clot fillers , intracranial aneurysm clips, artificial hearts ,ropes for the treatment of scoliosis , micropumps.[Koop et al.,2001] .Another area of interesting applications is orthopedics .The heating of fractured bones proceeds more rapidly if the fractured faces are under steady compressive stress. During surgery to reset fractures ,shape memory alloy plates can be attached on both sides of the fracture producing the necessary compressive stress in the fracture gap by exploiting the memory effect .[Li et al,1999].

The use of SMA has opened new frontiers also in terms of space applications. SM connectors are being developed to facilitate the joining of composite tube structural members. Such connectors are automatic catches and release systems based on SMA latching devices. SMA actuators are planned to be used to deploy shelters, control the dynamic of space structures and ensure the integrity of seals.[Turner, and patel,2004].There is also the promise of using

SMA_s in making high efficiency damping devices that are superior to those made of conventional materials, partially due to their hysteretic response ,specially ,porous shape memory alloys. The use of a torsion tube for trailing the edge trim tab control on helicopter rotors is a typical example of the smart blade technology whose main task is the attenuation of noise and vibrations in the surrounding environment.[Schweiger,2002].

2.Applications using superelasticity:

Super elasticity which is nonlinear pseudo elasticity as much as 7-8%,has been also applied in various fields. The first application was to orthodontic arch wire which made the orthodontic therapy much easier and effective.[Koop,K et al,2001].The second quite successful is to the antennas for cellular phones as shown in Fig.(1.3).Since superelastic wire is quite flexible and is not subject to damage. The third one is guide wires for catheters in medical use as shown in Fig.(1.4).A catheter which is a tube made of plastics , is a standard tool for diagnosing the circulatory system by injecting a contrast medium into vessels or for medical treatment by dilating a humen of blood vessel at the site of the obstruction .To introduce the catheter in a required place of the vessel in brain, heart , lever , a guide wire is necessary .It is being overtaken by NiTi superelastic wire recently since the Nitinol wire is more flexible and is not permanently bent, thus this application is expanding rapidly.[Mantovan,2000].By using the super elastic property of shape memory alloys, eyeglass frame components can withstand extreme deformations and spring back completely .[Chute,and Hodjson.1990 Queted in Aurcchio,1995].Further more ,many products in medical application such as braces, dental implants, stents and orthodontic wires are used of shape memory alloys.

Fig.(1.3) Superelastic antenna for a cellular phone.(adapted from Otsuka & Ren 1999)

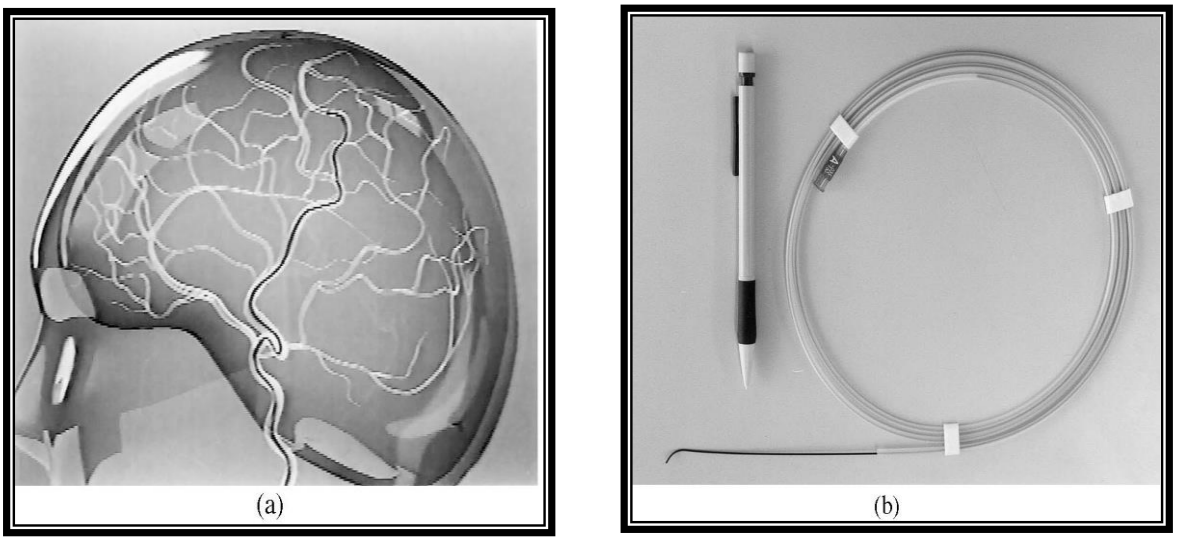

Fig.(1.4) Superelastic guide wire for a catheter in medical use.
(a)Applications for brain; (b) appearance of a guide wire. (adapted from Otsuka & Ren 1999)

1.5 Objectives

The objective of this work is to prepare, develop and investigate porous (CuAlNi) base shape memory alloys produced by powder metallurgy technique

in order to increase shape memory effect and super elasticity of copper based shape memory alloys. In this study ,several material parameters are studied through the addition of alloying element such as (Ti,B,Fe,Si,Co,Zr) and the combination of Ti and Mn and B and Mn in the other hand. In addition, different heat treatment such as solution treatment, direct quenching, aging and step quenched treatment.

Furthermore, different process parameters such as compacting pressure, rate of loading, period of maximum load, sintering time and sintering temperature have also been studied to know their effects on shape memory effect and super elasticity of prepared alloys.

On the other hand, numerical analysis and modeling of CuAlNi porous shape memory alloys are presented using finite element technique with two approaches. In the first ,unit cell finite element analysis with square and hexagonal arrangement of periodic distribution of pores has been used. In the second, the real microstructure of porous shape memory alloys is analyzed using image processing and image analysis for light optical microscope structure combination with finite element method to analyze stresses and strains in the real material microstructure.

Review of Literature

2.1 General view:

Research on shape memory alloys is becoming a target of physicists as well as materials scientists and engineers, and martensitic transformations are being studied by various approaches both experimental and theoretical. For these reasons, rapid progress has been made recently in both fundamentals and applications. one form of these studies current study for copper based high temperature shape memory alloys used for space systems based upon shape memory effect or super elasticity characteristics . Cu Al Ni shape memory alloys have been prepared using powder metallurgy process in the present study .

2.2 Ni-Ti based shape memory alloys:

In the 1960 Buehler and Wiley developed a series of nickel-titanium alloys with a composition of 53 to 57% nickel by weight, that exhibited an unusual effect: severely deformed specimens of the alloys with residual strains of 8-15%,regained their original shape after a thermal cycle. This effect became known as the shape memory effect and the alloys exhibiting it were named shape memory alloys.[Buehler and Wiley,1965 Quoted in Auricchio 1995].

Eucken and Duerig (1989),studied underage Ti-50.85 at % Ni wire tensile specimens which were pseudo elastically pre strained between 2 and 8% .A second deformation to the same strain was found to occur at stresses some 60Mpa lower than the flow stresses measured during the pre straining. The transformation temperatures were measured in the unstressed state using differential scanning calorimetric (DSC) and tensile testing was done using extensometer in a temperature chamber.

Li et al.,(1999) used TiH_2 powder which is added as a reactant and pore-forming agent to produce porous NiTi shape memory alloys. The transformation behavior of porous NiTi alloys was investigated as it has been relevant to engineering and medical applications of SMA_s .It was found that the behavior of porous NiTi alloys is different from that of cast NiTi alloys. They showed that the characteristic transformation temperatures of porous NiTi alloys are independent of sintering temperature, sintering time and TiH_2 content, but latent heats of transformation increase with increasing sintering temperature ,time and TiH_2 content.

Li et al.,(2000)prepared equiatomic porous NiTi SMA_s by self propagating high temperature synthesis (SHS) using elemental nickel and titanium powder. It was found that the combustion temperature increases with increasing preheating temperature and results in melting of NiTi compound above 450 $^{\circ}$C.

Erbstoeszr et al (2000) presented an experimental investigation for NiTi shape memory alloys to stabilize the shape memory effect in cast NiTi. It was found that the most stable one –way shape memory effect in NiTi was a five minutes 475°C salt bath followed by water quench .

Mantovni (2000) presented an overview about properties and biomedical applications of NiTi shape memory alloys. Detwining process and its anisotropy in Nitiol shape memory alloys have been studied by Liu (2001).He showed that the maximum shape recovery strain is intrinsically related to lattice geometry and twining mode. While the magnitude of shape recovery strain is related to a competition of detwinning versus dislocation generation responsible for the macroscopically observed martensite deformation . It has been shown that the anisotropy in detwinning process allows the possibility of maximizing the potential of the polycrystalline shape memory alloys.

Wu(2001) reviewed Nitiol fabrication processes such as melting , forming , shaping , cutting, joining and finishing commonly employed for manufacture of Nitinol material and components.

The thermally induced recovery of microscopic deformation in a Ni-Ti shape memory alloy was examined by Ni et al (2002). Surface deformation was evaluated by indenting the alloy in the martensite phase at room temperature using spherical and pyramidal indenters. They showed that deformation in spherical microindents can be almost completely reversed by heating whereas partial recovery observed for pyramidal impressions formed by Vickers indenter. It was shown that the recovery ratio is independent of load for Vickers geometry .

Crone et al (2002) prepared NiTi shape memory alloy with refined grain size synthesized by mechanical alloying process through a cold rolling fabrication of elemental nickel and titanium layered foils. After the layer thickness was reduced to the nano scale by multiple cold rolling and folding passes, an alloying and intermediate phase formation reaction was initiated. X-ray diffraction profiles confirmed that the present was intermetallic NiTi phase.

Tension-torsion tests were conducted on thin walled tubes of the polycrystalline super elastic and shape memory Nitinol alloy using various loading / unloading path under isothermal conditions by the workers Macnany et al (2003).Their experimental results showed significant variations in the mechanical response a long the two loading axes.

Brinson et al (2003) studies micro and macro mechanical transformation behavior of polycrystalline NiTi shape memory alloys. Special attention was paid to macroscopic banding , variant microstructure , effect of cyclic loading, strain rate and temperature effects. It has been shown that use of interference filter on the microscope enabled observation of grain boundaries and martensite plate formation and growth without recourse to etching or other chemical surface preparation.

Crone et al(2003) used atomic force microscopy (AFM) to reveal that the thermally induced martensitic transformation of NiTi shape memory thin films allows for partial indent recovery on the nano scale and the recovery was nearly complete at indentation depths of less than 100nm.

Fan et al (2004)presented comparative study between single crystals and polycrystals from NiTi shape memory alloys and found that all single crystals exhibit normal two stage transformation being independent of Ni content where as polycrystals with Ni content show three stage transformation but those with high Ni content (51.5 Ni %) exhibit normal two stage transformation.

Nasser et al(2005)investigated compressive response of NiTi shape memory alloys at high strain rates using modified split Hopkinson pressure bar and a mini- Hopkinson bar with specially designed striker bars. It was shown that the transition stress from the austenite to the martensite phase shows strain rate sensitivity. Porous NiTi alloy with several different porosities was processed by spark plasma sintering by Zhao et al (2005). The compression behavior of the porous NiTi was examined as a high energy absorbing material.

2.3 Copper base shape memory alloys:

Planes et al (1981) presented study of ordering in a β phase of CuZnAl alloy and the influence of ordering on the martensitic transformation temperature using differential scanning calorimetric. Barcelo and Ahlers (1982) showed that it is possible to induce a hexagonal long range ordered martensite phase in a Cu ZnAl alloy with $M_s = 50^{\circ}C$ and an electron concentration e/a=1.48. From their measurements of the critical stress and retransformation to β after re heating , it was concluded that the hexagonal and original 3R martensite have the same formation free energy thus, the two structures can not be described by their difference in stacking fault density (compared to a face centered lattice). The application of martensitic alloys in shape memory devices requires reproducible and stable transformation temperatures. In certain CuZnAl alloys,

the reverse transformation temperatures A_s and A_f progressively increase with prelonged holding at temperatures below A_s .

Study of the increase in A_s as a function of the stabilization temperature and time had been reported by Humbeeck et al(1984). The crystal structure and reordering of stabilized step-quenched copper zinc aluminum martensite using x-ray diffraction technique had been reported by Delacy et al (1984).

During the stabilization of step-quenched Cu Zn Al martensite

(quenching above the M_s temperature) ,precipitation and changes in the microstructure of martensite had been occurred. Extra contrasts were observed which are not present in non stabilized martensite by Graef et al (1985).

A study of crystallography of the martensitic transformation in a Cu-26.71Zn-4.15Al shape memory alloy by means of group theory was presented by Juany et al (1985). They had obtained the irreducible representation and 24 martensite variants associated with the martensitic transformation in this alloy system.

Thermal analysis data for CuZnAl in ribbon form were analyzed as a function of degree of stabilization by Scrasbrook and Stobbs (1987). The relatively high sensitivity of rapidly quenched ribbon material to both quench and equilibrium stabilization was discussed using differential calorimeter.

The influence of the average grain size and ordering degree of the parent phase on the starting temperature of thermoelastic martensitic transformation in a Cu-25.62 Zn-3.97 Al-0.0018B (wt %) shape memory alloy was studied by Jianxin et al (1988).

Adachi et al (1988) presented crystallographic analysis using transmission electron microscopy taking into account the various combinations of martensitic plate variants which meet at the boundaries formed between different self accommodating plates groups in CuZnAl martensites.

The process of the thermo elastic β´to martensite transformation and reverse transformation was studied as a function of temperature and applied

stress using electric resistance measurements and metallographic observation in a Cu-29%Zn-3%Al alloy by Deg, Ansell(1990).

Mellor et al (1990) presented the training of polycrystalline Cu-6.57%Al -20.18%Zn-0.72%Co alloy using stabilized stress induced martensite. The mechanism responsible for the development of two way SME by stabilized stress induced martensite had been studied using optical and scanning electron microscopy.

The ordering temperatures of β to B_2 (ordered body center cubic) and from B_2 to another order crystal lattice structure ($L2_1$ as shown in chapter three)had been studied in CuAlNi shape memory alloys with different concentrations using electrical resistively by Recarte et al, (1997).

Franz and Horbegen(1998) had been shown that the lattice defects in the stable austenite (β) phase of a Cu-27%Zn-4%Al shape memory alloy by a hot rolling and quenching process (Ausforming) lower the temperature range of martensitic transformation cycles and improve strength properties through increase dislocation density.

The neutron texture analysis had been perform on the pseudo elastically transforming CuAlZn Mn shape memory alloy specimens by Neov et al (1999). Pons and Cesari (1999) had been shown that variety of distribution of γ-phase precipitates in CuZnAl single crystals shape memory alloy with different size , shape , distribution density and nature can be obtained by some suitable heat treatments.

Recarte et al (1999) have studied the influence of quenching and post quench aging treatments on the atomic order of the β phase obtained by quenching in CuAlNi shape memory alloys using thermoelectric power measurements. The initial evaluation of thermoelectric power during aging showed two clear stages where thermoelectric power value decreases.

The microstructural and transformation characteristics were studied by Aslanidis et al (1999), including the effect of thermomechanical cycling and

using torsional actuation mechanism for Cu Al Ni shape memory alloy. Recent developments with nearly 10 years on shape memory alloys (specially for NiTi) and martensitic transformations on which shape memory effect and super elasticity are based, were reviewed by Otsuka and Ren (1999).

Ferreira et al (2000) were shown that boron and iron were refining and stabilizing the microstructure in the Cu-15.5%Zn-8.0%Al alloy. The pre-alloyed melt of Cu-13.1Al-3.16Ni alloy was atomized by argon at pressure of 2.3 Mpa by Raul et al(2000). They used hot isostatic pressing (140 Mpa pressure at 850 $^{\circ}$C)during 2hr to compact pre alloyed powder. After the compaction , hot rolling temperature of 850°C to improve mechanical properties of product was used . The main result had been shown that fracture occurred after deformation higher than 12% and the maximum recoverable tensile strain was 7 %.

Cakmak et al (2001) studied aging behavior of Cu-21.62%Zn-5.68%Al martensite at 24°C by analyzing diffraction line profiles obtained by x-ray diffractometry and change of the lattice parameters associated with aging time at room temperature .

In (2002) , Pana et al presented characterization of dry sliding wear behavior of the Cu Zn Al shape memory alloys in their different phases using adhesive wear tests (pin-on-Disk).Characterization of wear surfaces were carried out by optical microscopy , scanning electron microscopy , Dsc and x-ray diffraction.

The nucleation and propagation of cracks in Cu Al Ni shape memory alloy were observed using atom force microscope (AFM) by Lu et al(2002) . The results indicated that in Cu Al Ni shape memory alloy the martensitic transformation first occurred at crack tip upon loading and the micro crack nucleated and propagated along martensite interface. Neutron powder diffraction and texture studies of Cu Al Mn Zn shape memory alloy were preformed under tensile loads by Neov et al (2002) . The specimens were deformed up to 3% strain .

The effect of high velocity impact loading on the structure , transformation temperatures , elastic and an elastic properties had been studied for a CuAlNi shape memory alloy in the β'_1 martensitic phase by(Golyandin et al,2002). The impact loading of crystals had been preformed by means of a light gas gun producing compressive plain strain wave pulses with a duration of about $2*10^{-16}$ sec. It had been shown that the stability of the temperature range and hysteresis of martensitic transformation are a scribed to the rather stable martensitic variant structure .

Kim (2003) had used a simple constrained heating technique to realize the two-way shape memory effect (which is a phenomenon that a material can alternate between two shapes as it undergoes a thermal cycle) and had studied the effect of heating time and temperature for Cu-33.1%Zn-1.3%Al alloy prepared by induction furnace casting and hot rolled.

Silva and Lima(2005) prepared Cu-13%Al-2%Nb shape memory alloy by mixing pure elemental powders. A ball to powder weight ratio 6:1 and rotation rate of 15rpm in argon atmosphere were the main processing parameters changes in microstructure as a function of milling time were studied using x-ray diffraction analysis and scanning electron microscopy. Obtained results had been shown that high energy ball milling combined with pressing with (900Mpa) and sintering at 850°C , can be used to promote the formation of copper aluminum solid solution with density of 91% of theoretical density .

Sampath (2005) studied effect of addition of zirconium (0.2, 0.4 and 0.6%Zr) on the microstructure and transformation temperatures of Cu-11%Al-3.82%Ni shape memory alloy . The differential scanning calorimeter studies had been shown that zirconium increases the martensitic transformation temperature up to 0.4% additives but further addition of zirconium decreases M_s to below room temperature .

From the previous review , it has been clear that very little studies for copper base shape memory alloys by powder metallurgy technique using process

parameters and various alloying elements such as [B, Fe, Si, Co, Mn, Zr, Ti] were presented.

2.4 Analysis of shape memory alloys:

Turner et al(1994) presented finite element analysis of the random response suppression of composite panels reinforced with NiTi shape memory fibers. The preliminary results demonstrated that the SMA fibers can completely eliminate the thermal post buckling deflection and reduce the random response at elevated temperatures.

Lubliner and Auricchio(1996) presented a first attempt to apply generalized plasticity to the behavior of shape memory alloys. Trochu and Qian (1997) suggested a methodology to simulate the nonlinear thermo mechanical behavior of shape memory alloys by finite element method. A general and simplified constitutive law was formulated based on plastic flow theory using a bilinear model as uniaxial material law. Auricchio et al (1997) proposed constitutive models based upon generalized plasticity taking into account super elasticity and the single variant martensite reorientation only. Numerical simulation of uniaxial loading, four point bending and three point bending tests were presented . The computation tool to be used during the design of SMA-based devices had been also proposed by Auricchio & Taylor (1997). Constitutive model included super elastic behavior of shape memory alloy at finite strains.

Rebelo and Perry (1999)developed algorithms which allow for analysis of Nitinol medical devices by finite element method. They assumed multi linear elastic behavior to explain super elasticity of Ni-Ti shape memory behavior.

Thermo mechanical one dimensional constitutive model based on the use of strain and temperatures control variables and able to reproduce the basic response in tension and compression and shape memory effect had been presented by Auricchio and Sacco (1999) . The model was implemented in a small deformation beam finite element.

The structure of a twinned martensite plate in NiTi shape memory alloy was examined based on micro mechanics by Liang et al(1999).

Koop et al (2001) analyzed stent material Nitinol using Ansys type 4.5 software and user material program to present individual model for the material. They used multi linear elastic model with different Young ′s modulus for austenite and martensite phases to compute super elastic under loading and unloading behavior of Nitinol stent material. Thermo mechanical model of a super elastic shape memory wire under cyclic stretching –bending loading had been proposed by Auricchio and Sacco (2001).

Qidwai et al (2001) presented modeling of thermo mechanical behavior of porous shape memory alloy. The porous SMA was assumed to be made of two components , the dense shape memory alloy matrix and the pores . Rate – independent type constitutive model was employed to describe the matrix behavior using unit cell finite element method and averaging micro mechanic method . Cylindrical and spherical shape were considered as approximations of open and closed pores respectively.

The radial displacement control of an externally pressurizes elliptic composite cylinder where the SMA strip actuators are bonded on its in and out surface was studied numerically using finite element method by Kim and Lee(2003) .

Turner and Patel (2004) analyzed of shape memory alloy hybrid composite structure using thermo mechanical model of SMA actuators and hybrid composite models to implement in the commercial finite element codes.

2.5 Summary

Shape memory alloys (SMA) are being increasingly used in various industrial applications as actuators , connectors, eyeglass frames , stents or damping materials so that a significant a mount of research in last few years has

greatly advanced in thermo mechanical characterization, material fabrication and numerical modeling and simulation of SMA.

In the light of previous review of literature shape memory alloys included NiTi base alloys for medical and for fiber reinforced advanced composites and copper base shape memory alloys for space systems specially Cu Zn Al and Cu Al Ni alloys . Most of those studies were prepared by casting in control atmosphere (in Argon or in vacuum) except NiTi shape memory alloys for medical applications . The previous studies were emphasized on thermo mechanical characterization and martensitic transformation and their crystallographic changes during phase transformation . Very few work has been done for porous copper base shape memory alloys processed by powder metallurgy taking into consideration compacting and sintering parameters effects.

Perhaps, there is no comprehensive study on the copper base shape memory alloys prepared by powder metallurgy taking into consideration all manufacturing parameters and analysis of porous shape memory alloy depends upon real microstructure of size , shape and distribution of pores in the material.

In this study , CuAlNi shape memory alloys have been prepared from elemental powder and developed of their behavior by two ways as follows:

1. Chemical compositions of alloys through adding of various alloying element into base used alloys such as Ti, B, Co ,Zr ,Fe , Si, Mn.
2. Heat treatments in what solution heat treatments at different times and temperatures has been taken further more, effects of aging treatment and step-quenched treatment are also explained on the microstructure , shape memory effect and super elastic behavior of prepared alloys from different physical and mechanical tests.
3. Until cell finite element analysis of porous shape memory material has been presented in this study. Proposed square and hexagonal unit cell for

pore distribution have been used to represent periodic arrangement of pores.

4. Unit cell finite element analysis of real microstructure of porous shape alloy has been taken in this study. Real images from optical microscopy with suitable magnification have been pictured and analyzed using image analysis technique to calculate pores and their distribution in the image, further more transform these image to engineering geometry to analyze mechanical behavior using finite element method .

Theoretical Consideration

3.1 General View

The term shape memory alloy (SMA) is applied to that group of metallic materials that demonstrate the ability to return after deformation, to some previously defined shape or size when subjected to the appropriate thermomechanical procedure. Although a relatively wide variety of alloys and also compounds are known to exhibit the shape memory effect, only those that can recover substantial a mounts of strain are of commercial interest. To date , this has been the case for Ni-Ti and copper based alloys such as CuZnAl , CuAlNi or CuAlBe which are the subject of the present work.

In this chapter, shape memory effect and superelasticity behavior, martensitic transformations and their microscopic and macroscopic perspectives have been presented with enhanced for copper base alloys. Furthermore, theoretical considerations of powder metallurgy technique for copper base alloys taking into consideration types of compaction and sintering processes have been presented. Finally, effects of alloy elements, thermal treatments and aging treatments have also explained in this chapter, but we begin with martensitic transformation due to understand the origin of shape memory effect.

3.2 Martensitic Transformations:

One can not obtain an understanding of even the most elementary engineering aspects of shape memory effect without first becoming familiar with some basic principles of martensite and its formation. Martensitic transformation can be explained in two manners as follows:

3.2.1 Microscopic Prospective of Martensite

Solid state transformations are two types diffusion and diffusionless (displacive). Diffusion transformation are those in which a new phase can only

be formed by moving a toms randomly over relatively long distances . long rang diffusion is required because the new phase is of a different chemical composition than the matrix from which it is formed. Since atomic migration is required, the progress of this type of transformation is dependent upon both time and temperature. In contrast, displacive transformations do not require such long range movements in these cases atoms are cooperatively rearranged into a new more stable crystal structure but without changing the chemical nature of the matrix. Because no atomic migration is necessary, displacive transformations generally progress in a time –in dependent fashion . They are referred to as a thermal transformation since the amount of new phase present is usually dependent only on temperature and not the length of time at temperature. Martenesitic transformations are generally of this second type and are formed upon cooling from a higher temperature phase called the parent phase or austenite. (Wayman and Duerig 1990).

The terms "Martensite" and "austenite " were originally intended to refer only steel phases but the more generalized definition referring to the type of transformation product and not the particular material is now widely accepted. In physical metallurgy, the term martensite is used to describe any diffusionless transformation product which the individual atomic movements are less than one interatomic spacing. (Porter and Easterling 1992).

Martensitic transformations are first order transformations which mean that heat liberated when martensite is formed, there is a hysteretic associated with the transformation and there is a temperature range over which austenite and martensite coexist. [Ahlers 2002]. Martensite is formed based upon cooling with the volume fraction of martensite increasing as the temperature is reduced but with the volume fraction being independent of time, and that it inherits the composition and atomic order of the parent phase.[Wayman and Duerig,1990] .

The transformation from parent phase to martensite is often thought of in two parts, the Bain strain and the lattice invariant shear. The Bain strain or lattice deformation consists of all the atomic movements needed to produce the

new structure from the old.[Reed-Hill,1964].In Fig.(3.1),the austenite structure is illustrated in diagram(a)and the martensite structure is illustrated by diagram (d).

As the interface progresses one atomic layer, each atom is required to move by only a very small amount as shown in Fig. (3.1) c. The end results of all these small coordinated movements are the new martensitic structure. The movements needed to produce the new structure are called as Bain strain.(Reed-Hill, 1964) .

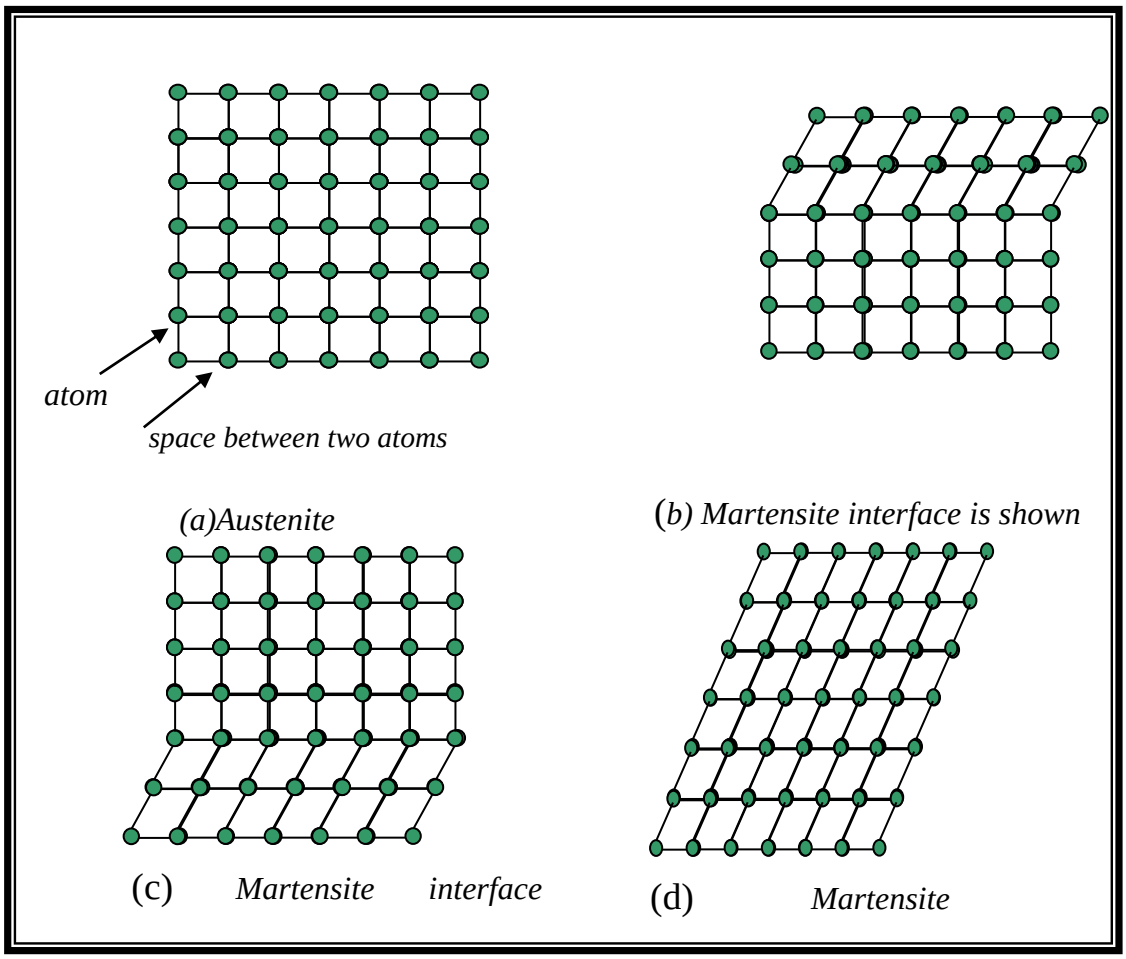

Fig.*(3.1) The transformation from austenite to martensite .a. austenitic phase b.and c. interface advance and d. completely martnsitic phase*

The second of a martensitic transformation, the lattice invariant shear which is an accommodation step. The martensitic structure produced by the Bain strain is of a different shape and often volume than the surrounding austenite.[Smallman and Bishop,1999].

Martensite in steel involves both volume and shape change where as shape memory alloys such as NiTi and Cu-base alloys undergo basically only a shape change. Either the overall shape of the new phase or the surrounding austenite must be attend to accommodate the new structure .[Wayman and Durig ,1990]. For example, one cannot change the shape of single brick in the center of brick wall, either the surrounding bricks must deform, or the new brick must accommodate its form to the space available.

There are two general mechanisms by which this can happen: slip and twinning as shown in Fig. (3.2) . In both cases, each individual cell has the new martensitic structure, but the overall shape is that of the original austenite. Slip is a permanent process and is a common accommodation mechanism in many martensites.[Reed-Hill,1964].

Twinning is unable to accommodate volume changes which should be necessary, but can accommodate shape changes in a reversible way [Porter and Easterlng,1992] . For shape memory to accur to any significant extent, the accommodation must be required fully reversible, in other words, twinning be the dominant accommodation process. [Otsuka and Kakestia,2002].

In the two–dimensional model shown in Fig. (3.2) , only two directions or variants of shear are required to restore the original overall shape of the matrix. In three dimensions, the situation can be complicated. For example, in CuZnAl martensites require four martensites variants for full three dimensional accommodation.

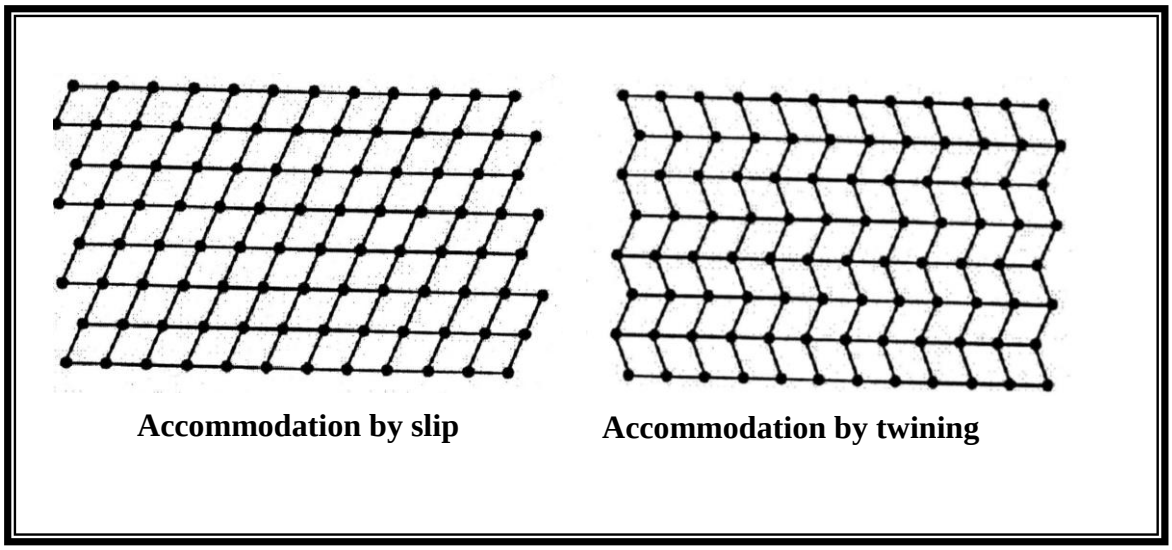

Fig.(3.2): The two mechanisms of accommodating the shape change due to atomic shear of a martensitic transformation a. by slip b. by twinning(Wayman and Duerig,1990)

The twin boundary is a mirror plane and when positioned on the boundary, the view in one direction is mirrors of the other as shown in Fig. (3.3).The atoms situated on the boundary have the same number and types of bonds in both directions. The twin boundaries have very low energy and they are quite mobile thus the relative stability of a martensite phase is not strongly affected by the number of location of these boundaries .[Reed-Hill,1964].

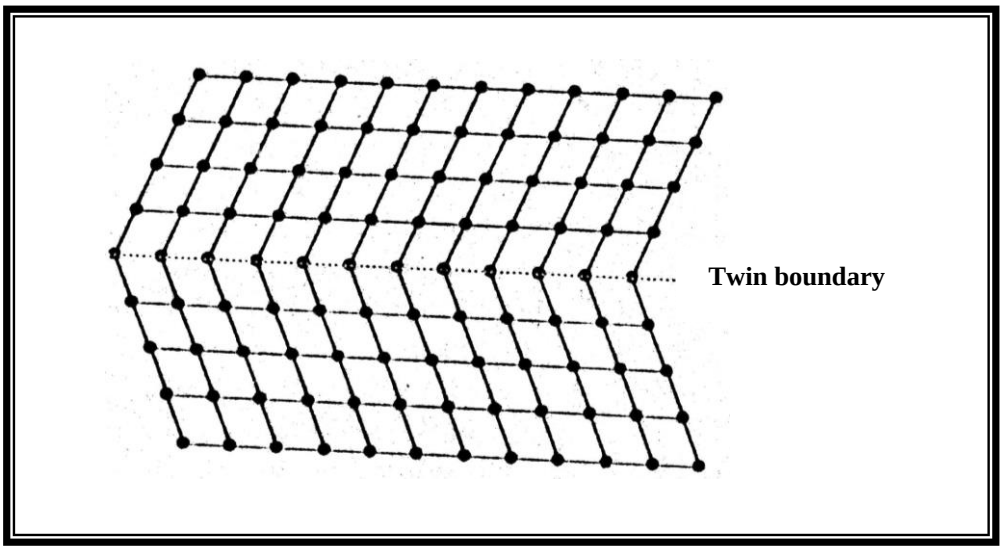

Fig.(3.3) Schematic view of a twin boundary.(Reed-Hill,1964)

Atomic bonds are broken in the slip accommodation while all bonds remain intact in the twinned structure. If a stress is applied to the structure as

shown in Fig. (3.2.b), the twin boundaries will easily move producing a shape which better accommodates the applied stress as clear in Fig.(3.4).

The result of moving a twin boundary is to convert one orientation or twin variant into another. That variant will be chosen which is most favorably oriented to the applied stress. A single variant of martensite can be produced by straining a sufficient amount. The condensation of many twin variants into a single favored variant is called as detwinning . The boundaries between martensite plats also behave as twin boundaries. [Reed-Hill,1964].

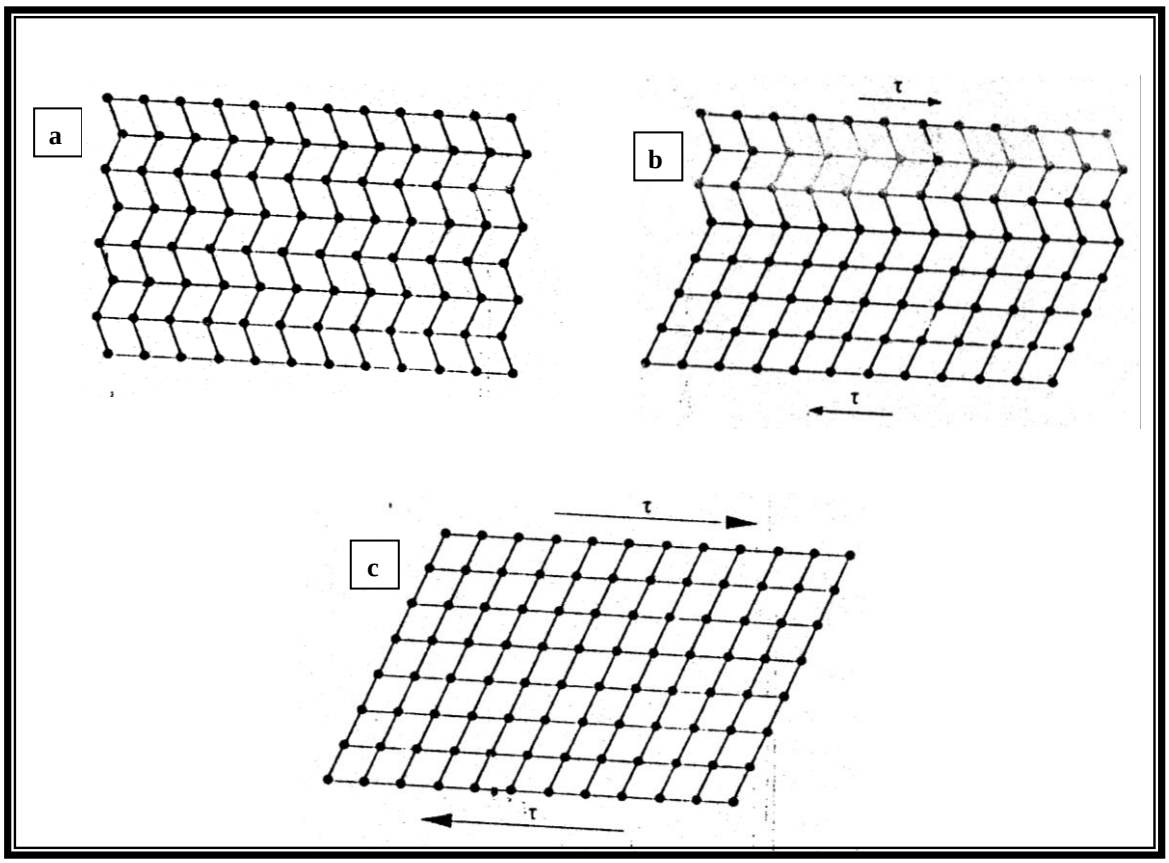

***Fig.(3.4) Twin boundaries in martensite can be removed by applied shear stress*(Reed-Hill,1964)**

In steel , the atoms are disordered , meaning that different elements are randomly distributed on the lattice sites, where as in CuZnAl and CuAlNi atoms are on very specific sites so that atoms are ordered.

During a martensitic transformation, the martensite takes on the same ordering of the austenite which is called inherited ordering. [Porter and Easterling,1992].

Shape memory alloys are generally based upon a Bcc symmetry , some with Bcc structure , more often with B_2 (premitive cubic) order structure and some with an even more complex ordering called Do_3 (face centered cubic) [Wayman and Duering ,1990].

3.2.1.1.Structure of martensite and morphology:

The formation of martensite appears from micrographs to be a random process and way it is observed to develop is illustrated in Fig. (3.5) . It has been shown that the martensitic phase is often in the shape of lens and spans initially an entire grain diameter. The density of plates does not appear to be a function of the grain size of the austenite . [Porter and Easterlng,1992] .

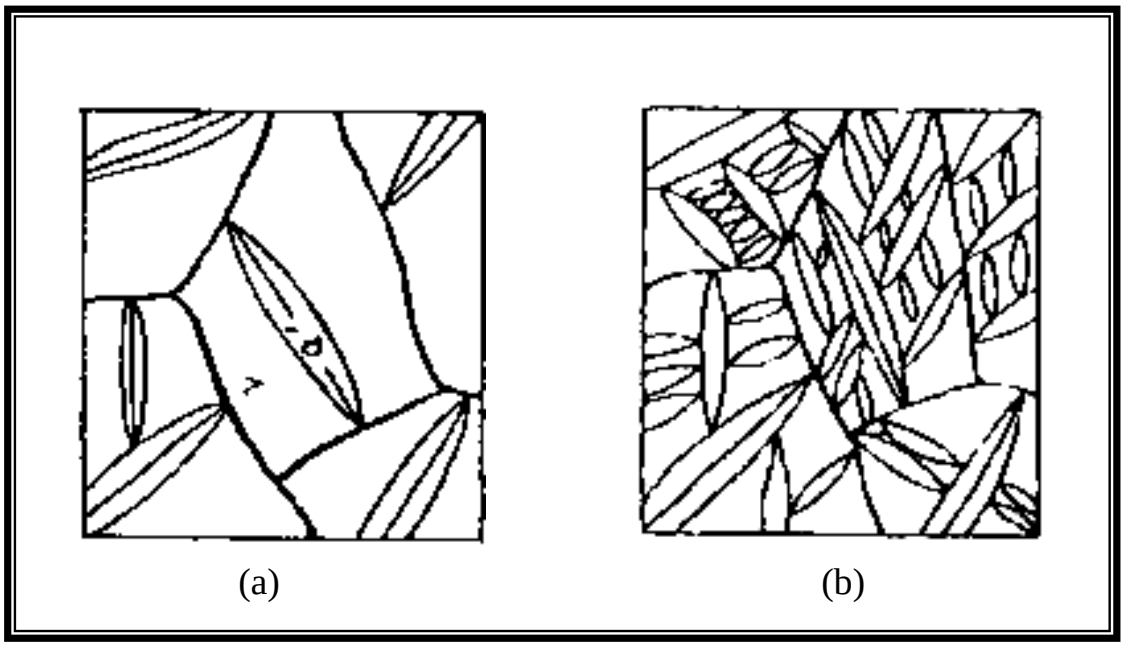

Fig.(3.5)growth of martensite with increasing cooling below M_s ,for both (a) and (b) **[Porter and Easterlng,1992]**

The transformed regions appear coherent with the surrounding austenite which means that intersection of the lenses with the surface of the specimen does not leads to any discontinuity . It has been shown that a fully grown plate spanning a whole grain may form within 10^{-7} second which means that the martensite / austenite interface reaches the speed of sound in a solid. Martensite is thus able to grow independently of thermal activation although some Fe-Ni

alloys to exhibit isothermal growth characteristics . This great speed of formation makes martensite nucleation and growth as a difficult process to study experimentally.[porter and Easterling,1992]. The volume fraction of martensite increases by the systematic transformation of the austenite remaining between the plates that have already formed as shown in Fig. (3.5.b). The first plates form at the martensite start temperature (M_s) which is associated with a certain driving force for the diffusionless transformation from austenite to martensite as shown in Fig. (3.6)

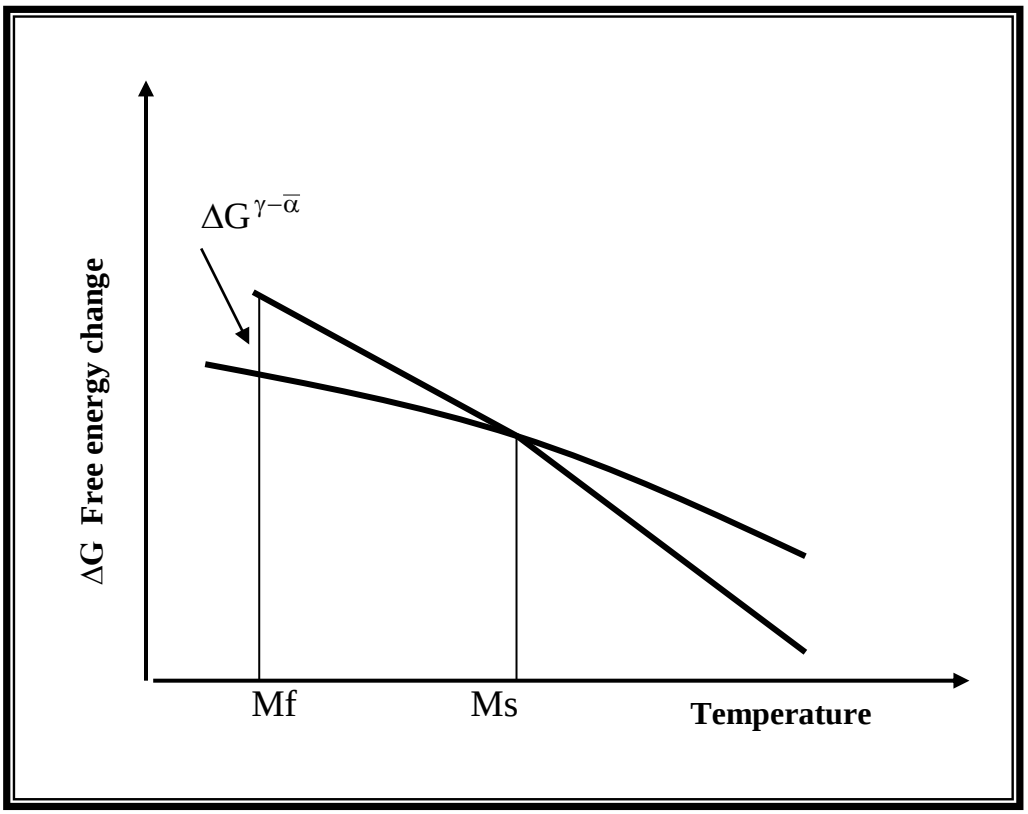

Fig.(3.6)Free energy temperature diagram for austenite to martensite phase change

The martensite finish temperature (M_f) correspond to that temperature below which further cooling does not increase the martensite amount.[Reed-Hill,1964]. Because the martensitic transformation is a lattice –distortional diffusionless structural change having a dominant deviatory component and an associated change in shape , strain energy dominates the kinetic and morphology of the transformation . The driving energy required for martensitic

transformation is much higher (especially for irreversible martensite) than that needed for diffusion decomposition such as precipitation.[Meyers and Chawla,1999]. If a diffusion-induced transformation competes with martensitic transformation, the cooling in the region where to M_s (Fig. 3.6), has to be fast enough to avoid the former transformation on the other hand, if to is low enough , there is essentially no diffusion and slow cooling leads to produce martensite .For irreversible martensites the gap in which $M_s \rightarrow A_s$ is a few handred Kelvin while for reversible martensites, the gab is a few tens of Kelvin.[Meyers and Chawla,1999].Martensite can be exhibited a variety of morphologies depending upon the composition of the alloy, conditions in which it is formed and its crystalline structure . The three most common morphologies are the lenticular (lens shaped), lath (a large number of blocks juxtaposed in a single like arrangement) and the a circular (needle shaped) .

In spite of these differences in morphology , some unique features are common to all martensites . The most important is the existence of an undistorted and un rotated plane which has the same indices in the two structures , parent and martensite phases. This undistorted and unrotated plane is called as the habit plane . The macroscopic shape deformation in the formation of martensite plate is believed to be shear parallel to the habit plane and a simple (uniaxial) tensile or compressive strain perpendicular to the habit plane . A strain of this nature called as invariant plane strain .[Reed-Hill,1964].

3.2.1.2.Martensite Crystallography:

Knowledge the crystal structure of martensite is a first step toward understanding the mechanism of the martensitic transformation. Lattice parameters and lattice correspondence between parent and martensite are required in the phenomenological theoretical calculation and the exact atomic positions are not required , since small suffles are considered not to a contribute to the shape strain . The correct band structure of martensite can not be obtained unless actuate atomic parameters are used . Since martensites usually appear in a

self-accommodating manner, a single crystal of martensite is not usually obtained.[Otsuka and Ren,1999].In Au-Cd alloys two types of martensite appear depending upon Cd content which are γ_2' (B19) martensite appear near Au-47.5% Cd while ζ'_2 martensite appear near Au-50.0%%Cd. The structure of the γ_2' martensite is an orthorhombic unit cell where as ζ'_2 martensite is Trigonal (R-phase)unit cell structure .[Otsuka and Ren,1999]. R –phase transformation is a martensitic transformation which competes with the monoclinic martensitic transformation. In Ti-50% Ni alloy , the structure of martensite is monoclinic (B19) martensite where as R-phase appears in Ti-Ni-Fe ternary alloys. Table (3.1) present a number of systems in which martensitic transformation have been observed .

Table (3.1) systems in which martensitic transformation occurs .

Adapted from (Meyers and Chawla,1999).

Alloy	***structure change***
Fe-Mn , Fe-Cr-Ni	Fcc→Hcp
Fe-Ni	Fcc→Bcc
Fe-Mn-C	Fcc→BcT
Fe-Ni-C	Fcc→BcT
Fe-C	Fcc→BcT
In-Ti and Mn-Cu	Fcc→FcT
Cu-Zn	Bcc→FcT
Cu-Sn	Bcc→FcT
Cu-Al	Bcc→disordered HcP Bcc→orthorhomic Bcc→monoclinic
Au-Cd	Bcc→orthorhomic Bcc→Trigonal
Mn-Cu	Fcc→BcT
Ti	Fcc→HcT
Ti-Cu	bcc→HcP
Ti-Fe	bcc→HcP

3.2.1.3.Martensite Nucleation:

The nucleation of martensite plates is a subject of great interest and also of considerable controversy. It is generally accepted that nucleation occurs heterogeneously at defects as is the case with nucleation in most other transformations or phase changes. (Ahlers,2002). Because of the great speed of growth of martensite , it is extremely difficult to study this transformation experimentally . It has been assumed that the initial nucleus should be coherent with the parent austenite phase. So the total increase in Gibbs free energy associated with the formation of a fully coherent inclusion of martensite in a matrix of austenite can be expressed as : [Porter and Easterling,1992].

$\Delta G = A\gamma + V\Delta G_s - V\Delta G_v$ ----------Eq.(3.1)

where :

γ –The interfacial free energy

ΔG_s –strain energy

ΔG_v –volume free energy

A- surface area

There is a balance between surface and elastic energy on the one side and volume free energy on the other .In the martensitic transformations , the strain energy of the coherent nucleus is much more important than the surface energy so that the Bain distortion strain produces large strains in the surrounding austenite .

The interfacial surface energy of a fully coherent nucleus is relatively small.[Porter and Easterling,1992]. It has been thought that surfaces and grain boundaries are not significantly contributing to nucleation so the transformation is being initiated with other defects within the crystal.[Reed-Hill,1964].

In order to reduce the elastic energy of martensite plate should be as thin as possible being determined by the decrease in volume free energy compared with the increase from the habit plane energy. In addition the amount of the martensite shear should be as small as possible.[Ahlers,2002].

3.2.1.4.Martensite Growth

Martensite plates grow to their final sizes with great rapidity. Recent measurements show that the growth velocity is of the order one –third the velocity of sound in the matrix , and the growth velocity is independent of temperature . If the growth of martensite plates occurred as the results of atoms jumping over energy barrier from the parent phase to the product phase then the jump rate should be a decreasing function of the temperature and at some finite temperature a noticeable dropping off in the martensite growth rate should become apparent. This does not occur. Martensite has been observed to form with great rapidity even at $4K^{\circ}$. [Reed-Hill,1964].

During the growth of the thin planar plates of a constant thickness a low-energy interface between the martensite and the matrix, the habit plane is created right to the tip of the growing plate. The orientation of this interface is found generally to have high miller indices.[Ahlers,2002].Because of the martensite shear the matrix around the tip is distorted elastically, provided that the stresses do not activate plastic deformation by the movement of dislocations in the martensite or matrix . All the redistributions of the atoms from the matrix to the martensite structure occur near the tip and thus must not consume too much energy in order to possible . Once a thin martensite plate is created it often but not always, thickness by the movement of interfaces. During this step the mobility is more important than the necessity to keep an undistorted habit plane which leads to a bending of the interface and to an change in microstructure as often observed .[Ahlers,2002].

3.2.1.5.Origin Of The Martensitic Transformation:

Although it is still a subject of dispute ,items that on the level of lattice dynamics almost all different first order martensitic transformations can find a common origin . First order martensitic transformations is driven dominantly by phonon entropy differences between parent phase and martensite .[Otsuka and Ren,1999]. The parent phase has higher vibrational entropy because its low

lying or soft phonon branch contributes significantly to the entropy of the system where as stiffer martensite has lower vibrational entropy due to its higher phonon energy . As a result, a transformation from a higher entropy state to a lower entropy state will occur at some temperature .

According to the basic principle of thermodynamics that a low entropy state is favored at low temperatures and a high entropy state is favored at high temperatures . It has been shown that a dominant phonon contribution to entropy in martensitic transformation of copper base shape memory alloys using elastic constant measurements and calorimetry measurements .[Comas and Manosa ,2000].It has been suspected that many martensitic transformation can be caused by certain electron effect which can induce a phonon a normally through electron phonon coupling where as in ferrous alloys, martensitic transformation has different origin which is largely due to the magnetic contribution.

For example , there has been some clear evidence indicating the softening in elastic constants in Fe-Ni and Fe-Pt alloy can be ascribed to the magnetoelastic coupling between magnetization and phonon. Therefore ,items that the microscopic origin of martensitic transformation may be diverse and depends upon specific alloy system .[Otsuka and Ren,1999].

3.2.2.Macroscopic Perspective Of Martensite :

Most of mechanical and physical properties of austenite and martensite are different so through the transformation variety of significant property changes will be occurred .The temperatures, M_s,M_f ,A_s and A_f are indicated in Fig. (3.7),which refer to the temperatures at which the transformation to martensite starts and finishes, and the temperature at which the reversion to austenite starts and finishes. As shown in Fig.(3.7),the transfer matrix temperatures differ upon heating and cooling .

This difference causes a hysteresis associated with martensitic transformation. Yield strength is an one property that changes in a most significant way. The martensitic structure can deform by moving twin

boundaries which are quite mobile so, the yield strength of martensite is extremely low compared with yield strength of austenite which must deform by dislocation generation and movement .[Wayman and Duerig,1990].

Only a certain a mount of martensitic deformation can be accommodated by this twin movement process and once this is exceeded , the material will deform elastically and eventually yield a second time , this time by irreversible processes (dislocation movement).

The tensile behavior of a twinned martensite material is explained in Fig.(3.8) .the plate all stress is related to thermal hysteretic in that both are controlled by the frictional stress of the twin boundaries . The ratio of resistances to reversible and irreversible deformation is characterized by the yield strength ratio of martensite to austenite . In general, in shape memory alloy , this ratio is maximized so that all deformation can be recovered upon heating .Typically ratios would be 0.1to 0.2. [Wayman and Duerig,1990] .

3.2.2.1.Stress Induced Martensite and Superelasticity:

The formation of martensite is a thermoelastic process. Which means that an incremental decrease in temperature between M_s and M_f results in a slight growth of existing martensite plates and the nucleation of new ones , but when the temperature is incrementally raised , the newly nucleated plates disappear and those which grew slightly on incremental cooling correspondingly shrink back a little . There is an equivalence between temperature and stress ,a decrease in temperature is equivalent to an increase in stress, both of them stabilizing martensite. The martensite is also crystallographically reversible.

Normally on cooling, the martensite forms at M_s under no stress , but in the same material ,martensite can form above M_s if a stress is applied , martensite is termed stress-induced martensite (SIM). The deriving force for the transformation in this case, is mechanical.

Above M_s the stress required to produce SIM increases with increasing temperature as shown in Fig. (3.9). The variation in the stress needed to produce

(SIM) increases linearly with temperature above M_s . The linear variation in stress to induce martensite as a function of temperature obeys the Clausius-Clapeyron equation written as : [Gaskel,1978]

$d\sigma/dM_s = - \Delta H/T\varepsilon_t$----------Eq.(3.2)

where:

σ-applied stress

ε_t- transformational strain resolved a long the direction of the stress

T-temperature

ΔH-The transformation latent heat

The increase in difficulty to stress induce martensite continues to increase with temperature until M_d ,above which the critical stress for inducing martensite is greater than that needed to move dislocations. M_d is the highest temperature at which it is possible to have martensite thus the temperature range for (SIM) is from M_s to M_d . Above the temperature M_d, superelastic behavior can not occur and M_d is above A_f with few degrees. [Keefe, 1999].

Fig. (3.10) shows typical measurements from differential scanning calorimeter (DSC)for shape memory alloy. The (DSC) plot illustrates the power required to heat the material at a constant rate of temperature increase versus temperature . Energy is either absorbed or released during phase changes resulting in sharp peaks when the heat flow is plotted versus temperature . The transformation temperatures are measured from the intersection of the slopes in the linear portions of the peaks and the single phase , horizontal sections [Keefe,1999].

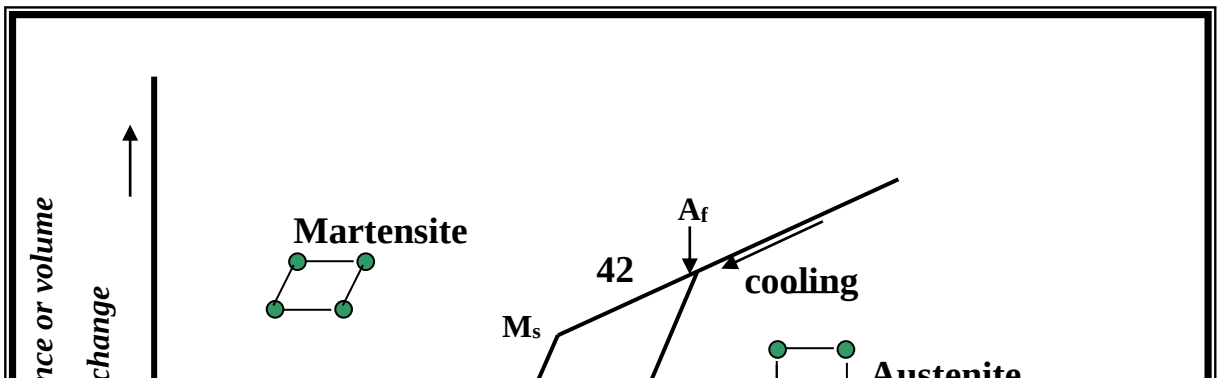

Fig. (3.7) property change with temperature for martensite transformation occurring in a shape memory alloy (Wayman and Duerig,1990).

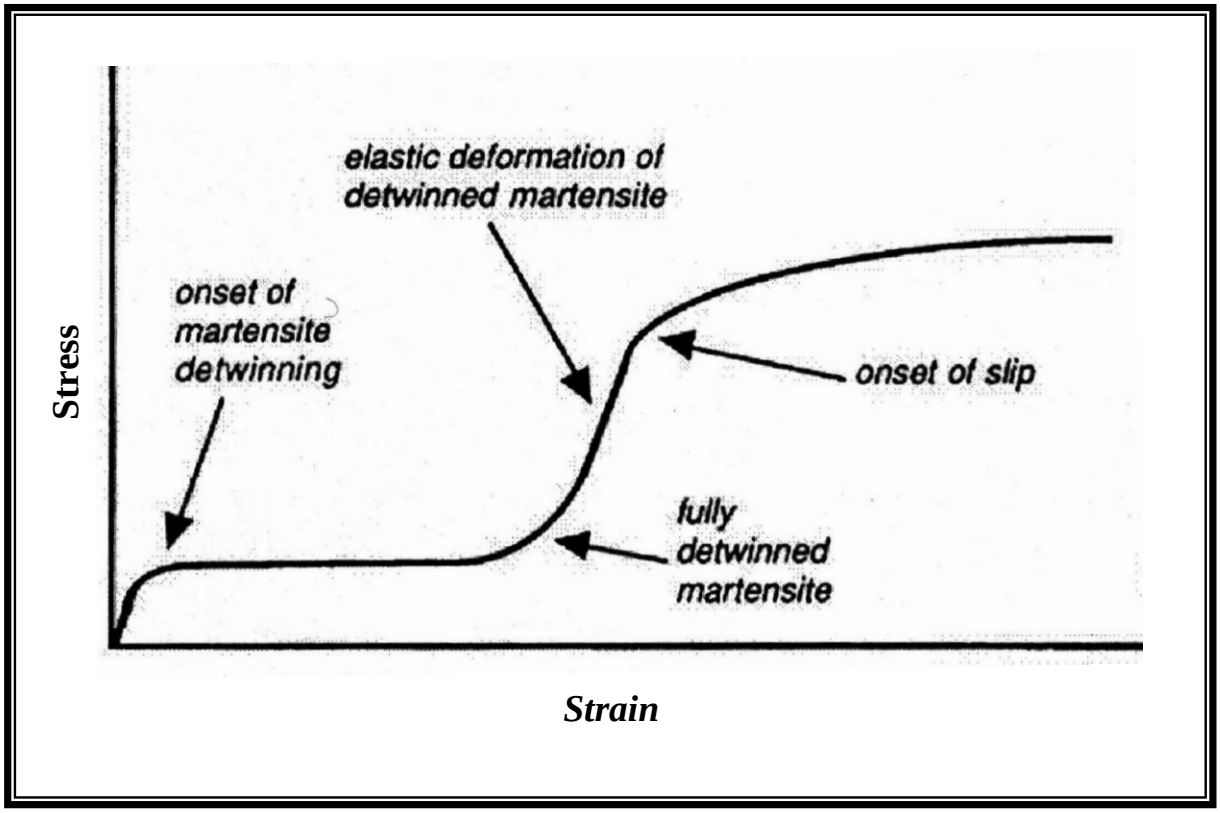

Fig. (3.8) typical stress-strain curve for a twinned martensitic material(Keefe,1999).

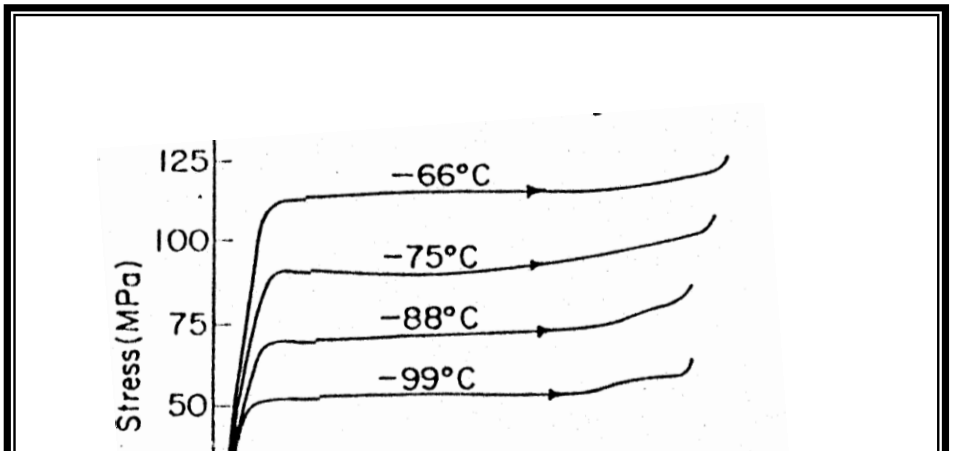

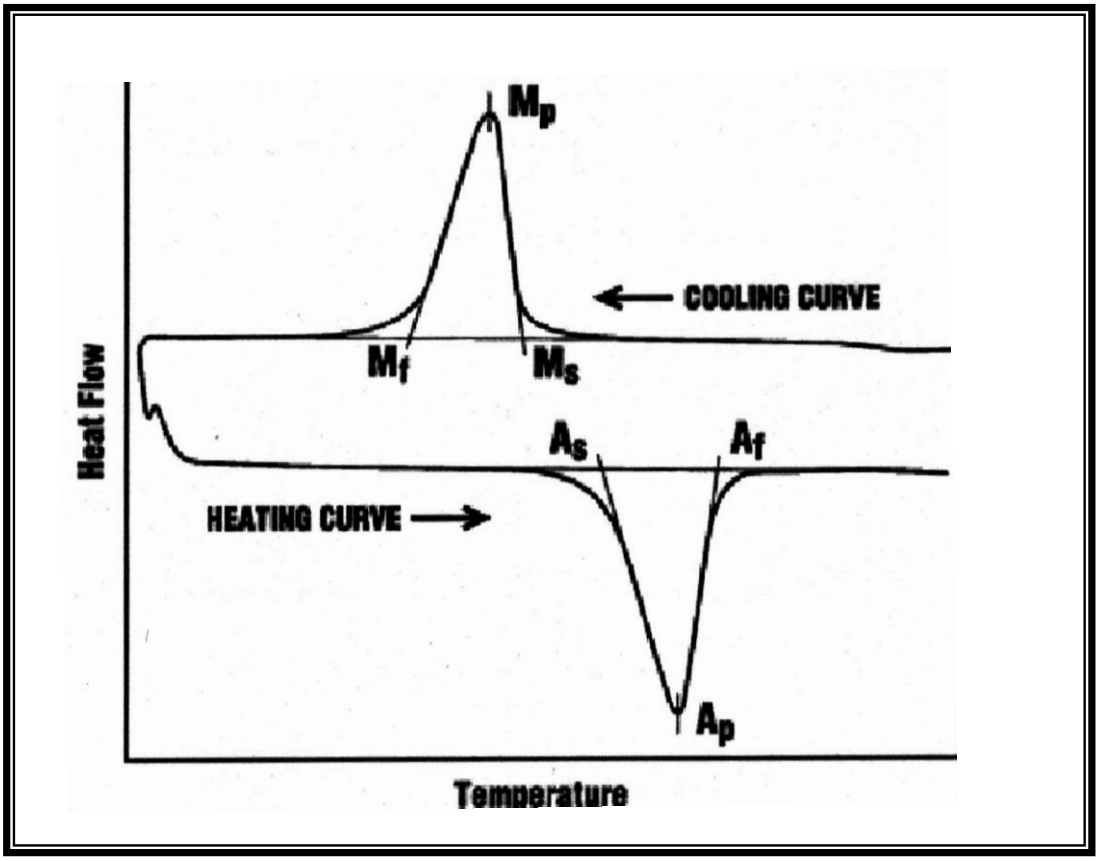

Fig. (3.10) A typical(DSC) curve for shape memory alloy **(Keefe,1999).**

Depending upon temperature , the material will generally behave in one of three ways: when cold below M_s the alloy will be in the martensitic phase, when hot above A_f the material will be in the austenitic phase and when between A_f and M_d ,the material can behave superelsticity alloy .

The behavior of the alloy is distinctly different in each temperature regime .Fig. (3.11) shows three different stress-strain responses for one shape memory alloy .[Keefe,1999].

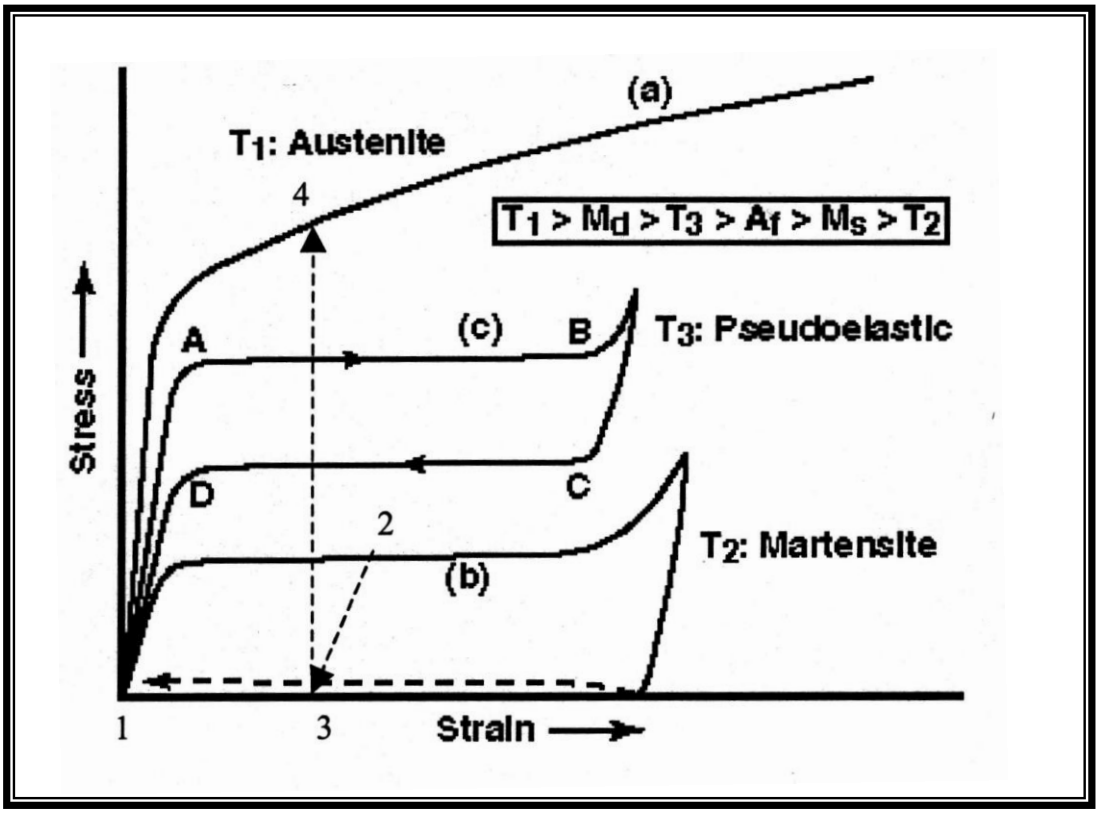

Fig. (3.11) Generic loading curve for SMA (Keefe,1999).

The shape memory effect is outlined in Fig.(3.11) by following numbers (1-4). The material is strained in martensite (1-2). At point 2, the specimen is unloading and left with some apparent plastic deformation at 3.If the simple is unconstrained and heated into austenite , all of this deformation will be completely recovered and return to point 1. However , if the piece were held fixed and heated , the stress would increase to point 4, when the (SMA) becomes fully austenitic .Point 4, corresponding to the maximum stress that can be achieved for the given amount of preset deformation .

3.2.2.2.Martensite Aging and Stabilization:

Martensite aging effect is a puzzling phenomenon unclear for over 60 years and has been found in Au-Cd ,Au-Cu-Zn,Cu-Zn-Al,Cu-Al-Ni and In-Tl . It involved two time dependent phenomena during martensite aging. One is called martensite stabilization , the other is called rubber like behavior .[Otsuka and Ren,1999].Martensite stabilization refer to the phenomenon that martensite appears to be more stable with respect to the parent phase during aging so that the reverse transformation temperatures are increased. The rubber like behavior refers to the phenomenon that martensite exhibits a recoverable or pseudo-elastic deformation behavior after aging together with an increase in critical stress as shown in Fig. (3.12).

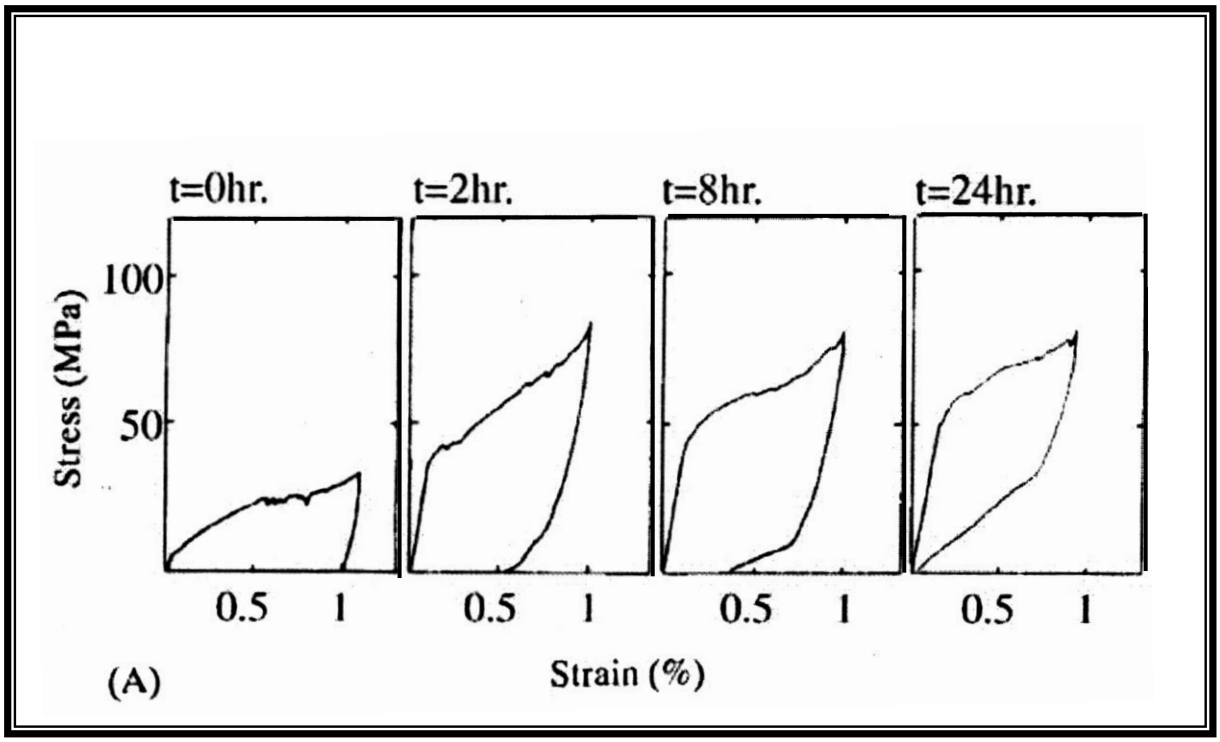

.

Fig. (3.12) The change of stress-strain curves of furnace-cooled Au-47.5Cd alloy after aging in martensite for various times t.[Otsuka and Ren ,1999]

Stabilization is a phenomenon associated with samples cooled to some temperature intermediate between M_s and M_d ,held there for a period of time and then cooled again. In such case , transformation does not immediately continue and the total amount of transformed martensite is less than obtained by

continuos cooling throughout transformation range. It has been observed that existing plates do not continue to grow after stabilization ,but the new plates are nucleated.

The degree of stabilization is a function of the time held at temperature.[Porter and Easterling,1992]. However , a general mechanism applicable to all martensites explained what is occurring during martensite aging which gives rise to stabilization and rubber like behavior , is not found.
Many previous studies using Cu-based alloys concluded that some structure change during aging in martensite is necessary to cause the aging effect.

However , martensite of these alloys are unstable and thus they have an born tendency to decompose simultaneously during aging. Therefore , the observed structure change may be just due to the inadvertent decomposition while aging itself may be independent of the decomposition. [Asanovic et al,2006].

3.3.Martensitic Transformation in Cu-based Shape Memory Alloys.

Cu-based alloys are Hume- Rothery alloys for which the phase stability is mainly controlled by the average number of valence electrons per atom. At high temperatures the crystal structure is bcc (β phase).

The β phase can be retained as a metastable phase below its stability limit by means of a suitable quench . During this quench the alloy becomes configurationally ordered.[Comas and Manosa,2000].

The body center cubic (β) phase is unstable thermodynamically at low temperature as shown in phase diagram of Cu-Al and Cu-Al-Ni in Fig.s(3.13)and (3.14).

It transforms martensitically to 3R,9R,18R or 2H . Its stability at elevated temperatures is due to the vibrational entropy from the low energy transverse phenon modes .[Ahlers ,2002].

Shears on the low –index {110} $<\bar{1}10>$ systems are therefore good candidates to describe the martensitic transformation .

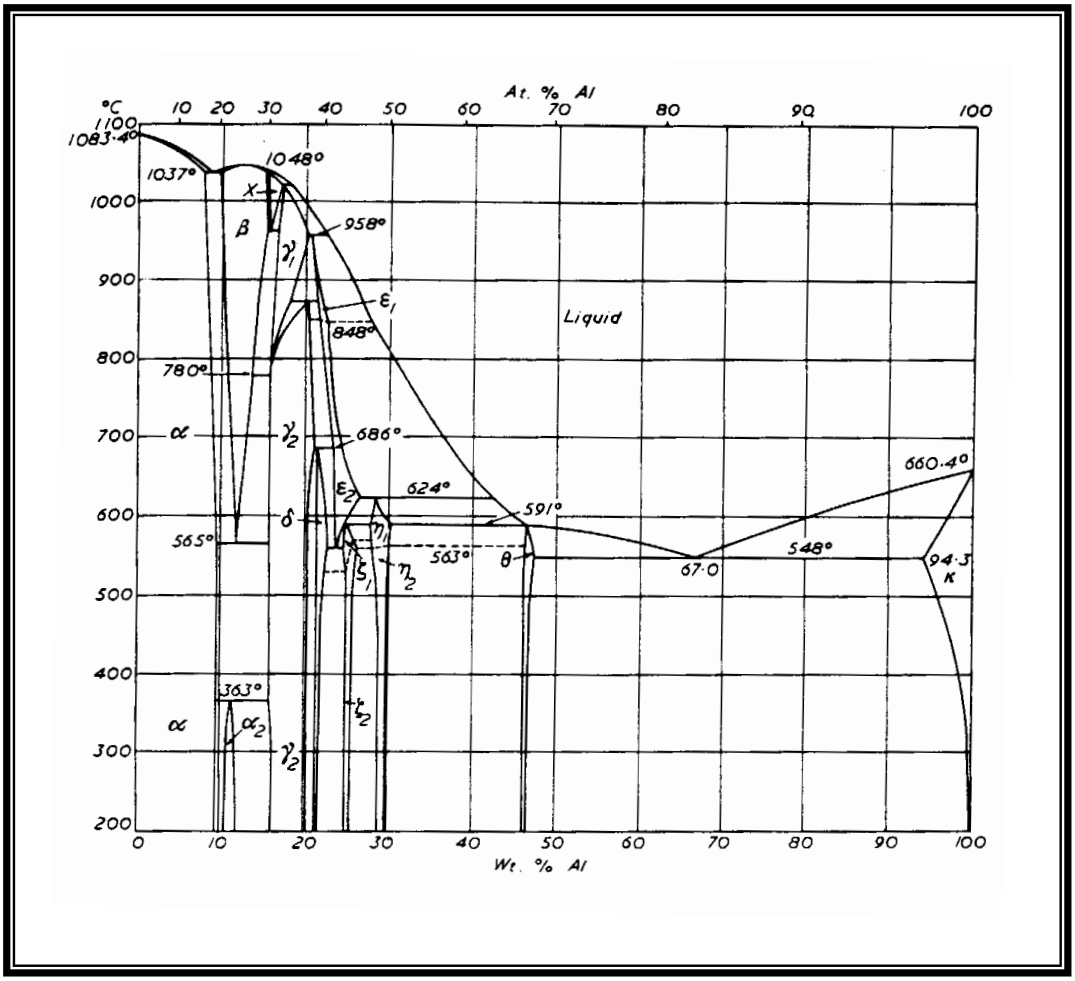

Fig. (3.13) Cu-Al equilibrium phase diagram(Higgins 1977)

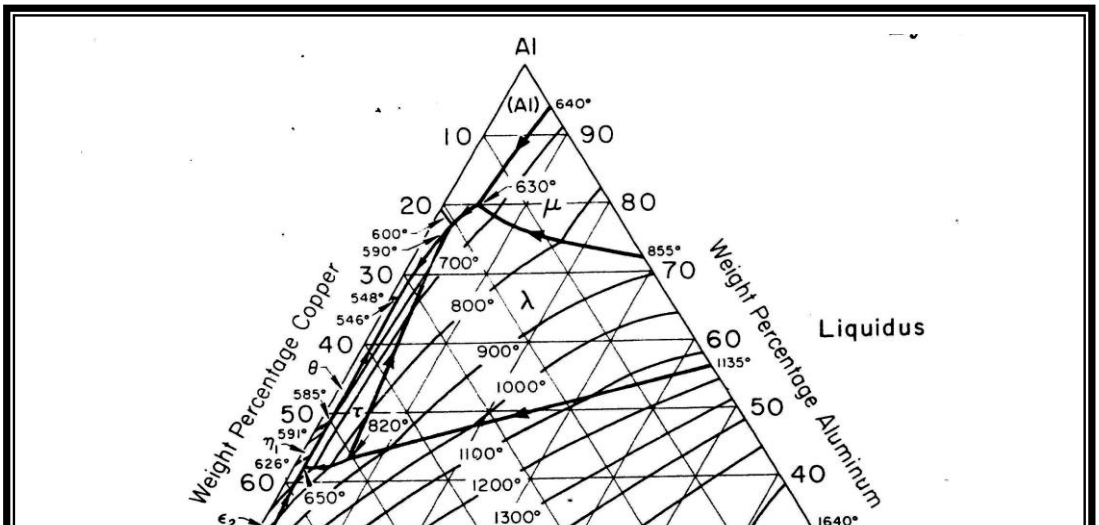

The {110} planes are also common slip planes in the bcc structures. A long wave "primary" shear combined with an additional secondary "shuffle" shear on an inclined (011) plane can indeed account for the movements of the atoms at the tip of growing thin martensite plates. It also leads to the correct martensite crystallography . For illustration consider Fig. (3.16)in which B_2 (Fig. 3.15) unit cell with the two sublattice sites and a(110) plane are indicated. The same (110) plane is plotted in Fig.(3.16)b . The circles belong to the atoms in one plane and the square to the atoms in the neighboring plane .The two different sublattice sites are shown as open and full symbols. Along-wave shear by which each consecutive plane is displaced with respect to the neighboring plane is indicated by the shifts A $\rightarrow A^{-}$ and D$\rightarrow D^{-}$, which place the atoms into the middle between the three atoms on the neighboring plane. This primary shear already transforms an inclined (011) plane into a close packed plane of martensite structure a shown in Fig. (3.16)c .[Ahlers,2002] .

Its stacking is not correct yet, and therefore additional secondary shear of these planes are required which is represented by the shift from D^{-} to $D^{=}$.

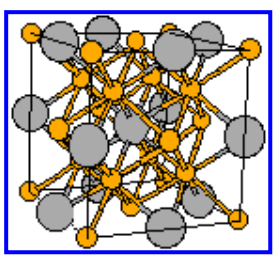

$D0_3$

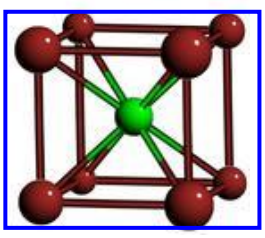

B2

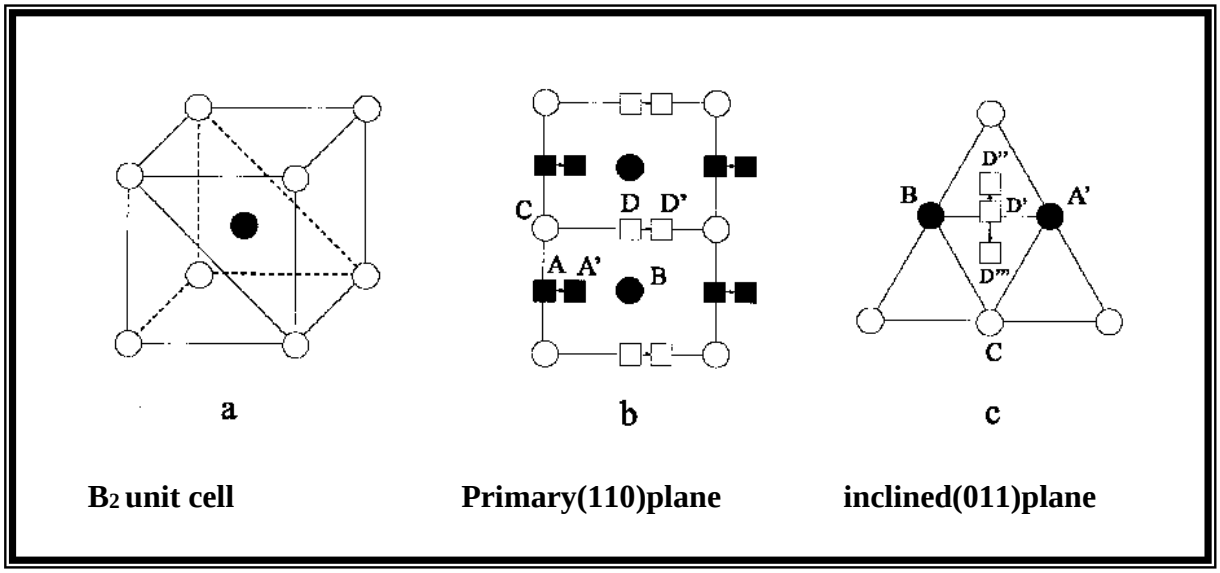

Fig. (3.16) The B_2 unit cell and primary (110) plane.(○),(●) positions in one plane whereas (□),(■), positions in the neighboring plane(Ahlers 2002).

The fraction of planes shuffled in one direction and in other direction is determined by the condition that an undistorted habit plane is created . The net amount of these shuffles has been calculated to be close to zero. This means that the number of planes shuffled the larger distance from D^{-} to $D^{=}$ must be compensated by double their number in the opposite direction .

The most homogenous distribution leads to the 9R structure with the stacking sequence ABC ,BCA,CAB .A less homogenous distribution is obtained by the shift of a whole stack of planes in one direction followed by a shift in the opposite direction . This configuration leads to the formation of twinned FCC martensite.[Ahlers,2002].

In reality the two shear occur simultaneously at the tip of the expanding martensite plate which means that the atoms on the shuffle plane are displaced continuously with its progressing distortion by the primary shear starting from the original positions on the inclined (011) secondary plane. They move symmetrically in the two possible opposite directions towards the final positions $D^{=}$ to $D^{\equiv}$ in the close-packed lattice . The 9R structure has a more homogenous interface than the twinned 3R.Once the thin plate has formed, it starts to thicken.

This process consumes little energy . It is due to the very favorable atom fit at the boundary between the two structures because of the small orientation change of the based planes.[Lovey et al,1987 Quoted in Ahlers, 2002]. Therefore the energy consuming process during martensitic transformation is the expansion of the thin plates at constant thickness in addition to nucleation.

The long range ordered Cu-based alloys retransform back to the original shape of β phase matrix. In order for this occur, two conditions have to be met .The first is that the flow stress of the matrix is so high that the distortion at the tip of the growing martensite is not relaxed by dislocation glide. A second important factor is the multiplicity of the transformation-retransformation paths of the atoms. It has been shown that in order to obtain a martensitic transformation with little energy loss two requirements have to be met. The resistance against the shears and shuffles should be small, and the transformation –retransformation path of the atoms must be single valued.[Ahlers,2002].

3.5.Origin of Shape Memory **:**

The martensite phase is generally a lower symmetry phase than is the austenite . The consequence of this is that there are several ways in which martensite can form from austenite but there is only one possible route which will return the austenite structure .Two shear directions can be applied to the squares to produce two different rhombus variants but there are no other possible variants of austenite so both of these rhombus shapes would have to return to same square geometry .This simple geometrical concept becomes the foundation for the shape memory effect. Upon cooling from austenite , the self accommodating variants of martensite are formed. The twin boundaries migrate during deformation resulting in a biased distribution of martensite variants. There is only one possible reverted structure and with reversion to austenite must return to original shape . Thus the shape accommodation due to twin boundary movement can only be supported by the less symmetrical martensitic structure and when the more symmetric austenite structure is return , the twinning deformation must also disappear .[Wayman and Duerig,1990].

The shape memory effect can be described according to the cooling and heating curves with respect to electrical resistance property.There is no change in shape of a specimen cooled from above A_f to below M_f.

When the specimen is deformed below M_f it remains so deformed until it is heated. The shape recovery begins at A_s and is completed at A_f .Once the shape is recovered at A_f , there is no change in shape when the specimen is cooled to below M_f and the shape memory can only be reactivated by deforming the martensitic specimen once again. The shape memory effect is a one time only occurrence which referred as one way shape memory. In contrast , in the two way shape memory behavior ,the specimen changes its shape upon cooling to below M_f .For example, way shape memory spring extends when heated above A_f and contracts again when cooled below M_f .Special thermomechanical treatment is required to produce two way shape memory behavior .[Wayman and Duerig ,1990].

When the external stress is applied , the variants that have shear strains tend to grow and the unfavorable oriented variants shrink as shown in Fig.

(3.17) only two variants are shown for simplicity. All unfavorable variants disappear and the favorable variant stakes over the structure. On heating, the structure reverts to the original one. Composed of equal distribution of the two variants giving the strain recovery.

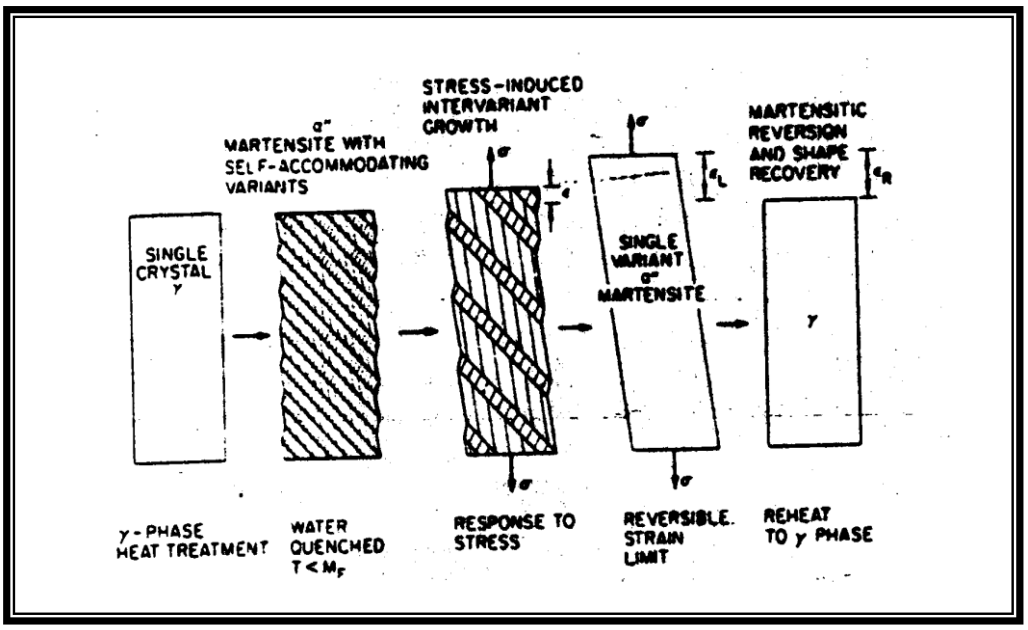

Fig. (3.17) Growth of one martensite variant and shrinkage of others.(adapted from Meyers and Chawla,1999)

The shape memory effect in tension, compression and bending loading are shown in Fig. (3.18).

Only two martensite variants are shown , A and B . variant B favors tensile strains where as variant A produces compression in the direction of loading. Under compressive stresses. Variant grows at the expense of B. Under tensile loading , the opposite is true. Under bending ,variant B grows in the outside while variant A grows in the inside. The situation in a real material is much more complex.

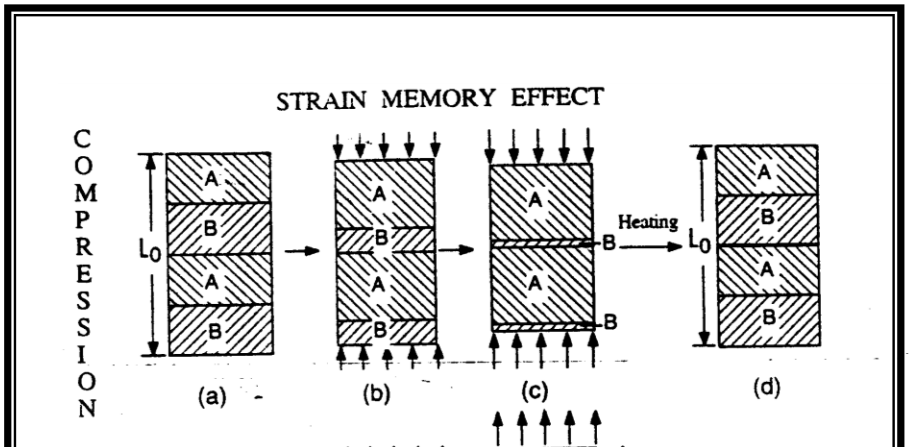

3.6. Copper-Based Shape Memory Alloys:

Both Ni-Ti and Cu-based shape memory alloys such as CuZnAl and CuAlNi, are presently available for commercial shape memory applications. In many applications, Cu-based alloys provide a more economical alternative to Ni-Ti.

Early Cu-based alloys suffered from intergranular failure causes by coarse grain structure but, recent development of fine–grain Cu-based alloys has improved mechanical properties.

Current Cu-based shape memory alloys are derived from three binary alloy systems: Cu-Zn and Cu-Sn. The martensitic transformation in Cu-Sn alloys is not ideally thermoelastic and suffers from a rapid degradation of shape memory properties during aging.[Wayman and Duerig,1990].

Cu-Zn base with al, Si, Ga, Mn as alloying elements and Cu-Al with alloying elements of Ni, Be, Zn, Mn have been explored for their shape memory properties.

In this study, CuAlNi alloys have been prepared using powder metallurgy process. These alloys are also grain refined by additives such as b, Ti, Co, Zr, Fe, Si and Mn. Further more , CuAlNi+(Ti+Mn) and CuAlNi+(B+Mn)with different percent of additives have also been studies.

3.6.1.Effect Of Alloy Elements :

The shape memory properties of Cu-based shape memory alloys are very sensitive to alloying elements which are added to adjust the martensitic transformation temperatures and to optimize mechanical properties.

The martensitic transformations in cu-based alloys occur from ordered bcc (β phase). The high temperature β phase has a disordered A_2 structure (Fig. (3.15))but upon cooling the structure goes through a nearest-neighbor ordering transition and develops the B_2 supperlattice structure .Further cooling induces next-nearest neighbor ordering and the structure eventually becomes the Do_3 or L_2,superlattice structure depend up on alloy composition and cooling rate .[Barrett and Massalski, 1980].

Martensite structure in Cu-based shape memory alloys are more complex than are those of Ni-Ti system. All are of along period stacking order type such as 3R, 6R, 9R, 18R and 2H or 4H. The thermally induced martensites in both CuZnal and CuAlNi alloys consist predominantly of β^{-}(9R) martensites. γ^{-}(2H) martensites are usually found in alloys with higher aluminum content. Mixtures of both β^{-} and γ^{-} martensites have been observed in cu-21.0Zn-5.95Al and Cu-13%Al+ 4.09% Ni. In both systems, the stability of γ^{-} martensite increases with aluminum content .

The stress–induced martensite from parent β phase normally have the same structure as thermally induced martensites ,further more , β^{-} martensites can also

be induced upon stressing the γ' martnsites .the stability of β' and γ' marteensites depend upon stress and temperature .[Wu,1990].

3.6.2.Effects Of Heat Treatment:

Cu-based shape memory alloys are affected by heat treatment such as solution (Betatizing) treatment and aging through changing of transformation temperatures (A_s,A_f,M_s.M_f) .All transformation temperatures are increased with increasing betatizing temperature.[Wu,1990].Also ,extending of betatizing time from 10 to 60minuts raises transformation temperature . This effect is related to grain growth during solution treatment.

Both the parent phase (β) and martensite in Cu-based shape memory alloys are susceptible to aging effects. For CuZnAl alloys, a direct quench into the austenite β phase results in depressed transformation temperatures which increase and stablize during subsequent aging at low temperatures.[Asanovic et al,2006].

When CuZnAl alloy is stabilized by post-quench aging and is then subjected to exposure at temperatures of 100-350 C°, the change in transformation temperatures can be classified into three stages as shown in Fig. (3.19). The first is characterized by a rapid drop of transformation temperatures which are then recoverable during subsequent aging at temperatures below 70 C° . The amount of depression increases with aging temperature up to 300 C° and then decreases with further increases in the aging temperature .

The transformation temperatures increase only moderately with time during the second stage.

The temperatures decrease drastically and the hysteresis is widened, in third stage. [Wu,1990].

It has been shown that the post quench aging effect and the first stage behavior are related to the ordering in CuZnAl alloys . The second stage is probably related to the growth of ordered domains where as the third stage aging

characteristics have been demonstrated to be caused by the decomposition of the β phase into bainite or α phase .[Asanovic et al,2006].

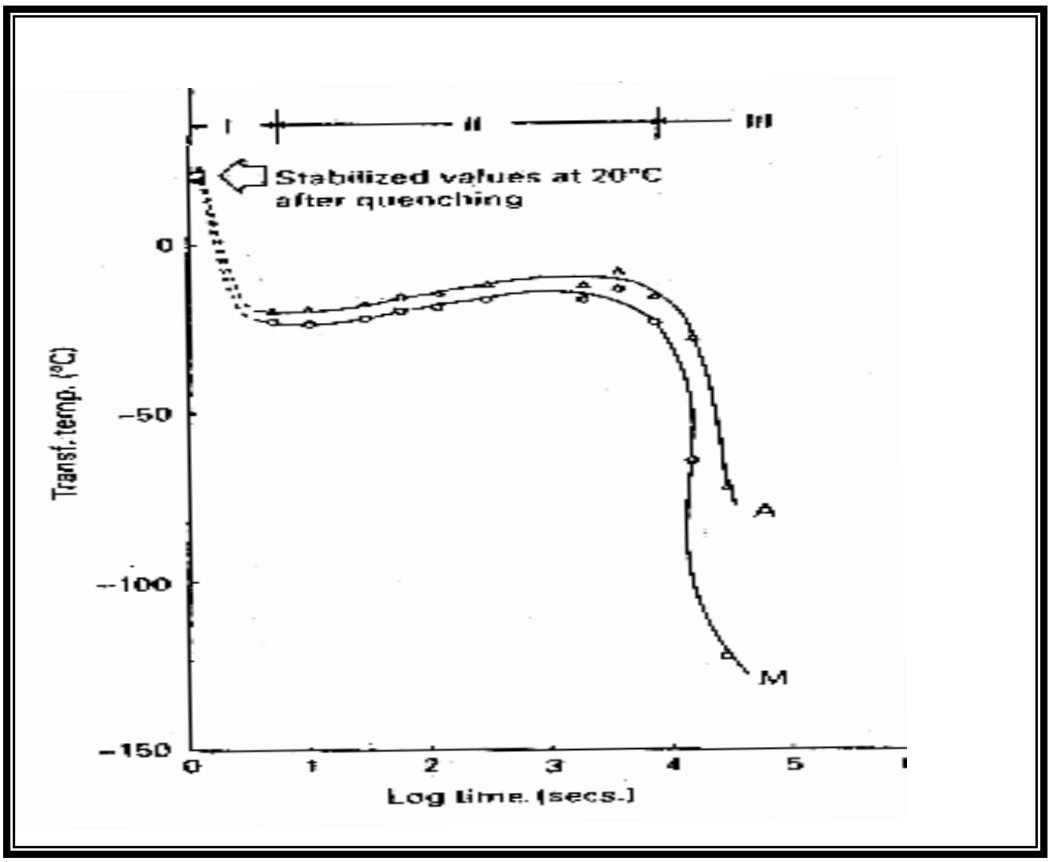

Fig. (3.19) Changes in M and A temperatures of cu-26.67Zn-4Al alloy during aging at 200 C° .(Wu,1990) .

Direct quenching of CuZnAl alloys into martensitic state causes stabilization of martensites which may not transform back to the parent phase during subsequent heating up to 150 C° as shown in Fig. (3.20) which clear the resistivity curve of Cu-25.8%Zn3.58Al alloy with M_s =100 C° after directly quenching from the solution treatment to the ambient. No transformation is detected whereas step-quench process with intermediate aneal in the parent phase(β) state at 150 C° gradually restore transformation as shown in Fig. (3.20) .[Wu,1990].

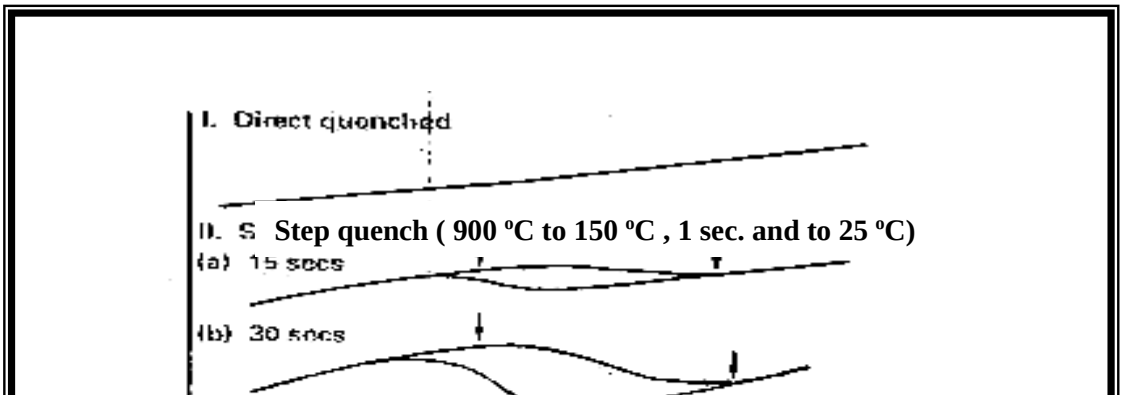

Fig. (3.20) Effects of quenching on transformation resistivity curve for Cu-25.8Zn-3.6%Al alloy. [Wu,1990].

Aging of CuZnAl martensites also causes martensite stabilization through increase A_s and A_f to higher temperature.[Asanovic,2006].

The aging effects in CuAlNi alloys are sensitive to Ni content. For most alloys containing 3-5%Ni, the transformation temperatures increase with aging time at 200-300 C° temperatures and decrease at higher aging temperatures .e.g.400 C° . The aging characteristics are related to reordering at the early stage and later to the precipitation of γ_2. Which causes the depression of transformation temperatures. [Wu,1990].

3.7.Powder Metallurgy of Cu-Based Shape Memory Alloys:

Fine grain copper based shape memory alloys without grain-refining element additions can be produced by powder metallurgy. A grain size of around 30μm has been obtained in a powder processed CuZnal alloy which was water atomized to an averaged particle size of 150 μm and subsequently cold

Powder processed CuZnAl shows better resistance to cycling degradation

in recoverable strain than conventionally processed alloys. A powder processed CuAlNi alloy with grain size of 20 μm exhibits a significantly improved ductility from 5 to 7% compared to 0.6% in cast alloys.[Wu,1990].

Porous shape memory alloys exhibit all the same properties as their dense counterparts but with added benefit of low density and the ability to undergo larger deformation before failure. Furthermore , porous SMA would take advantage of the inherent damping of shape memory alloys while at the same time providing structural rigidity and decreased weight.[Penrod,2003].

Porous SMA_s are manufactured by several different ways based upon application, structure and properties which can be adjusted to meet a specific need.In the following , general explanation for copper based alloys powders preparation , mixing, compacting and sintering have been presented.

3.7.1.Preperation of Copper Powder:

Because of the majority of copper content in copper base shape memory alloys , great attention for production of copper powders, has been presented in this section . Copper powder containing more than 99% Cu is available commercially . The four major methods for producing unalloyed copper powders are oxide reduction, atomization , electrolysis and hydrometallurgy .[stevenson,1984]. Brief description of these processes are presented in the following :

3.7.1.1.Production of copper Powder by the reduction of Copper Oxide:

reduction of copper oxide is the oldest and by tonnage ,the most extensively used process for the production of copper powder . In the this process , particulate copper oxide is reduced with gaseous reducing agents at elevated temperatures. The product is essentially a sintered porous cake of copper that must be ground to powder . Raw materials include copper scale, cement copper , particulate copper scrap and atomized copper. Particulate copper scrap and atomized copper are roasted to form cuprous and cupric oxide. Various approaches for producing copper powder by oxide reduction . They differ

mainly in the degree of oxidation of the starting material prior to reduction .[Stevenson,1984].

3.7.1.2 .Production of Copper powder by Atomization:

Atomization of copper is the disintegration of a molten stream of high quality copper with high pressure water jets, which produces copper powders of compacting grade quality. The resulting denied powder may be subjected to an elevated temperature treatment to modify its engineering properties.

Nearly spherical powders result from the atomization of liquid copper with inert gas or air. These powders are used to produce fake copper powders. Spherically shaped copper powders have insufficient green strength for use in conventional powder metallurgy.[Dowson,1990].

Liquid copper is superheated to about 1150 to 1200 C° utilizing flow rates of 27Kg/min or more with water pressures of 10-14Mpa.Atomization may be conducted in an air or inert(N_2 gas)environments.

3.7.1.3.Production of Copper Powder by Electrolysis:

Production of electrolytic copper powder as shown in Fig. (3.21) , depends upon electrochemical principles that apply to the electro refining of copper . The conditions of deposition are changed to yield spongy deposit instead of the strongly adherent product. The formation of powdery deposits is favored by low copper ion concentration, high acid content in the electrolyte and high cathode current density.

Although , these conditions yield spongy deposits, control of additional variables such as temperature, circulation rate of the electrolyte , size and type of anode and cathode and electrode spacing, is necessary to produce copper powders.[Jasim,2006].

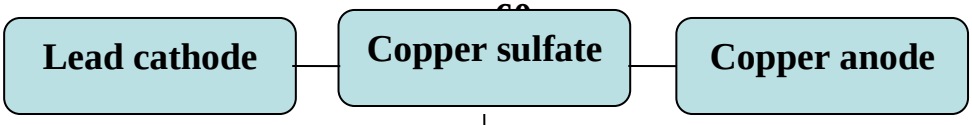

Fig.(3.21) flow chart for production of electrolytic copper powder[adapted from Klar,1984]

3.7.1.4.Production of Copper Powder by Hydrometallurgyical Processing :

Copper powder can be produced by hydrometallurgical methods which consist of preparing pregnant liquor by leaching ore or another suitable raw material followed by precipitation method of the metal from this solution. The most important precipitation methods are cementation , reduction with H_2 or sulter de oxide and electrolysis .Use of several leach precipitation steps or the inclusion of floatation , solvent extraction or ion exchange improves the purity of the final material.

3.7.2 Blending and Mixing processes:

Blending is an operation of through intermingling of powders of the same composition or substance while mixing is defined as the through intermingling of powders of several or more different materials .Mixing is extremely desirable in the preparation of alloys from elemental powders .[Sinha,1995].

Additives such as binders or lubricates are usually included in both types of processes to facilitate pressing and achieve the required green strength and controlled porosity in the final product. Mixing of powders is a most complex process which relies on the movement of mass of one powder component into that of another powder component. This movement is dependent upon powder material, particle size and shape and surface conditions.[Sinha,1995].

The main purpose of mixing is to produce uniform distribution of powder and to control the powder characteristics .It must produce a homogenous mixture in the least possible time .

Time of mixing is of great importance. It is very difficult to determine the optimum mixing time in advance because of our limited knowledge of the friction in powder mass. Some problem that can take place during mixing, are variation in particle size distribution through agglomeration , oxidation of powder particles and segregation of powder during transfer from the mixer.

Time of mixing may vary considerably from a few minutes to 24 hours or more. It may be accomplished in air , under protective atmosphere or under suitable liquid to avoid partially or completely oxidation or segregation.

Mixing is accomplished by various types of blenders and mills such as ball mills, road mills and double cone mixers.

It has been shown that there are three mechanisms which occur in mixing process included the following :

1.Transfer of groups of adjacent particle from one location to another called as "connective mixing".

2.Distribution of particles over a newly developed surface known as "diffusive mixing".

3.The formation of slipping planes within the mass called as "shear mixing"

All of them are always occurred in operation but the degree of any one of these will depend upon the mixing machine .[Sinha,1995].

Mixing may be either dry or wet based on the medium in which the milling is carried out. Wet mixing is used to produce more fine and uniform mixture of powder particles. Wet mixing may be obtained by the addition of alcohol, benzene, glycerin or acetone as a liquid medium in adequate amount in order to bring the powder to the consistency of a thin paste. After completion of the mixing process, benzene or acetone is removed by during the mix in air or in a controlled oven up to 50 C° .

Mechanical alloying is a relatively new technology that enables a large variety of advanced material obtaining. It consists of material milling in a high energy mill process producing repeated powder particle deformation ,work hardening , fracturing , clean surface , local heating and solid state welding. Re-fracturing and so on, under the impact energy transferred to them from collisions of the chaotic moving balls. Pure solid solutions of alloys of an extended solubility limit are obtained if components does not react each other.[Orban,2004].

It has been shown that mechanical alloying and powder metallurgy techniques can be used to prepare Cu-based shape memory alloys. Mechanical alloying can reduce oxidation because a new phase is formed and produces a pre-alloyed powder that shortens the sintering time. For CuAlNb shape memory alloy prepared by mechanical alloying, the ball to powder weight ratio is 6:1 with 150rpm rotation rate.[Silva and Lima,2005].

3.7.3.Particle Shape and Powder Density:

Although shape of powder particle is importance it is not normally specified or determined directly . It is not easy factor to measure and almost impossible to quantity. There is a number of commonly occurring shapes such as granular, a circular, irregular ,flaky and spheriodal. Particle shape has a major influence on the packing density of powders and this is a factor that can be measured.

Spherical powders pack most density and the density decreases as the irregularity of the particle shape increases.

There are two was of expressing this bulk density that are in general use in powder metallurgy. The most widely used is apparent density ($\rho_{ap.}$) which is

the density of powder mass expressed as grammes per cubic centimeter of a standard volume of powder gently loaded under specified conditions into a cylindrical container of specified volume .

In the other test a weighed sample is placed in a graduated cylinder which is tapped or otherwise vibrated in a standard way until the volume is constant. This gives the tap density or tapped density which is higher than the apparent density.[Dowson,1990].

Most powder are three dimensional in nature. These powder may be equiaxed and nodular but uniformity of shape does not completely exist within anyone type of powder. However, advancements in qualitative analysis are based on the use of the scanning electron microscope(SEM) for determination of particle shape. In addition to its high magnification capability, this device produces an image with a three dimensional appearance.

3.7.4.Particle Size and its Distribution:

particle size and size distribution have a significant effect on the behavior of metal powders during processing thus to a considerable extent, they govern the properties of the final products made from powder.

It affects most of the properties such as mould strength, density of compact, porosity , expulsion of gases, dimensional stability, flow and mixing characteristics .[Ullrich, 1984].

Particle size is expressed by the diameter for spherical shaped particles and by the average diameter for non-spherical particles. Average diameter is defined in different ways according to the method employed for size distribution .When the method involves sizing ,the particle size is measured as the opening of a standard screen which just retains or passes the particle. When determined by microcount method ,the diameter is measured by averaging several dimensions. According to the sedimentation method the particle size is defined as the diameter of the spherical particle having the same specific gravity and setting velocity as the non spherical particle under test. In practical metal powders are divided into three distinct classes sieve, sub sieve and sub micron or ultra fine . The screen with the opening of finest standard mesh sieve for production purposes is the 325 mesh screen having the aperture of 44 micron.

Whereas sub sieve particles are smaller than the aperture of mesh screen but greater than 1 micron. There are several techniques of particle size measurement which have been shown in table (3.2).

In this study optical microscopy has been used to analyze shape, size and distribution of particles for elemental powders and their alloys through taking digital images for optical microstructure with suitable magnification and analyzing of these image with image analysis program taking into consideration image analysis and image processing .

Table (3.2) Common methods of particle size measurement and their limit of useful size range.[Sinha,1995].

Method of analysis	*Particle size range (micron)*
1.i- sieving using mechanical shaking ii-Micro mesh sieve	44→840 5→44
2.Microscopic analysis i-light microscopy ii-SEM	 0.1→100 0.001→10
3.Sedimentation method i-Sedimentation and decantation ii-Gravitational iii-Centrifugal	 2→50 0.05→50 0.05→10
4.Elutration method i- Elutration ii-Roller air analyzer	 5→100 5→40
5.Permeability method i-Permeability ii-fisher sub-sieve size	 0.5→100 0.2→50
6.Adsorption method (gases)	0.002→20
7.Electrolytic resistivity method (coulter counter)	0.3→300

3.7.5.Powder Compaction of Cu-based Alloys:

Powder of copper–based alloys is usually preformed in a closed die although other means such as hot pressing, roll compaction, isostatic pressing, extrusion and forging can be used. Brief description of these processes has been presented as follows:[Stevenson,1984].

3.7.5.1.Die Compaction:

Compaction in metal dies is one of the most important methods for shaping metal powders. When the die cavity is uniformly filled with copper powder it gives rise to certain packing density (apparent density) but a certain amount of bridges are also formed, when the powder is slightly pressed by the application of one punch or more punches as shown in Fig.(3.22), the first densification occurs by particle movement and rearrangement causing improved packing density which all bridges are collapsed. The degree to which this occurs is dependent upon particle size distribution, particle shape, amount of lubricants.

The interparticle movement produces superficial abrasion of surface film comprising oxides which absorbed atmospheric gases which are usually present or wedged between the metallic surfaces. These films obstruct the occurrence of direct metal contact and thus the formation of appreciable interparticle bonding due to the interparticle movement, the films surrounding the particles are ruptured which are more brittle with respect to the metal underneath.

The initial contact areas between the particles are so small that even a slight punch load causes very high pressure on these areas there by breaking up the surface films at the areas of contact. At this stage compacting produces only dense packing of powder particles.

There is no deformation or adhesion between the individual particles. If the pressure is more increased, the clean particles are brought close enough together and they adhere to each other with some strength. Further increase in pressure causes deformation of particles and large areas of contact of neighboring grains will take place companied by filling of voids by the

squeezing of small particles, due to this , strength and density are increased.[Sinha,1995].

Deformation is the major mechanism of densification with regard to production of high density parts.

Both elastic and plastic deformation may be took place. Most of elastic deformation will be recovered on removal of stress from the compact. This occurs before, during and after ejection from the die cavity.

Most of metal powders work hardens to a suitable extent so that they become more difficult to improve densification of the compact by increasing pressure of compacting. However ,low pressures may be more effective since plastic deformation may occur at ease and the external pressure will be become less effective with increasing pressure.[Sinha,1995].

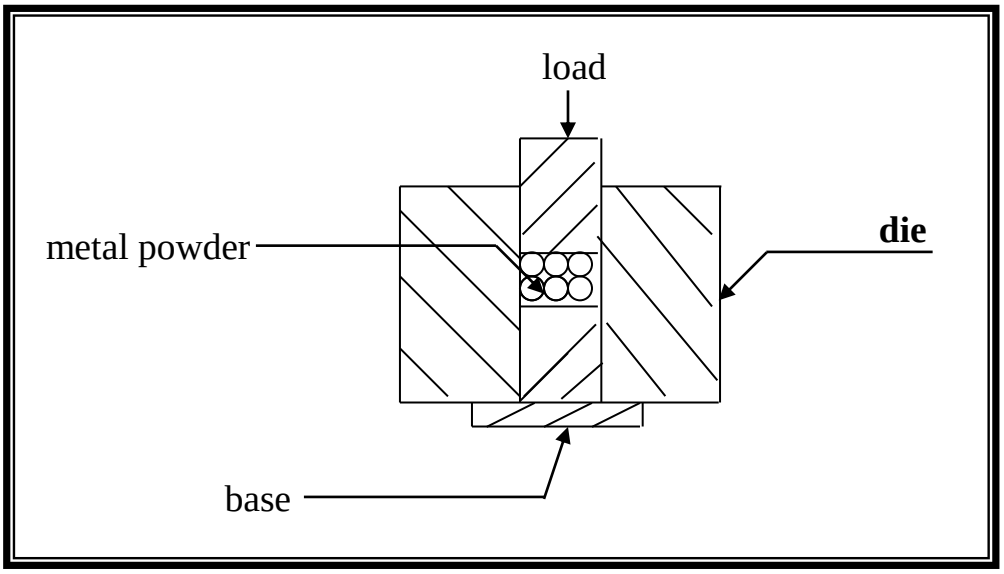

Fig. (3.22) Tools Die Compaction

During compaction, several types of friction will be occurred as follows:

1. Friction between moving punches and die wall which is relatively small.
2. Friction between adjacent particles which is insignificant and play a minor part in compaction .

3. Internal friction within the powder particles during deformation.
4. Friction between powder particles and the die wall which is the most important factors which effects the uniformity of density throughout thr compacted part.
5. Friction between the green compact and the die wall ejection which based upon powder material, die finish and compacting pressure.[Sinha,1995].
6. To reduce the effects of all above friction, lubricants from low melting materials such as Li, Zn, Al strearates can be used. It has been shown that the lubricant Zinc stearate forms a protective film on the powder surface and hinders diffusion between Aluminum and Copper in CuAlNb shape memory alloy.[Silva and Lima,2005].

There are several different types of die compaction techniques but here ,two important types are considered as follows:

1.Single-action compaction which is used for manufacture of flat, thin parts such as washers , discs and thin rings or short rods. The die and the lower punch are stationary during application of pressure by the motion of upper punch acting from one direction only on the powder placed in the die cavity. This type of compaction has been used in this study to prepare disc samples and cylindrical samples.

2. Double–action compaction denotes a system in which powder is compacted simultaneously from opposite directions by both the top and bottom punches. Equal or different amounts of movements and pressure may be used from each direction as shown in Fig.(3.23).

Upper punch

Fig.(3.23) Double action compaction system

3.7.5.2.Isostatic Pressing:

Isostatic pressing is the consolidation (refers to the production of coherent metal structures using metal powders as the major raw material) of powdered material contained in a tightly sealed flexible mould into shaped bodies in which uniform pressure is applied simultaneously and equally in all directions which leads to achieve uniform density and strength.

If the pressure transmitting medium is liquid such as water , glycerin or various hydraulic oils, the term more specifically used is hydrostatic pressing whereas gases, powders, rubber or plastic medium refers to as isostatic pressing process .[Sinha,1995].

3.7.5.3.Roll compacting:

Roll compacting refers to the continuous compaction of metal powders by a rolling mill in which metal powders are fed from a hopper to a set of rolls that produce a continuous green strip or sheet as shown in Fig. (3.24).[Knopp et al,1984].

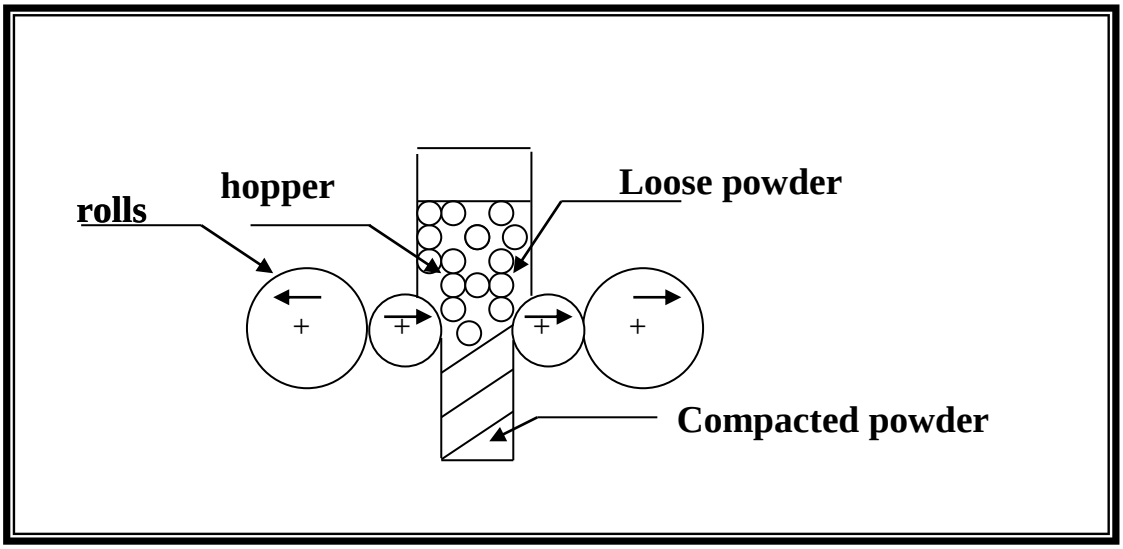

Fig. (3.24) Typical roll compaction of copper strip.

3.7.5.4.Powder Extrusion:

This process consists of extruding the mixture of powders at high pressures and high temperatures (850 for copper base alloys) through the suitable die.

In this process, binding material such as paraffin wax is used to binds the powder particles and to minimizes the friction against the die wall. Extrusion of bars, rods, tubes and thin sheets may be used to satisfy extremely high densities.[Sinha,1995].

3.7.5.5.Powder Forging :

In this process, pressed powder perform by die compaction or isostatic compaction is heated to hot working temperature in a protective atmosphere and immediately transferred to close die and forged. After forging, the component is quenched or cooled in protective medium to minimize oxidation. This produces densification up to 100% and involves lower sintering temperature. The green

compacts are given the combination of sintering and forging preheating instead of sintering in a normal way.

3.7.5.6.Hot Isostatic Pressing (HIP):

Hot isostatic pressing is a material processing technique in which high isostatic pressure is applied to powder compact at elevated temperatures to produce particle bonding. This process usually results in the manufacture of a fully dense body.

During compacting, the compact is subjected to equal pressure from every side. Elevated temperature ranges from 480 C° for aluminum alloy powders compacting to 1700 C° for tungsten powder compacting. High density argon gas is the most common medium used in the process and pressure range from approximately 20 to 300 Mpa .[Price and Kohler,1984].

A pressure of 140 Mpa at 850 C° which is applied during 2 hours, has been used to hot isostatic compacting of CuAlNi shape memory alloys.[Raul et al,2000] .

3.7.6.Sintering of Copper-base alloys:

Sintering is the thermal treatment of a powder or compact at a temperature below the melting point of the main constituent for the purpose of increasing its strength by bonding together of the particles.[Dowson,1990].

Sintering is carried out at a temperature in the range of 0.7-0.9 of the absolute melting point of the base metal in a multi component powder system. Sintering is a very complex process in which physical, chemical and metallurgical effects interact simultaneously. Sintering process is concerned with the following:

1. Diffusion of particle to particle.
2. Formation of grain boundaries.
3. The closing of voids present in the green compacts.

Furthermore, the decrease in free energy due to the decrease in surface area is the main driving force of sintering.[Sinha,1995] .

Typical sintering furnace temperatures for Bronze range from 815 to 860 C° with total sintering time in hot zone from 15 to 30min depending on the furnace temperature selected, required dimensional change and the mechanical properties desired after sintering .

For brasses, sintering temperatures range from 760 to 925 with time from 10 min to 45 min.[Mathews,1984].

3.7.6.1.Stages of Sintering:

The fundamental aspect of sintering is that it is carried out at constant temperature and time is varied to obtain the desired results. There are three stages of sintering as follows [Sinha,1995]:

I.Adhesion without shrinkage:

Initial bonding and neck growth occur rapidly and very early in the sintering process when the powder compact is being heated up. In this stage, great extended of bonding within the sinter mass may continue for some more time.

This first stage of consists of volume diffusion of vacancies from the neck region to the convex portion of the system remote from the neck and surface diffusion between surface regions with different radii of curvature.

II. Stage of Densification and Grain Growth:

Here, most of the shrinkage occurs in which more pore rounding takes place so that network of pores is formed and grain growth continue. Closed pores with increase pore size and decreased numbers of total pores are obtained by volume diffusion of voids from the interior towards the surface. Smaller pores must have been absorbed more rapidly by the larger ones.

III. Elimination of the last isolated and rounded pores:

Here, the spheroidization of isolated pores rapidly increases and pore shrinkage has been occurred more quickly in the vicinity of the grain boundary.

Further densification proceeds at a low rate.

3.7.6.2.Mechanisms of Sintering:

Several mechanisms of sintering are considered as follows:

I. Adhesion Mechanism:

Adhesion between metal surfaces is an elementary bonding process which does not involve material transport. Adhesion processes exert a decisive influence on sintering but not during intermediate and last stages of sintering.[Sinha,1995].

II. Material Transport Mechanisms:

There are six possible mechanisms of material transport which are briefly explained here in the following:

1.Recovery and Recrystallisation :

It involves the movement of atoms over very small distances which are observed in powders having severe lattice distortions and are related with grain growth during densification.

The removal of stress in the micro-contacts also promotes mutual binding between the particles in the initial stages.[Sinha,1995].

2.Viscous Flow:

under the effect of applied pressure , it is expected that the plastic flow of material will slowly fill up the pores. Viscous flow occurs according to the equation :

$\tau = \eta \, d\varepsilon_{xy} / dt$ ----------Eq.(3.2)

where :

τ –shear stress

η-viscosity

$d\varepsilon_{xy} / dt$ -shear strain rate

For other materials which behave as a solid with a yield point which vary with temperature, the equation of viscous flow becomes :

$r_n^2 / r_p = 3/2 \, (\gamma/\eta) \, t$ ----------Eq.(3.3).

where:

r_n -radius of neck between two particles

r_p - particle radius η- viscosity

γ- surface tension t-time

This mechanism relied on the rate of increased contact area between two spherical powder particles to calculate the rate of sintering solid mass. This theory has been established in hot pressing. [Sinha,1995].

3.Evaporation and Condensation Mechanism:

It involves material transport through a gas phase, in which evaporation from the convex portions or the surfaces of spheres and condensation in the neck area due to higher vapor pressure over the convex surface comparison with neck region have been occurred. Because most metals do not have high vapor pressures at temperatures near their melting points, evaporation and condensation contribute normally to material transport in metallic systems.[Lenel et al,1984].

4.Lattice Diffusion Mechanism:

Diffusion flow is the most important mechanism of material transport which is based on the concept that a certain concentration of vacancies exist in crystal lattice of a metal.

Vacancy gradient exists between neck area and the interior of the system , between points on the surfaces having different curvatures. Further more ,vacancy gradient exists between distorted and undistorted lattice and particles centenss and midpoints of contact with adjacent particles.

Vacancy diffusion during sintering is obtained by the geometrical arrangement and type of vacancy sources and sinks. Vacancies diffuse from the neck area or high curvature regions to the interior or regions of low curvature while atoms diffuse in opposite direction to cause welding.[Sinha,1995].

Smaller pores and concave surfaces act as the vacancy source and grain boundary, convex surfaces and larger pores act as vacancy sinks. Lattice or volume diffusion works at elevated temperatures at which the value of surface

diffusion diminishes due to the decrease in particle specific surface and large temperature dependence of the lattice (volume) diffusion coefficient at high temperature as shown in eq.(3.4).[Sinha,1995].

$r_n^2 / r_p^2 = (Kv\gamma/RT)^* D_v .t$ ----------Eq.(3.4)

where:

D_v -volume (lattice) self diffusion coefficient

K- constant dependents upon surface geometry of the system and nature of vacancy sinks.

R- gas constant, T- absolute temperature ,T-time,γ-surface tension , v- volume

Fig. (3.25 a) illustrates a cross section of a two shape model. The radius r_c is the radius of curvature , r_n is the neck radius and radius of particle r_p. In Fig.(3.28 b) volume diffusion indicated by path (a) and surface diffusion indicated by path (b).

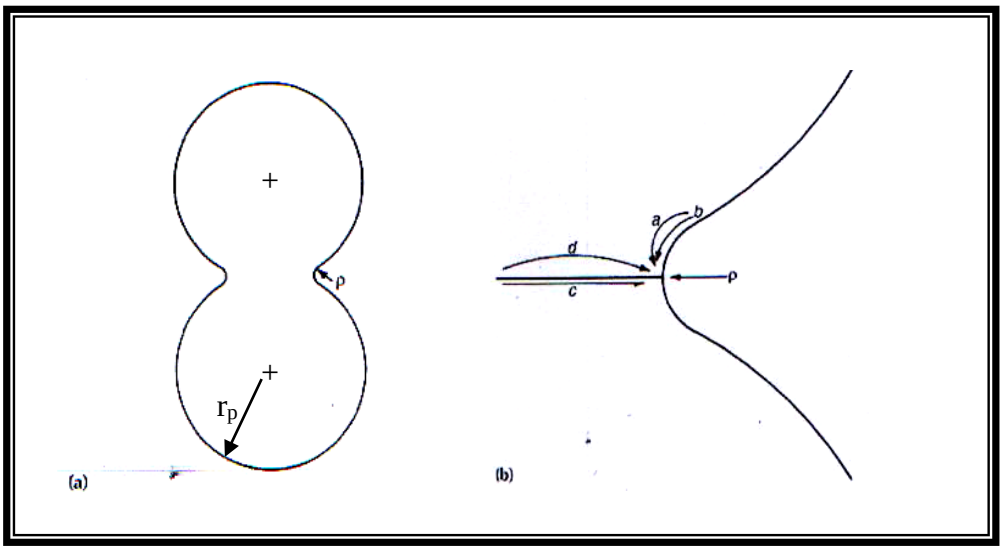

Fig. (3.25) Cross section through two spheres sintering together in [a] and volume diffusion and surface diffusion baths in [b], where path (a) , volume diffusion from flat surface to the neck. Path (b) , surface diffusion from the flat surface to the neck. Path (c), grain boundary diffusion from the grain boundarythe neck. Path (d) ,volume diffusion from the grain boundary to the neck.[Lenel et al,1984].

Assuming that the two particles are single crystals with different orientations, a grain boundary is formed at the neck. The difference in curvature at the neck with r_c and adjacent flat surfaces causes a difference in stress and chemical potential between two points which produces a gradient in the

concentration of vacancies between highly curved neck surface and the adjacent flat surface the high and low concentration of vacancies respectively.

5.Surface Diffusion Mechanism:

It refers to the movement of atoms on external surfaces therefore, exchange between surface atoms and surface vacancies is occurring during sintering. Surface diffusion occurs in all sintering processes which is responsible for the neck formation between adjacent particles. It is significantly important for sintering fine powders at low temperature where the effect of volume (lattice) diffusion is insignificant. Path (b) in Fig.(3.25 b) illustrates the surface diffusion . Surface and volume diffusion flow cause rounding and spheroidization of irregular pores in compacts. However, they do not explain shrinkage which may be represented by a decrease in the distance between the centers of the two spherical particles.

6.Grain Boundary diffusion Mechanism :

Grain boundary is considered to be formed between adjacent particles in the original sinter compact and it is expected that vacancies are moving directly along grain boundaries to external surfaces. In grain boundary diffusion, a slow displacement of grain boundaries takes place through a region of voids which remove them.

Elimination of last isolated pores during the last stage of sintering is due to grain boundary diffusion.[Sinha,1995].

The atoms from either the external surfaces or locations along the grain boundaries would diffuse down the grain boundaries which result in neck growth , rounding of pore or shrinkage of pore . This mechanism is found to be more effective with decreasing sintering temperature .

3.7.7.Liquid Phase Sintering :

In system involving mixed powders, liquid formation is possible because of differing melting ranges of the components. Common systems involving

liquid phase sintering for copper base alloys include copper-cobalt, copper-tin, copper-zinc, copper-phosphorous and copper-aluminum.

Heating of a mixed –phase system begins with a mixture of elemental powders. When the liquid forms, it flows and wets the solid particles and begins acting on the solid phase. Melt penetration between the solid particles can cause swelling of the compact especially if the green density is high and the particles are coarse. However, along with melt penetration, there is possible rearrangement of the particles.

The combination of wetting, liquid flow and particle rearrangement contributes to a rapid change in the volume of the compact. When heating is continuing in the presence of a liquid phase, the solid phase begins to dissolve.[Lenel et al,1984].

Based upon experimental observations, the stages of liquid phase sintering are given as follows:

1. Melting and liquid flow involving a rearrangement of the solid particles.
2. Rapid dissolution of the small solid constituent and reprecipitation on the larger ones.
3.coal essence of solid of solid particles involving slow densification.

The characteristics of typical liquid phase sintering include that the liquid phase wets the solid so there is a solubility of the solid in the liquid , and the amount of liquid phase should be large enough to occur an appreciable densification.[Sinha,1995].

The first stage refers to large scale bulk movement of particles within the liquid phase causing rearrangement of the particles and densification. It has been noted that densification increases with the increasing the amount of liquid phase. The densification is very rapid in this stage.

It has been shown that a liquid drop in contact with a solid surface (as shown in Fig. (3.26)) obeys the following equation [Parker ,1981]:

$\cos\theta = (\gamma_{GS} - \gamma_{SL}) / \gamma_{LG}$ ----------Eq.(3.5).

Where:

θ -contact angle

γ_{GS}-surface tension of solid –gas interface .

γ_{SL}-surface tension of solid-liquid interface.

γ_{LG}-surface tension of liquid –gas interface .

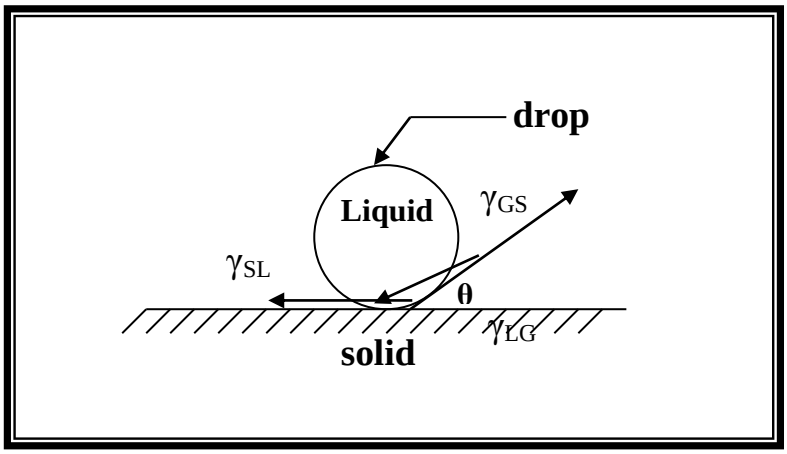

Fig. (3.26) Interfacial surface tension between gas, liquid and solid phases.

If the liquid phase completely wet the solid particles , contact angle θ=0. In order to liquid phase sintering successfully occurs, it is necessary that contact angle is less than 90˚. In case of non wetting liquid phase, contact angle equal or greater than 90˚. Therefore, partial exudations from the compact will occur in the form of droplets during sintering. It has been noted that partial exudations from CuZnAl and CuAlNi compacts occur during sintering at 850 C˚ as a droplets in many experiments of this work.

The amount of wetting can be improved by lowering the liquid-solid interfacial energy by diffusion or absorption method at the interface . A measure of penetration of a liquid phase by the liquid between the two grains is given by angle (φ) as shown in Fig.(3.27) . Complete penetration into grain boundary takes place when the liquid-solid interfacial energy or tension is less than one half of the grain boundary energy.[Sinha,1995].

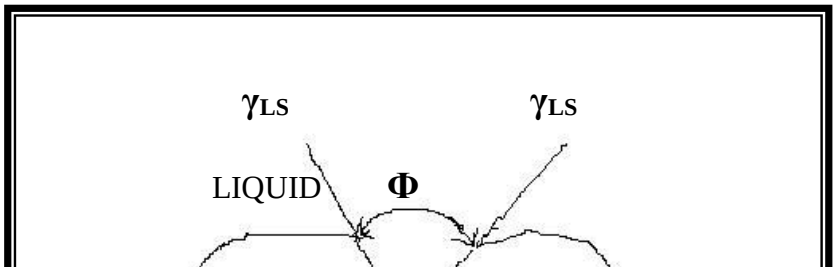

Fig. (3.27) Interfacial energy between solid and liquid phases when liquid phase penetrates between two grains.

The second stage is controlled by the surface and interfacial tension of the phases. After the completion of the rearrangement stage, second stage including solution and reprecipitation take place. It must be at least limited solubility of the solid in the liquid phase. Because there is dissolution and material transport by diffusion through the liquid, slow densification occurs as compared with first stage. Small particles have high curvature so they have interfacial tension and therefore higher solubility compared with large particles. These small particles dissolve first to form supersaturated liquid phase while re precipitation occurs on the largest solid particles having lower interface tension.

Third stage includes coalescence and grain growth. In the case of incomplete wetting of the solid by liquid, there is no complete separation of the solid particles by the liquid but there is some contact between solid particles. This may be considered in terms of low grain boundary energy with regard to one half the interfacial energy between the solid and the liquid .This condition causes the formation of solid skeleton within the compact.[Sinha,1995].

Liquid phase sintering kinetics generally are more sensitive to temperature than to sintering time. For solution and reprecipitation shrinkage, the transport path is through the liquid phase.

In the final stage, solid state sintering is predominant and the rate of densification is quite low. The combination of wetting, liquid flow and particle rearrangement contributes to a rapid change in the volume of the compact.

3.7.8.Homogenization During Sintering :

alloys may be produced by powder metallurgy techniques either by sintering compacts pressed from homogenous pre alloyed powder particles or by first mixing different powders for compacting and sintering which is based in this study . Compacted blends of powder exist as solute-rich particles surrounded by a matrix of solvent particles such as aluminum particles as solute particles and copper particles as solvent particles in the case of copper-aluminum alloys.

The density to which the powder is pressed determines the degree of residual inter particle porosity. Density differences between two different types of particles often cause mixing difficulties; therefore, such problems are minimized by varying the size of the particles used.

Sintering causes solid state diffusion of the solute atoms in to solvent matrix and diffusion of solvent atoms in to the solute-rich particles. Homogenization as a function of time at temperature may be described in terms of concentration and distance profiles that exhibit discontinuities in the as compact condition and that approach the average compact composition as concentration gradients are eliminated due to inter diffusion.

The compact behaves as a collection of many small diffusion couples that are allowed to undergo inter diffusion to the point where atomic fluxes become negligible and homogenization is achieved. [Lenel et al,1984].

Variation in sintered density with sintering temperature and time during homogenization is frequently different compared to the variation that exists if compacts are composed of particles of identical composition.

This is due two phenomena which have opposing effects on the densification of the compact and occur simultaneously. The matrix is densified due to pore shrinkage .A net flow of vacancies from one particle to other occurs if there is a difference in the fluxes of the atomic species to and away from a specific type of particle.

These vacancies can accumulate in the form of fine pores which called as Kirkendall porosity. The formation of Kirkendall porosity may cause expansion of the compact with subsequent reduction in density of compact.[Lenel et al,1984].

There are several parameters can affect the rate and extent of densification or expansion during homogenization such as:

1. Extent of the difference in the diffusivities of the particles.
2. Size of the particles in the compact.
3. Composition of the compact.
4. Compacting pressure.
5. Oxygen content of the starting powders.
6. Entrapped gases within powder particles.

The form of the density-time relationship for a specific homogenization treatment may vary and is more complicated for multi phase systems.

Multi phase binary systems must be described by the solute solubility and inter diffusion coefficients of each of the phases present. In such complexities the parameters required to analyze the homogenization process are not available.

The duration of sintering required to achieve a desired degree of homogeneity is dependent on temperature because inter diffusion coefficient (D) are exponentially dependent on temperatures in the following equation.

[Thornton and Colangelo,1985].

$D=D_{\circ} \exp(-Q/RT)$----------Eq.(3.6)

Where:

D- diffusion coefficient (cm^2 /sec)

$D_{\circ}$-diffusivity coefficient(cm^2 /sec)

Q- activation energy (cal/mol/K)

R- gas constant

T-absolute temperature (K)

Direct experimental techniques for the determination of the progress of homogenization include microscopy , composition analysis of microstructure using atomic probe analysis, scanning electron microscope and by x-ray diffraction technique .[Lenel et al ,1984].

Experimental Procedure

4.1. General View

In this chapter, materials and equipment used in this study are presented. Experimental procedure used to prepare samples from the elemental powders through the blending of powders in the mixing operation, compaction and finally sintering based upon typical steps of powder metallurgy technique, have been also presented in detail. Several physical tests such as apparent density, porosity expansion, etc and mechanical test such as hardness and compression in different form, furthermore, phase identification by X-ray diffraction and microstructure are also explained.

4.2. Materials

The elemental powders used in this study to prepare several alloys with average particle size, purity and origin are shown in table 4.1.

Table 4.1. powders used in this study.

Powder	Average particle size (μm)	Purity %	Origin.
Copper	75	99.98	Merck co.
Aluminum	75	99.80	Merck co.
Nickel	150	99.98	Bucks Fluka AG Co. Germany
Iron	150	99.9	Merck co.
Titanium	150	99.9	Merck co.
Cobalt	2	99.8	Merck co.
Zirconium	600	99.8	Merck co.
Manganese	45	99.8	Merck co.
Boron	22	99.9	Indian product.
Silicon	45	99.0	Merck co.

4.3. Equipments

The preparation of blended powders with different chemical compositions requires many equipments and instruments which are used not only in preparation of powder mixture but also in compaction and sintering stages. These equipments and instruments include the following:

1-Microbalance type L2205-D with accuracy (±0.001) manufactured by sartorius GMBH Gottigen –Germany.

2-Polyethylene zip-lock bags.

3-Calibrated micrometer with accuracy ±0.001mm.

4-Electrical oven up to 350 C.

5-Quartz type (0.038m in diameter with 0.38 m length).

6-Alumina gars with alumina balls manufactured by Berlin-Germany.

7-Dial gage with accuracy ±0.01mm manufactured by Germany with magnetic arm.

8-Proving ring with max. 50KN with dial gage ±0. 001mm accuracy manufactured by England.

9-Hydraulic press with hand-lever pressing with 32 ton maximum power.

10-Electric hydraulic press type soil test, Inc. USA with 120-ton capacity.

11-Electric tube furnace manufactured in this study up to 1200°C with alumina tube and type K thermocouple and digital thermostat controller with accuracy ±1.0 °C.

12-Double action dies with different dimensions made from alloy steel treated with suitable heat treatment have been used in this study.

13-Lithium striate lubricant.

14-Electric tube furnace up to 750°C manufactured in this study with type k thermocouple.

15-Argon cylinders with pressure gages from 1 to 15 bars.

16-Digital multimeter type (Honeytek A930)

17-Digital miliohmeter type (Hioki 3220 mΩ Hi tester)

18-Magnetic stirrer with thermostat hot plate up to 350°C. type (Gallenhamp)

19-Digital camera type (Mercury, Cyberpix S-550V).

20-Transparency glass slides.

21-Electric rolling mixer.

4.4. Preparation of blended mixtures

Blended mixtures from elemental powder given in table (4.1) with different weight percent have been prepared in this stage. Three main mixtures include Cu +13% Al + 3.98% Ni and Cu + 11% Al + 3.82% Ni , have been prepared. Furthermore; additives from Ti, B, Fe, Si, Co, Zr and Ti + Mn and B + Mn to the base mixture of Cu + 13Al + 3.98% Ni have also been prepared to explain the effects of alloying element on the shape memory effect and super elasticity of prepared alloys. Compositions of prepared alloys from elemental powders used in this study have been shown in table (4.2).

4.5. Mixing

The blending of an elemental powders mixture improves as the number of contacts between the different components of the mixture increases . Wet mixing for constituents of the mixtures has been done by electric rolling mixers as shown in Fig.(4.1).Alumina balls with different diameters as shown in Fig.(4.2) and alumina gars have been used to mix and refine metal powders for about 15 hours. Athyle alcohol has been used in wet mixing. In the light of this statement, mechanical mixing by hand for 2 hours has been used at first for alloys 1,2,3and 6 using athyle alcohol but it has been shown that chemical segregation in the final samples is found. Therefore, mechanical mixing by hand in zip-polyethylene locked bags is not satisfied. Chemical segregation of powder components has been shown macroscopically in samples as shown in Fig. (4.3).

Table 4.2. Mixtures and their compositions prepared in this study.

Alloy No.	Composition (weight parent of powders)
1	Cu + 11.0 Al + 3.82 Ni
2	Cu + 13.0 Al + 3.98 Ni
3	Cu + 12.6 Al + 3.98 Ni + 0.4 Ti
4	Cu + 12.2 Al + 3.98 Ni + 0.8 Ti
5	Cu + 11.8 Al + 3.98 Ni + 1.2 Ti
6	Cu + 12.6 Al + 3.98 Ni + 0.4B
7	Cu + 12.2 Al + 3.98 Ni + 0.8B
8	Cu + 11.8 Al + 3.98 Ni + 1.2B
9	Cu + 12.6 Al + 3.98 Ni + 0.4 Fe
10	Cu + 12.2 Al + 3.98 Ni + 0.8 Fe
11	Cu + 11.8 Al + 3.98 Ni + 1.2 Fe
12	Cu + 12.6 Al + 3.98 Ni + 0.4Si
13	Cu + 12.2 Al + 3.98 Ni + 0.8 Si
14	Cu + 11.8 Al + 3.98 Ni + 1.2 Si
15	Cu + 12.6 Al + 3.98 Ni + 0.4 Co
16	Cu + 12.2 Al + 3.98 Ni + 0.8 Co
17	Cu + 11.8 Al + 3.98 Ni + 1.2 Co
18	Cu + 12.6 Al + 3.98 Ni + 0.4 Zr
19	Cu + 12.2 Al + 3.98 Ni + 0.8 Zr
20	Cu + 11.8 Al + 3.98 Ni + 1.2 Zr
21	Cu + 12.2 Al + 3.98 Ni + (0.4 Ti + 0.4 Mn)
22	Cu + 11.8 Al + 3.98 Ni + (0.4 Ti + 0.8 Mn)
23	Cu + 11.4 Al + 3.98 Ni + (0.4 Ti + 1.2 Mn)
24	Cu + 12.2 Al + 3.98 Ni + (0.4 B + 0.4 Mn)
25	Cu + 11.8 Al + 3.98 Ni + (0.4 B + 0.8 Mn)
26	Cu + 11.4 Al + 3.98 Ni + (0.4 B + 1.2 Mn)

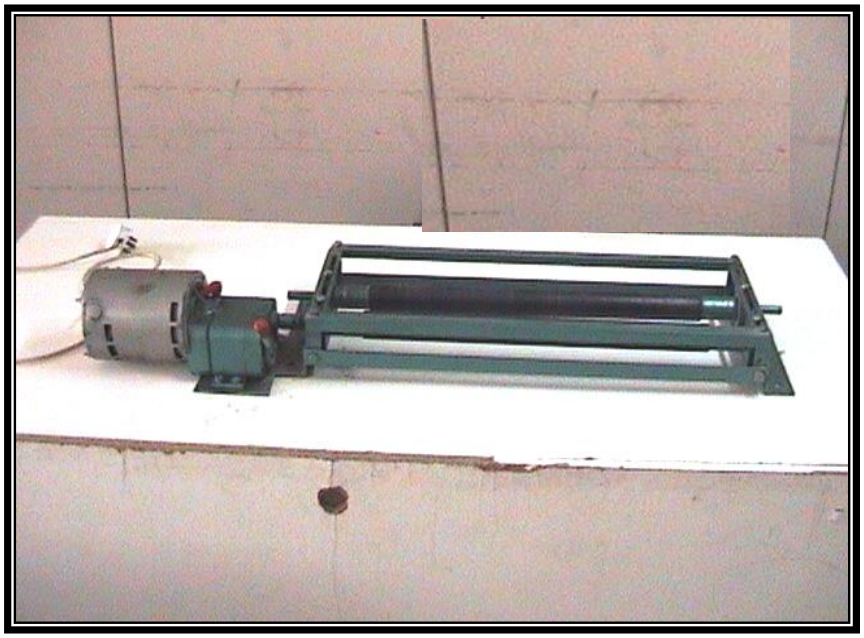

Figure.(4-1) Electric rolling mixing equipment.

Figure.(4.2) Alumina balls used for mixing powders mixture.

The wet mixtures of powdered alloys are dried in air at room temperature for about 1.0 hour and placed in polyethylene zip-locked bags. Lubricants are

not used in the mixture in order to avoid any oxide formation through the sintering process which leads to inhibit martensitic transformation. Based upon knowledge of oxide formation from lubricant in sintering process in Cu + 13% Al + 2% Nb which presented (Silva and Lima, 2005).

They showed that lubricant zinc stearate with milling and mixing of blended powders leads to form protective film on the powder surface and hinders diffusion between Aluminum and copper,

4.6. Compaction

In this stage, cold uniaxial pressing in double action dies has been used. Electric hydraulic press with uniaxial pressing as shown in Fig. (4.4) is used to compact green samples for compression test and disc samples for physical and micro structural tests.

Various compression stresses from (118.695; 237390; 356.086, 474.781, 593.476, 712.171, 830.867 and 949.562 Mpa) using double action alloy steel dies fixed in the electric hydraulic press with 120 ton capacity.

Alloy steel dies are heat treated by quenching from 850 for 1 hour in oil at room temperature and tempered in 200°C for 30 min to stress relieve due to quenching.

Samples with dimension (14.5 mm in diameter and 5mm thickness) and (10 mm diameter and 20mm height) have been prepared for hardness, microstructure tests and compression tests respectively.

Three loading rates have been used to press green compact as follows:
a-Rate (1) = 10 ton/ min,b-Rate (2) = 5 ton/ min , c-Rate (3) = 0.3 ton/ min

Furthermore; period of applied pressure time at maximum amount taken into consideration as a process parameter which are 1, 5, 10 minutes. Several

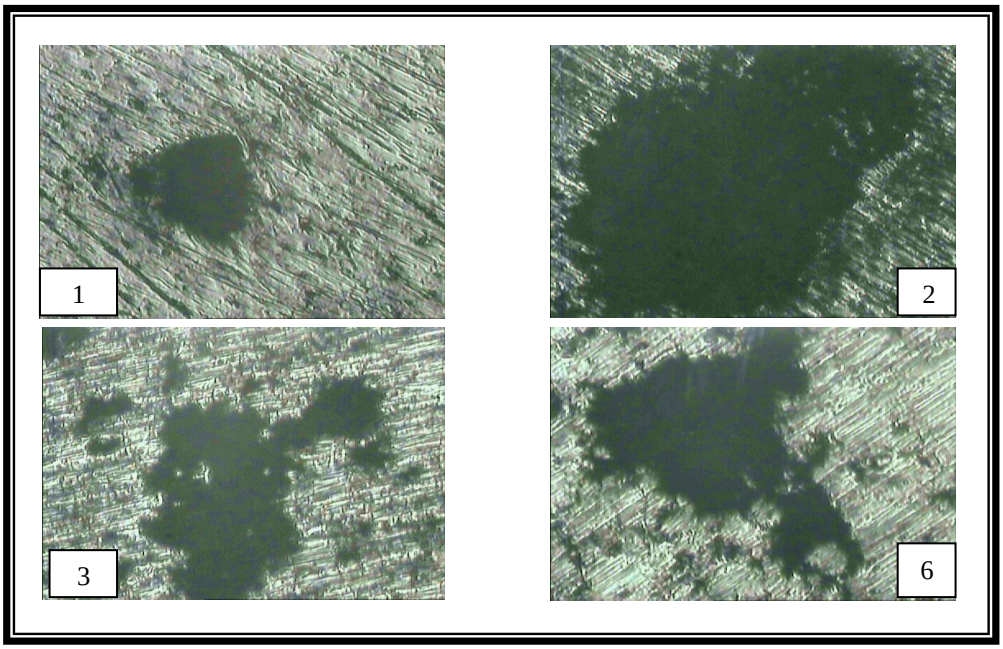

Fig.(4-3) chemical segregation of alloying element prepared by hand mixing for alloys 1.2.3 and 6.

Figure.(4-4) Uniaxial hydraulic press machine

physical tests such as apparent density, porosity, expansion and macrocracking after final sintering are based to determine optimum amount of pressure, rate of loading and period of time of maximum compression stress.

From experiments during experimental works, it has been shown that very small amounts from lithium stearate as lubricant for double action alloy steel die walls avoid cracking in the sample through the ejecting process from die specially cracks in the surface of samples. After each cycle of pressing, cleaning of die parts by acetone is used. Essential steps to form green compact from metal powder mixture include:

1-Full die cavity by some what 6 gram of mixture.

2-Pressing of mixture in double action dies by movement of upper punch and remain the base of frame fixed completely up to maximum load (tons) with different rates of loading and different soaking time.

3-Ejecting of green compact from the die by remove of the base and movement of the same upper punch.

Amount of compression stresses, rate of loading and periods of applying maximum compression stresses have been used for mixtures from alloy 1, 2, 3 and 6 .

4.7. Sintering

Several attempts have been used in this study to sinter green compacts from alloys, 1, 2, 3 and 6 using different heating cycles. Many of these attempts have been failed where complete cracking or melting of some particles on the surface causes burst of samples in the other hand, have been occurred. However, some of other attempt has been succeeded but with high porosity so, optimal experimental procedure for sintering of green compacts prepared in this study, has been reached in this investigation. All samples are placed in quartz tube which placed in tube furnace as shown in Fig. (4.5). Attempts used in this study include the following heating cycles.

I. First attempt

1. Heating green compacts from room temperature (27°C to 850 °C) with heating rate 5°C/min.
2. Soaking time for 15 min at 850°C.
3. Slow cooling in furnace.

All samples are failed with cracking and burst completely as shown in Fig.(4.6).

II. Second attempt

1-Heating green compact up to 850 from R. T. with 5°C/ min rate of heating.

2-Soaking time 15 min in 850°C.

3-Air cooling.

All the samples are also failed by creaking.

I*II. Third attempt*

1-Heating the furnace up to 550°C and entered the samples immediately and continue the heating up to 850°C.

2-Remain the green compacts in 850 for 10 minutes.

3-Air cooling.

All the samples are also failed by cracking and formation of melt bubbles on the surface.

IV. Fourth attempt

1-Heating the furnace up to 550°C and the green compact have been entered and closed the furnace to continue heating up to 900°C for 10 minutes.

2-Slow cooling in furnace.

All samples are also failed completely.

V. Fifth attempt

1. Heating the furnace up to 850°C.
2. Entered the green compact immediately.
3. Remain the samples in 850°C for 10 minutes.
4. Air cooling.

This cycle has been satisfied and accessed but with high porosity of final sintered samples and with low apparent density. (Porosity in the range of 16 - 35%).

The proposed heating cycle for sintering of prepared alloys in this study includes two stages of sintering as the following.

VI. Sixth attempt

1-Heating green compact from room temperature up to 600°C.

2-Soaking time is 3 hours.

3-Increase heating of samples in the furnace up to 850 for different times 10 min, 30 min, 1, 2 and 3hr.

4-Slow cooling in furnace.

This sintering heating cycle is shown in Fig.(4.7). The sintering of all samples has been satisfied and successfully occurred with low porosity (approximately 8~14).

Several higher sintering temperatures such as 850, 900, and 950°C have been taken to study their effects on the final physical properties. It has been shown that sintering in 850°C gives low evaporation of zinc in alloy I and low thermal effects compared with sintering in 900 or 950°C.All previous attempts of sintering have been done using argon atmosphere with 1.5 bar/min at a first minute to remove all air in quartz tube and with 0.5 bar/min for remain time.

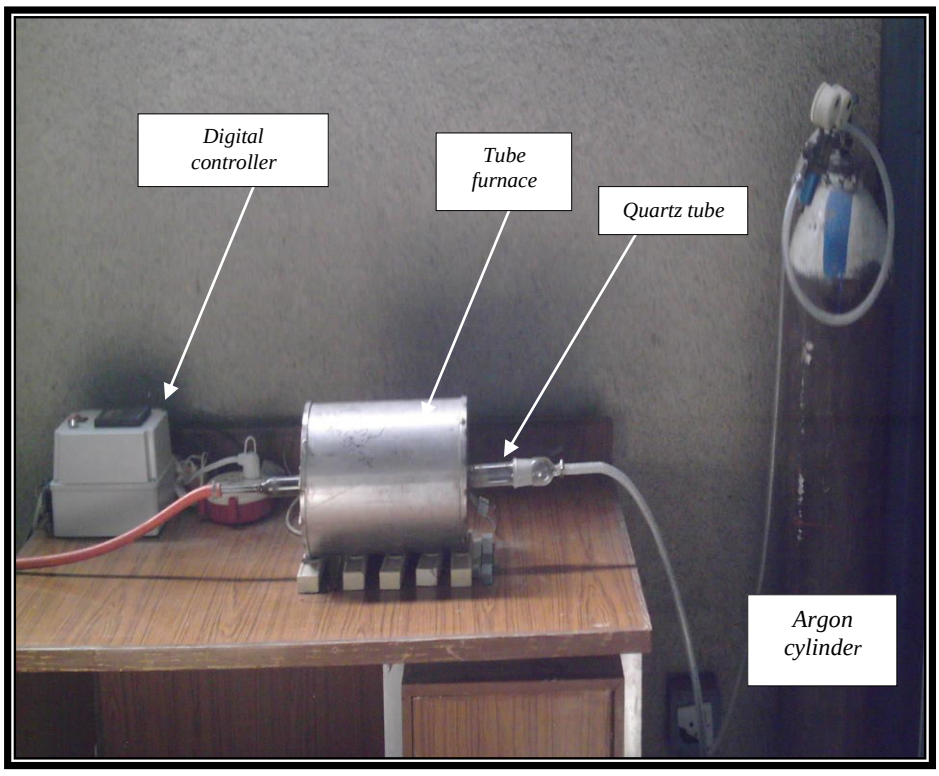

Figure. (4-5) Tube furnace used in this study.

Figure.(4-6) Failed samples in 1,2,3,4 attempts on sintering.

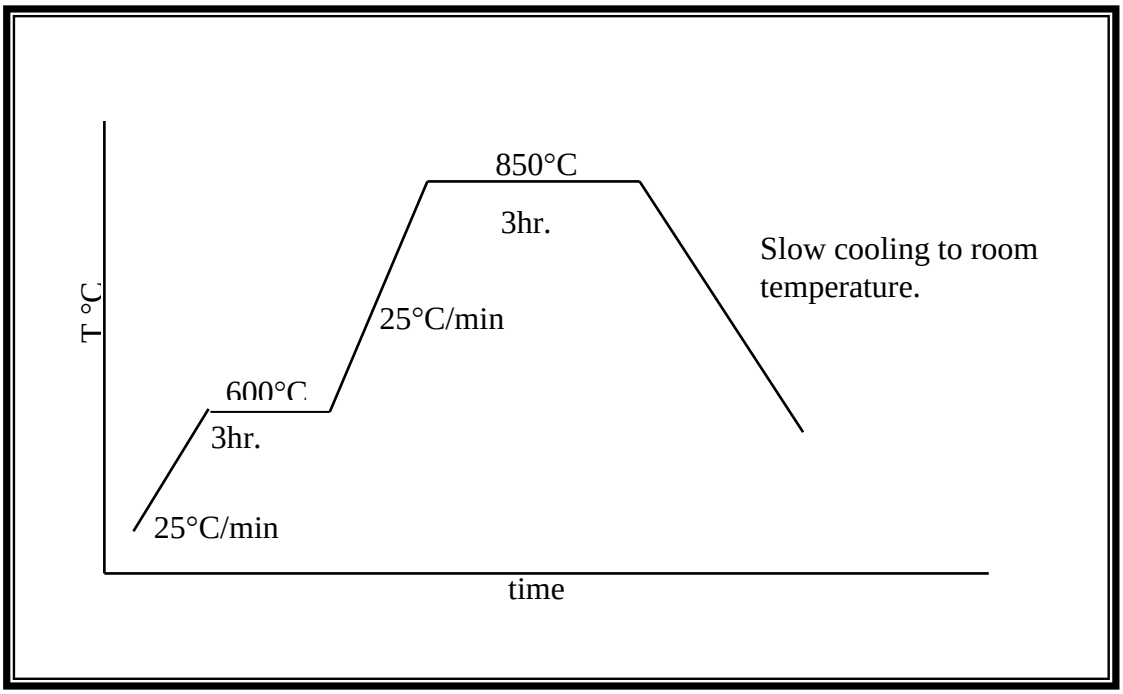

Fig. (4.7) heating cycle used in sixth attempt of sintering

Temperature in heating zone of type furnace is calibrated using external digital thermometer type (ELD Mod.9710,prodit ,Italy) and with digital multimeter with type k thermocouple. For different furnace temperature include

(250, 350, 500, 550, 600, 750, 800, 850, 900, 950). Digital controller of tube furnace has ±5 degrees as a temperature interval for switch on and switch-off of conductor operation.

4.8. Heat treatment

Several heat treatments have been used in this study including solution (betatizing) heat treatment , step quench treatment and aging heat treatment (post quench). Furthermore , heat treatment including shape memory effect of prepared alloy. The details of these treatment are given in the following:

4.8.1. Solution (betatizing) heat treatment

After sintering, all sample are solution treated by heating the samples up to (850°C) for different time as (30,60 and 140 min) and followed by rapid quenching in ice water at 3 ~ 4°C in order to avoid decomposition of β phase into equilibrium phases including ($\alpha + \gamma_2$) which is eutectoid reaction. taken in 565°C for aluminum bronze (Cu + 0.4 $\rightarrow$ 15.6 wt % Al). solution treatments are occurred in argon atmosphere with 0.5 Bar per min as a flow rate to avoid oxidation of samples. One of the most important and used of solution treatment in this study is shown in Fig. (4.8).

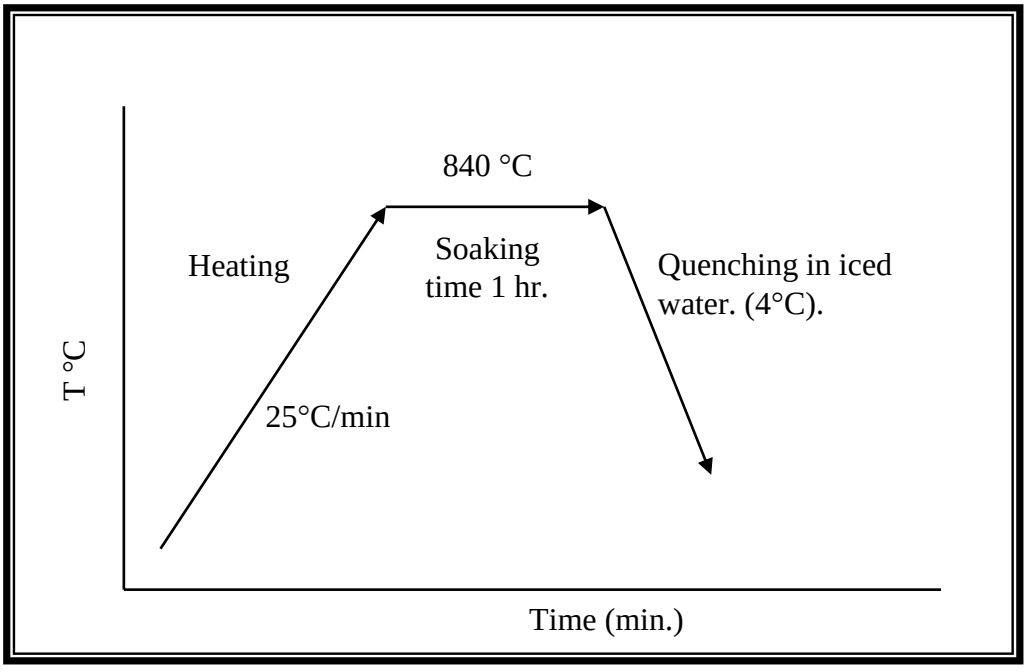

Fig. (4.8): solution treatment heating cycle for CuAlNi base alloys

.

4.8.2. Aging Treatment

Aging treatment is a thermal treatment occurred after rapid quenching in ice water to age some intermetallic compounds in the microstructure to modify their properties in suitable temperature. Here 200°C for 30 min is taken as aging treatment for all prepared alloys. Thermal cycle is shown in Fig. (4.9).After aging, samples are also post aging quench in iced water (3~4°C) in order not to occur any phase decomposition during slow cooling. There is no enough time to decompose β phase to $\alpha+\gamma_2$ phase.

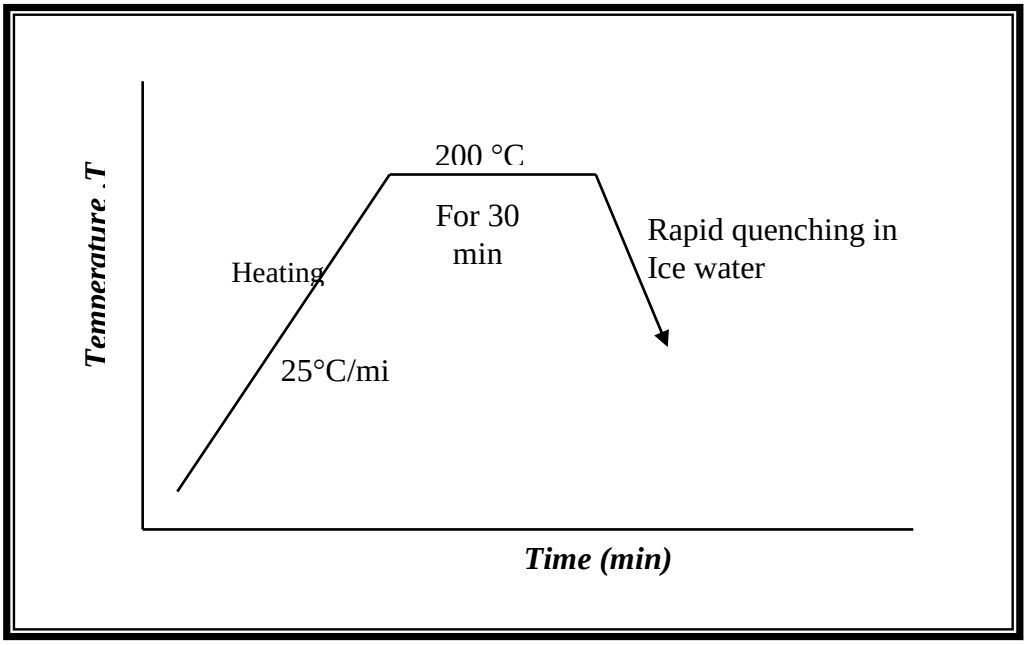

.

Fig. (4.9) Post quenching, aging treatment

4.8.3. Step quench heat treatment

Step quench treatment is not continuous rapid cooling but, it is an isothermal cooling through quenching from 850°C to 95°C at approximately (2-3) seconds. After this, remain in 95°C for 15 min and quenching in ice water at later. Thermal cycle of step quench is shown in Fig. (4.10).

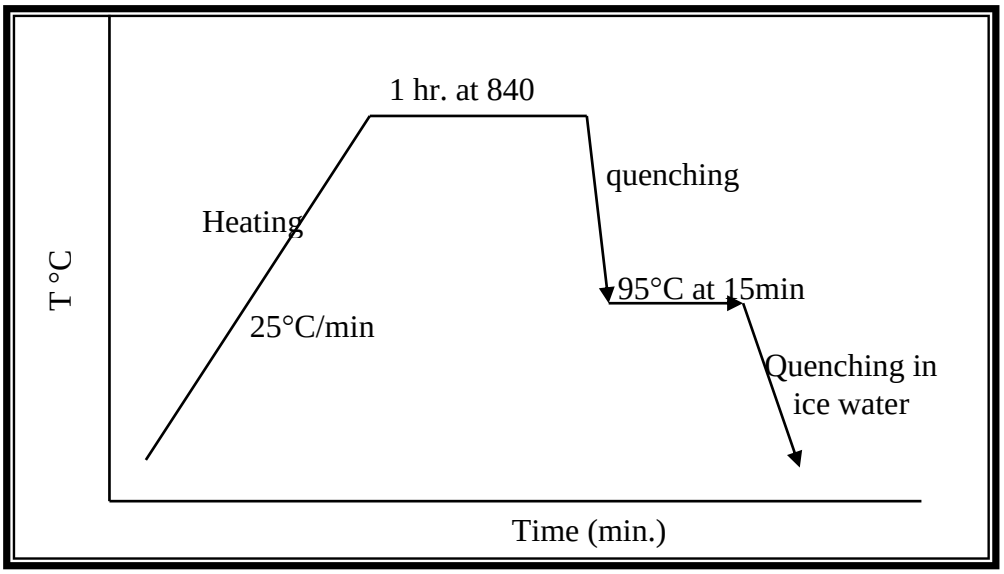

Fig. (4.10) Step quench heating cycle for prepared alloys.

4.8.4. heat treatment including shape memory effect

In order to obtain shape memory effect , which is determined by cold working by hardness indenter not only Brinell indentor but also micro and macro Vickers indenter and by compression test in different temperatures, heating to several temperatures such as 150°C, 200°C and 450°C for 10 and 30 minutes have been taken into consideration.

Different temperature and times have been taken into consideration due to different composition of prepared alloys and wide ranges of alloying element.

4.9. Phase identification and analysis

Phases analysis of prepared alloys is based upon X-ray diffraction technique and microstructures examination using optical microscope with different magnification. At a first, mixture of blended powders from alloys, 1, 2, 3 and 6 samples has been identified by X-ray diffraction technique in order to compare these diffraction pattern with sintered diffraction pattern for the same samples to enhance good sintering process. Furthermore, after solution

treatment, aging treatment and step quench heat treatment X-ray diffraction have been taken.

All X-ray diffraction tests are carried out at S.C. of Geological survey and mining. Low angle X-ray diffraction is preformed. X-ray generator with Cu Kα radition at 40 Kv and 20 mA is used.

The X-ray is generated by general electric diffraction type Philips (Pw 1840) operating at scanning speed of 6°(2θ) per minute. The specimen has been held at a fixed angle of θ=5 degrees relative to the incident X-ray been while the detector is moved through an angle of 2θ= 10° to 90 degrees.

4.10 Light Optical Microscopy (LOM)

Microstructure evolution with (40, 75, 100, 150, 400, 600 and 1000 X) magnification using two different microscope as shown in Fig.(4.11) has been examined for (40, 100, 400 and 1000X) Olympus microscope manufactured by Japan has been used where as with (75, 150, 600) union microscope has been used which is also made in Japan –in the metallurgical laboratory in material engineering department. Carl Zeiss. Microscope with low magnification (1.0, 1.6 and 5x) has also used to capture the macroscopically Brinell indentors. With all microstructure examination, digital camera type (Mercury, Cyberpix S-550V) has been used. The prepared samples from all categories with dimensions of (14.5 mm in diameter and 5mm in thickness) as can be seen in Fig.(4.12) have been wet ground using 180, 400, 800 and 1200 grit silicon carbide papers. These samples are then cleaned with water and dried with hot air. After drying , the samples are stored in polyethylene zip – lock bags with silica gel and sent to X-ray diffraction test where as another categories of the same alloys are polished with fine alumina type (0.02μm fine polishing alumina, struers made in Denmark) with fire cloth for ductile non ferrous alloys. Polishing and grinding wheel has been used to prepare metallographic sample. Samples are etched with two etching solution which are:

1-5 gram $FeCl_3$ + 10 ml HCl + 100ml H_2O

2-20 ml NH40H + 10 ml H_2O_2 + 20 ml H_2O

The ammonium hydroxide / hydrogen peroxide/ water solution (etching two) is the most widely used etching for copper and copper alloys. [Récksecker, 1985].

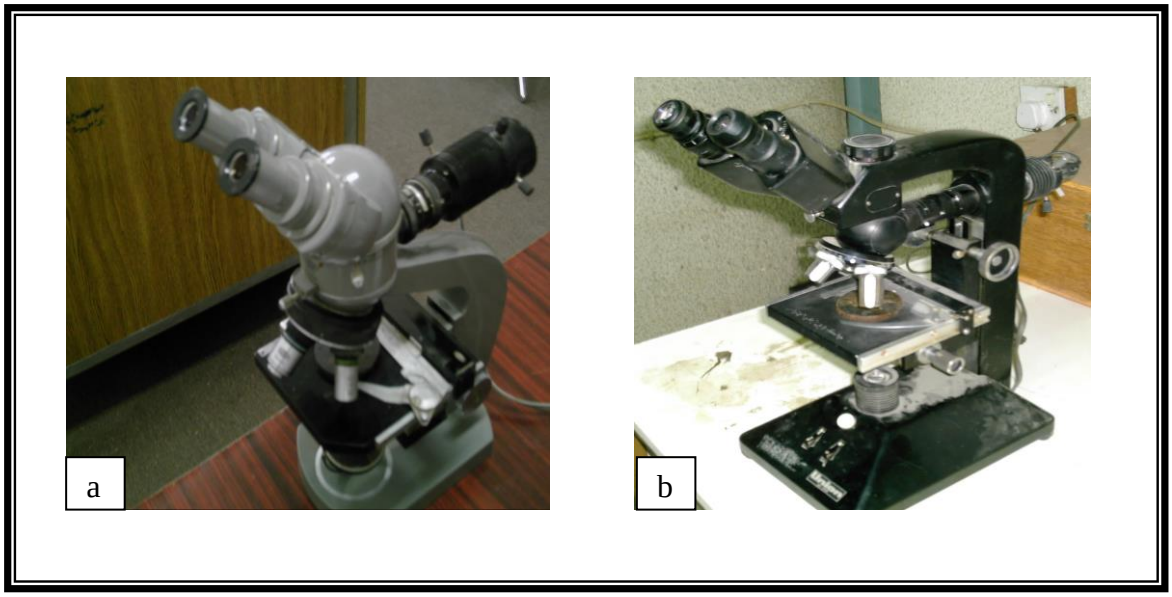

Figure.(4-11) Light optical microscopes.(a.Olympus and b.Union type).

Fig.(4.12) samples used for metallographic examination and physical tests.

4.11 Scanning electron microscopy (SEM)

Scanning electron microscope examination is used to reveal the microstructure of specimens for both unetched and etched conditions. SEM is used after direct quench , aging treatment and after step-quenched heat treatment . Several magnification has been captured with box, 2500x, 5000 x and 1000x for all specimens. SEM examination has been done in advanced metallurgical and material laboratory in the faculty of engineering, university of Tehran.Its specification is vega tescan, obducat camscan,Oxford instrument ,U.K.

4.12. Physical Tests

Several physical tests for elemental powders, green compacts and sintered samples as well as heat treated samples have been carried out. These tests include the following:

4.12.1. Particle size and particle distribution

Particle size of elemental powders [Cu, Al, Zn, Ni, Zr, Co, Fe, Mn, Ti, Si and B and blended powders from alloys, 1,2 ,3 and 6 is determined by image analysis technique..

Digital image for microstructure of certain powder sample using low magnification light optical microscope (LOM) has been captured by digital camera. This image is analyzed through image processing and image analysis using matlab program. The main steps for image processing and analyzing are shown in Fig. (4.13).

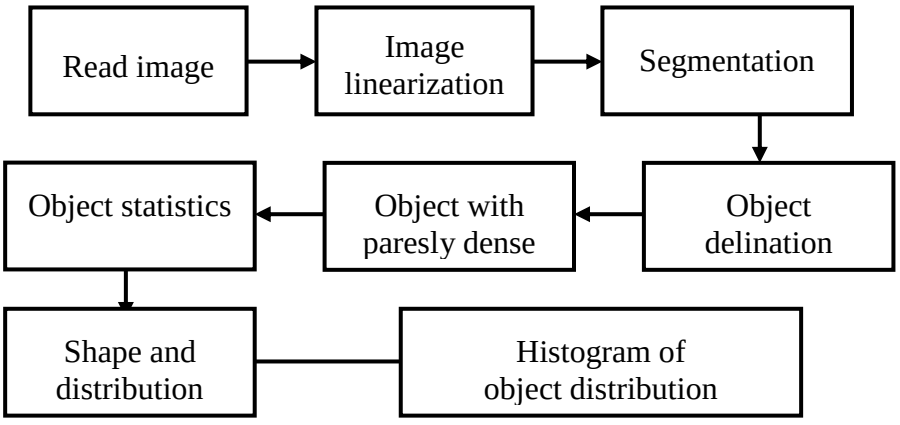

Figure. (4.13). Image processing and image analyzing using matlab version 7 program

Various techniques are used to measure the size of irregularly shaped particle when viewed through a microscope. This has resulted in different measurements which are used to classify these two dimensional particle image in terms of an equivalent spherical particle or equivalent rectangle in the direction of particle with feret's length and width, as shown in Fig. (4.14).

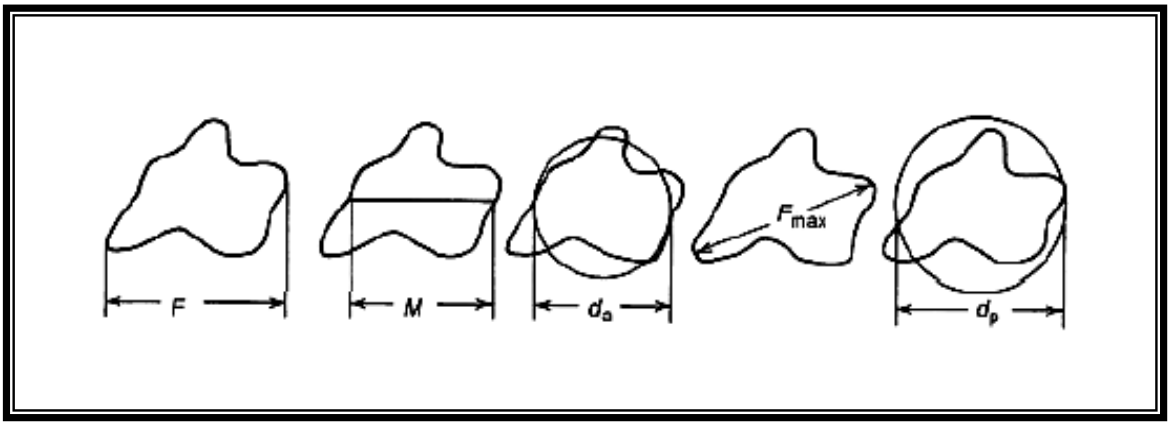

Figure. (4.14) Techniques for measuring size of irregular shaped particles.

Where M the Martin's diameter is the length of the line that bisects the area of the particle image, all particles measured in the same direction. [Hubbard, 1984].

In this study, direct measurement of particle dimensions in X and Y direction or any directions for one particle and for all particles can be used. Average of these dimensions has been taken as average particle size based upon equivalent spherical shape for spherical particle shape and equivalent elipse for non spherical particles.

Histogram curves for normal particle size distribution and acumulative plot used in determining median particle size have been also obtained by image analysis of LOM image.

4.12.2. Apparent density of powders and blended powders

The weight of unit volume of loose powder expressed in grams per cubic centimeter is the apparent density of a metal powder which is the one of the

fundamental properties of a powder. This characteristic defines the actual volume occupied by a mass of loose powder which directly affects processing parameters such as the design of compacting tooling and the magnitude of press motions required to compact and density loose powder.

Apparent density determinations are made by pouring powder into standard graded cub with 10 ml maximum volume into suitable grade. Care must be exercised to prevent physical densification of the powder in the cup when leveling. Weight of cup with and without powder is calculated using microbalance with accuracy of ±0.001 grams. Apparent density in grams per cubic centimeter is then determined by the following equation.

$$\rho_A = \frac{m_2 - m_1}{V_p} \quad \text{.....Eq.(4.1)}$$

Where:

ρ_A = Apparent density of powder (g/ cm^3).

m_1 = weight of cup without powder (unfilled cup (g).

m_2 = weight of cup with powder (g).

V_p = volume of powder in cup (cm^3)

4.12.3. Green porosity and density

The weight of unit volume of compacted blended powder expressed in grams per cubic centimeter is the green density of the compact. It is calculated from dimensions evaluations and weighting of compact sample as follows:

$$\rho_g = \frac{m_g}{V_g} \text{.....Eq. (4.2)}$$

Where:

ρ_g = green density (g/ cm^3). , m_g = green mass of the compact (g).

V_g = volume of the compact (cm^3).

Green porosity is determined from the knowledge of the theoretical density of blended powders (mixture) which is calculated by the weight percent of elemental powder multiply by it's theoretical density as follows:

$$\rho_{tB} = \sum_{i=1}^{n} Wt_1 * \rho_1 + Wt_2 * \rho_2 + Wt_3 * \rho_3 + ... + Wt_n * \rho_n \quad \text{.....Eq.(4.3)}$$

Where:

ρ_{tB} = theoretical density of blended powder (g/cm^3). , n = No. of elemental powders.

W_t = weight percent (%). , $\rho_{1,2,3,....n}$ = density of elemental powder (g/ cm^3).

So the green porosity is calculated from the equation:

$$P_g = \left(1 - \frac{\rho_g}{\rho_{tB}}\right) \times 100\% \quad \text{.....Eq. (4.4)}$$

Where:

P_g = green porosity (%). , ρ_g = green density (g/ cm^3).

ρ_{tB} = theoretical density of blended mixture (g/cm^3).

4.12.4. Pore size and pore distribution

The pore size and pore distribution in the samples for both compacted and sintered states have been determined by using image processing and analyzing through capture of light optical microscopy digital image for compacts and two stages of sintering. Histogram of natural distribution of pores and acumulative distribution have also determined.

4.12.5. Apparent density, porosity and water absorption of sintered compacts

The following procedure is used to evaluate apparent density, apparent and true porosity and water absorption of sintered samples according to ASTM-C 373 standard.

1-The specimen is dried up to 100°C for 24 hours in argon atmosphere then cooled to room temperature. The weight dry specimen is measured as (m_d).

2-The specimen is placed in a beaker of distilled water for 24 hours. The weight wet specimen is measured as (m_w).

3-The specimen is placed in a bayrex beaker of distilled water and boiled for 3 hours taking into consideration that the specimen must be covered by the water at all time. After boiling time , the specimen is left to soak form an additional 24 hours. After impregnation of the tested specimen, suspended mass (m_s) is measured when the specimen is suspended in water.

4-Directly, after calculation of (m_s), the specimen is cleaned with cotton cloth to remove all excess water from its surface. Immediately the specimen is weighted to determine the saturated mass (m_{sa}). The apparent density, apparent and true porosity and absorption of water are calculated from the following relations:

$$\underset{(g/cm^3)}{\text{apparened density}}\ (\rho_a) = \frac{m_d}{(m_{sa} - m_s)/\rho_w} \quad \text{.....Eq.(4.5)}$$

Where ρ_w = density of water (1.0 g/cm^3).

$$\underset{(\%)}{\text{apparened porosity}} = \frac{(m_w - m_d)}{(m_{sa} - m_s)} \times 100 \quad \text{.....Eq.(4.6)}$$

$$\text{true porosity} = (m_{sa} - m_d) \quad \text{.....Eq.(4.7)}$$

$$\underset{(\%)}{\underset{(cm^3)}{\text{absorption of water}}} = \frac{m_w - m_d}{m_d} \times 100 \quad \text{.....Eq.(4.8)}$$

4.12.6. Dimensional change of sintered compacts

Dimensional change for the sintered compact specimen is calculated from the following equation [Feerby, 1984].

$$\text{Dimensional change}(\%) = \frac{L_S - L_D}{L_D} \times 100 \quad \text{.....Eq. (4.9)}$$

Where:

L_D = is the die cavity dimension (mm). ,

L_S = is the sintered specimen dimension (mm).

Expansion is indicated by a plus sign and shrinkage is indicated by a minus sign (-). Dimensional changes are determined as the difference in dimensions between green and sintered compacts in the parallel and/or perpendicular direction of pressing. From a technological stand point , the dimensional change during sintering of greatest importance is the difference between the dimensions of the die and the sintered compact in the radial direction that is the direction perpendicular to that of pressing. Therefore, L_s and L_D in equation (4.9) refer to diameter of sintered compact and diameter of die compact respectively in this work.

4.12.7. Electrical resistance

Electrical resistance for sintered compacts and heat treated alloys [step quenched, direct quenched and aging specimens] has been determined using mili ohmmeter type [Hoyki 10100] manufactured in Japan as shown in Fig.(4.15). Electrical resistance is evaluated in different temperatures [8°C to 250°C] with increment of 1°C degree. Small tube furnace up to 750°C with type k thermocouple manufactured in this study has been used to carry out electrical resistance measurements with different temperature. Voltage transformer (variac) has been used to control heating rate through the experiments. Specimen is placed in alumina cell and both of furnace and sample in cell have been insulated with glass wool and E-glass fabric ravings to insulate heat to the surroundings as low as possible. Fig.(4.16) shows the tube furnace and cell used to calculate electrical resistance as a function of temperature. This test is used to know phase transformation temperatures which indicate suddenly variation in electrical resistance of the specimen with tested temperature.

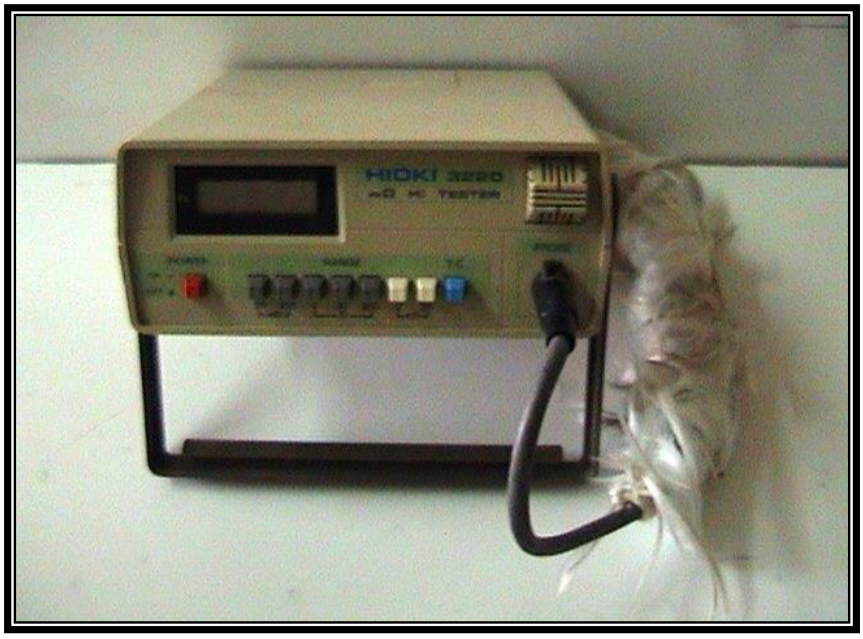

Figure(4-15) milliohm-meter equipment.

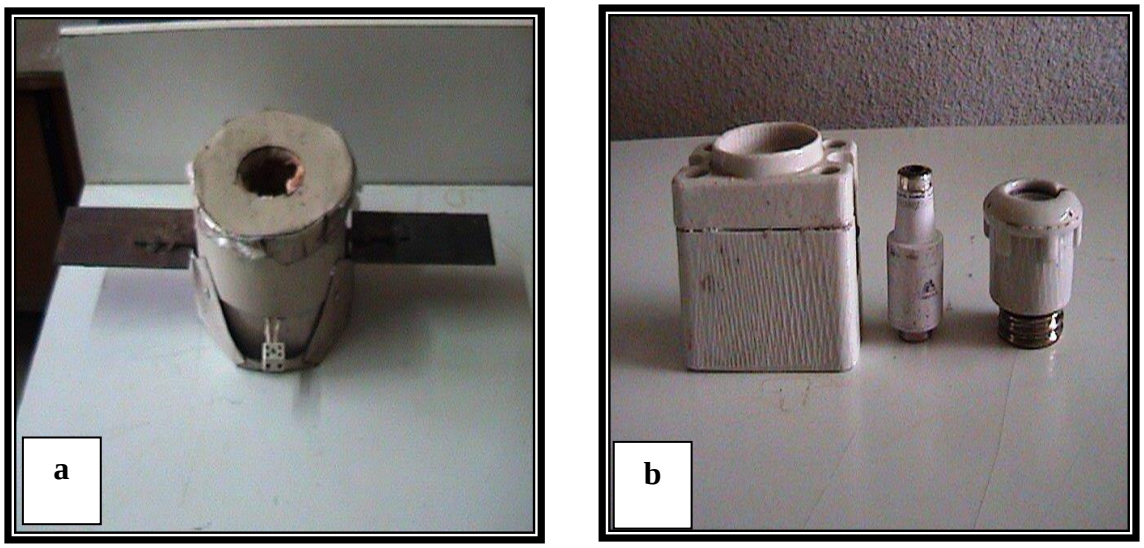

Figure(4.16) tube furnace (a)and the cell (b) used for electrical resistance with different temperatures.

4.12.8 Ultrasonic wave test.

Ultrasonic wave test is used for cylindrical specimens (10 mm in diameter , 35mm in length). This test has been done after compressing the direct quenched specimens up to 10 % strain and after recovery heat treatment which include heating the specimen upt to 150 ^{o}C for 15 min. Low frequency with high wave length of Ultrasonic equipment used especially for test the reinforced concrete is used . Digital monitor appears directly the time of transferred of ultrasonic wave. The wave length is 2.5 cm .

4.13. Mechanical Tests.

Mechanical tests including micro and macro hardness and compression test are done for sintered and heat treated samples. Shape memory effect has been concered in all mechanical tests.

4.13.1. Microhardness measurements

Microhardness Vickeres tester type [Microhardness Tester Hv-1000] is used to measure hardness with 100, 200 and 500g load and holding time of 20 seconds compined with optical microscopy to measure the diagonal length of Vicker's impression. The Vicker's microhardness (H.V.) is defined as follows:

$$HV = 1.854\,P/d^2 \quad \text{.....Eq.(4.10)}$$

Where P = applied load.

d = average length of diagonal μm.

Two reading are reordered for each sample. This test shows great variation in hardness number 50, it is based for shape memory effect only not to determine the hardness value of tested sample because there are many pores in the surface of the sample.

4.13.2. Macrohardness measurements

Two main methods are used not only to determine hardness values of tested specimens but also to evaluate shape memory effect through the indentation of tests impression. These include the following:

4.13.2.1. Vicker's macro harness measurements

Macrohardness Vicker's tester type [Hardness Tester model mat24/crbv,Brooks inspection equipment Ltd.] is used to measure the hardness with 3Kg primary load and 30 Kg as major load. Four readings are recorded for each specimen. Macrohardness is given directly by digital monitor with test machine. Dimensions of Vicker's impression are calculated using low magnification light optical microscopy type [Carl Zeiss] and by image analysis.

4.13.2.2. Brinell macrohardness measrments

Brooks universal hardness tests is used to measure Brinell hardness with 2.5mm ball diameter as indentation ball and 137.5Kg major load with 10Kg as micro load digital readings for Brinell hardness number is given directly-where as the impression of indentation ball is given by using low magnification light optical microscopy with digital camera and by image analysis and image processing.

4.13.3. Compression test

Sample with (10 mm in diameter and 20 mm height) dimension as shown in Fig.(4.17) have been compressed using calibrated universal testing machine as shown in Fig. (4.18) at room temperature and at 50 ^{o}C. However, strain-temperature test curves of prepared direct quench samples achieved using Calibrated, compression equipment. Proving ring manufactured in England with 50 KN maximum load is used to measure the load applied in to specimen and dial gage with 0.01mm accuracy is used to evaluate displacement in the designed equipment as a shown in Fig. (4.19). All equipment are calibrated with three compression machine, universal testing machine with 30KN max. load type phwye, Marshal compression machine with 20KN max. load and with another universal testing machine manufactured in Germany in Kufa university.

Compression tests are done in room temperature and in different temperature using tube furnace with digital controller and type K-thermocouple which is stacked with sample directly.

It has been shown that samples from Cu+45%Ti+5%Co with 6mm in diameter and 8mm height have the following experimental data:

Table (4.3) verification of compression equipment

Type of equipment	Max. load	Max. displacement
Universal testing machine with 30KN max. load type phywe	17	2.1
Universal testing machine with 20KN max. load.	16.9	2.2
Hydraulic compression machine used in this study	16.87	2.25

Therefore; due to the limit of loads in universal testing machine and there is slight or small variation in he corded readings for max. load and max. displacement furthermore , no one accept heating system placed with universal testing machine, hydraulic compression machine with designed heating equipment has been used in this study.

Fig.(4.17) compression samples

4.13.4. Shape memory effect

Shape memory effect is determined from Vickers impression or brinell indentation follows:

$$\text{Shape memory effect (SME \%)} = \frac{d_b - d_a}{d_b} \times 100 \quad \text{.....Eq. (4.11)}$$

Where:

d_b = average impression diameter in (μm) before heating.,

d_a = average impression diameter in (μm) after heating.

Shape memory effect is also determined from compression test as follows [Ariapour, 1998]:

$$SME\ (\%) = \frac{L_2 - L_1}{L_0 - L_1} \times 100 \quad \text{.....Eq. (4.12)}$$

Where:

L_0 = initial distance between two indentation reference marks on the surface of a specimen parallel to the compression direction.

L_1 = is the distance between the indentation marks after compression and direction.

L_2 = is the distance between the indentation marks after recovery heating.

The reported values are the average of three measurements. Further more, strain recovery percentage during shape memory effect is also calculated as follows:

$$\in_r = \frac{L_2 - L_1}{L_0} \times 100 \quad \text{.....Eq.(4.13)}$$

Where :

$\in_r$ = recovery of strain percentage (%). ,

The reported values are the average of three measurements.

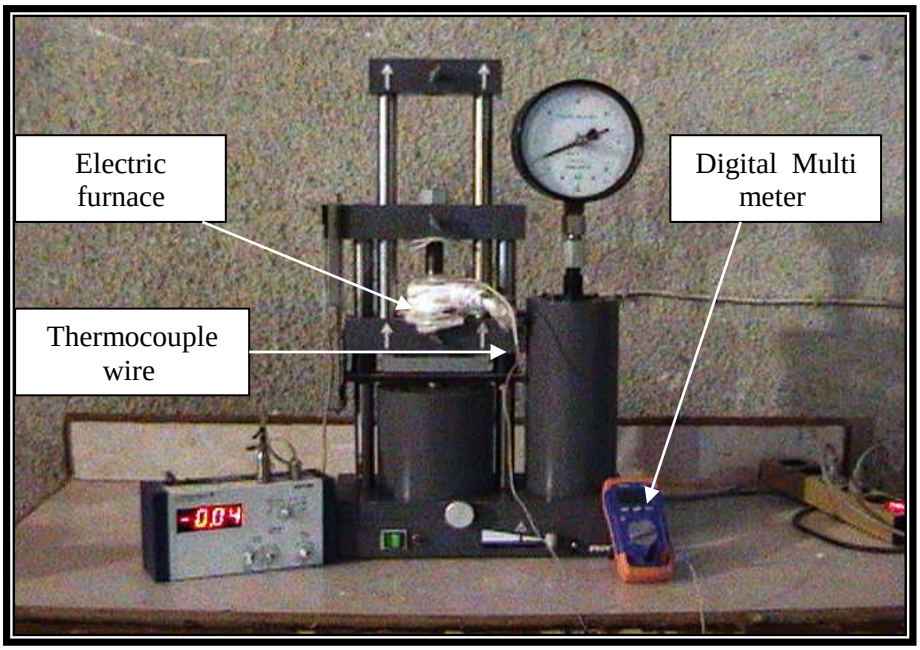

Fig.(4.18) Universal testing machine used for compression test in room temperature and 50 ^{o}C.

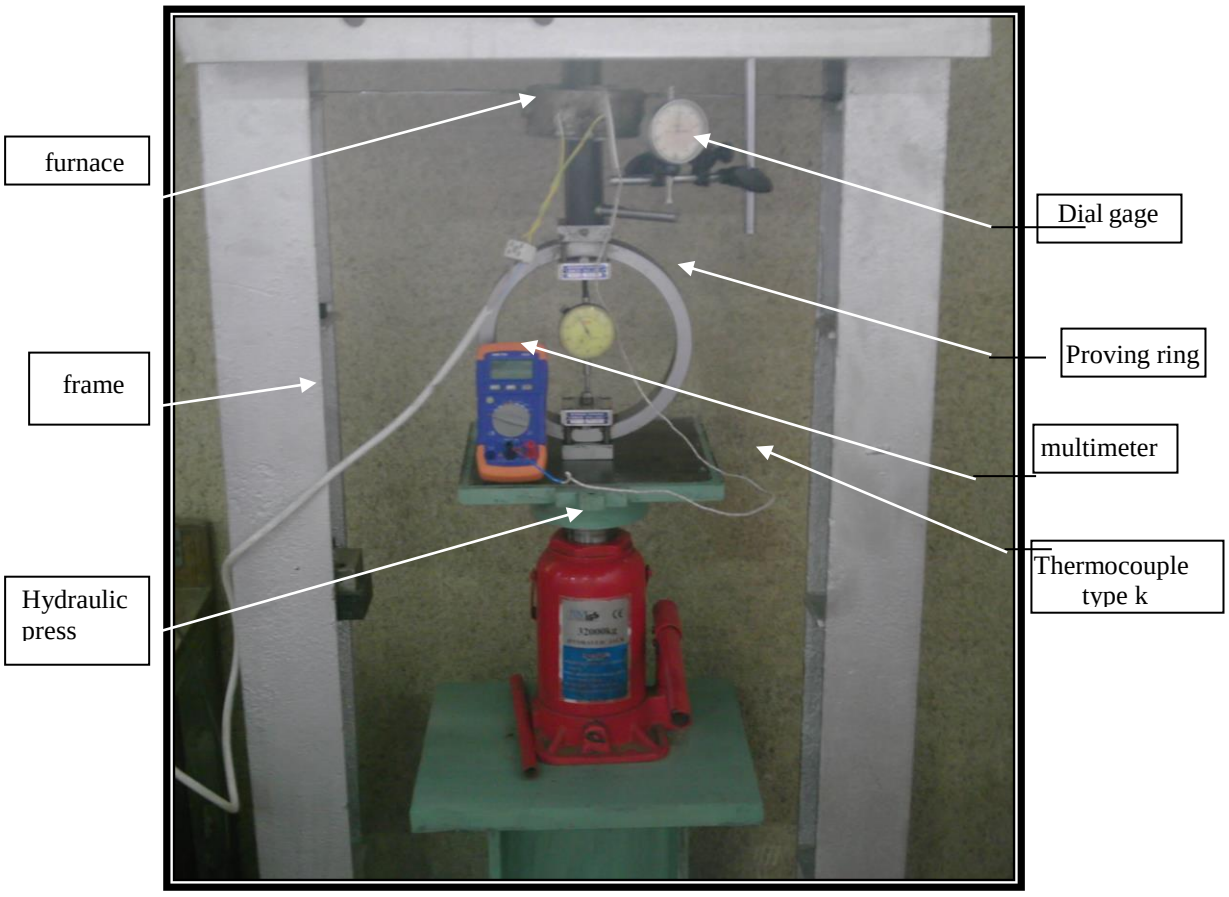

Fig.(4.19) compression equipment with required heating system.

Modeling and Numerical Simulation of Shape memory Alloys

5.1.Gernal View

In this Chapter , the attention on the constitutive modeling of shape memory alloys has been presented. Several shape memory alloys models have been explained in attention to temperature- dependent inelastic model of shape memory alloys used in packages such as Abquas and Ansys version 9.

In this study, two approaches are used to analyze shape memory effect through using unit cell finite element analysis using square and hexagonal unit cell to study of shape memory structures with pores and, the real microstructure using digital image have been used to analyze porous shape memory alloy with finite element method. For both of the two approach ansys ver. 9. has been employed. Verification of used model with case studies has also been presented.

5.2. Shape memory models

Constitutive laws which according to the recent literature ,seem to be the most used and efficient for simulating the response of shape memory allays based devices , are present in the following:

5.2.1 Ozdemir model

This model introduced by Ozdemir [Queted in Fugazza , 2003] allows to study the mechanical responded material showing hystersis. The mathematical expressions that described it are the following :

$$\frac{d\sigma}{dt} = E[\frac{d\varepsilon}{dt} - \left|\frac{d\varepsilon}{dt}\right|(\frac{\sigma-\beta}{Y})^n] \qquad \text{------- Eq.(5.1)}$$

$$\frac{d\beta}{dt} = \alpha E\left|\frac{d\varepsilon}{dt}\right|(\frac{\sigma-\beta}{Y})^n \qquad \text{------- Eq.(5.2)}$$

Where

σ : Stress

ε : strain

E : elastic modulus (Gpa)

Y: Yield stress (MPa) which represents the beginning of the stress-induced transition from austenite to martersite in SMA.

β : one dimensional back stress (N/m^2).

α : Constant controlling the slope of the $\sigma - \varepsilon$ curve .

n : Constant Controlling the sharpness of transition form elastic to plastic state.

The equation (5.1) can be rearranged as following :

$$\frac{d\varepsilon}{dt} = \frac{d\sigma/dt}{E} + \left|\frac{d\varepsilon}{dt}\right|\left(\frac{\sigma-\beta}{Y}\right)^n \qquad \text{------- Eq.(5.2)}$$

The total strain as shown in equation (5,3) is made up of two separate components as follows :-

1. Linear elastic component σ/E and .
2. nonlinear strain component $\dot{\varepsilon}$, described by the expression

   $\dot{\varepsilon} = |\dot{\varepsilon}|[(\sigma-\beta)/Y]^n$.

Where (.) is the ordinary time derivative. This inelastic component is a function of both the strain rate ($\dot{\varepsilon}$) and the over stress ($\sigma-\beta$).

It would be possible to show that for equation (5.1 and 5.2) , the strain is in dependent of the applied rates of loading which means not dependent on either $\dot{\sigma}$ or $\dot{\varepsilon}$). By subtracting expression in equation (5.2) from expression (5.1), we may obtain the following equation :

$$\dot{\sigma} - \dot{\beta} = E\,\dot{\varepsilon}\left[1 - (1+\alpha)\left(\frac{\sigma-\beta}{Y}\right)^n\right] \qquad \text{Eq.(5.4)}$$

Which it is useful to rewrite in a more Convenient differential form as :

$$d\varepsilon = \frac{d(\sigma - \beta)}{E\left[1 - (1+\alpha)\left(\frac{\sigma - \beta}{Y}\right)^n\right]} \qquad \text{...Eq.(5.5)}$$

and by integration , we get the solution for the total strain .

$$\varepsilon = \frac{Y}{E(1+\alpha)^{1/n}} \int \frac{d(\sigma - \beta)}{1 - (\sigma - \beta)^n} \qquad Eq.(5.6)$$

The integral in Equation (5.6) is a function only of the overstress $\sigma - \beta$ therefore , equations (5.1 and 5.2) represent a rate – independent stress – strain behavior . and this model does not permit to capture the behavior exhibited by shape memory alloys .

5.2.2.Cozzarelli model :

Here , the mechanical characterization of shape memory alloys is accomplished by extending the rate independent model of Ozdemir [Graesser and Gozzerelli 1991] when equation (5.1) is divided by $\dot{\varepsilon}$, the slope of the stress –strain curve is obtained as :

$$\frac{d\sigma}{d\varepsilon} = E\left[1 - Sgn(\dot{\varepsilon})\left(\frac{\sigma - \beta}{Y}\right)^n\right] \qquad \text{Eq.(5.7)}$$

Where

$$Sgn(\dot{\varepsilon}) = \begin{cases} -1 & \text{if} \quad \dot{\varepsilon} < 0 \\ 0 & \text{if} \quad \dot{\varepsilon} = 0 \\ +1 & \text{if} \quad \dot{\varepsilon} > 0 \end{cases} \qquad \text{...Eq. (5.8)}$$

This model has ability to predict super elastic and simplicity to be extended to three dimensional case but still rate and temperature independence . It is unabled to predict the behavior after that the transition from austenite to martensite is completed .

5.2.3 Tanaka model

On the basis of the analysis of thermo- mechanics and Continuum mechanics . Tanaka presents the following constitutive relation [Fugazza ,2003]

$$\dot{\sigma} = D\dot{\varepsilon} + \theta\dot{T} + \Omega\dot{\zeta} + \psi\dot{\eta} \qquad \text{...Eq}(5.9)$$

Where ,

σ - Stress tensor

ε - Strain tensor

T - Temperature

D - Stiffness matrix

θ - Thermo elasticity tensor

Ω - Range of strain resulting from martensite

ψ - Range of strain resulting from R-phase transformation

ζ - Volume percentage of martensite phase

η - Volume percentage of R phase .

It is also possible to evaluate the volume percentage of austenite phase which results from the expression $1-(\zeta+\eta)$ the volume Percentage of martensite transformation ζ Can be written as :

$$\zeta = 1 - \exp\left[b_M C_M (M_S - T) + b_M \sigma\right] \qquad \text{Eq}(5.10)$$

and for austenite

$$\zeta = \exp\left[b_A C_A (A_S - T) + b_A \sigma\right] \qquad \text{Eq}(5.11)$$

Where b_M ,C_M ,b_A and C_A are material coefficient for martensite and austenite phase respectively .

M_S and A_S represent the initial temperature of the martensite and austenite transformation under no stress conditions respectively

The volume Percentage of R-phase , η assume the form :

$$\eta = b'_M C'_M (T - M'_S) - b'_M \qquad \text{...Eq.(5.12)}$$

and

$$\eta = 1 + b'_A C'_A (T - M'_S) - b'_A \sigma \qquad \text{...Eq.(5.13)}$$

Where again b'_M, C'_M, b'_A, C'_A are material coefficients .M`s and A`s are the temperature of initial of the martensite and reversed R-phase transformation under condition of no stress . This model has an ability to account for the R-phase and temperature dependence but it is still rate independent ..

5.2.4. Auricchio model :

The general inelastic theory used for development of constitutive models for materials has been presented by Auricchio (1995) and Lubliner and Auricchio (1995) .

Auricchio applied generalized plasticity to analyse shape memory alloy behavior .For simplicity , a one dimensional model is presented here .

Auricchio model assumed that the stress and strain are – rate independent and isotropy of martensite single variant and austenite phase , Therefore , in the most general case , three phase transformation are considered as follows :

1) Conversion of austenite to single Variant martensite($A \to M$) .

2) Conversion of Single Variant martensite to austenite phase ($M \to A$) .

3) Single Variant martensite reorientation ($M \to M$)

As control Variables , we assume the uniaxial stress , σ and relative temperature T , As internal Variables we may choose either Single –Variant martensite fraction ζ_M or austenite fraction ζ_A [Auricchio et.al,1997] which are assumed to satisfy the following relation at each time :

$$\zeta_M + \zeta_A = 1 \qquad \text{...Eq.(5.14)}$$

Accordingly there is only one independent internal variable , chosen herein to be ζ_M . From equation (5.14) we get relation between the rates of the fractions as :

$$\dot{\zeta}_M + \dot{\zeta}_M = 0 \qquad \text{...Eq.(5.15):}$$

To reproduce the Superelastic behavior in a uniaxial State of stress only two phase transformations Can be considered , the conversion of austenite into single Variant martensite($A \rightarrow M$) and the conversion of single variant martensite into austenite ($M \rightarrow A$).

As showed experimentally , for uniaxial stress- temperature changes and in the usual range of applications , the region s in which phase transformation may be occurred are delimited with good approximation by straight lines [Melton , 1990] So that ,

$$\dot{\zeta}_M = \dot{\zeta}_M^{A\rightarrow M} + \dot{\zeta}_M^{M\rightarrow A} \quad \text{...Eq.(5.16)}$$

$$\dot{\zeta}_A = \dot{\zeta}_A^{A\rightarrow M} + \dot{\zeta}_A^{M\rightarrow A} \quad \text{...Eq.(5.17)}$$

5.2.4.1 Single Variant martensite Production :

To describe the region corresponding to the Single variant martensite production Process , the following functions are introduced (Auricchio et al 1997) .

$$F^{A\rightarrow M} = \sigma - C^{A\rightarrow M} * T \quad \text{...Eq.(5.18)}$$

$$F_S^{A\rightarrow M} = F^{A\rightarrow M} - R_S^{A\rightarrow M} \quad \text{...Eq.(5.19)}$$

$$F_f^{A\rightarrow M} = F^{A\rightarrow M} - R_f^{A\rightarrow M} \quad \text{...Eq.(5.20)}$$

With

$$R_S^{A\rightarrow M} = C^{A\rightarrow M} M_S \quad \text{...Eq.(5.21)}$$

$$R_F^{A\rightarrow M} = C^{A\rightarrow M} M_F \quad \text{...Eq.(5.22)}$$

Where $C^{A\rightarrow M}, M_S$ and M_f are material Parameter include stress to temperature Coefficient , initial and final transformation temperatures from $A \rightarrow M$ at zero stress respectively . whereas σ is the applied stress and F is the pressure causes flow in the Material . The region in which the transformation may take place is evaluated from

$$F_S^{A\rightarrow M} > 0 \text{ and } F_f^{A\rightarrow M} < 0 \quad \text{…Eq.(5.23)}$$

As can be shown in Fig. .(5.1) .

To activate the production of single – variant martensite , the stress should be increased or temperature should be decreased . so ,we require to,

$$\dot{F}^{A\to M} > 0 \qquad \text{Eq.(5.24)}$$

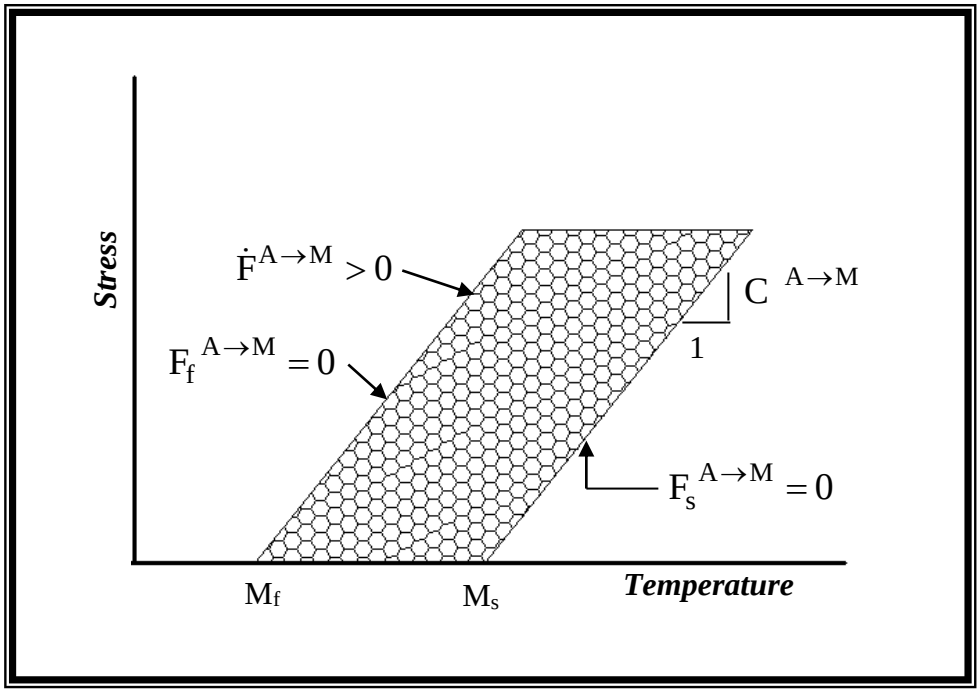

Fig.(5.1) production of single variant martensite

5.2.4.2. Austenite production

Similarly to the previous equations , the functions are introduced as :

$$F^{M\to A} = \sigma - C^{M\to A}T \qquad \text{...Eq.(5.25)}$$

$$F_S{}^{M\to A} = F^{M\to A} - R_S{}^{M\to A} \qquad \text{...Eq.(5.26)}$$

$$F_f{}^{M\to A} = F^{M\to A} - R_f{}^{M\to A} \qquad \text{...Eq.(5.27)}$$

With

$$R_S^{M\to A} = C^{M\to A}A_S \qquad \text{...Eq.(5.28)}$$

$$R_f^{M\to A} = C^{M\to A}A_f \qquad \text{...Eq.(5.29)}$$

Where $C^{M\to A}$ is the stress to temperature coefficient for reveries direction of transformation A_S and A_f are the initial and final transformation temperature from martensite to austenite zero stress .The region in which the transformation may take place is described by Fig. (5.2) as :

$$F_S^{M\to A} < 0 \quad \text{and} \quad F_f^{M\to A} > 0 \qquad \text{Eq.(5.30)}$$

So , to activate the production of austenite ,the stress should be decreased or the temperature should be increased or proper combination of these actions should be occurred , so.

$$\dot{F}^{M\to A} < 0 \qquad \text{...Eq.(5.31)}$$

The material behavior is assumed to be isotropic. The pressure dependency of the phase transformation is modeled by introducing the Drucker –Prager loading Function as [Auricchio , 2001]

$$F = q + 3\alpha p \qquad \text{Eq.(5.31)}$$

Where

α – material parameter

p- pressure

$$p = \mathrm{Tr}(\sigma)/3 \qquad \text{...Eq.(5.32)}$$

Where :

Tr – trace operater

σ – stress vector

$$q = \left[\frac{1}{2}\sigma^T[M]\sigma\right]^{1/2} \qquad \text{...Eq.(5.33)}$$

σ^T - Transpose of stress vector

M – matrix defined as

$$[M]=\begin{bmatrix}1&0&0&0&0&0\\0&1&0&0&0&0\\0&0&1&0&0&0\\0&0&0&2&0&0\\0&0&0&0&2&0\\0&0&0&0&0&2\end{bmatrix} \quad \text{...Eq.(5.34)}$$

Auricchio model (1997) assumed the linear form for evolution of the Volume fraction of martensite and which is defined as :

$$\dot{\zeta}_M=\begin{cases}-H^{A\to M}(1-\zeta_M)\dfrac{\dot{F}}{F-R_f^{A\to M}} & A\to M \text{ Transformation}\\ H^{M\to A}\zeta_M\dfrac{\dot{F}}{F-R_f^{M\to A}} & M\to A \text{ Transformation}\end{cases} \quad \text{..Eq.(5.35)}$$

where :

$$R_f^{A\to M}=\sigma_f^{A\to M}(1-\alpha) \qquad \text{Eq.(5.36)}$$

$$R_f^{M\to A}=\sigma_f^{M\to A}(1+\alpha) \qquad \text{Eq.(5.37)}$$

Where $\sigma_f^{A\to M}$ and $\sigma_f^{M\to A}$ are material Parameters as shown in Fig. .(5.3)

$$H^{A\to M}=\begin{cases}1 & \text{if}\begin{pmatrix}R_S^{A\to M}<F<R_f^{A\to M}\\ \dot{F}>0\end{pmatrix}\\ 0 & \text{otherwise}\end{cases} \quad \text{...Eq(5.38)}$$

$$H^{M\to A}=\begin{cases}1 & \text{if}\begin{pmatrix}R_f^{M\to A}<F<R_s^{M\to A}\\ \dot{F}>0\end{pmatrix}\\ 0 & \text{otherwise}\end{cases} \quad \text{...Eq(5.39)}$$

Where :

$$R_S^{A\to M} = \sigma_S^{A\to M}(1+\sigma) \qquad \text{Eq.(5.40)}$$

$$R_S^{A\to M} = \sigma_S^{M\to A}(1+\sigma) \qquad \text{Eq.(5.41)}$$

Where $\sigma_S^{A\to M}$ and $\sigma_S^{M\to A}$ are the material Parameter as shown in Fig.. (5.3).

Fig. (5.3) idealized stress – strain carve of linear super elastic behavior of SMA .The incremental stress relation is

$$\Delta\sigma = [D]\,(\{\Delta\varepsilon\} - \{\Delta\varepsilon^{tr}\}) \qquad \text{Eq.(5.41)}$$

$$\{\Delta\varepsilon^{tr}\} = D\overline{\zeta}_M\bar{\varepsilon}_L\frac{\partial F}{\partial\{\sigma\}} \qquad \text{Eq.(5.42)}$$

Where

$\{D\}$- elastic –strain matrix. , $\{\Delta\varepsilon^{tr}\}$ = incremental transformation strain

$\bar{\varepsilon}_L$ = maximum transformation strain which is the material parameter as shown in Fig. (5.3).

This model assumed isotropic behavior for both austenite and martensite phase , furthermore , it is applied to evaluate only super elastic behavior not the shape memory effect for both linear and exponential approach in this study , Ansys version 9 is taken for modeling super elastic behavior of shape memory alloy which is based upon Auricchio model for only linear approach .up to date , there is no unique model for modeling and numerical simulation for both super elastic an shape effect of shape memory materials further more , there is no package or software deals with porous shape memory alloys not only for modeling but also for numerical simulation of engineering devices.

Many workers in the field of analysis of shape memory alloys assume the multilinear elastic model to analyze super elastic behavior of shape alloys especially for nitinol devices with appropriate approximations and assumptions . [koop et al , 2001]

The previous material parameters as shown in Fig. (5.3), are determined from experimental tensile or compression tests for shape memory alloy sample .

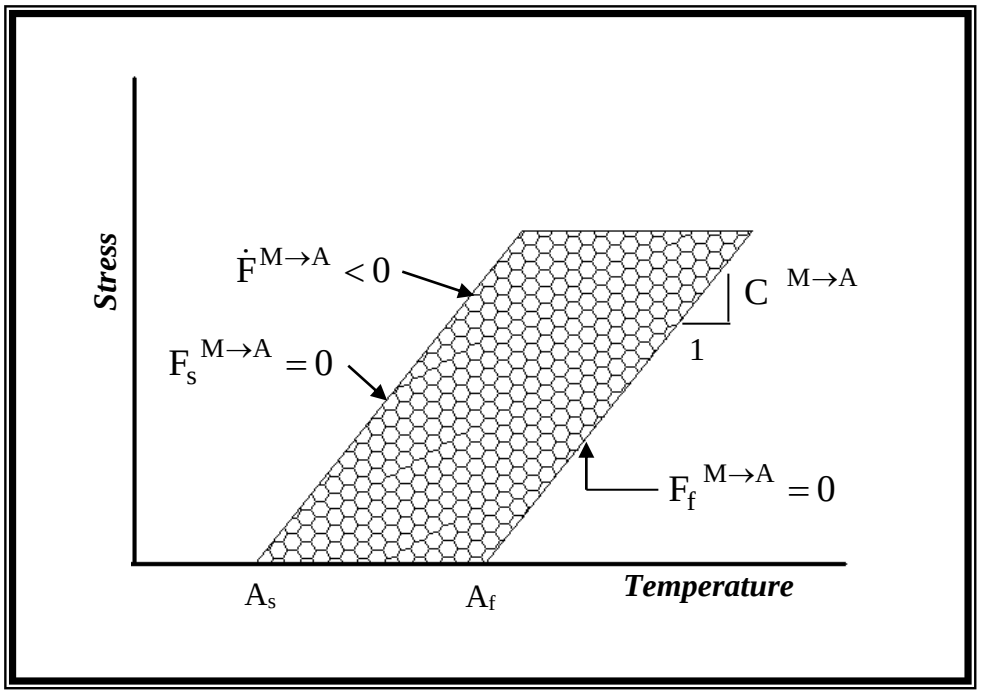

Fig.(5.2) production of austenite phase .

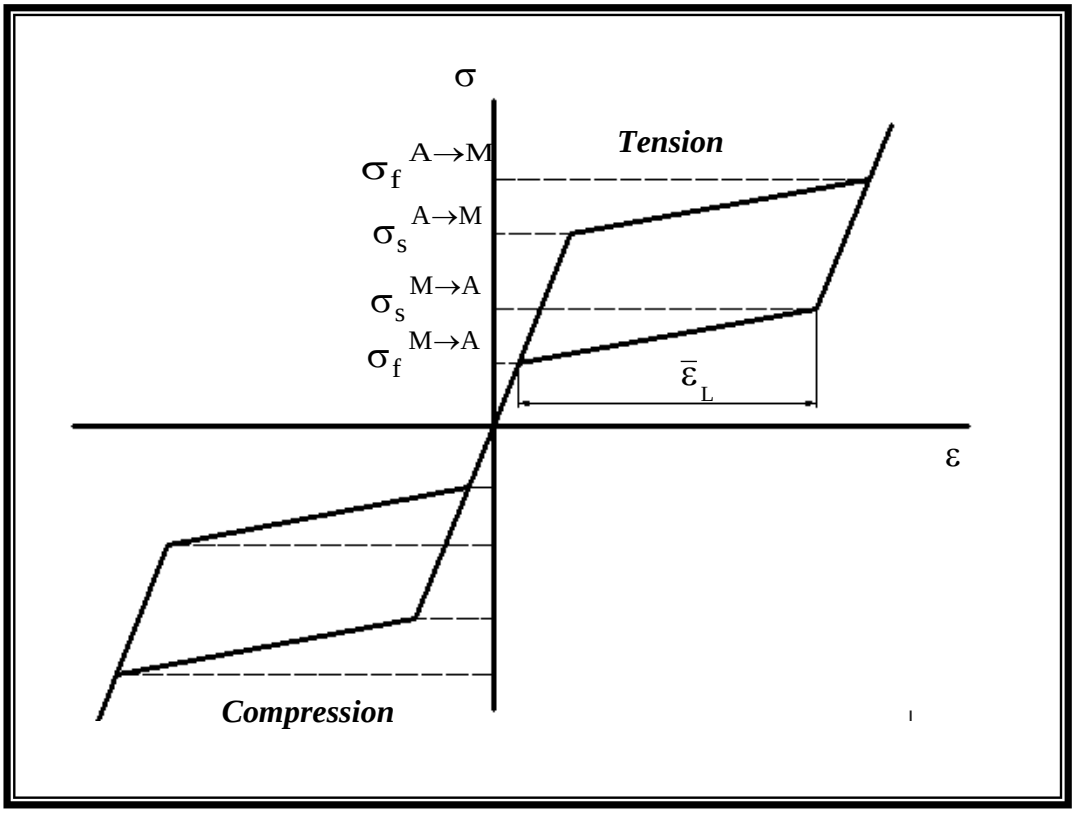

Fig.(5.3) idealized stress-strain curve of linear super elastic behavior of SMA.

5.3 modeling of porous shape memory alloys :

Porous shape memory alloys have been developed and used primary for bone be construction (Ni – Ti base) also due to it's lower density compared to fully dense shape memory alloys, they use in a number of light weight applications. Another advantage of porous shape memory alloys is the possibility of creating a functionally gradient material by controlling the porosity . The expectation is that the porous SMAs will retain some of the desirable characteristics of fully dense SMAs such as shape memory effect and super elasticity while enhancing shape recovery and energy absorption capabilities.

While both theoretical and experimental work are equally important, in this section focuses on the micromechanical modeling of porous shape memory alloys under quasi- static loading.

The modeling of porous materials has been performed assuming either periodic or random distribution of pores. Periodic arrangement of pores in a real porous shape memory material is an approximation assumption, but this assumption provides insight into global material behavior in the form of useful limiting values for the overall properties.

Furthermore, an approximate local variation of various field such as stress and strain indicating areas of concentration due to porosity can be obtained. So , these results may give design limitations in order to minimize or even avoid micro-buckling , yielding and consequently loss of capacity of phase transformation. The assumption of periodicity and symmetry boundary conditions reduce the analysis of porous shape memory material to the analysis of the unit cell. Thus , appropriate loading conditions need to be used. In the case of the porous material with random distribution of pores , micromechanical averaging techniques can be used to determine the averaged macroscopic response. In this case the material is treated as a composite with two phases, dense matrix and pores. The two most widely used are the self- consistent method and the Mori-Tanaka method. Both methods are based on the assumption that the effective response of the composite can be obtained by considering a single in homogeneity embedded in an infinite matrix.

Furthermore , the two approaches are assumed uniform shape of pores such sphere or cylindrical . but with random distribution.

In this study , unit cell finite element analysis taking into consideration tetragonal and hexagonal distribution of pores has been studied using Ansys. version 9.

Furthermore , randome distribution with non uniformed shape of pores in shape memory alloy matrix has also studied using real microstructure image taken from digital camera sticked with light optical microscope. Microstructure images have analyzed and processed in order to know the two phases, matrix shape memory alloy and embedded pores clearly and to convert image (pixels) into geometry (area in X and y coordinates) . This object is not easy due to the complex image of microstructure of porous shape memory alloy because there are multiphase in addition of pores.

Two dimension analysis is used for both approaches. Circle, ellipse or any non uniformed shape can be used as pore shape In the image of microstructure porous shape memory alloy may contain open, closed pores or a combination of both types. In this study two dimension analysis is based , so either open or closed pores are assumed to exist in the sample.

5.4. Unit Cell Finite element method

Two main periodic arrangement of pores are studies as follows:-

5.4.1. Tetragonal arrangement of pores.

An in plane square arrangement of pores is assumed at a first step in the present study. the cross section of such arrangement for open pores is shown in Fig.. (5.4) . The xy-plane forms the cross section of the material specimen and z is the out of plane axis along the length of the specimen.

As shown in Fig.(5.4) the open pores are assumed to be in the form of cylinders with circular cross-section and generators parallel to the out of plane z-axis

5.4.2. Hexagonal arrangement of pores. :-

Hexagonal arrangement of pores is also assumed in this study. The cross section of hexagonal arrangement of pores is shown in Fig..(5.5).

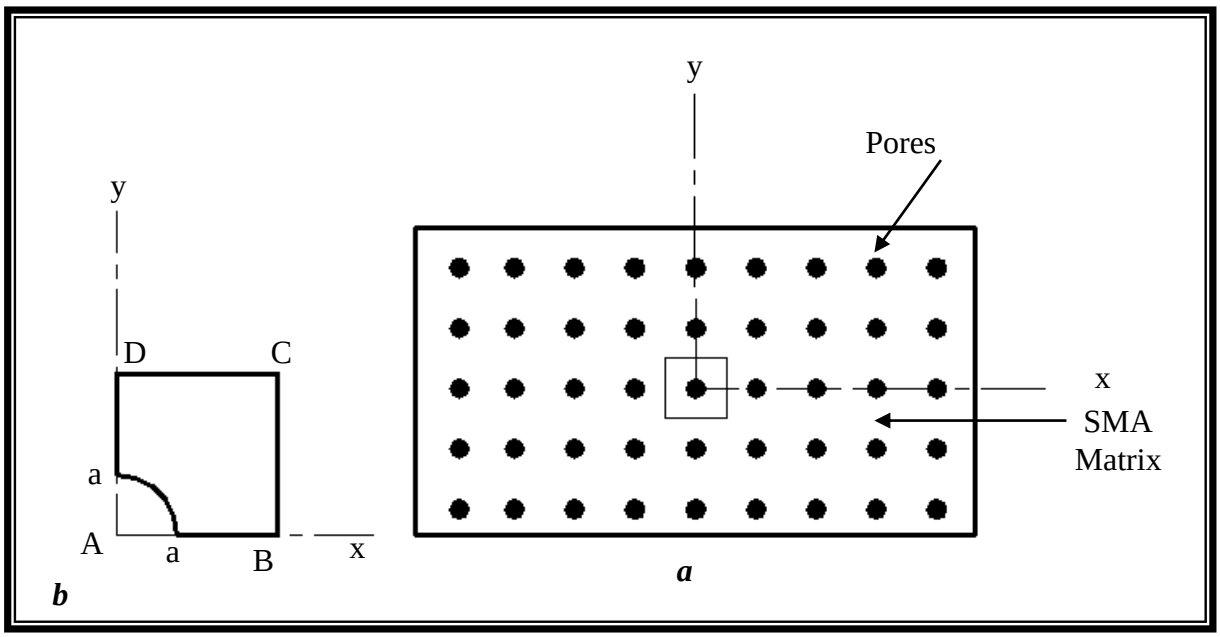

Fig..(5.4) square arrangement of pores in a and b squire unite cell

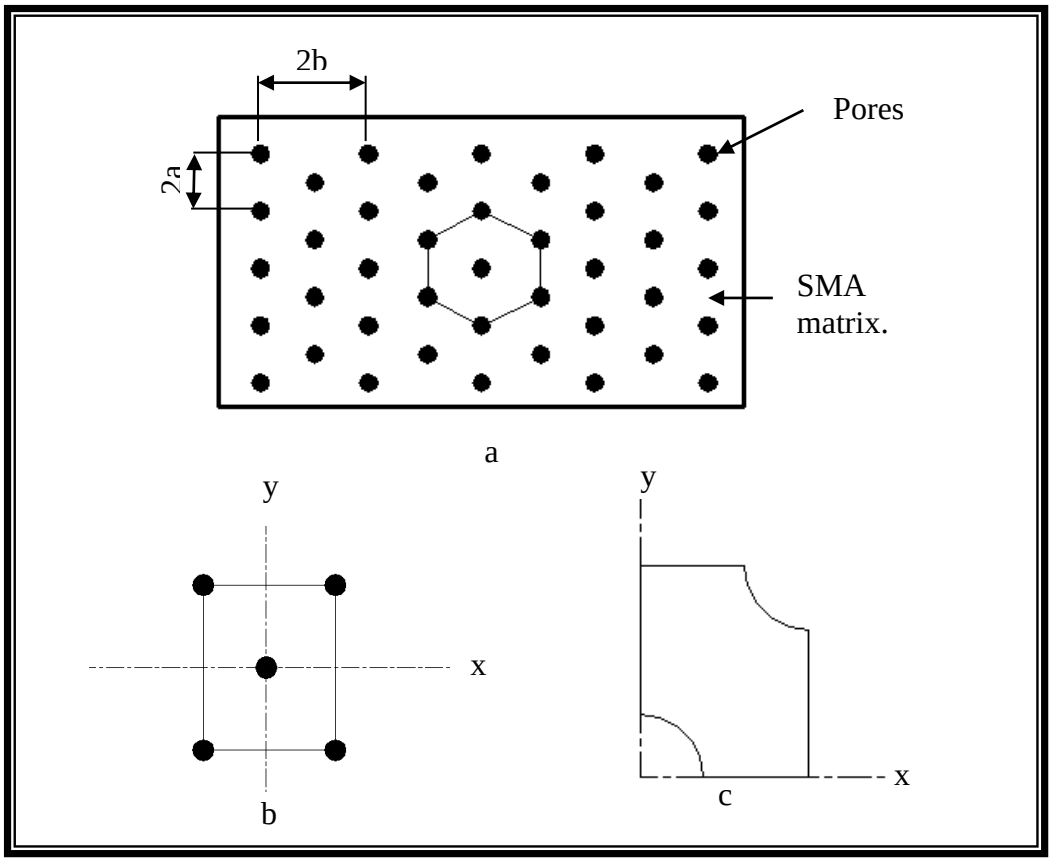

Fig.(5.5) Cross-section schematic of periodic hexagonal arrangement of open pores in a dense shape memory alloy matrix. a. Hexagonal arrangement of pore b. Repeated unite of pore arrangement C. Hexagonal unit cell .

In this case , the unit cell is a rectangle with length a and width b, So the cross section of each unit cell is a rectangle with cross section [2a × b]where b= 0.866 a . The unit cell has a uniform depth in the z- direction. Assuming that the applied loads do not violate the geometric symmetry of the unit cell.

5.5.1 real representation of microstructure image using image analysis and processing.

In this section several parameters and topics must be explained as follows:-

5.5.1. Image processing :-

Scanned surface section images of microstructure examination specimens have been used in both experimental and modeling studies. Image processing is applied to the microstructure light optical microscope image. The image is processed by Microsoft picture manger at first to obtain image without black edges taken from optical microscope as shown in Fig. (5.6).

Matlab version 7 imaging toolbox is used in order to convert the original images to a binary (black and white) image , with white signifying the shape memory alloy matrix and black being the pores. The image has a resolution of (118 pixels /cm) which captured by digital camera fitted by hand on the microscope. The processing of image involves creating a uniform background in the image and converting the image in to binary image . This stage includes the following steps in matlab version 7:-

Step 1. Read and display an image .

Clear the matlab workspace of any variable and read and display the microstructure image such alloy I image for example as shown in Fig. (5.7) using the command : I = imread (alloy I. JPg); imview(I)

Step 2. Estimate the value of background pixels:

This is very important step to recognize objects and background of image .There are many functions in morphological operations used to see the estimated background of image in matlab Toolbox software.

Step3. Create an image with uniform background .

step4. Create a binary version of the image .

Create a binary version of the image by using there sholding. The function gray threshold automatically computes an appropriate there to use to convert the image to binary as shown in Fig. (5.8).

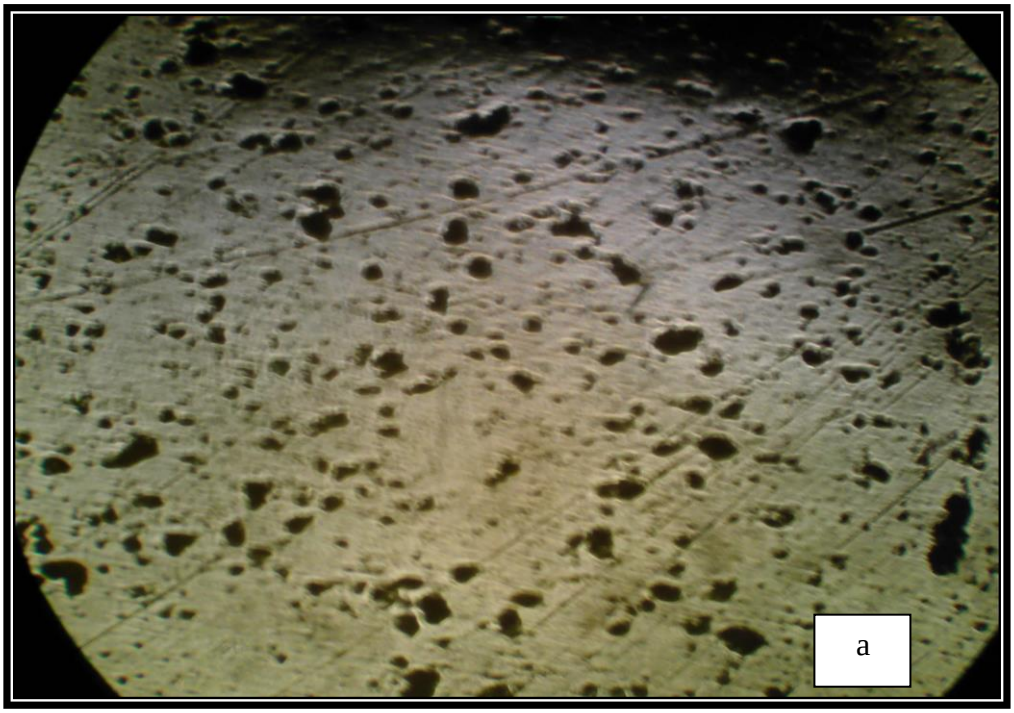

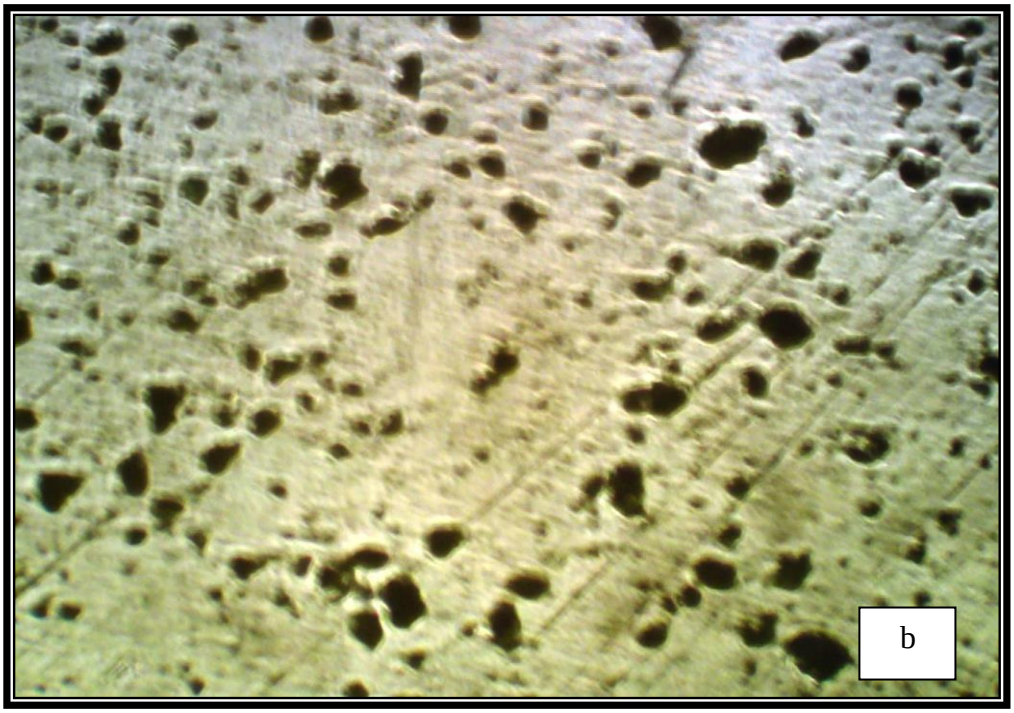

Fig. (5.6)LOM images for alloy 13 in the case of : a. original image b.neutralized image with Microsoft picture manger.

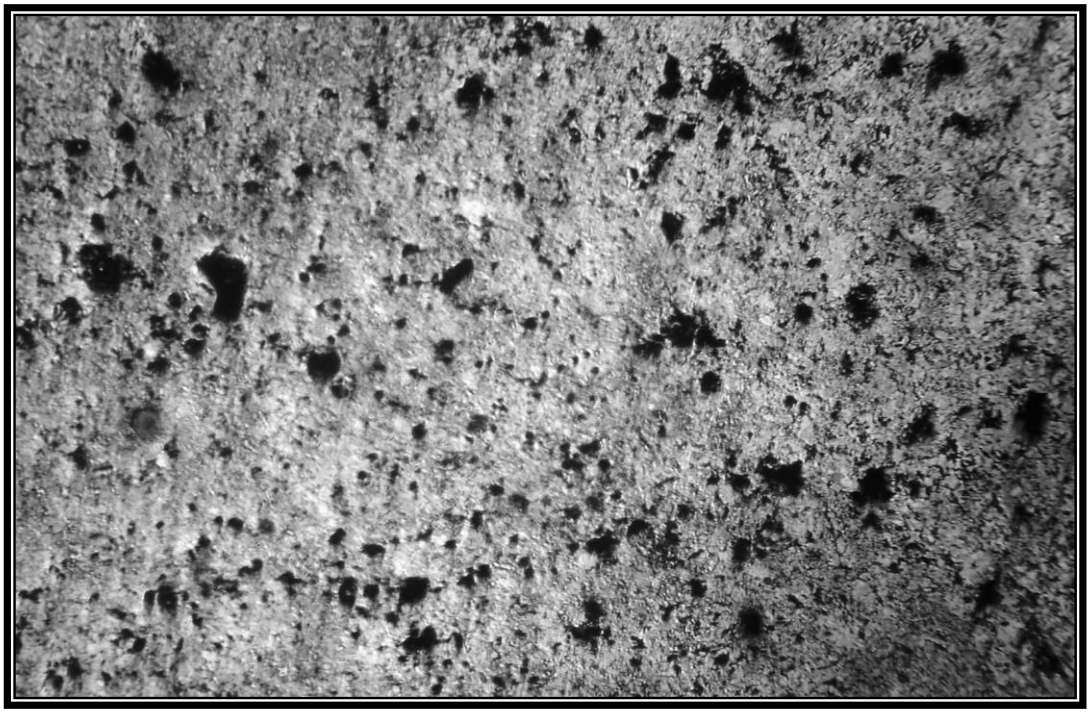

Fig.(5.7) LOM image with uniform background for alloy 10.

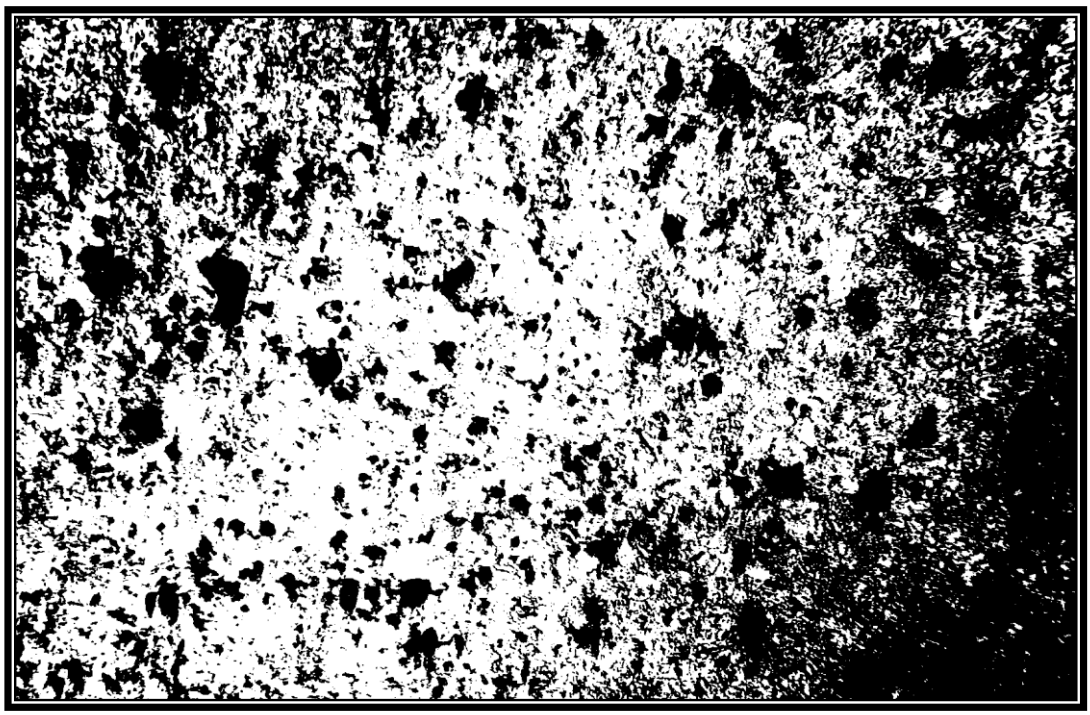

Fig.(5.8) LOM binary image for alloy 10.

5.5.2. Image Analysis:

After converting the image to a binary image (white and black), several functions have been used to determine the number of objects (black in image) which are pores , their distribution ,area , centroid and bounding box. The bounding box represents the smallest rectangle that can contain a region on in this case a pore. Further more , statistical properties of objects in the image may be obtained using matlab functions . statistical properties include maximum diameter of pore area , circle or ellipse fitted object and mean of all pore sizes.
This field of knowledge is new and very important in material engineering applications such as analysis of particles , shape and size and distribution of particles in the field of powder metallurgy as in this study, and in the analysis of final product microstructure for example pores size and their distribution , grain size and grain growth in complex metallurgy microstructure. The main problem in the field of image processing and analysis is the image segmentation which is the hardest task and main problem in computer vision . If target objects cannot be detected correctly, it is difficult to do object measurement , analysis and reconstruction. Since objects are complex in shape and size and its distribution, there is no universal segmentation algorithm.

There are several Segmentation algorithms based upon the type of images and requirements of measuring objects. These algorithms include:-

- ***threshold .***
- ***split and touching objects on shape.***
- ***edge detection.***

The algorithm based on edge detection is very useful for delineating objects with a valuable edge whereas threshold is suitable for image with either uniform object or uniform background. The algorithm based on split and merge is suitable for image on that objects have similar surface properties[wojnar,1999]. Object in our images are the pores in the analysis of microstructure of porous shape memory alloys and are the particles in the analysis of particles of pure

powders and blended powders before compaction. In this study image analysis and processing used to give the following :-

1. Particle size and shape using suitable scale calibration .
2. particle distribution based up on accumulated particle number and histogram of particle sizes.
3. particle size with suitable circle ellipse and Feret rectangle best fit with Particle shape .
4. pore size and shape in the sintered compact image .

5.6.Finite element Analysis of porous shape memory alloys using Ansys Software:

Ansys program is an open system where the user has various possibilities for constricting an individual model for the material .Ansys program is based up on finite element analysis. Our problem which in reality is composed of continuous fields (fields of displacements , strains , stresses temperature and state variables) can be solved by an approximate discrete element based solution.

Shape memory alloys have a complex behavior and are not similar than all other material behavior .They have several non linearities such as follow:

1. The deformations in the model are so large that the relationship between strains and displacements become non linear .
2. Material behavior is non linear .

3- The loadings may be non linear .

Thus all geometrical non linearities and material non linearities are employed in the analysis of shape memory alloys alone , further more the presence of pores also increased the complexity of the analysis .

After processing and analyzing microstructure images of porous shape memory alloys , Ansys parametric Design Language (APDL) script is used to input coordinates of pores with best fit ellipse , best Fit ferret rectangles and / or best fit circle .In Ansys version 9 (2005) there are two elements deal with shape

memory alloy which are plane 182 and plane 183. These element may be used to model only the super elastic behavior of shape memory alloys depend up on Auricchio model .

Plane 182 element is used for two dimensional modeling which is defined by four nodes having two degree of freedom at each node .where as plane 183 is defined by eight nodes with also two degree of freedom per node as shown in Fig..(5.9)

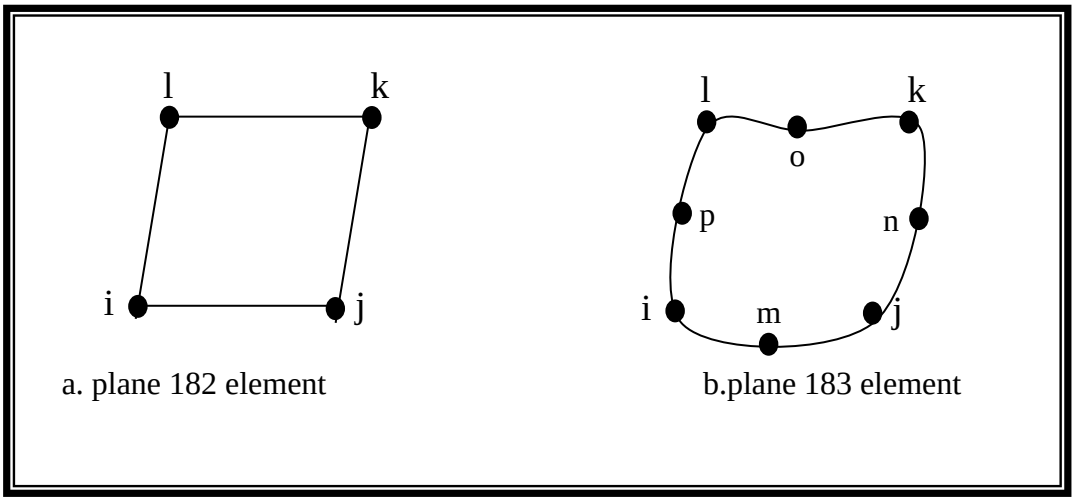

.

Fig.(5.9) Plane element use to model super elastic behavior of shape memory alloy in Ansys ver 9 Environment

5.6.1. Boundary Conditions

The following boundary conditions need to be applied regardless of pore geometry for unit cell finite element analysis .

$$U(0,y) = V(x,0) = 0 \qquad \text{Eq.}(5.43)$$

$$U_{max}(x,y) = C_1 \quad \text{and} \quad V_{max}(x,y) = C_2 \qquad \text{Eq.}(5.44)$$

Where U and V are displacements in the X and Y directions respectively and C_1 and C_2 are constants which impose the boundary conditions that all material points on respective unit cell boundaries have the same normal displacement. The stress and strain field in the unit cell can be extended for the whole porous shape memory alloy by virtue of the periodicity and symmetry conditions .

The reflective symmetries imply that shear stresses components are vanished on all boundaries of the unit cell (square and hexagonal Unit cell). So .

$$\tau_{xy}(0,y)=\tau_{xy}(x,0)=0 \qquad \text{...Eq.(5.45)}$$

Where τ_{xy} - in plane shear stress .

Fig.(5.10) shows the meshes of the unit cells used and mesh of real microstructure image with plane 182 element. Plane 182 with four nodes is used and based for finite element analysis formulation in order to decrease time of analysis and running addition to complexity of the structure.

Non linear load increment procedure has been done for 10 load steps with 50 steps with 50 and 5 sub steps of loads for maximum and minimum sub steps respectively.

5.6.2. Materials properties

In this study Auricchio model is based to model the superelastic behavior of shape memory alloy which described by six constants previously mentioned as follows:

$\sigma_S^{A\to M}$-starting stress value for austenite phase toward martensite phase (martensite starting stress).

$\sigma_f^{A\to M}$ - Martensite finishing stress.

$\sigma_s^{M\to A}$- starting stress value for martensite to austenite reverse phase transformation.

$\sigma_f^{M\to A}$- Final stress value for martensite to austenite reverse phase transformation.

ε_L^- - maximum transformation strain.

α - parameter measuring the difference between material responses in tension and compression.

These constants are input in the ansys program as show in Fig. (5.11). All material constants are measured experimentally from compression test of compression samples prepared in the experimental work..

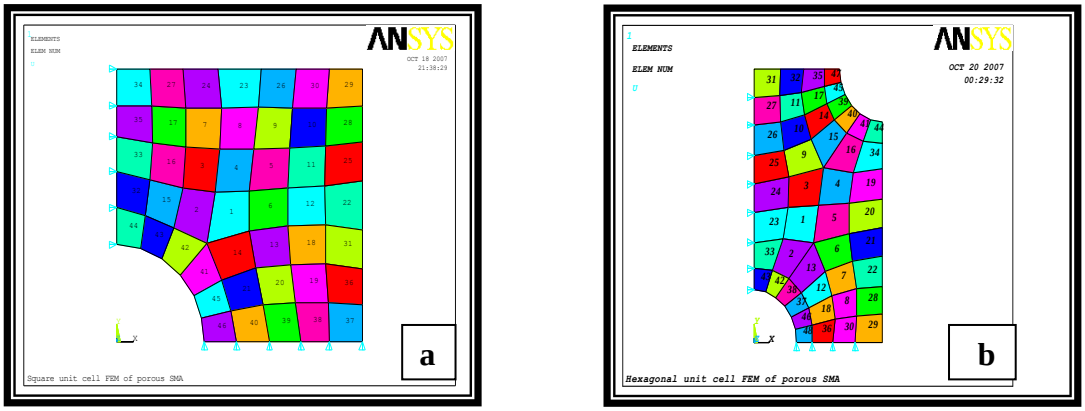

Fig.(5.10) Mesh of Square (a) and hexagonal (b) unit cell FE.

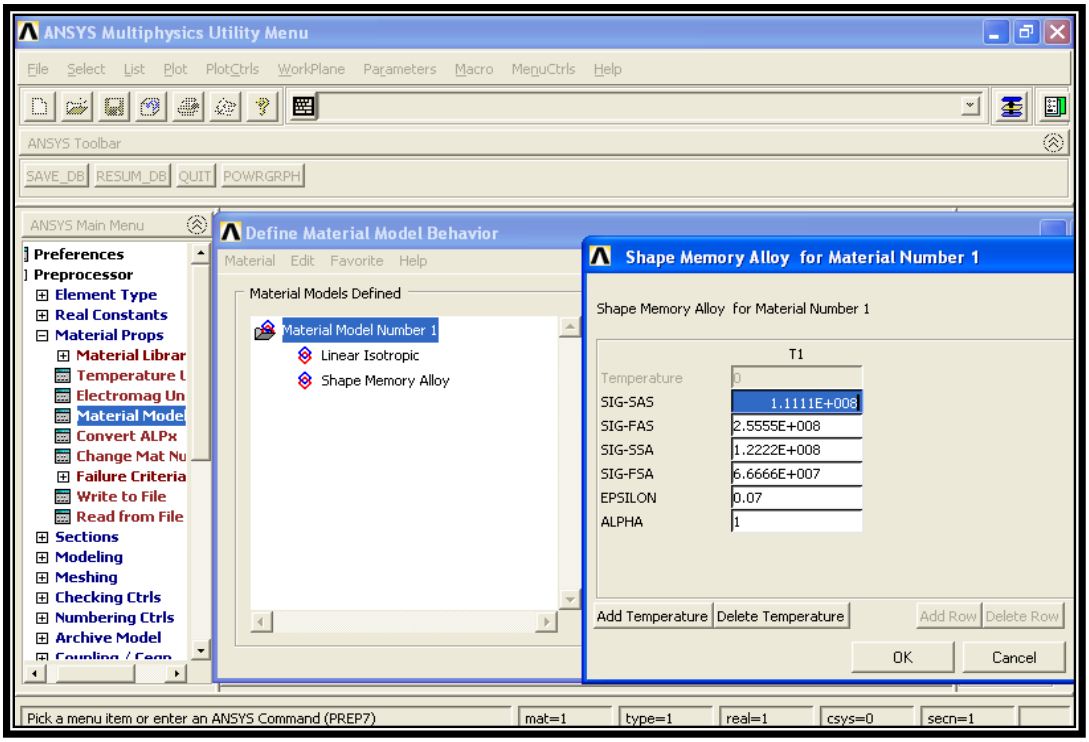

Fig.(5.11) Material properties of shape memory alloy input in Ansys program .

5.7. verification of the shape memory alloy model.

According to review of literature , there is very few papers about the analysis of porous shape memory alloys used unit cell finite element method. Perhaps there is no study of porous shape memory alloy based upon real micro structural image with ansys program. All previous studies deal with dense shape memory alloy manufactured by casting and their models have been done in another programs with user material subroutine (such as in Abquas program) . All researchers used unit cell finite element method and no one depend upon real microstructure of porous shape memory alloys. Therefore in this section two case studies have been presented for dense shape memory alloy.

1.First verification case study:

The First case study is a circular wire of diameter D= 1.49 mm and length 20 mm. The experimental loading unloading history was applied to the specimen reaching a maximum 8% strain by wick 1994(Queted in Auricchio etal 1997). The material parameters are in the following :

$E = 60$ GPa , $\nu = 0.3, \varepsilon'_L =$ 7.5 % , $\sigma_s^{A\to M} = 520MPa$, $\sigma_f^{A\to M} = 600MPa, \sigma_s^{M\to A} = 300MPa,$ $\sigma_f^{M\to A} = 200MPa$

In our verification, element plane 182 is used to mesh the specimen with its material parameters and applied incremental nonlinear loads as tensile stress. Fig.(5.12) showed the comparison between experimental and analyzed behavior. Good agreement has been obtained.

2. Second verification case study.

Nitinol tube (49.2 wt % Ti ,50.8 wt% Ni) with a 4.64 mm outer diameter and .37 mm thickness had prepared by (McNaney et. al, 2003) The tube was cut into 75 mm long specimens and ground along 25 mm long center test section to an outer diameter of 4.3 mm in order to obtain tensile specimen with 0.2mm thickness ,with the following material properties:

$E = 180\ GPa$, $\nu = 0.3, \varepsilon'_L = 6\%$, $\sigma_s^{A\to M} = 360\,MPa$, $\sigma_f^{A\to M} = 440\,MPa, \sigma_s^{M\to A} = 150\,MPa,$ $\sigma_f^{M\to A} = 100\,MPa$

Good agreement has been obtained with experimental study as show in Fig.. (5.13). For both examples , the material is nitinol 50/50 Ni-Ti base shape memory alloy. We choose these experimental studies because all material parameters are defined experiments alloy whereas many other studies on Ni-Ti or copper base alloys are studied from the point of view either focuses on physical properties such as x-ray diffraction , electrical resistance, DSC studies of some mechanical tests such as stress-strain curves or only hardness with nanoscale so we not comparison with these studies as a numerical study.

Note.

It must be shown that numerical modeling and simulation of porous shape memory alloys either by unit cell finite element analysis or by microstructure-based finite element analysis where the porous shape memory matrix and pore as particulate impeded in the matrix, shape memory material parameter for fully densed material must be presented. In this study all samples prepared by experimental work are porous so the following acceptable relation are based to calculate dense material parameters (See Zhao etal, 2005).

$$\sigma_{sp}^{M\to A} = (1-P)\sigma_{sD}^{M\to A} \quad \text{---------- Eq(5.46)}$$

$$\sigma_{fp}^{M\to A} = (1-P)\sigma_{fD}^{M\to A} \quad \text{---------- Eq(5.47)}$$

$$\sigma_{sp}^{A\to M} = (1-P)\sigma_{sD}^{A\to M} \quad \text{---------- Eq(5.48)}$$

$$\sigma_{fp}^{A\to M} = (1-P)\sigma_{fD}^{A\to M} \quad \text{---------- Eq(5.49)}$$

Where :

p-apparent porosity

p and D subscript refer to porous and fully densed respectively for all stresses which defined as material parameters .

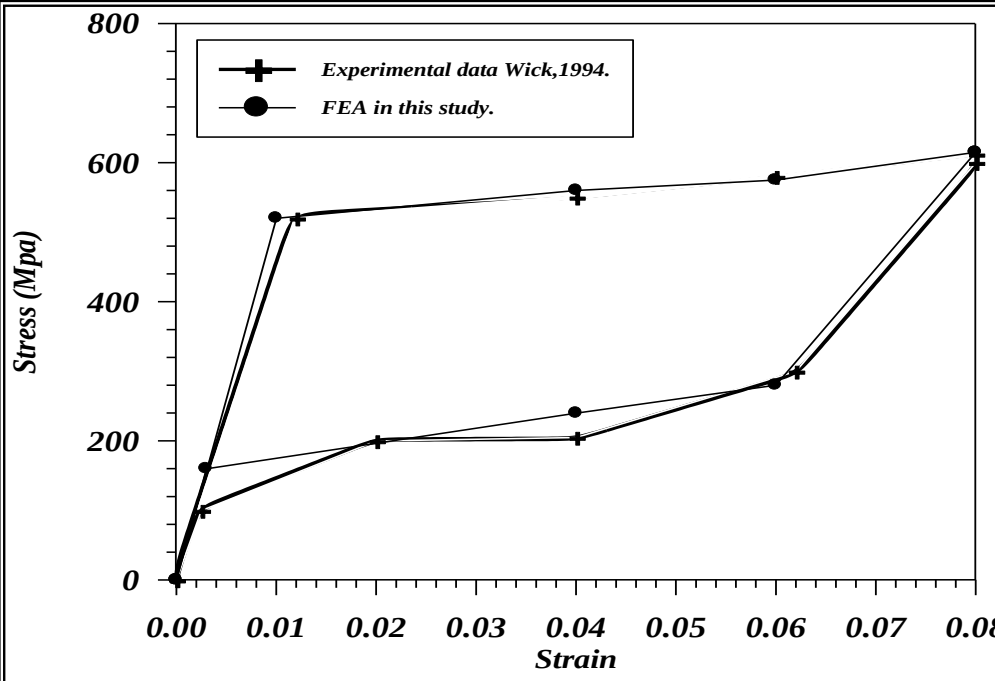

Fig.(5.12) Stress-Strain curve for nitinol wire under tension ,comparison between experimental and FEA for case study 1.

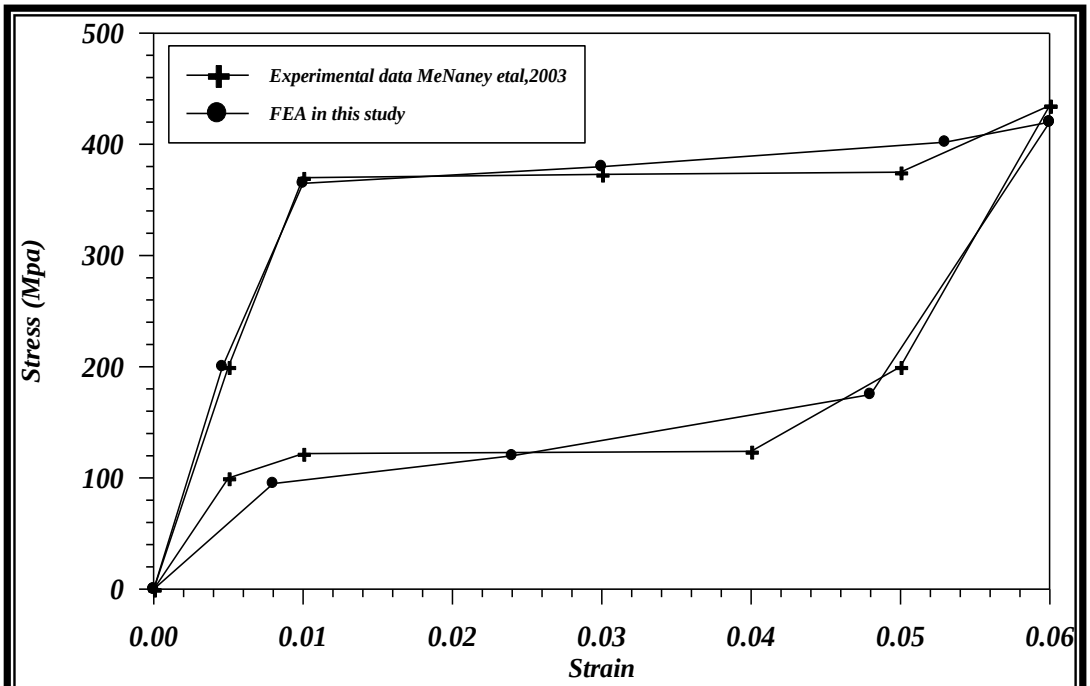

Fig.(5.13) Stress- strain curve for nitinol tube under tension, comparison experimental with FEA for case sudy 2.

Results and Discussion

6.1 General View :

In this chapter , experimental results which include physical and mechanical tests results for both before sintering and after sintering process have been presented . At a first , physical properties measured in this study for elemental and blended powders such as apparent density , particle size and shape and particle distribution have been presented .It has been Concluded that all experimental results are classified into before sintering and after singeing in order to avoid any ambiguous arrangement of results . Furthermore, numerical results and comparison with experimental work based up on unit cell finite element analysis and microstructure based finite element analysis have also presented .

6.2.Results before sintering of compacts :

In this part many physical tests results and several parameters have been studied and presented as follows:

6.2.1 Apparent density of elemental and blended powders :

Apparent density of elemental powders used to prepare blended mixture of alloys has been measured and shown in Fig.(6.1). The apparent density of iron and nicked are the highest density compared with other powders due to high density of the solid material for be both iron and nicked .

Apparent density of a metal powders depends upon the density of the solid material , particle size and its distribution , particle shape and surface area , Apparent density is strongly affected by particle size and its distribution, in

addition , As particle shape becomes less spherical apparent density decreases due to the increase in frictional surface area and less uniformity powder particle during packing .

Apparent density of blended powders for mixtures of alloys [1,2,3 and 6] is shown in Fig .(6.2). Apparent density of mixture of alloy (1) is the highest with comparison with other mixtures due to the high content of higher solid density of copper. The measured apparent density of blended powders and elemental powders , has been affected by the flow rate and internal friction between particles in the same or different composition and friction between particles and wall of baffle box and small funnel . Decreasing surface area to volume ratios and decreasing surface roughness tends to reduce frictional forces between setting particles , This tendency thus increases apparent density by allowing the particles to move with more effectively to fill the free spaces between previously settled particles. An effective way to increase the apparent density of the elemental or blended powders is to fill the spaces between particles with smaller particles as can be seen in the next section.

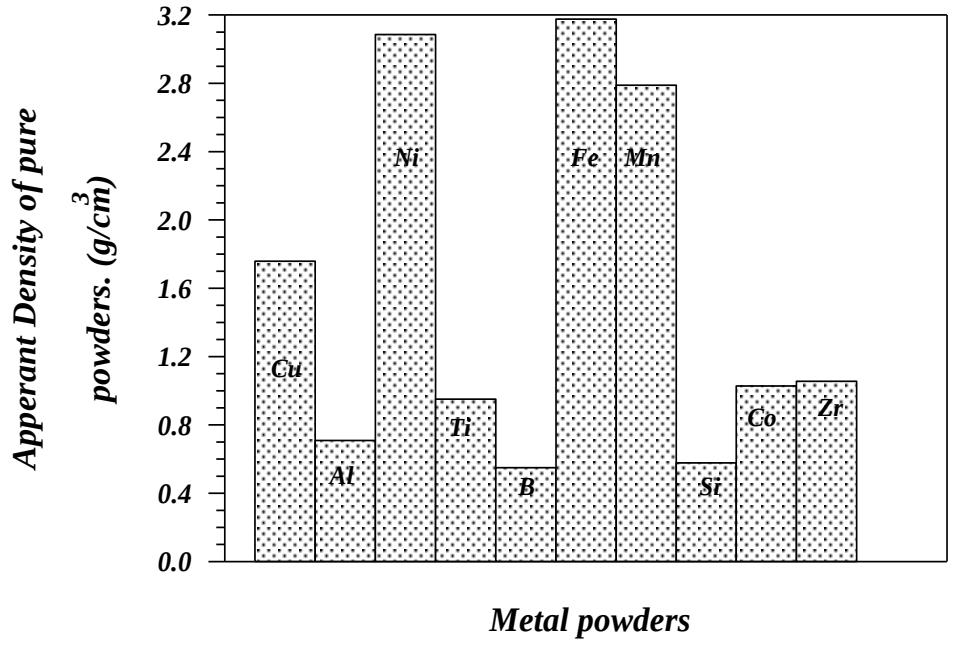

Fig.(6.1) Apperant density of pure metal powders used in this study.

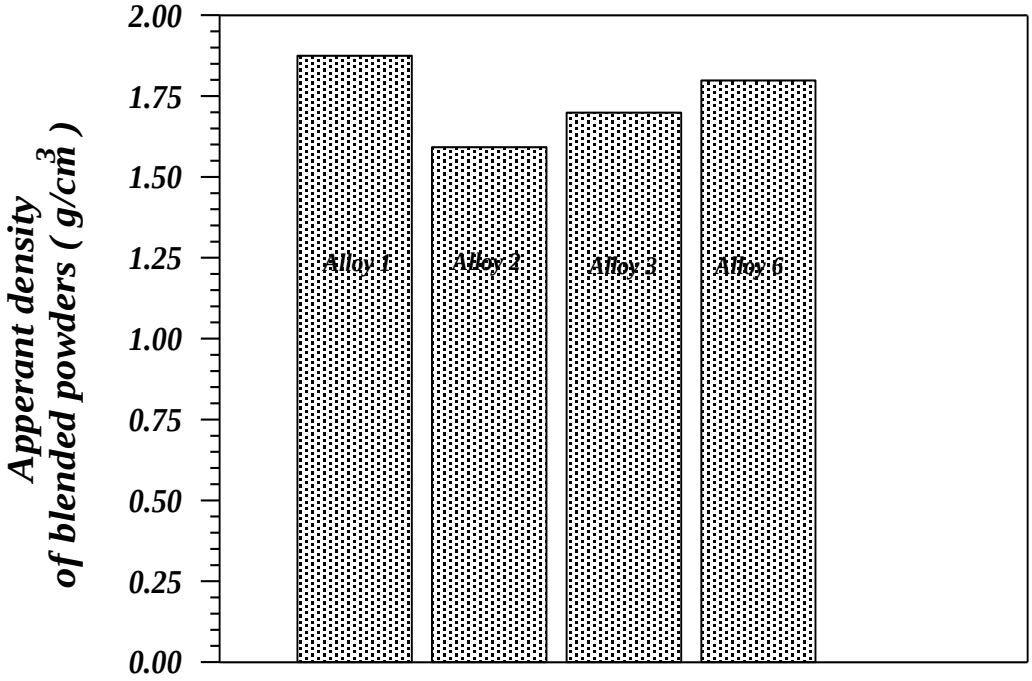

Fig.(6.2) Apparent density of blended mixtures of alloys.

6.2.2 particle size and distribution :

Particle size and its distribution for both elemental and blended powders have been measured in this work using light optical microscopy images which are analyzed and processed using image analysis toolbar in matlab version 7 program image in white and black (binary image) and accumulative plot for each powders are shown in Figures (6.3 - 6.12).

In all these image middle particle size are used in the image analysis to find particle size of metal powders. Mean particle size is determined at 50 % point on the accumulative plot , accumulative plot is weighted by particle size .In all these image , agglomerate of particles in the glass slide is the main problem which may be occurred so wrong result about particle size may be obtained .Furthermore ; the best fit ellipse or circle or feret width and feret length used to capture particles shape and size are estimated technique and affected on the final results accuracy . Mean of particles size for elemental and blended powders are given in table (6.1) .

Decreasing particle size generally decreases apparent density because the smaller particles have greater specific surface of the powder which the later leads to increase the friction between particles and subsequently decreases the apparent density.

On the other hand , most powders used for compaction have irregular shape. The addition of fine spherical powder such as powder Ni effectively increases apparent density while the addition of flake powders such as Cu decreases apparent density .

The relative amount of coarsest and finest particles and the percentage of particles between the two types determine apparent density .

Binary image and accumulative plot for blended mixture of powders from alloy(1,2,3and 6) are shown in Fig .(6.13-6.16) .respectively .

Different particle size ranges are preferred for good compacts and also for good properties of the final sintered Products .

Table(6.1) Average particle size of metal powders and blending mixtures

No.	Material	Average particle size
1	Cu	1
2	Al	2
3	Ni	8
4	Ti	75
5	B	80
6	Co	0.8
7	Zr	8.2
8	Fe	20
9	Mn	1.2
10	Si	4
11	Alloy 1	9
12	Alloy 2	5
13	Alloy 3	16
14	Alloy 6	8

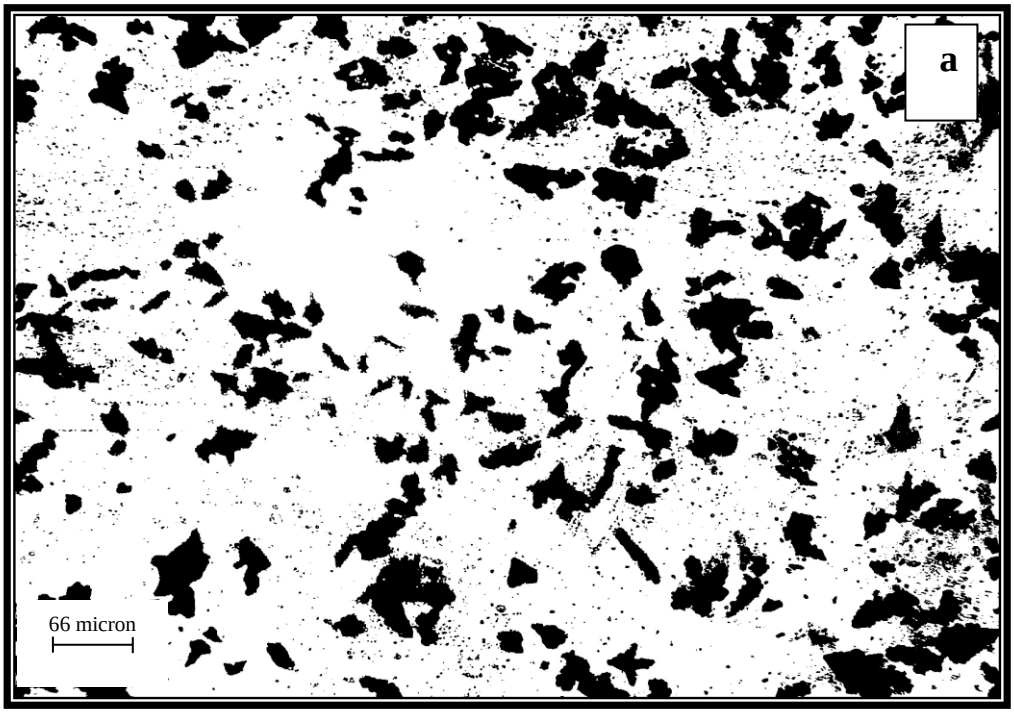

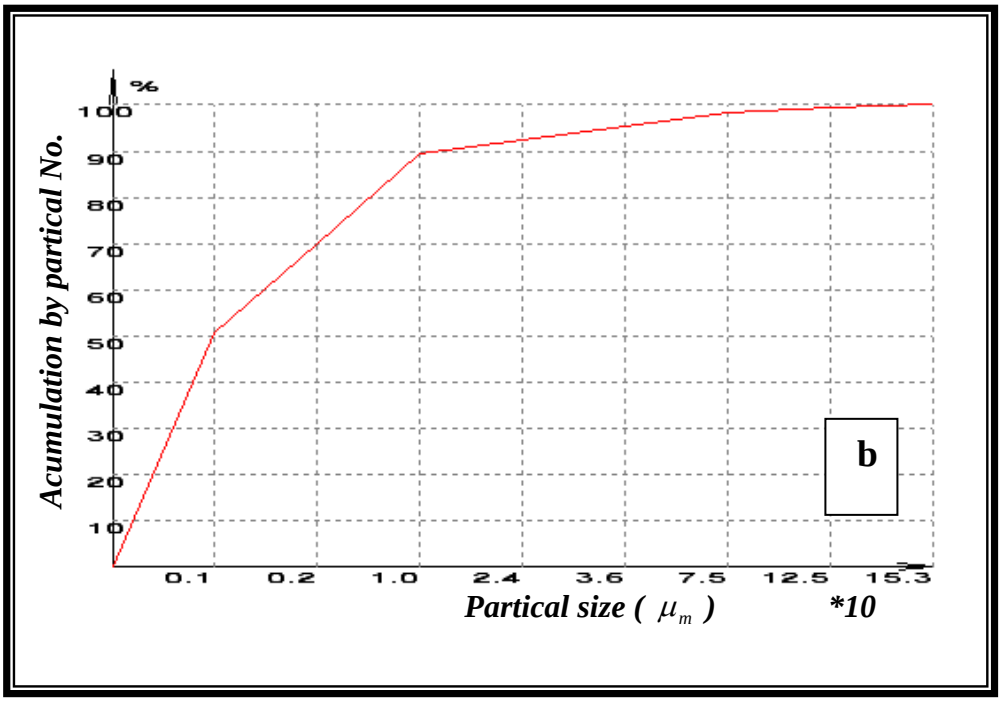

Fig.(6.3) Binary Image and Accumulative size Distribution in (a) and (b) respectively of Cu Powder.

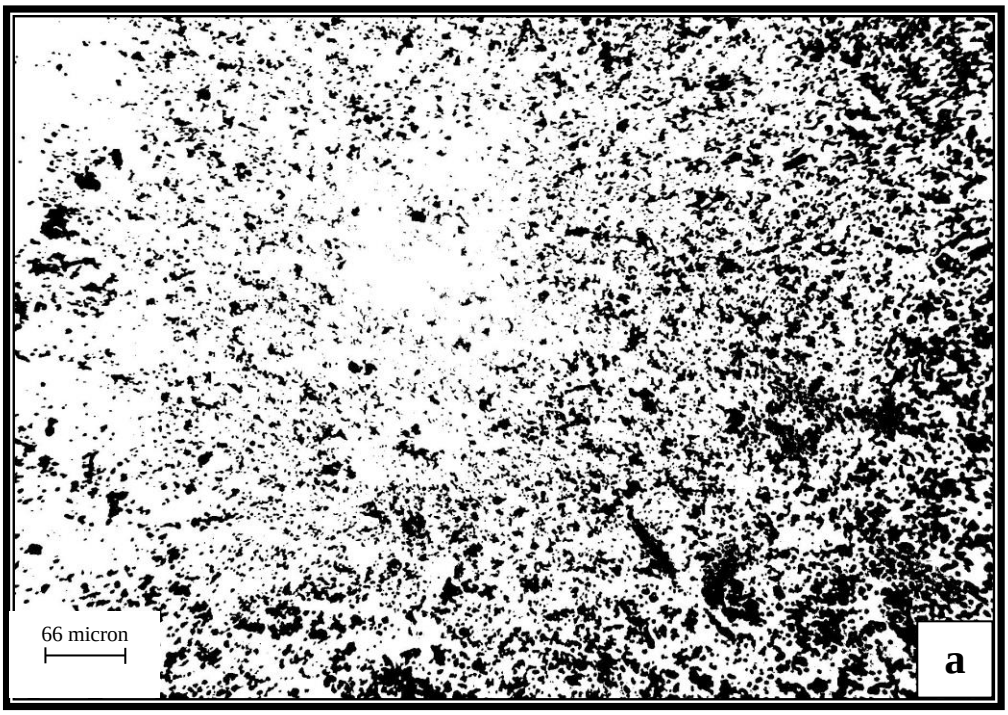

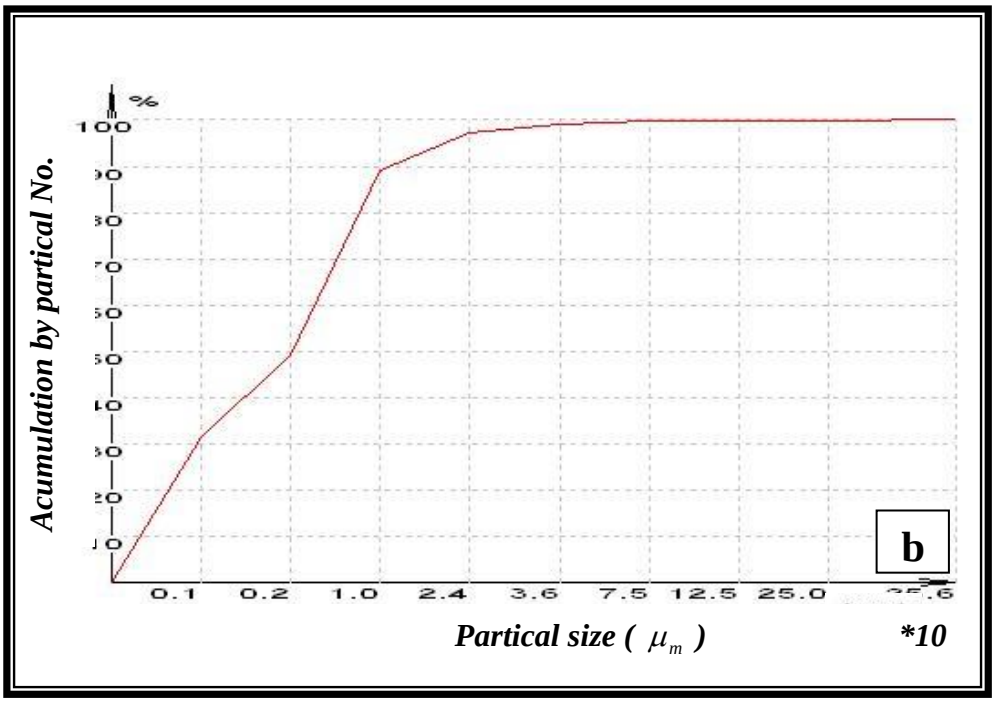

Fig.(6.4) Binary Image and Accumulative size Distribution in (a) and (b) respectively of Al Powder.

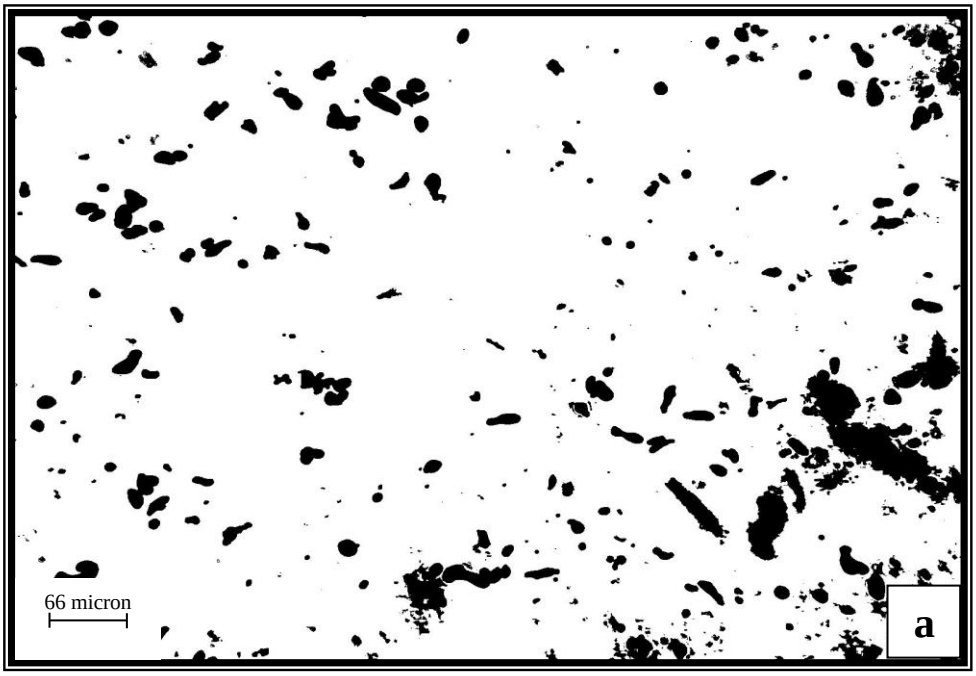

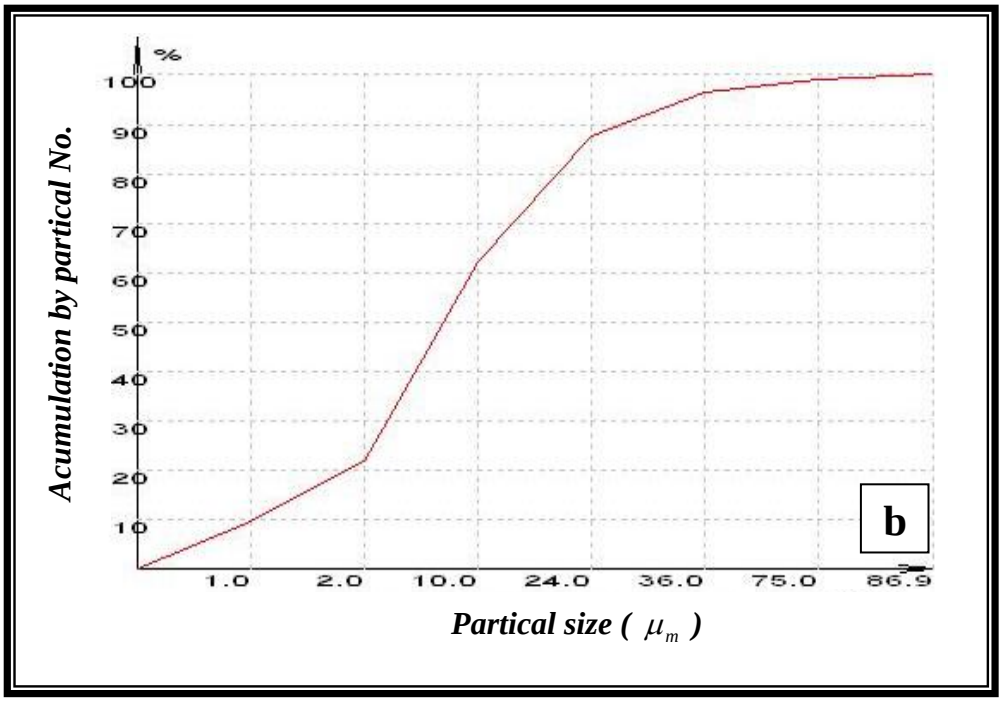

Fig.(6.5) Binary Image and Accumulative size Distribution in (a) and (b) respectively of Ni Powder.

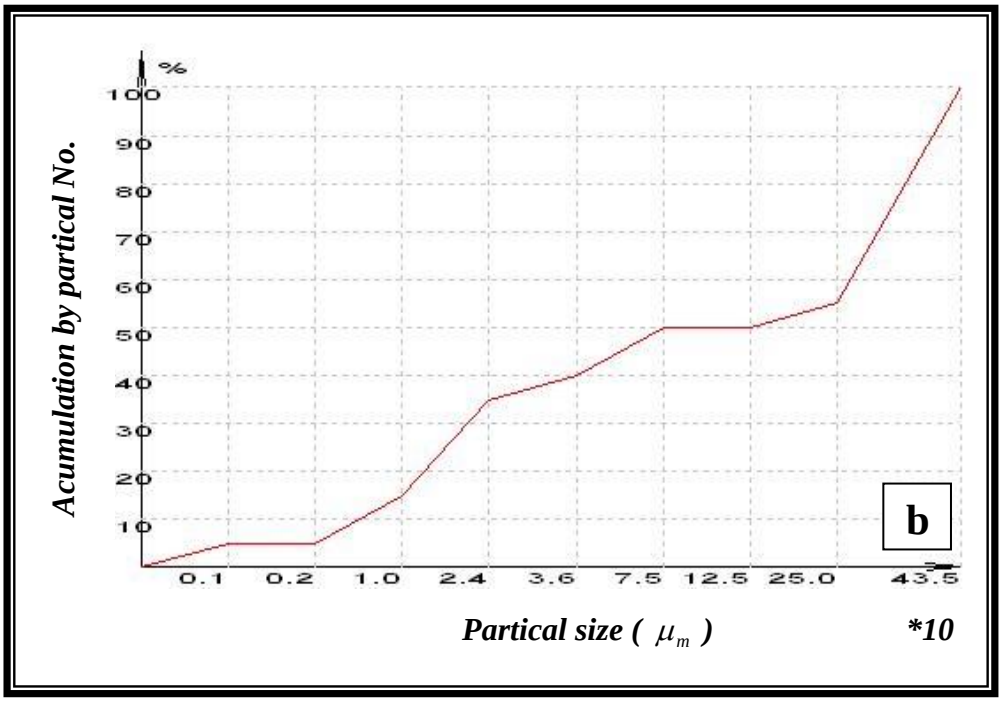

Fig.(6.6) Binary Image and Accumulative size Distribution in (a) and (b) respectively of Ti Powder

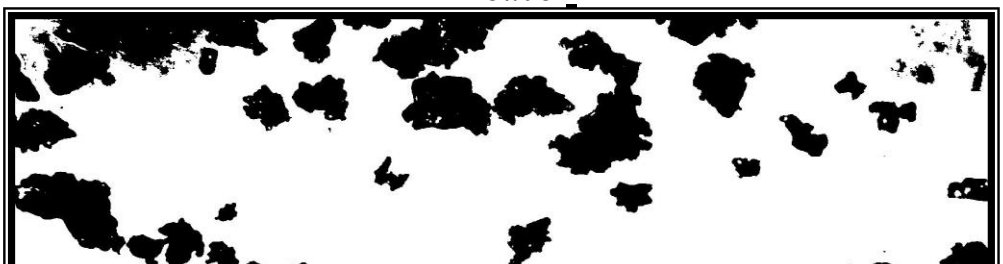

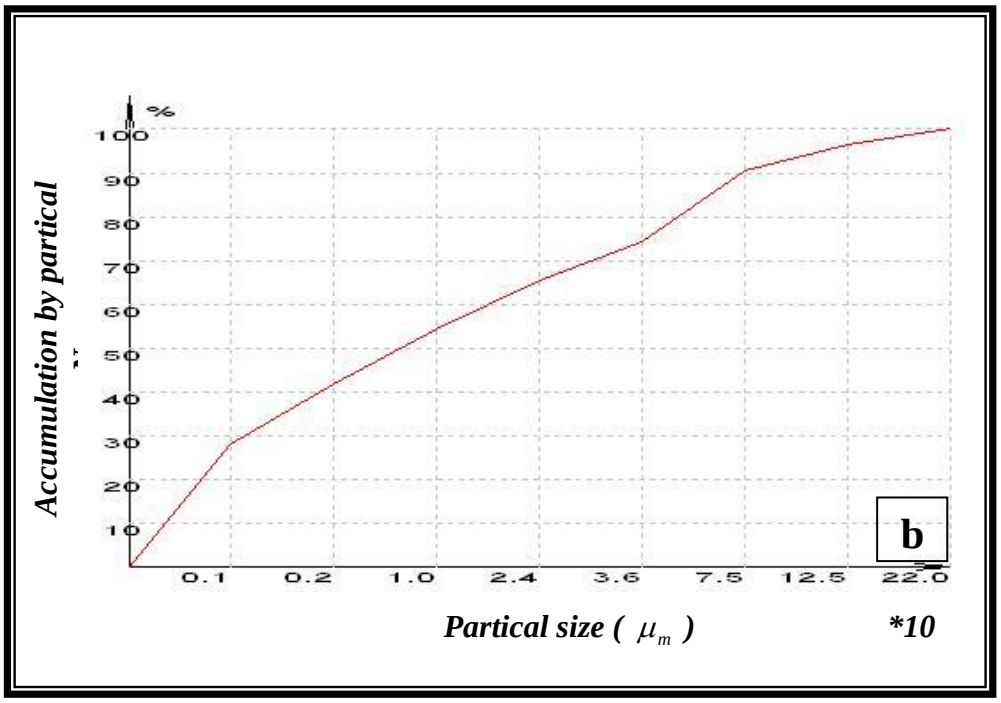

Fig.(6.7) Binary Image and Accumulative size Distribution in (a) and (b) respectively of B Powder

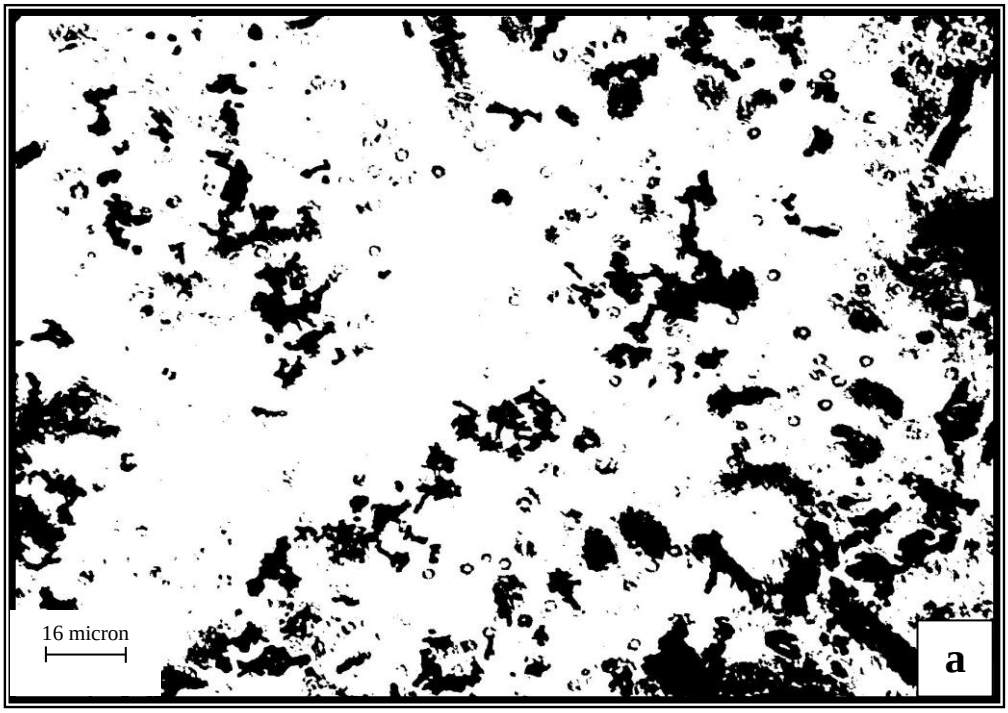

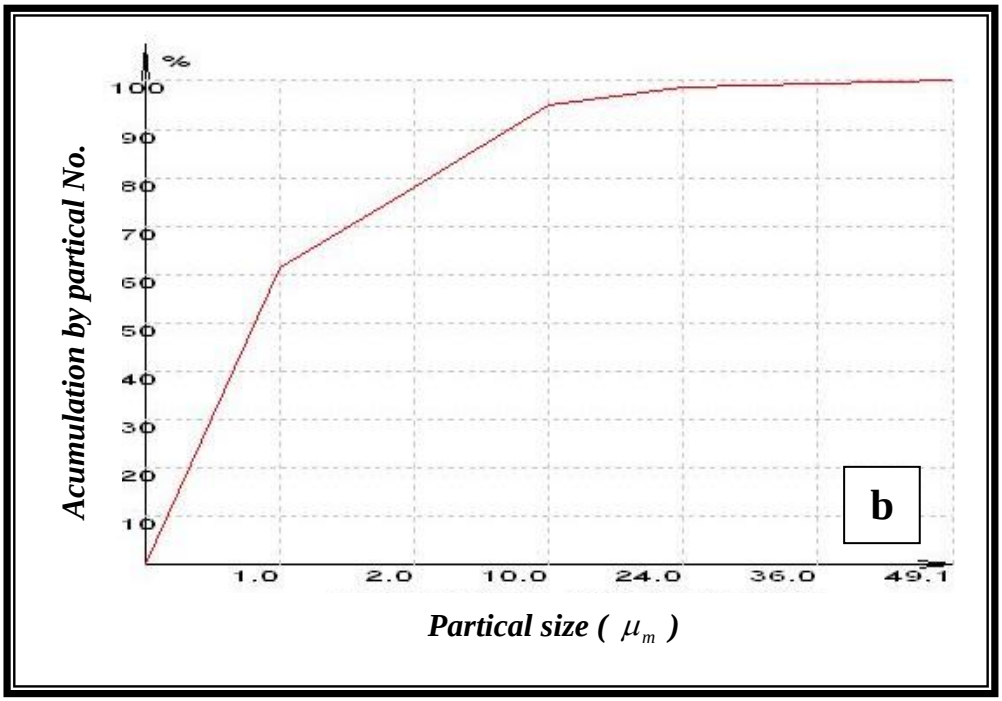

Fig.(6.8) Binary Image and Accumulative size Distribution in (a) and (b) respectively of Co Powder

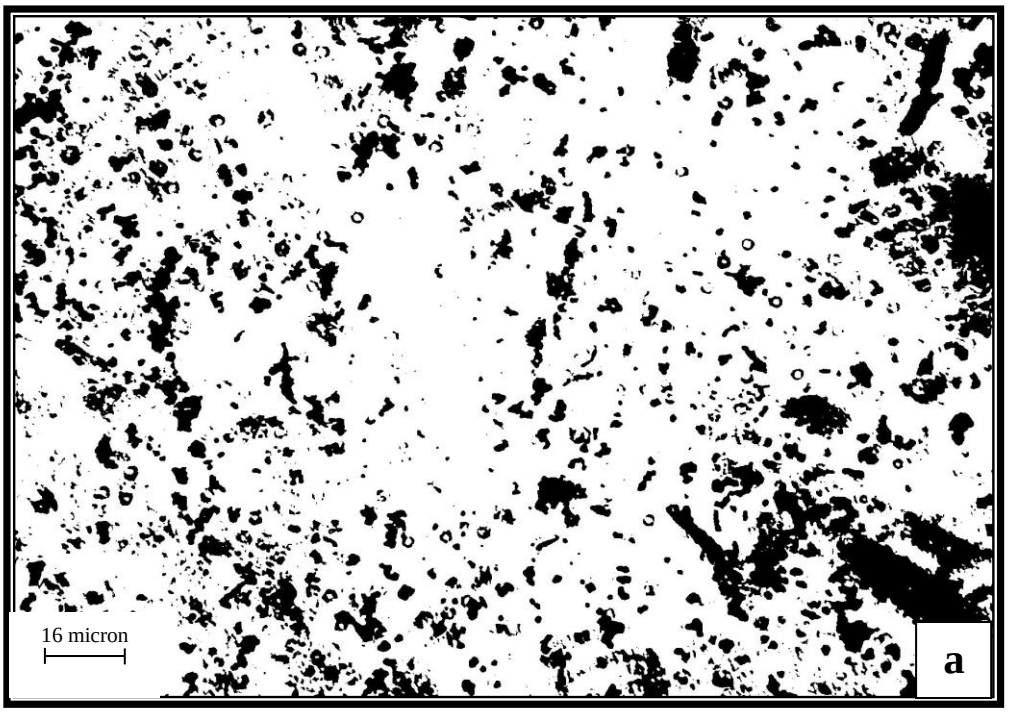

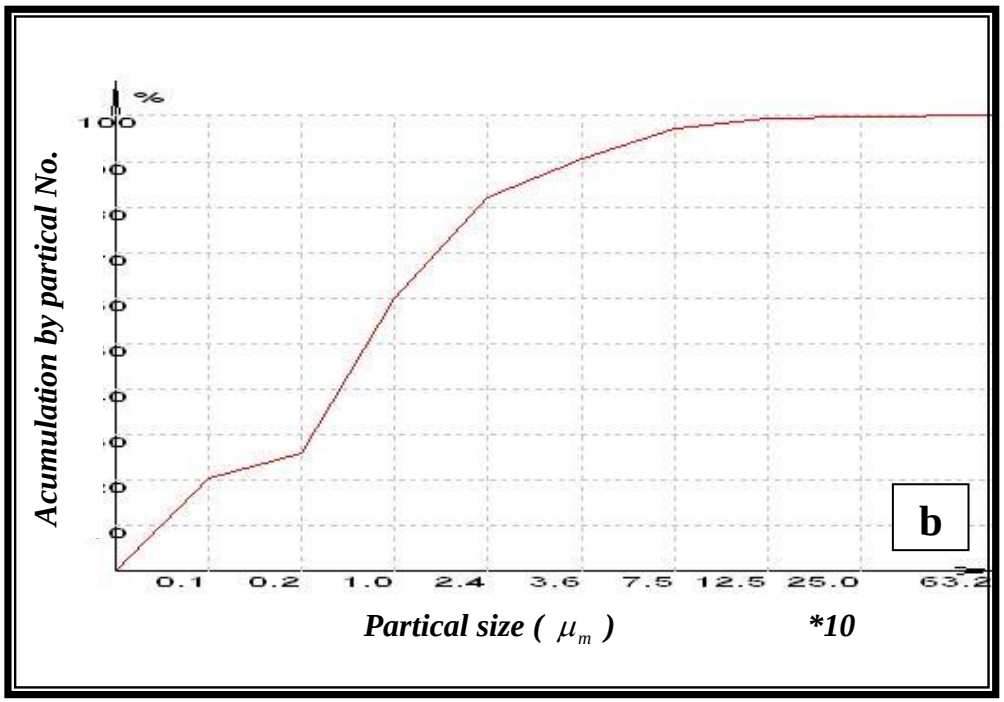

Fig.(6.9) Binary Image and Accumulative size Distribution in (a) and (b) respectively of Zr Powder

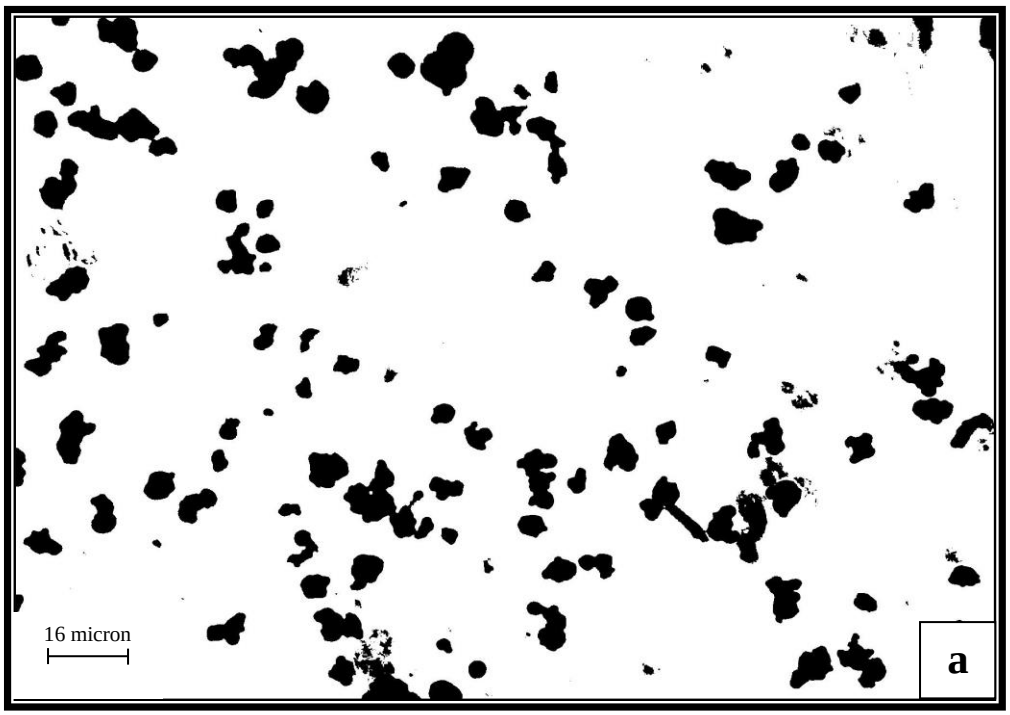

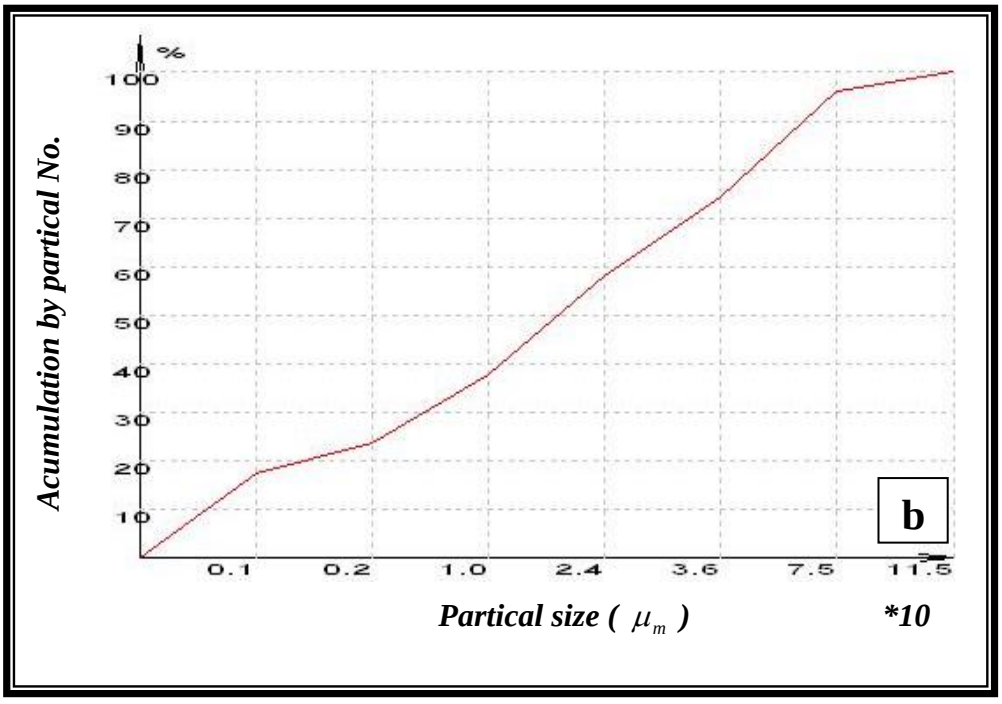

Fig.(6.10) Binary Image and Accumulative size Distribution in (a) and (b) respectively of Fe Powder

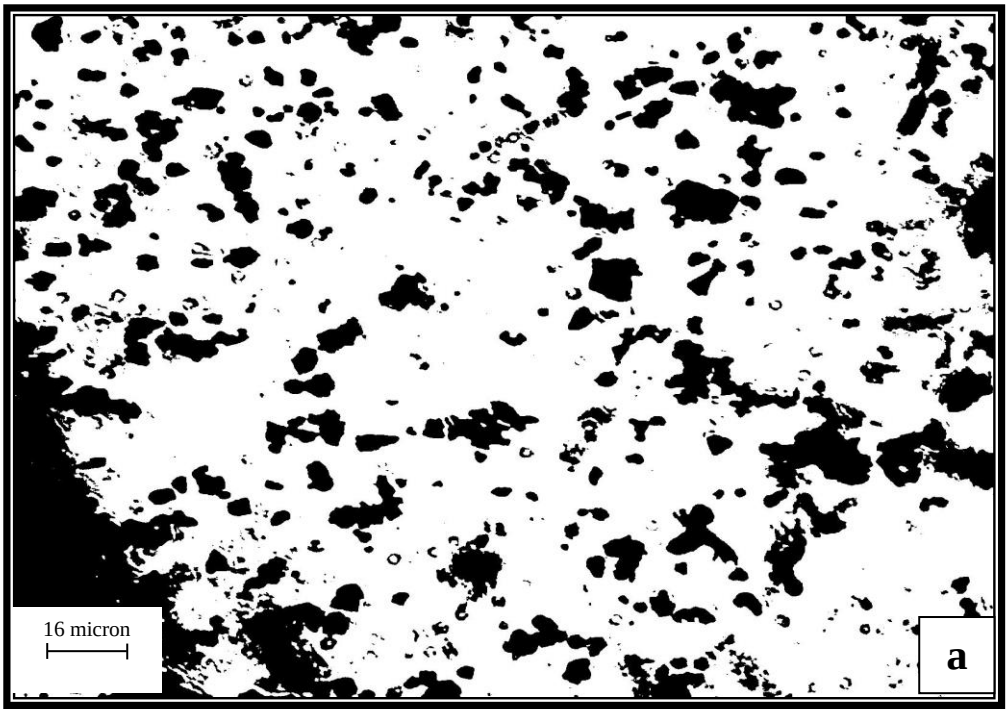

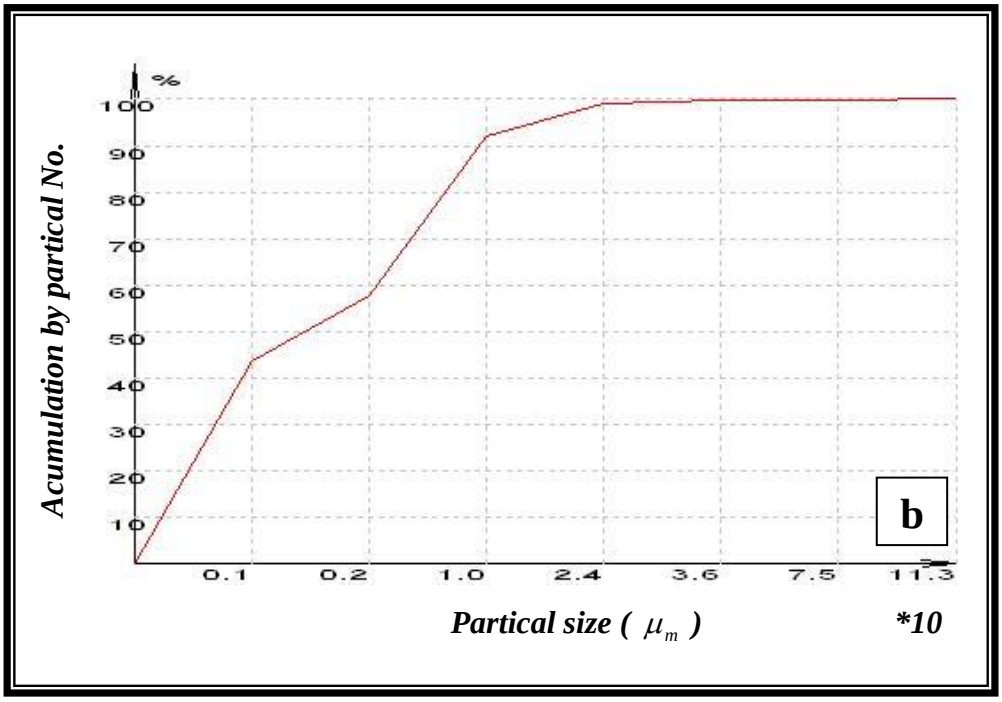

Fig.(6.11) Binary Image and Accumulative size Distribution in (a) and (b) respectively of Mn Powder

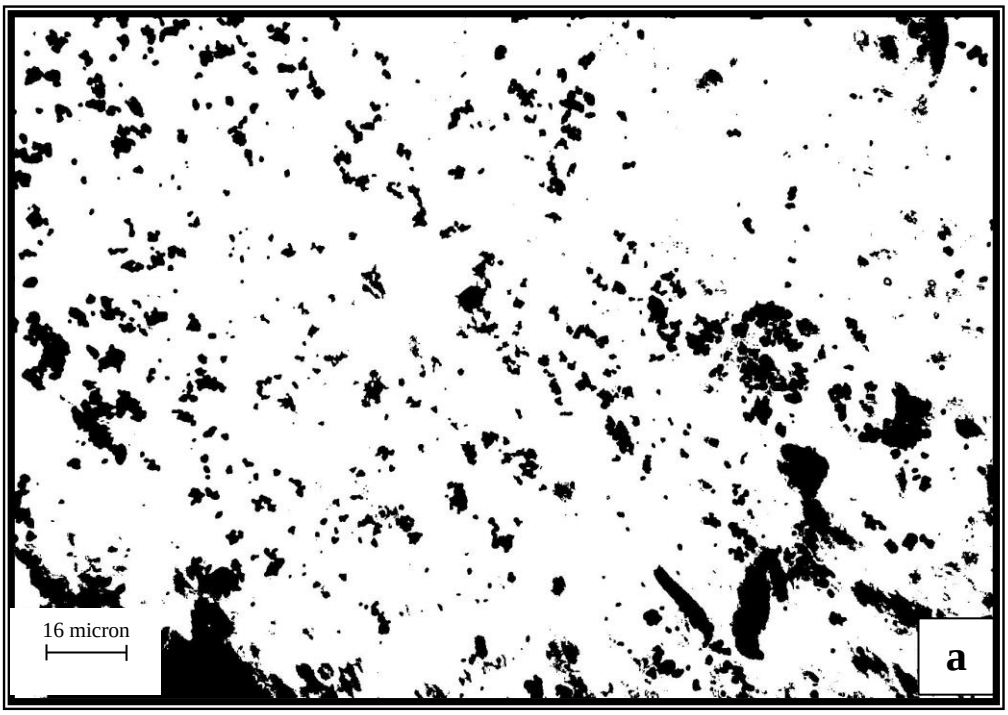

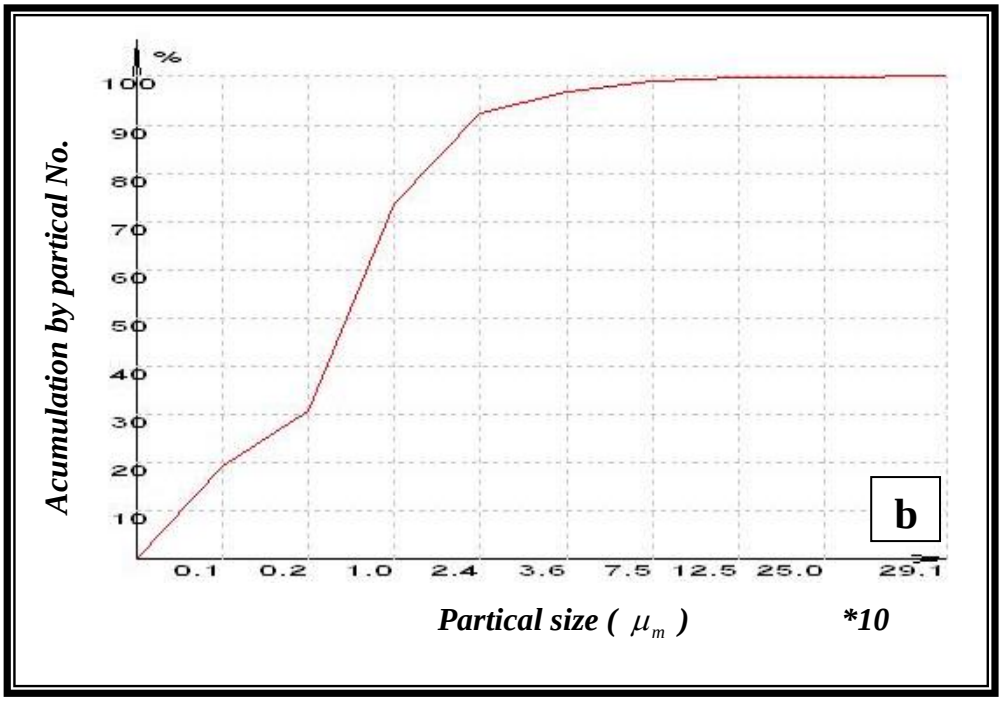

Fig.(6.12) Binary Image and Accumulative size Distribution in (a) and (b) respectively of Si Powder

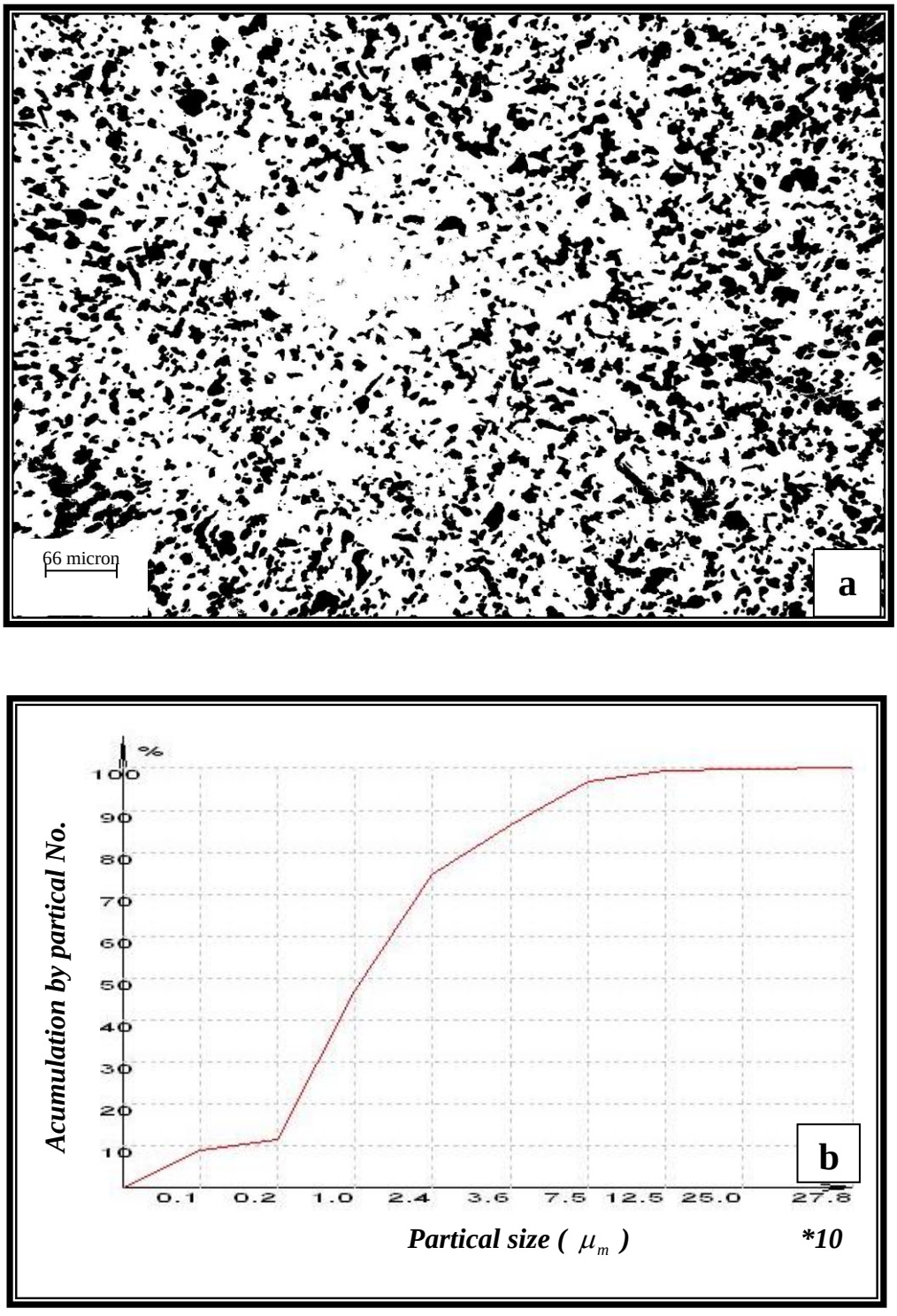

Fig.(6.13) Binary Image and Accumulative size Distribution in (a) and (b) respectively of blended mixture of alloy1 Powder.

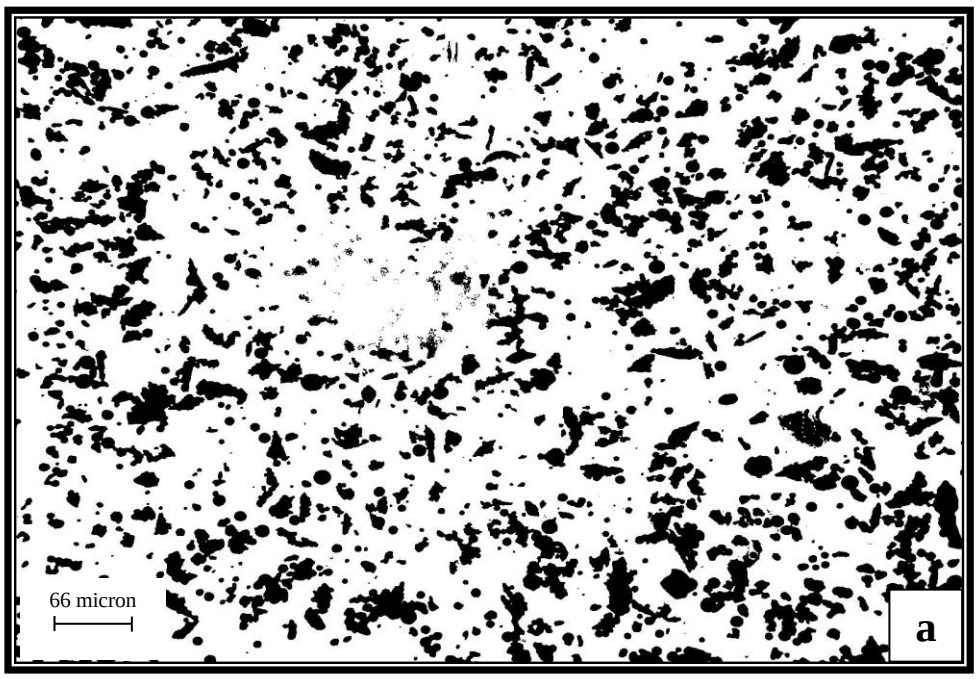

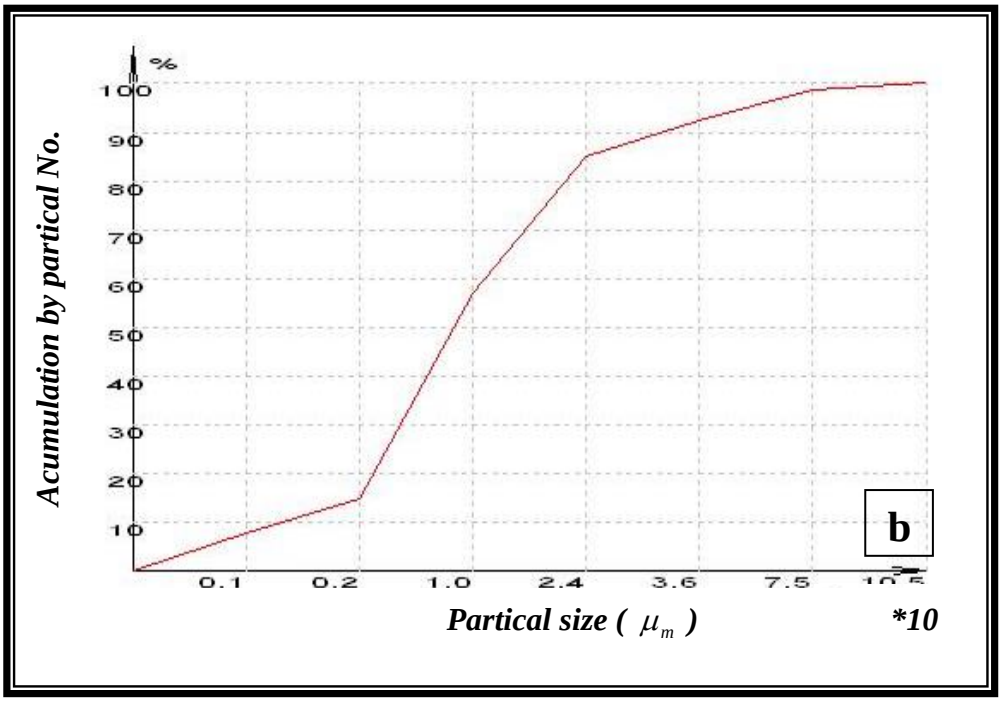

Fig.(6.14) Binary Image and Accumulative size Distribution in (a) and (b) respectively of blended mixture of alloy2 Powder

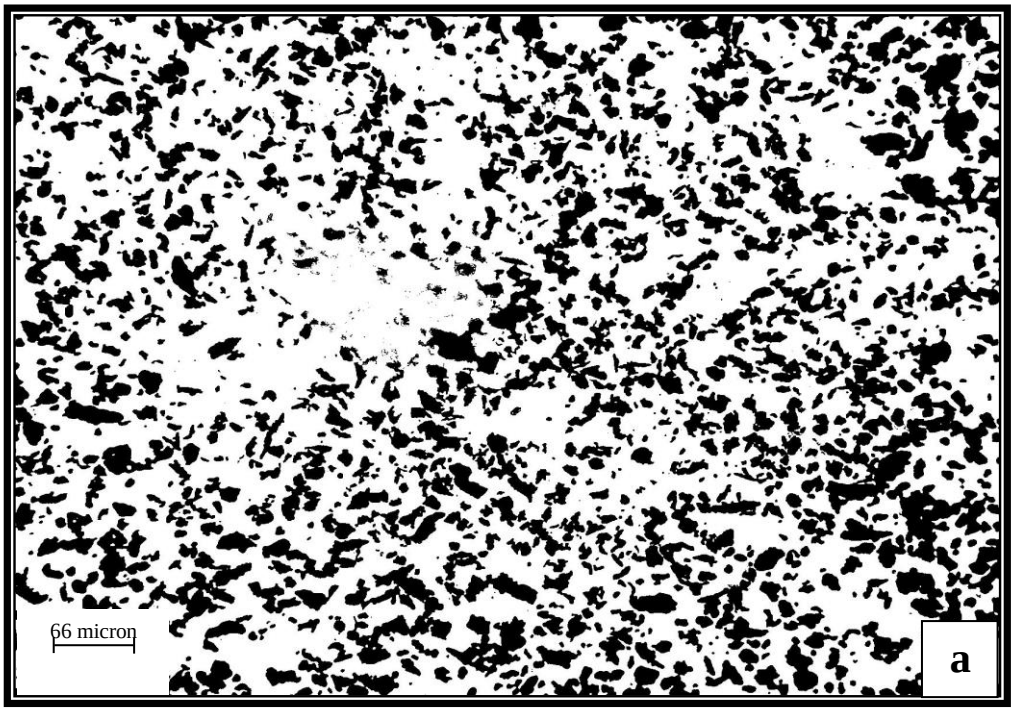

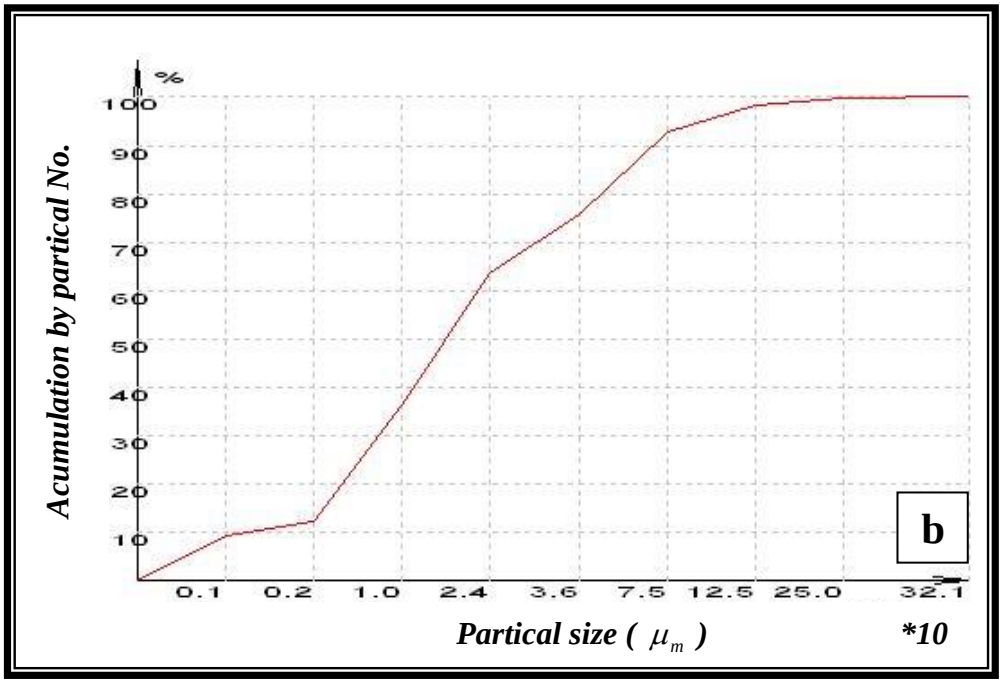

Fig.(6.15) Binary Image and Accumulative size Distribution in (a) and (b) respectively of blended mixture of alloy3 Powder

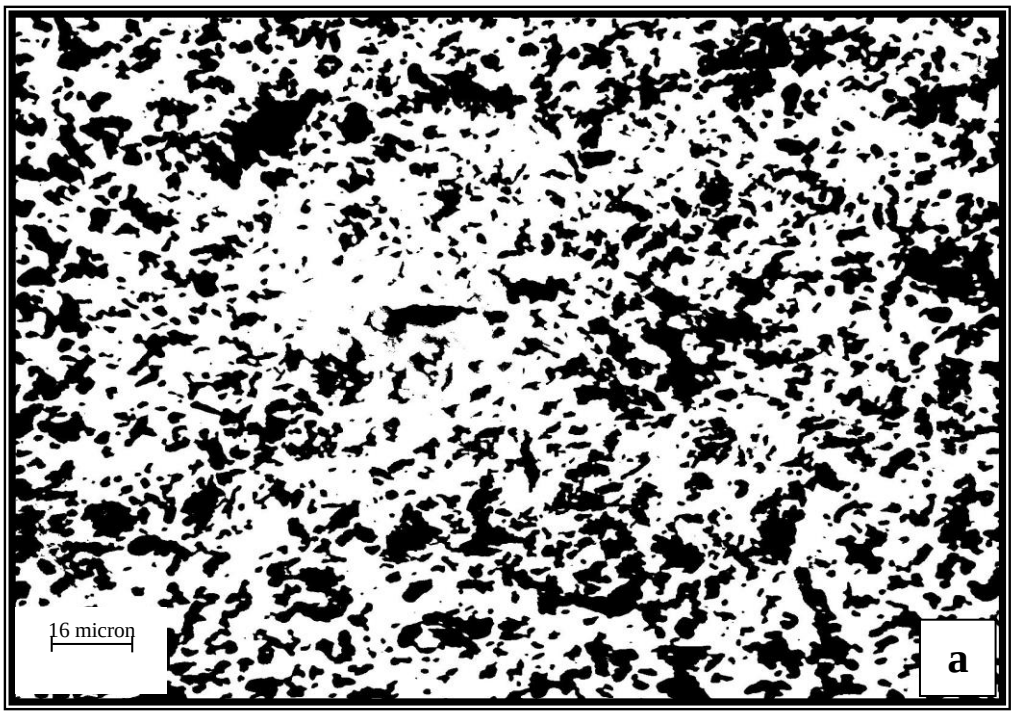

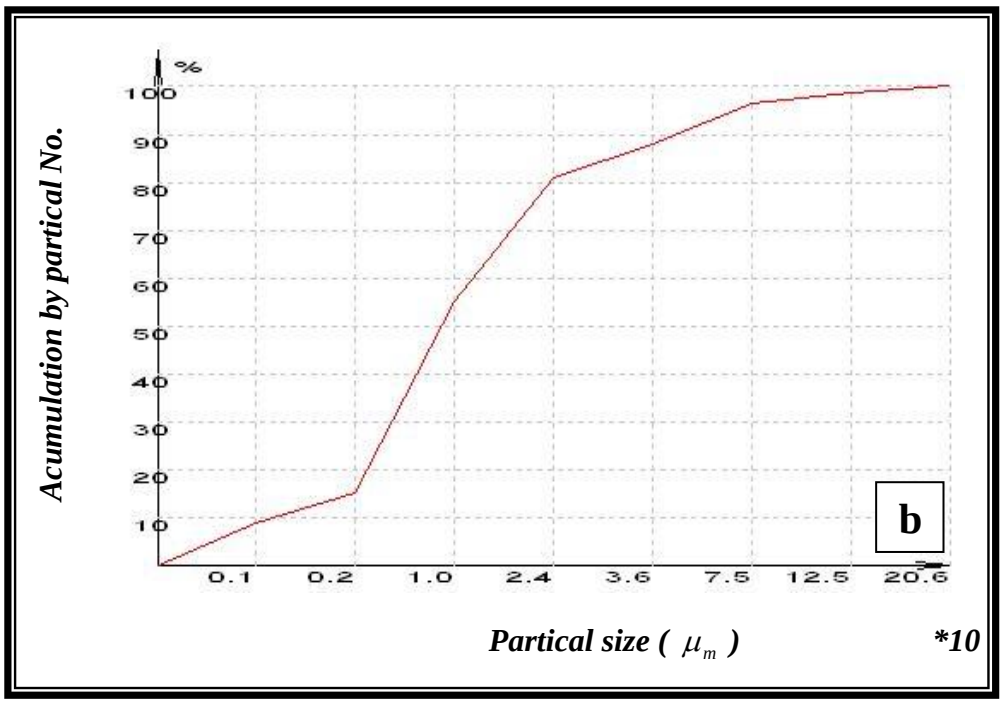

Fig.(6.16) Binary Image and Accumulative size Distribution in (a) and (b) respectively of blended mixture of alloy6 Powder

6.2.3.Green density and green Porosity of compacts :

Green density of alloys 1,2,3 and 6 compacts are shown in Fig.(6.17) .with respect to compacting pressure . For all Compacts , green density increases with increasing pressing stress , from 100 MPa to 950 MPa .As show from Fig.(6.17) , slight increment in green density for all blended compacts are obtained when compacting pressure increases from 800 MPa to 1000 MPa thus , 850 MPa as compacting pressure is based for all next studies of all other parameters such as rate of loading , period of maximum load and all parameters in the sintering process.

In the first stage of compaction , powder particles are rearranged so that bridging that alloys occurs in a randomly arranged stack of loose powder particles is partially eliminated. In the second stage elastic and plastic deformation of the particles have been took place . The amount of plastic deformation depends up on the ductility of the powder material which is here the matrix copper Powder , copper powder has much ductility than the other powders such as Al, Ni , Ti, B, Co , Mn , Si, Fe and Zr. In the light of this statement , when plastic deformation of powder particles has been done , powder Particles are strain hardened.

The third stage of compaction includes fracture of powder particles which have been embrittled through work hardening , under the applied stress increment . The plastic flow stage of densification of powders may be divided in to two substages as deformation in the region surrounding the particles contacts and filling of remaining cavities by local extrusion.

Green porosity which the complimentary of green density , has been shown in Fig.(6.18) for green compacts from alloys number 1, 2, 3 and 6 . With increasing of compacting pressure , the density of the powder mass increases because the total amount of porosity in the mass decreases , however , the pore size and pore distribution will change as well. The uniform compacting stress

applied to the upper punch when a single level cylindrical compact is pressed from one direction as used in this study, is not transmitted uniformly for both direction and magnitude of the stress. throughout the compact. This leads to variation in density in the pressing direction due to the friction between the die wall and the powder. This friction is reduced by using lubricants . In this study, Paraffin lubricant has been applied as a thin coating to the wall of rigid dies. The ratio of the compact to which pressure is applied to the area of contact between the powder and the side walls of the die also affects density. The highest density is found at the top of the outer circumference where wall friction causes maximum relative motion between particles. The density at the circumference decreases rapidly from the top downward with the lowest compact density near the bottom. Density distribution at the centerline of the compact is more uniform due to minimum influence of friction between die wall and powder.

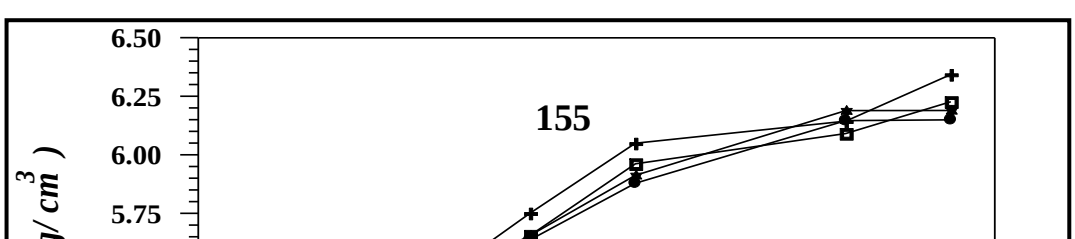

6.2.3.1. Effect of rate of loading

To explain effect of rate of loading on the green density of compacts , three rates (0.2 ,6 and 10 ton/ min) have been studied. Figure (6.19) shows effect of loading rate on the green density of blended mixtures of alloys 1,2,3 and 6. It has been shown that increasing rate of loading leads to decrease green density for all blended powders . when the rate is slow (0.2 ton/ min) , there is a period that the powder particles move and slide together so many pores are filled with small particle size. In addition , most gases are remove from the compact under action of stress because there is enough time to escape gases. Furthermore ,any motion of powder particles requires increasing applied stress and period of time as well like the diffusion process which depends upon time , temperature and activation energy which is a function of stress.

6.2.3.2 Effect of period of maximum load.

when pressing stress is applied to metal powders, behavior is not similar to solid material. The maximum compacting (850 MPa) is applied to powder particles in the metal die at the first moment but this amount of pressure is decreased gradually through the period of time . Thus, powder particles in die have smaller compressive stress than at first moment . In the light of this statement, there is a relaxation time that the elastic deformation of powder particles will be returned and this deformation will not grow to give additional plastic deformation so the green density of compacts decreases with more time of loading as shown in Fig. (6.20) for all alloys.

Powdered compacts have spring-back behavior therefore their mechanical stress- strain curves do not obey traditional elasto-plastic metallic behavior It is like soil behavior thus , Drucker-Prager model may be used to analyze mechanical behavior of powders in the dies during compaction process.

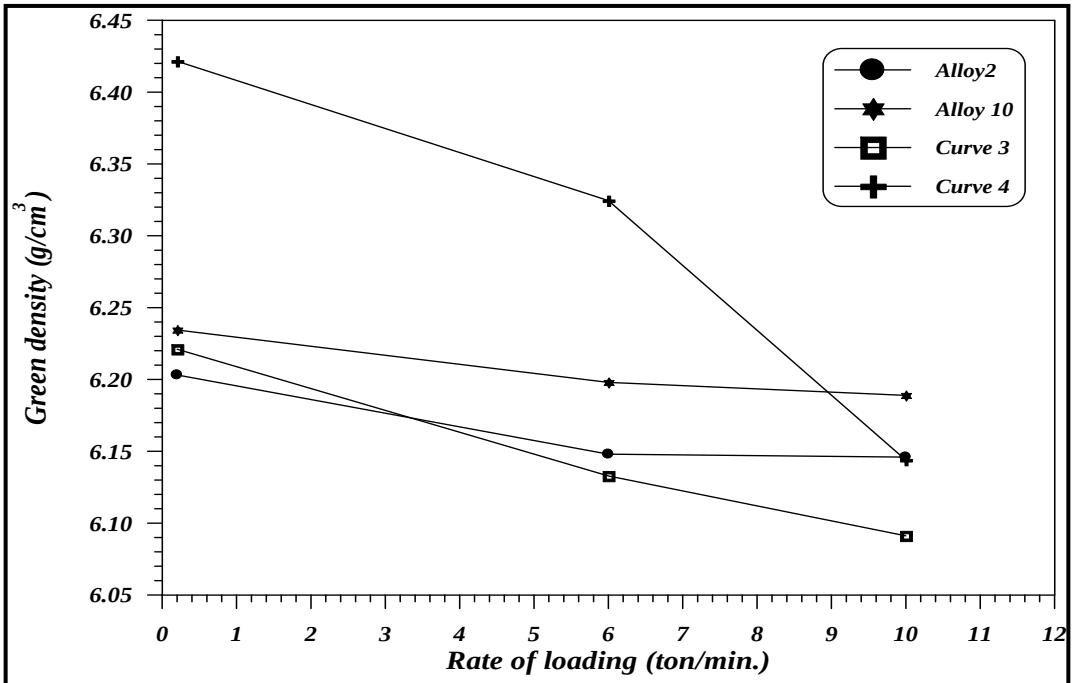

Fig.(6.19) Green density of compacts as a function of rate of loading at 850 Mpa compacting pressure and 1 min. as period of load.

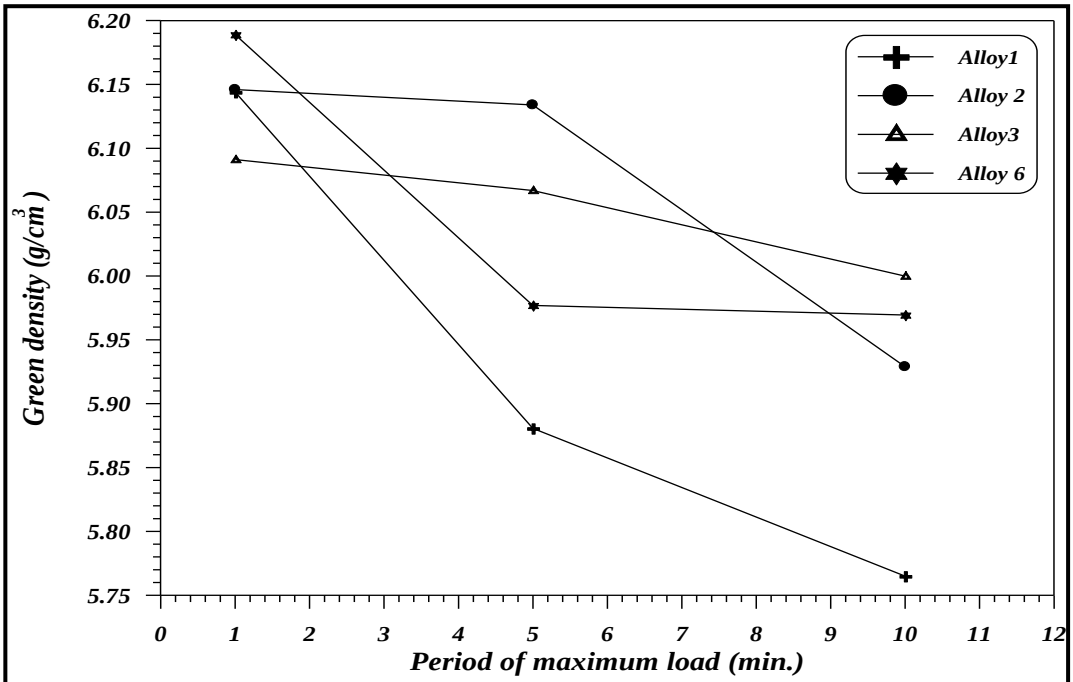

Fig(6.20) Green density as a function of period of maximum load at rate 3 and 850 Mpa compacting pressure.

6.2.4. x-ray diffraction pattern of compacts:

X-ray diffraction analysis of powdered compacts form alloy 1,2,3 and 6 has been studied in order to identify metal powders used in this study and to satisfy two stages of sintering later. In order not to repeat figures and to comparison with sintering samples x-ray diffraction pattern of compacts have been discussed later with sintering results.

6.2.5. Microstructure of compacts and pore size and its size distribution.

Microstructures of unetched samples from alloy compacts 1,2,3 and 6, have been taken using light optical microscope and digital camera. 0.2 ton/ min and one minute as period of maximum loading which is 850 MPa are based. Pore size at 50% point in the accumulative plot is calculated and shown in Fig.(6.21). It has been shown that grinding with 1200 grit silicon carbide paper may be closed then open pores in the surface which is affected on the microstructure and next affected on the accuracy of pore size and pore size distribution analysis. In the pore size distribution analysis using digital image analysis technique , best fit circle has used to represent the pores.

6.3 Result after sintering of compacts.

X- ray diffraction patterns for alloy 1,2,3 and 6 for both stage I and stage II sintering have been studied. In addition physical tests include apparent density, apparent porosity , water absorption and true porosity for different temperatures of sintering and different time of sintering have also been explained. At a first , It must be satisfied that all powdered compacts transform to alloys, so , we begin discussion about x-ray diffraction patterns as follows:

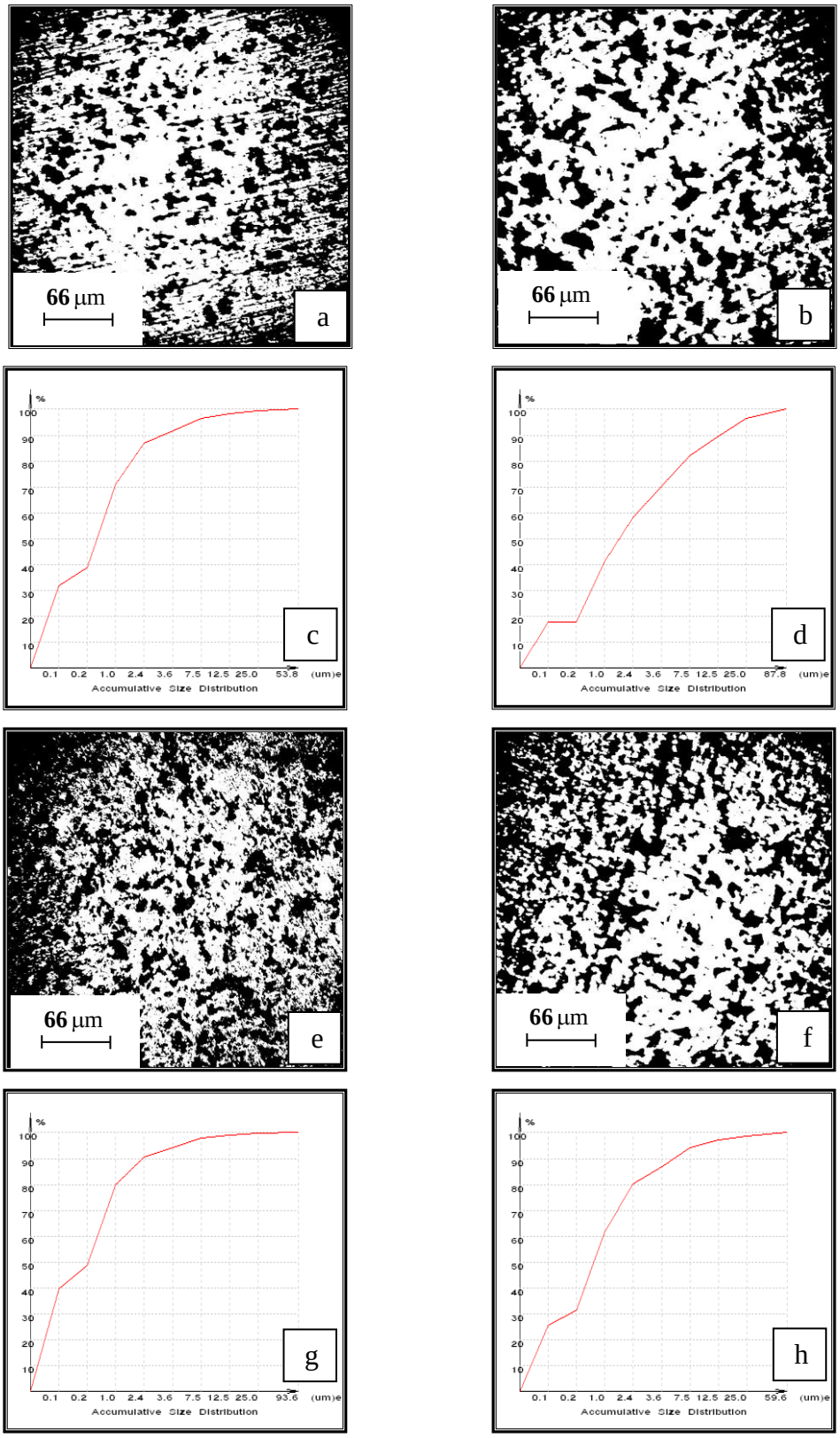

Fig.(6.21) LOM binary images and pore distribution for compact:

a. alloy1 b. alloy2 e. alloy 3 f.alloy 6 for images.

c. alloy1 d.alloy2 g.alloy 3 h.alloy 6 for accumulative distribution .

6.3.1. x-ray diffraction analysis.

x-ray diffraction patterns for compacts 1,2,3 and 6 and for these sample after 3 hours at 600 ^{o}C stage one sintering and after 3 hours at 850 ^{o}C stage two sintering are shown in Fig. (6.22) ,Fig. (6.23), Fig.(6.24) and Fig.(6.25) respectively .

From Fig. (6.22) , It has been shown that most elemental powders (Cu, Al and Ni) form the intermetallic compound γ_2 (Cu_9Al_4) according to Cu-Al phase diagram. The phase (Al_4Cu_9) is the same phase formula (Cu_9Al_4) but is different by density and interatomic space parameter as can be seen from x-ray diffraction card in Appendix A. for (Cu_9Al_4) intermetallic compound the unitcell is cubic with a=b=c= 8.7027 ^{o}A whereas cubic unit cell of (Al_4Cu_9) compounds has a=b=c= 8.704 ^{o}A. This is for the first stage of sintering (600 ^{o}C for 3 hours soacking time) whereas all elemental powders which remained in the first stage of sintering, form the intermetallic compound γ_2. Of course, in this system there are α phase with nickel dissolves in the unit cell of Cu+Al and γ_2 phase . It has been shown that sintering of alloy one in the final stage for three hours is enough to get microstructure with solid solution alloy (α) and with intermetallic compound γ_2 which precipitates on the grain boundaries of α phase.

In the Fig.(6.23) , standard peeks of x-ray diffraction pattern for copper, Aluminum and Nickel are obtained for compact 2. These peeks tend to remove partially in the first stage of sintering. whereas completely new peeks are formed in the second stage of sintering which refers to success of sintering process.Due to the composition of alloy 2 which is hypereutectoid , the phase are α solid solution and γ_2 intermetallic compound. there is enough time to get (Al_4Cu_9) compound with bigger unit cell dimensions than (Cu_9Al_4) Compound.

The intermetallic compound from titanium aluminum copper $(Cu,Al)_2Ti$ is formed in alloy 3 system. In addition , complete formation of $(Cu,Al)_2Ti$ Compound from compact3 has been satisfied in the second stage of sintering. The small additives from titanium (0.4 Ti) to the base alloy 2 in not clear in the x-ray diffraction pattern of compact whereas the effect of titanium is clear in the alloy formation by forming the completely $(Cu,Al)_2Ti$ compound as can be seen from Fig.(6.24).

From Fig.(6.25), it has been shown that all element powders form combination between two phases which are intermetallic compounds (Al_4Cu_9) and (Cu_9Al_4) which are the same phases except the length of cubic unit cell and furetherly, theoretical density. Boron addition affects on the positions of pecks and their intensities compared with the base alloy 2. As can be seen from Fig.(6.25) , addition of Boron deos not lead to form boron compounds with copper or another constituent such as aluminum and /or nickel , in this amount of addition. This is probably due to not enough amount of boron addition which led to week affinity to form intermetallic compound.

X-ray diffraction technique may be used for the rapid determination of the degree of homogeneity. The progress of homogenization is seen clearly although qualitatively in Figs. (6.22) , (6.23) , (6.24) and Fig.(6.25). The copper (111) peak occurs at diffraction angle $2\theta = 43.0$ and the aluminum (111) peak at a diffraction angle $2\theta = 38.0$ as can be seen in Fig.(6.23a) for example . In Fig.(6.23 b). , it has been shown that the initial stages of homogenization (low temperature (600 ^oC) first stage of sintering) proceed by forming the complete range of compositions from copper and aluminum. This is the manifestation of the intial interdiffusion across the copper- aluminum interparticle boundaries. As shown in Fig. (6.23) C, later stage of homogenization (high temperature 850 ^oC

for three hours second stage of sintering) result in the formation 100% intensity of Al_4Cu_9 internetallic compound. Intermetallic compound (Al_4Cu_9) formation occurs at a diffraction angle between those of pure copper and pure aluminum. from Fig. (6.23) , it is shown that diffraction angle of 100% intensity of the product (Al_4Cu_9) is 42.2 deg. Which lies between 43 for copper and 38.0 for Aluminum pure metal respectively.

The characteristic of the powder particles either copper powder or aluminum powder that compose the mixture exert a significant effect on homogenization kinetics. The sizes of the particles in the mixture establish the distance over which interdiffusion must occur to achieve homogeneity. [Lenel et al , 1984] . In alloy mixtures where the elemental solvent particles from a continuous matrix around the dispersed solute – rich particles ,particle size of the dispersed particles become the important parameter in establishing the interdiffusion distance.

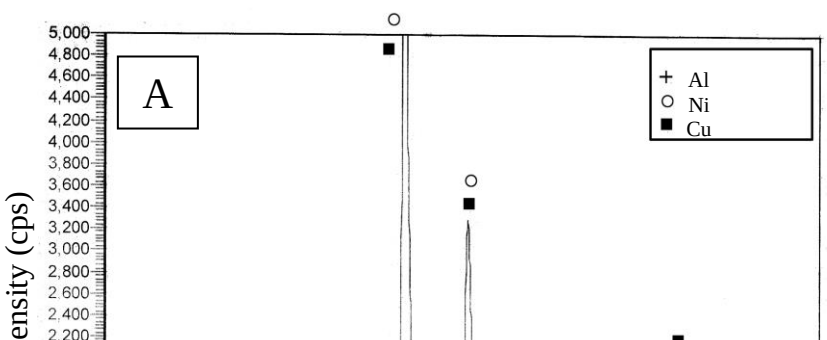

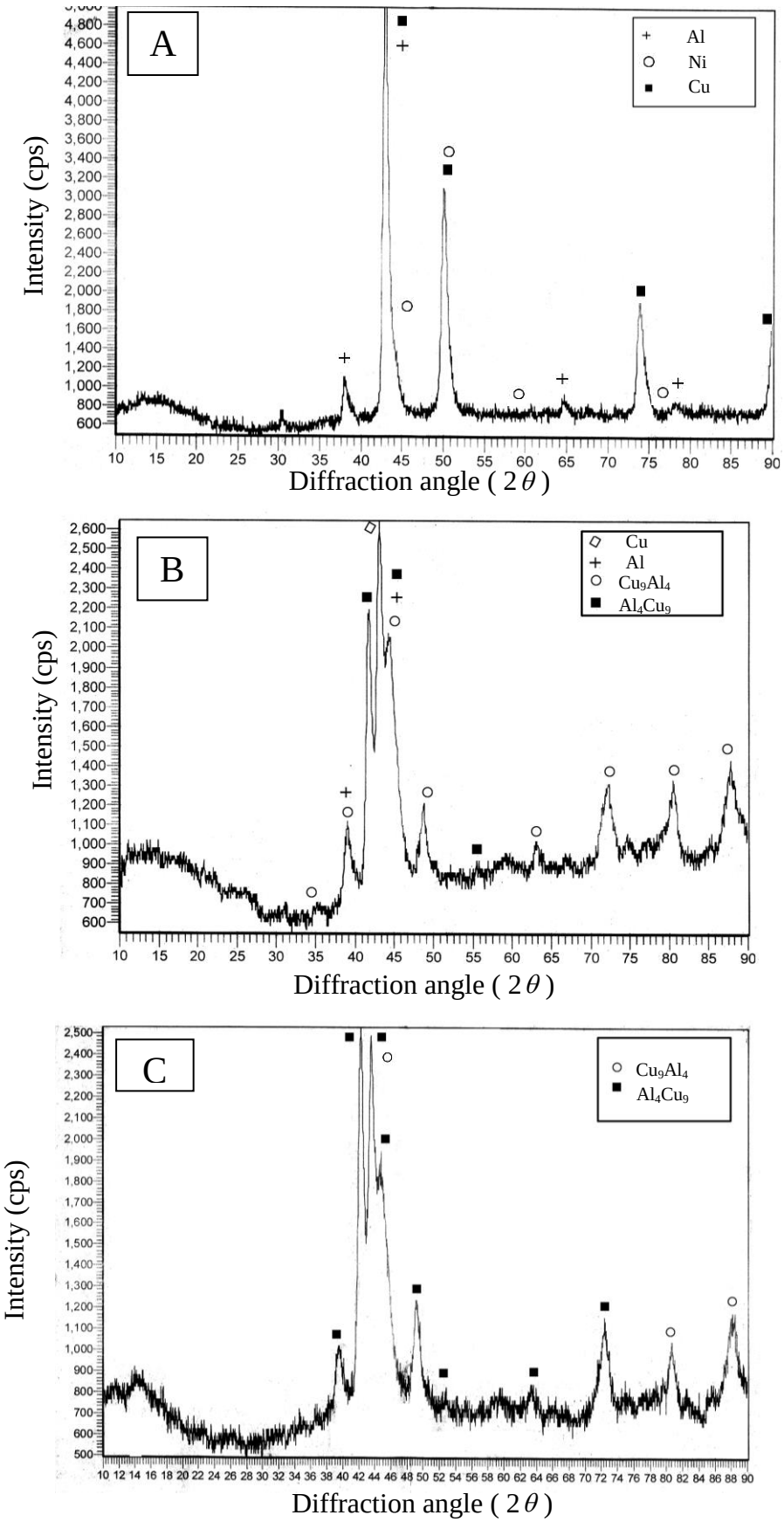

Fig.(6.23) XRD patterns for alloy 2 for :a. Compact . b. stage I sintering c.stage II sintering

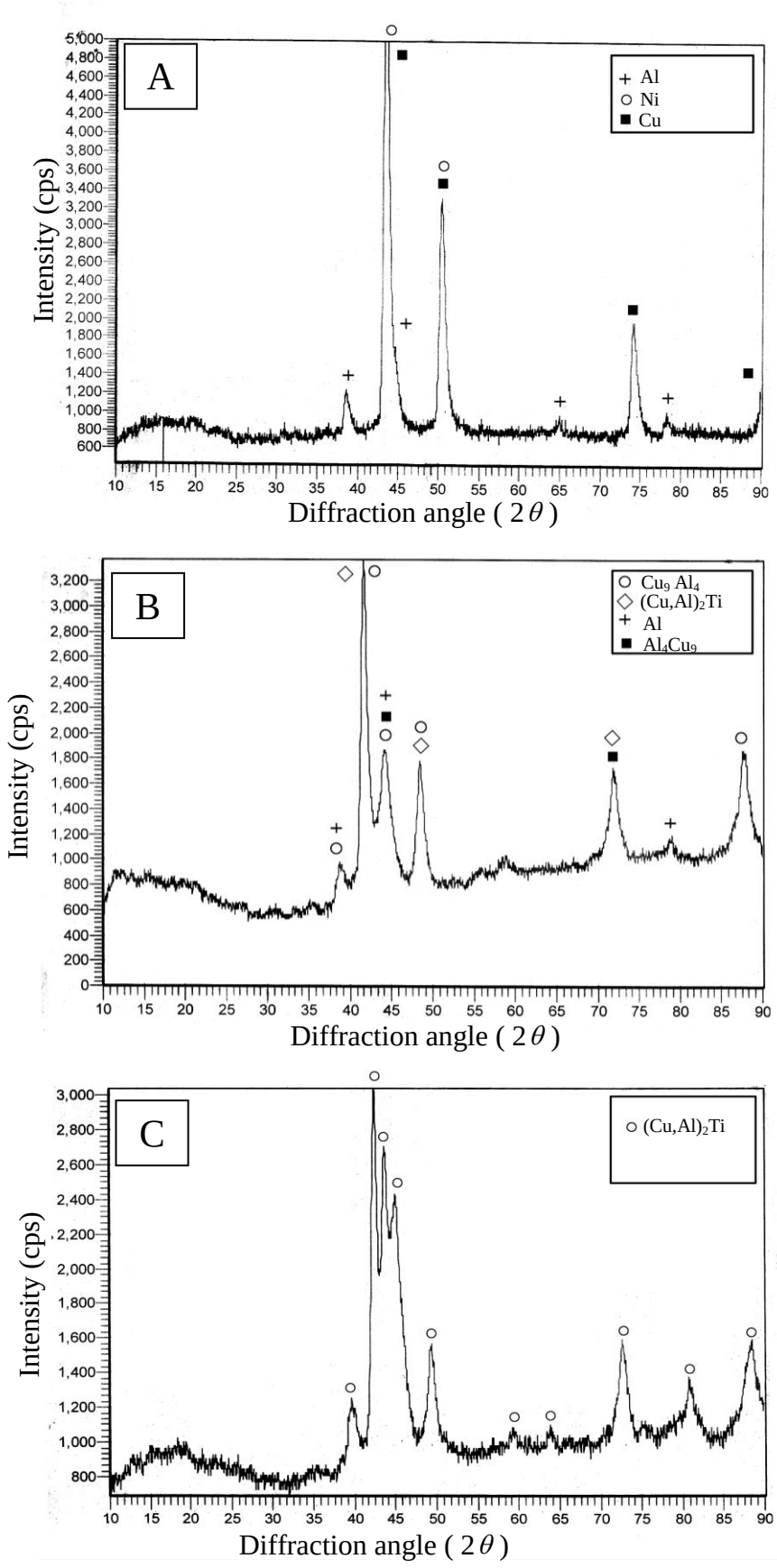

Fig.(6.24) XRD patterns for alloy 3 for :a. Compact . b. stage I sintering c.stage II sintering

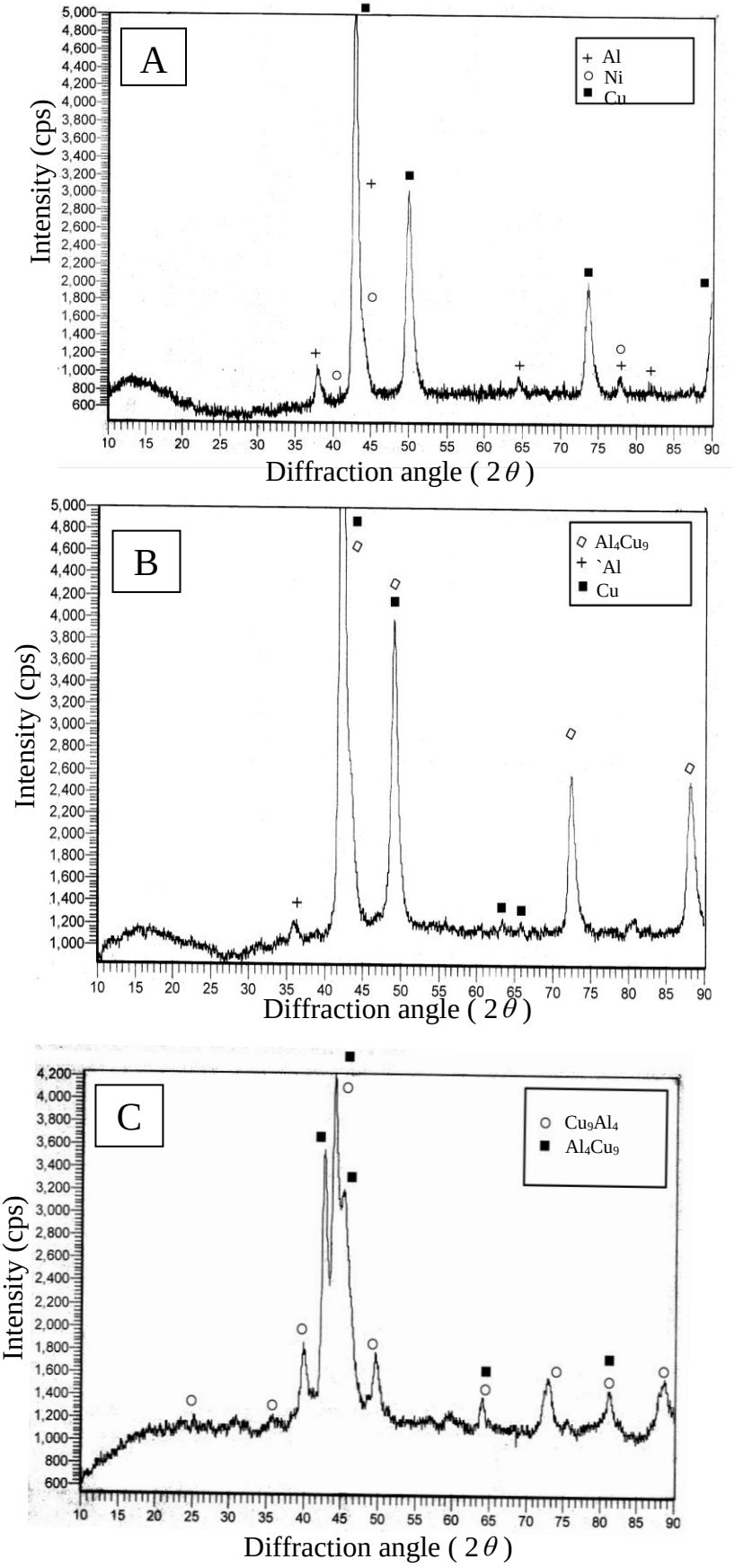

Fig.(6.25) XRD patterns for alloy 6 for :a. Compact . b. stage I sintering c.stage II sintering

6.3.2 physical test Results :

Several physical properties included apparent density , apparent porosity , water absorption , true porosity and expansion have been studied with respect to several parameter such as compacting pressure , time of sintering , temperature of sintering and rate of loading .These results are discussed and presented in the following :

6.3.2.1 Apparent density of sintered Compacts :

Apparent density of sintered compacts at 600^{c}c for three hours and at 850 ^{o}C for 10 minutes in addition , for alloy 1,2 ,3 and 6 is shown in Fig.(6.26) and Fig .(6.27) with respect to pressure of Compaction. the apparent density of alloys 1,2,3 and 6 in creases with increasing compacting pressure due to increase contacts regions in higher pressure which are the region of densification of compact under sintering . After 650 MPa Compacting pressure , slow increment in apparent density has been occurred Therefore , Compacts under sintering have traditional little pores and with high green density at higher Compacting pressure than that at lower Compacting pressure which lead to in crease apparent density at the final .It has been shown that sintered compacts have 72.3% from the theoretical density of Al_4Cu_9 compound (6.848 g/ cm^3) which measured from x-ray diffraction pattern for alloy 1,2,3 and 6 , at 950 M Pa compacting pressure . This ratio of density (apparent density relative to theoretical density) is not enough due to low time of sintering (10 min.) .The effect of time of sintering and sintering temperature have been explained later .It must be known that theoretical density of sintered compact is not calculated from elemental powders by summation of weight percent of constituents of compacts after sintering new material has been obtained and can not be compared with green elemental powders. So , theoretical density may be calculated from the equation :

$$\text{Theoretical density} = \frac{\text{No. of atoms per unit cell} \times \text{molecular weight}}{\text{Volume of unit cell} \times \text{Avogadro No.}} \qquad \text{Eq.(6.1)}$$

on the other hand , the effect of time of sintering on the apparent density of sintered compact has been shown in Fig.(6.28) and Fig.(6.29) for alloys 1,2,3 and 6. It has been shown that apparent density increases with increasing sintering time due to increase diffusion through the sintering process which leads to decrease porosity of sintered compacts .It is shown , density ratio between 80 -84% from the theoretical density , has been obtained alloy 1 and alloy 2 are more sensitive than alloys 3 and 6 for time of sintering because there is no fourth element additives (Ti or B) as in alloy 3 and 6 respectively These alloying elements need to more time and more temperature to diffuse in the matrix of alloy Some times , Compact swelling has been occurred .compact swelling is attributed to the diffusion of the primary or transient Al-metal into copper which is not transformed in the first stage sintering process (600 ^{o}C for 3 hours).

The effect of rate of loading of compacting pressure on the final apparent density of sintered compact has been shown in Fig.(6.30) and Fig .(6.31) .It is shown that apparent density is decreased loading because green density is decreased with increasing rate of with increasing rate of loading in beginning ,At low rate of loading , Compacts enter the sentencing process with low pores and with high initial green density so that all the activation thermal energy during sintering is went to density the compact through the diffusion of solute a tomes in the solvent a toms to form an alloys . whereas Compacts with high pores (low green density) heed more activation thermal energy either time or temperature in order to density through reduce the pores .

Apparent density as a function of temperature of sintering has been shown in Fig.(6.32) and Fig.(6.33) for alloy 2,6 and 1.3 respectively .

It is shown that apparent density increases from 850 ^{o}C to 900 ^{o}C for to min . as time of sintering . The highest point of apparent density is at 900 ^{o}C and after , this apparent density dropped in to lower amount at 950 ^{o}C . Variation in

sintered density with sintering temperature during homogenizations is frequently quite different compared to the variation that exists if compacts are composed of particles of identical composition . This is due to two phenomena which have opposing effects on the densification of the compacts which occur simultaneously .The matrix densities due to pore shrinkage .The net flow of vacancies from one particle to the other occurs if there is a difference in the fluxes of the atomic species to a specific type of particle Those vacancies may be accumulated in the form of fine pores which is called kirkendall porosity (Lenel et al , 1986) The formation of kirkendall porosity can result in expansion of the compact under sintering effect companied by reduction in density of the compact. From Fig .(6.32) and (6.33) , It has been shown that density of compact first increases and then decrease until a minimum is reached . It the initial stage of sintering (short time , low temperatures) the densification mechanism dominates and apparent density in creases sharply , later , a point is reached where density begins to decrease indicating that formation of kirkendall porosity has begin to dominate .Expansion of sintered compacts has been given for all compacts .The following processing parameters may affect the rate of densification and / or expansion during homogenization :

1. extent of difference in diffusivities of the particles in the compact (D_o for Cu, Al, Ni , Ti ,B, …etc)
2. size of the particles in the compact .
3. mean composition of the powder compacts .
4. Compacting pressure .
5. rate of loading during Compacting .
6. oxygen content of the starting Powders .

So , the form of the density –time – temperature relationship is frequently more complex for multi-phase systems .

Transient liquid phase sintering

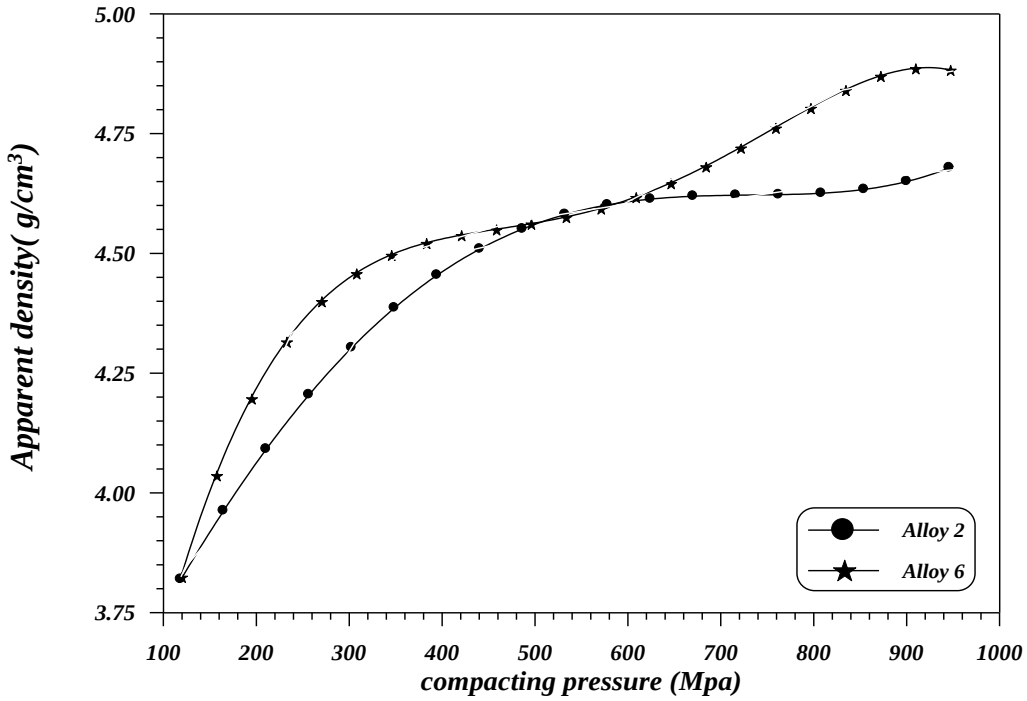

Fig.(6.26) Apparent density of alloy 2 and alloy 6 with respect to compacting perssure .

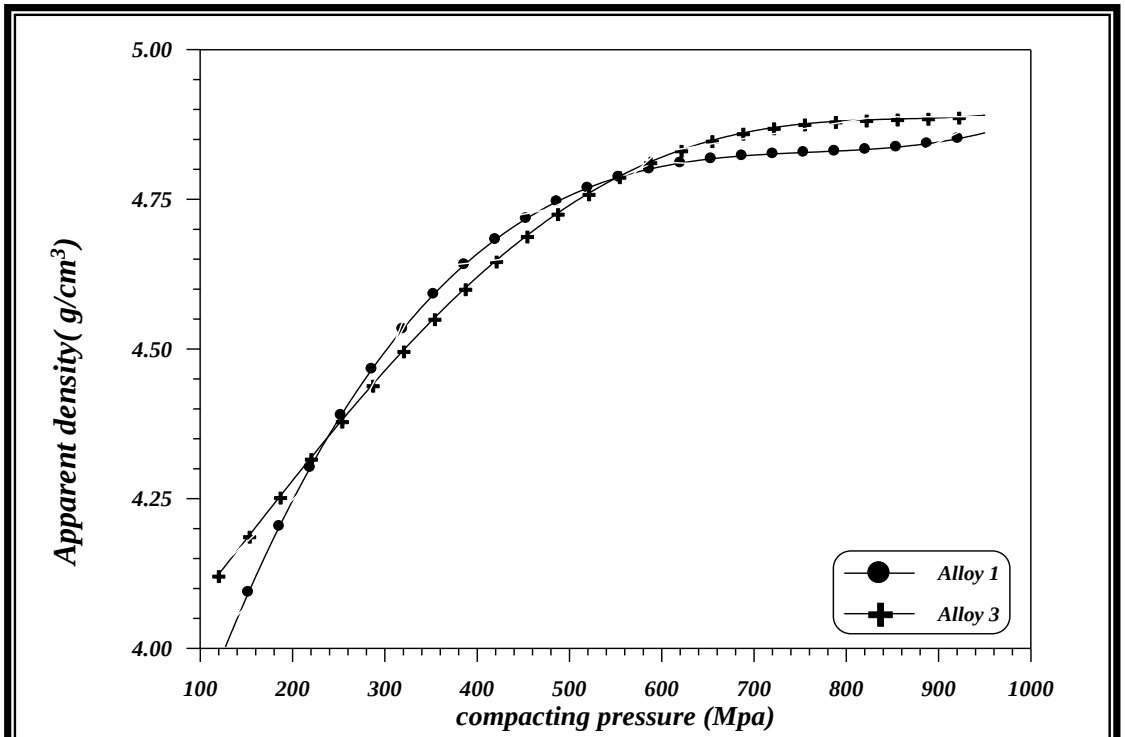

Fig.(6.27) Apparent density of alloy 1 and alloy 3 with respect to compacting perssure .

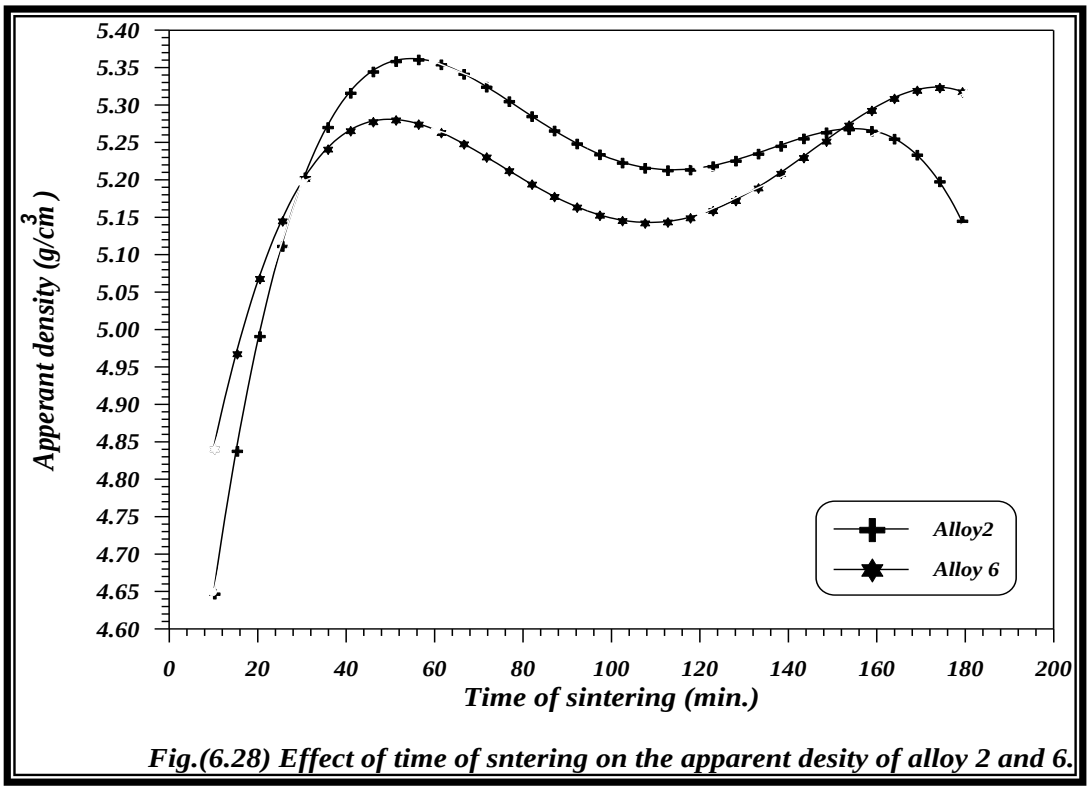

Fig.(6.28) Effect of time of sntering on the apparent desity of alloy 2 and 6.

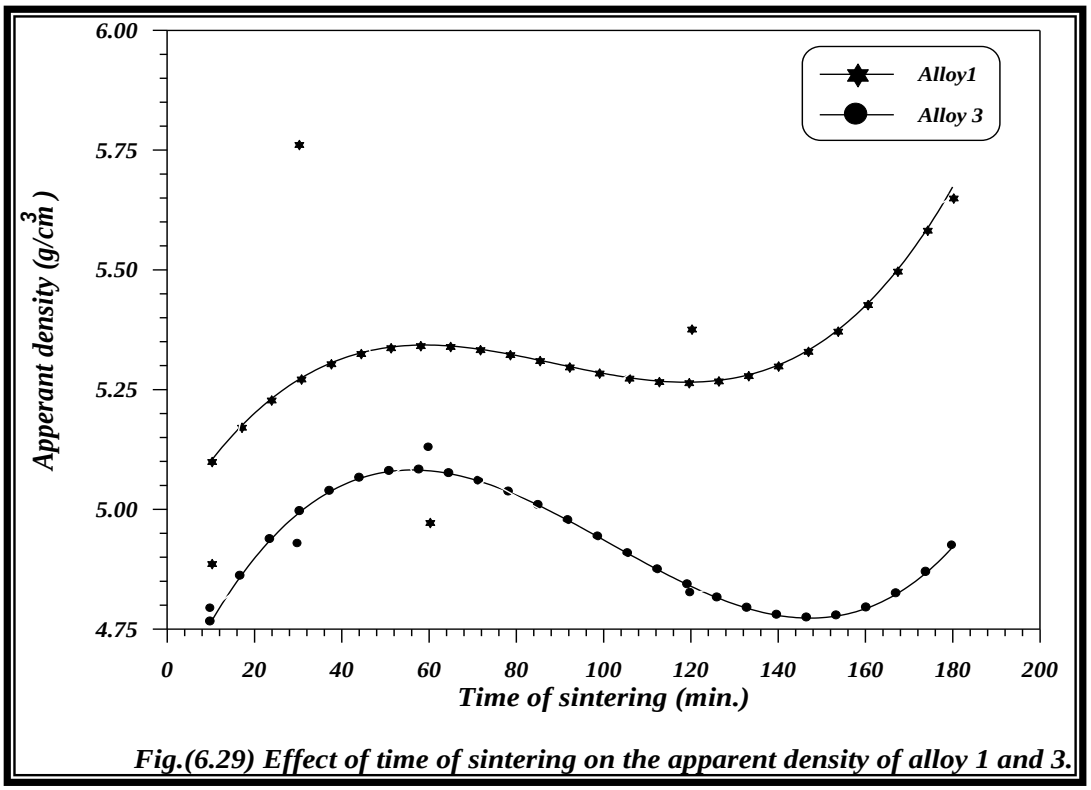

Fig.(6.29) Effect of time of sintering on the apparent density of alloy 1 and 3.

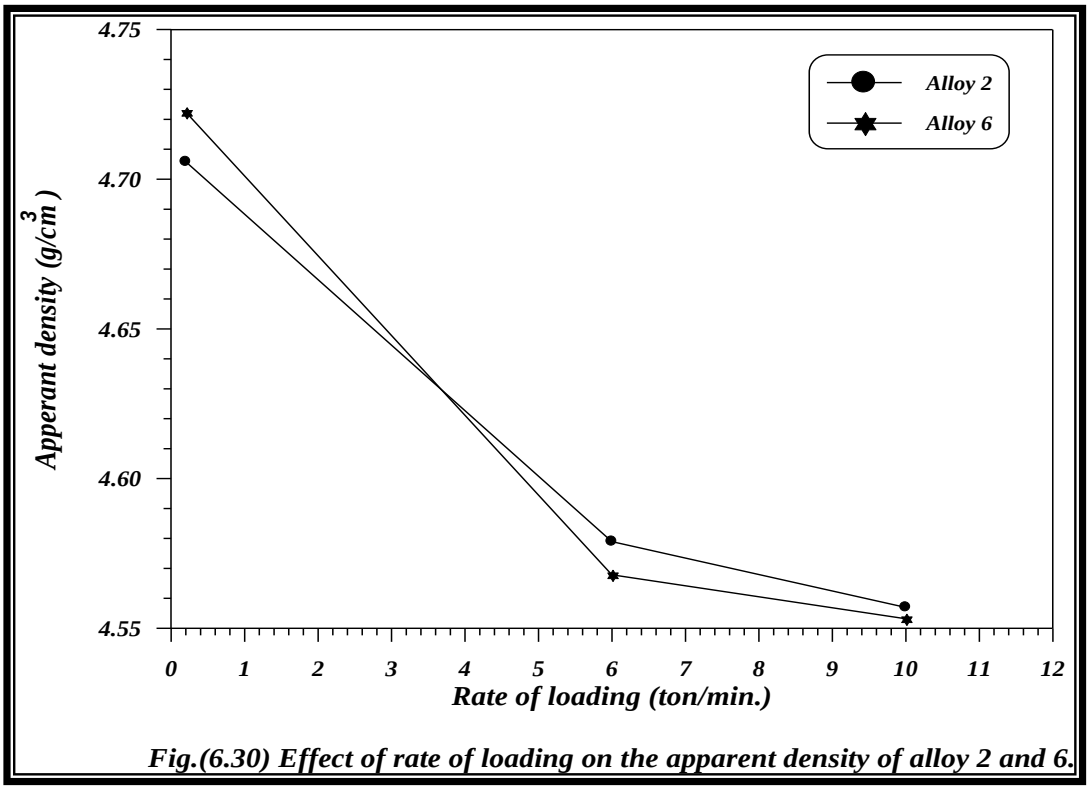

Fig.(6.30) Effect of rate of loading on the apparent density of alloy 2 and 6.

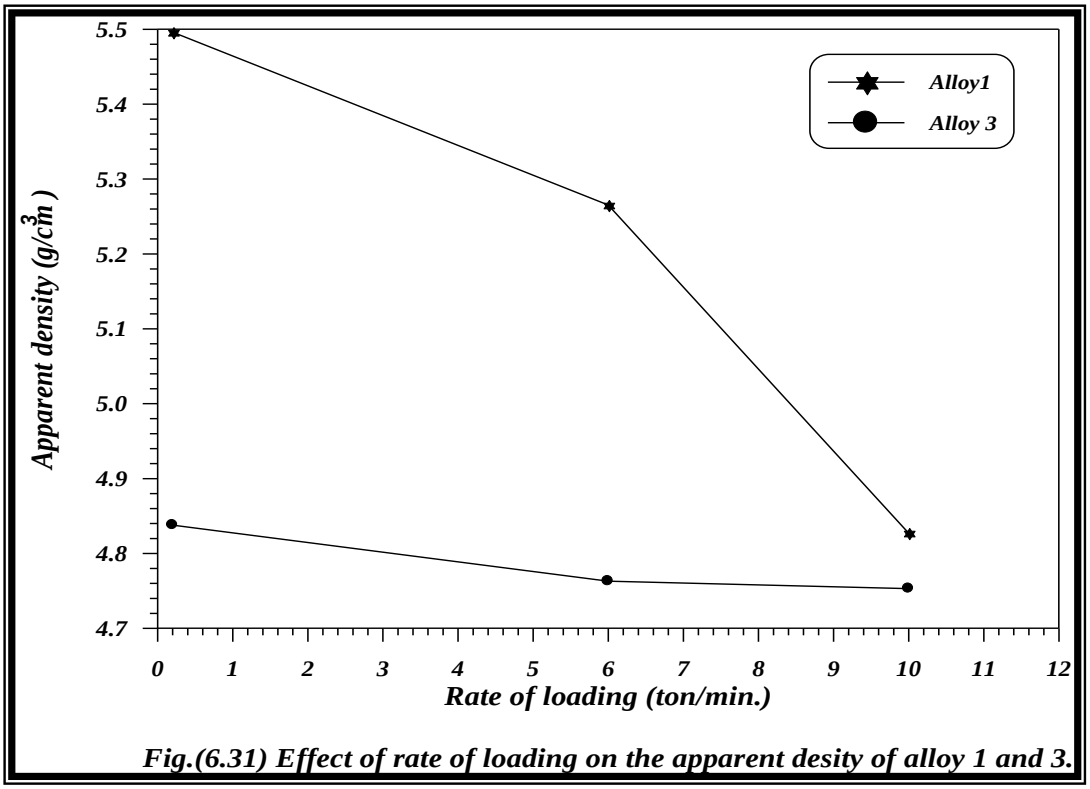

Fig.(6.31) Effect of rate of loading on the apparent desity of alloy 1 and 3.

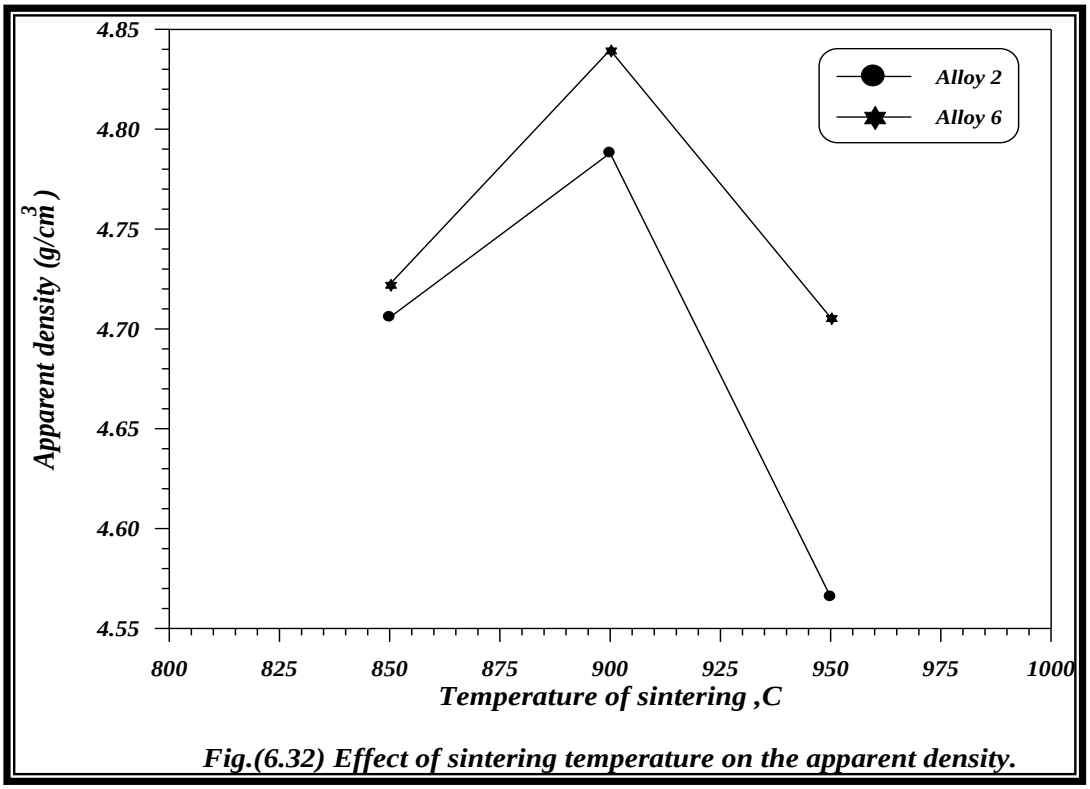

Fig.(6.32) Effect of sintering temperature on the apparent density.

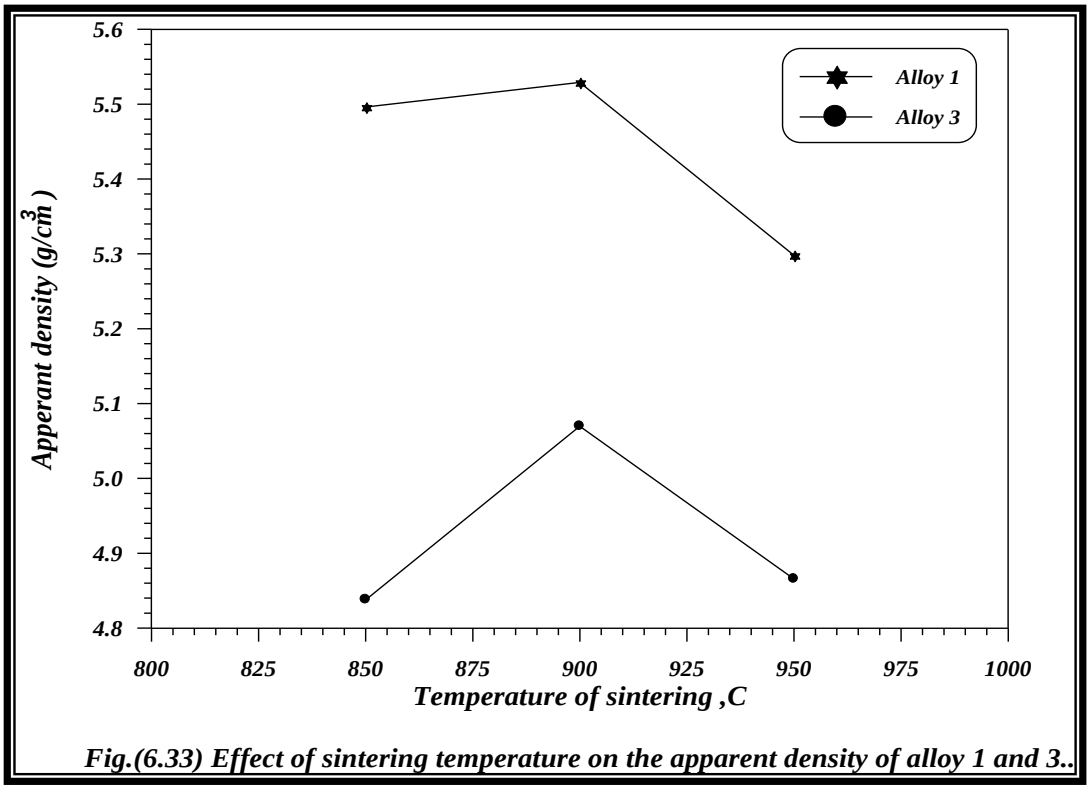

Fig.(6.33) Effect of sintering temperature on the apparent density of alloy 1 and 3..

6.3.2.2. Apparent porosity and absorption of water .

Apparent porosity is the amount of open pores in the volume of sintered compact. Apparent porosity as a function of compaction pressure is shown in Fig. (6.34) and Fig (6.35) for alloys 1,2,3 and 6.It has been shown that open pores volume fraction or apparent porosity for alloy 1,2,3 and 6 are decreased due to obtain densification at high compacting pressure so the pores are reduced on the other hand, apparent porosity is increased when rate of loading is increased due to decrease density of sintered compacts for alloy 1,2,3 and 6 as can be seen from Fig (6.36) and Fig.(6.37).

apparent porosity is the complimentary of apparent density as well, So the apparent porosity will be increased when temperature of sintering and or time of sintering increase because kirkendall porosity is simultaneously formed and reduce densification in the final stages of sintering as can be seen from Fig.(6.38) , (6.39) , (6.40) and Fig.(6.41). for temperature and time of sintering effects respectively.

Some open pores are connectedly between them in channels which facilitate water absorption from the surface to the bottom of alloy 1,2,3 and 6. This effect has been shown in polishing and wet grinding with water which leads to corrode the surface of specimens. Absorption of water is important property in wet or aqueous corrosion. Absorption water as a function of compacting pressure has been shown in Fig. (6.42) and Fig.(6.43) for alloy 2 and 6 for alloy 1 and 3 respectively. Water absorption is decreased for all alloys when compacting pressure is increased due to increase density of sintered compacts and decreased open pores.

when high loading rate is used in compaction of compacts , there is no enough time to escape air from pores and there is no time required to reduce pores by displacing of particles . thus absorption of water is increased when rate

of loading is increased as can be, seen in Fig.(6.44) and Fig.(6.45).It has been shown that alloy 2 and 3 are less sensitive than alloy 1 and 6 for absorption of water with rate of loading. Absorption of water is increased from 3.2% to 4.2% for alloy 6 and to 6.4% for alloy 2 respectively as can be seen from Fig.(6.46).

This is because of increasing of apparent porosity with increasing of sintering temperature . However, for alloy 1 and 3 , absorption of water decrease the beginning with increasing temperature of sintering but at later, water absorptions is increased at 900 ^{o}C for alloy 3 whereas water absorption of alloy 1 is continuously reduced with further increasing of sintering temperature as shown in Fig.(6.47) . This is probably due to kirkendall porosity which depends upon chemical composition of compact during sintering. In the light of this statement , alloy 1 has a smaller aluminum content than the other alloys so that compact swelling is not preferred in this alloy. Thus densification phenomena is the predominant at these temperatures.

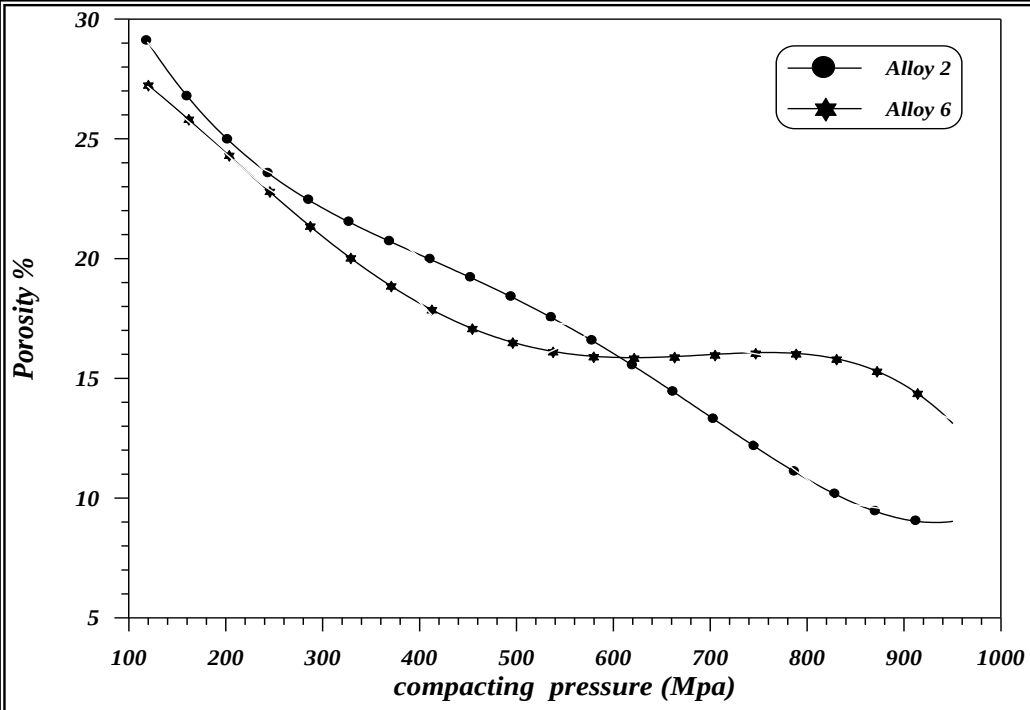

Fig(6.34) Effect of compacting pressure on th e apparent porosity of alloy 2 and 6.

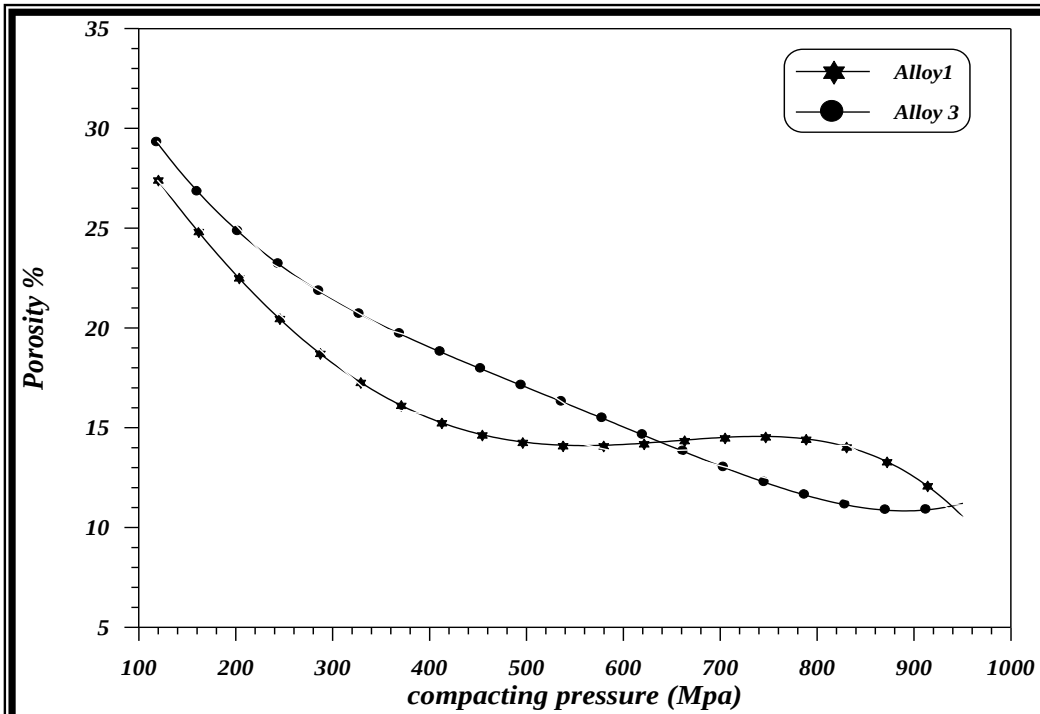

Fig.(6.35) Effect of compacting pressure on the apparent porosity of alloy 1 and 3.

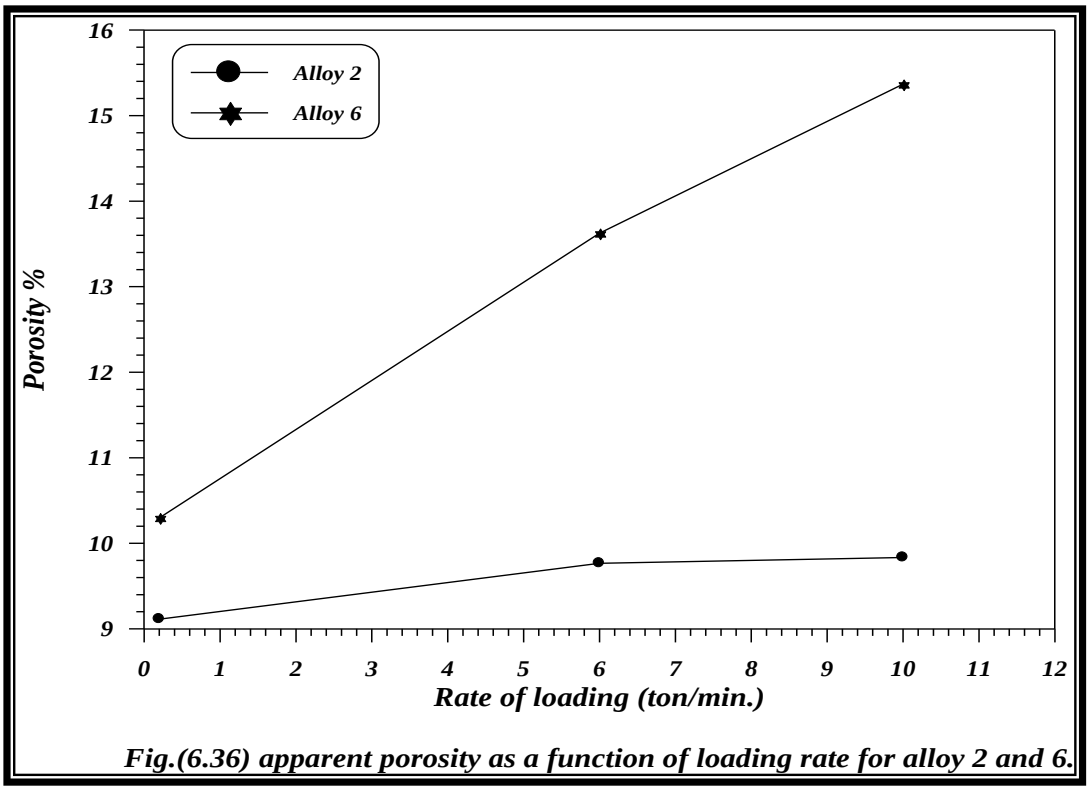

Fig.(6.36) apparent porosity as a function of loading rate for alloy 2 and 6.

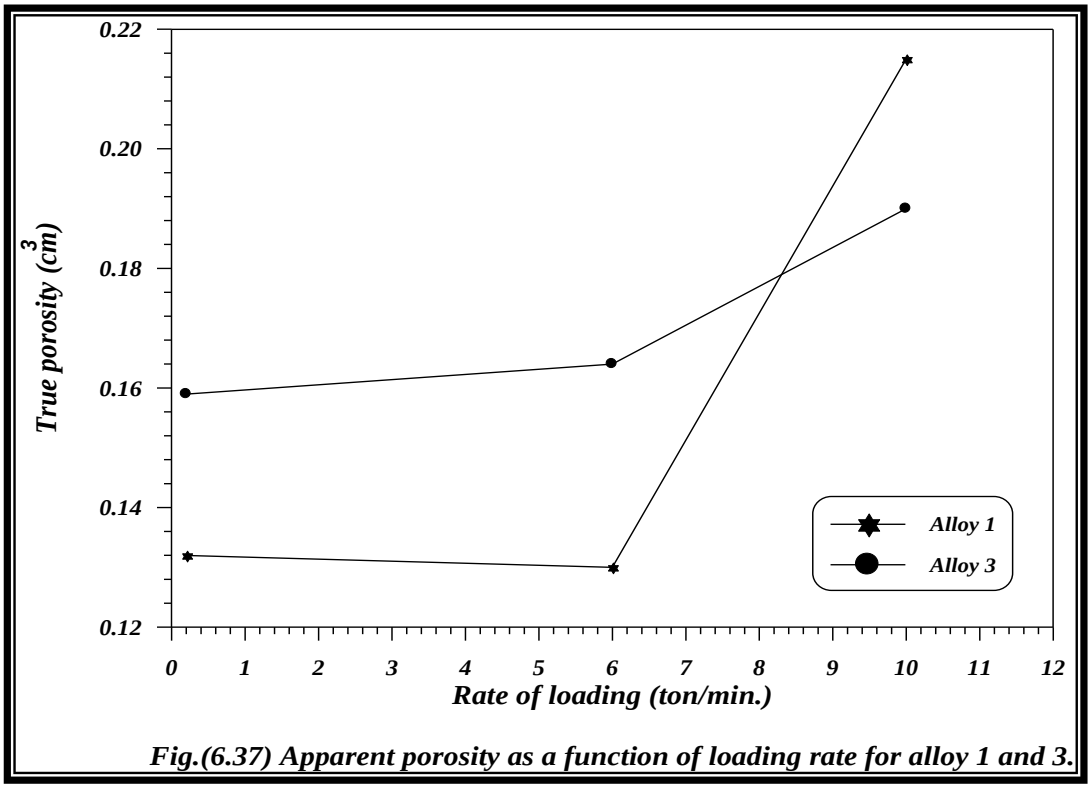

Fig.(6.37) Apparent porosity as a function of loading rate for alloy 1 and 3.

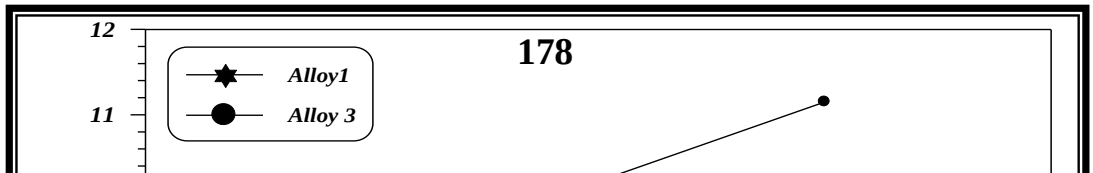

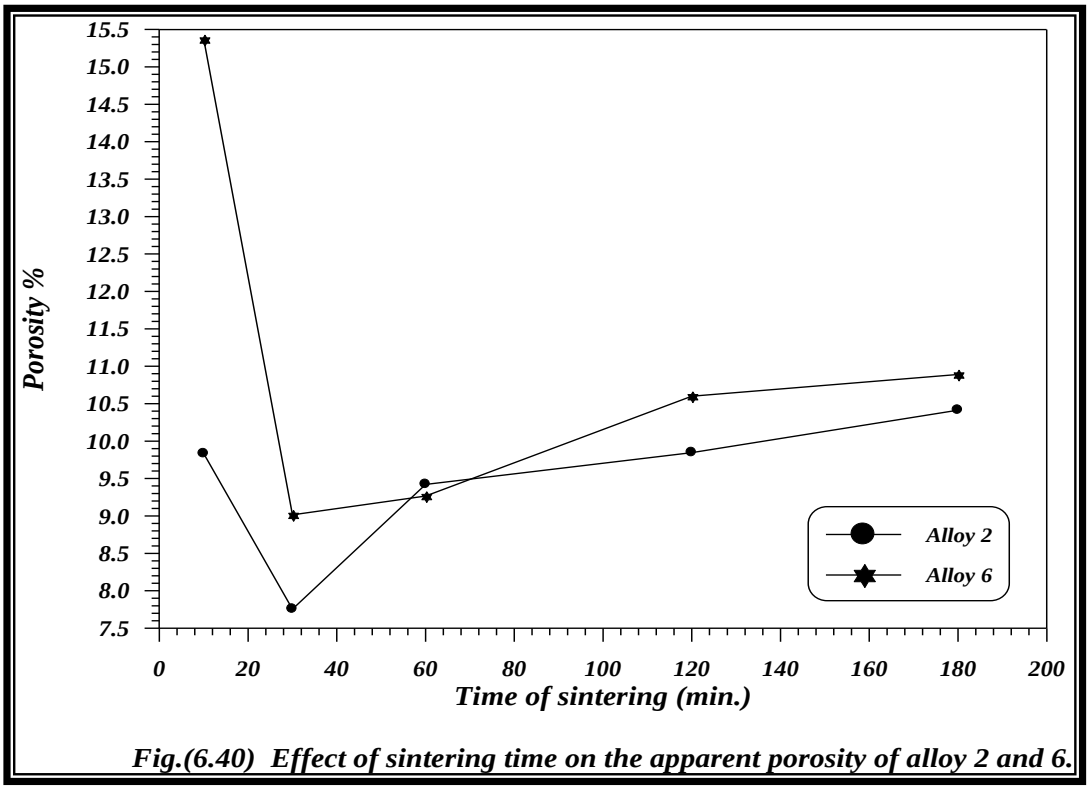

Fig.(6.40) Effect of sintering time on the apparent porosity of alloy 2 and 6.

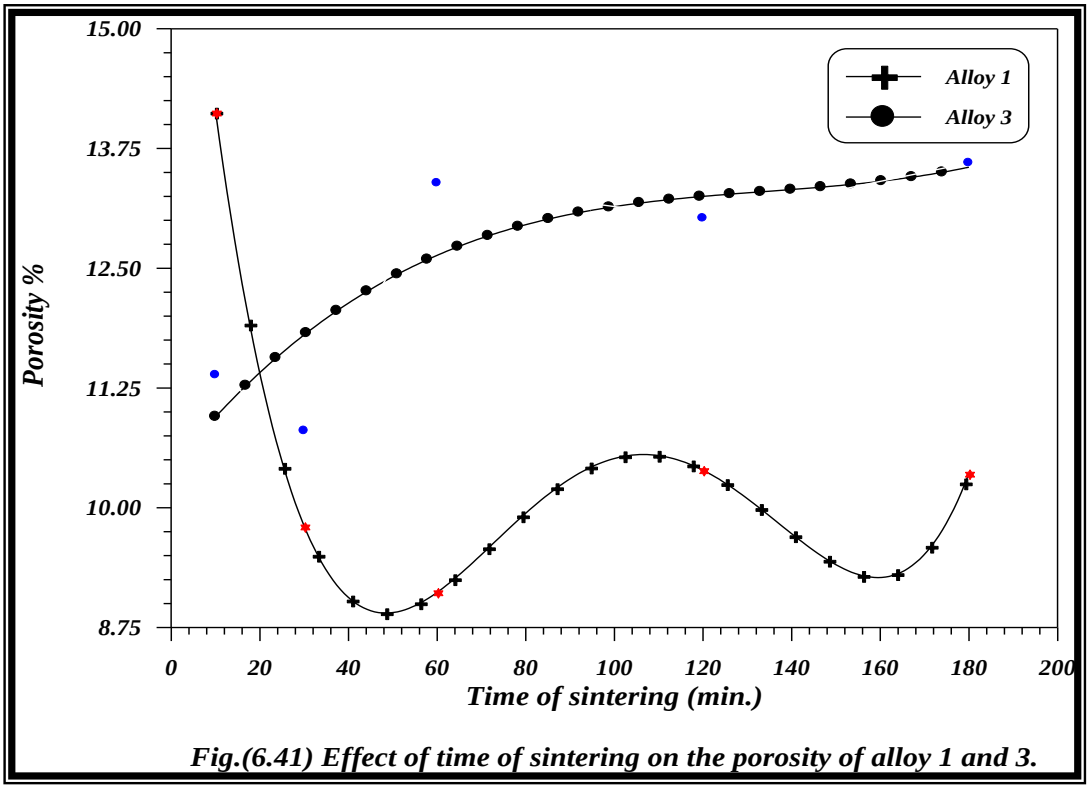

Fig.(6.41) Effect of time of sintering on the porosity of alloy 1 and 3.

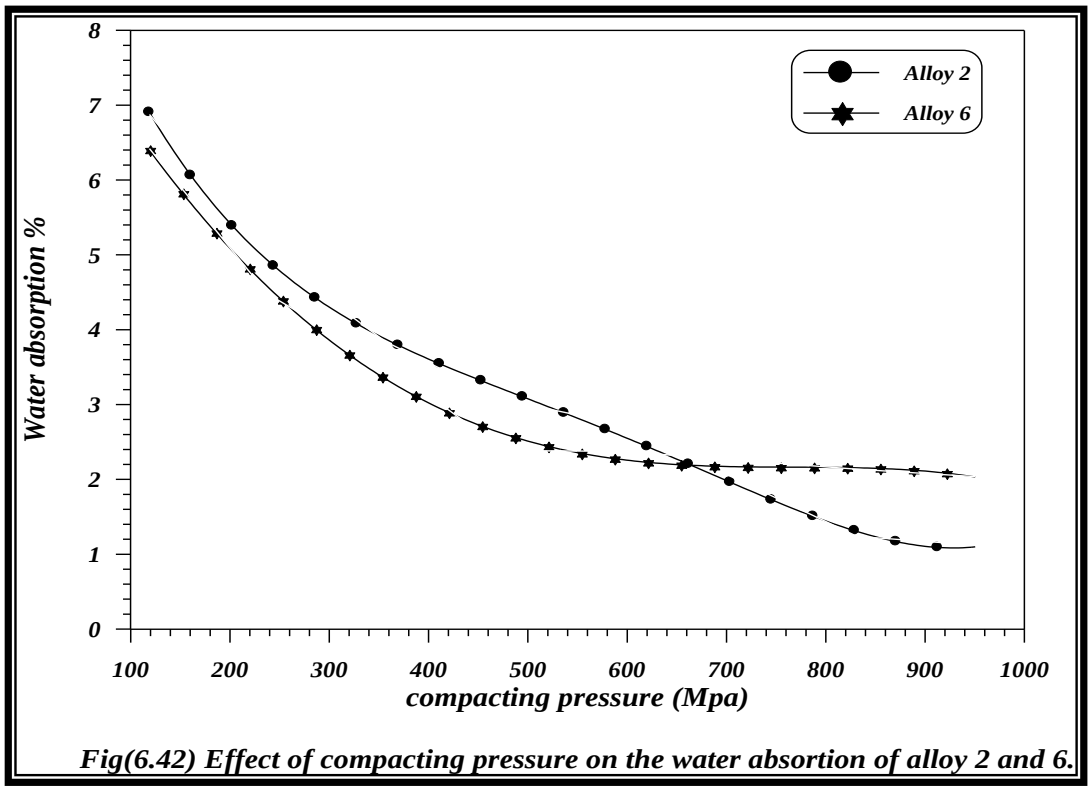

Fig(6.42) Effect of compacting pressure on the water absortion of alloy 2 and 6.

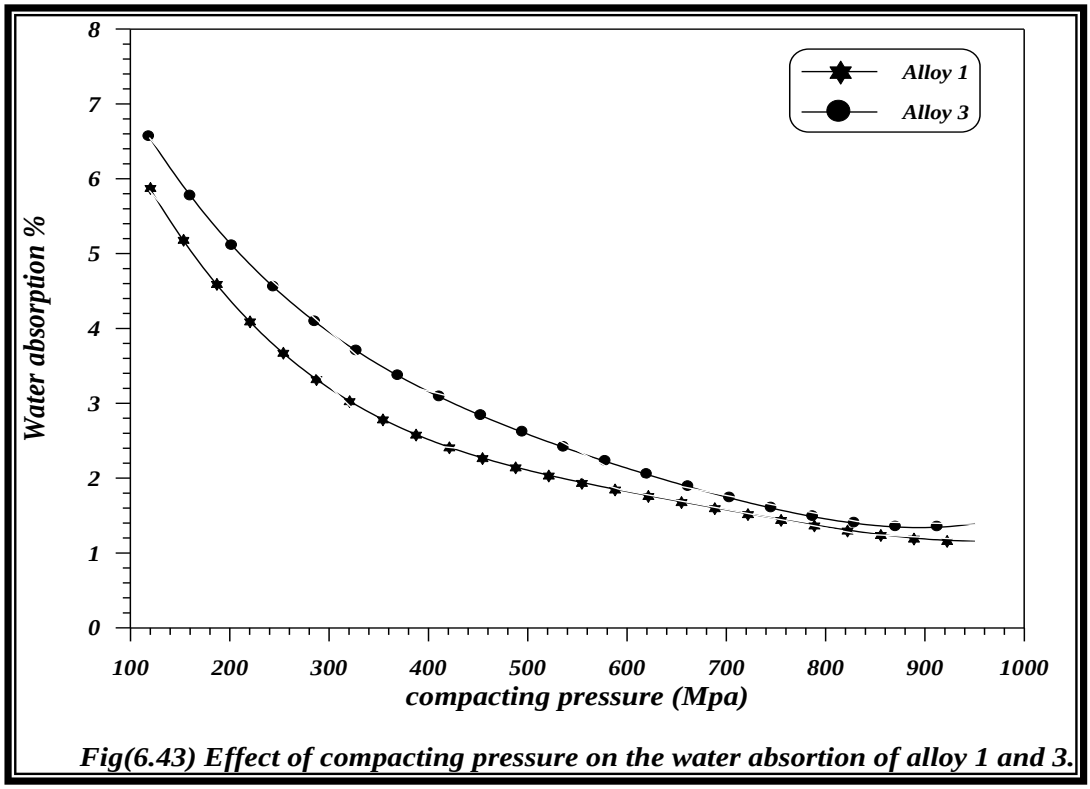

Fig(6.43) Effect of compacting pressure on the water absortion of alloy 1 and 3.

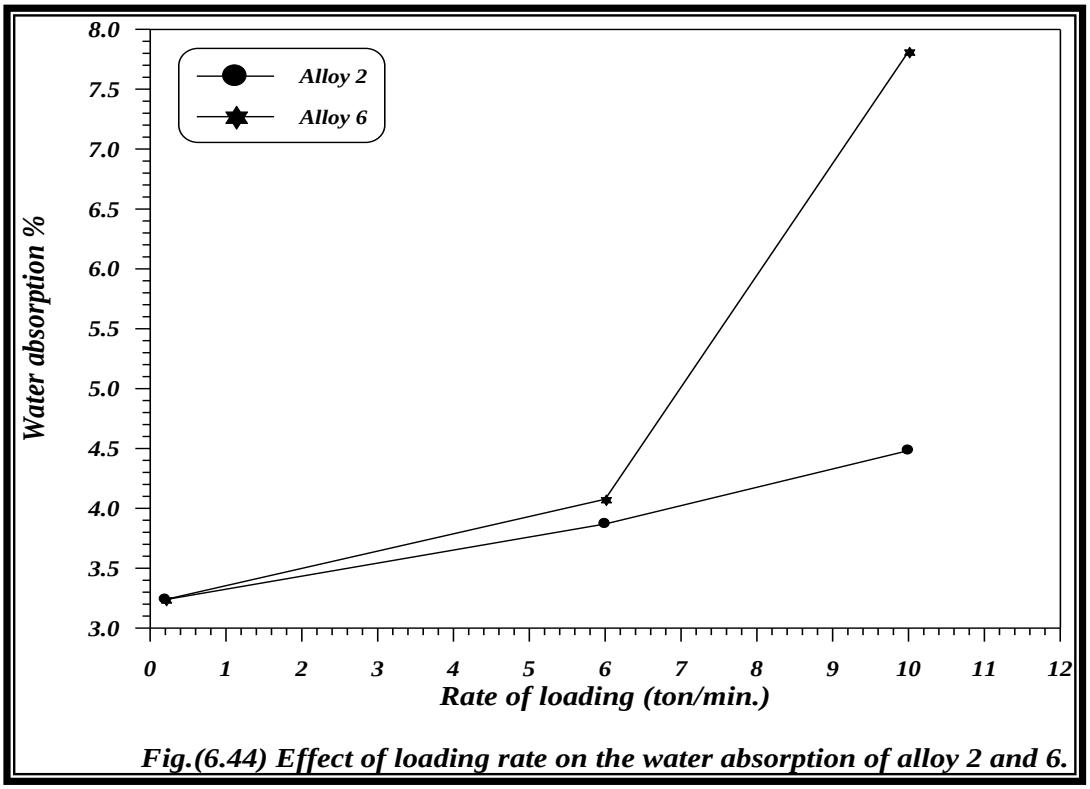

Fig.(6.44) Effect of loading rate on the water absorption of alloy 2 and 6.

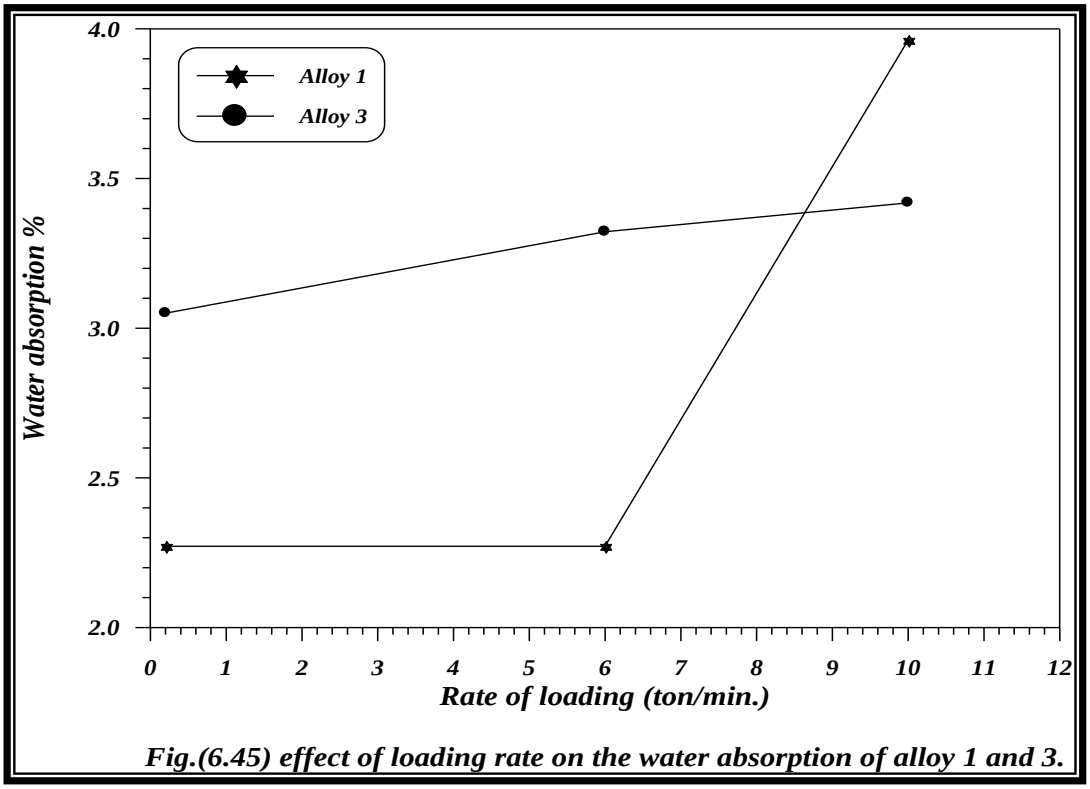

Fig.(6.45) effect of loading rate on the water absorption of alloy 1 and 3.

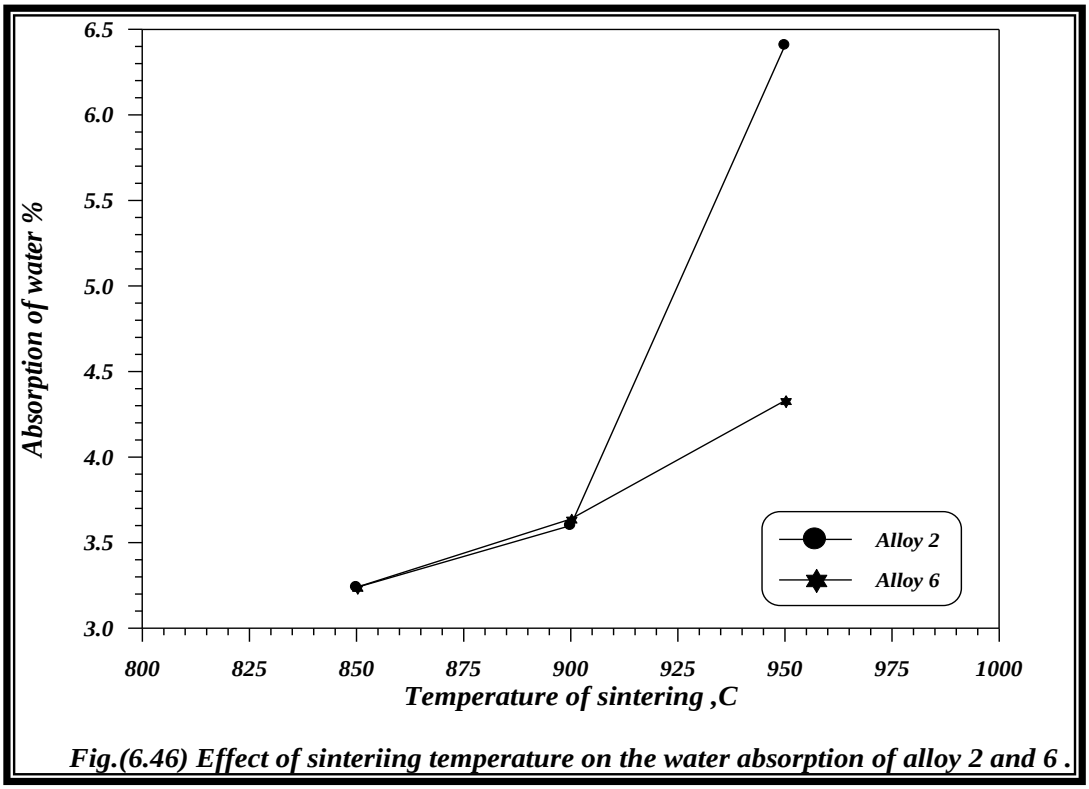

Fig.(6.46) Effect of sinteriing temperature on the water absorption of alloy 2 and 6 .

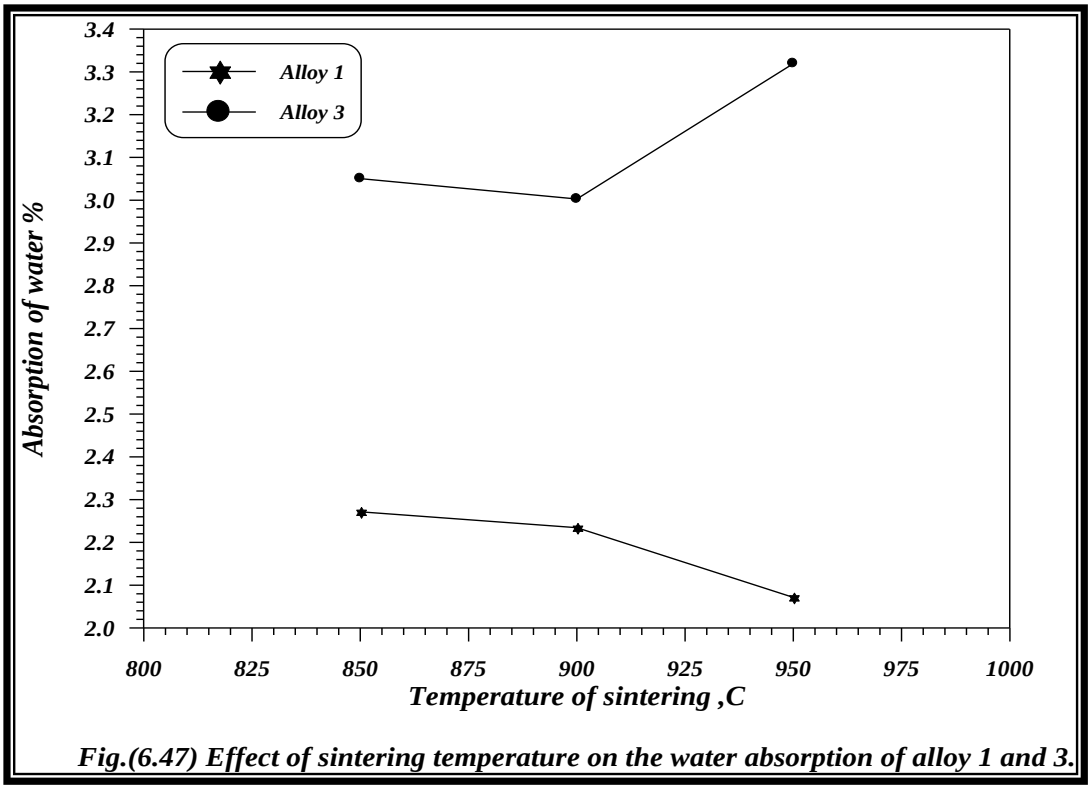

Fig.(6.47) Effect of sintering temperature on the water absorption of alloy 1 and 3.

6.3.2.3. True Porosity

True porosity is the measuring of closed and open pores in the volume of sintered compacts. True porosity decreased with increasing of compacting pressure for alloys 1,2,3 and 6 in Fig.(6.48) and (6.49).

In has been shown that closed pores is decreased when the compacting pressure is increased initial green density and increase apparent density with increasing pressing stress. On the other hand the effect of rate of loading on the true porosity of alloy 1,2,3 and 6 has been taken in to consideration as shown in Fig.(6.50) and Fig.(6.51).

High closed and opened pores concentration at high loading rate because the is no time to move of diffuse particles in the compact under the action of sintering. In the light of this statement, true porosity has been increased when temperature of sintering increased. It is probably due to form kirkendall porosity at high temperature which lead to occur the expansion of compacts under sintering. This is truly took place in all specimen. So that sintering at 850 ^{o}C is taken and higher temperatures (900 or 950 ^{o}C) have been avoided. The effect of sintering temperature on the true porosity is shown in Fig.(6.52) and Fig.(6.53). Because the expansion of compacts under sintering condition depends upon composition of alloy and because the lower aluminum content in alloy 1 tan in the other alloys , true porosity has been decreased up to (0.116 cm^3) at the sintering temperature of 900 ^{o}C. After this , open and close pores have been increased with increasing sintering temperatures.

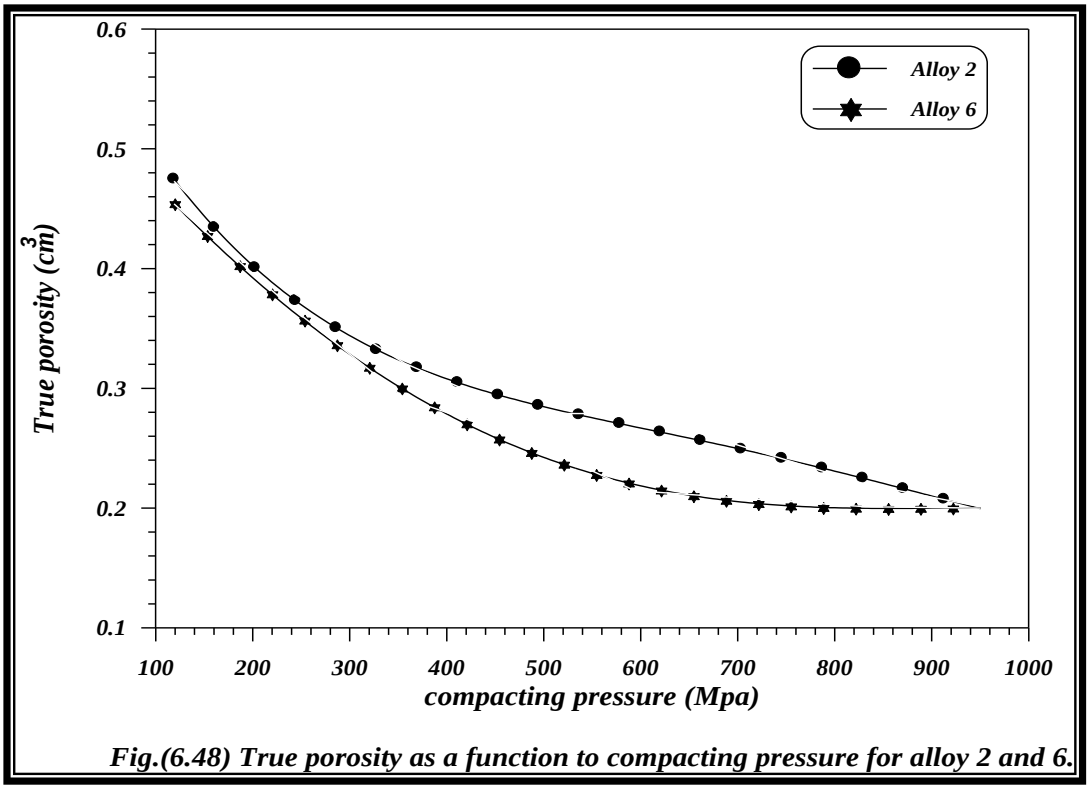

Fig.(6.48) True porosity as a function to compacting pressure for alloy 2 and 6.

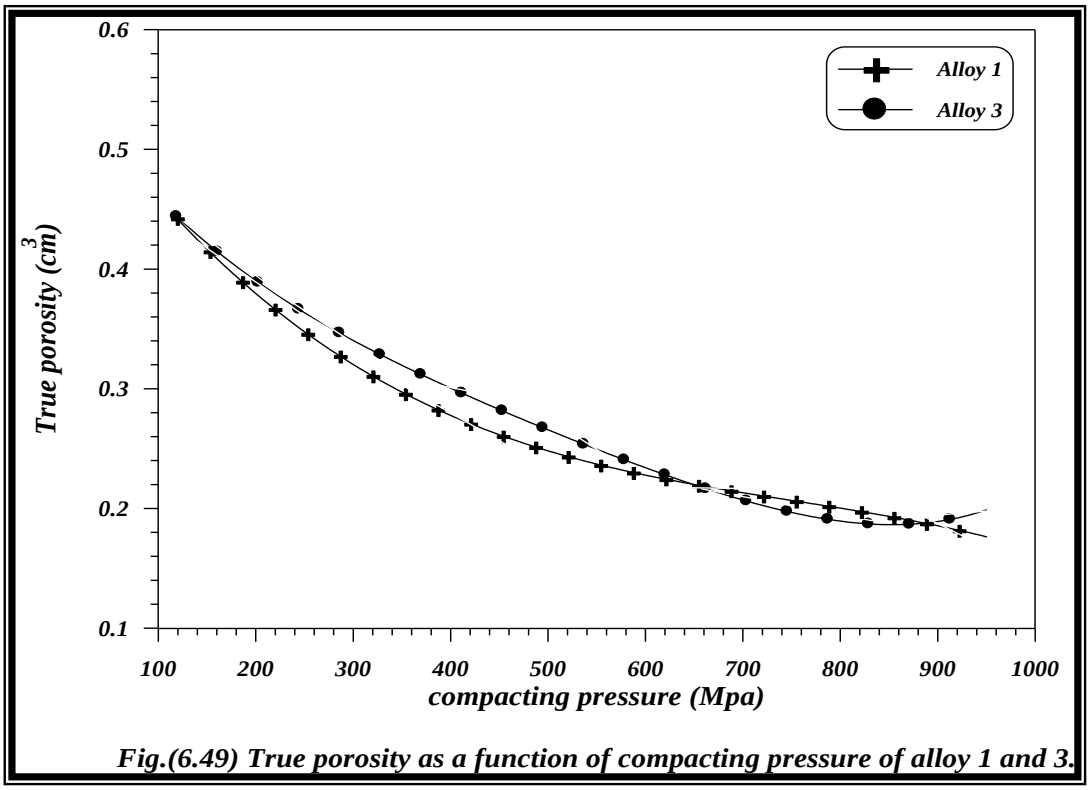

Fig.(6.49) True porosity as a function of compacting pressure of alloy 1 and 3.

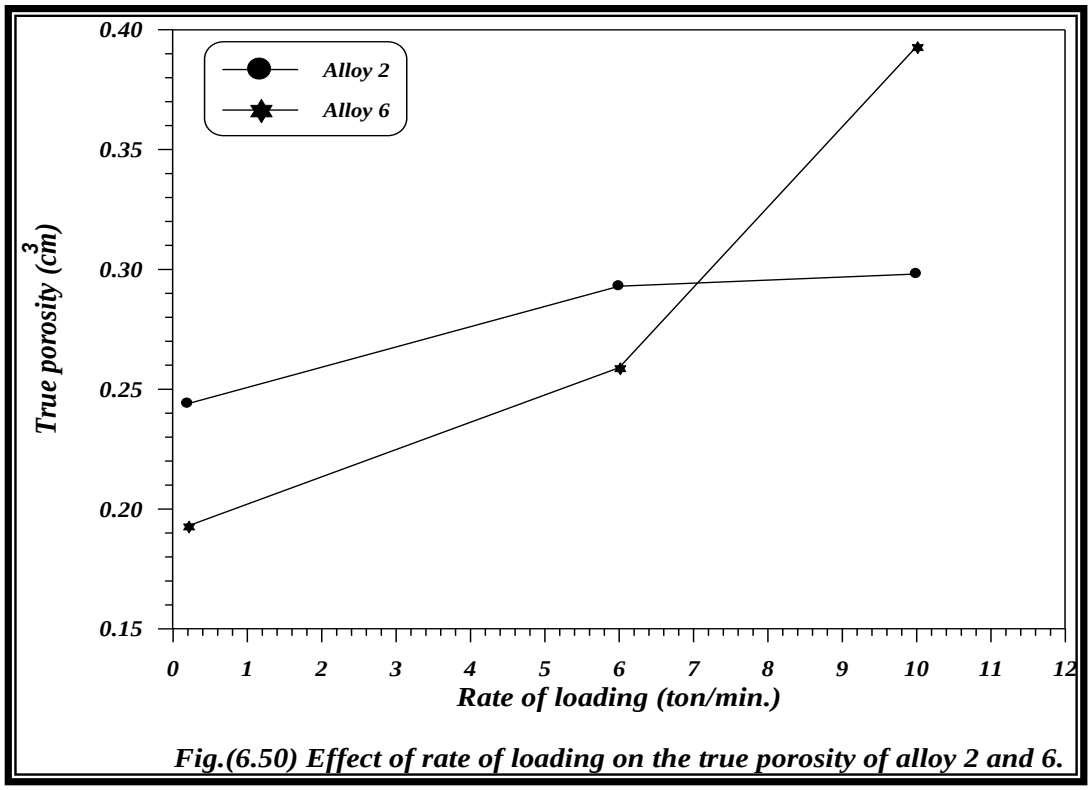

Fig.(6.50) Effect of rate of loading on the true porosity of alloy 2 and 6.

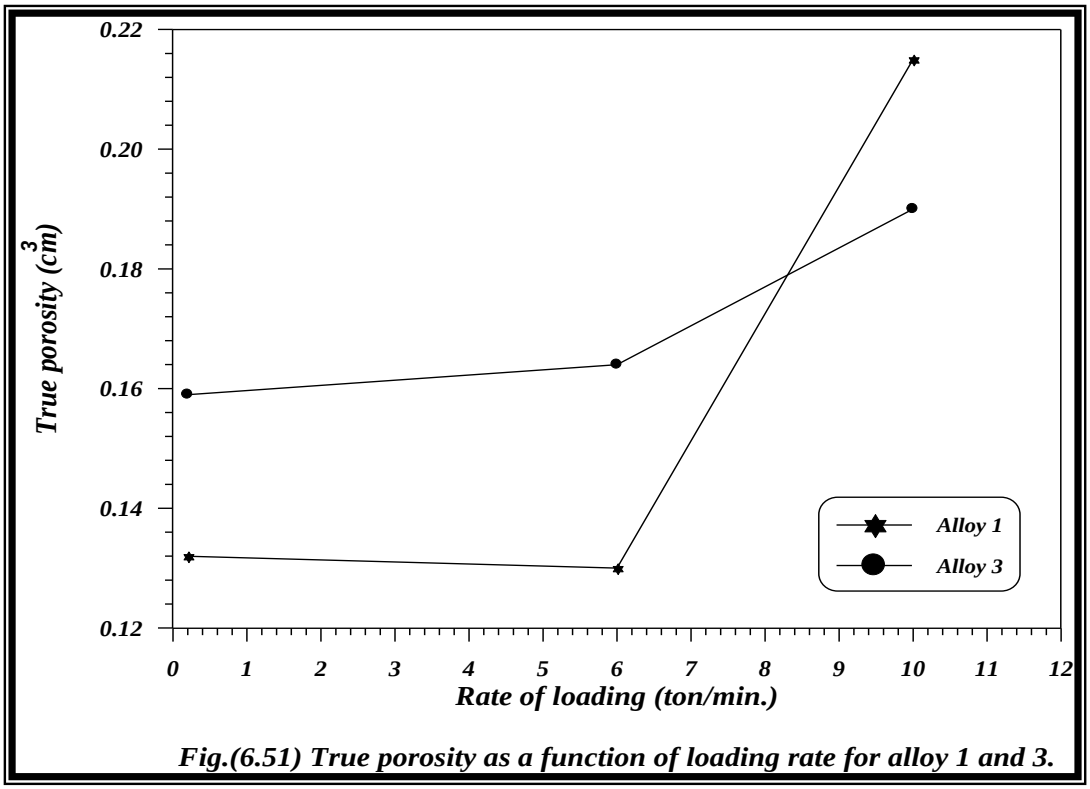

Fig.(6.51) True porosity as a function of loading rate for alloy 1 and 3.

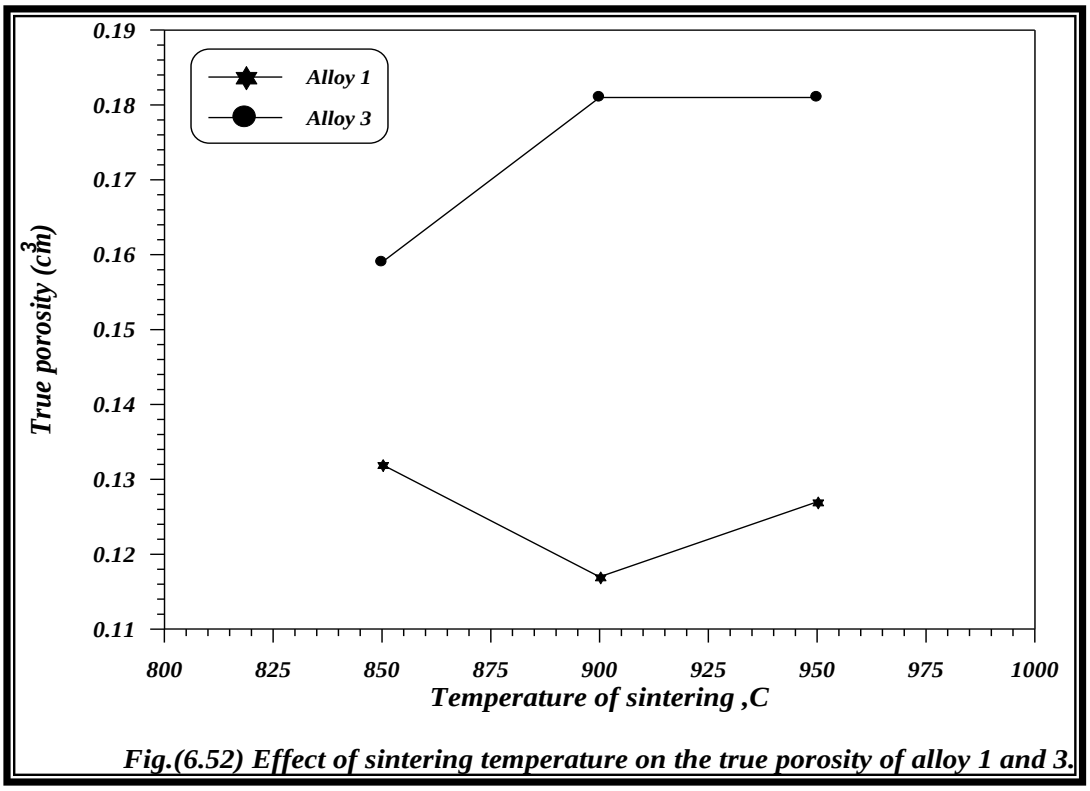

Fig.(6.52) Effect of sintering temperature on the true porosity of alloy 1 and 3.

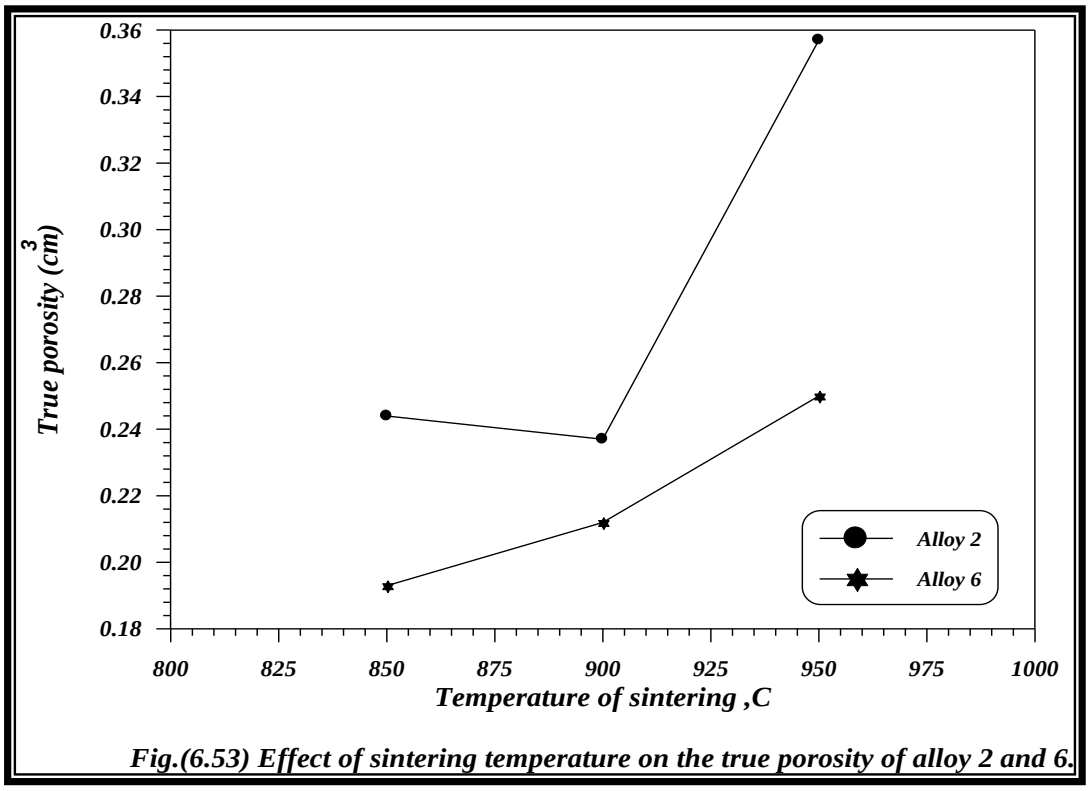

Fig.(6.53) Effect of sintering temperature on the true porosity of alloy 2 and 6.

6.3.2.4. Expansion of sintered compacts

Changes in the dimensions of compacts are important considerations in the sintering. Dimensional changes are determined as the difference in dimensions between green and sintered compacts parallel and perpendicular to the direction of pressing and are expressed in the percent of the green dimensions.

The effect of compacting pressure on the expansion of alloy 1,2,3 and 6 has shown in Fig. (6.54) and Fig.(6.55) . It has been shown that expansion of alloy 1,2,3 and 6 are increased with increasing compacting pressure from 1.32 % at 120 MPa a study state value of 3.35 % at compacting pressure greater than 660 MPa. This expansion is due to gases entrapped in closed off pores of the compact. Gases may be entrapped during compacting or may be formed by chemical reactions such as the formation of water vapor by reaction of oxide skins on the surface of the particles with the hydrogen of the sintering atmosphere which diffuses in to the closed pores. In the case of Aragon atmosphere , there is no hydrogen but it is probably that Aragon enters the closed pores at high temperature sintering which leads to expand the compact under sintering .

Furthermore, thermal expansion due to increase in temperature of sintering with high coefficient of thermal expansion of copper particles , increases and arises from high thermal expansion coefficients of other constituents under cooling of sintered compacts.

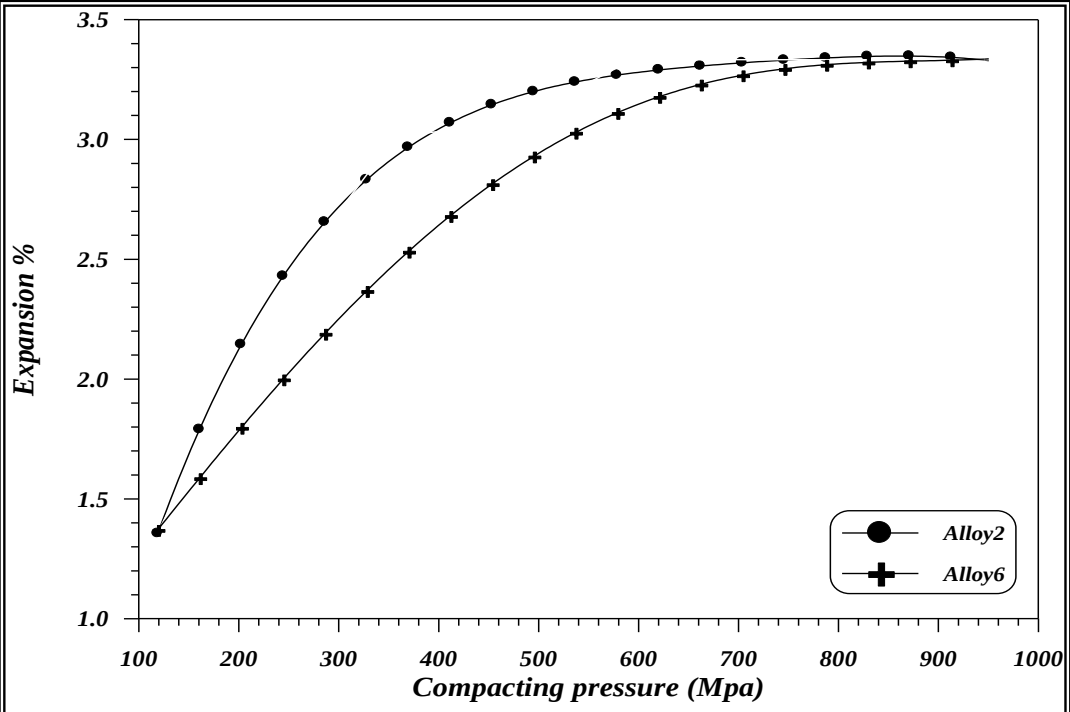

Fig(6.54) Expansion as a function to compacting pressure for alloy 2 and 6.

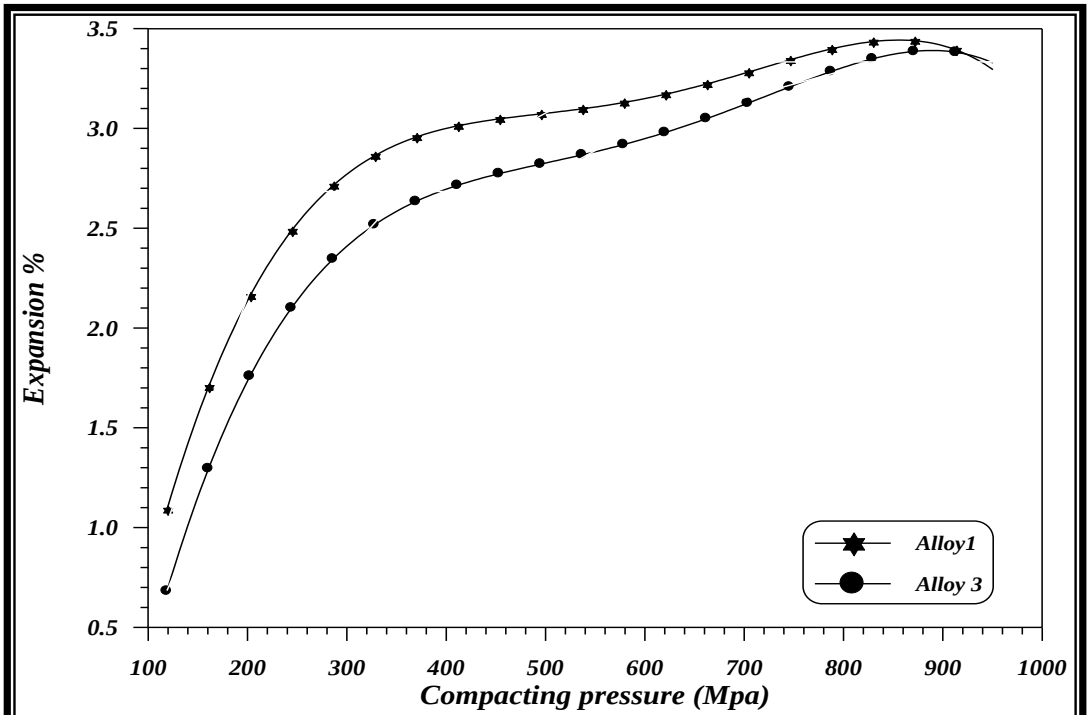

Fig.(6.55) Expansion as a function to compacting pressure for alloy 1 and 3.

6.3.3 Microstructure of sintered compacts.

The microstructure image by (LOM) for first stage sintering (3 hr at 600 ^{o}C) and second stages sintering (3 hr. at 600 ^{o}C and 3 hr. at 850 ^{o}C) have been shown in Fig.(6.56). The principal difference between the microstructures of the first and second stage sintering is in the shape of pores within the powder particles which have become rounded during sintering. The first stage sintering temperature is in the shape of pore within the powder particles which have become rounded during sintering. the first stage sintering temperature is too low to produce adequate bonding between powder particle. The specimens have been etched with ($NH_4OH + H_2O_2 + H_2O$) etchent to reveal the grain boundaries in the microstructure. Pores of different size are no longer cusp-shaped and irregular but have become rounded. The transition in microstructure form that of a green compacts to that of a well sintered compacts is a function of sintering time and temperature.

The effect of time of sintering which achieved at 850 ^{o}C on the microstructures has been shown in Fig. (6.57). While the temperature of sintering at constant time (10 min.) effect on the microstructures of alloys 1,2,3 and 6 has been shown in Fig.(6.58) and Fig.(5.59).

During annealing of cold worked wrought material, a recrystallization temperature is reached. The nuclei of strain-free grains are formed which grow into the recrystallized structure so that grain growth has been occurred. recrystallization temperature and amount of cold work. However, the temperature of sintering is higher than the recrystallization temperature of wrought material. Compacting pressure has a relatively minor effect on the temperature range at which the sintering structure is formed. The effect of compacting pressure on grain growth during sintering may be to facilitate contact between particles. Sintered structure of compact requires that grain growth occurs across particle boundaries. This grain growth is restricted until material transport has progressed to point where a substantial increase in the contact area between particles has been took place.

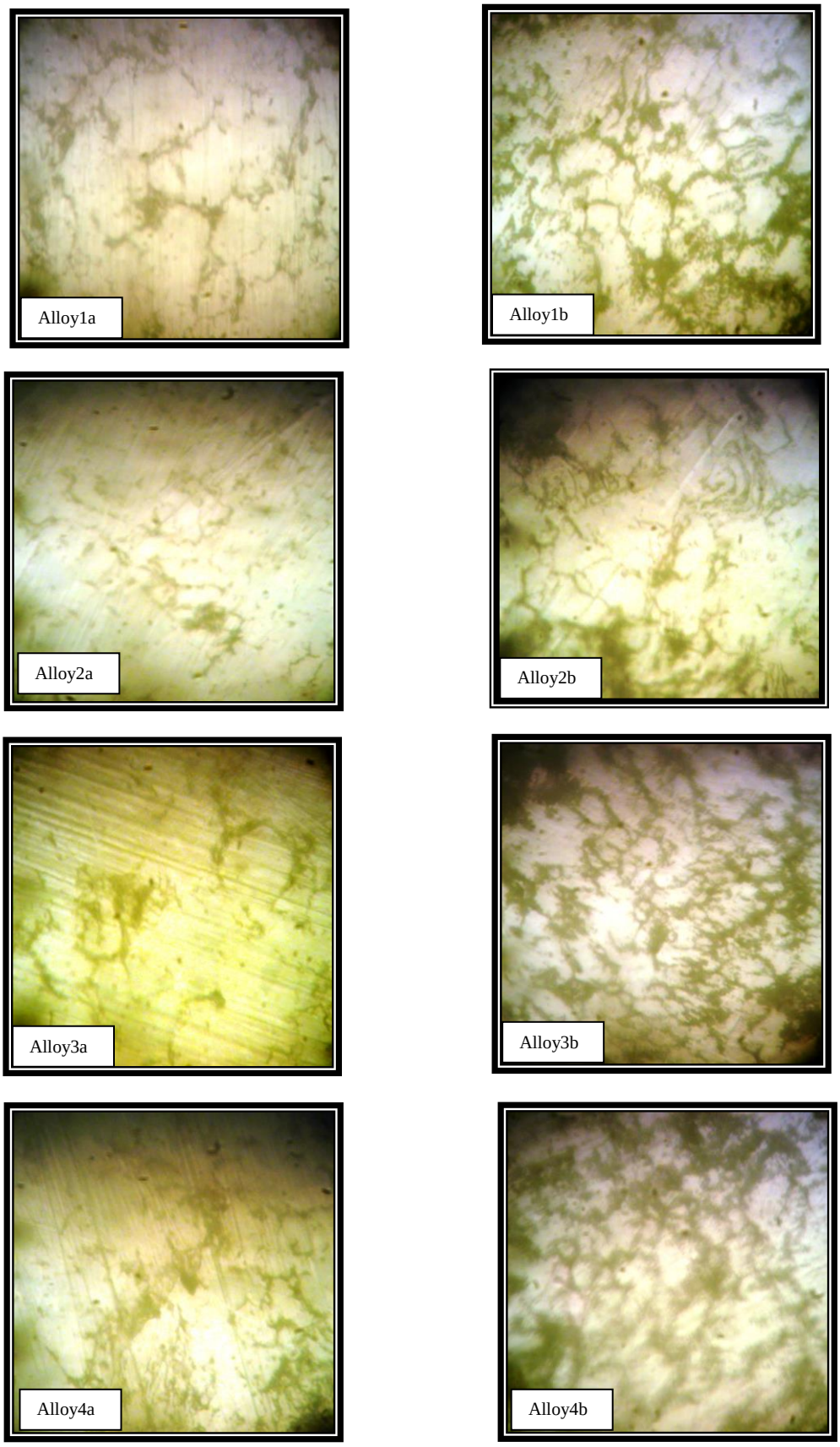

Fig.(6.56) LOM images for the microstructure of alloys1,2,3,6 for: a.stage I sintering b.stage II sintering 1000X .

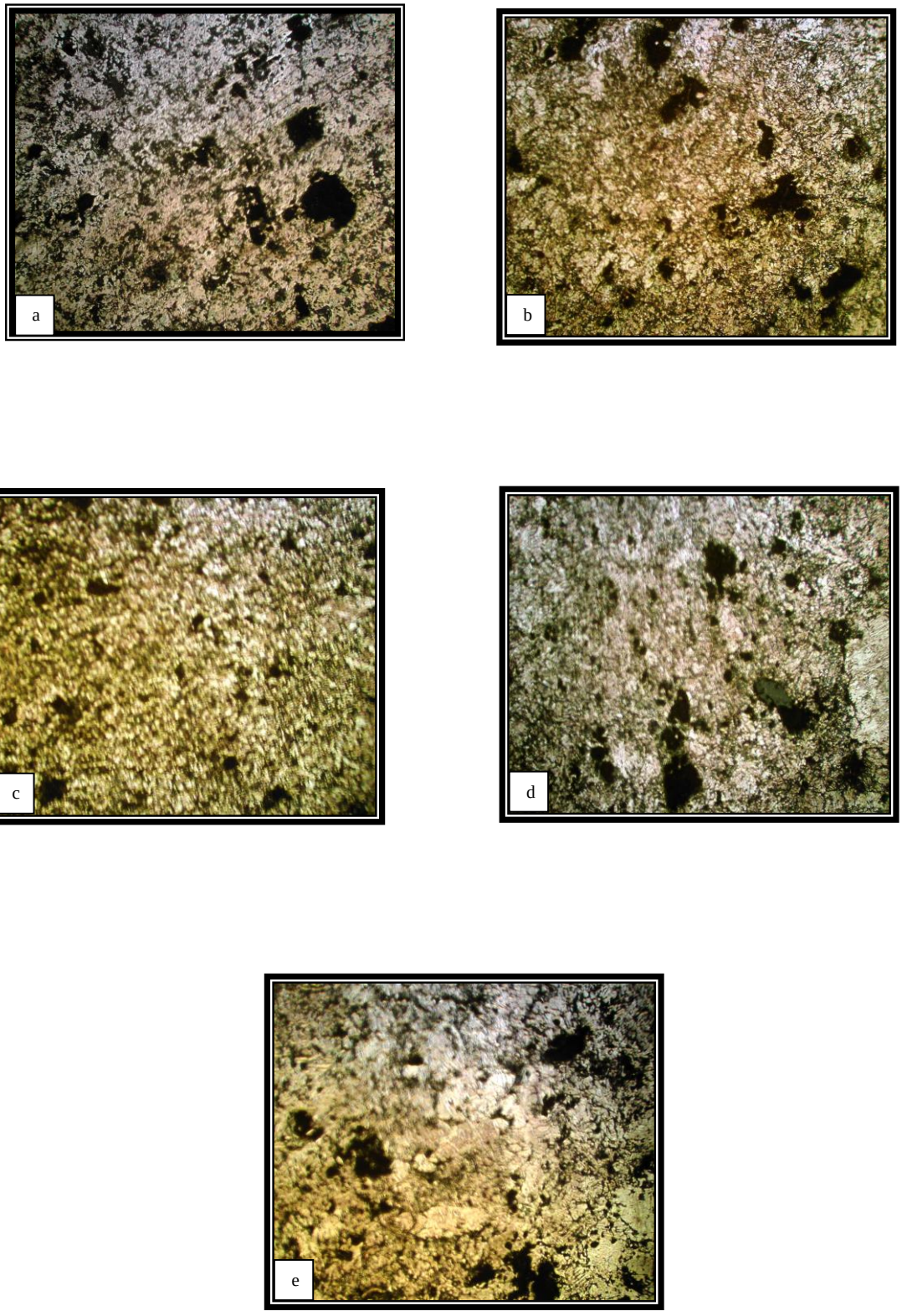

Fig.(6.57) LOM images for the microstructure of alloys2 for different sintering time as: a.10 min. b.30 min. c.60 min. d.120 min. e.180 min 150X.

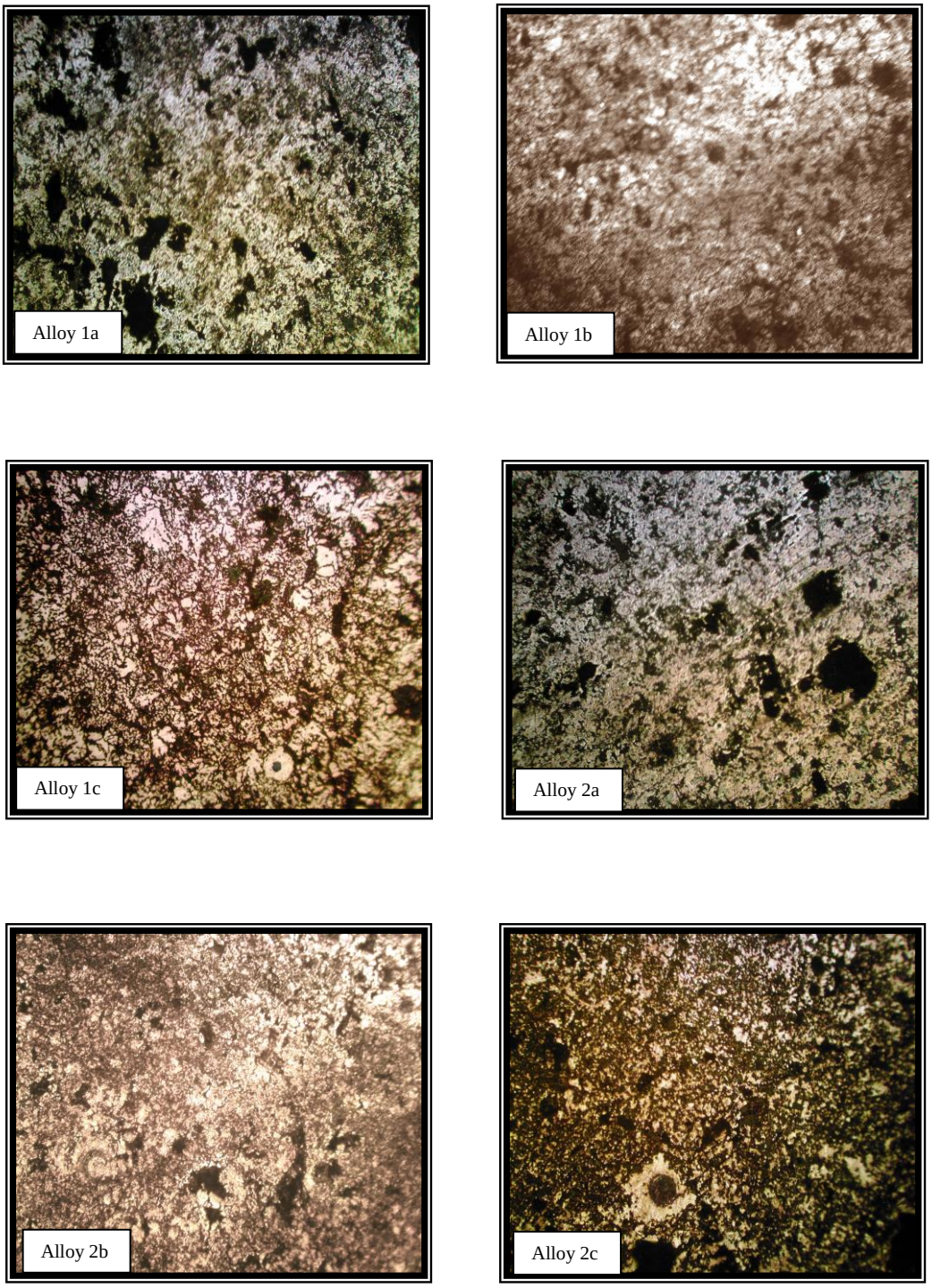

Fig.(6.58) LOM images for the microstructure of alloys 1 and 2 for different sintering temperature as: a.850 ^{O}C. b.900 ^{O}C. c.950 ^{O}C 150 X.

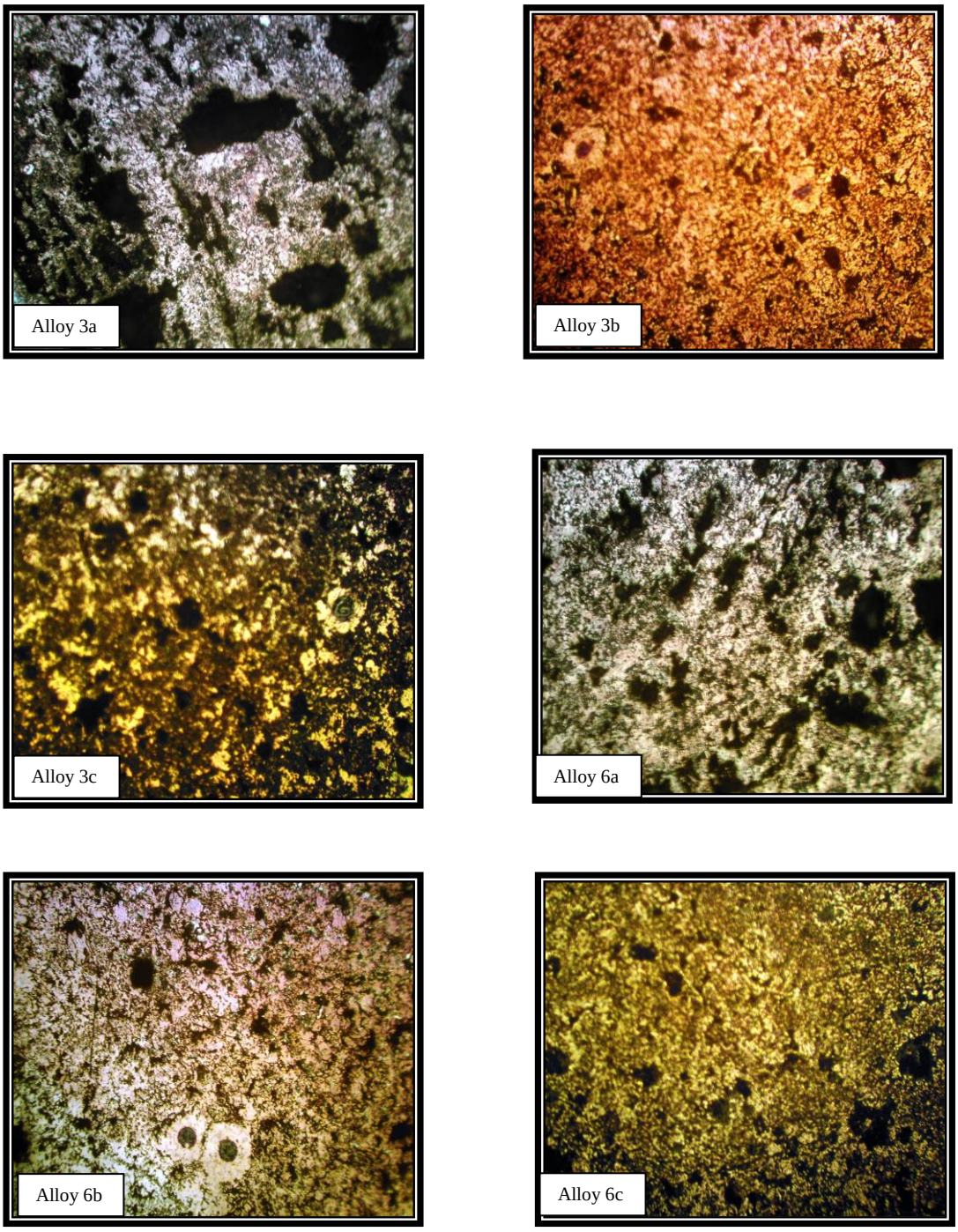

Fig.(6.59) LOM images for the microstructure of alloys 3 and 6 for different sintering temperature as: a.850 ^{O}C. b.900 ^{O}C. c.950 ^{O}C 150 X.

6.3.4. Pore size and distribution

LOM image of microstructures for first stage sintering and second stage sintering with corresponding a accumulative plots for alloy 1,2,3 and 6 have been shown in Fig.(6.60) and Fig.(6.61).

It is shown that pores are irregular and non uniform in shape and distribution in the first stage sintering due to low temperature of sintering with respect to the matrix alloying element (Cu). However , pores are rounded some what at the second stage sintering. The average pore size is determined at 50% point on the accumulative plot which is (8 , 10 , 7 and 10 μm) for alloys 1,2,3 and 6 respectively. For first stage sintering. However. the average pore size of alloys 1,2,3 and 6 for second stage sintering case is determined form Fig.(6.61) as [2,8,6 and 6 μm] respectively. Sometimes ,powder particles which are not formed alloy in the first stage sintering, appear as black regions in binary image so that not all black regions are pores. Any way , pores tend to round in the second stage sintering as possible.

Difference in composition and quantity of phases $(\alpha + \gamma_2)$ in the microstructure of sintered specimens affect on the distribution , of pores in the microstructures. In addition, silicon carbide particles of grinding paper may be impeded in sectioned surface of polished specimens specially alloy 1 due to low content of aluminum in the chemical composition which leads to lower γ_2 concentration phase in the matrix of ductile α. This effect may also affect on the real pore distribution which based upon binary image analysis. Therefore , more attention must be taken in the preparation of polished specimen to reveal real pores and the next pore distribution base up on white and black objects image analysis. Rounded and less of pores in the second stage of sintering refer to access of sintering process of compacts.

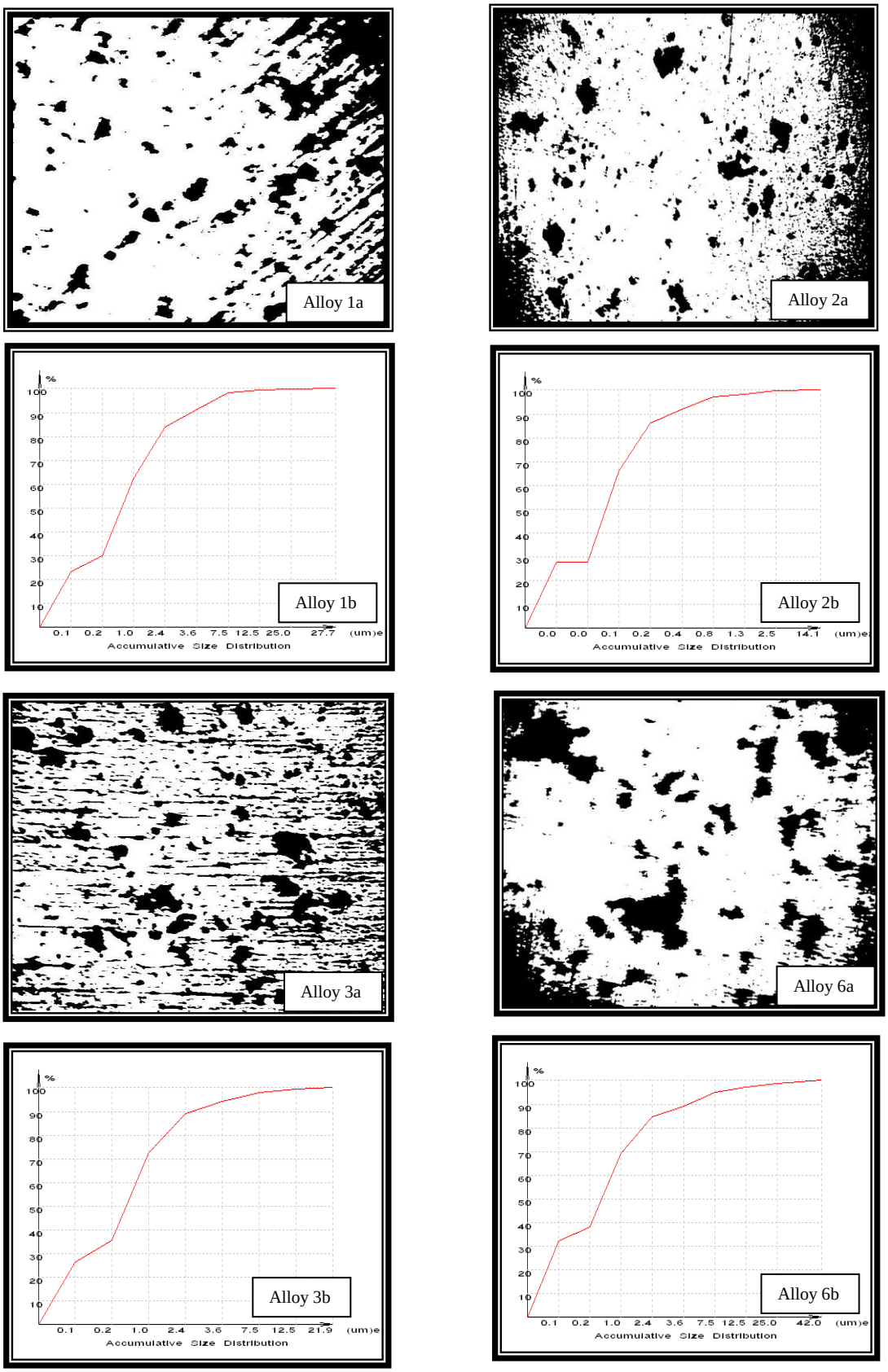

Fig.(6.60) LOM binary images and accumulative pore distribution of alloys 1 , 2 ,3 and 6 as: a. micrograph stage I sintering b. accumulative plot for stage I sintering 150 X .

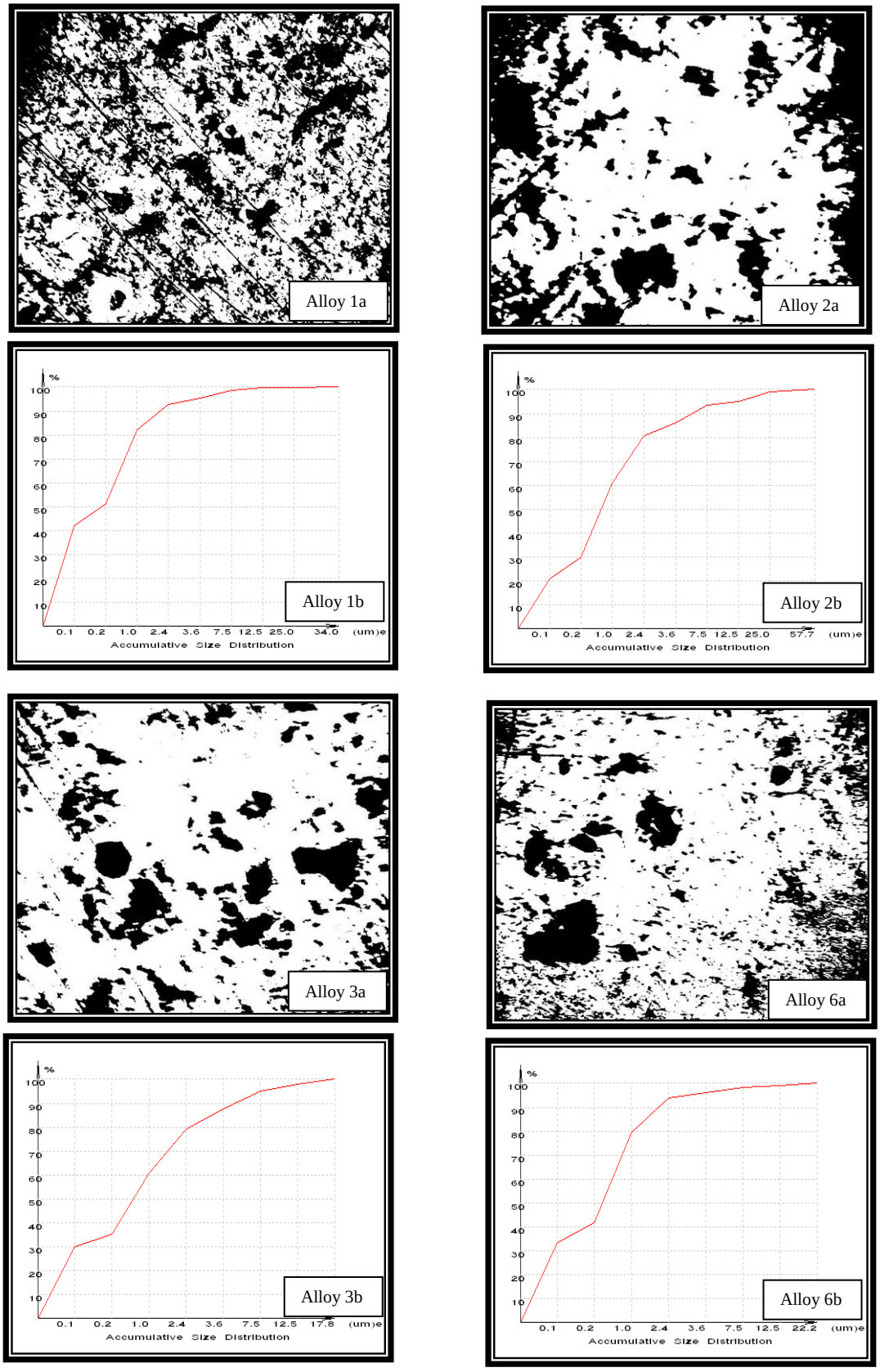

Fig.(6.61) LOM binary images and accumulative pore distribution of alloys 1 , 2 ,3 and 6 as: a. micrograph stage II sintering b. accumulative plot for stage II sintering 150 X .

6.3.5. Vicker's macrohardness test results

Vicker's macrohardness tester with digital monitor is used to determine the macrohardness of sintered compacts for both first and second stage sintering. Four readings are based for each specimen and apply this condition for all alloys Fig.(6.62) shows Vicher's macrohardness with 30 kg majer load and 3 kg as minor load, for alloys 1,2,3 and 6 . It has been shown that vicker's macrohardness for first stage sintering of alloy 1,2,3 and 6 are higher than that in the second stage sintering of these alloys because the sintering of alloy 1,2,3 and 6 at 600 ^{o}C and 3hr. as holding time is not enough to transform all intermetallic compound (γ_2) in to solid solution of β at the temperature greater than 564 ^{o}C for Eutectiod composition. In other words , sintering in temperature of 600 ^{o}C leads to form microstructure in $(\alpha+\gamma_2)$ region according to (Cu +Al) phase diagram. Alloy 1 consists of 11 % Al so that it is not enough to form β phase. Alloys 2,3 and 6 have 13% Al percent so that they are hypereutectoid and also sintering in 600 ^{o}C hot from β phase . There fore , γ_2 in $(\alpha+\gamma_2)$ microstructure is the predominant phase and because this intermetallic compound is very hard , alloys 1, 2,3 and 6 have high hardness. while the sintering in 600 ^{o}C for 3 hr and the next 850 ^{o}C for 3hr. addition , produce β' phase in this temperature and during cooling (Which is high rate in type furnace used in this study) Small amount from γ_2 phase may be precipitated in the matrix of α phase specially at grain boundaries regions. This reason produce low hardness of α phase with comparison with $(\alpha+\gamma_2)$ in the first stage sintering case.

Furthermore, in the first stage sintering case, not all metal powders transform to alloy so that these particles impeded in the matrix and not solved in the α phase and no form any intermetallic compound which lead to remain these particles near the surface and affect on the vicker's macrohardness. Thus ,

in the second stage there is no powdered particles not dissolved in the microstructure which form alloyed solid solution that the third and /or fourth alloying elements dissolve in the matrix of solvent metal.

After presentation of studying of process parameters for both in green and sintered compacts, martensitic transformation during different heat treatment are being presented in the following :-

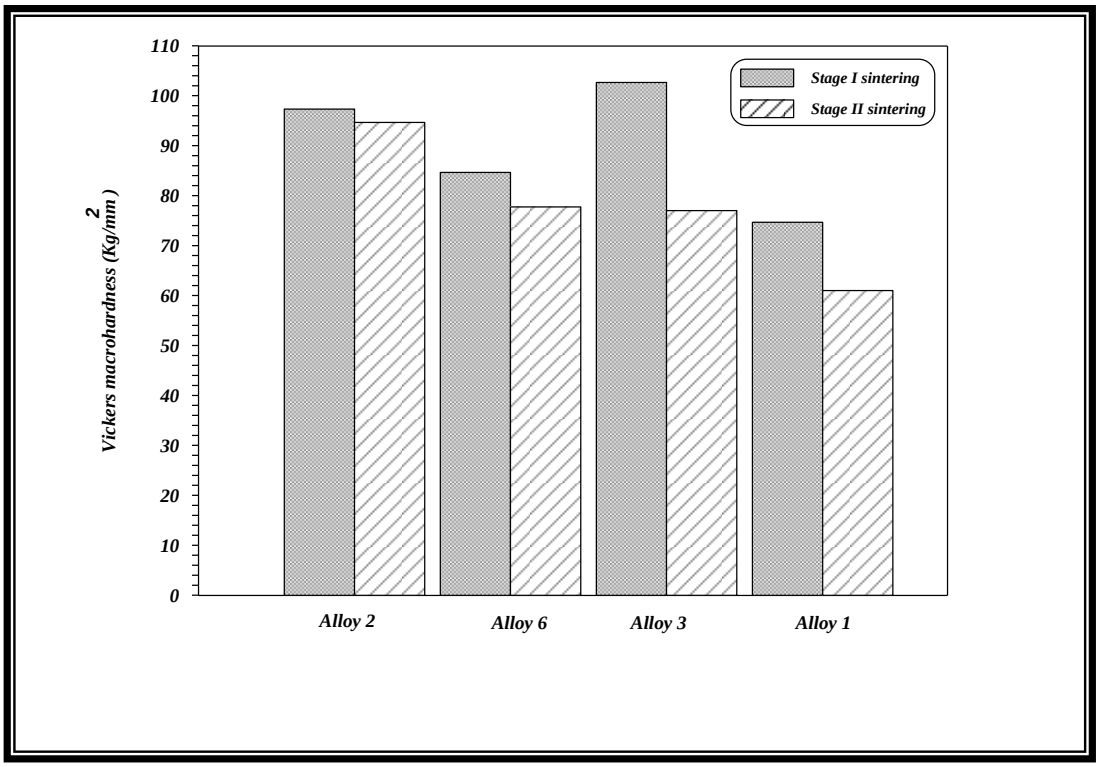

Fig.(6.62) Vickers macrohardness for sintered compacts 1,2,3 and 6 after stage I and stage II sintering.

6.4. Effect of heat treatment after sintering .

Different heat treatment such as direct quenching step – quench and aging after quenching are studied. Effects of these heat treatments on the X- ray diffraction patterns, LOM image, SEM image , hardness and compression are discussed and presented as follows:

6.4.1 X-ray diffraction Patterns for Direct quench treatment .

The sintered samples from (1 to 26) are heated from room temperature to 840 ^{o}C for 30 min., 60 min, and 140 min . After this , all heated samples are quenched in ice water at 2- 4 ^{o}C. To identify martensitic structure, x-ray diffraction technique is based . It is achieved from 10 deg. to 90 degree of diffraction angle (2θ). After x-ray diffraction patterns for alloys (from 1 to 26) are obtained , the same samples are heated to 450 ^{o}C for 30 min. and slow cooling in furnace up to 150 ^{o}C and cooling air from 150 ^{o}C. These reheated specimens are analyzed with x-ray diffraction in order to identify phases and to identify phases and to compare with direct quench x-ray diffraction patterns.

Fig. (6.63) shows x-ray diffraction patterns of alloy 1 for direct-quench treatment in a whereas b. shows x-ray diffractogram for reheating up to 450 ^{o}C for 30 min. treatment. It is shown that typical pattern of $\beta'(Cu_3Al)$ martensite phase has been formed during quenching. The crystallographic of β' phase is orthorhombic with primitive space group. Whereas $\gamma_2(Al_4Cu_9)$ precipitates in the reheating heat treatment without any retained $\beta'(Cu_3Al)$ which has cubic unit cell. It is probably that martensite is decomposed in to $\alpha + \gamma_2(Al_4Cu_9)$ phase completely due to low transformation temperatures with respect to the other alloys due to low content of aluminum in alloy 1.

Several empirical relationships are useful in obtaining estimated transformation temperature as: [Wu, 1990].

$$M_s(^oC) = 2020 - 45(wt\%Ni) - 134(wt\%Al) \quad \text{----- (6.2)}$$

It is shown from Fig.(6.63) that the intensity of (1210) plane is 3117 whereas the intensity of γ_2 in the plane (330) is 3313 (cps) which is greater than the first. Most intensities of martensitic structure (orthorhombic) is lower that in the case of $\gamma_2\,(Al_4Cu_9)$ phase due to high atomic packing in the γ_2 phase which cubic.

Fig.(6.64a) shows the diffractogram of martensitic transformation in alloy 2 which is hybereutectoid alloy. There is only one phase which is martensite in the x-ray diffraction pattern of retained martensite and γ_2 phase are explained in Fig.(6.64b.).Note that in order to decompose all β' phase into $\alpha + \gamma_2$ phase , it is required additional timer or high temperature. 30 min at 450 ^oC is not enough decompose $\beta' \rightarrow \alpha + \gamma_2$ Completely. Therefore, It is probably that alloy 2 has shape memory properties at higher temperature than alloy 1 because there is remain martensite phase up to 450 ^oC . High intensity about 2568 (cps) occurs at diffraction angle (2θ) = 44.6 degree for β' phase whereas the maximum intensity (4176 cps) of γ_2 phase at diffraction (2θ) = 42.5 degree.

For Fig. (6.65) which has titanium additive to alloy 2 as base alloy as (0.4 wt %) , It is shown that this alloy forms completely martensite phase ($\beta' = Cu_3Al$) when their sample are quenched in ice water at (2-4 ^oC) Titanium additive refine the microstructure and rise the martensitic transformation temperatures. Thus these alloys have desired shape memory properties at reasonable high temperatures. It is apparent that an addition of Ni in combination with Al form strong intermetallic compounds which leads to increase hardness in copper-aluminum base alloys. In addition , it is also apparent that Titanium functions together with Ni and Al to stabilize the bata phase (β) of Cu- Al alloys and retard the eutectoid reaction of

$\beta \rightleftarrows \alpha + \gamma_2$ and prevent emergence of the brittle ($\alpha + \gamma_2$) structure. It is shown that during heating up to (450 ^{o}C) there is intermetallic compound with titanium alloying element as $[Cu, Al]_2 Ti$

The effect of boron additive as 0.4 wt% on the x-ray diffraction patterns is shown in Fig.(6.66) . It is dear that decomposition of β phase into $\alpha + \gamma_2$ phase is occurred even though high rate of cooling has been used. Addition of boron in Cu Al Ni shape memory alloys effectively suppress subsequent grain growth during betatizing heat treatments. Boron additives have remarkable effects in refining the microstructure. Refining is largely due to the formation of small insoluble particles which either assist grain nucleation or inhibit grain growth so that boron additives have only very slight effects on transformation temperature. It is also shown that there is retained martensite (β') phase during reheating heat treatment as can be seen from Fig. (6.66b) .However , the predominate phase is γ_2 phase which refers to decompose of β phase through eutectoid reaction.

From all x-ray diffraction patterns of most alloys, It has been shown that direct quenching heat treatment promote and stabilize martensite phase for both quench state and even after reheating . It is apparent later that in order to promote reverse direction $\beta \rightleftharpoons \alpha + \gamma_2$ we need to step quench and / or aging treatments However , phase change included martensitic transformation has been satisfied during quenching.

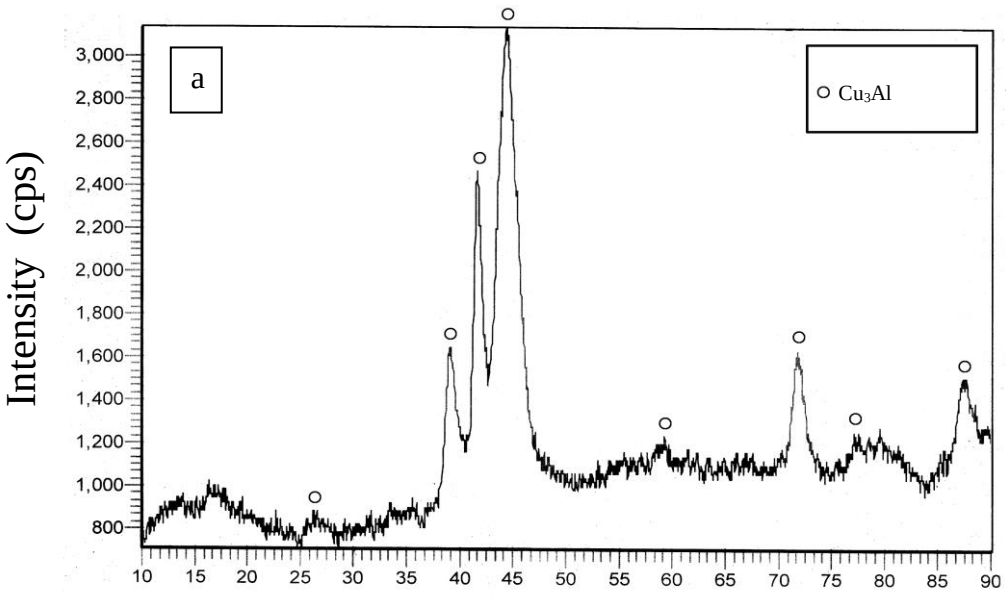

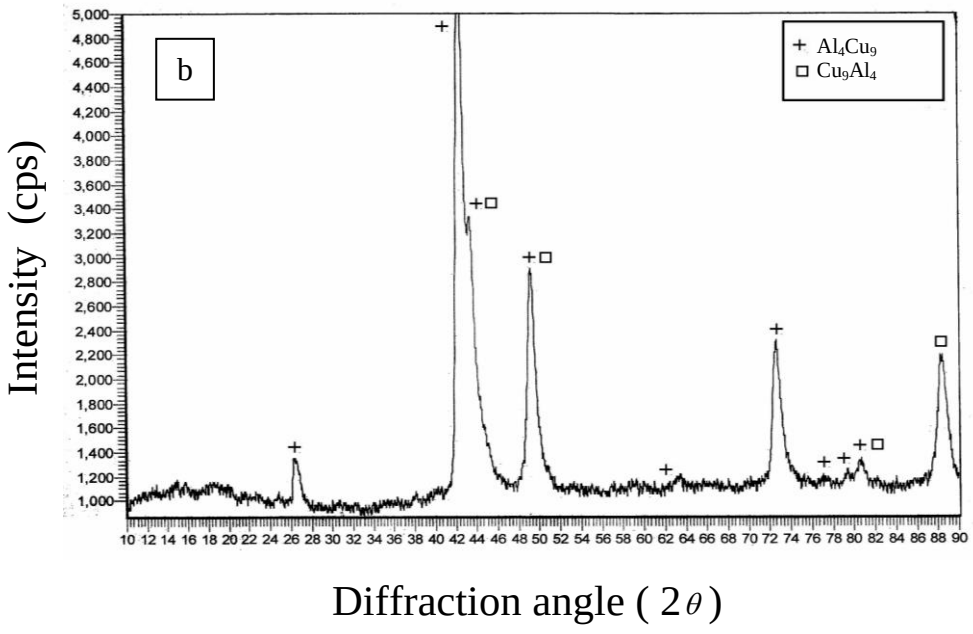

Fig.(6.63) XRD patterns for alloy1 at: a. after quenching from 840 °C for 60 min.to ice water. B. after reheating up to 450 °C for 30 min heat treatment

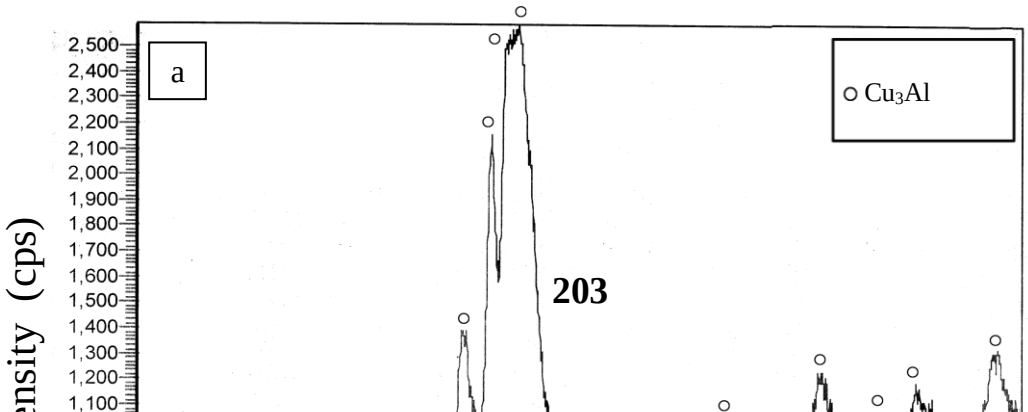

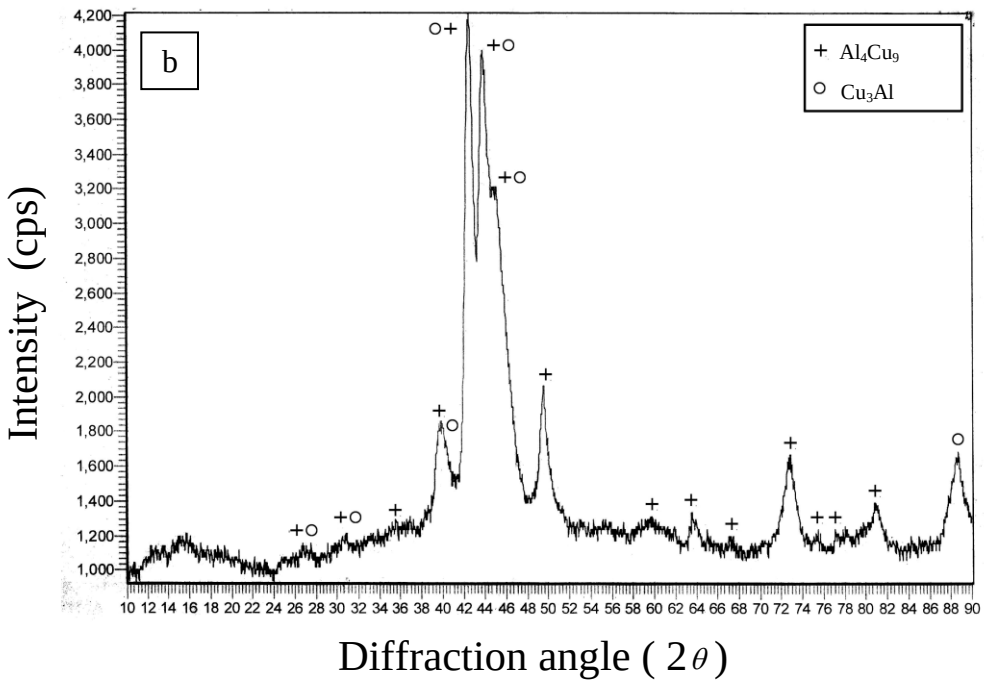

Fig.(6.64) XRD patterns for alloy2 at: a. after quenching from 840 °C for 60 min.to ice water. B. after reheating up to 450 °C for 30 min heat treatment

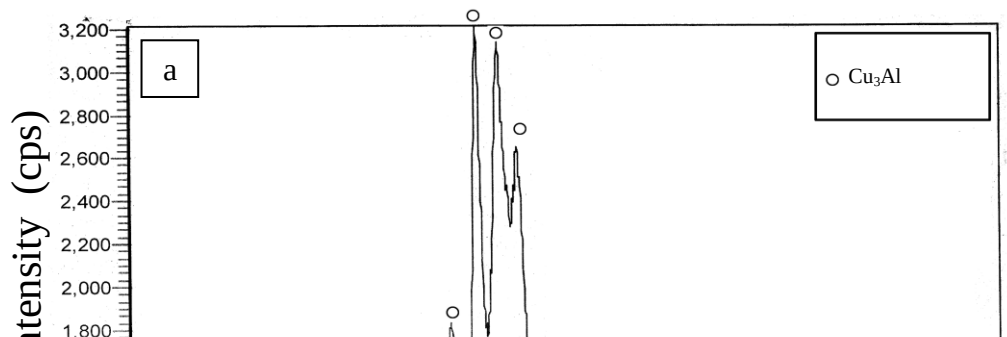

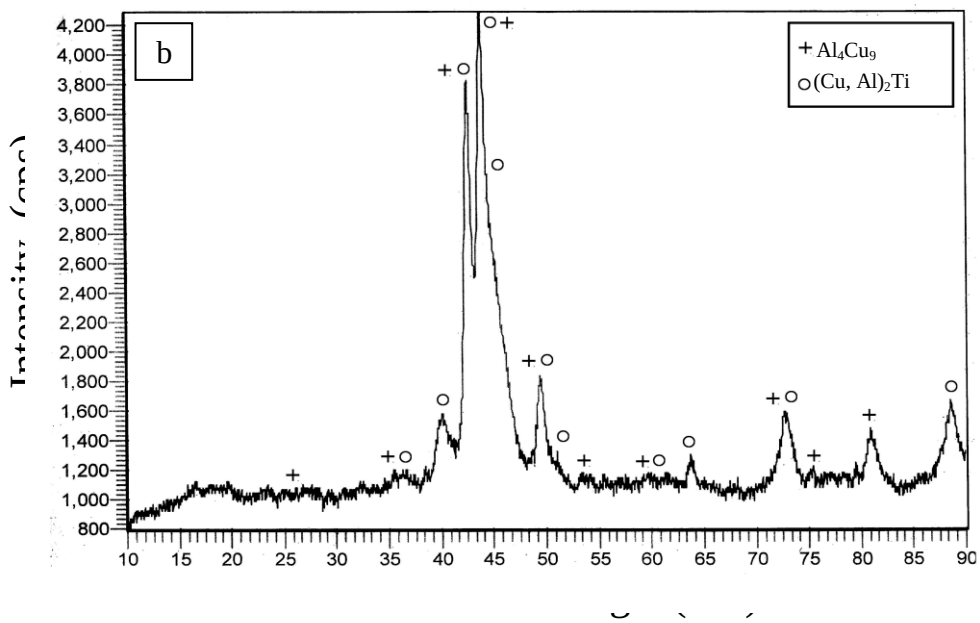

Fig.(6.65) XRD patterns for alloy3at: a. after quenching from 840 ºC for 60 min.to ice water. B. after reheating up to 450 ºC for 30 min heat treatment.

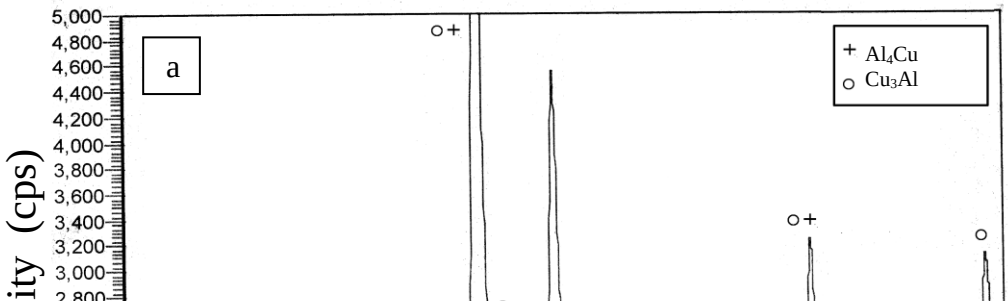

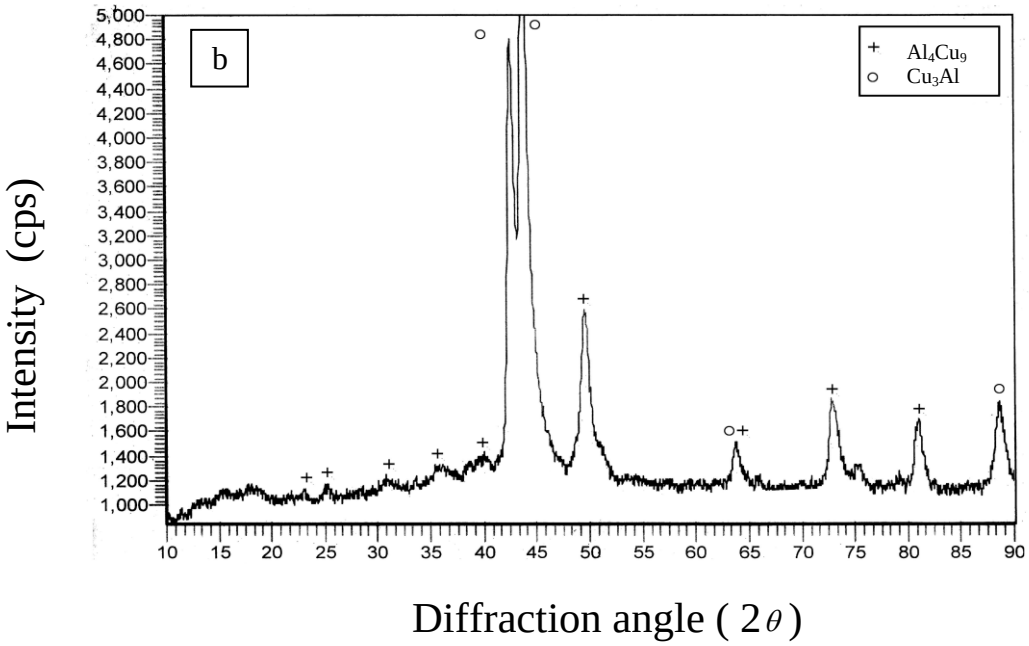

Fig.(6.66) XRD patterns for alloy 6 at: a. after quenching from 840 °C for 60 min.to ice water. B. after reheating up to 450 °C for 30 min heat treatment.

6.4.2.Light optical microscope images for Direct quench heat treatment.

Light optical microscope images for alloys (1,2,3, ….. 26) have been shown in Figs. (6.67) , (6.68) , (6.69) and Fig.(6.70).

The microstructure of these alloys are fine grains for etched specimens with [NH_4OH+ H_2O_2 + H_2O] etching . Sometime , martensite platelet has been clear but others is not clear due to fine structures and probably due to type of used etching.

It is apparent that martensite phase is formed near the pores in all specimen microstructures. Thus , pores as a defect may be promoted the martensitic phase transformation in porous alloys. It has been shown that martensitic structures viewed using (LOM) nearly always consist of plates that are very similar in appearance regardless of the alloys composition in which they have formed.

The internal microstructure of the martensite however , varies greatly among different alloys and con not be resolved by LOM.

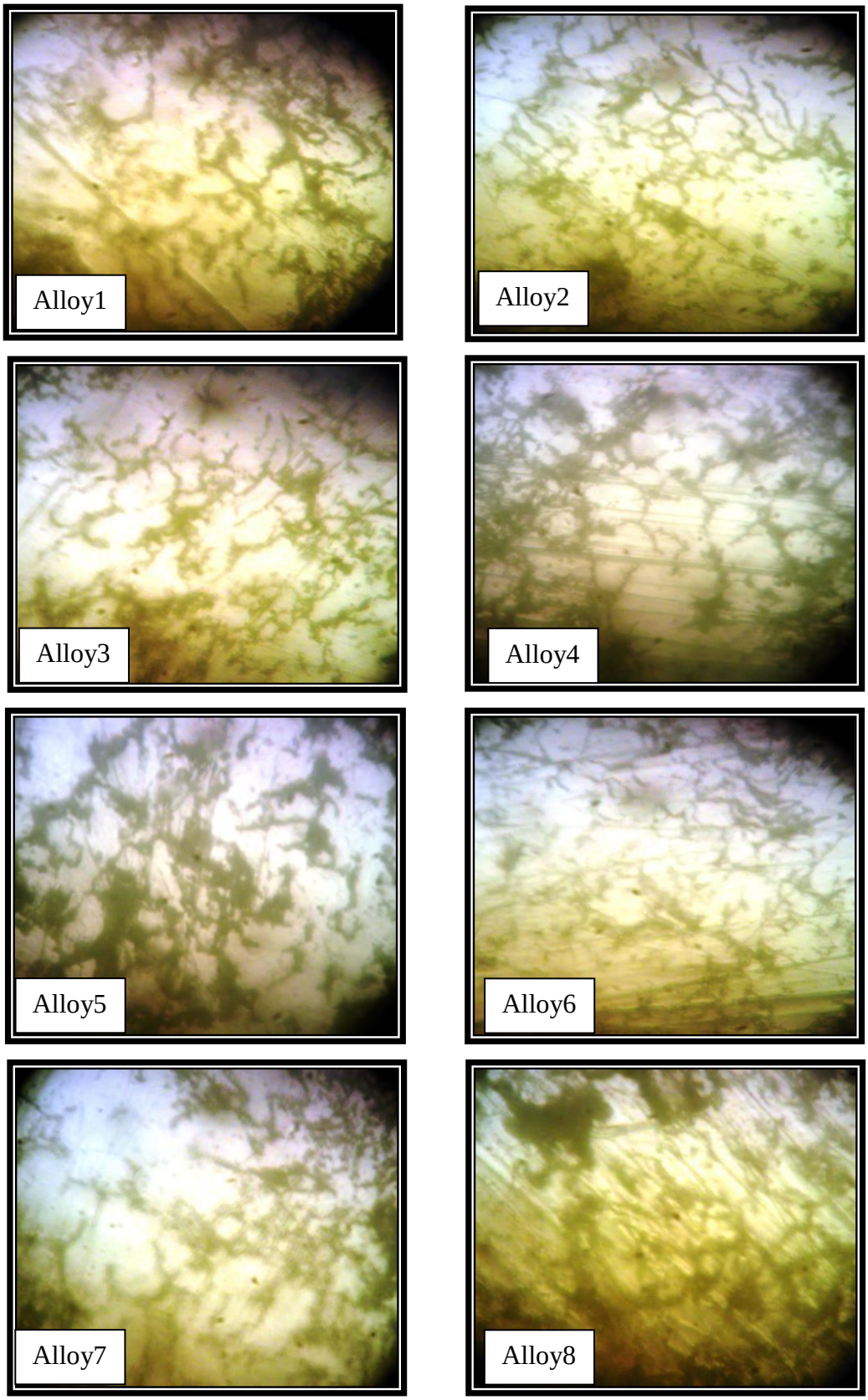

Fig.(6.67) LOM images for direct quench alloys 1,2,3,4,5,6,7 and 8 1000X.

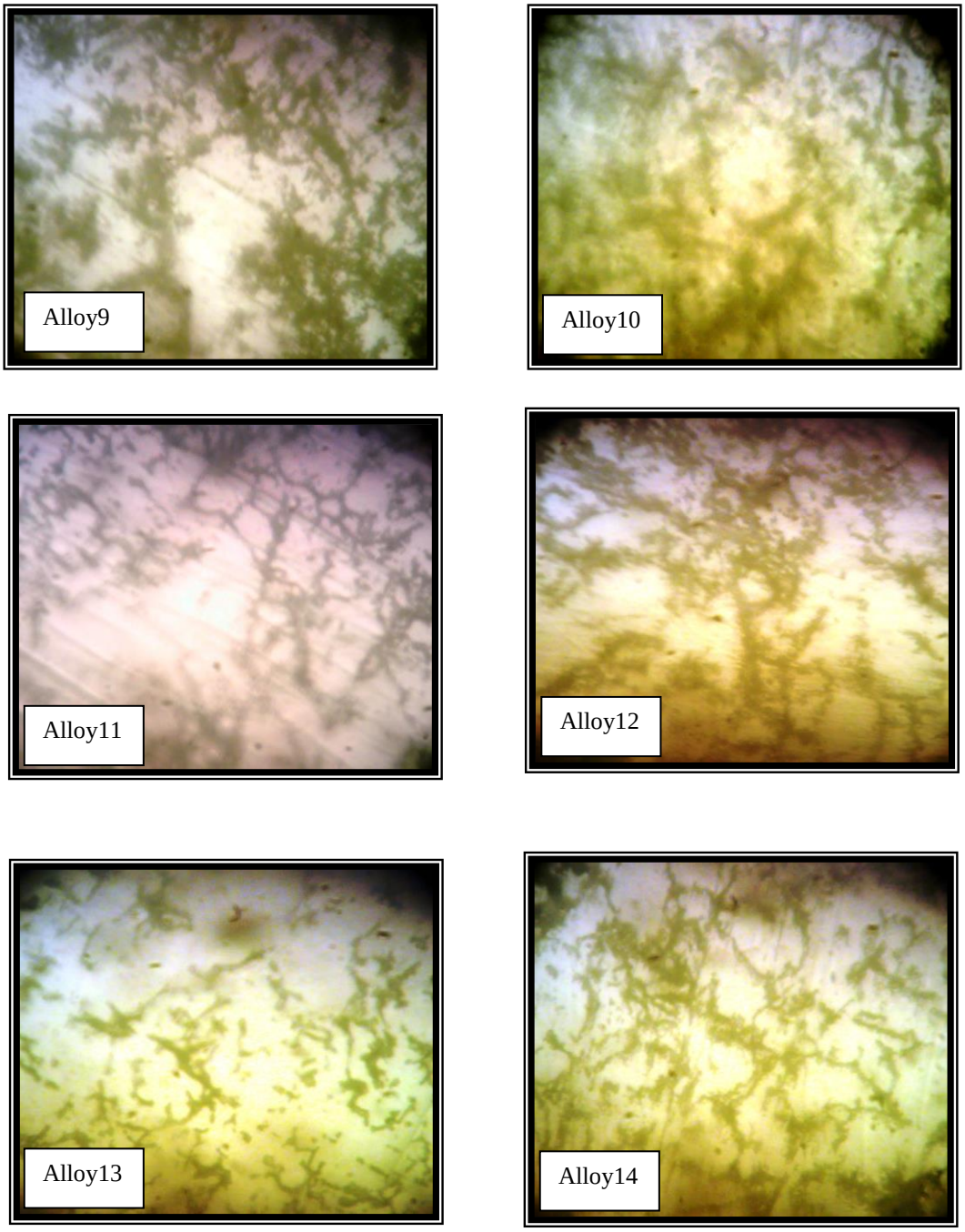

Fig.(6.68) LOM images for direct quench alloys 9,10,11,12,13 and 14 1000X.

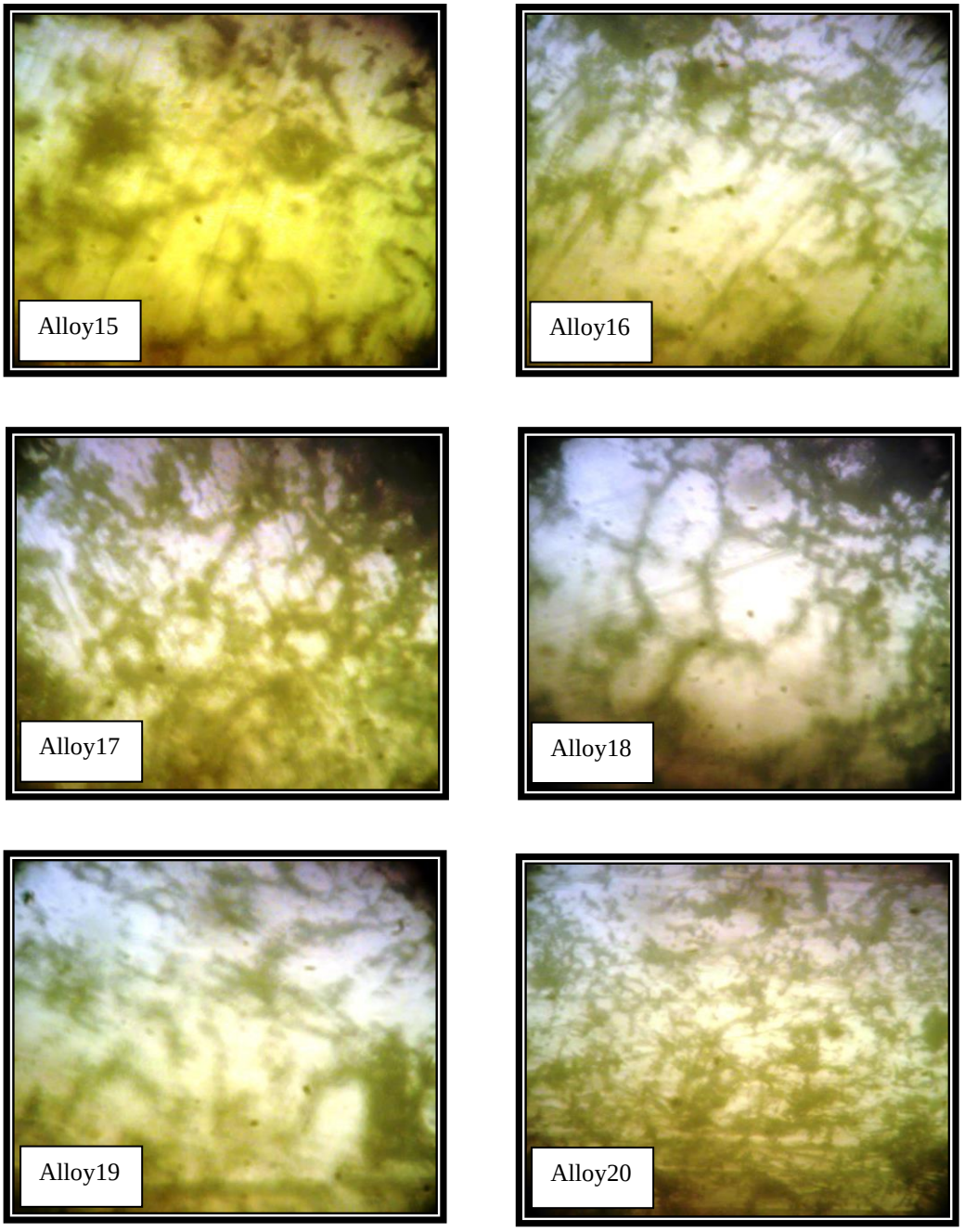

Fig.(6.69) LOM images for direct quench alloys 15,16,17,18,19 and 20 1000X.

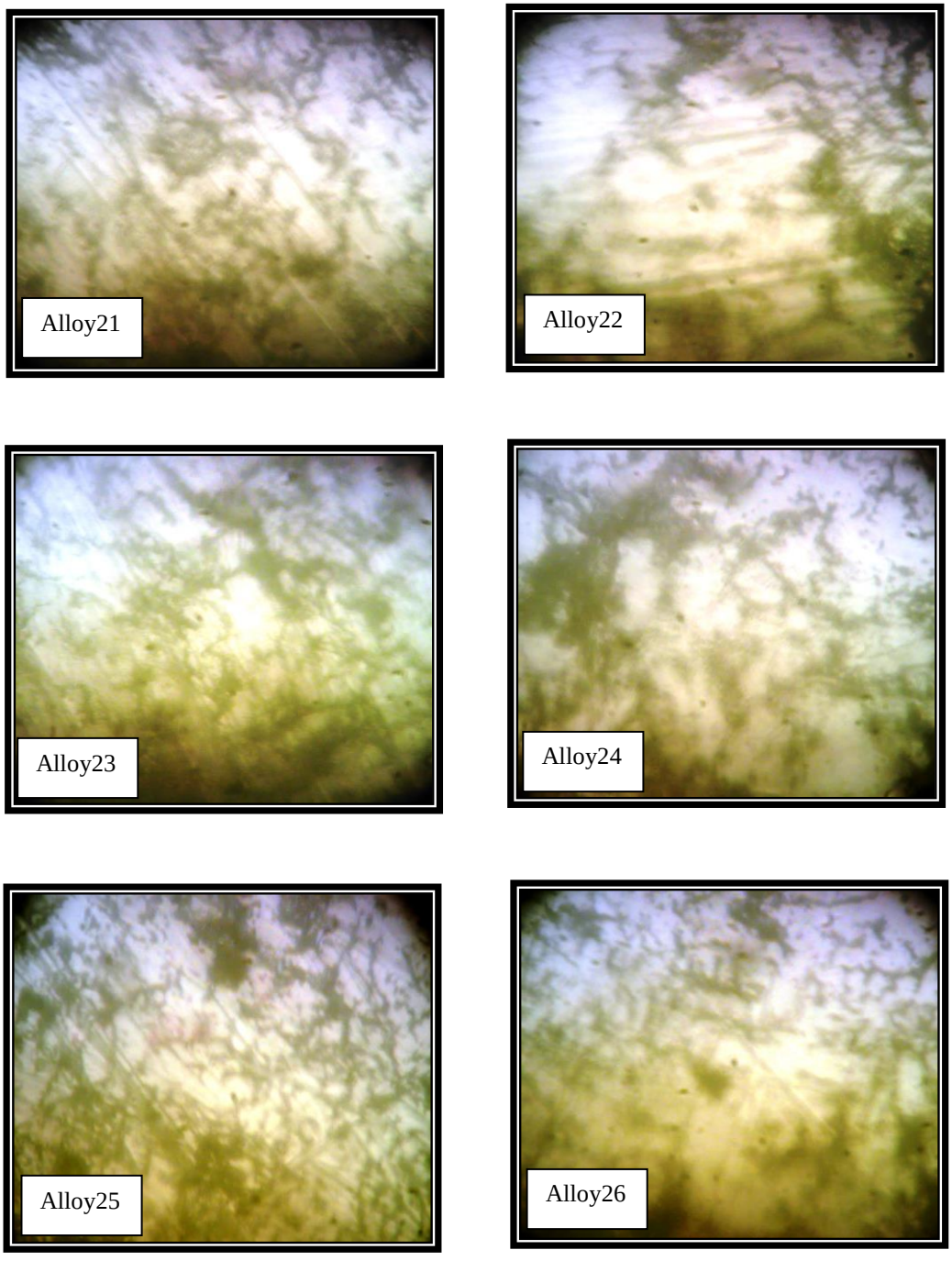

Fig.(6.70) LOM images for direct quench alloys 21,22,23,24,25 and 26 1000X.

6.4.3 Scanning electron microscope images.

Scanning electron microscope images for unetched specimen of alloys 1,2,3 and 6 are shown in Fig.(6.71), (6.72) , (6.73) and Fig. (6.74) .It is very important to examine sintered parts in the unetched condition which displays the number and distribution of original particle boundaries present.

Scanning electron microscope images for etched specimen of alloys 3 and alloy 6 are shown in Fig.(6.75) and Fig.(6.76) respectively. Etching reveal grain boundaries which are easily confused with the particle boundaries that also appear as thin gray or black lines. Cracks , particles and pore shape are easier to locate in the absence of distracting features.

The martensite formed in all alloys has a plate shape . This appearance is independent of the following parameters: -

1) The crystal structure of the martensite phase.
2) Whether the internal structure is twinned or faulted.
3) The presence or absence of crystallographic order.

Because of diffusionless feature of martensitic transformation , the order or disorder of the parent phase (β) is transferred in to martensite. Disordered B_2 copper- aluminum alloys (β) form disordered hcp martensite (β') whereas ordered B2 in Cu- Al system forms ordered orthorhombic martensite that is internally faulted (β').Growth of martensite plates is restricted by the grain boundaries of the parent phase or by previously formed plates.

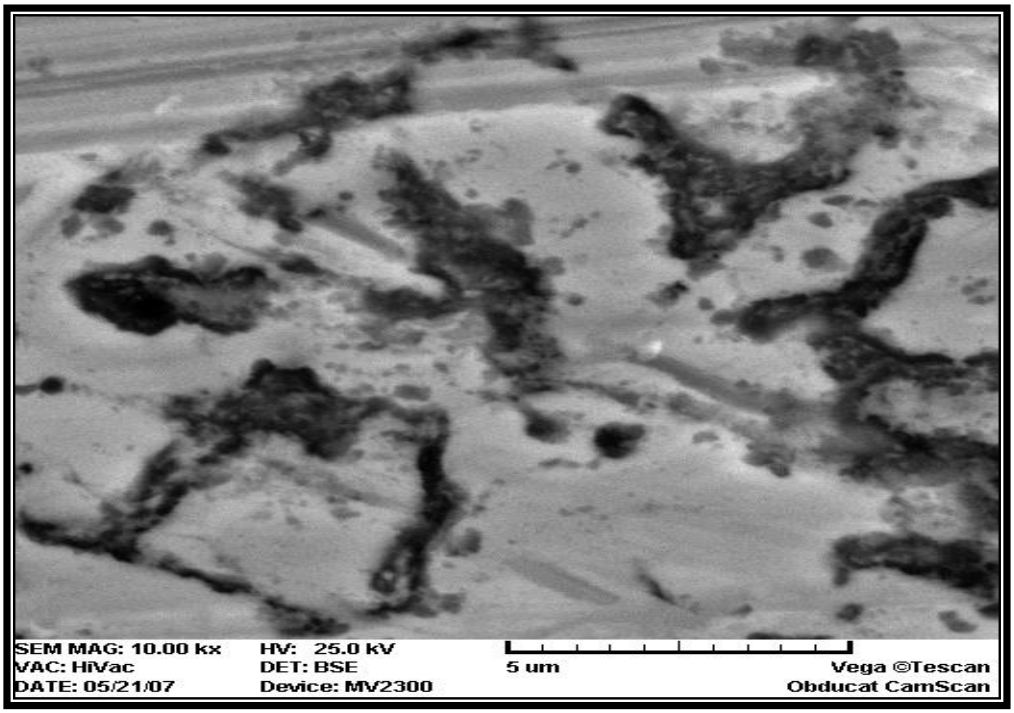

Fig.(6.71) SEM image for unetched alloy 1 in direct quenching state.

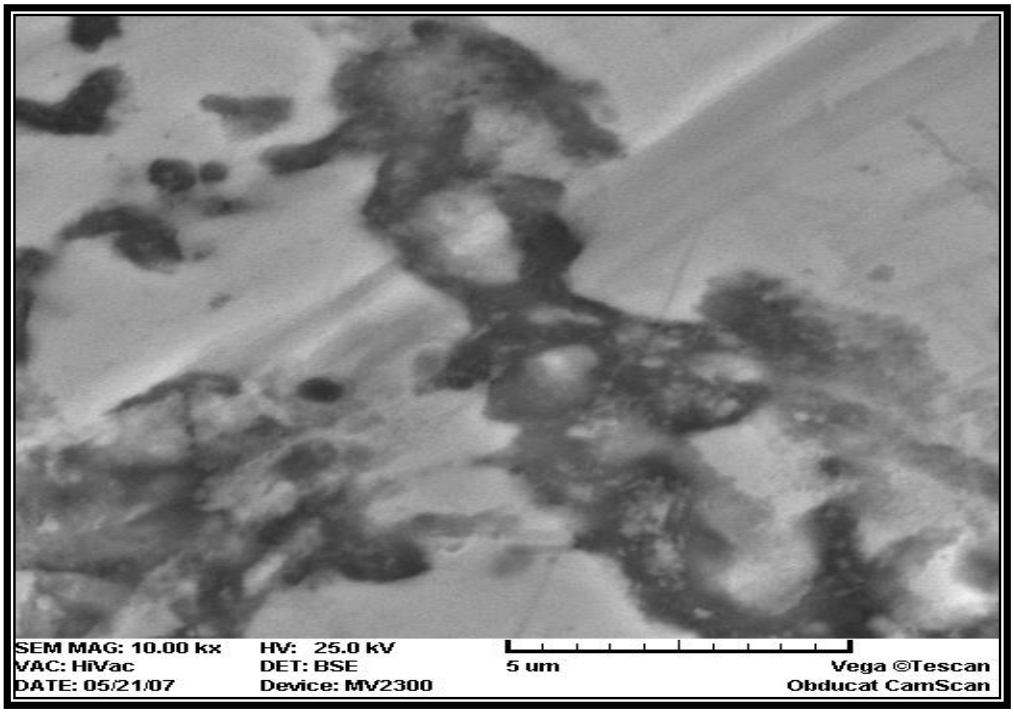

Fig.(6.72) SEM image for unetched alloy 2 in direct quenching state.

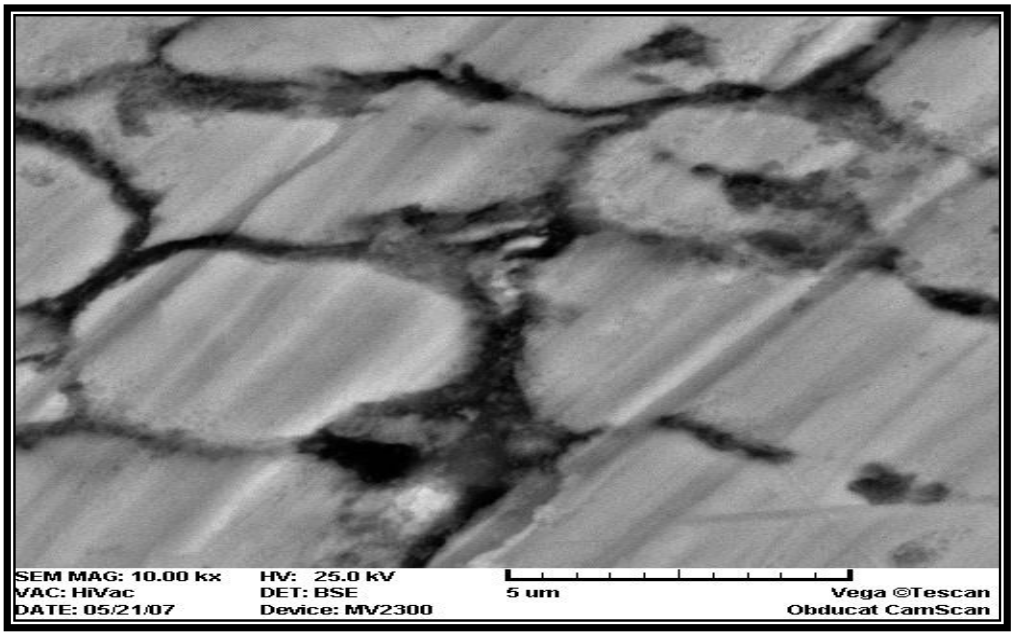

Fig.(6.73) SEM image for unetched alloy 3 in direct quenching state.

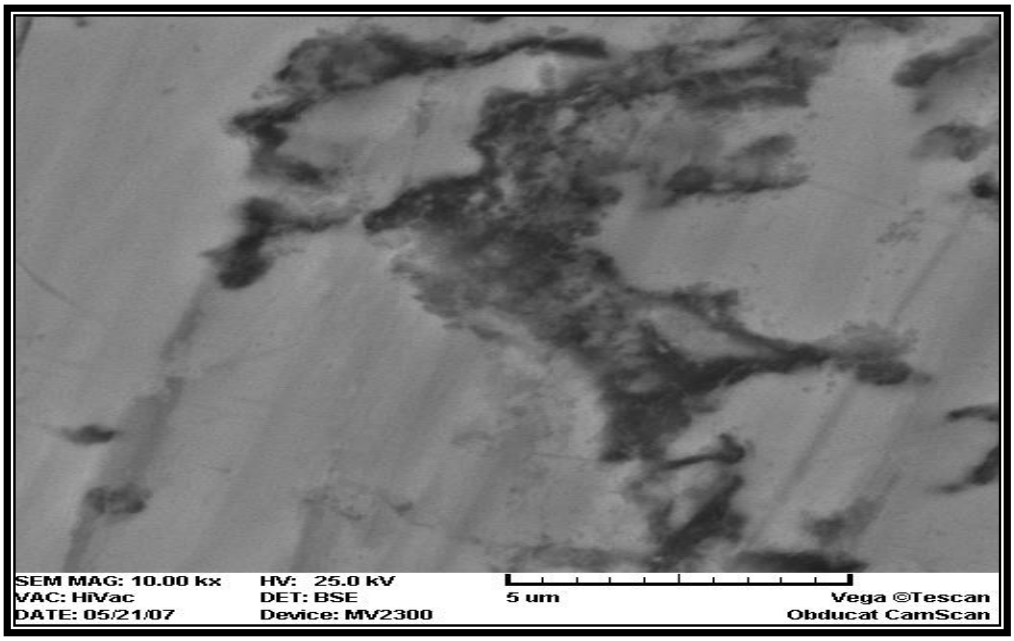

Fig.(6.74) SEM image for unetched alloy 6 in direct quenching state.

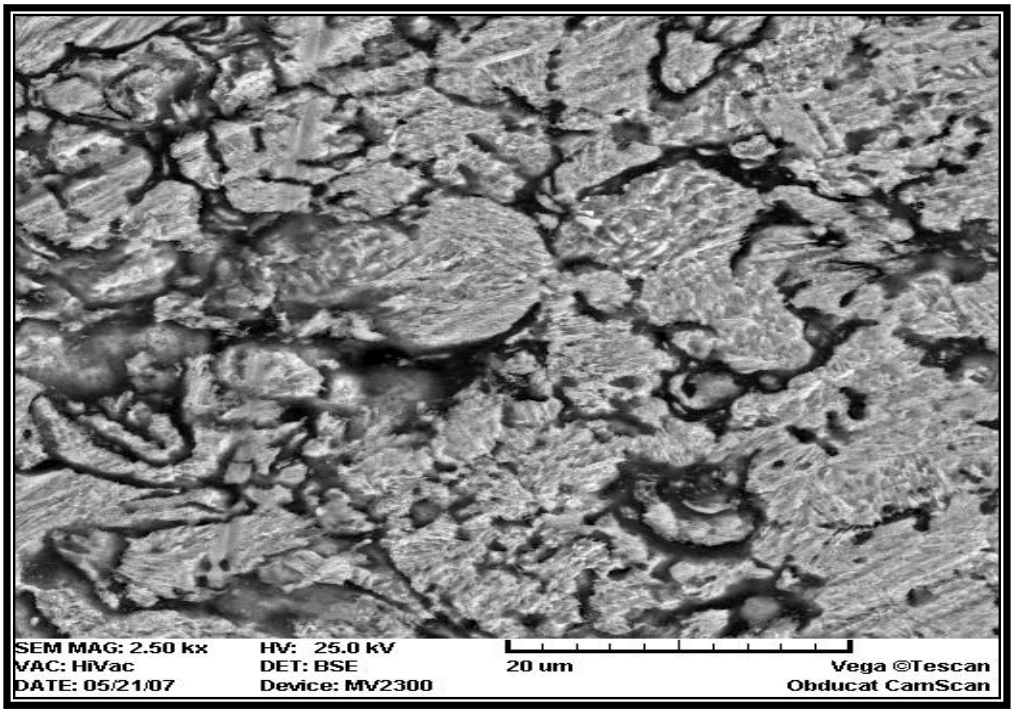

Fig.(6.75) SEM image for etched alloy 3 in direct quenching state.

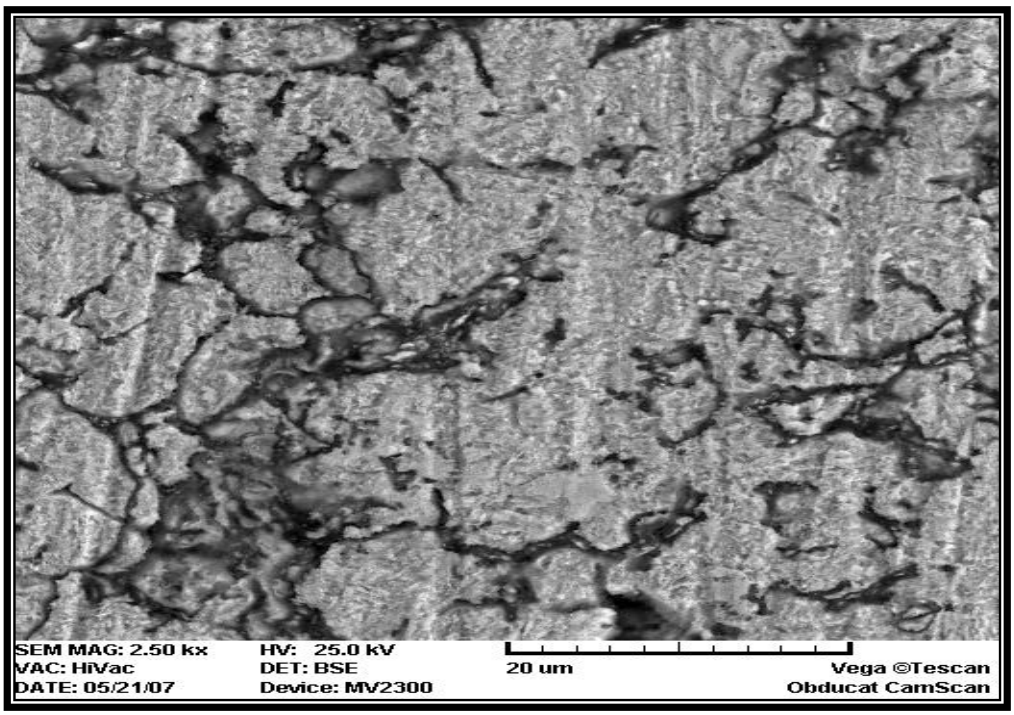

Fig.(6.76) SEM image for etched alloy 6 in direct quenching state

6.4.4 Hardness Test results for direct quenching heat treatment .

Vicker's microhardness using 500 g as maximum load as a function of weight percent of alloying element is shown in Fig.(6.77). These results for 26 alloys with three readings when the holding time at 840 ^{o}C is 60 min. when holding time is 30 min. microhardness is shown in Fig.(6.78) whereas for 140 min. as holding time of direct quench heat treatment it's results for microhardness is shown in Fig.(6.79).

It has been clear that Vicker's microhardness is fluctuated according to weight percent of most alloying element. This is probably due to presence of pores and its distribution through the specimen. Furthermore , Vicker's microhardness indenter may be lied on the pore or pore edge which leads to fluctuate reading results. In addition , not all alloying element added to based alloy have the same function on the hardness. Thus ,some of these alloying elements such as silicon gives hardness increment with its weight percent whereas a combination of(Ti+ Mn) leads to give higher hardness of the base alloy. It is probably that manganese stabilizes the intermetallic compound formed with fourth element (Ti or Zr for example) with Cu+Al+Ni systems. In general 0.4 wt % of alloying element has the greatest value of vicker's microhardness for most holding time from (30 min to 140 min.).

Brinell macrohardness with returned ball tester , has been shown in Fig.(6.80) for alloying element action . It is apparent that fluctuating of Brinell hardness valves are less than that is for vicker's microhardness. This is due to the large indentation ball with comparison with vicker's indenter. It is also apparent that Brinell hardness decreases with higher content of alloying element as 1.2 wt% of these elements. This is probably that when alloying weight percent is increased, holding time to dissolve this percent must also be increased to diffuse this higher weight percent so that it is probably that 60 min.as holding time is not enough so some intermetallic compounds does not form. Martensite phase during quenching through promoting decomposition of β phase $\alpha + \gamma_2$ phases.

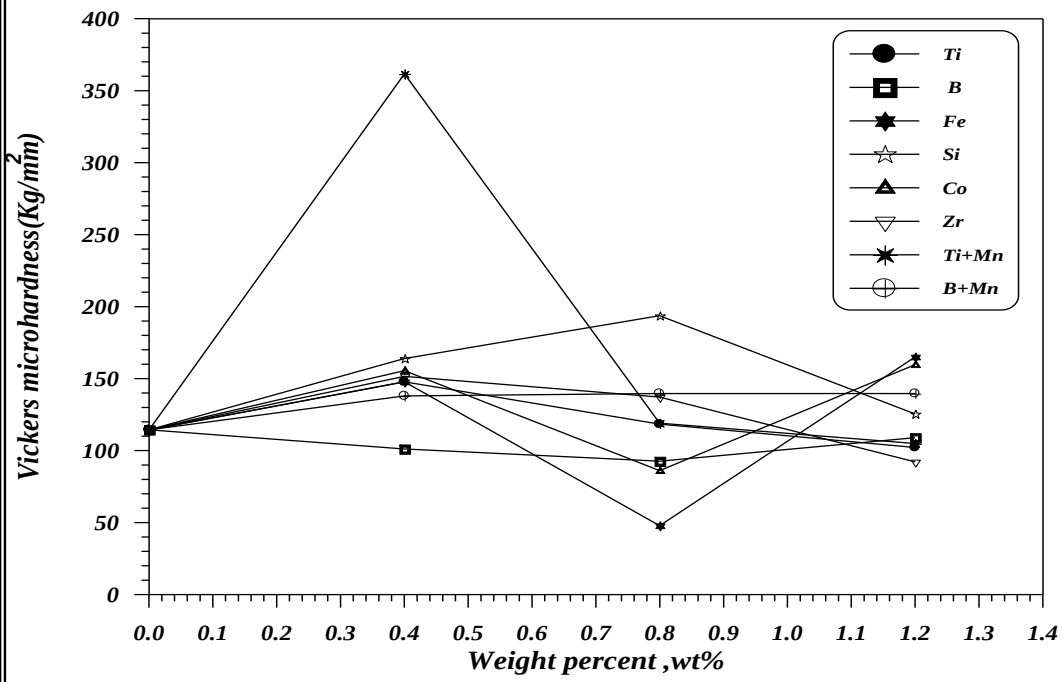

Fig.(6.77) Vickers microhardness as a function of alloying element for30 minute holding time of solution treatment.

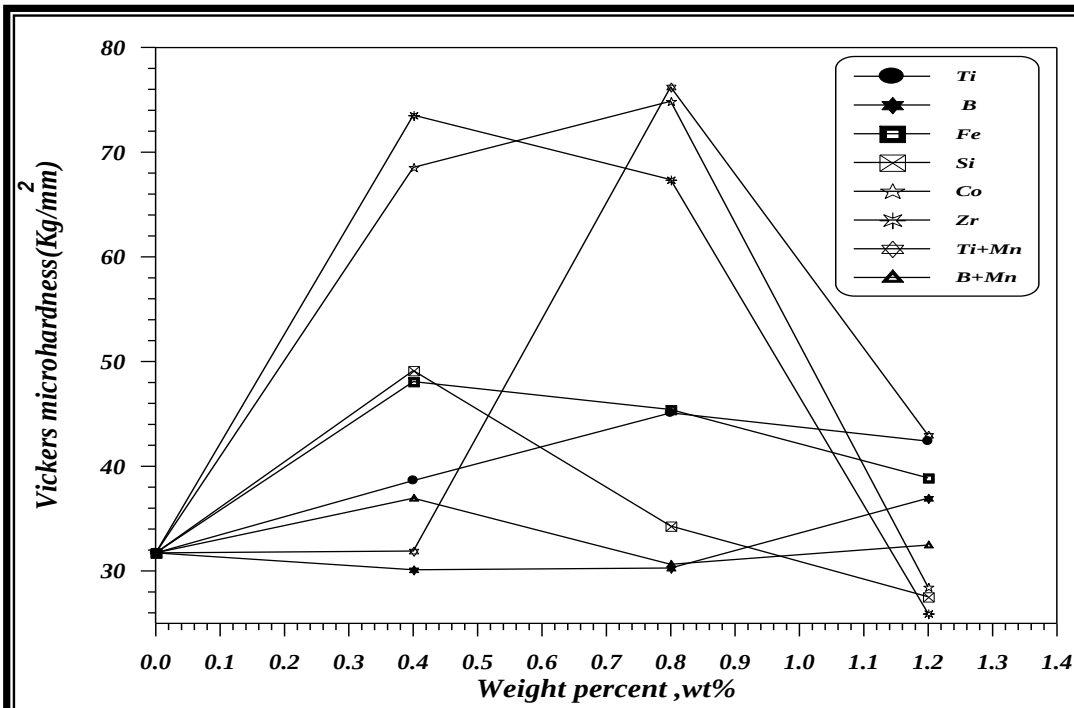

Fig.(6.78) Vickers microhardness as a function of alloying element for60 minute holding time of solution treatment.

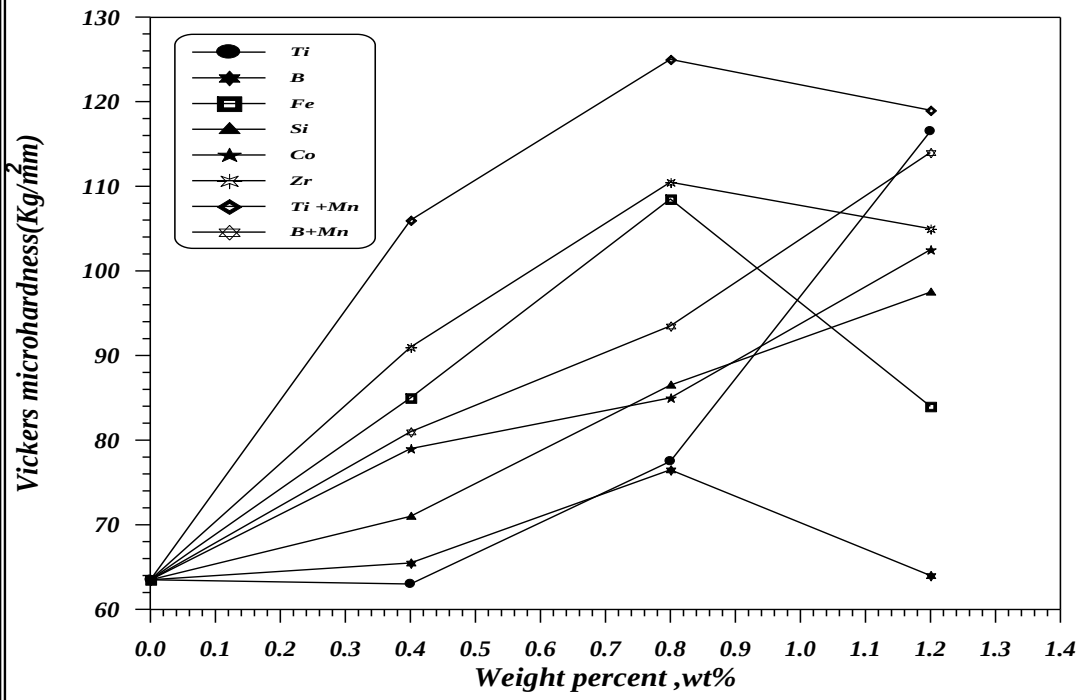

Fig.(6.79) Vickers microhardness as a function of alloying element for140 minute holding time of solution treatment.

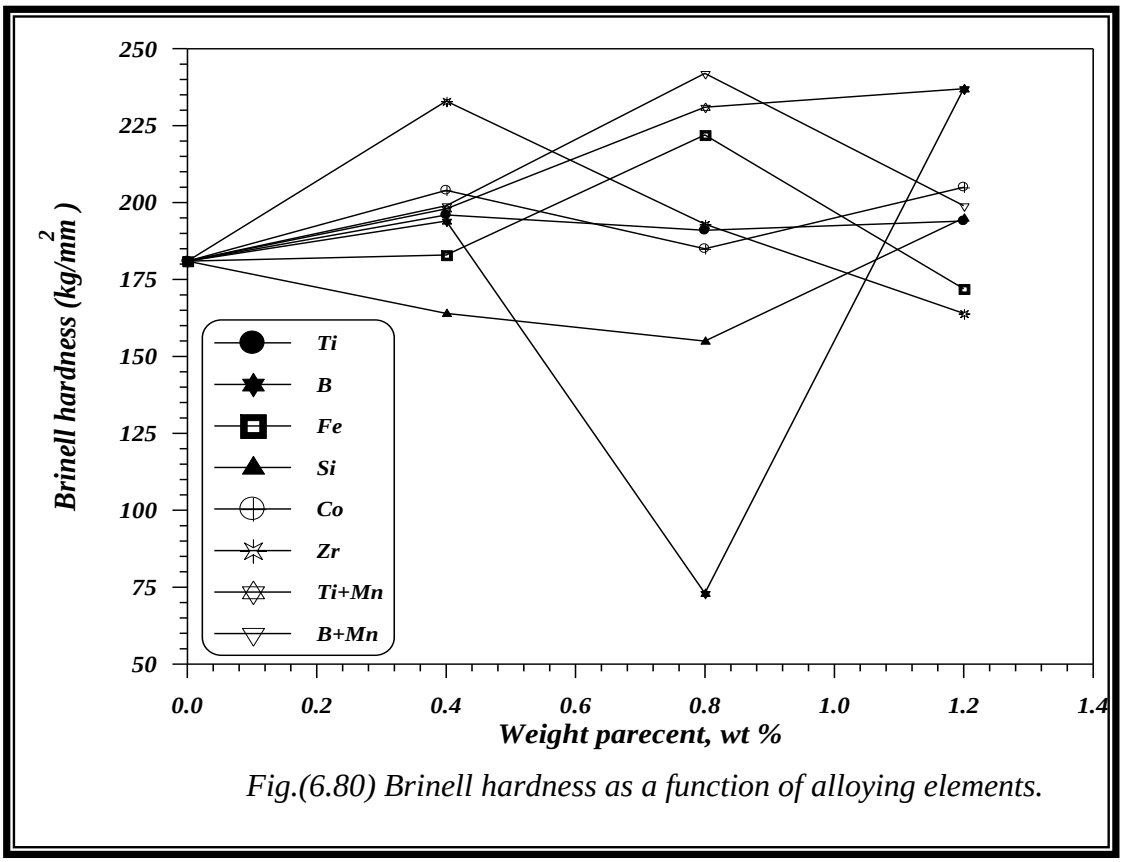

Fig.(6.80) Brinell hardness as a function of alloying elements.

6.4.5 Electrical Resistance test results

Electrical resistance test has been done for quenched specimen by heating them up to 170 ^{o}C and further cooling them to room temperature or slow below room temperature using cold water in the surrounding container. Electrical resistance results for both heating and cooling for alloy 1 have been shown in Fig. (6.81).

It is clear that there is wide range of transformation temperature during heating (A_s and A_f) and through cooling (Ms and Mf) . This is probably due to presence of pores which isolate the internal structure for heating and cooling. Thus , the specimen has been required more time to stabilize the temperature .During heating ,the first peek is referred to begin transformation in to parent phase (β) but the second peek or sharp change in electrical resistance curve referred to end of phase transformation. However, during cooling the first peek is referred to martensite final and the second referred to martensite final. Electrical resistance as a function of temperature for alloy 2 has been shown in Fig. (6.82) , whereas Figs. (6.83) and (6.84) show the electrical resistance results as a function of temperature for both heating and cooling for alloys 3 and 6 respectively.

It is apparent that the same wide range of transformation temperature for both of heating and cooling have been occurred due to presence of pores and non uniform pores distribution which are affected on the distribution of heat or temperatures through the specimen. Relative units of electrical resistance of specimen refer to divide electrical resistance for specimen to electrical resistance of the equipment (wires and cell).

It is clear that electrical resistance of metals and alloys are increased when temperature is raised but here, when phase transformation is occurred , drop or peak. Of electrical resistance readings have been obtained where the internal phase change is occurred in the specimen.

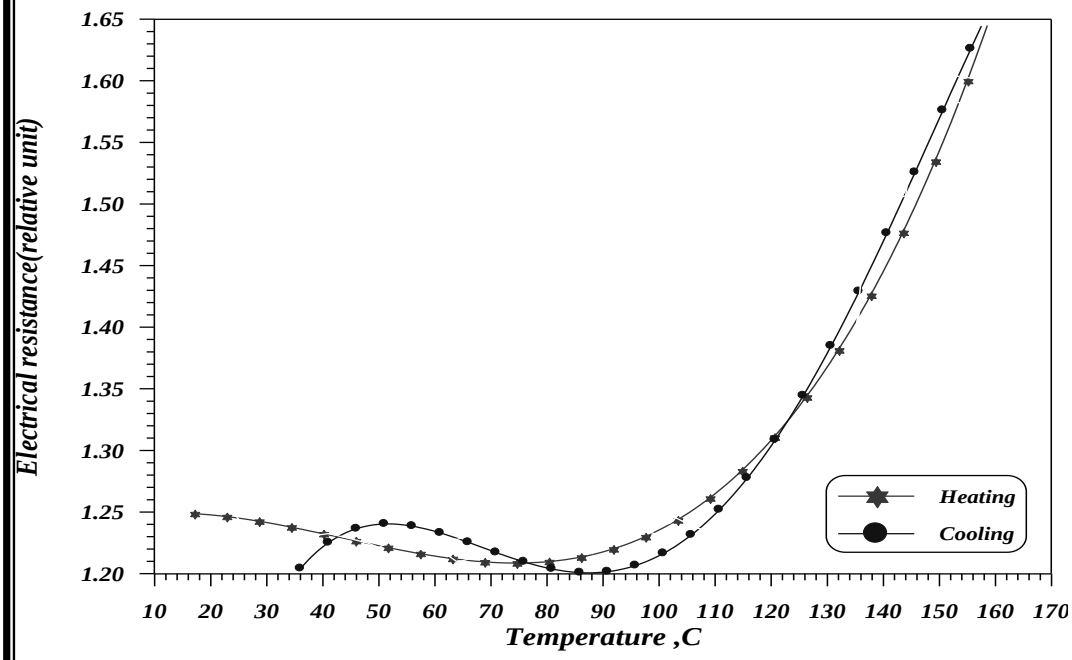

Fig.(6.81) Electrical resistance as a function of temperature for direct quench alloy 1 specimen.

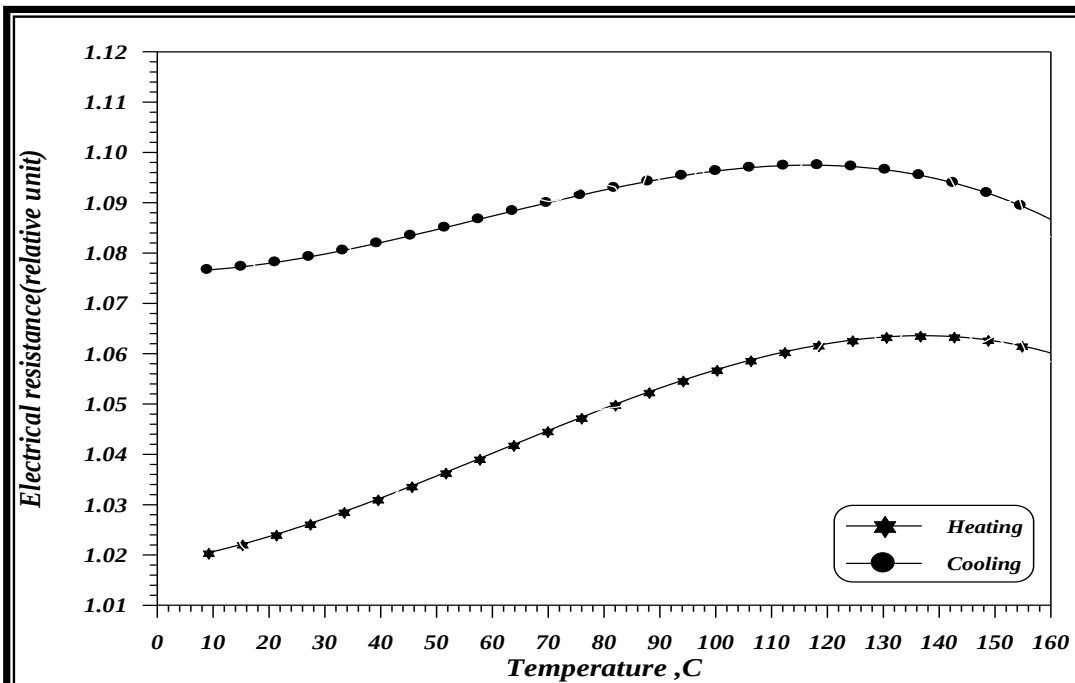

Fig.(6.82) Electrical resistance as a function of temperature for direct quench alloy 2 specimen.

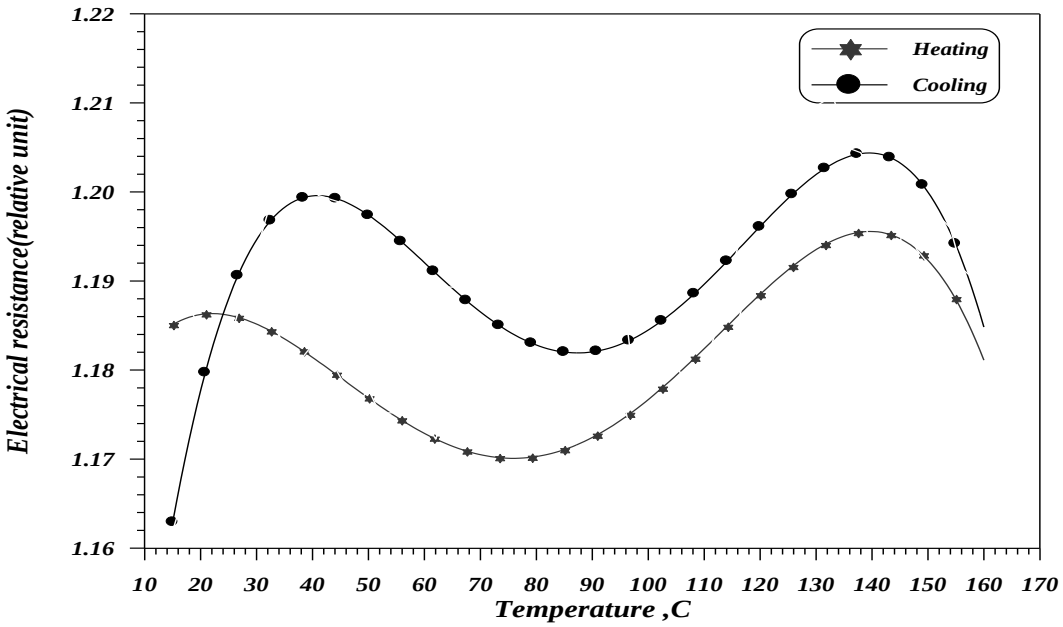

Fig.(6.83) Electrical resistance as a function of temperature for direct quench alloy 3 specimen.

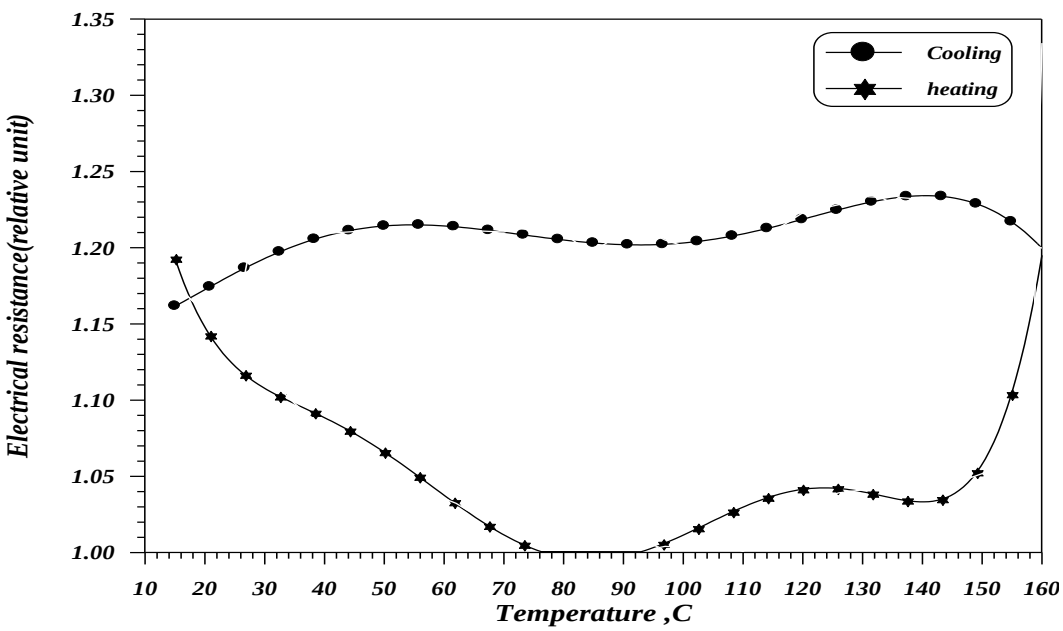

Fig.(6.84) Electrical resistance as a function of temperature for direct quench alloy6 specimen.

6.4.6. Ultrasonic test results

The aim of ultrasonic test is to satisfy the phase transformation of all specimens in quenched states and in reheating states.

Ultrasonic test has been done for cylindrical specimens with (0.01) m diameter and (0.04) m height.

After compression up to 8 % total strain in martensitic state and after reheating up to 150 ^{o}C for 10 min. state , ultrasonic test has been carried out. Time of ultrasonic test has been carried out. Time of ultrasonic wave transferred as a function of weight percent of Ti , B , Fe ,Si , Co, Zr, Ti+ Mn and B+Mn for both two case are shown in Figs.(6.85) , (6.86) , (6.87) (6.88) ,(6.89), (6.90) , (6.91) and Fig. (6.92) respectively.

It is clear that all alloying elements decrease time of wave transferred except Boron element. In addition , there is a difference between time of wave transferred through compressed specimens and reheated specimens due to change in phases for both cases. It is also apparent that time of ultrasonic wave for parent phase is lower than martensitic phase in the range of addition between (0.8 % to 1.2 %).

Ultrasonic test as nondestructive inspection is useful to calculate mechanical properties such as young modulus , shear modulus and poison's ratio. In this study , modulus of elasticity and other mechanical properties have been determined by destructive compression tests. Any way , comparison between experimental data in cases may be given with suitable correcting factor.

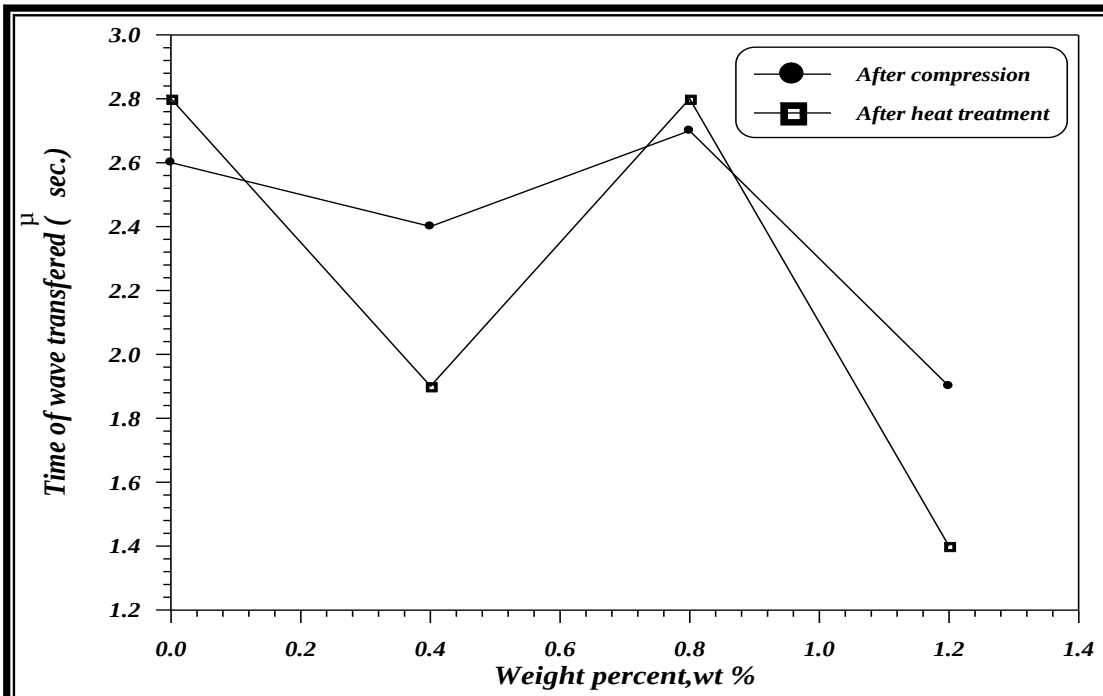

Fig.(6.85) Time of wave transferred as a function of weight percent of Ti.

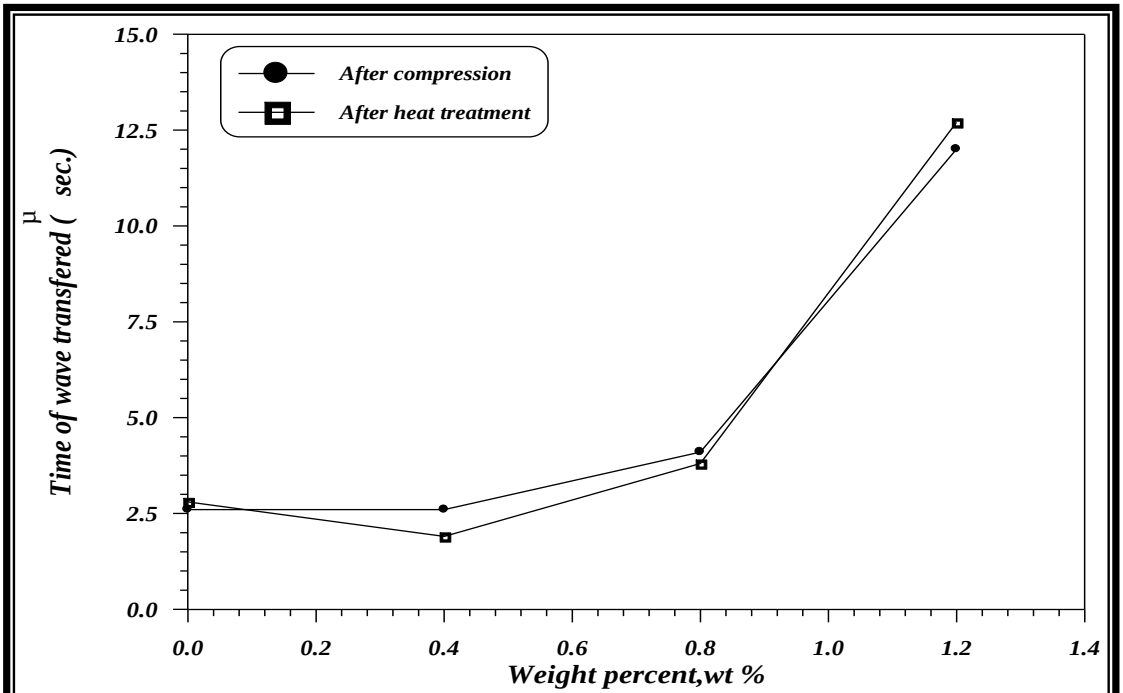

Fig.(6.86) Time of wave transferred as a function of weight percent of B.

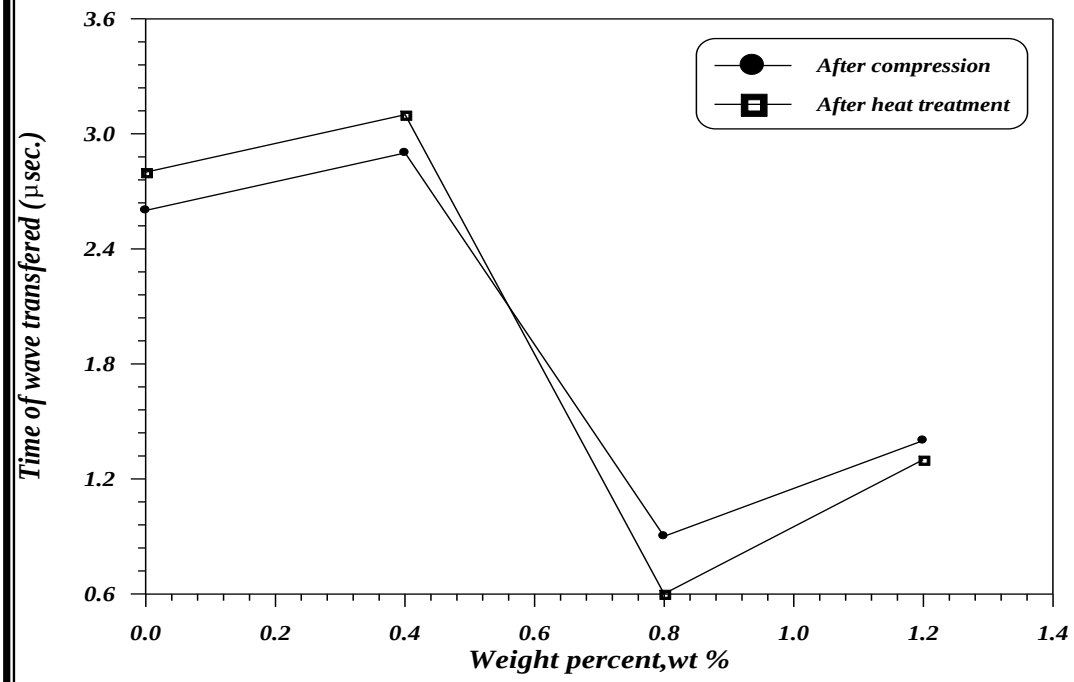

Fig.(6.87) Time of wave transferred as a function of weight percent of Fe.

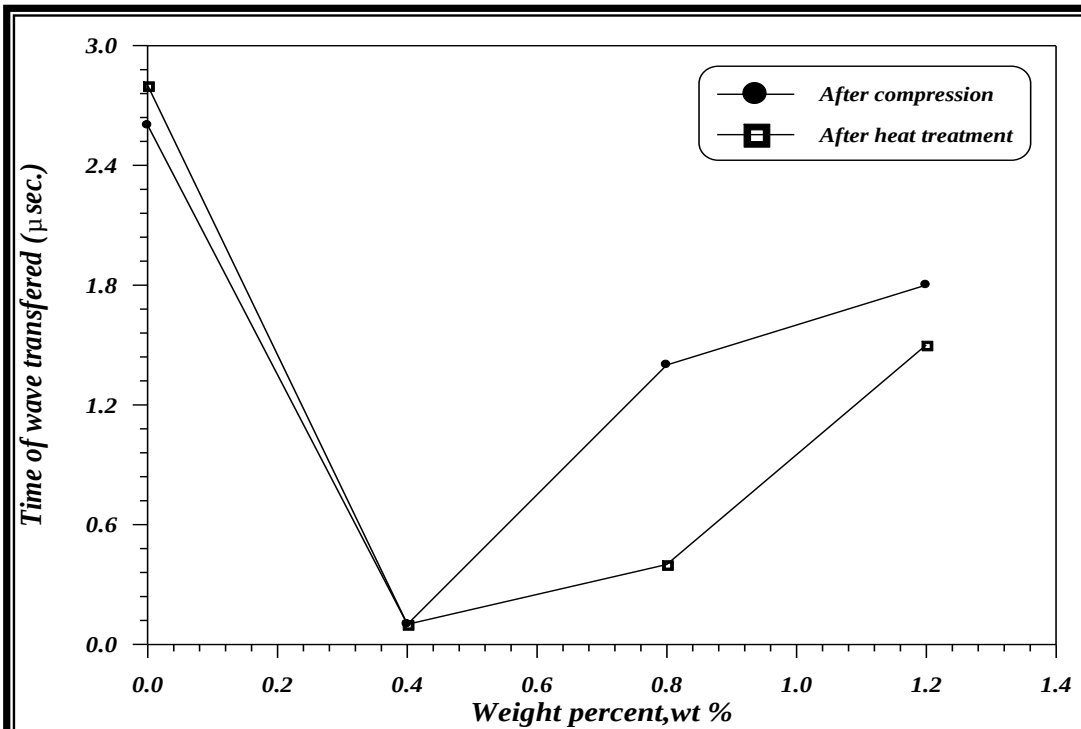

Fig.(6.88) Time of wave transferred as a function of weight percent o f Si.

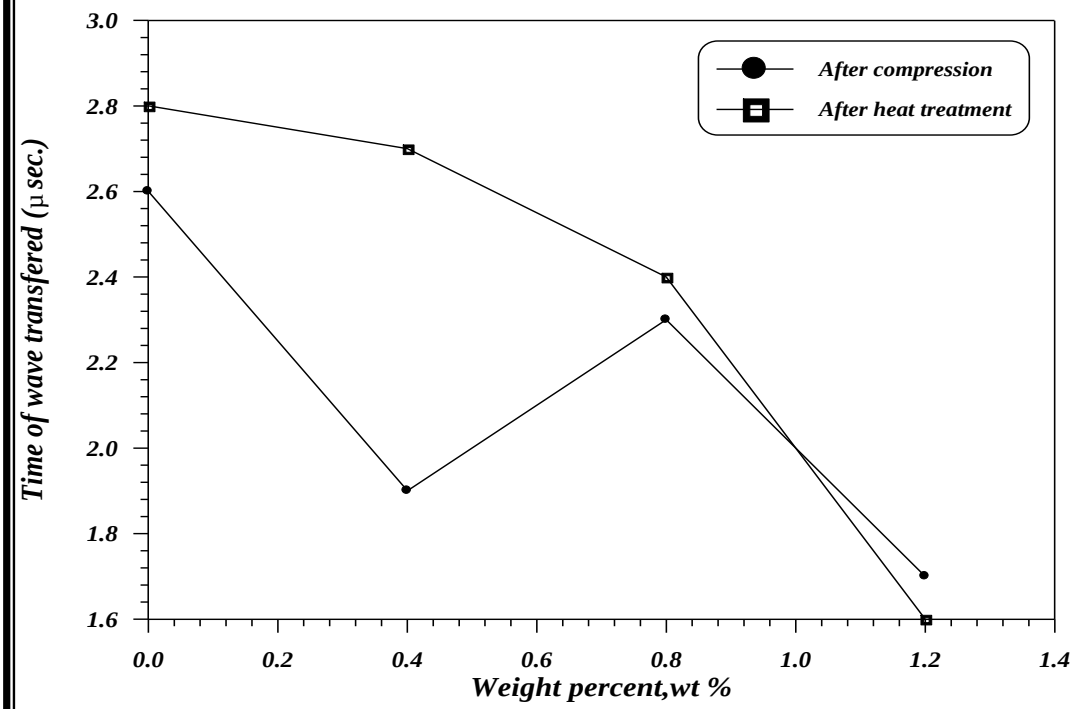

Fig.(6.89) Time of wave transferred as a function of weight percent of Co.

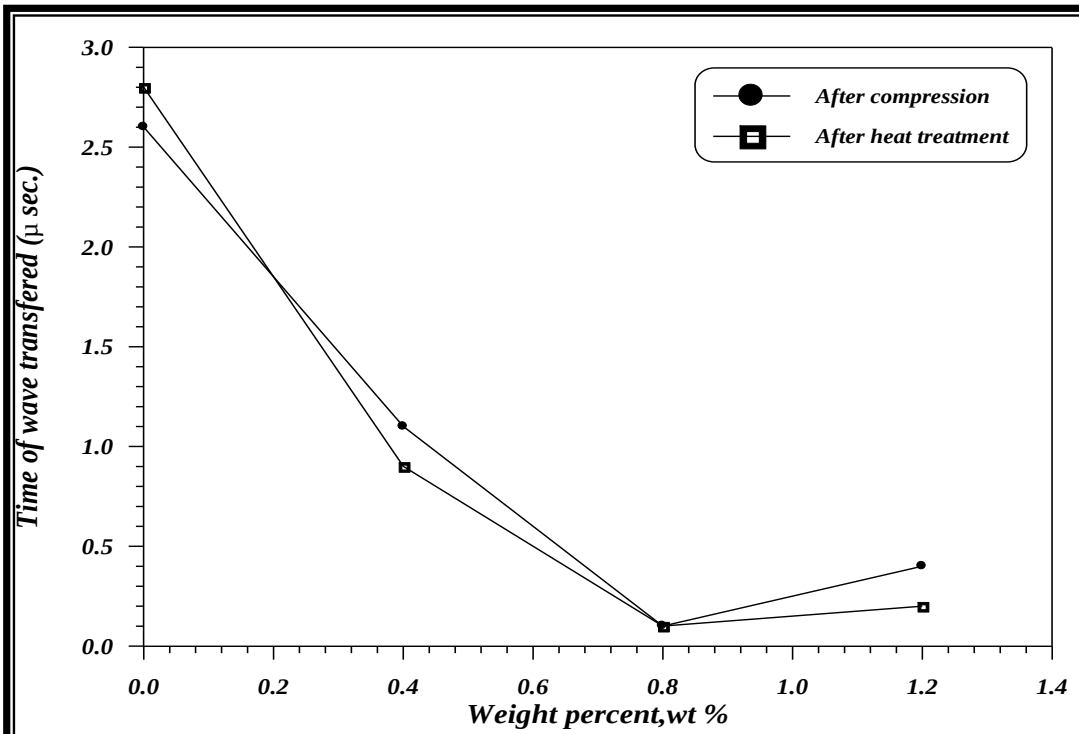

Fig.(6.90) Time of wave transferred as a function of weight percent of Zr.

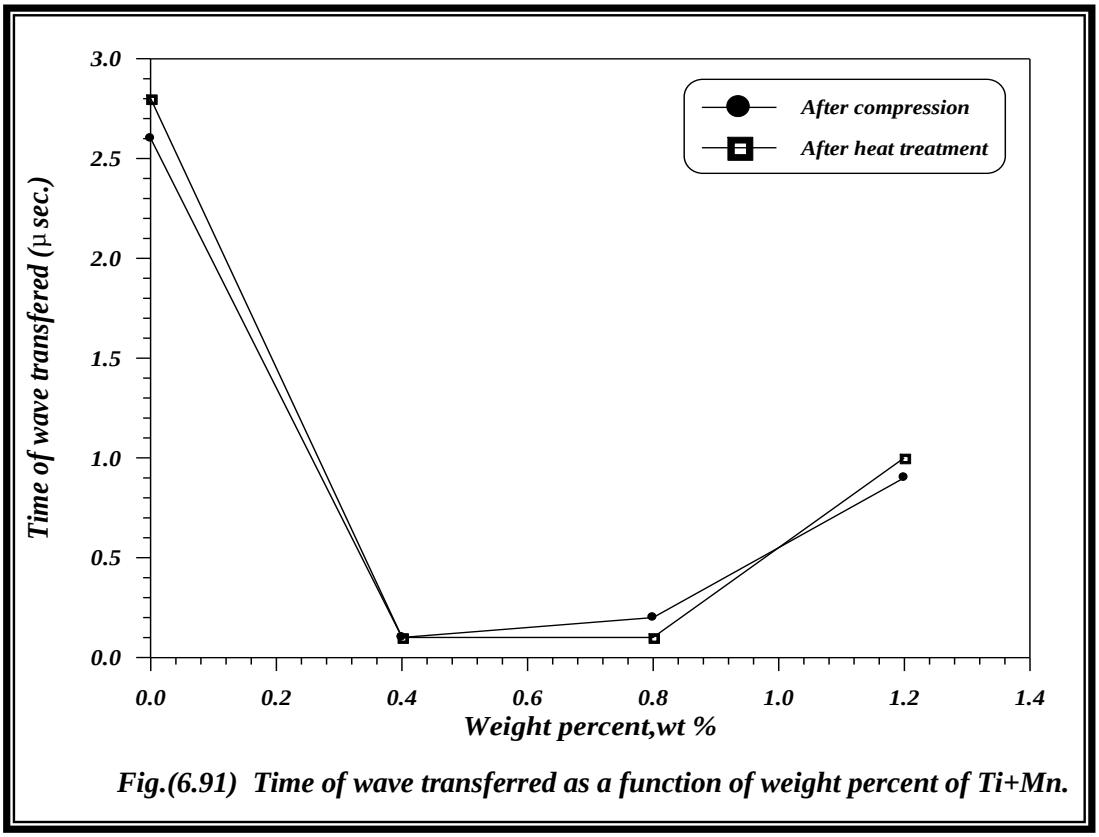

Fig.(6.91) Time of wave transferred as a function of weight percent of Ti+Mn.

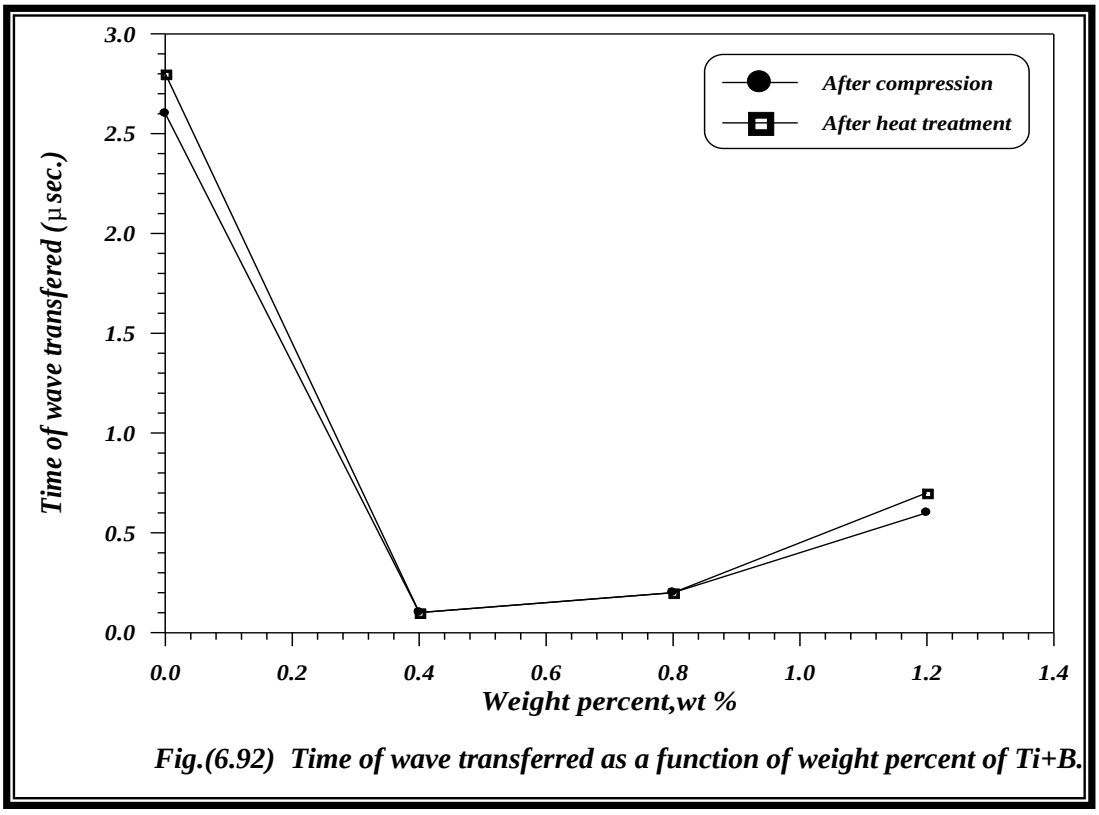

Fig.(6.92) Time of wave transferred as a function of weight percent of Ti+B.

6.4.7. Shape memory effect and shape recovery:

In order to test for shape effect and shape memory and shape recovery , the specimen is cooled below martensite finish temperature (M_f) and then loaded at a temperature at least below starting of parent phase (austenite) temperature (A_s) to detwin the martensite. After unloading , the sample is heated to recover austenite and the original shape.

Fig.(6.93) shows compression stress-strain curve for alloy1 under two conditions at room temperature as shown in a. and at 50 ^oC as shown in b. respectively.It is clear that hyctersis of stress- strain for loading and unloading is different for both cases. It is also clear that elastic recovery during unloading is approximately 3 % from the total strain – However , after heating up to 150 ^oC for min., shape memory effect and shape recovery are (5.52% and 0.294%) respectively for specimen compressed at room temperature In addition , shape memory effect and shape recovery are 3.85 % and 0.134 % respectively for specimen compressed at 50 ^oC as test temperature. It is apparent that specimen under loading unloading conditions has martensitic structure so that shape effect and shape recovery are obtained through heating cycle not at unloading condition so as to take place for super elastic behavior.

Compression stress- strain curve for alloy 2 tested at R.T. and at 50 ^oC have been shown in a. and b. in Fig. (6.94). It has been shown that low elastic strain (2%) with comparison with alloy 1 has been recovered during unloading. Thus this alloy has shape memory effect greater than alloy1 when tested at room temperature. However , low strength (approximately 150 Mpa) has been obtained for specimen tested in 50 ^oC and the specimen tends to have super elastic behavior during the first stage of loading. Any way , After heating specimen , shape memory effect is 24.996 % when tested this specimen at room temperature whereas specimen tested at 50 ^oC , shape memory effect is 1.44 % which is very low amount comparison with that at room temperature It is

probably that alloy2 specimen has superelastic behavior at 50 ^{o}C So it returns to original shape at unloading condition and not required to addition heating this is apparent from Fig.(6.94b.) by increasing superelastic strain as 3.4%.

Effect of titanium addition as (0.4 wt %) to base alloy (alloy2) on the compression stress strain curves for both cases at R.T. and at 50 ^{o}C are shown in Fig. (6.95) .

It is clear that titanium addition leads to increase strength at 50 ^{o}C and tends to browder hystersis of stress- strain loading- unloading cycle specially for specimens tested at 50 ^{o}C. Thus this alloys may be used as energy absorber material for damping application. It is probably that increasing titanium content leads to change martensitic transformation temperatures (M_s, M_f) which affects up on shape memory effect and shape recovery.

Effect of boron additions on the stress- strain curve have been shown in Fig. (6.96) for 0.4 wt% B. It is apparent that elastic strain is decreased when boron addition is increased and hystersis of loading and unloading is narrow specially for samples tested at 50 ^{o}C. However, shape memory effect after heating at 150 ^{o}C for 10 min. is (44.2 % , 9.6 % and 2.5 %) for (0.4 %, 0.8 % and 1.2 %) respectively when sample tested at room temperature thus , small additions from boron are preferred more than greater quantity due to boron effect on grain size of base alloy as grain refiner. For each content of boron, specimens tested at 50 ^{o}C have more Superelastic behaviors than that compressed at room temperature , this is probably that martensitic structure $(\bar{\beta})$ tends to transform into parent phase (β) under stress as possible in this temperature.

In addition , Summery of shape memory effect shape recovery for all alloys (1,2,3,4,…….., 26) are Presented in table (6.2).

Table (6.2) shape memory effect and shape recovery for all alloy under compression at room temperature at 50 °C.

Alloys	Compression R.T.		Compression at 50	
	SME%	S.R%	SME%	S.R.%
1	5.52	0.294	3.85	0. 134
2	24.99	0.0363	1.44	0.0116
3	58.82	1.382	2.94	0.110
4	5.90	0.113	2.97	0.131
5	15.34	0.290	10.28	0.149
6	44.18	0.217	1.96	0.034
7	9.58	0.238	4.53	0.115
8	2.49	0.113	2.05	0.057
9	14.35	0.365	2.84	0.120
10	12.80	0.319	2.50	0.066
11	28.01	0.443	1.64	0.061
12	19.16	0.465	6.63	0.184
13	27.23	0.365	10.58	0.214
14	11.71	0.180	8.69	0.189
15	1.36	0.030	1.67	0.103
16	8.45	0.177	7.53	0.220
17	5.23	0.166	2.16	0.048
18	53.97	1.357	2.25	0.084
19	11.84	0.154	5.78	0.147
20	25.93	0.564	8.69	0.111
21	5.29	0.056	1.10	0.025
22	7.71	0.156	4.92	0.171
23	7.53	0.185	1.35	0.043
24	5.21	0.0896	0.36	0.0061
25	35.45	0.896	0.99	0.024
26	6.92	0.142	2.31	0.104

It is clear that maximum shape effect is 58.82% from total strain (10%) at 0.4 wt % Ti of alloy3 whereas the minimum shape memory effect is

1.36 % for alloy 15 which contains 0.4 wt % Co. In addition , alloy 3 has a maximum shape recovery as 1.357%.

Furthermore , shape memory effect is calculated from hardness test by using image analysis technique for ball indenter of Brinell hardness and / or vicker's macrohardness indenter. Shape memory effect and shape recovery are function of load , temperature and composition as well as transformation temperature. Thus, it is believed that shape memory effect for microhardness is more than shape memory effect for vicker's macrohardness or Brinell hardness due to (large applied load used in the last two tests. Figs.(6.97), (6.98) and Fig.(6.99) show indenter image for alloys (1,2,3,4, …., 26) after direct quenching heat treatment in (a) and after heating up to 150 ^{o}C for 10 min. and air cooling in (b) . It is clear that difference in indentation dimension between a and b image is apparent in these Figures. This difference refer' to obtain shape memory effect for prepared alloys in this study. Brinell test with reciprocal ball is used to generate indenter which is taken an image using suitable magnification of optical microscope.

It must be taken the same digital camera to the same magnification of equipment in order and really compare between the two images.

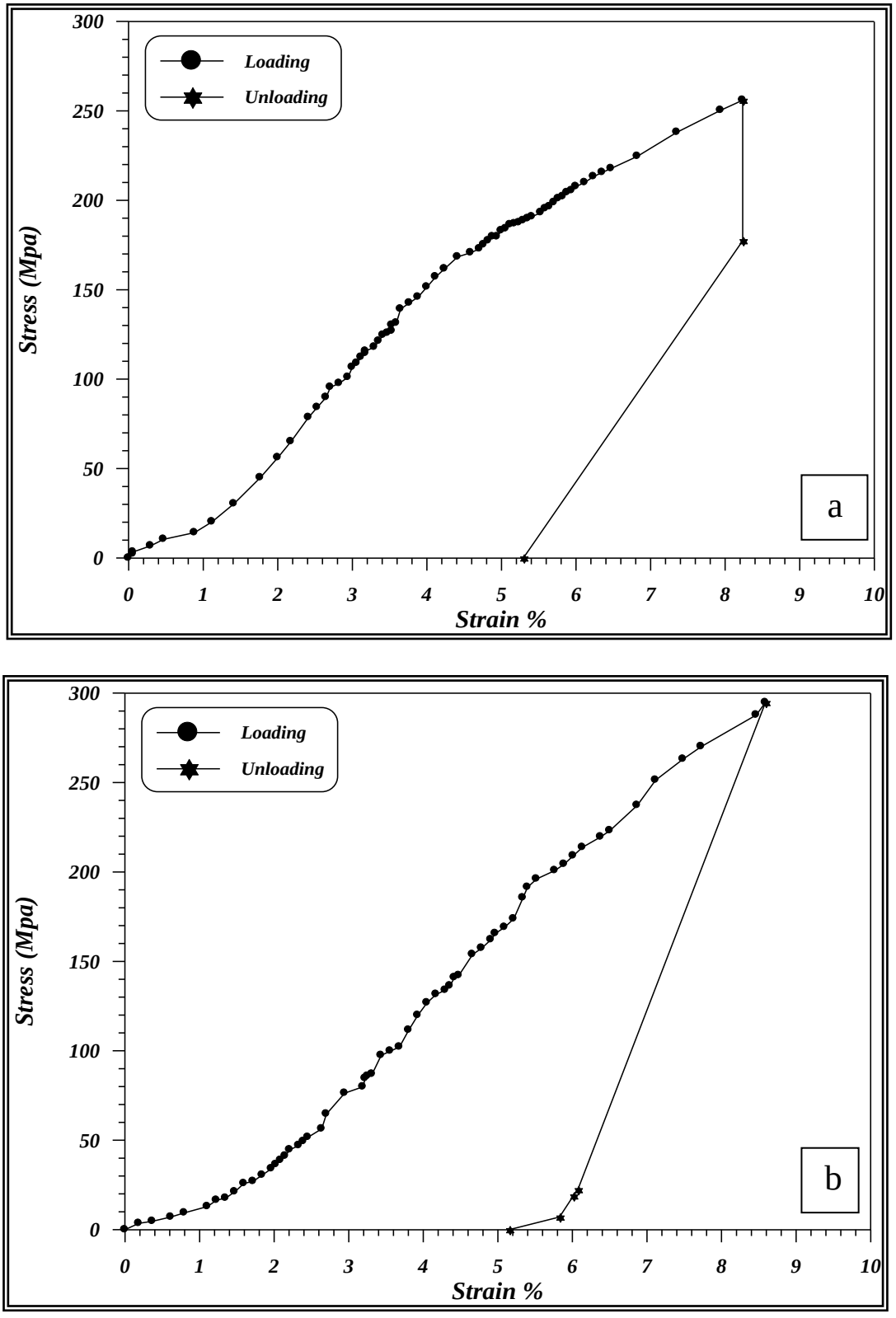

Fig.(6.93) Compression stress strain curve for alloy 1 at R.T. in a. And at 50 ˚C in b.

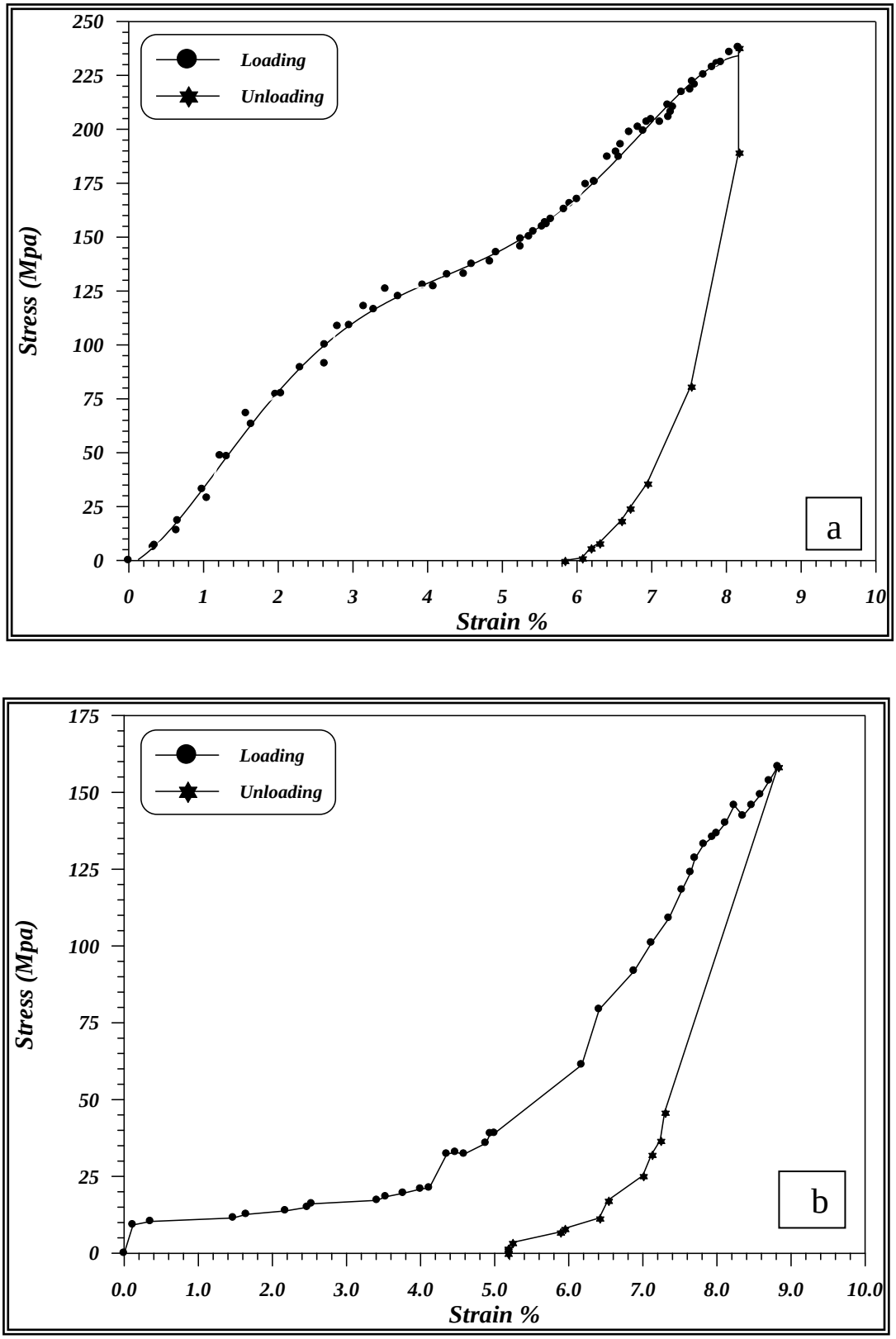

Fig.(6.94) Compression stress strain curve for alloy 2 at R.T. in a. And at 50 ˚C in b.

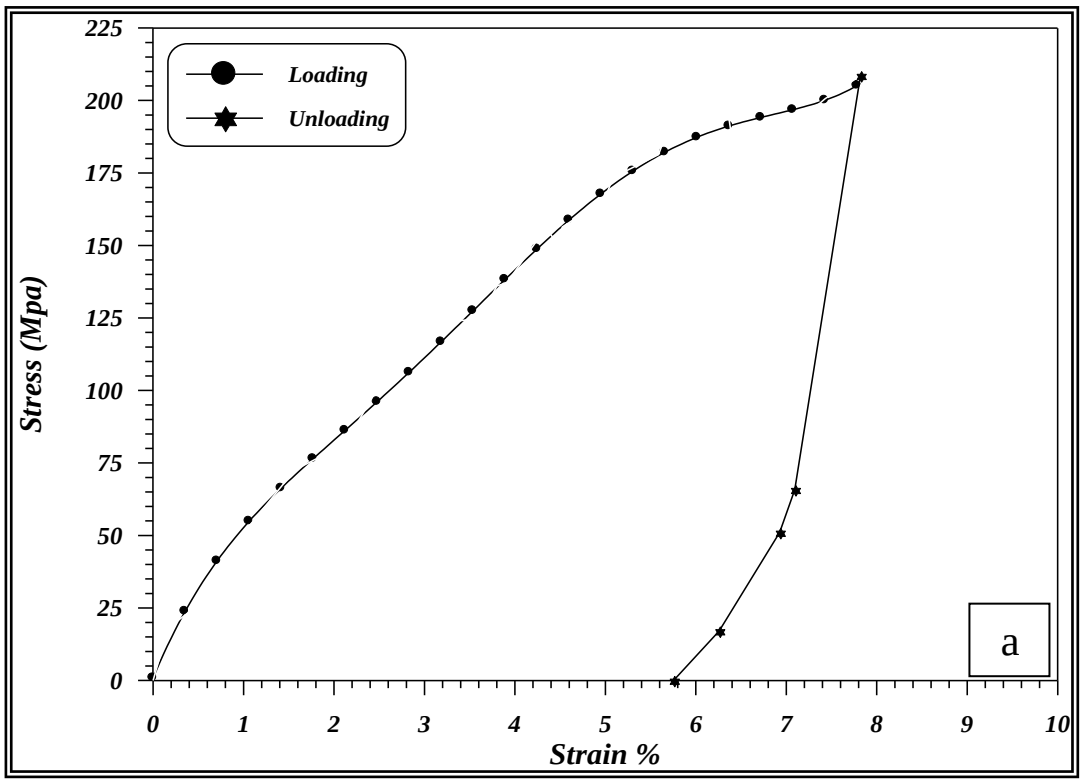

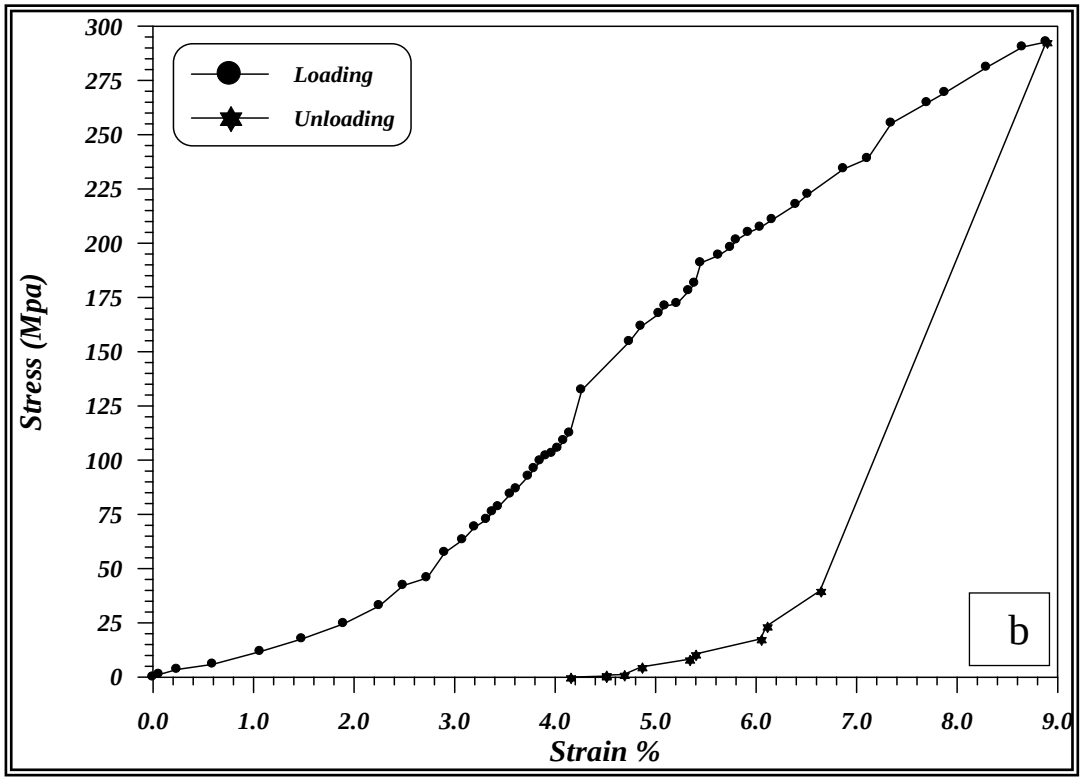

Fig.(6.95) Compression stress strain curve for alloy 3 at R.T. in a. And at 50 ˚C in b.

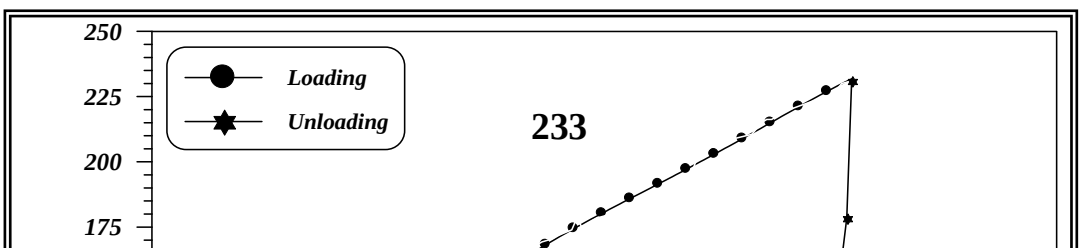

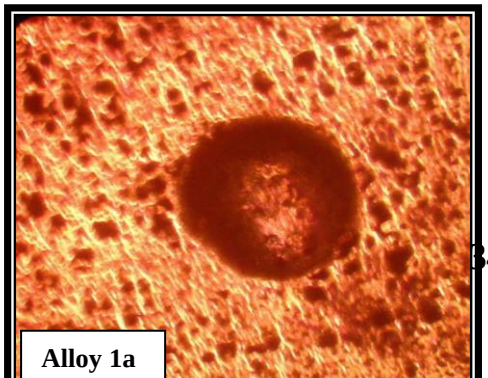
Alloy 1a

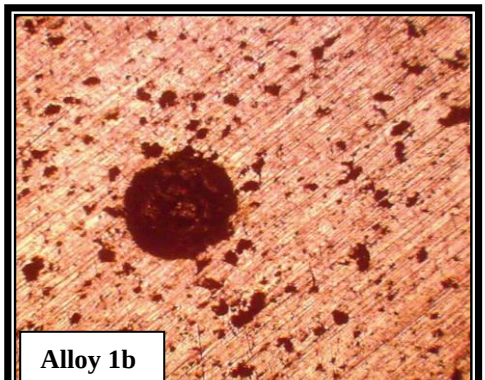
Alloy 1b

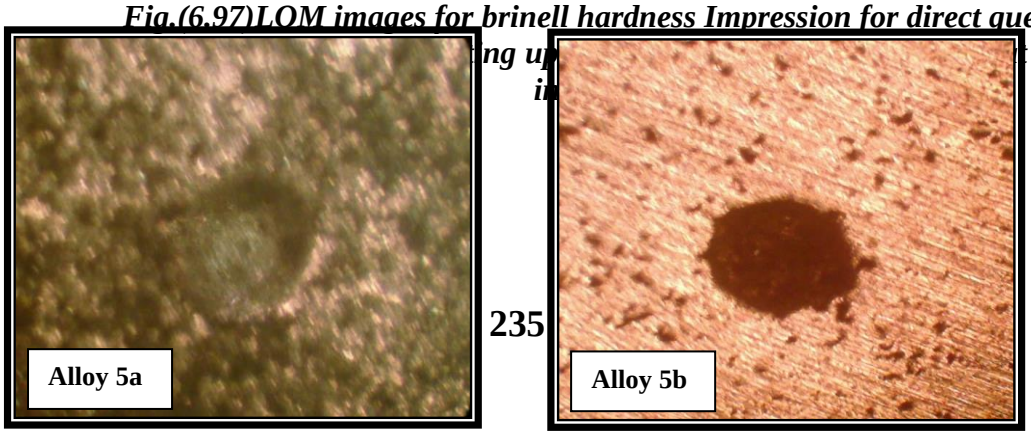

Fig.(6.97)LOM images for brinell hardness Impression for direct quenched ng up treatment in

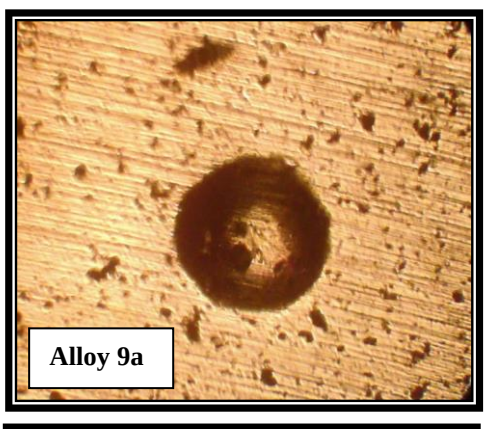
Alloy 9a

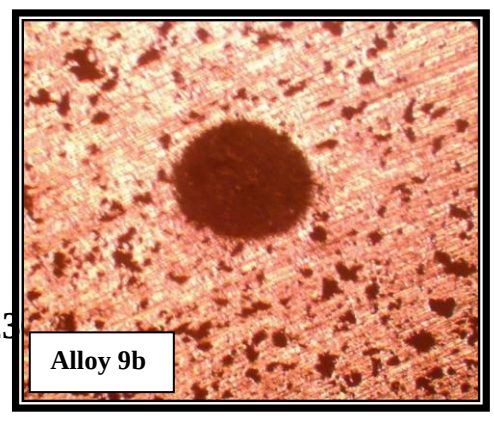
Alloy 9b

6.5. Aging heat treatment .

Aging heat treatment includes heating the direct quenched specimens up to 200 ^{o}C for 30 min. and followed by quenched in ice water . The origin of

martensite aging and the associated superelastic behavior has been a long standing puzzle for alloys having martensite transformation.

The martensite aging causes an increase in reverse transformation temperatures. Martensite aging includes martensite stabilization by which martensite becomes more stable with aging such that it is probably that the reverse transformation temperature (A_s and A_f) increase with aging time. In the following, X-ray diffraction technique has been done for aged specimen. In addition, optical microscopy image and scanning electron microscopy image have been presented. Furthermore , Vicker's macrohardness and shape memory effect have also been presented.

6.5.1. X-ray diffraction for aged specimens

X- ray diffraction pattern for alloy 1 which heat treated by aging treatment has been shown in Fig. (6.100).

It is clear that intermetallic compound (Al_4Cu_9) has been formed during aging of martensite $\overline{\beta}$ at 200 ^oC for 30 min. It has been shown that martensite of this alloy is unstable (i.e non equilibrium phase) and thus it has tendency to decompose simultaneously during aging decomposition of $\overline{\beta}$ phase which may be partially took place in this alloy because the martensite phase ($\overline{\beta}$) is the major phase in this alloy system.

Decomposition process is a diffusion process which is time dependent effect. It is required to more time or high temperature above (200 ^oC) to decompose all martensite phase in to ($\alpha + \gamma_2$) phase which are more stable (equilibrium phase than martensite phase).

Decomposition has also been occurred in alloy 2 as can be seen from X-ray diffraction pattern in Fig.(6.101). However, small amount of γ_2 phase has been form by decomposing of martensite phase with comparison with that it is occurred in alloy 1.

This is due to low transformation temperature of $\beta \rightleftharpoons \alpha + \gamma_2$ reaction as can be seen from (Cu+Al) phase diagram for for hypereutectoid alloys.

Fig.(6.102) shows x-ray diffraction pattern for alloy3 which aged in 200 ^{o}C for 30 min. It has been shown that the intermetallic compound (Cu, Al)$_2$ Ti precipitates in martensite matrix ($\overline{\beta}$) phase. In this temperature martensite phase is stable and may not be decomposed in to ($\alpha + \gamma_2$) through eutectoid reaction. It is probably that 0.4 wt % Ti addition satisfies this stability at 200 ^{o}C So that this alloy has shape memory effect at higher temperatures compared with alloy 1 and alloy 2.

In addition, aging of martensite structure of alloy 6 is more stable because there is no decomposition into $\alpha + \gamma_2$ phase during aging treatment as can be seen from x-ray diffraction pattern in Fig. (6.103). It is believed that boron addition as 0.4 wt % stabilized martensite phase and prevent decomposition by increasing transformation or increasing activation energy that is required to decompose ($\overline{\beta}$) in to $\alpha + \gamma_2$ phases. Thus , it is also apparent that alloy 6 may be used as high temperature shape memory alloy applications. In addition , it has been shown that aging is not dependent on the structure of martensite and it is occurred in any martensite for both ordered and disordered martensite. Aging of martensite is a time- dependent process so that it is diffusion process. Furthermore, it has been shown that points defects in shape memory alloys play a central role in determining martensite aging effects. Most shape memory alloys are ordered alloys or intermetallic and the defect structure and its concentration is quite different from that in pure metal or disordered alloys. Therefore, information on the defect structures and concentration is important for deep understanding of effect of defects on aging .

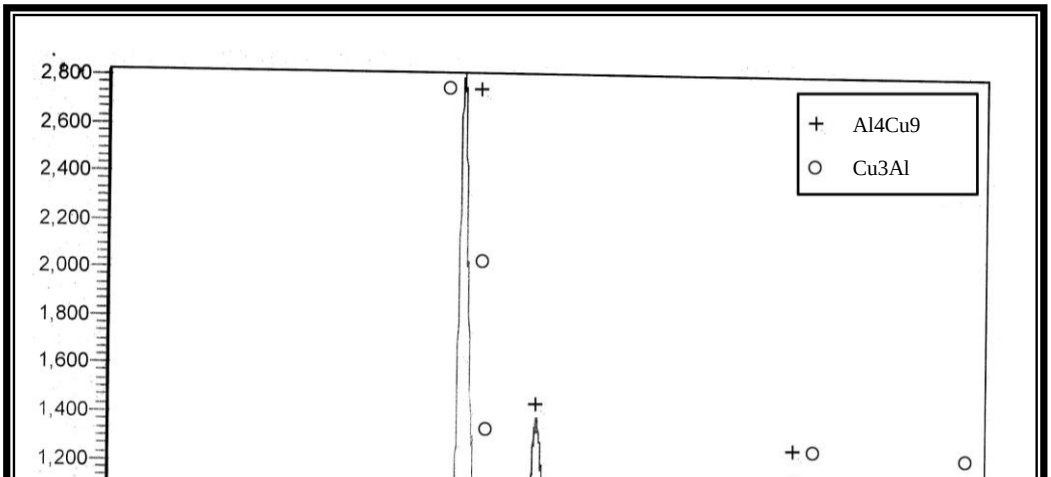

Fig.(6.100) XRD pattern for alloy1 which aged in 200 °C for 30 min.

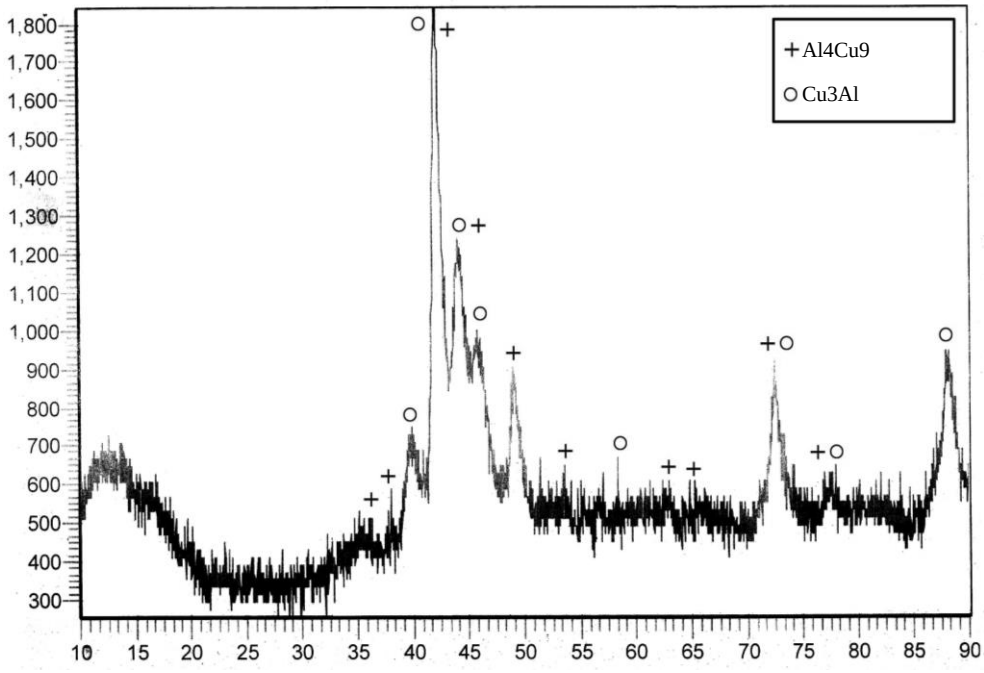

Fig.(6.101) XRD pattern for alloy2 which aged in 200 °C for 30 min.

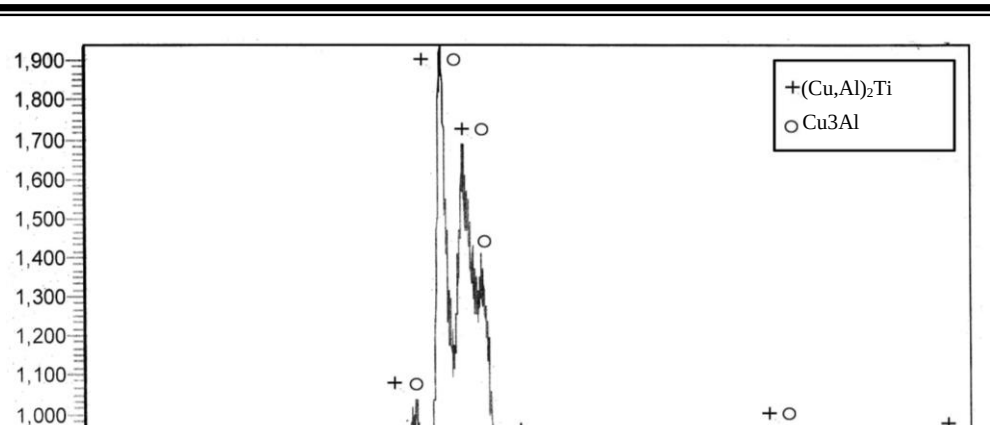

Fig.(6.102) XRD pattern for alloy3 which aged in 200 °C for 30 min.

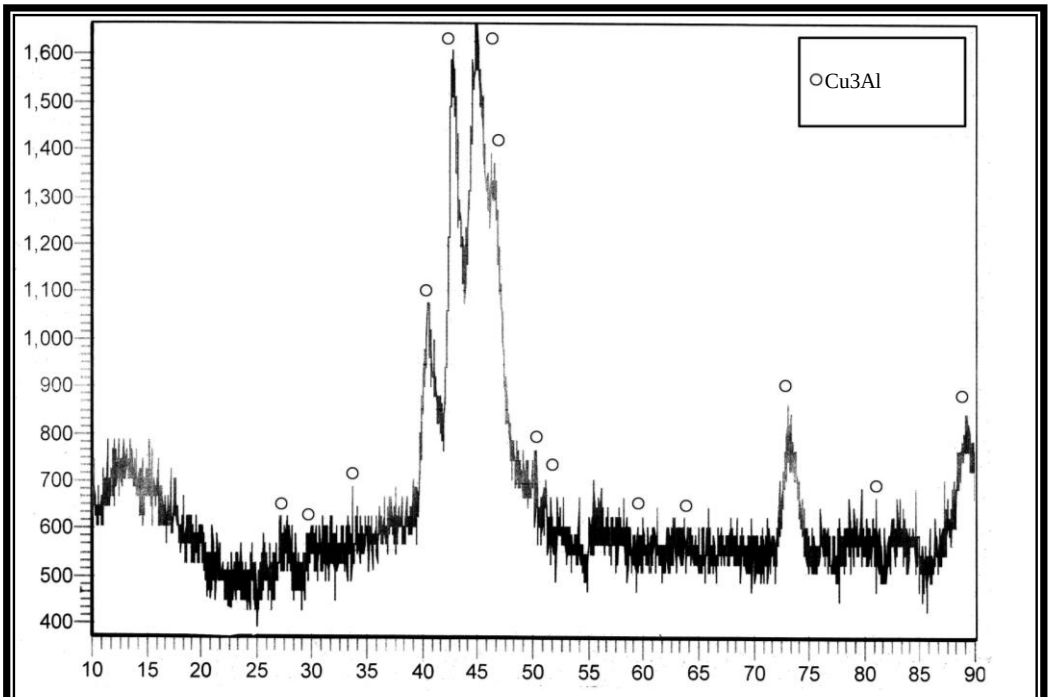

Fig.(6.103) XRD pattern for alloy6 which aged in 200 °C for 30 min.

6.5.2 Light optical microscope image:

Microstructure of twenty-six alloys using two etchants by optical microscope with two different magnification (1000 X and 2400 X) has been shown in Fig.(6.104 to 6.107) for alloy 1,2,3 and 6 respectively. Unfortunately , it has been shown that etching with ($NH_4OH + H_2O_2 + H_2O$) for all alloys dos not appear precipitation of intermetallic compounds in the microstructure but it is good etchant to appear grains and grain boundaries as shown from these Figures in a. Therefore , another etchant which is (Fecl3 + HCl + H2O) solution has been used to appear precipitates of intermetallic compounds in all alloys during aging treatment with (2400X) as magnification force . It has been shown that intermetallic compounds appear as gray or black fine spots in the microstructure near the grain boundaries or near the particles edges. It is also apparent that etching with ($NH_4OH + H_2O_2 + H_2O$) Solution reveals grain boundaries more than the second etchant which are easily confused with the particle boundaries that also appear as thin gray or black lines. Light optical microscope with polarized light is better than normal light optical microscope to reveal microstructure of martensite in non ferrous alloys. Unfortunately, there is no polarized light optical microscope in the university of Babylon.

During aging treatment ,(Cu, Al)2Ti intermetallic compound precipitates on the grain boundaries of martensite phase ($\overline{\beta}$) for alloy 3,4 and 5 . However, intermetallic compound of γ_2 phase (Cu_9Al_4) may be precipitated as gray fine spot near the boundaries in the region which do not include titanium intermetallic compound. However, the presence of precipitates produce changes in the martensitic transformation temperatures and the hystersis accompanying the forward and reverse transformations. Precipitates of γ_2 phase may be uncleared and grown through aging heat treatment which depend upon time , temperature and chemical composition of alloy. The γ_2 precipitates are rather well accommodated with the parent phase (β) . They are either fully coherent or at most semi coherent depending on the precipitates size. This is due to the cubic-cubic orientation relationship between (β) parent phase γ_2 phase.

Nevertheless , when the matrix surrounding one precipitate is transformed to single variant martensite , the hole left in the β matrix phase occupied by the precipitate is quite severely deformed due to the intrinsic deformation accompanying the transformation.

However, the precipitate itself maintains its shape which means that the γ_2 phase does not transform mathematically. Deep understanding of the interaction between γ_2 phase precipitates and martensite phase required high resolution transmission electron microscope (TEM).

However, the precipitation of γ_2 phase in the matrix of ($\overline{\beta}$) martensite phase is considered as one of strengthening the copper based shape memory alloys through producing dual phase shape memory alloys. Matrix of martensite in dual phase is responsible for shape memory properties and the precipitates (γ_2) is responsible to give high strength and high hardness of overall alloy.

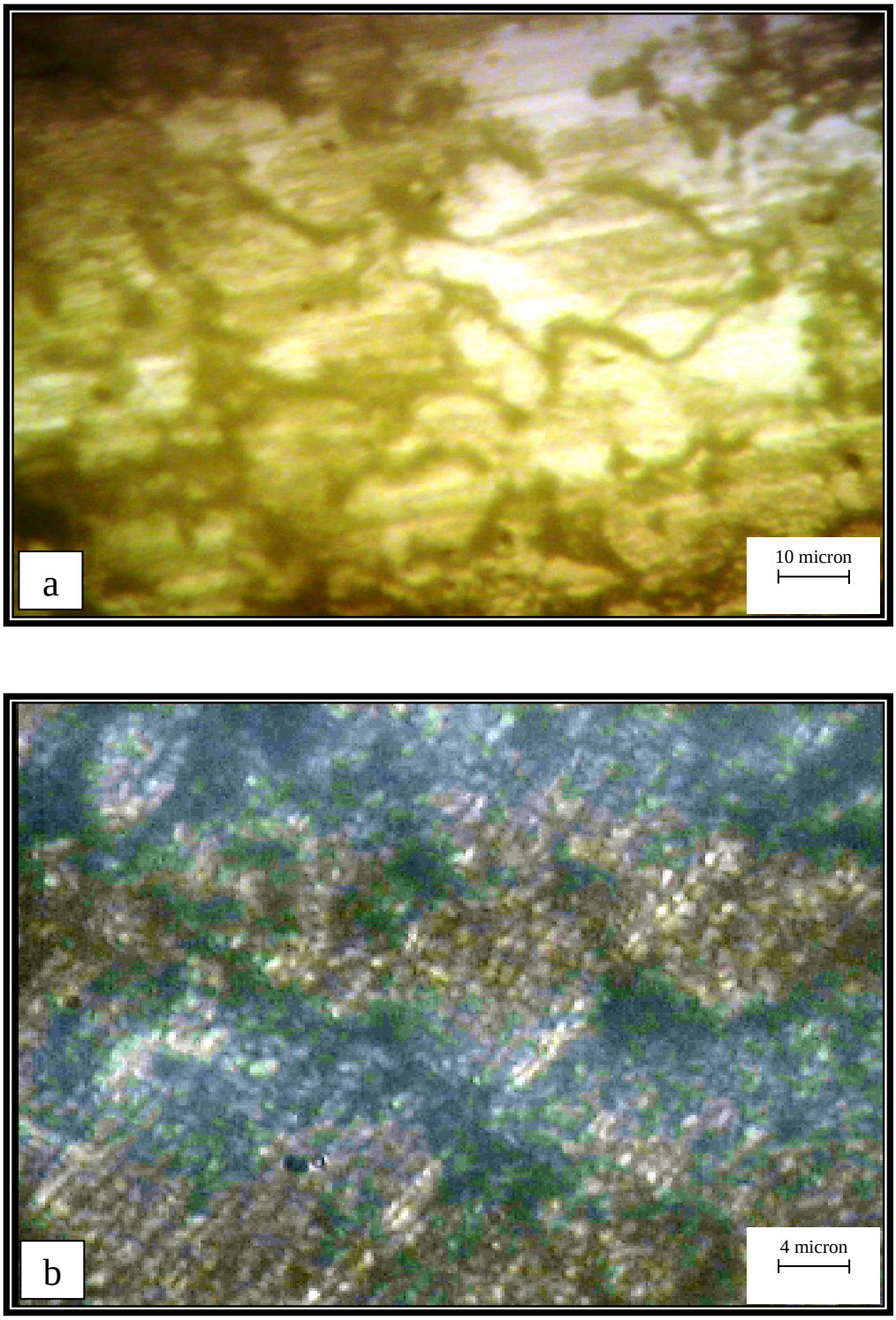

Fig(6.104) LOM images for alloy 1 aging in 200 C for 30 min. and followed by quenching in ice water for a:etched in (NH4OH+H2O2+H2O) solution, b: etched in(FeCl3+HCl+H2O) solution.

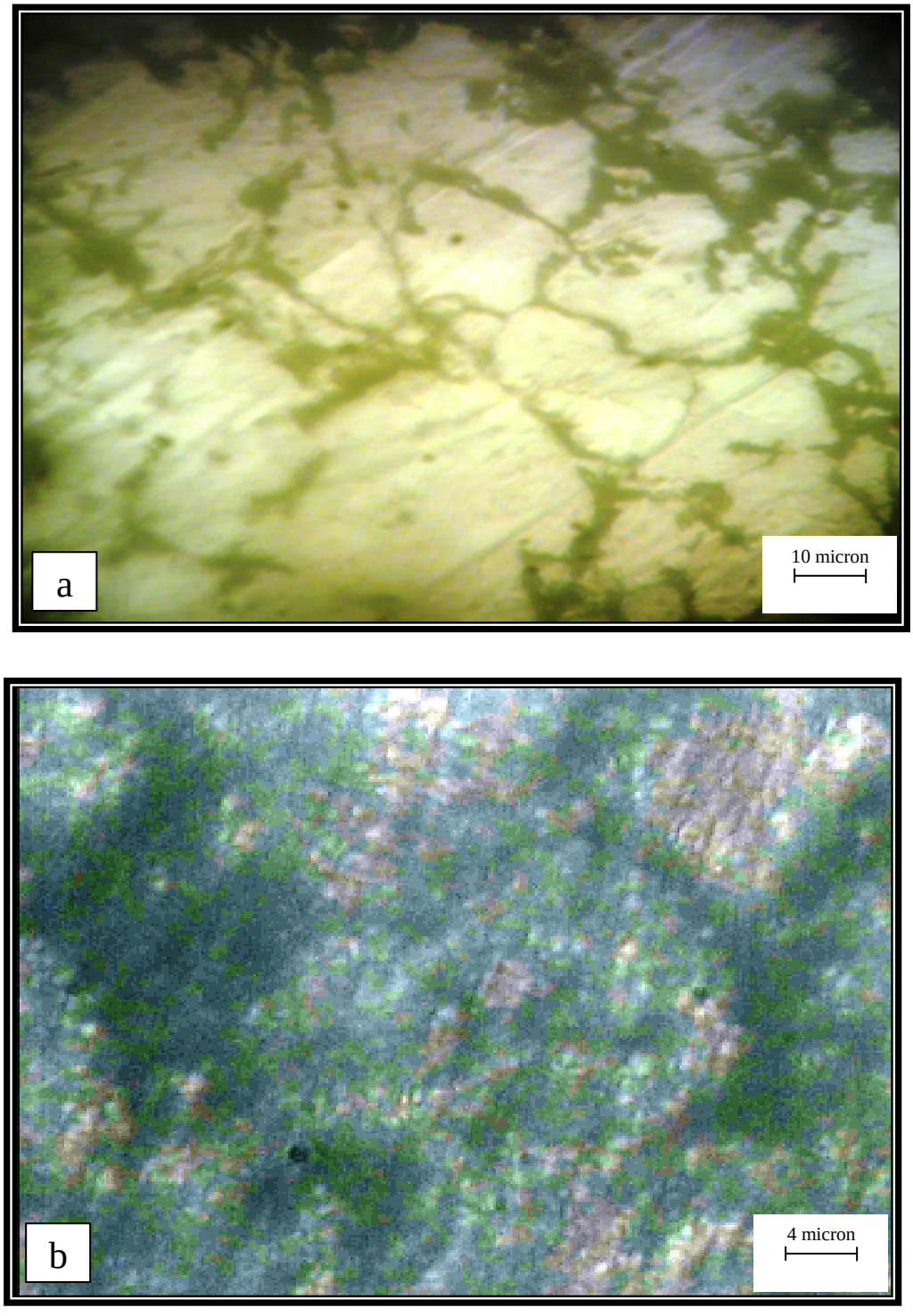

Fig(6.105) LOM images for alloy 2 aging in 200 C for 30 min. and followed by quenching in ice water for a:etched in (NH4OH+H2O2+H2O) solution.b: etched in(FeCl3+HCl+H2O) solution.

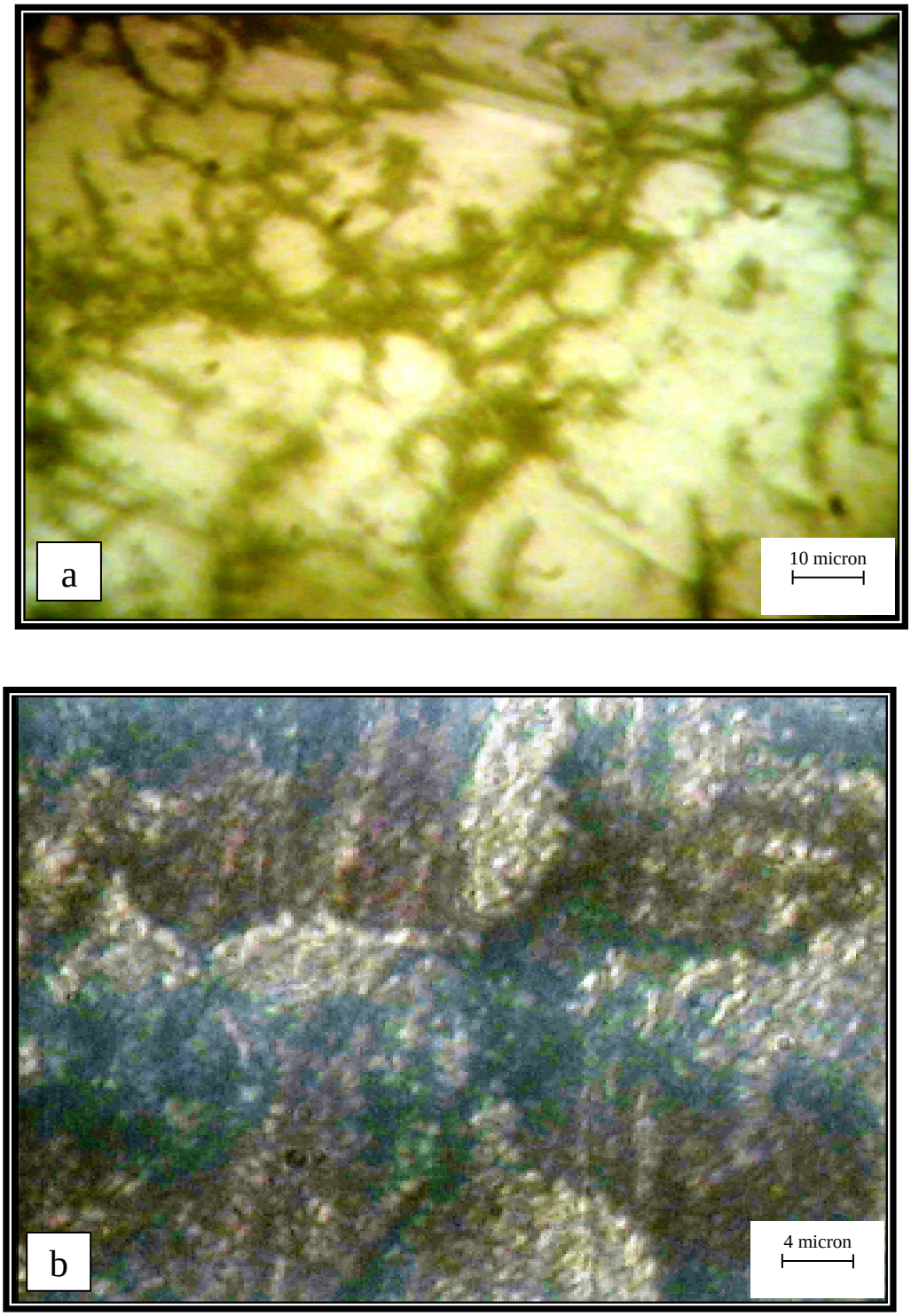

Fig(6.106) LOM images for alloy 3 aging in 200 C for 30 min. and followed by quenching in ice water for a:etched in (NH4OH+H2O2+H2O) solution.b: etched in(FeCl3+HCl+H2O) solution.

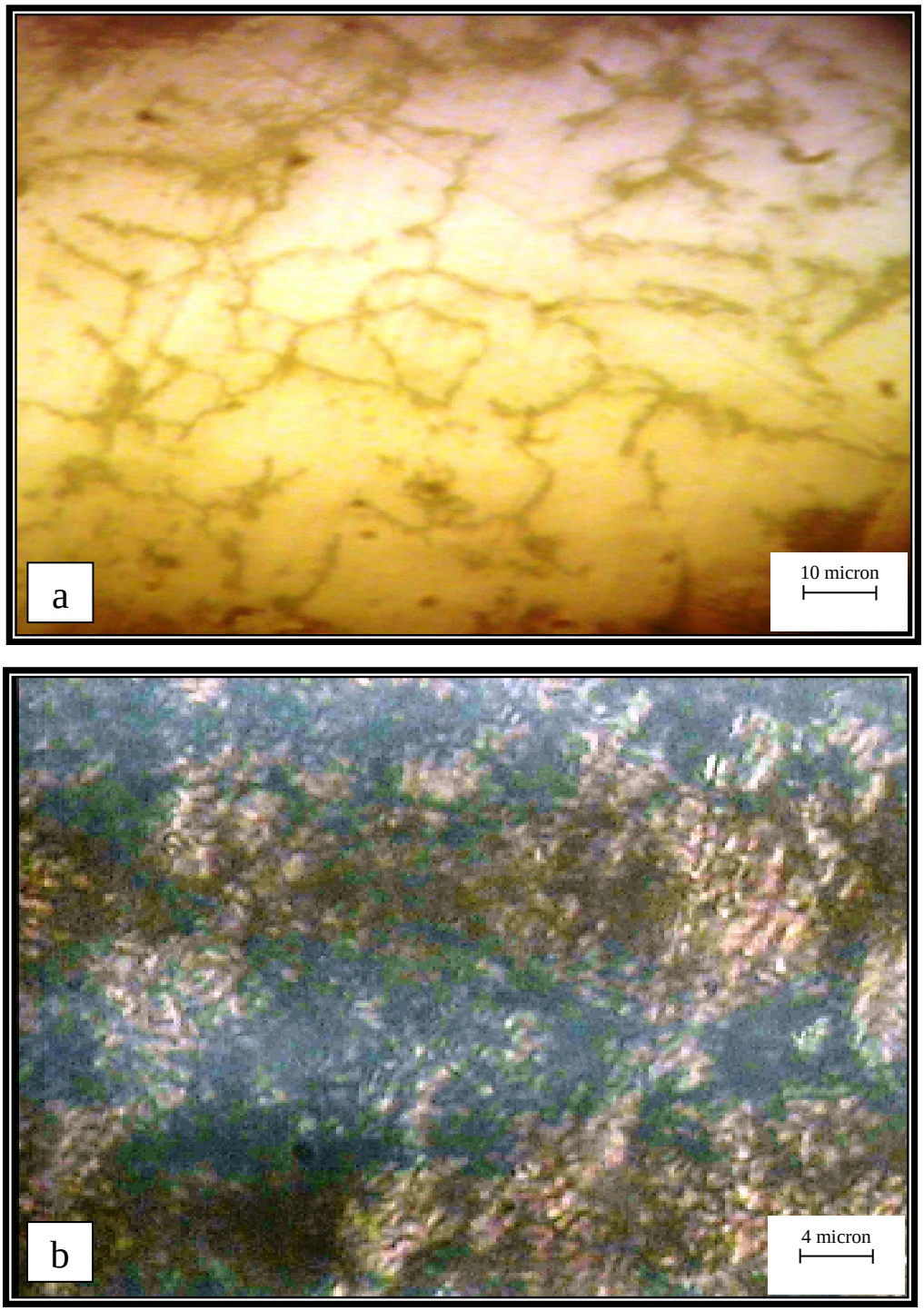

Fig(6.107) LOM images for alloy 6 aging in 200 C for 30 min. and followed by quenching in ice water for a:etched in(NH4OH+H2O2+H2O) solution.b: etched in(FeCl3+HCl+H2O) solution

6.5.3 Scanning electron microscope images:

Scanning electron micrographs of alloy 1, 2,3 and alloy 6 have been shown in Figs.(6.108) , (6.09) , (6.110) and Fig.(6.111) respectively. It has been shown that precipitates from γ_2 phase (dark black regions).blue precipitates are the intermetallic compounds of the above phases. It is also clear that scanning electron after solution treatment and aging treatment. It is apparent that pores and precipitates are lied near the grain boundaries or near the particle boundaries. Scanning electron micrographs for etched specimen of alloy2 and alloy3 etching with [$FeCl_3$+ HCl + H_2O] solution have been shown in Fig. (6.112) and Fig.(6.113) respectively.

6.5.4 Vicker's macrohardness test results

Vicker's macrohardness results as a function of weight percent of alloying elements have been shown in Fig. (6.114). It is apparent that vicker's hardness is decreased when weight percent of alloying elements is increased up to 0.8 wt%. After this decreasing, Vicker's hardness tends to increase secondly at 1.2 of alloying element except boron addition which continue in decreasing . It is probably that 0.4 % of alloying element forms critical weight percent which makes the precipitates of intermetallic compounds coherent with martensite matrix phase. This leads to increase hardness of alloys. However, when the weight percent of alloying elements is increased , precipitates of intermetallic compounds (γ_2 or $(Cu,Al)_2Ti$) may be semi coherent or no adherent stick with martensite matrix phase which also leads to decrease hardness. In addition, presence of pores make hardness data random in its distribution.

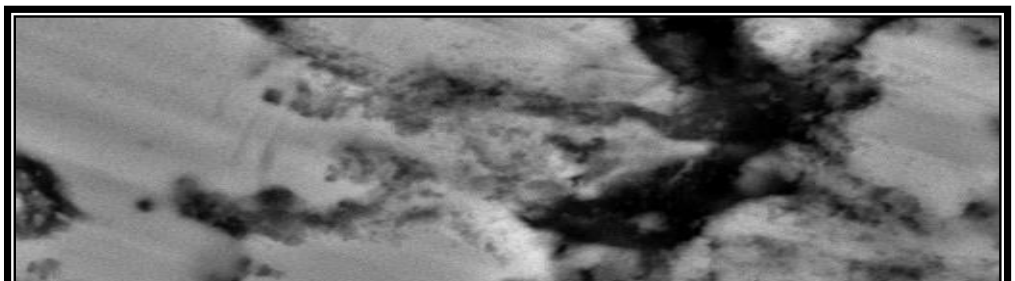

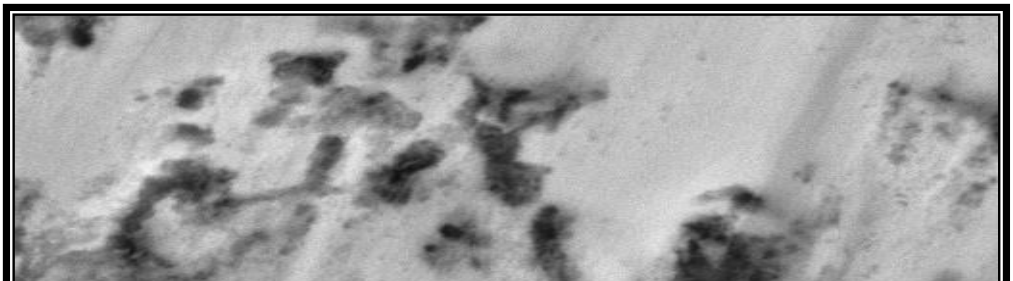

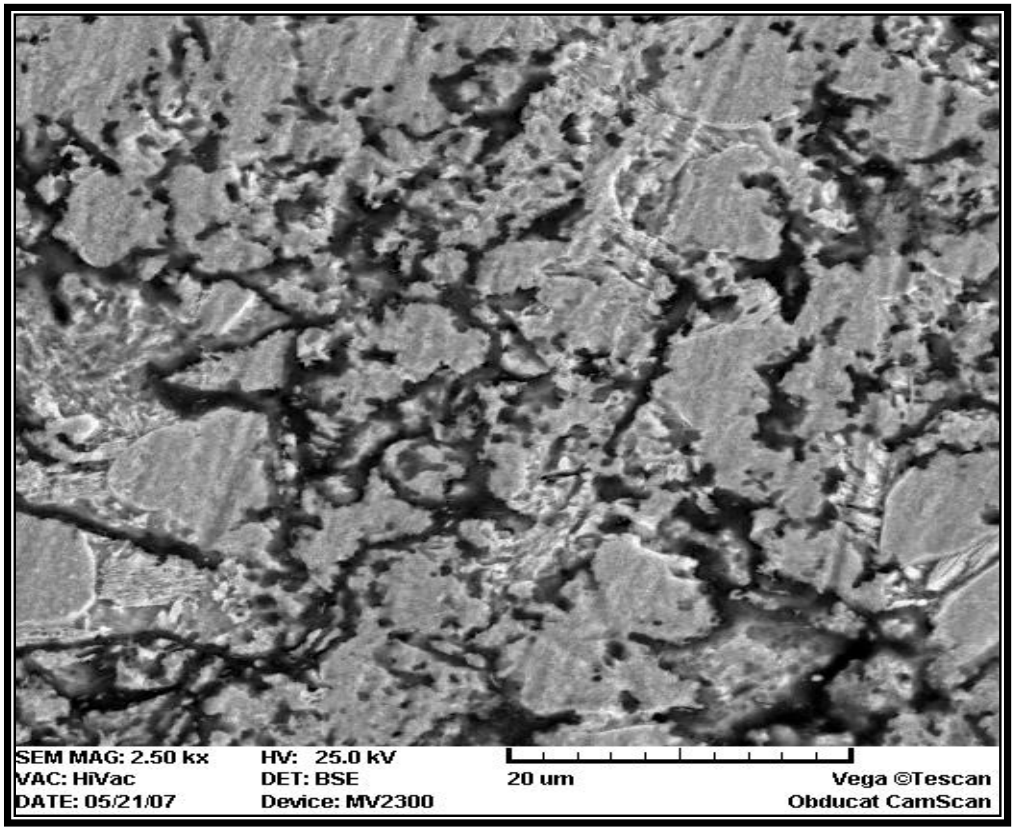

Fig.(6.112) SEM image for alloy 3 etched in (FeCl3+HCl+H2O) solution.

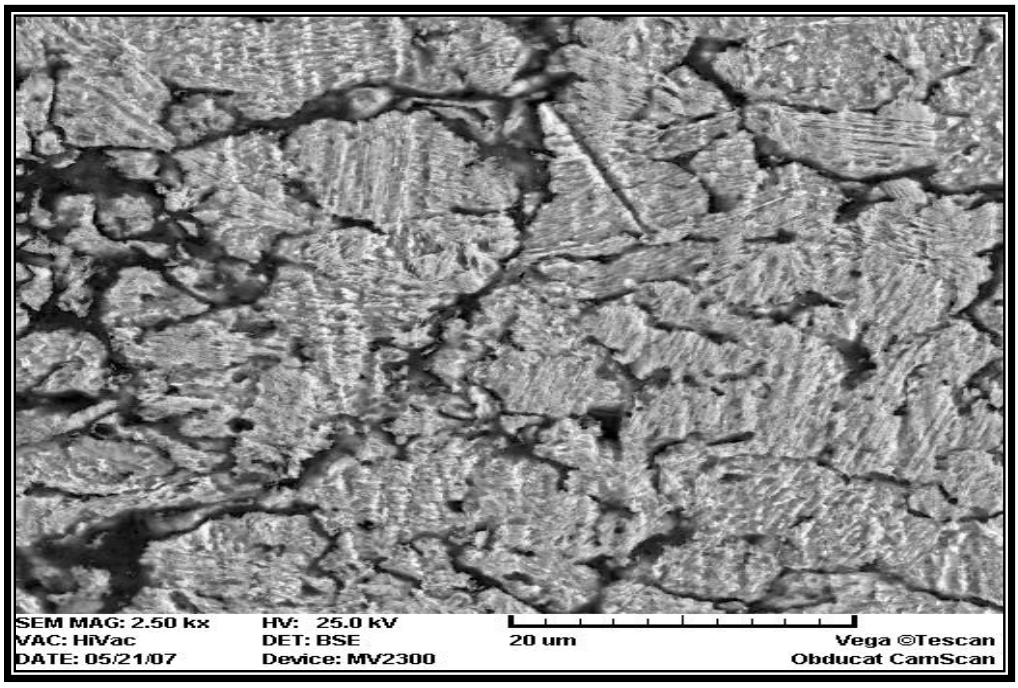

Fig.(6.113) SEM image for alloy 6 etched in (FeCl3+HCl+H2O) solution

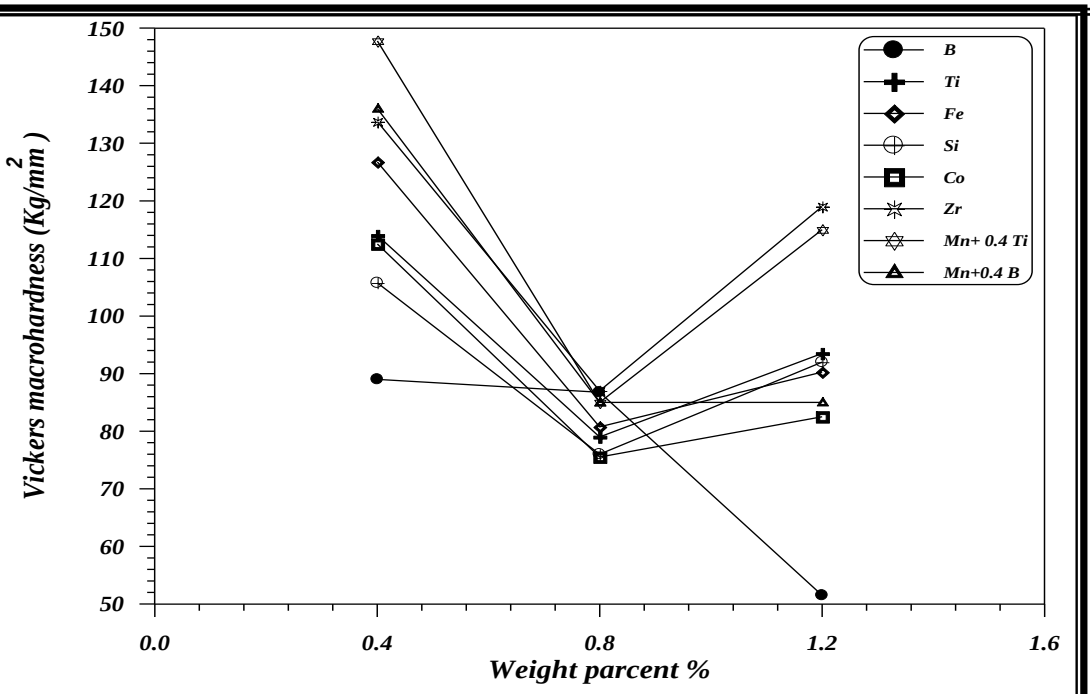

Fig.(6.114) Vickers macrohardness results for aged specimens with respect to weight percent of alloying elements

6.5.5 Shape memory effect for aged treated specimens:

Shape memory effect for aging heat treated specimen in calculated by using macrohardness test indenter. Vicker's macrohardness indenter after aging treatment is pictured for all alloys. After this , indenter for reheating up to 150 ^{o}C for 10 min. specimens is also pictured using digital camera fitted with light optical microscope with low magnification. These two image are analyzed and processed in real dimensions in order to determine dimensions of indenter (d1 and d2) before and after reheating heat treatment. Shape memory effect is calculated and presented in table (6.3). It is clear that alloy 6 has the maximum shape memory effect (**4.288365** %) whereas alloy 1has a minimum shape memory effect (**0.821182** %) in the other hand.

6.6. Step- quenched heat treatment:

Step- quenched heat treatment consists of solution treatment up to 840 ^{o}C for one hour and quenching in hot water at 95 ^{o}C for 15 min. After this , quenching in ice water has been done . In most copper—based shape memory alloys, the reverse transformation temperatures (A_s and A_f) increase with prolonged holding at temperatures below A_s[Humbeeck et. al , 1984] .

Therefore , transformation temperature may be changed after direct quenching treatment through the application of shape memory alloy and because the application of martensitic alloys in shape memory devices requires reproducible and stable transformation temperatures, martensitic structure must be stabilized either by aging or by step- quenched heat treatment. In this study, step-quenched specimen are used for the following reasons:

1. The disordered β-phase undergoes upon quenching disordered- ordered transformation. This transformation can not be suppressed even by rapid quenching and the degree of long range order is not equilibrium. Because M_s and A_s are affected by the degree of order in β-phase , holding the specimen at a temperature above M_s for a suitable time will be necessary in order to obtain equilibrium degree of order prior to transformation. The Transformation temperatures such as A_s , A_f , Ms and M_f obtained after step-quench treatment are Considered as true transformation temperatures.
2. quenching stresses which might affect the transformation temperatures , are minimized by step-quench heat treatment.

Table(6.3).Shape memory effect by impression Vickers's hardness for aged specimen.

Alloy No.	After aging treatment (by ferret's rectangle)		After recovery treatment		SME %	
	Length (Pixel)	Width (Pixel)	Length (Pixel)	Width (Pixel)	by length	by width
1	404.45	390.9	400.12	387.69	1.07059	0.821182
2	380.85	344.88	372.23	332.25	2.263358	3.662143
3	445.55	392.64	441.75	386.13	0.852878	1.658007
6	435.56	377.3	431.31	361.12	0.975755	4.288365

6.6.1. X-ray diffraction patterns for step- quenched specimens.

x-ray diffraction pattern for alloy 1 which step- quenched heat treated has been shown in Fig.(6.115). It is clear that intermetallic compound which is γ_2 , is precipitated through step- quench treatment with enough amount so as to appear in x-ray diffraction pattern. However, there is still martensite ($\overline{\beta}$) phase in the microstructure of alloy.

1.During step – quench treatment , decomposition of β phase in to $\alpha + \gamma_2$ phase through eutectoid reaction may be occurred. This is due to high temperature of decomposition line of alloy 1 which has low content of aluminum (11% Al) . It is hypoeutectiod alloy as can be seen from (Cu-Al) alloy phase diagram.

In addition X-ray diffraction pattern for alloy2 has been shown in Fig.(6.116). It is clear that the predominant phase is ($\overline{\beta}$) martensite phase but with small percent of intermetallic compound (γ_2) phase. This alloy is hypereutectoid alloy with (13% Al) . According to equation (6.2) , alloy 2 has M_s equal to 102 ^oC so that step- quench treatment temperature (95 ^oC) may be made the instable disordered ($\overline{\beta}$) phase suffer from decomposition into $\alpha + \gamma_2$ phase which are more stable and equilibrium than disordered ($\overline{\beta}$) at this temperature. It is also apparent from Fig.(6.18) that ratio of γ_2 phase is less that the ratio of ($\overline{\beta}$) martensite phase in the internal structure of step-quenched alloy2.

On the other hand, Fig(6.117) shows the x-ray diffraction pattern for alloy3 which contains titanium additions of 0.4% Ti. It has been shown that the major phase is ($\overline{\beta}$) martensite phase in which high intensity of ($\overline{\beta}$) phase has been obtained. It is also apparent that precipitates from [(Cu9Al)2Ti] intermetallic compound in the matrix of martensite phase are precipitated through step- quench treatment .It is clear that the ratio of intermetallic

compound is very little compared with the presence of major matrix phase from $(\overline{\beta})$ phase.

X-ray pattern for alloy 6 which contains boron addition is shown is Fig.(6.118). Decomposition of unstable (β) phase in to $\alpha + \gamma_2$ phase through eutectoid reaction has been occurred. However, most of the matrix of alloy 6 is still $(\overline{\beta})$ martensite phase. It is clear that step-quench treatment of alloys 1,2,3 and 6 leads to form dual phase shape memory alloys in which martensite is the matrix which intermetallic compounds precipitates.

This means that step-quenched shape memory alloys may be more strength as well more stable transformation temperature than that indirect quench specimens .

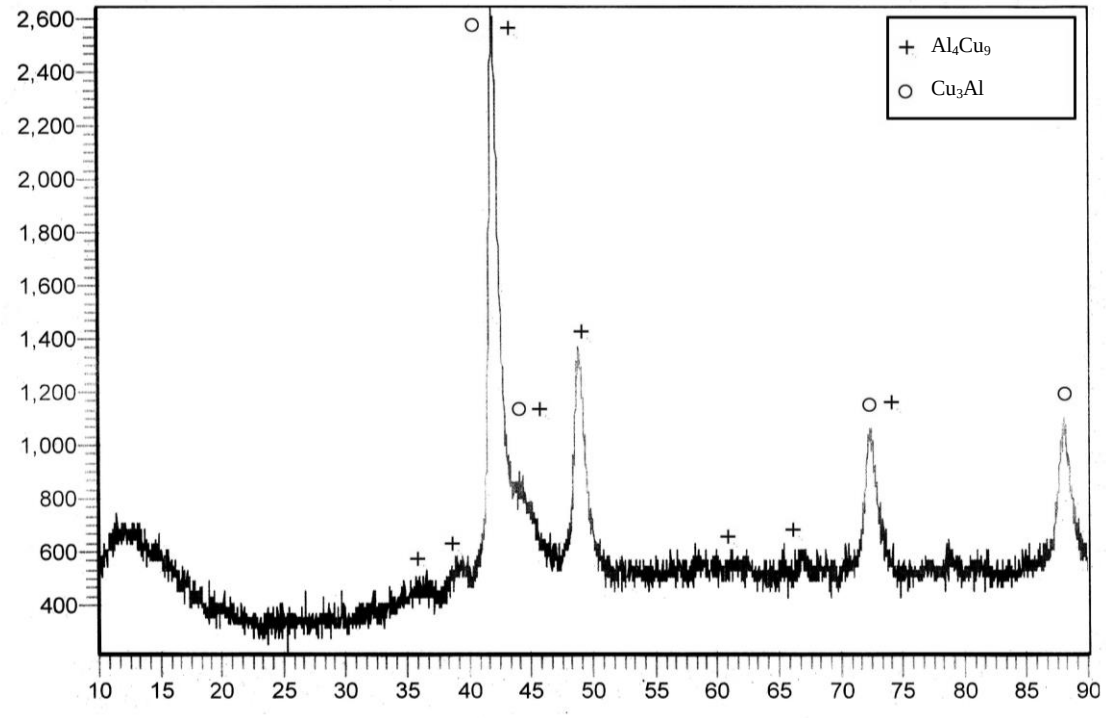

Fig.(6.115) XRD pattern of alloy 1 for step - quenched in 95 °C for 15 min.

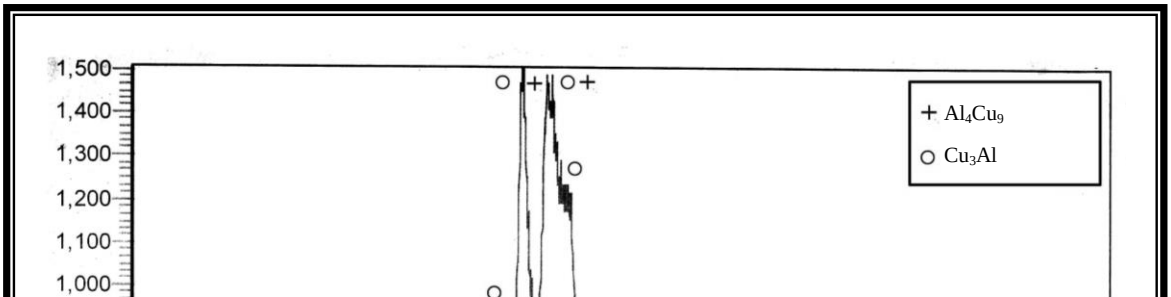

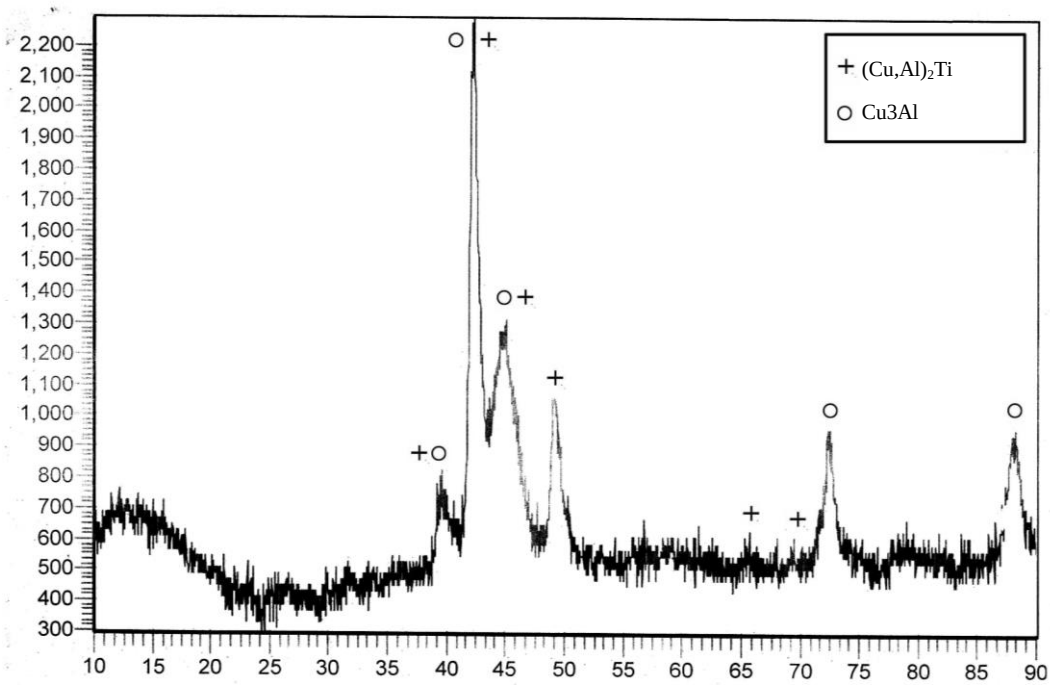

Fig.(6.117) XRD pattern of alloy 3 for step - quenched in 95 ºC for 15 min.

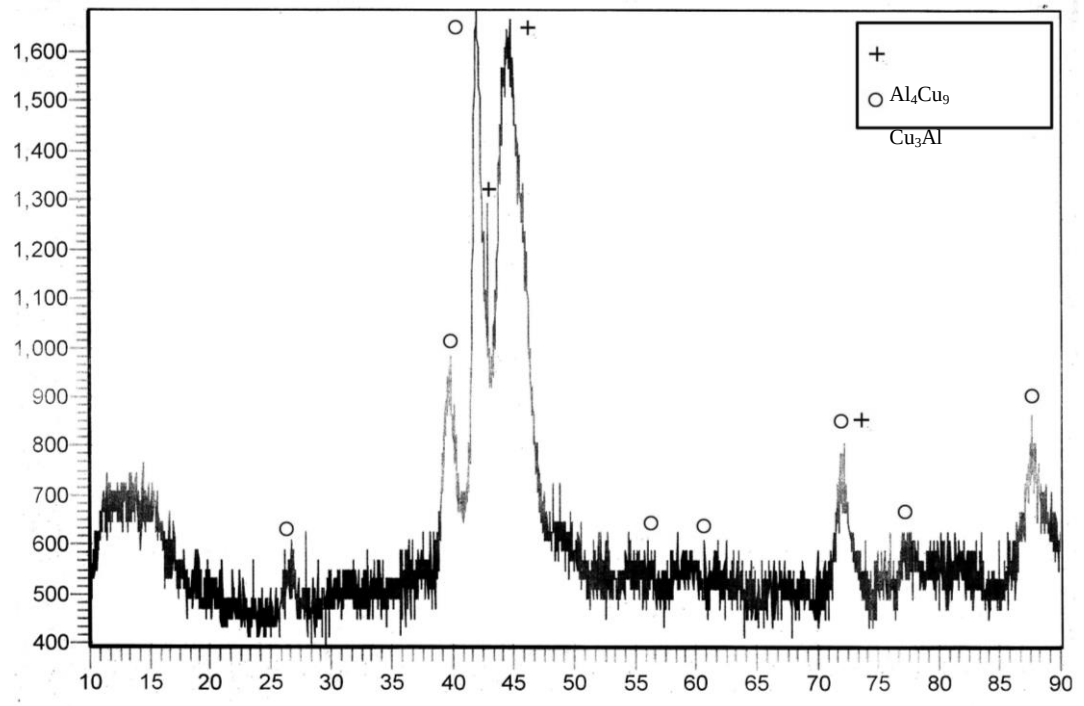

Fig.(6.118) XRD pattern of alloy 3 for step - quenched in 95 ºC for 15 min.

6.6.2. Light optical micrographs:

Here ,light optical micrographs for alloy 1,2,3 and 6 are considered to be attention in order not to scatter many microstructure image Two magnification resolution have been used as 1000 X and 2400 X . In addition two etchant solutions are also used to reveal grain boundaries and phases in the alloys microstructures. Etching the specimens with (NH_4OH + H_2H_2 +H_2O) solution reveals grain boundaries whereas etching specimens with (FeCl3+ HCl + H2O) solution reveal particle boundaries which is similar than grain boundaries in colors , and phases in the microstructure of alloys. The microstructure of alloys is complex due to presence of pores , multiphase and sometimes quench micro cracks rear pores which avoided them by step-quench treatment as possible.

Fig.(6.119) shows microstructure of alloy1 with 1000 x in a with(NH_4OH + H_2O_2+ $2O_2$+ H_2O) solution as etchant and 2400 x in b which the alloy is etched with solution of ($FeCl_3$ + HCl + H_2O). Note some intermetallic compounds from γ_2 precipitate near the grain boundaries or particle boundaries. This case it self may be applied in Figs.(6.120) , (6.121) , and Fig.(6.122) but for alloy 2,3 and 6 respectively . Unfortunates intermetallic compounds do not clearly appear in the micrographs. This is probably due to presence of pores and their distribution which makes complexity of microstructure in addition which

makes complexity of micrographs. This is probably due to presence of pores and their distribution which makes complexity of microstructure in addition to very fine structure of intermetallic compound itself.

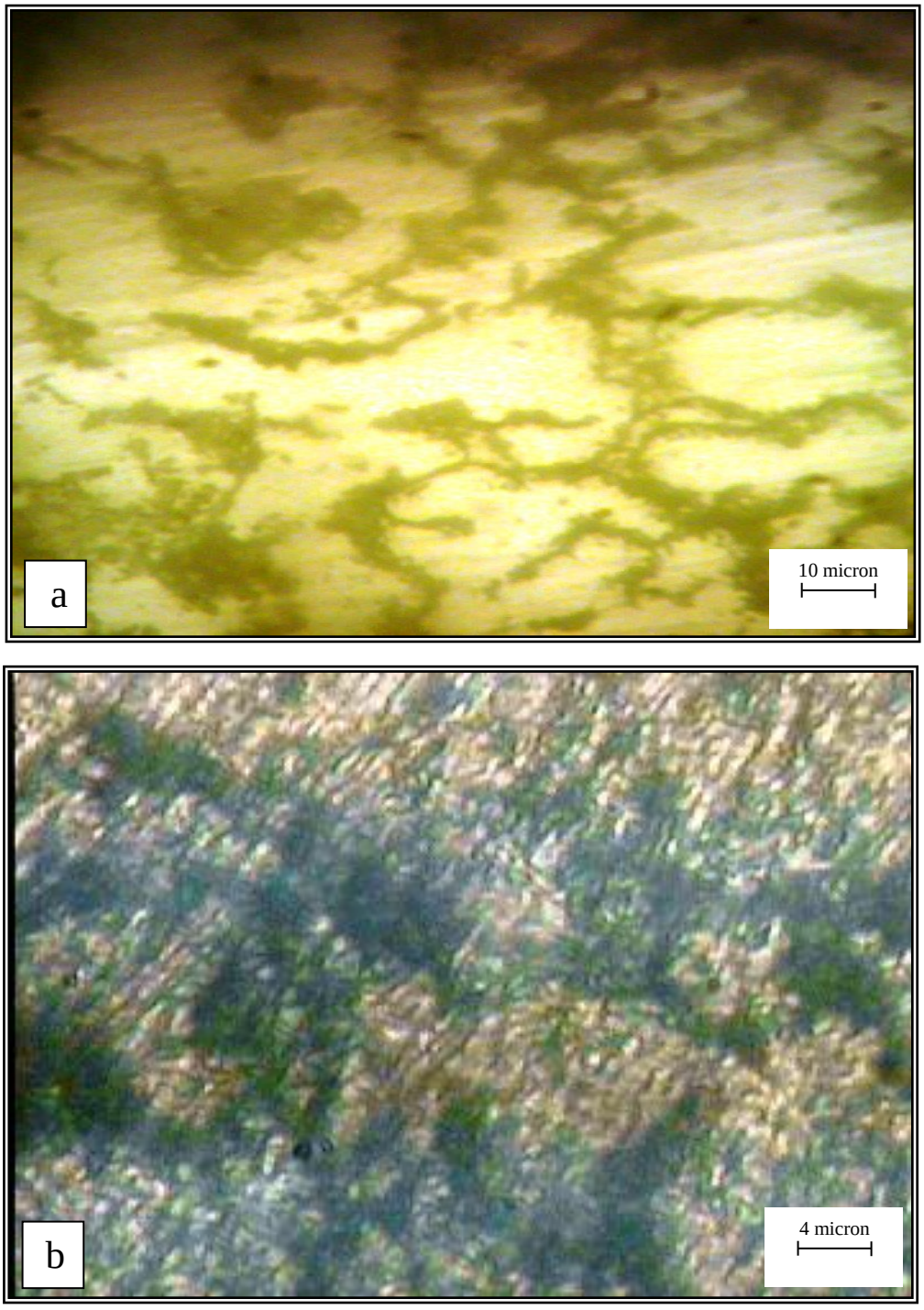

Fig.(6.119)LOM image for step-quenched of alloy 1 in 95 C followed by quenching in ice water for :a. etched in (NH4OH+H2O2+H2O) solution, b: etched in(FeCl3+HCl+H2O) solution.

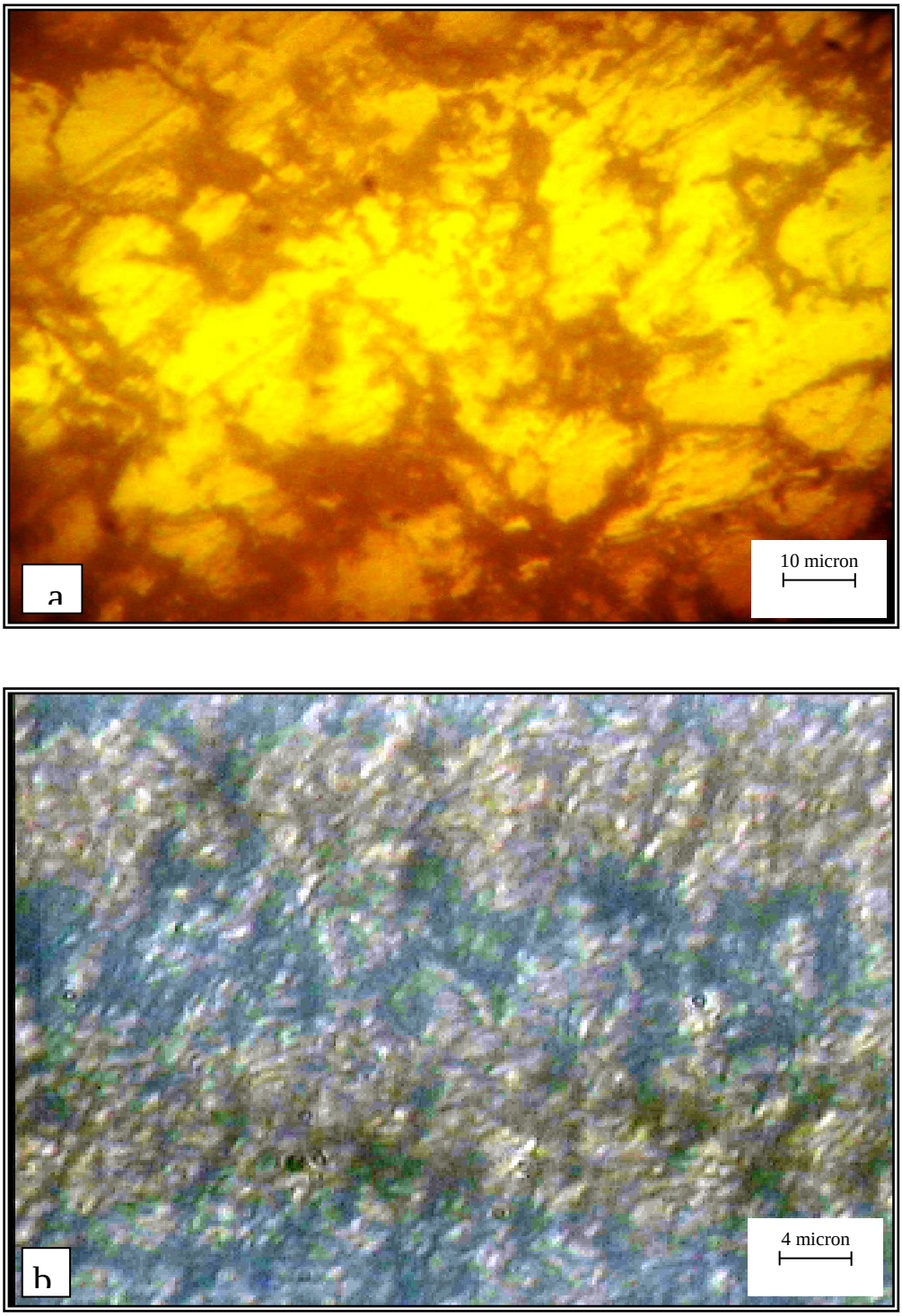

Fig.(6.120)LOM image for step-quenched of alloy 2 in 95 C followed by quenching in ice water for :a. etched in (NH4OH+H2O2+H2O) solution, b: etched in(FeCl3+HCl+H2O) solution

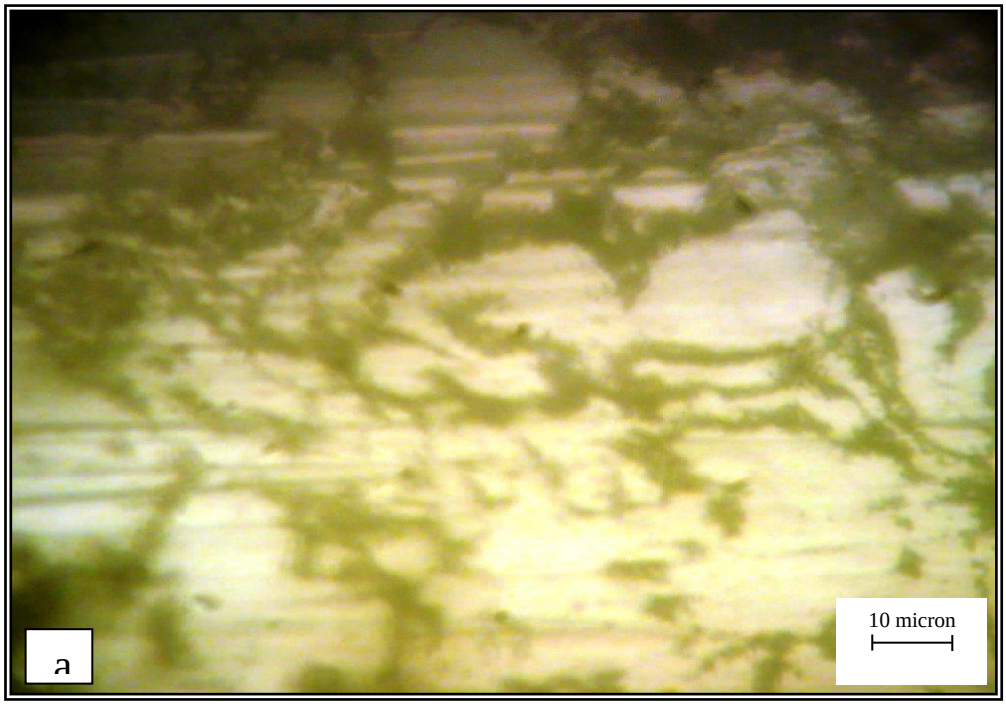

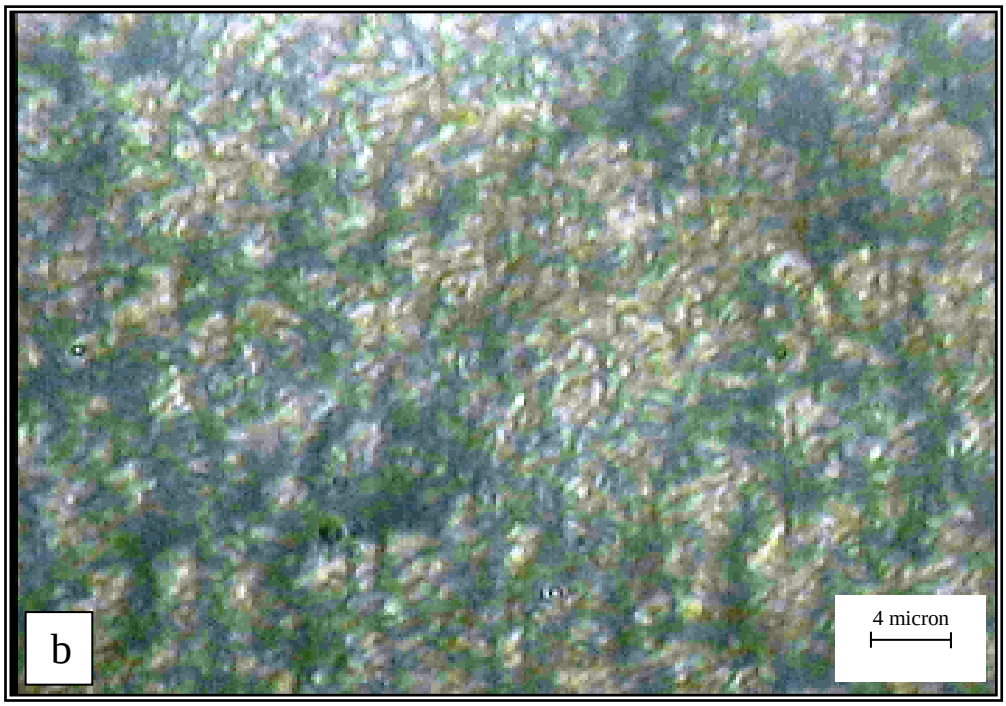

Fig.(6.121)LOM image for step-quenched of alloy 3 in 95 C followed by quenching in ice water for ∶a. etched in (NH4OH+H2O2+H2O) solution, b: etched in(FeCl3+HCl+H2O) solution

10 micron

4 micron

6.6.3. Scanning electron micrographs :

Scanning electron image for alloy 1 in the case of unetched has been shown in Fig.(6.123). The image reveals pores size and pores distribution on the surface of specimen. It has been shown that sintering difficulties of (Cu+Al) systems arise from aluminum content when aluminum content increase , porosity may be raised. All pores are agglomerated on the particle boundaries. Pores have non uniform shape as can be seen from Fig.(6.122).

It is clear that some regions in the surface of specimen are corroded when they are step- quenched in hot water. Unetched scanning electron image for alloys 2,3 and 6 are shown in Figs.(6.124) , (6.125) and Fig.(6.126) respectively. It is clear that using alloying element as grain refiner such as Ti or B causes small and low content of pores in the microstructure as can be seen in Fig.(6.125). It is probably that precipitates of intermetallic compounds require to high resolution of transmission electron microscope in which nanoscale has been taken into consideration. As clearly seen in Figs.(6.124) , (6.125) and Fig.(6.126), only distribution of pores and their shapes are clearly revealed whereas precipitates are not clearly appeared in the SEM image.

6.6.4. Vicker's macrohardness test results .

Vicker's macrohardness value as a function of alloying elements for step-quenched specimens, is shown in Fig.(6.127) In general speaking, aged martensitic specimens have vicker's macrohardness than in step- quenched specimens due to precipitate fine intermetallic compound in the aged treatment. However, the behavior of hardness profile is similar to the behavior of hardness profile of aged specimen in which the hardness is decreased with increasing weight percent of alloy elements. This is clearly seen is Fig.(6.127) . Generally , 0.4 wt % of alloying elements is optimum value for most elements to satisfy

suitable hardness number . In spite of using four readings for vicker's macrohardness value , standard deviation is high for each specimen. This is probably due to presence of pores in different shape and in nonuniform distribution .

6.6.5. Shape memory effect

Shape memory effect for step-quenched specimens has been determined using image analysis and image processing technique for impression of vicker's indenter using suitable low magnification resolution of optical microscope. Shape memory effect of all step- quenched specimens is shown in table (6.4).

As clearly seen from table (6.4) alloy 1 has maximums shape effect value (**23.63**%) whereas alloy 6 has a minimum value(**2.89934** %).

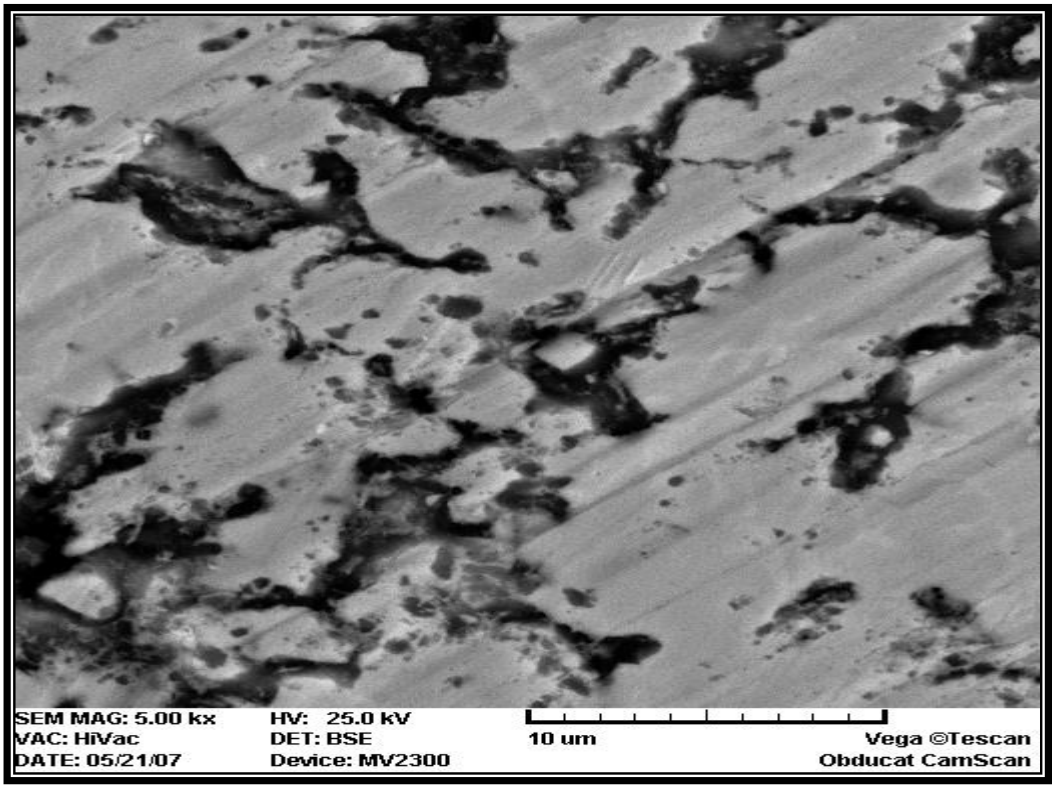

Fig.(6. 123) SEM image for alloy 1 under step quenched at 95 C for 15 min. and quenched in ice water.

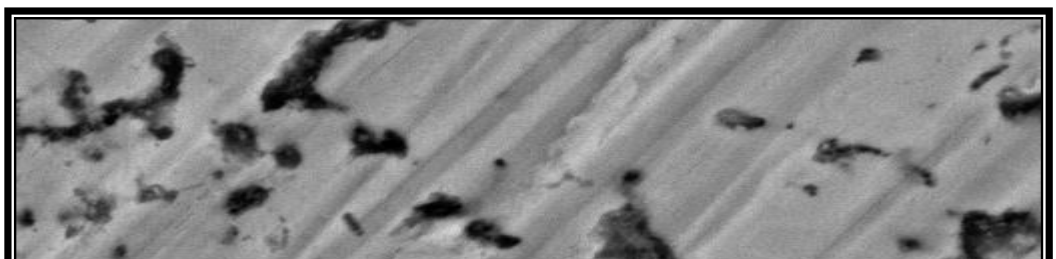

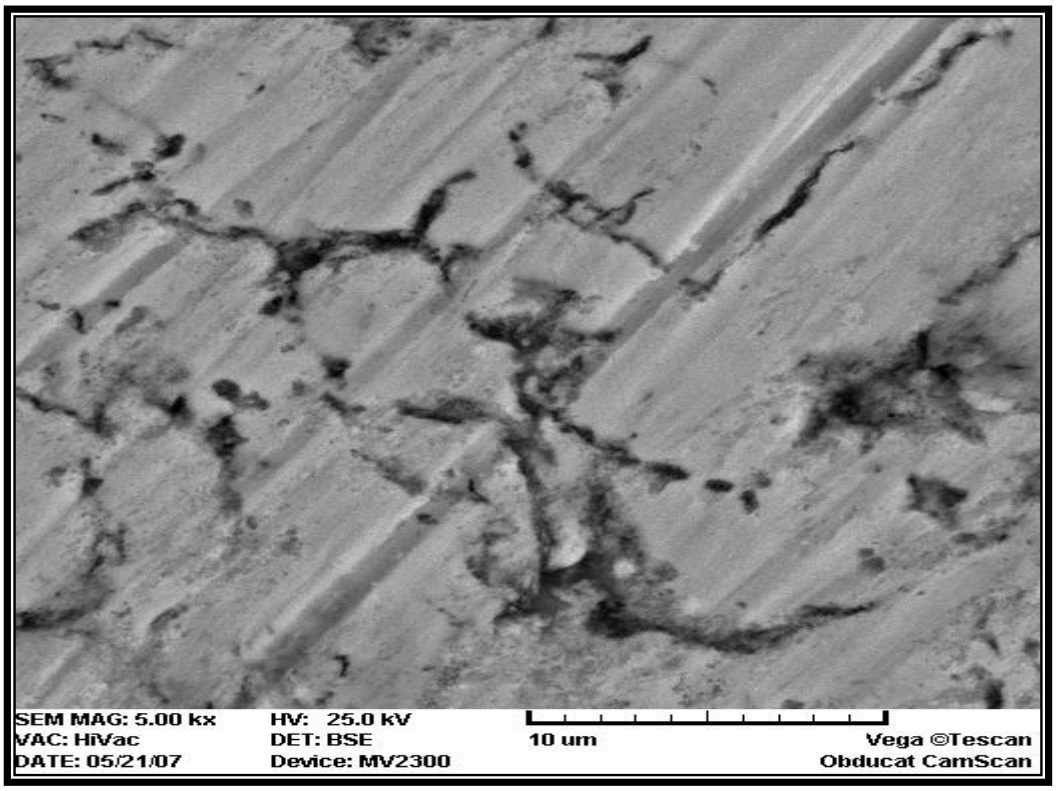

Fig.(6. 125) SEM image for alloy 3 under step quenched at 95 C for 15 min. and quenched in ice water

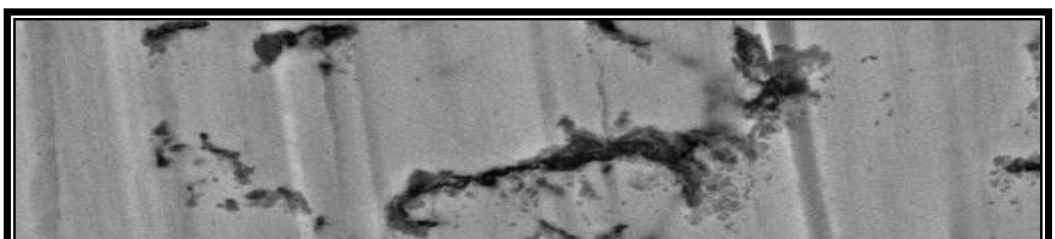

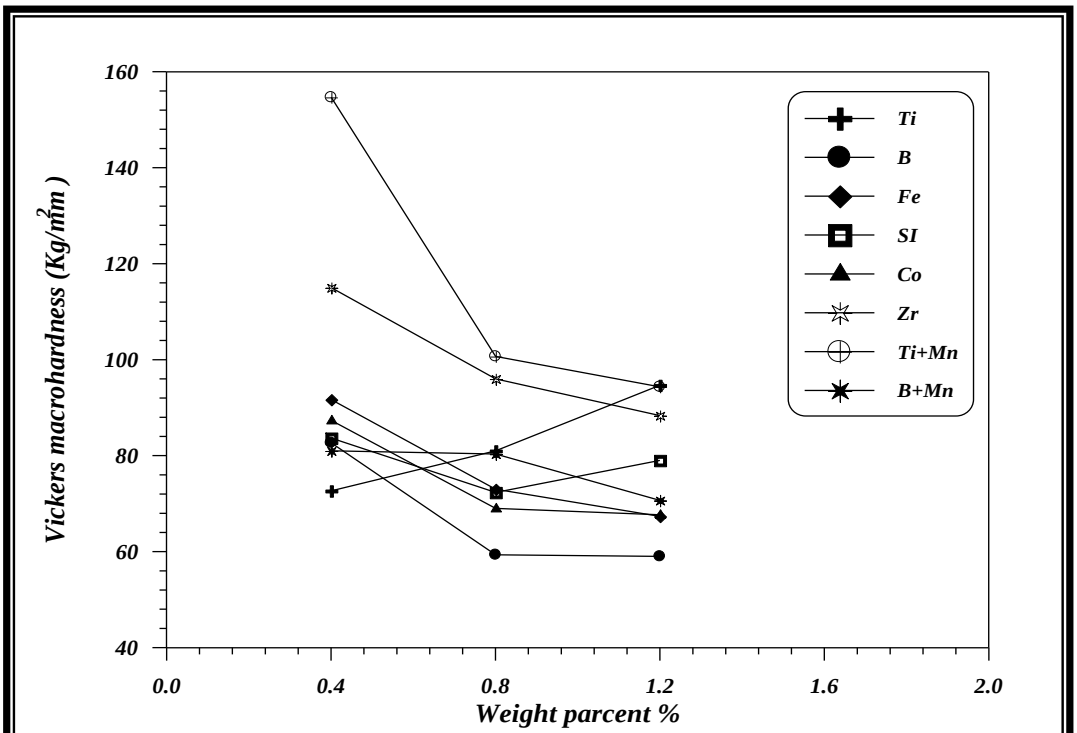

Fig.(6.127) Vickers macrohardness results for step-quenched samples according to weight percent of alloying elements.

Table(6.4).Shape memory recovery by Vickers hardness for step queched specimen.

Alloy No.	After aging treatment (by ferret's rectangle)	After recovery treatment	SME %

	Length(Pixel)	Width(Pixel)	Length(Pixel)	Width(Pixel)	by length	by width
1	824.73	661.83	629.84	570.46	23.63076	13.80566
2	446.29	434.58	434.52	414.73	2.637299	4.567629
3	526.04	491.95	470.67	455.84	10.52582	7.340177
6	422.51	417.50	410.26	403.43	2.89934	3.37006

6.7 Strain-temperature curves

Strain as a function of temperature at constant stress (100 Mpa) has been studied in order to know the amount f strain recovery and to know the range of transformation temperature during heating and cooling specimen. To conduct this test, direct quenched specimen in compressed up to the amount of stress of 100 Mpa and then placed in the furnace. The furnace was the heated from just above room temperature to (175 – 250 ^{o}C) according to tupe of alloy content of the specimen.Strain – temperature data is recorded by by dial guage with (0.001mm) accuracy and digital thermocouple curve for alloy 5 and alloy 6 has been shown in Fig.(6.128) and Fig.(6.129) respectively. The features of importance on these graphs are the two sharp changes in slope which corresponding to the beginning and end of transformation from martensite to oustensite during heating . Although the temperatures seen to have wide range and shiffed slightly slightly from that predicted form equation (6.2), the difference con be accounted for by consideration that the heating rate of the furnace in too high to allow stabilization at each temperature. This causes that the outer sections of the specimen reachs temperature before the inner section which which means that the majority of the specimen material is cooler than the indicated temperature. This may cause that the strain readings is to lag slightly behind the temperature readings . It is clear from this test that the compression testing does not significantly permanently impact the transformation temperatures . As can be seen Fig.(6.128) that small strain (0.16 %) is recovered during heating up to 225 ^{o}C. This is probably due to pore connections reopening or from edge effects. In addition, as can be seen from Fig.(6.129) , the recovery strain is 0.25 % but there a difference between the hystersis compared with that in Fig.(6.128) of alloy 5. After testing, specimen may be heated up to 450 ^{o}C and the strain measured to know the total shape recovery when the temperature just above A_s.

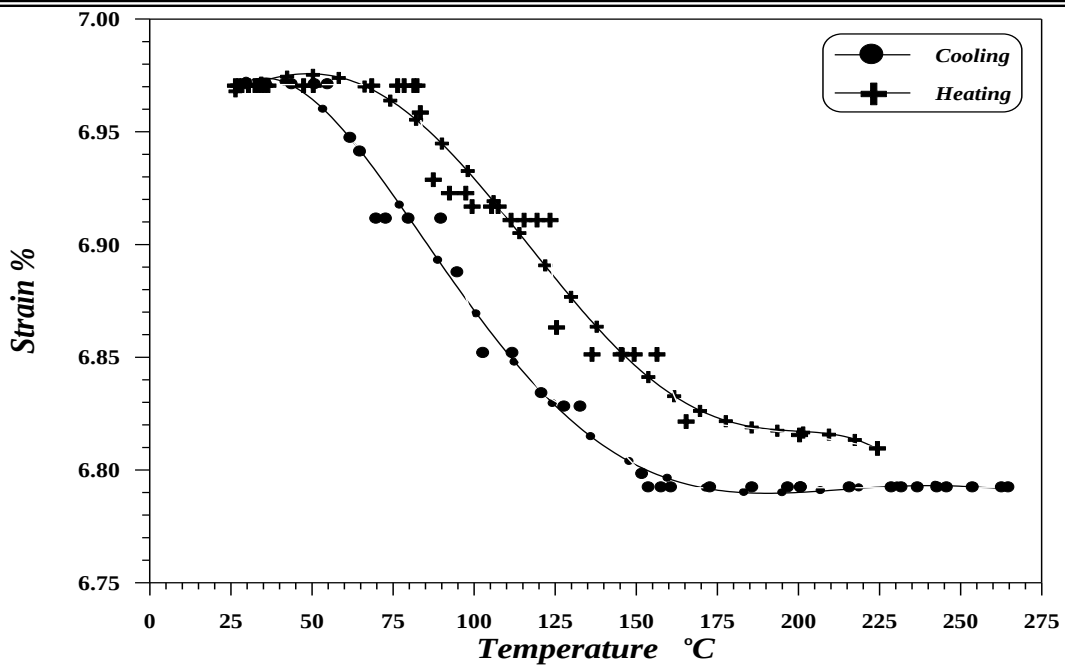

Fig.(6.128) Strain – temperature curve for alloy 5 at constant stress (100 MPa)

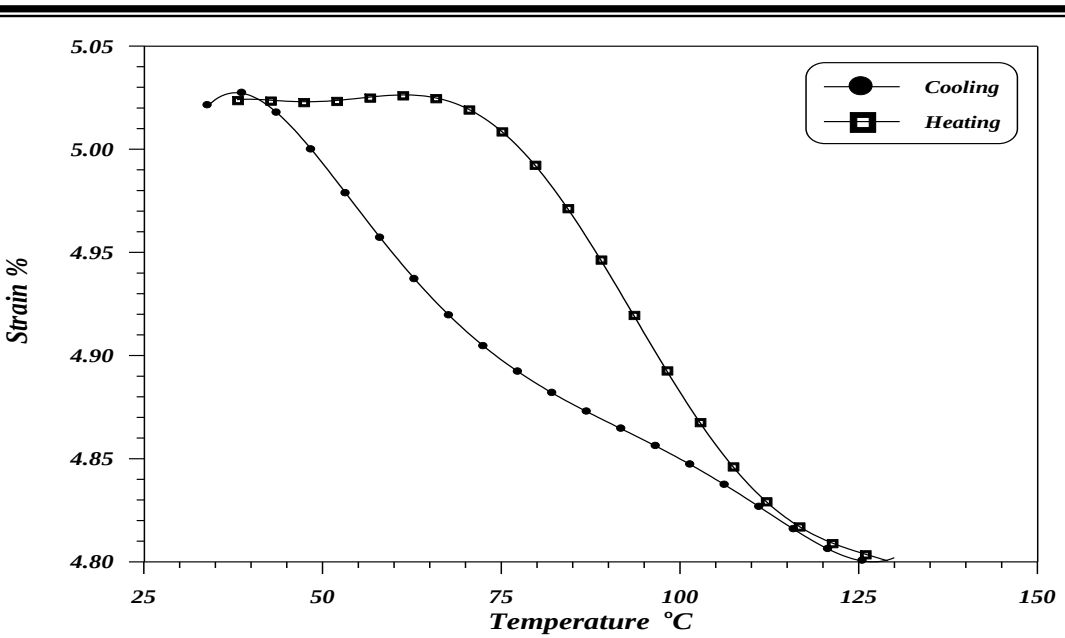

Fig.(6.129) Strain – temperature curve for alloy 6 at constant stress (100 MPa)

6.8 Numerical Results

Finite element analysis results for porous shape memory alloys prepared by powder metallurgy technique have presented here according to the pores distribution as follows:

6.8.1 Unit cell finite element results

Results obtained from unit cell finite element can be classified into the following manner according to assumption of periodic pores distribution.

6.8.1.1 Square unit cell FEA.

Fig.(6.130)shows the stress contour for (0.01*0.01mm) dimension of square unit cell for 10% as volume fraction of pores. This figure shows the distribution of normal stress in the x direction in which the maximum value of stress is obtained near the pore region in the last step of load increment. However, Fig.(6.131) shows the stress contour in the x direction for unloading case which also represents the maximum values near the holes (pores) which considered as stress concentration. It is clear that the region near pores are stressed enough to enhance stress-induced martensite more than the other regions.

In addition, Fig.(6.132) and Fig.(6.133) show the strain contour in x direction for the last load increment and unloading case (very small amount of loading but not equal to zero) respectively. It is apparent that some regions in the unit cell are strained up to 6.82 % that they will recover during unloading case up to 0.1 % which is very small elastic strain .furthermore, Fig.(6.134) and Fig.(6.135)show the stress- strain curve for loading and unloading cases for stress in the x and y direction respectively. It is apparent that small hystersis during loading and unloading paths has been observed. It is also apparent that the slope of the first stage of stress-strain curve is the same for the third stage due to the assumption of Auricchio model.

6.8.1.2.Hexagonal unit cell FEA results.

Fig.(6.136) shows the stress contour of x component in maximum load increment. It is apparent that maximum values of stress are occurred near the pores which means that pores may be promoted stress- induced martensite. In addition Fig.(6.137) shows the same stress contour but at the unloading case. It is clear that stresses may be released through unloading case in which phase transformation is occurred. Fig.(6.138)shows the high super elastic strain in which 9.46 % strain is given that is recovered into 1.0 % through unloading case as can be seen in Fig.(6.139).

In addition ,stress- strain curve for node 55 in x and y components are shown in Fig.(6.140) and Fig.(6.141) respectively. It is clear that hystersis throughout loading-unloading cases has been obtained for both components.

6.8.2.Real representation of microstructure FEA results.

Fig.(6.142) shows the image of microstructure of unetched alloy 12 specimen with 150X magnification. The equivalent finite element mesh of this image is shown in Fig.(6.143).

Fig.(6.144) and Fig.(6.145) show the total strain in the x direction for maximum load increment and during unloading step. It is apparent that regions strained up to 6.19 % are recovered into 1.2 % throughout unloading.

Fig.(6.146) shows the stress contour in the x direction for last load step. It is appeared that maximum stress is obtained near the pore region. However, Fig.(6.147)shows the same stress contour but at the unloading increment step. It is apparent that regions near the pores are stressed regions even after unloading case with comparison with the other regions which mean that these regions firstly transform into martensite and finally return to austenite during unloading.

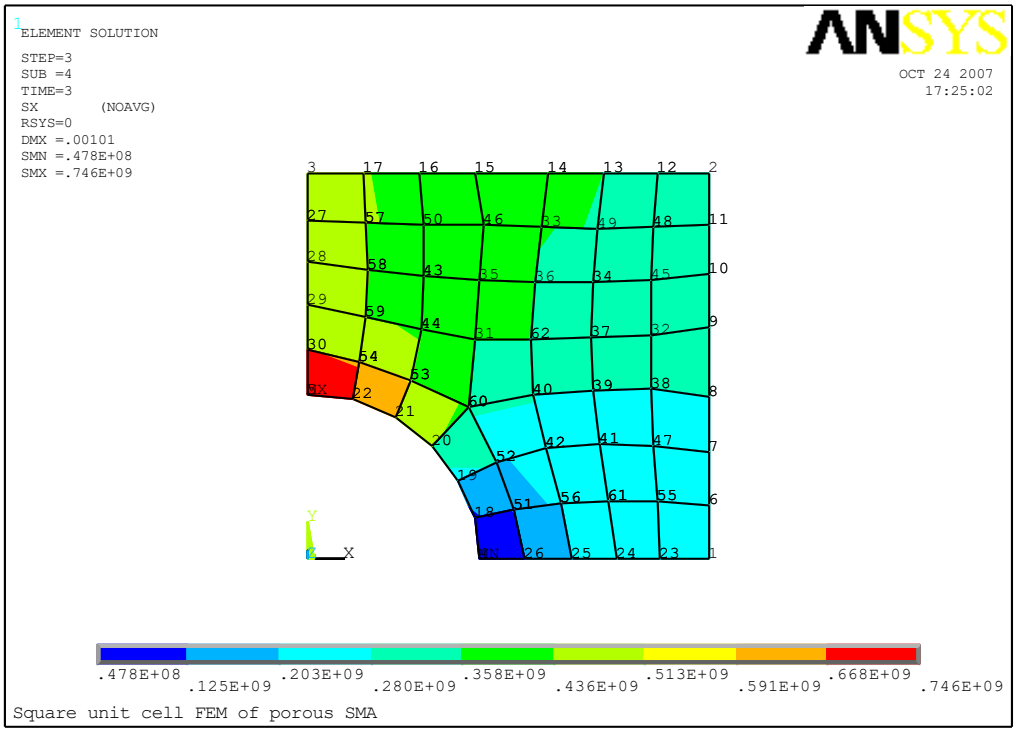

Fig.(6.130) Stress contour in x direction for square unit cell FEA For final maximum increment load step.

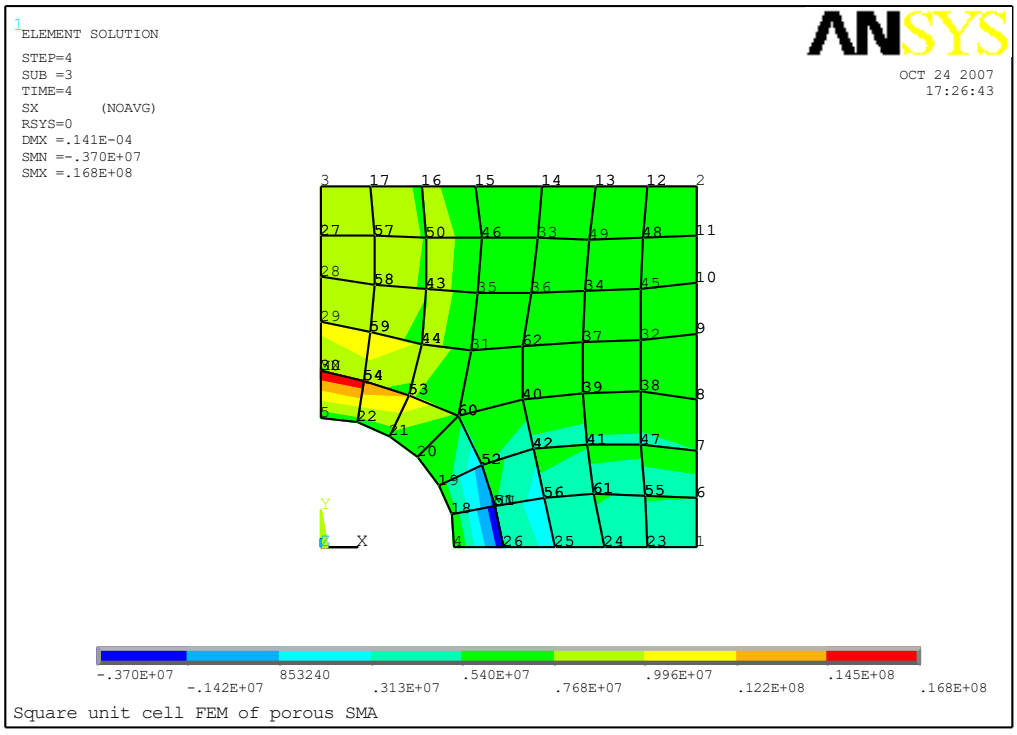

Fig.(6.131) Stress contour in x direction for square unit cell FEA For unload step.

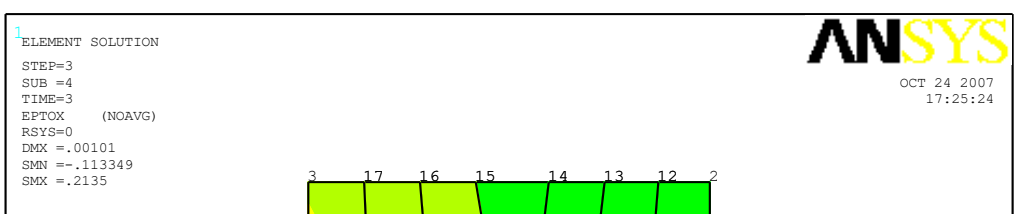

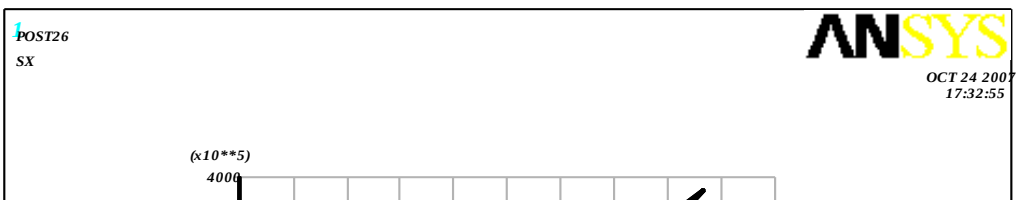
1
POST26
SX
ANSYS
OCT 24 2007
17:32:55
(x10**5)
4000

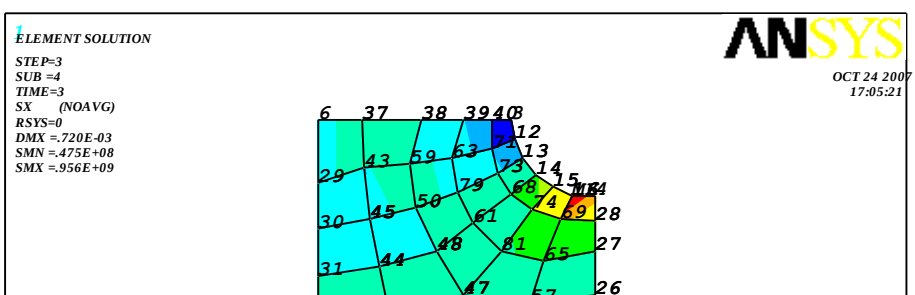
1
ELEMENT SOLUTION
STEP=3
SUB =4
TIME=3
SX (NOAVG)
RSYS=0
DMX =.720E-03
SMN =.475E+08
SMX =.956E+09
ANSYS
OCT 24 2007
17:05:21

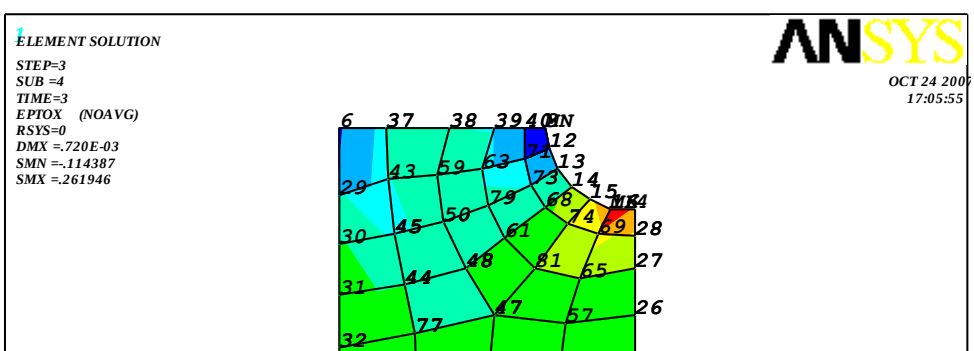
1
ELEMENT SOLUTION
STEP=3
SUB =4
TIME=3
EPTOX (NOAVG)
RSYS=0
DMX =.720E-03
SMN =-.114387
SMX =.261946
ANSYS
OCT 24 2007
17:05:55
6
37
38
39
40
MN
12
13
14
15
43
59
63
73
29
79
68
74
69
28
30
45
50
61
27
48
81
65
31
44
47
57
26
77
32

1
POST26
SX
ANSYS
OCT 24 2007
04:32:37
(x10**5)
4500
4000
3500
3000
2500
2000
ss (N/m2),Sx

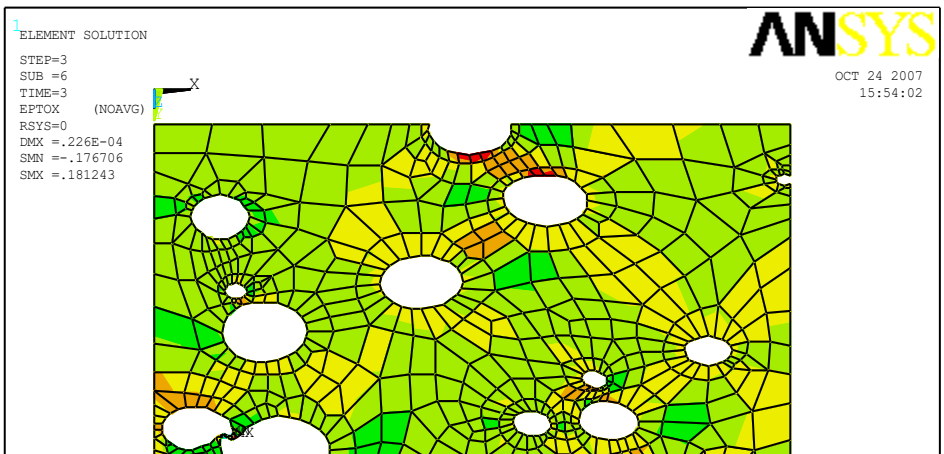
1
ELEMENT SOLUTION
STEP=3
SUB =6
TIME=3
EPTOX (NOAVG)
RSYS=0
DMX =.226E-04
SMN =-.176706
SMX =.181243
ANSYS
OCT 24 2007
15:54:02
Y
Z
X
MN
MX

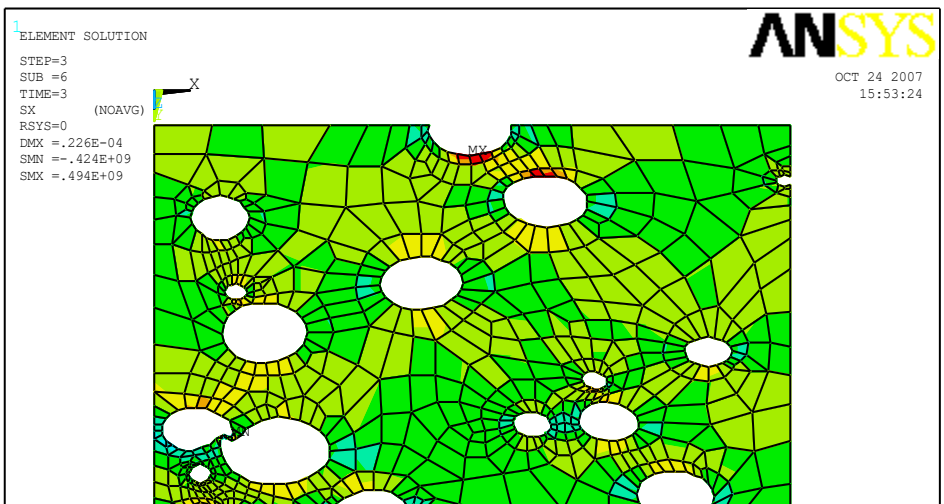
ELEMENT SOLUTION
STEP=3
SUB =6
TIME=3
SX (NOAVG)
RSYS=0
DMX =.226E-04
SMN =-.424E+09
SMX =.494E+09
ANSYS
OCT 24 2007
15:53:24
X
MX
MN

Conclusion and Recommendations For future works.

7.1 Conclusions

The main conclusions form the experimental and numerical study of the examined copper-based shape memory alloys in this research are :

1. The addition of (0.4 wt% Ti) to (Cu +13wt %Al +3.8wt % Ni) alloy causes a shape memory effect of (59 %) from 10 % of total strain.
2. shape memory effect obtained in this work is (5.9 %) in comparison with standard copper aluminum nickel base shape memory alloys of (4-7 %).
3. In comparison with standard (Ni/Ti) base shape memory alloys (8-10%) the SME observed in this study is (80 %).
4. It appears that the lower porosity leads to the higher SME.
5. Using image processing and images analysis of LOM images of elemental and blended powders is efficient to determine particle size and particle distribution before compacting of powders in addition to pore size and pore distribution in the microstructure of sintered compacts.
6. x-ray diffraction technique used to identify phases, shows that sintering at 600 ^{o}C for 3hr followed by sintering at 850 ^{o}C for 3hr. is efficient to satisfy sintering process in which elemental powders are completely transformed into alloy structure.
7. Martensitic transformation is occurred in Cu Al Ni based shape memory alloys completely by direct quenching form 840^{o}C into ice water(2-4 ^{o}C) whereas aging and step-quenched heat treatments tend to stabilize martensite phase with γ_2 intermetallic compound precipitates in the microstructure as clearly shown from x-ray diffraction analysis.
8. Phase transformations occurred in a temperature range of (70-130 °C) as indicated by electrical resistance test.
9. Ultrasonic results also support the occurrence of shape memory effect in all the examined alloys.

10. The use of unit cell finite element technique with periodic square and hexagonal arrangement of pores is efficient for analysis of porous shape memory alloys prepared with powder metallurgy technique.
11. Real represent of microstructure LOM image using image analysis with combination of finite element analysis is more accurate than unit cell finite element approach.
12. It has been shown that titanium addition to Cu Al Ni base shape memory alloys tends to form (Cu, $Al)_2Ti$ as intermetallic compound rather than $\gamma_2 (Al_4Cu_9)$ through recovery heating up to 450 ^oC and during aging treatment.
13. Numerical analysis for the hystersis of SMAs showed that regions around pores are preferred sites for martensitic transformations.
14. porous Cu Al Ni based shape memory alloys have suitable shape memory effect and shape recovery in addition to law weight which make them as suitable material for energy absorption applications.
15. It appears that Auricchio model is only applied to analyze superelastic behavior of shape memory alloy.

7.2 Suggestions and recommendation for future work.

The following suggestions should be taken into consideration for future work of copper-based shape memory alloys prepared by powder metallurgy technique.

1. Differential scanning calorimetric (DSC) test should be used in order to measure transformation temperature for the prepared alloys in heating and cooling cycles.
2. Transmission electron microscopy (TEM) should be used to reveal the structure of martensite, its form and the degree of ordering for obtained martensite .
3. In order to increased density of sintered compacts, double action press or hot isostatic pressing should be used.
4. To investigate shape recovery and superelastic behavior of prepared alloys in high temperature , stress- strain curve should be tested at high temperature in heating cycle and cooling subzero temperature during cooling cycle .
5. Corrosion and wear behavior of prepared alloys may be investigated in future in different mediums.
6. Advanced composite material in which metal matrix reinforced with shape memory alloy particles of prepared alloys may be studied and developed in future.
7. Fatigue behavior of copper based shape memory alloys should be studied to use them in space applications.

الخلاصة

ان التطورات السريعة في الصناعات الفضائية و العسكرية و الطبية تتطلب العديد من براءات الاختراع او تطوير بعض المواد. إحدى أهم هذه التطورات في هذا المجال هو استخدام السبائك التي تستعيد شكلها.

في هذه الدراسة تم تحضير ودراسة سبائك ذات أساس من النحاس- الألمنيوم – النيكل(CuAlNi) باستخدام تقنية ميتالورجيا المساحيق وذلك بإضافة عناصر سبك مختلفة من (Ti,B,Fe,Si,Co,Zr,Ti+Mn,B+Mn) وبأضافات مختلفة تتضمن (0.4,0.8 ,1.2 wt %.) من هذه العناصر. تم دراسة متغيرات التصنيع مثل مقدار ضغط الكبس ومعدل تسليط الضغط و الفترة الزمنية لبقاء الضغط وكذلك درجة حرارة التلبيد و زمن التلبيد. تم استخدام عدة معاملات حرارية من شانها تأكيد خواص استعادة الشكل مثل المعاملة المحلولية ومعاملة التعتيق ومعاملة الإخماد بالإضافة إلى المعاملات الحرارية التي تستعيد الشكل. أجريت الفحوصات الفيزيائية و الميكانيكية للسبائك المحضرة بعد عملية الكبس وبعد عملية التلبيد مثل فحص الكثافة الضاهرية و المسامية وامتصاصية الماء وتغير أبعاد النموذج بالإضافة إلى قياس صلادة النماذج الملبدة. تم قياس تأثير استعادة الشكل من خلال نماذج فحص الصلادة ونماذج فحص الانضغاط بعد أن أجريت عدة معاملات حرارية.

تم قياس المقاومة الكهربائية عند درجات حرارية مختلفة باستخدام فرن أنبوبي وكذلك تم قياس زمن مرور الموجات فوق الصوتية للنماذج المعاملة بالإخماد المباشر بعد التشكيل ومن ثم المعاملة حراريا ولجميع السبائك المحضرة .اجري فحص حيود الأشعة السينية للنماذج بعد عملية الكبس وبعد عملية التلبيد للتحقق من نجاح عملية التلبيد وكذلك اجري الفحص بعد المعاملات الحرارية المختلفة للكشف عن التحولات الطورية في حين استخدم المجهر الضوئي والمجهر الإلكتروني الماسح لكشف البنية المجهرية للسبائك المحضرة .تم حساب حجم المسامات وطبيعة توزيعها بالاضافة الى حجم الدقائق

وتوزيعها باستخدام تقنية معالجة الصور وتحليلها المأخوذة من المجهر الضوئي باستخدام برنامج (Mat lab ver 7) .

اعتمدت طريقة الشرائح المتناهية باستخدام خلية أحادية مربعة وأخرى سداسية لتمثل توزيع دوري للمسامات الدائرية لتحليل البنية للسبائك المسامية التي تستعيد شكلها وكذلك تم اعتماد الطريقة لتحليل البنية المجهرية الحقيقية للسبائك المحضرة من خلال اخذ صور للبنى بالمجهر الضوئي ومعالجتها وتحليلها وتحويلها إلى شكل هندسي يمكن تحليله بواسطة الشرائح المتناهية باستخدام برنامج (Ansys ver 9) .

يبدو ان السبيكة(Cu+13 wt% Al+3.8wt%Ni) المضاف اليها (.4 wt % Ti) تمتلك أعلى تأثير لاستعادة الشكل (% 58.824) بالمقارنة مع السبائك المحضرة الأخرى.بالمقارنة مع السبائك القياسية ذات الاساس من(Ni/Ti) تمثل هذة النسبة (80%) من نسبة استعادة الشكل والتي تبلغ (% 12-8) .

تتراوح المسامية الضاهرية للسبائك المحضرة بين(% 38-10) ويبدو إن أعلى نسبة تأثير استعادة الشكل يكون عند اقل مسامية.

إن معاملات الإخماد المباشر أعطت أعلى تحول مارتنسايتي في حين معاملات التعتيق و الإخماد المرحلي أعطى اقل تحولا بسبب ترسب طور جاما في البنية.

اظهر تحليل الشرائح المتناهية باعتماد الخلية الأحادية وكذلك التمثيل الحقيقي للبنية المجهرية إن التحول المارتنسايتي الناتج بالإجهاد يكون في المناطق القريبة من المسامات والتي تعمل كمناطق لتمركز الاجهادات.

References

1.Adachi , K.,Perkins, J.and Wayman , C.M. " the Crystallography and boundary structure of interpolate- group combinations of 18 R martensite variants in Cu-Zn-Al shape memory alloys " Acta Met.,Vol.36 , No.5, P.1343, 1988.

2.Addington , M. and Schodek , D. " Smart materials and New technologies for architecture and design professions " Architectural press, P.8, 2005.

3.Ahlers ,M."The martensite transformation :mechanisms and Crystallography" philosophical magazine A , Vol. 82, No.6, P.1039,2002.

4.Ariapour , A. " Effect of Nitrogen on Fe-Mn- based shape memory alloys" PhD thesis , University of Toronto , Canada , 1998.

5.Asanovic,V., Delijic , k. and Jaukovic ,N." isothermal decomposition of the $\overline{\beta}$ phase in Cu-Zn-Al shape memory alloys " J.Materiali in tehnologije, vol.40,No.4,P.153, 2006.

6.Aslanidis ,D. , Serneels , A. and Mooriehgem ,W. V. " Cu-based shape memory alloy hinge for deployment application " proceeding of shape memory and super elastic Technologies , SMST -99, 5-9 Sept . , Antwerp, Belgium , Mkrieherm , P and Astanidis D. (eds) ,1999.

7.Auricchio , F. and Sacco, E. " A temperature dependent beam for shape memory alloys: Constitutive modeling , finite element implementation and numerical simulations " J. comput . Methods . appl. Mech . Eng,Vol 144, P. 171, 1999.

8.Auricchio, F., Taylor ,R.L. and Lubliner ,J." shape memory alloys : mecromodelling and Numerical simulation of the super elastic behaviour " J. Comput Method .Appl . mech . Engg. Vol. 146,P. 281, 1997.

9.Auricchio, F." shape memory alloys:applications micromechanics, macromodelling and numerical simulations phD thesis , university of California , 1995.

10.Barcelo, G.and Ahlers , M. " Stress induced hexagonal martensite in Cu-Zn-Al" J.Scrita Met.9 Vol.16, No.1, p.l, 1982.

11.Barrett, C.and Massalski, T.B. " structure of metals " 3rd revised Edition , Pergamon press, 1980.

12.Baz, A. , Iman , k. and Mcloy, J . " The dynamcs of helical shape actuators J. Intell . Mat syst. Struct. , Vol. 1, P. 105, 1990.

13.Brinson , L.C. , Schmidt , I and Lammering , R." Stress- induced transformation behaviour of a polycrystalline Ni Ti shape memory alloy: Micro and macromchanical investigations Via in situ optical microscopy " J. Mat . processing and system (MPS) , 2003.

14.Buehler, W.J.and Wiley. R.C" Nickel based alloys" technical report , 1965, us-patent 317851.

15.Buehler,W.J. and Wang, F.E" A summary of recent research on the Nitinal alloys and their potential application in Ocean engineering " J. Appl. Phys. 9Vol.34, P.1475, 1963.

16.Cadogan , D. P. , Scarborough , S. E. , Lin , J.k . and Sapna III, G. H. " shape memory Cmposite development for use in Gossamer space inflatable structures 43rd AIAA/ ASME/ ASCE/ AHS/ ASC Structures , structural daynamics and material conf. and exhibit AIAA Gossomer spacecraft forum , App, 22-25, 2002, Denver.

17.Cakmak ,S. , Artunc ,E., Kayali, N.and Adjguzed , O. Lattice change in shape memory CuZnAl alloys on aging at room temperature " Turk J.phys., Vol. 25, P.467, 2001.

18.Cando , A.M. and Lovey , F.C. " Interaction of twin boundaries with stacking faults in 2H martensite : a high resolution electron microscopy study " J.philosophical magazine, Vol.83, No. 12, P.1479. 2003.

19.Chute , J.D. and Hodgson, D.E. " Eyeglass frame and SMA the challenge and the product. In Duerig, T.w and Wayman , C.M . (eds) , " Engineering Aspects of shape memory alloys" . P.420, 1999.

20.Comes , A.G. and Manosa ,L. " Lattice stability and martensite transition in β-phase cu-based shape memory alloys : long –wavelength acoustic mode antarmonicity "philosophical Magazine A, Vol.80, No.70, P.1681,2000.

21. Crone , W.C. , Show , G.A. , Stone , D.S. , Johnson , A. D.and Ellis , A.B. " shape recovery after microindentation of Ni Ti thin films" Society for Exp.Mech. 2002 SEM annual Conf. Proceedings , Carlotte , NC, 2003.

22.Crone , W.C. , Yahya, A.N. and Perpezko, J.H. " Bulk shape memory NiTi with refined grain size synthesized by mechanical alloying " Mat.Sci. forum , Vol.386, P.597,2002.

23.Deng, Y, AND Ansell ,G.S " Investigation of thermoelastics martensitic transformation ia a Cu- Zn –Al alloys " Acta Met. Mat. , Vol . 38, No. 19 P. 69, 1990.

24.Dowson, G." powder metallurgy : the process and its products " IOP pub. LTd. 1990.

25.Erbstoeszer,B. , Armstrong , B.,Taya, M.and Inoue, K. " stabilization of the shape memory effect in NiTi: An experimental investigation " Acta Mat., Vol.42, P.1145,2000.

26.Euchen, S. and Duerig, T.W. " The effects of pseudoelastic prestraining on the tensile behaviour and two- way shape memory effect in aged NiTi" Acta Metall ; Vol.37, No.8 , P.2245.

27.Ferrira, R.A, Rocha Lima, E.P. , Filho, A.A., de Quadros , N.F., Araujo , O.O. and Yadava, Y.P." Microstructural Evolution in a Cu Zn A l shape memory alloy: Kinetics and Morphological Aspects" J.Mat. Research , Vol.3, No.4, P.119, 2000.

28.Franz, M.and Hornbogen , E."Martensitic transformation of a CuZnAl-shape memory alloy strengthened by hot rolling " J. science and engineering,A252,p.157,1998.

29.Freeby , C.L. " Dimensional change of sintered metal compacts" in metals handbook 9th edition ,Vol.7 , powder metallurgy " , P.290, 1984>

30.Fugazza, D. " shape memory alloydevices in earthquake engineering : Mechanical properties , constitive modeling and numerical simulations " Msc thesis , pavia, 2003.

31.Gaskell, D.R. " Introduction to metallurgical thermodynamics " McGraw Kogakusha LTD , 1973.

32.Golyandin ,S.,Sinani,A., Humbeeck, J.V., Sohaller, R. and DeBaties ,R." The effect of shock- wave loading on transformation temperatures, elastic and anelastic properties of $\overline{\beta}_1$ Cu-Al-Ni martensitic single crystals", philosophical Magazine A, Vol.82 ,No.12, P.2419 , 2002.

33.Graesser , E.J. and Cozzarelli , F.A." shape memory alloys as new materials for seismic isolation " J. Engg.Mech.9 Vol.117, P.2590,1991.

34.Greaf , M.,Humbeeck , J.V. , Andrade , M. and Deleay, L. " The stabilization of step- queched copper –zinc – aluminium martensite. Part IV: changes in the microstructure. " J. scripta met. ,vol. 19 , p.643, 1985.

35.Higgins , R.A. " Engineering Metallurgy part I: Applied physical metallurgy " 4 th edition, ELBs , 1977.

36.Hubbard, J.L. " microscopy and image analysis", in metals Handbook 9th edition , Vol.7, " powder metallurgy". P.225, 1984.

37.Humbeeck , J.V. , Janssen , J., Ngoie , M. and Delaey , L. " the stabilization of step- quenched copper –zinc-Aluminium martensite . part I: the reverse transformation temperatures " J.scripta Met., Vol.18 , No.9 , p.895, 198,1984.

38.Jasim, S.A. " Production of metal powder by using electrochemical process" Msc thesis , University of Babylon , 2006.

39.Jianxin , W., Bohang, J. and Hsu , T.Y. " Influence of grain size and ordering degree of the parent phase on μ_s in a CuZnAl alloy containing boron " Acta Met.,Vol.36,No.6, P.1521,1988.

40.Juang, Z.W. , YE, c.w and Hsu , T.Y." Group theory and crystal ography of the martensitic transformation in a Cu-26.71 Zn-4.15Al shape memory alloy J.Acta met. , Vol.33 , No.11, p.2075, 1985.

41.keefe, A.C. " Thermomechanical characterization of shape memeory alloy tube actuators " Msc thesis , University of California , USA, 1999.

42.Kim , H.W. " Two way shape memory effect of Cu-Zn- Al alloys induced by a constrained heating method " J.Mat.Science lett., Vol . 22, P. 1233,2003.

43.Kim , Y.D. and Wayman , C.M. " shape memory effect in powder metallurgy. Ni Al alloys" Scripta Met. Mat. , Vol.24, No.2, P.245, 1990.

44.Kim, C.and Lee , S.H. " Complex 3D behaviors of composite cylinders with 3-D shape memory alloy actuators." Int.J. modern phys.B, Vol.17, No. 8 and 9 , P.1851,2003.

45.Klar , E. " production of Copper powder by the reduction of copper oxide " in metals Handbook 9th edition, Vol. 7, " powder metallurgy " P.105 , 1984.

46.Knopp. W.V. , Duncan , W.R , Gordon , S., Moses , A.J. and Toaz. M.W., " Roll compacting of metal powders " in metals handbook 9th edition , Vol.7, " powder metallurgy, p.401.1984.

47.Koop,k.,Lootz ,D., Momma , C.,becher ,B.and Kieckbush, M." Stent material Nitinal determination of characheri stics and component simulation using finite element method" J. Biomedical research , 2001.

48.Lenel , F.V. " Mechanical Fundamentals of consolidation " in metals handbook 9th edition , Vo1.7, " powder metallurgy" , P.296. 1984.

49.Li, B.Y. , Rong , L.J . and Li , Y.Y. " the influence of addition of TiH_2 in elemental powder sintering porous Ni-Ti alloys" Mat. Sci. engg. A, Vol.P.169,2000.

50.Li, B.Y. , Rong, L.J. , Luo,X.H. and Li , Y.Y. " Transformation behaviour of sintered porous NiTi alloys J.Met.Mat. Transactions A, Vol. 30A, P.2753, 1999.

51.Li, B.Y., Rong, L.J. , Li, Y.Y. and Gjumter, U.E. " Synthesis of porous Ni-Ti shape memory alloys by self propagating high temperature synthesis: reaction, mechanism and anisortropy in pore structure ", Acta mat.,Vol.48 , P.3895,2000.

52.Liang,Y. , Taya , M. and Mori, T." Micromechanics of stress- induced martensitic transformation in mono and poly crystalline shape memory alloys NiTi Advanced materials for the 1st Century : the 1999 Julia R weertman symposium , 1999 , Cincinnati, USA , oct.31- NoV.4, P.385.

53.Lindquist,P.G and Wayman , C.M. "martensitic transformation shape memory effect " in " Ergineering Aspects of shape memory alloys " edited by Duering, T.W and Wayman , C.M , P.58, 1990.

54.Liu,Y." Detwinning process and its anisotropy in shape memory alloys" smart mate, proceedings of SPIE, Vol.4234,2001.

55.Lu, Y.H. , Liang , S., Chu , W.Y. and QiaO , L.J. " In situ AFM observation of crack propagation in CuNiAl shape memory alloy " J. intermetallics, Vol.10, P.823, 2002.

56.Lubliner, J. and Auricchio ,F " Generalized plasticity and shape memory alloys", Int .J. Sol.Struct. , Vol.33, No.7, P.991, 1996.

57.Lukkassen , D. and Meidell, A." Advanced materials and structures and their fabrication processes" 3rd edition , Narvik university collage , 2003.

58.Mantovani, D." Shape memory alloys: properties and biomedical applications " , 2000 available at website www.tms.orgL/ pubs / journals / JOM/ jom.htmp.

59.Mathews , P.E. " Apparent density of metal powders" in Metals handbook 9th edition , Vol.7 , " powder metallurgy", p.272, 1984.

60.Mathews , P.E. " Sintering of copper- based materials in metals handbook 9th edition,Vol.7, " Powder metallurgy" p.376, 1984.

61.McNaney , J. M . , Imbeni, V. , J. M. , Imbeni , V. , Jung, Y. , Papadopoulos , P. and Ritchie , R.O. " An experimental study of the superelastic effect in a shape memory Nitinol alloy under biaxial loading " J. Mech . Mat. , Vol. 35, P.969, 2003.

62.Mellor,B.G. , Guilemany , J.M. , Miguel , J.R. , Fernandez, J., Amengual, A., Lovey , F.C. and Torra, V." stabilized stress-induced martensite its use in two wayshape memory training processes " Scripta Met. ,Vol.24, No.2, P.241, 1990.

63.Melton , K.N. " Ni Ti based shape memory alloys " in Engineering Aspects of shape memory alloys, Duerig, T.W and Wayman , C.M. (eds). P.21, 1990.

64.Meyers , M.A.and chawla, k.K." Mechanical behaviour of materials", prentice hall co., 1999.

65.Miyazaki, S. " shape memory alloys" Inst. Mater.Sci. university of tsukuba, Ibaraki, Japan , 1999, E-mail: miyazaki @ ims.tsukuba.ac.jp.

66.Nasser, S.N., Choi, J.Y., Guo, W.G. and Isaacs , J.B. " Very high strain- rate response of a Ni Ti shape memory alloy" J.Mech. Mat. , Vol.37, P.287, 2005.

67.Neov, D., Viana, M.and Mikula , P., " Insitu high resolution neutron diffraction study of stress induced martensitic transformation in CuAlZnMn shape memory alloy " 5th European Conf. on Residual stresses , step. 28-30, 1999, The Netherlands.

68.Ni, W., Cheng, Y.T. and Grummon,"D.S. Recovery of microindents in a nickel-titanium shape memory alloy: A self healing effect", App. Phys. Lett., Vol.80 , No. 18, P.3310, 2002.

69.Orban, R.L."New research directions in powder metallurgy " J.Romanian reports in physics , Vol.56 , No.3, p.505 , 2004.

70.Otsuka ,K. and Ren ,X " Review about Recent development in the research of shape memory alloys " J.Intermetallics VOL.7, P.511, 1999.

71.Otsuka , k. and kakeshita , T. " science and technology of shape memory alloys : New developments " MRS bulletin ,Feb.2002. available en www.mrs org/ publications / bulletin .

72.Otsuka , K. and Ren , X. " Martensitic transformations in nonferrous shape memory alloys" J. Mat. Sci. and engg. , Vol.A273, P.89, 1999.

73.Parker, R. H. " An introduction to chemical metallurgy " ,2nd edition, Pergamon press,P.221,1978.

74.Pena , J., Gil, F.J. and Guilemany , T.M. " Effect of microstructure on dry sliding wear behavior in CuZnAl shape memory alloys " Acta Mat., Vol.50 , P.3115, 2002.

75.Penrod, L.E." Fabrication and characterization of porous shape memory alloys ", Msc thesis Texas A& M university , 2003.

76.Planes ,A. , Macqueron , J.L., Molin , M.and Guenin , G. Calorimetric study of ordering in a β Cu-Zn-Al alloy", J.Mat.science and Engineering ,Vol. 50 , P.53, 1981.

77.Pons, J.and Cesari, E. " Interaction between γ phase precipitates and martensite in Cu-Zn-Al alloys " J. Mat.Struct . , Vol. 6, No.2, 1999.

78.Porter , D.A. and Easterling , K.E." phase transformations in metals and alloys " 2nd Edition , Chapman and Hall , 1992.

79.Price, P.E. and Kohler , S.P. " Hot isostatic pressing of metal powders " in metals Handbook 9th edition , Vol.7 , " powder metallurgy ", P.419. 1984 .

80.Qidwai , M.A., Entchev, P.B., Lagoudas,D.C.and Degiorgi,V.G., " Modelling of the thermomechaincal behaviour of porous shape memory alloys " Int.J.solids and structures,Vol. 38 , p.8653,2001.

81.Qiu, J. , Tani , J. , Osanai, D. , Urushiyama, Y. and Lewinnek ,D. " High speed response of SMA actuators Int .J. Appl. Electromag .Mech. , Vol. 12, P.87, 2000.

82.Raul ,B., Perez,S., Recarte , V. Oscar, A. and Juan, S." Advanced shape memory alloys processed by powder metallurgy ", J.Advanced Engineering materials, Vol.2,No.1-2,p.49,2000.

83.Rebelo, N. and Perry ,M. " Finite element analysis for the design of Nitinol metical devices" Pacific consultants.Com.

84.Recarte ,V.,Perezsaez , R.B., No,M.L. and Juan, J.S." Ordering Kinetics in Cu-Al-Ni Shape memory alloys" J.Appl.phys., Vol.86,No.10 ,P.5467,1999.

85.Recarte ,V.Lambri , O.A., Perezsaez , R.B. , NO , M.L. and Juan, J.S." Ordering temperature in Cu- Al- Ni shape memory alloy " J.Appl. phys.Let.,Vol.70,No.269,P.3513,1997.

86.Reed-Hill , R.E. " physical metallurgy principles " van nostrand Co.1964.

87.Ricksecker, R.E." copper and copper alloys", in metals handbook 9th edition , Vol.9 ,Metallagraphy .P.733, 1984.

88.Sampath, V." Effect of Zr on microstructure and transformation temperatures of Cu-Al-Ni Shape memory alloys" Int. Conf. smart materials , structures and systems, Bangalore , India , July 28-30 , 2005.

89.Scarsbrook , G.and Stobbs , W.M. " The martensitic transformation behaviour and stabilization of rapidly quenched Cu-Zn-Al ribbons " Acta Met. , Vol.35, No.1, p.47,1987.

90.Schweiger, J. "Aircraft control , applications of smart structures" in Encyclopedia of smart materials, Vol. 1 and 2 , Schwartz, M.(editor) , P.42, 2002.

91.Silva , M.C. and Lima , S.J." Evaluation of mechanical alloying to obtain Cu-Al-Nb shape memory alloys" ,J. Materials research , vol.8, No.2,P.119, 2005.

92.Sinha, A.K. " powder metallurgy " Dhanpat Rai and sons Delhi , 2nd edition , 1995.

93.Smallman , R.E. and Bishop , R.J. " Modern physical metallurgy and materials engineering " sixth edition , Reed educational and professional publishing , 1999.

94.Stevenson , R.w. " P/ M copper- based alloys" in Metals Handbook 9th edition , Vol. 7 , " powder metallurgy", p.733, 1984.

95.Surbled, P., Pioufle , B.L. , Yang, E.H. and Fujita, H. " Shape memory alloys for micromenbranes actuation" available on website : www.Fujita3.iis.u-tokyo.ac.jp.

96.Szprynagcz, M., Enokizona, M.and Todaka , T. " Improvement of shape memory effect in Fe-Cr-Co Ni-Si-Mn ferromagnetic alloy with change of Mn contents" Int.J.Appl. electromag. Mech. , vol.20, P.149, 2004.

97.Thornton , P.A. and Colangelo , V.J. " Fundamental of engineering materials " Prentice- Hall , 1985.

98.Trochu ,F.and Qian,Y.Y." Nonlinear finite element simulation of Superelastic shape memory alloy parts" J. comput.struct., Vol .62, No.5, P.799,1997.

99.Trochu F., Brailovski, V.,Meunier, M., Terriault, P. and Qian , Y.Y." Thermomechanical analysis of shape memory devices" J.Biomedical Mat.Engg.,Vol.6, P.389,1996.

100.Turner , T., Zhong,Z.W. and Mei, C. " Finite element analysis of the random response suppression of composite panels at elevated temperatures using shape memory alloy fibers" J.AIAA ,1994.

101.Turner, T.L. and Patel. H.D. " Analysis of SMA hybrid composite structure using commercial codes" in smart structures and materials : modeling , signal processing of SPIE Vol.5383, No.12, CA, 14-18 March, 2004.

102.Van Vlack, F." Element of material science",2nd Edition,Adison wisely publishing Co. 1978.

103.Ullrich , W.J . " Sieve analysis" in metals Handbook 9th edition,vol 7 , " powder metallurgy " P.214, 1984.

104.Wayman, C.M. and Duerig , T.W "An introduction to martensite and shape memory " on Engineering Aspects of shape memory alloys ,P.3, 1990, Duerig ,T.W, Metton , K.N, Stockel ,D. and Wayman , C.M. (eds) .

105.Wei, Z.G. , Sandstrom , R.and Miyazaki, S." Review shape memory material and hybrid composites for smart systems" J. of Mat. Science, Vol. 33, P.3743,1998.

106.Wick, A. " the bending behaviour of Superelastic Ni Ti " MSC thesis , University of karlsruhe , 1994.

107.Wojnar , L. " Image analysis : Applications in material engineering " CRC,press, P.98,1999.

108.Wu, M.H. " Cu-based shape memory alloys " In Enginnering Aspects of shape memory alloys ,P.96, 1990, Duerig ,T.W , Melton ,K.N. , Stockel ,D, and Wayman ,C. M. (eds).

109.Wu,M.H." Fabrication of Nitinol materials and components" Proceedings of the internation conf. on shape memory and Superelastic Technologies, Kunming, china, P.285,2001.

110.Zhao ,Y., Taya , M. , kang , Y. and Kawasaki , A. " Compression behaviour of porous Ni Ti shape memory alloy" Acta Mat. , Vol. 53, P 337 , 2005 .

111.Zhao , C. " Relationships between martensite transformation temperatures and Compositions in Fe-Mn-Si based shape memory alloys " J. Inst. Mech .Engrs , , Vol .214 , Part L , P. 1739, 2000.

References

1.Adachi , K.,Perkins, J.and Wayman , C.M. " the Crystallography and boundary structure of interpolate- group combinations of 18 R martensite variants in Cu-Zn-Al shape memory alloys " Acta Met.,Vol.36 , No.5, P.1343, 1988.

2.Addington , M. and Schodek , D. " Smart materials and New technologies for architecture and design professions " Architectural press, P.8, 2005.

3.Ahlers ,M."The martensite transformation :mechanisms and Crystallography" philosophical magazine A , Vol. 82, No.6, P.1039,2002.

4.Ariapour , A. " Effect of Nitrogen on Fe-Mn- based shape memory alloys" PhD thesis , University of Toronto , Canada , 1998.

5.Asanovic,V., Delijic , k. and Jaukovic ,N." isothermal decomposition of the $\overline{\beta}$ phase in Cu-Zn-Al shape memory alloys " J.Materiali in tehnologije, vol.40,No.4,P.153, 2006.

6.Aslanidis ,D. , Serneels , A. and Mooriehgem ,W. V. " Cu-based shape memory alloy hinge for deployment application " proceeding of shape memory and super elastic Technologies , SMST -99, 5-9 Sept . , Antwerp, Belgium , Mkrieherm , P and Astanidis D. (eds) ,1999.

7.Auricchio , F. and Sacco, E. " A temperature dependent beam for shape memory alloys: Constitutive modeling , finite element implementation and numerical simulations " J. comput . Methods . appl. Mech . Eng,Vol 144, P. 171, 1999.

8.Auricchio, F., Taylor ,R.L. and Lubliner ,J." shape memory alloys : mecromodelling and Numerical simulation of the super elastic behaviour " J. Comput Method .Appl . mech . Engg. Vol. 146,P. 281, 1997.

9.Auricchio, F." shape memory alloys:applications micromechanics, macromodelling and numerical simulations phD thesis , university of California , 1995.

10.Barcelo, G.and Ahlers , M. " Stress induced hexagonal martensite in Cu-Zn-Al" J.Scrita Met.9 Vol.16, No.1, p.l, 1982.

11.Barrett, C.and Massalski, T.B. " structure of metals " 3rd revised Edition , Pergamon press, 1980.

12.Baz, A. , Iman , k. and Mcloy, J . " The dynamcs of helical shape actuators J. Intell . Mat syst. Struct. , Vol. 1, P. 105, 1990.

13.Brinson , L.C. , Schmidt , I and Lammering , R." Stress- induced transformation behaviour of a polycrystalline Ni Ti shape memory alloy: Micro and macromchanical investigations Via in situ optical microscopy " J. Mat . processing and system (MPS) , 2003.

14.Buehler, W.J.and Wiley. R.C" Nickel based alloys" technical report , 1965, us-patent 317851.

15.Buehler,W.J. and Wang, F.E" A summary of recent research on the Nitinal alloys and their potential application in Ocean engineering " J. Appl. Phys. 9Vol.34, P.1475, 1963.

16.Cadogan , D. P. , Scarborough , S. E. , Lin , J.k . and Sapna III, G. H. " shape memory Cmposite development for use in Gossamer space inflatable structures 43rd AIAA/ ASME/ ASCE/ AHS/ ASC Structures , structural daynamics and material conf. and exhibit AIAA Gossomer spacecraft forum , App, 22-25, 2002, Denver.

17.Cakmak ,S. , Artunc ,E., Kayali, N.and Adjguzed , O. Lattice change in shape memory CuZnAl alloys on aging at room temperature " Turk J.phys., Vol. 25, P.467, 2001.

18.Cando , A.M. and Lovey , F.C. " Interaction of twin boundaries with stacking faults in 2H martensite : a high resolution electron microscopy study " J.philosophical magazine, Vol.83, No. 12, P.1479. 2003.

19.Chute , J.D. and Hodgson, D.E. " Eyeglass frame and SMA the challenge and the product. In Duerig, T.w and Wayman , C.M . (eds) , " Engineering Aspects of shape memory alloys" . P.420, 1999.

20.Comes , A.G. and Manosa ,L. " Lattice stability and martensite transition in β-phase cu-based shape memory alloys : long –wavelength acoustic mode antarmonicity "philosophical Magazine A, Vol.80, No.70, P.1681,2000.

21. Crone , W.C. , Show , G.A. , Stone , D.S. , Johnson , A. D.and Ellis , A.B. " shape recovery after microindentation of Ni Ti thin films" Society for Exp.Mech. 2002 SEM annual Conf. Proceedings , Carlotte , NC, 2003.

22.Crone , W.C. , Yahya, A.N. and Perpezko, J.H. " Bulk shape memory NiTi with refined grain size synthesized by mechanical alloying " Mat.Sci. forum , Vol.386, P.597,2002.

23.Deng, Y, AND Ansell ,G.S " Investigation of thermoelastics martensitic transformation ia a Cu- Zn –Al alloys " Acta Met. Mat. , Vol . 38, No. 19 P. 69, 1990.

24.Dowson, G." powder metallurgy : the process and its products " IOP pub. LTd. 1990.

25.Erbstoeszer,B. , Armstrong , B.,Taya, M.and Inoue, K. " stabilization of the shape memory effect in NiTi: An experimental investigation " Acta Mat., Vol.42, P.1145,2000.

26.Euchen, S. and Duerig, T.W. " The effects of pseudoelastic prestraining on the tensile behaviour and two- way shape memory effect in aged NiTi" Acta Metall ; Vol.37, No.8 , P.2245.

27.Ferrira, R.A, Rocha Lima, E.P. , Filho, A.A., de Quadros , N.F., Araujo , O.O. and Yadava, Y.P." Microstructural Evolution in a Cu Zn A l shape memory alloy: Kinetics and Morphological Aspects" J.Mat. Research , Vol.3, No.4, P.119, 2000.

28.Franz, M.and Hornbogen , E."Martensitic transformation of a CuZnAl-shape memory alloy strengthened by hot rolling " J. science and engineering,A252,p.157,1998.

29.Freeby , C.L. " Dimensional change of sintered metal compacts" in metals handbook 9th edition ,Vol.7 , powder metallurgy " , P.290, 1984>

30.Fugazza, D. " shape memory alloydevices in earthquake engineering : Mechanical properties , constitive modeling and numerical simulations " Msc thesis , pavia, 2003.

31.Gaskell, D.R. " Introduction to metallurgical thermodynamics " McGraw Kogakusha LTD , 1973.

32.Golyandin ,S.,Sinani,A., Humbeeck, J.V., Sohaller, R. and DeBaties ,R." The effect of shock- wave loading on transformation temperatures, elastic and anelastic properties of $\overline{\beta}_1$ Cu-Al-Ni martensitic single crystals", philosophical Magazine A, Vol.82 ,No.12, P.2419 , 2002.

33.Graesser , E.J. and Cozzarelli , F.A." shape memory alloys as new materials for seismic isolation " J. Engg.Mech.9 Vol.117, P.2590,1991.

34.Greaf , M.,Humbeeck , J.V. , Andrade , M. and Deleay, L. " The stabilization of step- queched copper –zinc – aluminium martensite. Part IV: changes in the microstructure. " J. scripta met. ,vol. 19 , p.643, 1985.

35.Higgins , R.A. " Engineering Metallurgy part I: Applied physical metallurgy " 4 th edition, ELBs , 1977.

36.Hubbard, J.L. " microscopy and image analysis", in metals Handbook 9th edition , Vol.7, " powder metallurgy". P.225, 1984.

37.Humbeeck , J.V. , Janssen , J., Ngoie , M. and Delaey , L. " the stabilization of step- quenched copper –zinc-Aluminium martensite . part I: the reverse transformation temperatures " J.scripta Met., Vol.18 , No.9 , p.895, 198,1984.

38.Jasim, S.A. " Production of metal powder by using electrochemical process" Msc thesis , University of Babylon , 2006.

39.Jianxin , W., Bohang, J. and Hsu , T.Y. " Influence of grain size and ordering degree of the parent phase on μ_s in a CuZnAl alloy containing boron " Acta Met.,Vol.36,No.6, P.1521,1988.

40.Juang, Z.W. , YE, c.w and Hsu , T.Y." Group theory and crystal ography of the martensitic transformation in a Cu-26.71 Zn-4.15Al shape memory alloy J.Acta met. , Vol.33 , No.11, p.2075, 1985.

41.keefe, A.C. " Thermomechanical characterization of shape memeory alloy tube actuators " Msc thesis , University of California , USA, 1999.

42.Kim , H.W. " Two way shape memory effect of Cu-Zn- Al alloys induced by a constrained heating method " J.Mat.Science lett., Vol . 22, P. 1233,2003.

43.Kim , Y.D. and Wayman , C.M. " shape memory effect in powder metallurgy. Ni Al alloys" Scripta Met. Mat. , Vol.24, No.2, P.245, 1990.

44.Kim, C.and Lee , S.H. " Complex 3D behaviors of composite cylinders with 3-D shape memory alloy actuators." Int.J. modern phys.B, Vol.17, No. 8 and 9 , P.1851,2003.

45.Klar , E. " production of Copper powder by the reduction of copper oxide " in metals Handbook 9th edition, Vol. 7, " powder metallurgy " P.105 , 1984.

46.Knopp. W.V. , Duncan , W.R , Gordon , S., Moses , A.J. and Toaz. M.W., " Roll compacting of metal powders " in metals handbook 9th edition , Vol.7, " powder metallurgy, p.401.1984.

47.Koop,k.,Lootz ,D., Momma , C.,becher ,B.and Kieckbush, M." Stent material Nitinal determination of characheri stics and component simulation using finite element method" J. Biomedical research , 2001.

48.Lenel , F.V. " Mechanical Fundamentals of consolidation " in metals handbook 9th edition , Vo1.7, " powder metallurgy" , P.296. 1984.

49.Li, B.Y. , Rong , L.J . and Li , Y.Y. " the influence of addition of TiH_2 in elemental powder sintering porous Ni-Ti alloys" Mat. Sci. engg. A, Vol.P.169,2000.

50.Li, B.Y. , Rong, L.J. , Luo,X.H. and Li , Y.Y. " Transformation behaviour of sintered porous NiTi alloys J.Met.Mat. Transactions A, Vol. 30A, P.2753, 1999.

51.Li, B.Y., Rong, L.J. , Li, Y.Y. and Gjumter, U.E. " Synthesis of porous Ni-Ti shape memory alloys by self propagating high temperature synthesis: reaction, mechanism and anisortropy in pore structure ", Acta mat.,Vol.48 , P.3895,2000.

52.Liang,Y. , Taya , M. and Mori, T." Micromechanics of stress- induced martensitic transformation in mono and poly crystalline shape memory alloys NiTi Advanced materials for the 1st Century : the 1999 Julia R weertman symposium , 1999 , Cincinnati, USA , oct.31- NoV.4, P.385.

53.Lindquist,P.G and Wayman , C.M. "martensitic transformation shape memory effect " in " Ergineering Aspects of shape memory alloys " edited by Duering, T.W and Wayman , C.M , P.58, 1990.

54.Liu,Y." Detwinning process and its anisotropy in shape memory alloys" smart mate, proceedings of SPIE, Vol.4234,2001.

55.Lu, Y.H. , Liang , S., Chu , W.Y. and QiaO , L.J. " In situ AFM observation of crack propagation in CuNiAl shape memory alloy " J. intermetallics, Vol.10, P.823, 2002.

56.Lubliner, J. and Auricchio ,F " Generalized plasticity and shape memory alloys", Int .J. Sol.Struct. , Vol.33, No.7, P.991, 1996.

57.Lukkassen , D. and Meidell, A." Advanced materials and structures and their fabrication processes" 3rd edition , Narvik university collage , 2003.

58.Mantovani, D." Shape memory alloys: properties and biomedical applications " , 2000 available at website www.tms.orgL/ pubs / journals / JOM/ jom.htmp.

59.Mathews , P.E. " Apparent density of metal powders" in Metals handbook 9th edition , Vol.7 , " powder metallurgy", p.272, 1984.

60.Mathews , P.E. " Sintering of copper- based materials in metals handbook 9th edition,Vol.7, " Powder metallurgy" p.376, 1984.

61.McNaney , J. M . , Imbeni, V. , J. M. , Imbeni , V. , Jung, Y. , Papadopoulos , P. and Ritchie , R.O. " An experimental study of the superelastic effect in a shape memory Nitinol alloy under biaxial loading " J. Mech . Mat. , Vol. 35, P.969, 2003.

62.Mellor,B.G. , Guilemany , J.M. , Miguel , J.R. , Fernandez, J., Amengual, A., Lovey , F.C. and Torra, V." stabilized stress-induced martensite its use in two wayshape memory training processes " Scripta Met. ,Vol.24, No.2, P.241, 1990.

63.Melton , K.N. " Ni Ti based shape memory alloys " in Engineering Aspects of shape memory alloys, Duerig, T.W and Wayman , C.M. (eds). P.21, 1990.

64.Meyers , M.A.and chawla, k.K." Mechanical behaviour of materials", prentice hall co., 1999.

65.Miyazaki, S. " shape memory alloys" Inst. Mater.Sci. university of tsukuba, Ibaraki, Japan , 1999, E-mail: miyazaki @ ims.tsukuba.ac.jp.

66.Nasser, S.N., Choi, J.Y., Guo, W.G. and Isaacs , J.B. " Very high strain- rate response of a Ni Ti shape memory alloy" J.Mech. Mat. , Vol.37, P.287, 2005.

67.Neov, D., Viana, M.and Mikula , P., " Insitu high resolution neutron diffraction study of stress induced martensitic transformation in CuAlZnMn shape memory alloy " 5th European Conf. on Residual stresses , step. 28-30, 1999, The Netherlands.

68.Ni, W., Cheng, Y.T. and Grummon,"D.S. Recovery of microindents in a nickel-titanium shape memory alloy: A self healing effect", App. Phys. Lett., Vol.80 , No. 18, P.3310, 2002.

69.Orban, R.L."New research directions in powder metallurgy " J.Romanian reports in physics , Vol.56 , No.3, p.505 , 2004.

70.Otsuka ,K. and Ren ,X " Review about Recent development in the research of shape memory alloys " J.Intermetallics VOL.7, P.511, 1999.

71.Otsuka , k. and kakeshita , T. " science and technology of shape memory alloys : New developments " MRS bulletin ,Feb.2002. available en www.mrs org/ publications / bulletin .

72.Otsuka , K. and Ren , X. " Martensitic transformations in nonferrous shape memory alloys" J. Mat. Sci. and engg. , Vol.A273, P.89, 1999.

73.Parker, R. H. " An introduction to chemical metallurgy " ,2nd edition, Pergamon press,P.221,1978.

74.Pena , J., Gil, F.J. and Guilemany , T.M. " Effect of microstructure on dry sliding wear behavior in CuZnAl shape memory alloys " Acta Mat., Vol.50 , P.3115, 2002.

75.Penrod, L.E." Fabrication and characterization of porous shape memory alloys ", Msc thesis Texas A& M university , 2003.

76.Planes ,A. , Macqueron , J.L., Molin , M.and Guenin , G. Calorimetric study of ordering in a β Cu-Zn-Al alloy", J.Mat.science and Engineering ,Vol. 50 , P.53, 1981.

77.Pons, J.and Cesari, E. " Interaction between γ phase precipitates and martensite in Cu-Zn-Al alloys " J. Mat.Struct . , Vol. 6, No.2, 1999.

78.Porter , D.A. and Easterling , K.E." phase transformations in metals and alloys " 2nd Edition , Chapman and Hall , 1992.

79.Price, P.E. and Kohler , S.P. " Hot isostatic pressing of metal powders " in metals Handbook 9th edition , Vol.7 , " powder metallurgy ", P.419. 1984 .

80.Qidwai , M.A., Entchev, P.B., Lagoudas,D.C.and Degiorgi,V.G., " Modelling of the thermomechaincal behaviour of porous shape memory alloys " Int.J.solids and structures,Vol. 38 , p.8653,2001.

81.Qiu, J. , Tani , J. , Osanai, D. , Urushiyama, Y. and Lewinnek ,D. " High speed response of SMA actuators Int .J. Appl. Electromag .Mech. , Vol. 12, P.87, 2000.

82.Raul ,B., Perez,S., Recarte , V. Oscar, A. and Juan, S." Advanced shape memory alloys processed by powder metallurgy ", J.Advanced Engineering materials, Vol.2,No.1-2,p.49,2000.

83.Rebelo, N. and Perry ,M. " Finite element analysis for the design of Nitinol metical devices" Pacific consultants.Com.

84.Recarte ,V.,Perezsaez , R.B., No,M.L. and Juan, J.S." Ordering Kinetics in Cu-Al-Ni Shape memory alloys" J.Appl.phys., Vol.86,No.10 ,P.5467,1999.

85.Recarte ,V.Lambri , O.A., Perezsaez , R.B. , NO , M.L. and Juan, J.S." Ordering temperature in Cu- Al- Ni shape memory alloy " J.Appl. phys.Let.,Vol.70,No.269,P.3513,1997.

86.Reed-Hill , R.E. " physical metallurgy principles " van nostrand Co.1964.

87.Ricksecker, R.E." copper and copper alloys", in metals handbook 9th edition , Vol.9 ,Metallagraphy .P.733, 1984.

88.Sampath, V." Effect of Zr on microstructure and transformation temperatures of Cu-Al-Ni Shape memory alloys" Int. Conf. smart materials , structures and systems, Bangalore , India , July 28-30 , 2005.

89.Scarsbrook , G.and Stobbs , W.M. " The martensitic transformation behaviour and stabilization of rapidly quenched Cu-Zn-Al ribbons " Acta Met. , Vol.35, No.1, p.47,1987.

90.Schweiger, J. "Aircraft control , applications of smart structures" in Encyclopedia of smart materials, Vol. 1 and 2 , Schwartz, M.(editor) , P.42, 2002.

91.Silva , M.C. and Lima , S.J." Evaluation of mechanical alloying to obtain Cu-Al-Nb shape memory alloys" ,J. Materials research , vol.8, No.2,P.119, 2005.

92.Sinha, A.K. " powder metallurgy " Dhanpat Rai and sons Delhi , 2nd edition , 1995.

93.Smallman , R.E. and Bishop , R.J. " Modern physical metallurgy and materials engineering " sixth edition , Reed educational and professional publishing , 1999.

94.Stevenson , R.w. " P/ M copper- based alloys" in Metals Handbook 9th edition , Vol. 7 , " powder metallurgy", p.733, 1984.

95.Surbled, P., Pioufle , B.L. , Yang, E.H. and Fujita, H. " Shape memory alloys for micromenbranes actuation" available on website : www.Fujita3.iis.u-tokyo.ac.jp.

96.Szprynagcz, M., Enokizona, M.and Todaka , T. " Improvement of shape memory effect in Fe-Cr-Co Ni-Si-Mn ferromagnetic alloy with change of Mn contents" Int.J.Appl. electromag. Mech. , vol.20, P.149, 2004.

97.Thornton , P.A. and Colangelo , V.J. " Fundamental of engineering materials " Prentice- Hall , 1985.

98.Trochu ,F.and Qian,Y.Y." Nonlinear finite element simulation of Superelastic shape memory alloy parts" J. comput.struct., Vol .62, No.5, P.799,1997.

99.Trochu F., Brailovski, V.,Meunier, M., Terriault, P. and Qian , Y.Y." Thermomechanical analysis of shape memory devices" J.Biomedical Mat.Engg.,Vol.6, P.389,1996.

100.Turner , T., Zhong,Z.W. and Mei, C. " Finite element analysis of the random response suppression of composite panels at elevated temperatures using shape memory alloy fibers" J.AIAA ,1994.

101.Turner, T.L. and Patel. H.D. " Analysis of SMA hybrid composite structure using commercial codes" in smart structures and materials : modeling , signal processing of SPIE Vol.5383, No.12, CA, 14-18 March, 2004.

102.Van Vlack, F." Element of material science",2nd Edition,Adison wisely publishing Co. 1978.

103.Ullrich , W.J . " Sieve analysis" in metals Handbook 9th edition,vol 7 , " powder metallurgy " P.214, 1984.

104.Wayman, C.M. and Duerig , T.W "An introduction to martensite and shape memory " on Engineering Aspects of shape memory alloys ,P.3, 1990, Duerig ,T.W, Metton , K.N, Stockel ,D. and Wayman , C.M. (eds) .

105.Wei, Z.G. , Sandstrom , R.and Miyazaki, S." Review shape memory material and hybrid composites for smart systems" J. of Mat. Science, Vol. 33, P.3743,1998.

106.Wick, A. " the bending behaviour of Superelastic Ni Ti " MSC thesis , University of karlsruhe , 1994.

107.Wojnar , L. " Image analysis : Applications in material engineering " CRC,press, P.98,1999.

108.Wu, M.H. " Cu-based shape memory alloys " In Enginnering Aspects of shape memory alloys ,P.96, 1990, Duerig ,T.W , Melton ,K.N. , Stockel ,D, and Wayman ,C. M. (eds).

109.Wu,M.H." Fabrication of Nitinol materials and components" Proceedings of the internation conf. on shape memory and Superelastic Technologies, Kunming, china, P.285,2001.

110.Zhao ,Y., Taya , M. , kang , Y. and Kawasaki , A. " Compression behaviour of porous Ni Ti shape memory alloy" Acta Mat. , Vol. 53, P 337 , 2005 .

111.Zhao , C. " Relationships between martensite transformation temperatures and Compositions in Fe-Mn-Si based shape memory alloys " J. Inst. Mech .Engrs , , Vol .214 , Part L , P. 1739, 2000.